Plasma chemistry and surface kinetics modeling of plasma catalysis in a dielectric barrier discharge

Björn Loenders

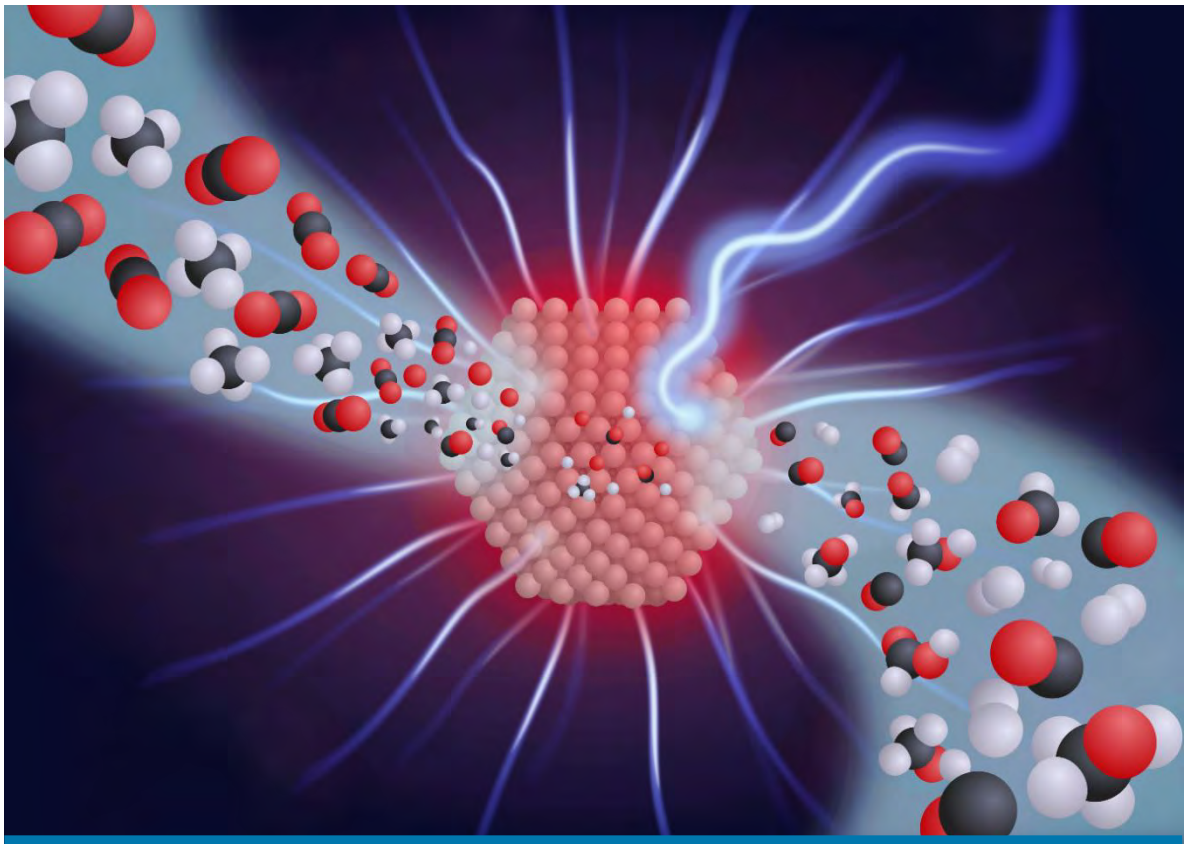

Supervisor **Prof. Dr. Annemie Bogaerts**

Thesis submitted for the degree of Doctor of Science: Chemistry
Faculty of Science | Antwerp, 2026

Universiteit Antwerpen

Universiteit Antwerpen

Faculteit Wetenschappen

Departement Chemie

Plasma chemistry and surface kinetics modeling of plasma catalysis in a dielectric barrier discharge

Proefschrift voorgelegd tot het behalen van de graad van doctor in de Wetenschappen: Chemie aan de Universiteit Antwerpen te verdedigen door

Björn Loenders

Promotor:

Prof. Dr. Annemie Bogaerts

Antwerpen, 2026

The PhD researcher and supervisor declare that the PhD research was conducted according to the principles of scientific integrity, as mentioned in the general PhD regulations and charter for PhD researchers of UAntwerp and the integrity charter for PhD researchers and supervisors affiliated with the University of Antwerp.

The research in this thesis was supported by the FWO-SBO project PlasMaCatDESIGN (FWO grant ID S001619N).

Nederlandse titel:

Plasmachemie- en oppervlaktekinetiekmodelleren van plasmakatalyse in een diëlektrische barrièreontlading

University of Antwerp
Faculty of Sciences
Groenenborgerlaan 171, 2610, Antwerp, Belgium

Research group PLASMANT
Plasma Lab for Applications in Sustainability and Medicine – ANTwerp

Disclaimer:

The author allows to consult and copy parts of this work for personal use. Further reproduction or transmission in any form or by any means, without the prior permission of the author is strictly forbidden.

Members of the jury

Chair

Prof. Dr. Erik Neyts
Modelling and Simulation in Chemistry (MOSAIC)
University of Antwerp, Belgium

Promotor

Prof. Dr. Annemie Bogaerts
Plasma Lab for Applications in Sustainability and Medicine – Antwerp (PLASMANT)
University of Antwerp, Belgium

Members

Prof. Dr. Vera Meynen
Laboratory of Adsorption and Catalysis (LADCA)
University of Antwerp, Belgium

Prof. Dr. Anton Nikiforov
Plasma Lab for Applications in Sustainability and Medicine – Antwerp (PLASMANT)
University of Antwerp, Belgium

Prof. Dr. Jan van Dijk
Elementary Processes in Gas Discharges (EPG)
Eindhoven University of Technology, The Netherlands

Prof. Dr. Ir. Leon Lefferts
Catalytic Processes and Materials (CPM)
University of Twente, The Netherlands

Prof. Dr. Joris W. Thybaut
Laboratory for Chemical Technology (LCT)
University of Ghent, Belgium

Acknowledgement

First of all, I would like to thank my promotor, Annemie Bogaerts, for giving me the opportunity to start a PhD at PLASMANT and for her continuous support throughout this journey. I am especially grateful that you were always available for questions or discussions, as well as for your quick responses to my emails whenever I needed feedback or guidance.

Next, I would like to thank the many colleagues that I worked with throughout the years, starting with my "*partner in crime"*, Joachim, with whom I shared many ups and downs during my PhD (including the setbacks of a global pandemic). I would also like to thank Senne, Elise, Eline and Claudia for their joyful and supportive attitude, and their willingness to share their experience as older PhD students. I also wish to express special thanks to Sara, Roel, Bart, Rani and Pepijn for the many interesting discussions and shared moments. I wish to thank Yannick for helping me get started with my research when I just joined the group, and Kevin van t' Veer for always taking the time to explain things to other people. Of course, I also would like to express my thanks to the various other wonderful people I had the pleasure of working with at PLASMANT, including (but not limited to): Joran, Callie, Stijn V. R., Stein, Robin, Elli, Sarah, Matthias, Helder, Ivan, Colin, Josh, Greg, Hamid, Mahdi, Sean, Parisa, Charlotte, Kristof, Omar, Yury, Angela, Eduardo, Fanny, Maxime, Vincent, Stijn H., Jonas, Maryam, Georgi, James, Frederica, Paola, Igor, Naresh, Shangkun, Yuxiang, Andrew, Matthew, Patrick, Nick, Edgar, Hanne, Ruben, Jana, Cecilia, Julien, and Abraham. To close this list of colleagues I would also like to express special thanks to the people that do a lot of work "behind the scenes", e.g., by maintaining the labs and servers: Karel, Luc, Karen, Priyanka and Herman.

Verder wil ik naast Joachim ook graag mijn andere vrienden en voormalig studiegenoten uit Antwerpen bedanken: Céderic, Dante en Manou. Bedankt voor jullie steun, geduld en

begrip, wanneer ik (misschien iets te vaak) mijn bezorgdheden en frustraties deelde, maar ook voor de vele leuke momenten tijdens onze studieperiode en daarna.

Ook wens ik mijn vrienden Stef en Dries te bedanken om mij te motiveren en voor hun interesse in (de status van) mijn doctoraat, alsook voor de vele momenten die we samen hebben gedeeld.

Tot slot, wil ik graag mijn familie bedanken, met in het bijzonder mijn ouders, Gert en Marie-Rose, en mijn grootouders, Marie-Louise, Leo, Jef en Jenny, voor hun steun en hulp, zowel tijdens mijn doctoraat en alle momenten daarnaast. Dankzij jullie ben ik geraakt waar ik nu ben.

Table of Contents

List of abbreviations 6

Summary 9

Samenvatting 12

Chapter 1. Introduction 15

1.1 Fossil resources: a blessing or a curse? 16

1.2 Greenhouse gases as resources 18

1.3 Plasma technology for CO_2 conversion 22

1.4 Combining plasma technology and catalysis 25

1.5 Synergy between plasma and catalyst: a complex puzzle 29

1.6 Physical interactions 32

1.6.1 Surface discharges vs. localized discharges 32

1.6.2 Effect of metal particles on the discharge behavior 35

1.6.3 Effect of the packing and reactor dimensions 37

1.6.4 Other material properties of the packing 40

1.6.5 Comparing packing materials at different residence times 43

1.7 Chemical interactions 46

1.7.1 Temperature dependence of plasma-catalyst synergy 47

1.7.2 Effect of plasma-catalyst synergy on trends in catalyst reactivity 54

1.7.3 The role of plasma species in plasma catalysis: vibrational excitation vs. radicals 64

1.7.4 Quantifying plasma-catalyst interactions 68
1.7.5 Tailoring the selectivities towards oxygenates 70
1.7.6 Complex mixtures of radicals 77
1.7.7 Eley-Rideal (E-R) reactions involving radicals 81
1.7.8 Radicals reaching the catalyst surface 83
1.7.9 Electric fields and charge accumulation 85
1.8 The aim of this thesis 88
Chapter 2. Methodology 91
2.1 0D Microkinetic modeling 92
2.2 Reactor models 93
2.3 Species balance equations 94
2.4 Reaction rates 97
2.5 Rate coefficients of gas reactions 98
2.6 Rate coefficients of surface reactions 100
Chapter 3. Plasma-catalytic partial oxidation of methane on Pt(111): a microkinetic study of the role of different plasma species 105
3.1 Introduction 106
3.2 Methods 108
3.3 Results and discussion 110
3.3.1 Thermal catalysis 111
3.3.2 Plasma catalysis: effect of vibrational excitation 114
3.3.3 Plasma catalysis: effect of radicals and stable intermediates 120

3.3.4 Additional remarks and suggestions....140
3.4 Conclusion....142
Chapter 4. Oxygenate production from plasma-activated reaction of CO_2 and ethane 147
4.1 Introduction....148
4.2 Methods....149
4.3 Results and discussion....153
4.4 Conclusion....160
Chapter 5. Is a catalyst always beneficial in plasma catalysis?....163
5.1 Introduction....164
5.2 Methodology....165
5.2.1 Surface kinetics simulations using the CatMAP code....166
5.2.2 Coupled plasma and surface kinetics simulations....168
5.3 Results and discussion....176
5.3.1 The role of CO hydrogenation in plasma-catalytic DRM....177
5.3.2 Insight from coupled plasma-surface simulations: effect of catalyst on DRM 187
5.4 Conclusion....201
Chapter 6. How plasma reaction conditions affect the optimal catalyst: A microkinetic study of plasma-catalytic CO_2 splitting....205
6.1 Introduction....206
6.2 Methods....209

6.2.1 Reactor geometry and conditions 210
6.2.2 Species balance equations 213
6.2.3 Solving the Boltzmann equation for electrons 215
6.2.4 Rate coefficients for glass surfaces 216
6.2.5 Rate coefficients for transition metals 221
6.2.6 Correction for diffusion to the wall 227
6.3 Results and Discussion 230
6.3.1 Importance of Eley-Rideal reactions for O atom recombination 232
6.3.2 Effect of E-R reactions in plasma-catalytic CO_2 splitting 236
6.3.3 The mechanism of low-pressure plasma-catalytic CO_2 splitting 241
6.3.4 Effect of temperature on plasma-catalytic CO_2 splitting 248
6.3.5 The optimal catalyst depends on temperature and residence time 256
6.3.6 Effect of pressure on plasma-catalytic CO_2 splitting 260
6.3.7 Effect of flow rate on plasma-catalytic CO_2 splitting 263
6.3.8 Discussion of the optimal catalyst properties 267
6.4 Conclusion 270
Chapter 7. Overall conclusions and future outlook 275
Appendix 283
References 391
List of Publications 453
Presentations 454
Other Achievements 455

List of abbreviations

0D	Zero-dimensional
1D	One-dimensional
APGD	Atmospheric pressure glow discharge
APPJ	Atmospheric pressure plasma jet
BEP	Brønsted-Evans-Polanyi
CCS	Carbon capture and storage
CCU	Carbon capture and utilization
CSTR	Continuous stirred tank reactor
DBD	Dielectric barrier discharge
DFT	Density functional theory
DRE	Dry reforming of ethane
DOF	Degree of freedom
DRIFTS	Diffuse reflectance infrared Fourier transform spectroscopy
DRM	Dry reforming of methane
EEDF	Electron energy distribution function
E-R	Eley-Rideal
GA	Gliding arc
GHG	Greenhouse gas
IPC	In-plasma catalysis
IR	Infrared
IUPAC	International Union of Pure and Applied Chemistry

L-H	Langmuir-Hinshelwood
LTE	Local thermodynamic equilibrium
MD	Molecular dynamics
mln/min	Normal liters per minute
MS	Mass spectroscopy
NTP	Non-thermal plasma
ODE	Ordinary differential equation
PCE	Partial chemical equilibrium
PES	Potential energy surface
PFR	Plug flow reactor
POX	Partial oxidation
PPC	Post-plasma catalysis
RF	Radio-frequency
RWGS	Reverse water-gas shift
sccm	Standard cubic centimeter per minute
SEI	Specific energy input
SRM	Steam reforming of methane
SVP	Sudden vector projection
TEA	Techno-economic assessment
TOF	Turnover frequency
TP	Thermal plasma
TS	Transition state
TST	Transition state theory

Summary

Our society is strongly dependent on fossil resources, both for energy production and as a feedstock for chemicals. Yet, the use of these resources comes with important drawbacks. On one hand, their combustion for energy production results in the emission of large amounts of CO_2, which together with other greenhouse gasses (GHG's) results in global warming and climate change. On the other hand, the reserves of fossil resources are limited and will eventually run out.

A potential solution to this issue is carbon capture and utilization (CCU), which involves collecting CO_2 and converting it into new chemicals and fuels. This can be achieved through various reactions, one of the most interesting of which is the dry reforming of CH_4 (DRM). This reaction converts the two most important GHG's, namely CO_2 and CH_4, into new feedstock chemicals for industry. However, DRM is a very energy-intensive reaction, due to the high thermodynamic stability of its reactants, and thus requires high temperatures using conventional thermal catalysis.

Plasma technology is an interesting alternative for gas conversion applications, as it is powered by electricity and hence can make use of renewable energy such as solar, wind and hydropower. Moreover, non-thermal plasma (NTP) can convert thermodynamically stable molecules at mild temperatures and pressures, due to its strong non-equilibrium character and high reactivity. However, a downside to this high reactivity is that NTP is typically not very selective. Plasma catalysis therefore combines plasma with a catalyst to improve the selectivity towards the desired products.

This thesis explores how the chemistry inside the plasma and on the catalyst surface are affected by the exchange of reactive species between both, using chemical kinetics modeling. Chapter 1 covers various chemical and physical interactions that occur

between the plasma and catalyst, to illustrate the high complexity of plasma catalysis. Chapter 2 subsequently discusses the main equations that form the basis of the kinetic models in the following chapters.

Next, Chapter 3 investigates the effect of vibrationally excited molecules, as well as radicals and stable intermediates on the surface kinetics and reaction pathways of CH_4 partial oxidation on a Pt(111) surface. We find that, while both vibrationally excited molecules and radicals improve the reaction rates, the latter clearly dominate the surface kinetics. Additionally, we also study the effect of different radicals and stable intermediates by varying their partial pressures in the gas phase.

Plasma-based DRM may also facilitate the valorization of the many remote natural gas reserves by locally converting CH_4 into liquid oxygenates, which are easier to transport. Although natural gas also contains around 10% C_2H_6 next to CH_4, only few studies have investigated the co-conversion of CO_2 and C_2H_6. Hence, in Chapter 4 we study the gas phase chemistry of C_2H_6 dry reforming in a dielectric barrier discharge (DBD) plasma. We discuss the reaction pathways that form C_1-C_4 hydrocarbons, syngas (CO/H_2) and various oxygenates. Moreover, we also study the effect of plasma power on the CO_2 and C_2H_6 conversions, as well as on the product selectivities.

In Chapter 5, we investigate the effect of different transition metal catalysts on the kinetics of plasma-catalytic DRM at typical DBD conditions and illustrate that the catalyst can also have a negative effect, by facilitating the recombination of adsorbed radicals back to the reactants.

Finally, Chapter 6 studies plasma-catalytic CO_2 splitting in a low-pressure discharge. Our results indicate that Eley-Rideal reactions play an important role in the recombination of O atoms to O_2 on the surface. Additionally, we illustrate that there is no single best catalyst, but rather that the optimal catalyst depends on reaction conditions, such as

temperature, pressure and flow rate. While this conclusion sounds quite evident, many experimental studies on plasma catalysis compare different catalysts for only a single set of reaction parameters. We therefore want to emphasize the importance of evaluating catalysts over a range of conditions. Hence, the findings presented in this thesis contribute to a better understanding of plasma-catalysis, with a focus on GHG conversion.

Samenvatting

Onze maatschappij is zeer afhankelijk van fossiele grondstoffen, zowel voor de productie van energie als chemicaliën. De verbranding ervan zorgt echter voor de uitstoot van grote hoeveelheden CO_2, hetgeen samen met andere broeikasgassen leidt tot opwarming van de aarde en klimaatverandering. Daarnaast zijn de voorraden van fossiele grondstoffen beperkt en zullen deze bijgevolg ooit uitgeput raken.

Een mogelijke oplossing hiervoor is *carbon capture and utilization* (CCU), waarbij CO_2 wordt opgevangen en omgezet in nieuwe chemicaliën en brandstoffen. *Dry reforming of* CH_4 (kortweg DRM) is een bijzonder interessante reactie in dit opzicht, aangezien deze tegelijkertijd de twee voornaamste broeikasgassen, CO_2 en CH_4, omzet in nieuwe grondstoffen voor de chemische industrie. DRM is echter zeer endotherm en vereist bijgevolg hoge temperaturen om uit te voeren via thermische katalyse.

Plasmatechnologie is een interessant alternatief op klassieke thermische katalyse op vlak van (broeikas)gasconversie, aangezien plasma hierbij wordt opgewekt met elektriciteit en dus kan gebruik maken van hernieuwbare energie. Daarnaast is niet-thermisch plasma (NTP) zeer reactief doordat het zich in een toestand bevindt die sterk afwijkt van het thermisch evenwicht. Hierdoor kan NTP thermodynamisch stabiele moleculen zoals CO_2 en CH_4 omzetten bij relatief milde reactiecondities. Een nadeel aan deze hoge reactiviteit is echter dat NTP vaak niet selectief is. Bij plasmakatalyse wordt plasma daarom gecombineerd met een katalysator om de selectiviteit van de beoogde producten te verbeteren.

Deze thesis onderzoekt hoe de chemie in het plasma en op de katalysator beïnvloed worden door de uitwisseling van reactieve deeltjes tussen beiden, m.b.v. modellen die hun reactiekinetiek simuleren. Hoofdstuk 1 bespreekt verschillende chemische en fysische interacties tussen het plasma en de katalysator, om het complexe karakter van

plasmakatalyse te illustreren. In hoofdstuk 2 worden vervolgens de belangrijkste vergelijkingen behandeld die de basis vormen van de modellen in de daaropvolgende hoofstukken.

Hoofdstuk 3 onderzoekt het effect van vibrationeel geëxciteerde moleculen en radicalen op de oppervlaktekinetiek en reacties van de partiële oxidatie van CH_4 met een Pt(111) katalysator. Onze resultaten geven aan dat zowel vibrationeel geëxciteerde moleculen als radicalen de reactiesnelheden verhogen, maar het effect van radicalen is duidelijk sterker. Verder bestuderen we ook de afzonderlijke effecten van verschillende radicalen en tussenproducten door hun partieeldrukken in de gasfase te variëren.

Het gebruik van plasmatechnologie voor DRM zou de ontginning van afgelegen aardgas voorraden kunnen vergemakkelijken door ter plaatse CH_4 om te zetten in vloeibare chemicaliën. Naast CH_4 bevat aardgas echter ook ongeveer 10% C_2H_6. Desondanks zijn er weinig studies die de co-conversie van CO_2 met C_2H_6 hebben onderzocht. Hoofdstuk 4 behandelt daarom de plasmachemie van *C_2H_6 dry reforming* in een diëlektrische barrière ontlading. We bespreken hierbij de reactiepaden die leiden tot de vorming van C_1-C_4 koolwaterstoffen, syngas (CO/H_2), alcoholen, aldehyden en carbonzuren. Daarnaast onderzoeken we ook het effect van het plasmavermogen op de conversies van CO_2 en C_2H_6, alsook op de selectiviteiten van de verschillende producten.

In hoofdstuk 5 onderzoeken we de invloed van verschillende transitiemetalen op de reactiekinetiek van DRM in een diëlektrische barrière ontlading. Hierbij tonen we aan dat de katalysator ook een negatief effect kan hebben, door geadsorbeerde radicalen terug te laten recombineren naar de reactanten (i.e., CO_2 en CH_4).

Tenslotte bestuderen we in hoofdstuk 6 plasmakatalytische CO_2 splitsing in een lage-druk plasma. Onze resultaten geven aan dat Eley-Rideal reacties een belangrijke rol spelen bij de recombinatie van O atomen naar O_2 op het katalysatoroppervlak. Daarnaast

illustreren we dat de optimale katalysator afhangt van reactiecondities, zoals temperatuur, druk en het massadebiet van het gas. Hoewel deze conclusie evident lijkt, worden in experimentele plasmakatalyse studies vaak slechts één set reactiecondities gebruikt om verschillende katalysatoren te vergelijken. Daarom wensen we hierbij aan te tonen dat het belangrijk is om katalysatoren te evalueren bij verschillende reactiecondities. De resultaten en bevindingen die zijn voorgesteld in deze thesis dragen bijgevolg bij aan een beter inzicht in plasmakatalyse, in het bijzonder voor broeikasgasconversie.

Chapter 1.

Introduction

1.1 Fossil resources: a blessing or a curse?

Fossil resources have been, and still are, incredibly important to the development of human civilization as we know it today. During the first industrial revolution, the use of coal as an energy source started to rise rapidly, later followed by oil and natural gas. Although efforts have been made to lower the share of fossil resources in our total energy supply, we currently still produce most of our energy from fossil resources. For reference, in 2023 fossil resources contributed about 77% to the global energy production, good for 140 PWh (1.40×10^{17} Wh).[1,2]

Moreover, fossil resources are not only an important energy source, but also the main feedstock for the chemical industry. Indeed, petrochemicals (i.e., chemicals derived from oil or natural gas) account for approximately 90% of the raw materials used for the production of chemicals.[3] Hence, we rely on fossil resources for the production of a broad range of products and materials, going from the plastics used in packaging, electronic devices, cars and various household items, to synthetic textiles, paints, coatings, medicines and even fertilizers used for agriculture.[3]

However, the use of fossil resources comes with a serious drawback. The combustion of fossil resources for energy production (for example, as fuels for vehicles or for electricity) results in the emission of large amounts of CO_2. Consequently, the concentration of CO_2 in the atmosphere is continuously rising. In November 2025 the globally-averaged CO_2 concentration reached a value of 426 ppm,[4] which corresponds to an increase of 52% compared to pre-industrial levels (280 ppm).[5]

The accumulation of CO_2 and other greenhouse gasses (GHGs) in the atmosphere in turn causes global warming. As such, the global surface temperature has risen by 1.1 °C in 2011-2020 compared to 1850-1900.[6] Moreover, the level of global warming is expected to keep rising in the near future, which results in increasing risks for human welfare

worldwide, such as rising sea-levels and extreme weather conditions (e.g., heat-waves, droughts, rainfall variability). These can in turn lead to water shortages, a decline in food production, damage to infrastructure, economical damage, a decrease in biodiversity, etc.[6] Needlessly to say it is essential that we find ways to decrease our CO_2 emissions and limit global warming.

Moreover, our reserves of fossil resources are not endless. While new or unconventional supplies of fossil resources, such as shale gas and oil, are still being discovered, their extraction raises several environmental concerns. Yet, even sources that are currently unexploited will eventually run out. Hence, if we do not lower the rate at which we consume coal, oil and natural gas, their reserves will inevitably become more and more depleted, forcing us to find alternatives for fossil resources.[7]

One approach to limit the CO_2 concentration in the atmosphere is by carbon capture and storage (CCS). As the name implies, CCS involves collecting CO_2 (e.g., by capturing it before release or by extraction from the atmosphere) and storing it, for example, underground, in depleted oil or gas reservoirs. While CCS can aid in reducing our net CO_2 emissions, it does not solve our dependence from the declining reserves of fossil resources. An alternative approach, namely carbon capture and utilization (CCU), involves collecting CO_2 and transforming it into new products. If these new products are platform chemicals that would normally be produced from fossil resources, then CCU can provide a solution to both the rising CO_2 levels in the atmosphere and our dependence on the diminishing reserves of fossil resources.[8] Hence, we can tackle both challenges simultaneously by recycling the CO_2 produced by energy production and industrial processes into a new feedstock for the chemical industry.

1.2 Greenhouse gases as resources

While recycling CO_2 (and other GHG's) into new chemicals might, at first glance, seem a straightforward idea, the reality is not so simple. During the combustion of fossil fuels, CO_2 is formed alongside other reaction products (like H_2O), and energy is released. However, this also means that recycling CO_2 in turn requires energy to convert this thermodynamically stable molecule back into new fuels or value-added chemicals.

For example, the simplest reaction for CO_2 conversion is its decomposition into CO and O_2, a reaction known as CO_2 splitting:

$$CO_{2(g)} \rightarrow CO_{(g)} + \frac{1}{2}\, O_{2(g)} \qquad \Delta H° = +283\ kJ/mol \qquad \text{R1.1}$$

As this reaction has a standard reaction enthalpy of +283 kJ/mol,[9] it is highly endothermic, meaning that a large amount of energy is consumed during the reaction.

The CO produced by CO_2 splitting can be separated from the reaction mixture and combined with H_2, to acquire a gas mixture known as syngas (CO/H_2). Syngas is used to produce various platform chemicals, such as aliphatic, olefinic and aromatic hydrocarbons via Fischer-Tropsch synthesis, as well as CH_3OH and other oxygenates (i.e., oxygen-containing organic compounds).[10–13] By varying the syngas ratio (i.e., the ratio between H_2 and CO) the selectivity towards different products can be modified.[12] For example, long chain hydrocarbons favor a low syngas ratio ($H_2/CO \approx 1$), whereas CH_3OH synthesis requires a high syngas ratio (e.g., $H_2/CO \approx 2$).

Because of the high endothermicity of pure CO_2 splitting, a co-reactant is often added to lower the reaction enthalpy and improve the conversion.[14] In CO_2 hydrogenation, for example, H_2 is added as a co-reactant.

Various products can be obtained from this reaction, such as CO, CH_4 and CH_3OH:

$$CO_{2(g)} + H_{2(g)} \rightarrow CO_{(g)} + H_2O_{(g)} \qquad \Delta H° = 41\ kJ/mol \qquad \text{R1.2}$$

$$CO_{2(g)} + 4\,H_{2(g)} \rightarrow CH_{4(g)} + 2\,H_2O_{(g)} \qquad \Delta H° = -165\ kJ/mol \qquad \text{R1.3}$$

$$CO_{2(g)} + 3\,H_{2(g)} \rightarrow CH_3OH_{(g)} + H_2O_{(g)} \qquad \Delta H° = -53\ kJ/mol \qquad \text{R1.4}$$

Thanks to the use of H_2 as co-reactant, the reaction enthalpies of these reactions are much reduced compared to pure CO_2 splitting (R1.1). The reverse water-gas shift (RWGS, R1.2) remains endothermic, but with a relatively low standard reaction enthalpy of 41 kJ/mol. Moreover, both CO_2 methanation (R1.3) and CO_2 hydrogenation to CH_3OH (R1.4) are exothermic, with standard reaction enthalpies equal to -165 and -53 kJ/mol, respectively.[9] Unfortunately, industrial H_2 production currently occurs predominantly through steam reforming of CH_4.[14] Hence, the potential of CO_2 hydrogenation for CCU remains limited until H_2 production processes that can utilize renewable energy (e.g., electrolysis) become economically competitive with CH_4 steam reforming. This is especially true for CO_2 methanation (R1.3), which would otherwise yield no net CH_4 production or CO_2 consumption.

Next to H_2, CH_4 is another common co-reactant for CO_2 conversion. The reaction between CO_2 and CH_4 is known as the dry reforming of CH_4 (DRM), and yields syngas with a theoretical H_2/CO ratio equal to 1:

$$CO_{2(g)} + CH_{4(g)} \rightarrow 2\,CO_{(g)} + 2\,H_{2(g)} \qquad \Delta H° = +247\ kJ/mol \qquad \text{R1.5}$$

As both CO_2 and CH_4 are very thermodynamically stable molecules, DRM is highly endothermic, with a standard reaction enthalpy of +247 kJ/mol.[9] Nevertheless, this is still 36 kJ/mol less compared to pure CO_2 splitting (R1.1), making DRM (R1.5) more thermodynamically feasible. This is illustrated in Figure 1.1, which shows the gas fractions

at thermodynamic equilibrium for pure CO_2 (a) and a 1:1 CO_2/CH_4 mixture (b). Indeed, CO_2 splitting (Figure 1.1 (a)) requires a temperature of approximately 3000 K before the products (CO and O_2) become thermodynamically favored over the reactant (CO_2). For DRM (Figure 1.1 (b)), on the other hand, the transition from the reactants (CO_2 and CH_4) to the products (CO and H_2) occurs at a considerably lower temperature (i.e., around 900 K).

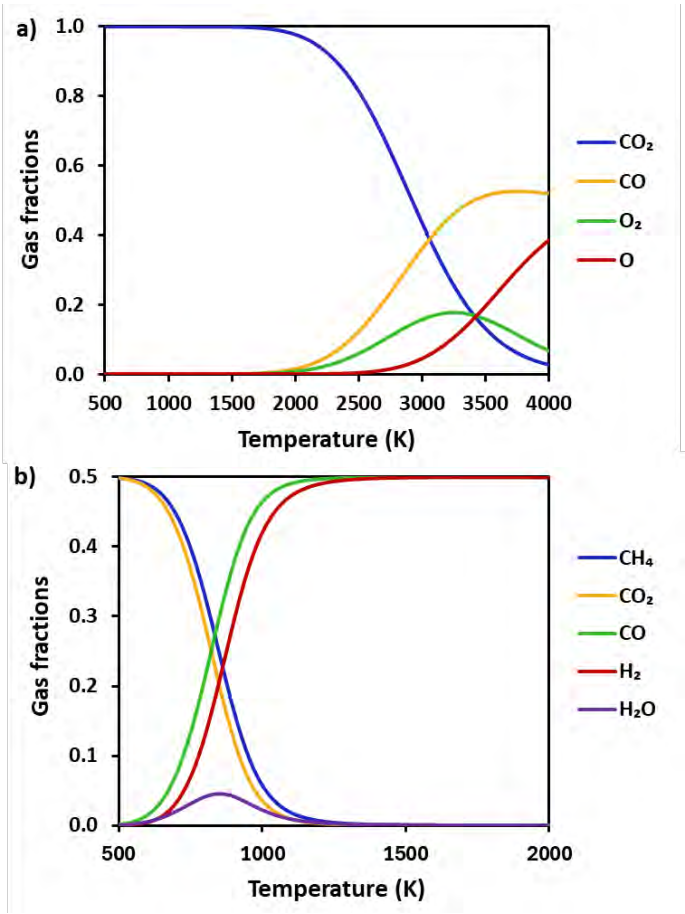

Figure 1.1. Gas fractions at thermodynamic equilibrium for pure CO_2 (a) and a 1:1 CO_2/CH_4 mixture (b) at a total pressure of 1 bar. Note that (a) is plotted over a broader temperature range (500-4000 K) than (b) (500-2000K). Also note the different y-scale between both figures. The thermodynamic equilibria were calculated according to the method described in ref. 15. The enthalpy and entropy values were acquired using the NASA Glenn polynomials.[16]

Not only can DRM proceed at a considerably lower temperature than pure CO_2 splitting, but it also converts a second GHG, next to CO_2, namely CH_4. While the atmospheric CH_4 levels are lower compared to those of CO_2 (i.e., 1.95 ppm[17] vs. 426 ppm[4] for CH_4 and CO_2, respectively), CH_4 has a 100-year global warming potential that is 27 to 30 times higher than that of CO_2.[18] As such, DRM can simultaneously reduce the emissions of the two most important GHG's. While CH_4 is predominantly acquired from natural gas, it can also be obtained from renewable resources, such as biogas: a gas mixture produced by anaerobic digestion of organic waste material.[12]

However, DRM is currently not yet economically competitive with the established method for syngas production in industry, CH_4 steam reforming:

$$CH_{4(g)} + H_2O_{(g)} \rightarrow CO_{(g)} + 3\,H_{2(g)} \qquad \Delta H° = +206\ kJ/mol \qquad \text{R1.6}$$

Like DRM, steam reforming produces syngas starting from CH_4 but using H_2O as the second reactant instead of CO_2. Steam reforming is also highly endothermic (+206 kJ/mol),[9] but less compared to DRM (+247 kJ/mol).[9] If the desired product is H_2 rather than syngas, reaction R1.6 can be followed by the water gas shift reaction, to improve the amount of produced H_2:

$$CO_{(g)} + H_2O_{(g)} \rightarrow CO_{2(g)} + H_{2(g)} \qquad \Delta H° = -41\ kJ/mol \qquad \text{R1.7}$$

$$CH_{4(g)} + 2\,H_2O_{(g)} \rightarrow CO_{2(g)} + 4\,H_{2(g)} \qquad \Delta H° = +165\ kJ/mol \qquad \text{R1.8}$$

R1.8 is the net reaction that results from combining R1.6 and R1.7. Note that R1.8 is the reverse reaction of CO_2 methanation (R1.3), and thus consumes CH_4 (from natural gas) while producing CO_2, which is of course undesirable from an environmental perspective.

Apart from DRM and steam reforming, syngas can also be produced through partial oxidation of CH_4 (POX):[19]

$$CH_{4(g)} + \frac{1}{2} O_{2(g)} \rightarrow CO_{(g)} + 2\, H_{2(g)} \qquad \Delta H° = -36\ kJ/mol \qquad \text{R1.9}$$

Yet, in contrast with the energy-intensive DRM and CH_4 steam reforming processes, POX is slightly exothermic with a standard reaction enthalpy of -36 kJ/mol,[9] giving it an advantage from an energy-based perspective. However, like steam reforming, POX does not utilize CO_2, which is a more important GHG than CH_4. Hence, there are various processes that convert CO_2 and/or CH_4 into value-added products, each with distinct advantages and disadvantages.

As is evident from the discussion above, many of the reactions that convert CO_2 (or CH_4) into value-added chemicals either require a substantial amount of energy or use co-reactants (like H_2) which are produced via energy-intensive processes. Hence, recycling CO_2 into value-added chemicals and fuels either directly or indirectly consumes energy. Several technologies are currently being explored that utilize different (renewable) energy sources to enable CO_2 conversion: thermal catalysis uses heat, photocatalysis and biochemical conversion (i.e., photosynthesis) use (sun)light, while electrochemical conversion and plasma technology use electricity.[14] While each of these technologies has their own advantages and disadvantages, the scope of this thesis is limited to the use of plasma technology for GHG conversion. However, interested readers are referred to a review by Snoeckx and Bogaerts,[14] who compared these technologies and their potential for CO_2 conversion.

1.3 Plasma technology for CO_2 conversion

Plasma is a (partially) ionized gas, i.e., a gas in which a large amount of energy is deposited, causing some of the gas molecules to lose an electron and form positively charged ions and free electrons. However, a variety of other highly energetic species are

typically also present, such as radicals, negatively charged ions, and (electronically and vibrationally) excited molecules. As plasma is formed by adding large amounts of energy to a gas, it is often referred to as the fourth state of matter.[20]

Plasma occurs in nature in different forms: stars like our sun, lightning, the aurora borealis, interstellar nebulae, to name a few examples. In laboratory conditions, plasma is typically created by applying a strong electric field to a gas. Electrons in the gas are then accelerated in the electric field and thus gain kinetic energy, which they can transfer to molecules upon collision. If the energy of the electrons is high enough, the collisions can ionize the gas molecules, thus creating additional electrons, which are also accelerated in the electric field, and in turn form more electrons, i.e., resulting in an electric discharge.[20]

Plasmas can be categorized into two sub-groups, namely thermal plasmas (TP) and non-thermal plasmas (NTP). TP's are characterized by a state of local thermodynamic equilibrium (LTE). This means that the reactions and transitions (i.e., excitation and de-excitation) in the plasma are governed by collision processes, and that for each collision process the forward and reverse rates are in equilibrium. Moreover, local gradients of the plasma properties should be small enough that particles have enough time to equilibrate when diffusing from one point in the plasma to another.[21] Consequently, the temperature of the electrons and the heavy species (molecules, radicals and ions) in TP is the same. This is not the case for NTPs, in which the electron temperature (T_e) is much higher (10^4-10^5 K) than the translational temperature of the bulk gas (T_g), which remains (relatively) close to room temperature. Moreover, due to excitation of the vibrational modes in the gas molecules, their corresponding vibrational temperature (T_v) often exceeds T_g, while the temperatures of the rotational degrees of freedom (T_r) and the ions (T_i) are close to T_g. Hence, the temperatures in NTP can typically be ordered as: $T_e >> T_v > T_r \approx T_i \approx T_g$.[20] Next to NTP and TP, a third category of plasma is so-called warm plasma.

This type of plasma is a transitionary state between NTP and TP, with gas temperatures of several thousand Kelvin (typically 2000-6000 K) which is substantially higher than room temperature but still much lower than the electron temperature.[14]

Because of its strong non-equilibrium character, NTP can activate very thermodynamically stable molecules, like CO_2, while maintaining low gas temperatures (300-1000 K). Since plasma technology involves the creation of electrical discharges to convert gas molecules into value-added products, it is directly powered by electricity. This means that the process can make use of renewable energy such as solar, wind or hydropower. Moreover, plasma technology for gas conversion is a so-called "*turnkey*" process, meaning that it can be rapidly switched on and off. Hence it can adapt to the variable, weather-dependent supply of renewable energy, as the process can be easily switched on when excess energy is available and off again when the energy supply is low. This makes plasma technology an interesting method for the renewable production of chemicals and fuels from CO_2 and other GHG's.[14] Figure 1.2. gives a schematic representation of the use of plasma technology for CO_2 conversion.

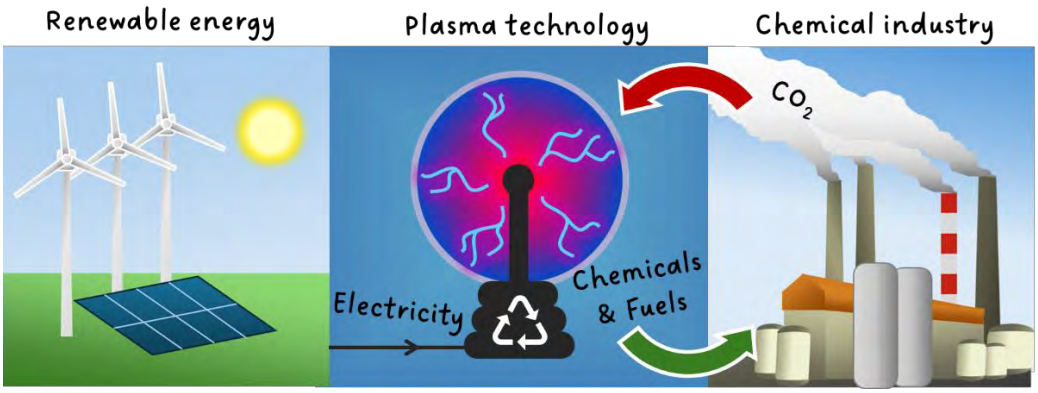

Figure 1.2. Schematic overview of plasma technology for CO_2 conversion. Renewable energy powers plasma technology, which takes CO_2 produced by industry and converts it into new chemicals and fuels, that are again used as resources for the chemical industry.

1.4 Combining plasma technology and catalysis

As mentioned in section 1.3, plasma can be formed by collision of highly energetic electrons with gas molecules, which results in a cocktail of reactive species. These plasma species react with each other, as well as with remaining gas molecules, giving rise to a complex reaction network that yields a broad range of different products. This again illustrates the advantages of the non-equilibrium character of NTP, as it may enable the formation of various products that are not favored by the thermodynamic equilibrium. For example, the use of NTP for DRM does not only yield syngas, but can also produce C_2 and C_3 hydrocarbons, as well as various oxygenates, including alcohols (CH_3OH, C_2H_5OH), aldehydes (CH_2O), carboxylic acids (HCOOH, CH_3COOH) and ethers (CH_3OCH_3).[22,23]

Nevertheless, the wide variety of different products also highlights that NTP is typically non-selective towards product formation, which can be cumbersome when aiming for specific end-compounds. Plasma may therefore be combined with a catalyst to improve the selectivity towards the desired products. This combination of plasma and catalysts is referred to as plasma catalysis.[24]

The International Union of Pure and Applied Chemistry (IUPAC)[25] defines a catalyst as: "A substance that increases the rate of a reaction without modifying the overall standard Gibbs energy change in the reaction." Hence, a catalyst facilitates a reaction by lowering the activation barrier of one or more reaction steps. Figure 1.3 illustrates the effect of a catalyst by means of a reaction energy diagram. The red curve represents the situation without catalyst; a high energy barrier needs to be overcome for the reaction to occur, due to the high energy of the transition state (TS). Yet, for the case with catalyst (blue curve) an alternative reaction path becomes available in which the reactants interact with the catalyst, resulting in catalyst-bound intermediates that react further to form the products. The formation of bonds between the catalyst and the involved species

stabilizes the intermediates and transition states (TS1, TS2, TS3), thus lowering the activation barriers and improving the reaction rate.

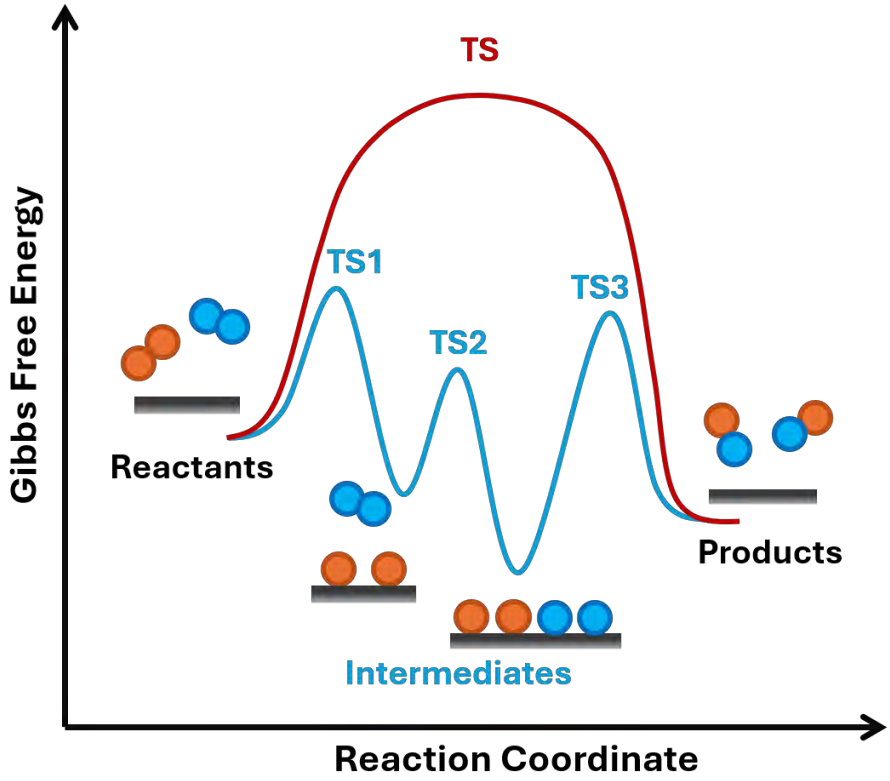

Figure 1.3. Reaction energy diagram that illustrates the principle of catalysis. Transition states are denoted as TS.

Although a catalyst does not alter the thermodynamic equilibrium, the choice of catalyst can sometimes be used to steer the selectivity towards a particular product via the reaction kinetics. If a catalyst does not improve all steps in the reaction pathway that leads to the thermodynamically favored product, the reaction may become kinetically trapped in a reaction intermediate. For example, the most thermodynamically stable products of CO hydrogenation are CH_4 and H_2O, but using Cu-based catalysts CH_3OH can be obtained with high selectivity. This is due to Cu being a weakly binding catalyst that is

unable to break the C-O bond in CO, while this metal does catalyze the dissociation of H_2 and the hydrogenation steps. Conversely, strongly binding catalysts, like Rh, Ru, Ir and Ni, do catalyze the breaking of the C-O bond and are thus selective towards CH_4.[26]

Although a catalyst enhances the rate of a specific reaction, thermal catalysis typically still requires high temperatures, either due to kinetic or thermodynamic constraints. This is in contrast with NTP which, due to its non-equilibrium character, is highly reactive, but also not very selective. Plasma catalysis therefore aims to combine the high reactivity of plasma with the selectivity of catalysts and thus combine the best of both worlds.[24,27]

Experimental setups for plasma catalysis can be divided into two large groups, namely in-plasma catalysis (IPC) and post-plasma catalysis (PPC). As the name implies, IPC involves placing a catalyst directly into the plasma, while in PPC the catalyst is placed after the plasma. Consequently, IPC is only possible using NTP which can maintain a relatively low gas temperature (i.e., 300-1000 K), i.e., to avoid damage to the catalyst. This is in contrast with warm plasmas, such as atmospheric pressure glow discharges (APGDs), gliding arc (GA) discharges and microwave plasma, as their high temperature (around 2000-6000 K) would be detrimental to the catalyst.[24]

Since the plasma and the catalyst are spatially separated in PPC, only long-lived plasma species (i.e., typically stable molecules) can reach the catalyst.[24,27] Hence, PPC may often result in gas conversion by plasma followed by thermal catalysis of the resulting product mixture. Yet, this is not necessarily the case. For example, at low-pressure conditions the radical recombination in the gas phase can become relatively slow, so that recombination of radicals predominantly occurs via surface reactions.[28,29] In a typical reactor for low-pressure plasmas, radical recombination occurs on the surface of the reactor walls, but if a catalyst is placed in the plasma afterglow, interaction between the radicals and the catalyst can also occur. Indeed, in this case the lifetime of plasma radicals becomes

sufficiently long to reach the catalyst. This is, for example, the case when the catalyst is placed in the afterglow of a low-pressure radio-frequency (RF) discharge.[30]

In IPC, the catalyst is placed inside the plasma, so short-lived species may also reach the catalyst.[24,27] Yet, the species still need to diffuse from the bulk plasma to the catalyst surface, so in practice the lifetime of these species and the distance between the (bulk) plasma and the catalyst particles will determine which plasma species can interact with the catalyst. Indeed, species with extremely short lifetimes may not be able to traverse the plasma sheet between the bulk plasma and the catalyst surface.

A common reaction setup for IPC is the so-called packed-bed dielectric barrier discharge (DBD) reactor, in which the catalyst is placed inside a DBD reactor.[24,27] Schematic representations of both an empty (a) and a packed-bed (b) DBD reactor are presented in Figure 1.4. A DBD reactor consists of two electrodes over which an alternating voltage is applied, at least one of these electrodes is covered by a layer of a dielectric material that prevents the formation of an arc discharge between the electrodes. Instead, the dielectric becomes polarized due to the applied voltage, and filamentary microdischarges are formed that transfer charge to the surface of the dielectric material. This accumulation of charge on the surface of the dielectric limits the formation of new microdischarges until the polarity is reversed.[20,31]

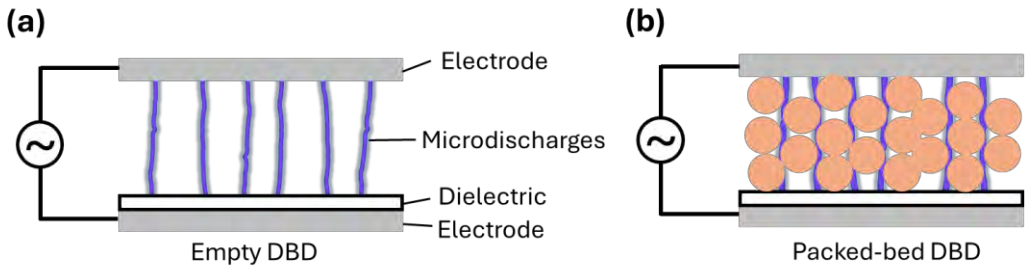

Figure 1.4. Schematic representation of an empty (a) and a packed-bed (b) DBD reactor.

1.5 Synergy between plasma and catalyst: a complex puzzle

If the selectivity or yield achieved with plasma catalysis is greater than the combined selectivities or yields of the plasma and catalyst alone, synergy occurs between the plasma and catalyst.[24,27] The exact cause for plasma-catalyst synergy is often unclear, as this can be the result of various physical and chemical interactions between the plasma and the catalyst. Whether or not synergy is achieved is the combined result of these effects. Hence, plasma-catalyst synergy does not always occur, and in some cases, plasma catalysis instead performs worse than plasma without catalyst.[32–36]

The plethora of interactions that can occur between the plasma and the catalyst makes plasma-catalytic systems highly complex. These interactions are either chemical or physical in nature and can be divided into effects of the plasma on the catalyst or effects of the catalyst on the plasma. Effects of the plasma on the catalyst involve changes in the catalyst's properties that are induced by the plasma. Examples of these effects include changes in the morphology of the catalysts, reduction or oxidation of the catalyst material, and alteration of its work-function (the energy required to remove an electron from the catalyst).[37,38] In addition, plasma-produced reactive species like radicals, ions, and vibrationally or electronically excited molecules might diffuse to the catalyst surface and partake in the surface chemistry. On the other hand, the catalyst can also alter the plasma. For example, in packed-bed DBD reactors, introducing a catalyst or packing material into the discharge gap can lead to localized electric field enhancement and alter

Section 1.5 is derived from the following publication:

Loenders, B.; Michiels, R.; Bogaerts, A. Is a Catalyst Always Beneficial in Plasma Catalysis? Insights from the Many Physical and Chemical Interactions. *J. Energy Chem.* **2023**, *85*, 501–533. DOI: 10.1016/j.jechem.2023.06.016

the discharge behavior of the plasma.[37,38] Since multiple of these interactions can occur simultaneously, it is often difficult to determine which effects contribute to the overall process, let alone correlating these to specific properties of the catalyst material or the plasma. A schematic overview of various physical and chemical interactions is presented in Figure 1.5. In the next sections these interactions will be discussed in more detail.

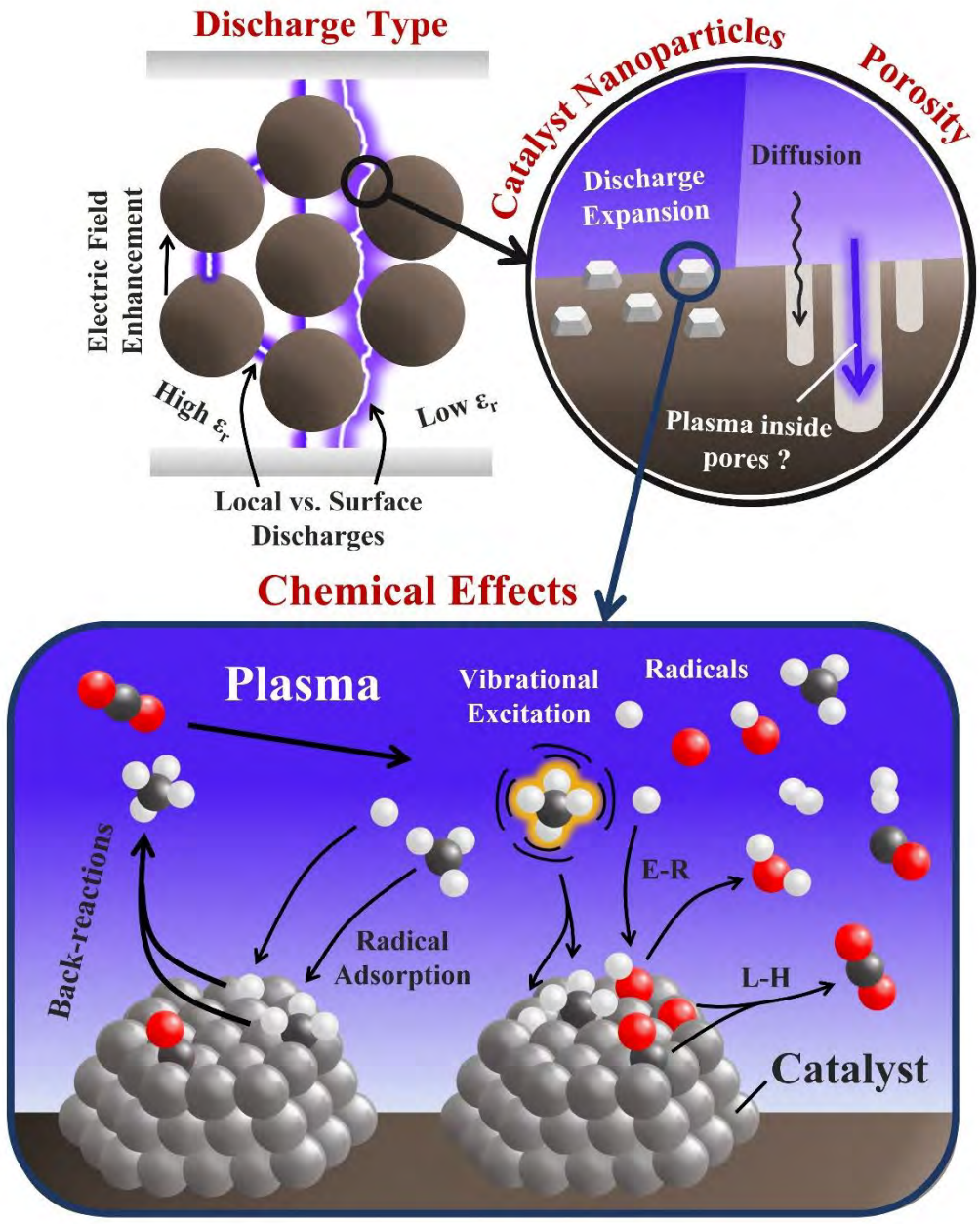

Figure 1.5 Schematic overview of the various physical and chemical plasma-catalytic interactions. E-R and L-H are abbreviations for Eley-Rideal (see section 1.7.7) and Langmuir-Hinshelwood reactions, respectively.[39]

1.6 Physical interactions

Strictly speaking, physical interactions between plasma and catalyst (or packing) are not catalytic effects. Yet, they can substantially affect the plasma chemistry by altering its discharge behavior and are therefore an important factor to consider when studying in-plasma catalysis. Since physical and chemical effects occur simultaneously in experiments, it is typically difficult or impossible to distinguish their individual contributions to the results. Nevertheless, by using carefully designed experiments or computational modeling, it is possible to isolate different (physical or chemical) interactions and study these separately. In the following subsections we will focus in more detail on the most important physical plasma-catalyst interactions.

1.6.1 Surface discharges vs. localized discharges

The introduction of a support material (with or without catalyst particles) in the discharge gap influences the plasma physics and can therefore alter its discharge behavior. In plasma catalysis, the catalyst is typically placed inside the plasma by loading it on packing beads of a few millimeters in diameter, which are inserted into a DBD plasma reactor. Both experimental[40] and modeling[41] studies for air plasmas have shown that the dielectric constant (ε_r) of the packing is an important material property in this regard, as it has a strong influence on the type of discharges that can occur in between the packing beads. Low dielectric constants (i.e., a low polarizability) give rise to surface discharges on the packing beads, while high dielectric constants (i.e., a high

Section 1.6 is derived from the following publication:

Loenders, B.; Michiels, R.; Bogaerts, A. Is a Catalyst Always Beneficial in Plasma Catalysis? Insights from the Many Physical and Chemical Interactions. *J. Energy Chem.* **2023**, *85*, 501–533. DOI: 10.1016/j.jechem.2023.06.016

polarizability) promote the formation of discharges localized at the contact points between the beads. These local discharges can serve as staging points that facilitate streamer propagation to adjacent beads. However, for materials with very high dielectric constants, such as $BaTiO_3$ ($\varepsilon_r \approx 2600$), streamer propagation does not happen, and only local discharges occur.

The effect of the dielectric constant on the discharge type is schematically displayed in Figure 1.6, which illustrates the change in discharge type in a packed-DBD as the dielectric constant rises. The dielectric constant of the packing material increases upon going from glass beads ($\varepsilon_r = 5$), to ZrO_2 ($\varepsilon_r = 25$), to $BaTiO_3$ ($\varepsilon_r \approx 2600$). Materials with a low dielectric constant, such as glass beads, predominantly form surface discharges, which connect to the surface of adjacent beads and thus spread out over the discharge gap. For materials with intermediate dielectric constants, such as ZrO_2, localized microdischarges start to occur at the contact points between the beads, while surface discharges are still present as well. For $BaTiO_3$, which has a high dielectric constant of approximately 2600, only localized microdischarges occur.[41]

The discharge type is expected to have important implications for the chemical plasma-catalyst interactions, as it determines the spatial distribution of the plasma in the reactor and its distance to the surface. Indeed, before reactive plasma species can partake in the surface chemistry, they need to diffuse from the plasma to the catalyst surface. Consequently, the number of species that reaches the catalyst will depend on the distance between the plasma and the catalyst particles, as well as the lifetime of the species.

Interestingly, computational modeling of air plasma by Wang et al.[41] revealed that the dielectric constant of the packing beads not only influences the discharge type, but also the concentration of the species inside the plasma. Higher dielectric constants (i.e., $\varepsilon_r = 1000$ vs. $\varepsilon_r = 5$) were found to enhance the concentration of N radicals and electrons,

while slightly suppressing O and O_3. This is caused by the stronger polarization of the beads with higher dielectric constants, which leads to stronger electric field enhancement at the poles, and thus higher electron temperatures. The higher electron temperatures improve the electron impact dissociation of N_2, while lowering the fraction of the electron energy that goes into electron impact dissociation of O_2.[41]

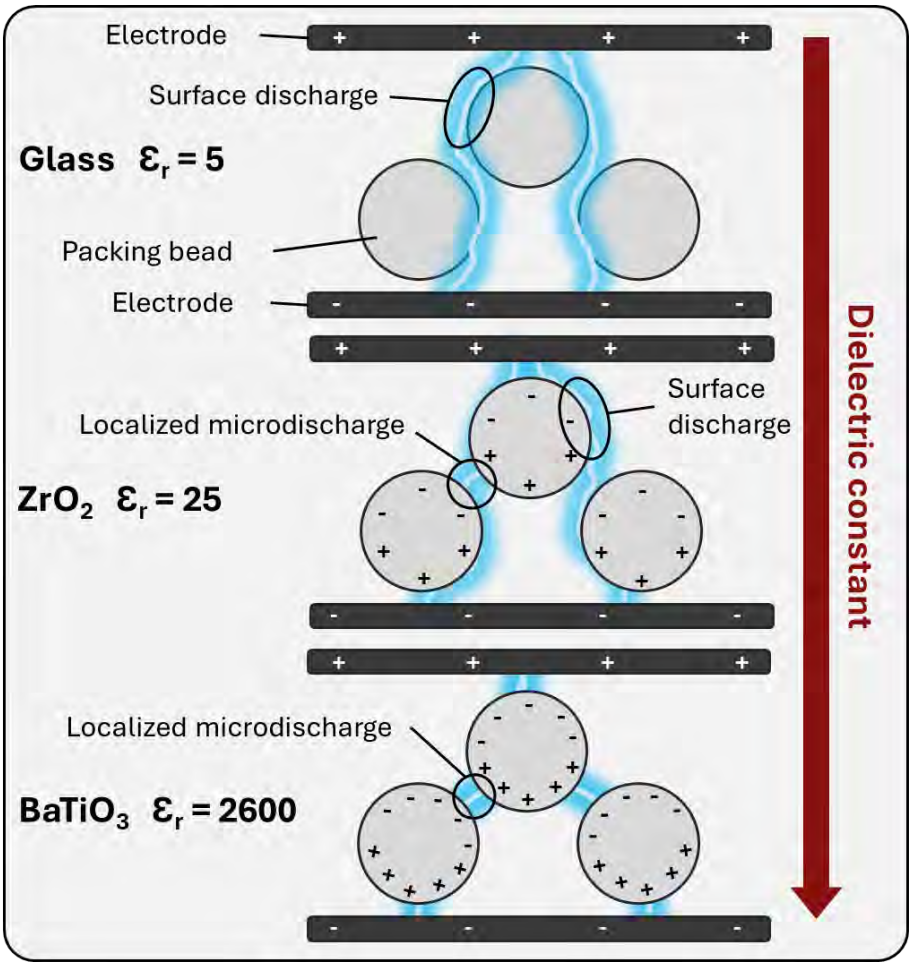

Figure 1.6. Schematic representation of the discharge behavior in a packed-bed DBD reactor for materials with different dielectric constants (ε_r), namely glass ($\varepsilon_r = 5$), ZrO_2 ($\varepsilon_r = 25$) and $BaTiO_3$ ($\varepsilon_r \approx 2600$). The discharge type changes from surface discharges at low ε_r to localized discharges at high ε_r. Based on ref. 41.

This example illustrates that the dielectric constant of the packing can be used to enhance or suppress the formation of specific plasma species. More generally, we can envision that low dielectric constants (and thus lower electron temperatures) are more beneficial if vibrational excitation is desired, while high dielectric constants can enhance electron impact dissociation. Indeed, energy thresholds for vibrational excitation are much lower than those for electron impact dissociation. For example, electron impact dissociation to the first vibrationally excited states of CH_4 or CO_2 requires a threshold energy in the range of 0.162–0.361 eV or 0.083–0.291 eV, respectively, depending on the model that is excited.[42] Electron impact dissociation reactions of CH_4 or CO_2, on the other hand, have energy thresholds starting at 8.6 eV[43] and 7.5 eV,[44] respectively.

Thus, the dielectric constant of the packing has a strong effect on the discharge type, with low dielectric constants favoring surface discharges along the beads, and high dielectric constants enhancing the formation of localized microdischarges between the beads. Consequently, the dielectric constant can be used to tune the discharge mode to optimize contact between plasma and catalyst. Indeed, it affects the distribution of the plasma between the beads, and thus whether plasma species are formed in the vicinity of the catalyst particles. In addition, the electric field enhancement due to polarization of the beads determines which plasma species are formed by certain electron impact processes.

1.6.2 Effect of metal particles on the discharge behavior

As described in previous section, experimental observations have shown that the presence of a catalyst or support material in the discharge gap can alter the plasma's discharge behavior.[40,41,45–47] While the dielectric constant of the packing material (the catalyst support) influences the discharge type, some authors reported a similar effect when the packing was loaded with a catalyst. For example, Tu *et al.*[45] observed a change in the discharge type from filamentary discharges in an empty DBD reactor to a mixture

of surface discharges and localized microdischarges when the reactor was packed with Ni/Al_2O_3. Moreover, when comparing the effect of a Ni/Al_2O_3 packing to an Al_2O_3 packing without Ni, the authors found that the additional presence of Ni resulted in a much wider spatial distribution of the discharges.[45] Likewise, Kim et al.[46,47] observed that the presence of other types of metal nanoparticles (e.g., Zr, Ag, and Cu) also causes expansion of the plasma, in addition to the effect of the support.[46,47] Furthermore, these authors found that the catalyst loading of Ag nanoparticles on a zeolite support also enhanced the number of microdischarges, next to the discharge volume. While packing the support in the DBD reactor on itself already resulted in more, yet less intense (i.e., lower current peaks) microdischarges, the effect was even stronger in the presence of Ag nanoparticles. Additionally, both the plasma expansion and the number of microdischarges were further enhanced at larger Ag loadings.[46,47]

Hence, to determine the chemical effect of the catalyst in plasma catalysis, results should ideally be compared to the reactor packed with the same support material but without catalyst particles. However, even this approach is not conclusive, as the presence of catalyst nanoparticles can also affect the discharge behavior compared to the bare support material.

It is also noteworthy that not all metals affect the discharge behavior in the same way. Indeed, Kim *et al*.[46] found that Cu nanoparticles were less effective in plasma expansion and plasma-catalytic benzene oxidation compared to Ag. In a follow-up work by the same research group,[40] loading Ag on γ-Al_2O_3 was found to enhance streamer formation relative to pure γ-Al_2O_3, while the presence of Pt was detrimental to streamer propagation. Moreover, Ndayirinde *et al.*[48] found for plasma-catalytic NH_3 synthesis that the addition of different promotors (Ce, La, and Mg) to Co-based catalysts significantly changed the discharge characteristics (e.g., plasma power and electrical current profile)

of the DBD plasma. In other words, depending on their composition, the catalysts can act as “plasma modifiers”, and may thereby possibly affect the plasma chemistry.

These results illustrate that different types of metals do not necessarily affect the discharge behavior in the same way. As such, a catalyst that is optimal from a chemical perspective, i.e., regarding the surface reactions, might not be beneficial for the plasma physics. It might, perhaps, be possible to counter such negative effects by choosing the support material accordingly, i.e. to optimize the discharge behavior of the plasma. This would also imply that the optimal support material may change for different catalysts.

To summarize, the presence of metal nanoparticles can further affect the discharge behavior, in addition to the effect of the support material. Metal nanoparticles may lead to expansion of the plasma, as well as a larger number of microdischarges, and their effect becomes more apparent for larger metal loadings.[45,46] Moreover, the physical interaction between the plasma and the catalyst nanoparticles varies for different metals,[40,46] which makes a direct comparison of their chemical effect challenging.

1.6.3 Effect of the packing and reactor dimensions

In addition to the composition of the packing, the diameter of the packing beads and the width of the discharge gap also strongly determine the discharge behavior in the reactor. Van Laer *et al*.[49,50] studied the effect of the bead and gap sizes on the discharge behavior computationally, by modeling the fluid dynamics of a helium DBD plasma. Their simulations showed that smaller bead or gap sizes, as well as higher dielectric constants (and thus stronger polarizability), enhance the electric field. However, the electric field enhancement stagnates at higher dielectric constants, and the electric field becomes constant upon further increasing ε_r. Moreover, this stagnation happens at lower values of ε_r for smaller beads or discharge gaps. Additionally, the enhancement of the electric field as well as the smaller voids resulting from smaller bead sizes cause a larger fraction

of electrons to be lost through collision with the walls. Hence, smaller beads and higher dielectric constants can enhance the electric field up to a certain point but also result in a drop in the (space- and time-averaged) electron density.[49,50]

Since gas conversion requires both a high electric field and high electron density, smaller bead and gap sizes or higher dielectric constants are no longer beneficial after the electric field stagnates. As such, materials with low ε_r can benefit more from smaller bead and gap sizes (i.e., to improve the electric field), while materials with (very) high ε_r may benefit more from larger bead and gap sizes (i.e., to improve the electron density).[49,50]

This agrees with results from CO_2 splitting experiments,[51] which showed that smaller beads (100–200 µm) were more beneficial in case of SiO_2 (ε_r = 3.9) and Al_2O_3 (ε_r = 9), while the trend was inversed for ZrO_2 (ε_r = 25), for which larger beads (300–400 µm) gave higher conversions. However, narrowing the discharge gap generally resulted in higher CO_2 conversions for gap sizes in the range 250–1250 µm, regardless of the packing material.[51] Given that the dimensions of the packing and the discharge gap affect the electric field, and thus the electron temperature, these parameters may also affect the species formed in the plasma, similar to the dielectric constant, as discussed in section 1.6.1.

Next to the dielectric constant of the packing, many other factors determine the optimum packing size. Butterworth *et al.*[52] studied the effect of packing particle size (180–2000 µm) on CO_2 splitting in a packed-bed DBD with an Al_2O_3 or $BaTiO_3$ packing. Their results showed that smaller packing particles improved CO_2 conversion, but on the condition that the applied voltage is high enough to generate discharges in the voids between the packing particles. However, the use of smaller particles (and thus smaller voids) also increased the burning voltage and led to partial discharging, i.e., not all the charges stored on the surface of the dielectric are transferred during a discharge cycle and thus less plasma is formed. The latter of course has a negative effect. As such, the

authors illustrated that to (fully) benefit from the use of smaller particles, breakdown should be facilitated by using higher voltages or gas mixtures with a lower breakdown voltage (e.g., by adding noble gasses to the feed). Indeed, their results showed that smaller particles for Al_2O_3 improved CO_2 conversion in CO_2/Ar feed mixtures. However, the beneficial effect of smaller particles declined when increasing the CO_2 fraction. Moreover, for pure CO_2 small particle sizes became detrimental, as no plasma could be generated for particles smaller than 850 µm. For $BaTiO_3$, on the other hand, plasma could still be generated in pure CO_2 for the smallest particles, likely due to electric field enhancement caused by the high dielectric constant. Yet, $BaTiO_3$ generally did not benefit from smaller particle sizes, except at the highest Ar fractions combined with plasma powers above 10 W.[52]

Additionally, smaller packing particles result in more contact points between the particles, where the electric field is enhanced, which increases the number of localized microdischarges. As such, the packing size might be used to tune the volume of the plasma relative to that of the non-ionized gas in the reactor.[53,54] This explains why even materials with a high dielectric constant, like $BaTiO_3$, can benefit from smaller packing particles to some extent, as has been observed experimentally.[55,56] Indeed, packings with high dielectric constants, result in the formation of localized discharges at the contact points between the beads, as discussed in section 1.6.1.

To summarize, not only the dielectric constant of the packing, but also the dimensions of the packing beads and of the discharge gap determine the discharge behavior. While the electric field is initially enhanced with rising dielectric constant and smaller bead or gap sizes, this trend is broken as the electric field stagnates. Consequently, the trends regarding bead size and discharge gap can be inversed for different packing materials, thus significantly complicating direct comparison between different experimental studies. Additionally, some packing materials can benefit significantly from smaller

particle sizes, on the condition that a sufficiently high voltage is applied. Yet, smaller particles also raise the breakdown voltage and can lead to partial discharging if the applied voltage is too low. Hence, the optimal packing and gap size depends on many parameters, including the dielectric constant of the packing, the gas mixture, and the applied voltage.

1.6.4 Other material properties of the packing

In the previous sections we discussed the effect of the dielectric constant of the packing, the presence of metal nanoparticles, as well as the dimensions of the beads and the reactor on the discharge behavior and electric field enhancement.

However, many other material parameters of the packing may affect gas conversion in a DBD. For example, in an experimental study on DRM in a packed-bed DBD reactor, Michielsen *et al.*[23] observed that α-Al_2O_3 spheres gave higher conversions than γ-Al_2O_3 spheres of the same size. Since both packing materials have the same dielectric constant, this indeed indicates that other material properties play a significant role as well. An important difference between the α-Al_2O_3 and γ-Al_2O_3 in ref. 23 is the higher porosity of the latter, e.g., with pore volumes of 8.47 $mm^3\ g^{-1}$ vs. 500 $mm^3\ g^{-1}$ for α-Al_2O_3 and γ-Al_2O_3, respectively.

We could speculate that part of the gas may be protected from the plasma by diffusion into the pores, which raises the question whether plasma formation inside the pores is possible. Particle-in-cell/Monte Carlo collision simulations have shown that plasma streamers can only penetrate into pores with a diameter larger than the Debye length, which is typically in the order of 0.5–1 µm for air discharges in DBD.[57] Using T_e = 2.5 eV and $n_e = 3 \times 10^{19}\ m^{-3}$ from ref. 58, we can estimate a Debye length, $\lambda_{de} \approx 7430 \times (T_e/n_e)^{1/2}$ = 2 µm for CH_4/CO_2 DBD plasmas. As the pore diameter of γ-Al_2O_3 in ref. 23 is determined to be 0.54 µm, this indicates the plasma is indeed not able to penetrate into the pores.

This may explain why the γ-Al_2O_3 packing gave lower conversion, despite its higher porosity, as the gas inside the pores could not be converted by the plasma due to a shielding effect. This principle is schematically presented in Figure 1.7; plasma can only reach into pores with a sufficiently large diameter, while smaller pores "shield" the gas from the plasma. This result is striking, and different from thermal catalysis, where higher porosity is typically beneficial, enabling more catalyst surface area to participate to the reaction. It again illustrates the additional complexity of plasma catalysis, compared to e.g., thermal catalysis.

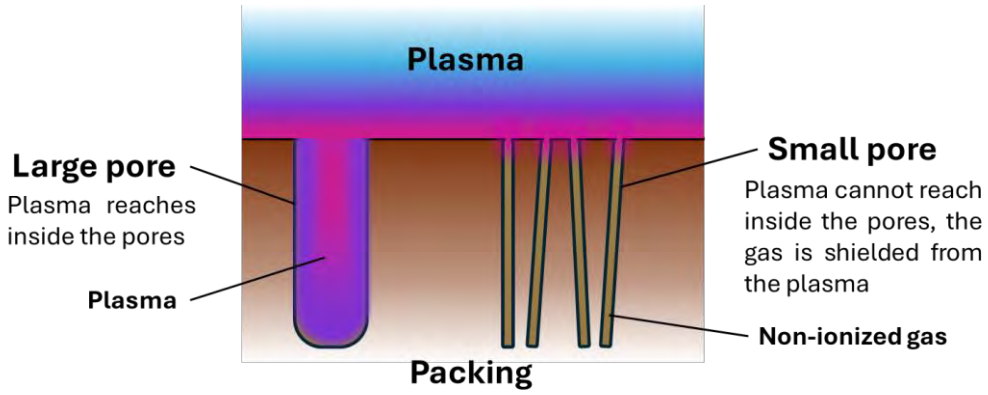

Figure 1.7. Schematic representation of the effect of the pore size of the packing in plasma catalysis applications. The plasma is only able to reach into the pores if their diameter is large enough (i.e., larger than the Debye length).[57] *Smaller pores, on the other hand, shield the gas from the plasma.*

It is noteworthy that most support materials have pore sizes in the microporous (< 2 nm) and mesoporous (2–50 nm) range,[59] meaning that the plasma will typically not reach into the pores. This is important to keep in mind for plasma catalysis applications, as any catalyst particles that are present in the pores will not be in direct contact with the plasma, and can thus only be reached by plasma species via diffusion. How far the plasma species will be able to reach into the pores will thus depend on their lifetime and diffusion coefficient. This was discussed in a review by Kim et al.,[60] who estimated

diffusion lengths of 0.74, 52, and 65 µm for $O(^1D)$, $O(^3P)$, and OH, respectively, based on lifetimes of 10 ns, 50 µs, and 100 µs, respectively. Assuming a typical diffusion coefficient around 0.2 $cm^2\ s^{-1}$, similar to the values reported in ref. 60, we might expect diffusion lengths of 6.3-63 µm for vibrationally excited CH_4 and CO_2, with lifetimes in the range of 1-100 µs.[22,61] Similarly, for CH_x radicals in CH_4 DBD plasma, with lifetimes of < 5 µs (CH), < 30 µs (CH_2), and > 1 ms (CH_3),[22] diffusion lengths of < 0.45 µm, < 1.1 µm, and > 200 µm may be reached, respectively. Note that the lifetimes and thus diffusion lengths are determined by the reactions in the plasma and will differ dependent on the gas mixture and reaction conditions, such as temperature, pressure, and plasma power. Apart from radicals and excited species, ions and electrons might also diffuse into the pores. However, estimating their diffusion lengths is more complicated, as positive ions can be accelerated into the pores due to the negative charge accumulated at the pore walls, while electrons experience repulsion.[59]

Next to physical affects, the chemical properties of the packing can also play a role. For example, some experimental studies have suggested that a higher basicity of the packing enhances CO_2 conversion in DRM and CO_2 methanation.[62–65] Indeed, it is known from thermal catalysis that basic sites on the support material interact with CO_2 due to the Lewis acidic properties of this molecule. Hence, a higher number of basic sites enhances CO_2 adsorption and can improve CO_2 conversion.[66–68] This effect likely also plays a role in plasma catalysis. For example, Mei *et al.*[65] studied plasma-catalytic DRM with Ni, Ag, and Pt catalysts supported on γ-Al_2O_3, as well as bare γ-Al_2O_3 and observed that the trend in CO_2 conversion was consistent with the number of basic sites on the catalyst material. Additionally, Mikhail *et al.*[63] investigated plasma-catalytic CO_2 methanation using Ni/$CeZrO_x$ catalyst with various dopants (Cu, La, Mn, Co, Y, Gd, and Sr) and observed that the amount of CH_4 produced (and CO_2 converted) was generally improved with a higher percentage of medium basic sites compared to strong basic sites. This was attributed to strong basic sites mainly forming strongly-bound and unreactive surface intermediates,

while CO_2 adsorbed on medium basic sites results in more reactive surface intermediates.[63,66,67] However, it is worth noting that it is difficult to establish a clear correlation between basicity and CO_2 conversion in plasma catalysis, due to the many factors that can play a role.

Furthermore, the effect of the packing in plasma-catalytic DRM is further complicated by the myriad of products that can be formed. Indeed, in the abovementioned work by Michielsen et al.[23] the selectivity and CO/H_2 ratio showed significant variation with packing material (SiO_2, α-Al_2O_3, γ-Al_2O_3, ZrO_2, and $BaTiO_3$) and bead size (1.25–2.24 mm).

In summary, next to the dielectric constant, metal loading, packing bead, and reactor gap size, many other packing properties can affect the conversions and product selectivity. These include other physical properties, such as porosity and pore size, which determine the fraction of the gas mixture and catalyst particles that are in direct contact with the plasma. On the other hand, chemical properties, such as basicity, may also play a role.

1.6.5 Comparing packing materials at different residence times

While various packing properties can affect the conversion, the optimal packing in terms of conversion can also differ depending on the residence time of the gas in the reactor. This was illustrated by Uytdenhouwen *et al.*,[69] who demonstrated the existence of a partial chemical equilibrium (PCE) for CO_2 splitting in a DBD reactor.

"Partial" chemical equilibrium refers to the fact that although the plasma is not in thermal equilibrium (and hence does not follow equilibrium thermodynamics), it can still reach a state resembling a chemical equilibrium. When the gas composition at a fixed point in the reactor remains constant with time, a steady state is reached at this position. However, the gas composition may still change with the position in the reactor. Yet, if the reactor (or the residence time) is sufficiently long, the gas composition will also become constant with position towards the end of the reactor. At these conditions, the difference

between the net production and destruction rates becomes zero for all species, hence this state is referred to as a "partial" chemical equilibrium. Note that the gas composition at PCE depends on the plasma conditions and that the PCE can be reached both from the reactant, as well as from the product side of the reaction equation.[69]

Uytdenhouwen *et al.*[69] found that the CO_2 conversion stabilized at different values depending on the size of the discharge gap and the choice of packing, but the residence time needed to reach PCE also changed independently of the conversion at PCE. To illustrate this, Figure 1.8 schematically presents four possible cases for the evolution of the conversion with residence time; cases A (red curve) and B (blue curve) both evolve quickly towards a PCE, but for case A the conversion at the PCE is higher than for case B. For cases C (black curve) and D (green curve) the conversion evolves more slowly with residence time compared to cases A and B and thus requires a longer residence time to reach a PCE. For case C the conversion at the PCE is high, while for case D the conversion at the PCE is low. Hence, in cases A and D the conversions are always high and low, respectively, regardless of the residence time. However, case B (fast evolution, low PCE) outperforms case C (slow evolution, high PCE) at short residence times, while case C outperforms case B at long residence times. As such, the optimal reaction parameters may change depending on the residence time.

Indeed, in the abovementioned work, Uytdenhouwen *et al.*[69] found that placing a ZrO_2 packing in a DBD reactor with a 455 µm discharge gap, resulted in the same PCE as the empty reactor, but a longer residence time was required to reach the same conversion (i.e., 91.3 s vs. 37.1 s, respectively). In other words, the ZrO_2-packed and empty reactor performed the same at long residence times, while the empty reactor performed better at short residence times. However, when SiO_2 was packed in the reactor, the PCE shifted to a higher conversion (71%) relative to the empty (54%) and ZrO_2-packed (55%) reactor. Moreover, for a larger (4705 µm) gap, the trend changed and ZrO_2 reached the highest

conversion at PCE (57%), followed by SiO_2 (40%), with the empty reactor giving the lowest conversion (23%).[69] Hence, even direct comparison of two different packing materials in the same DBD reactor is not necessarily straightforward, as the observed trend in conversion might change for different residence times.

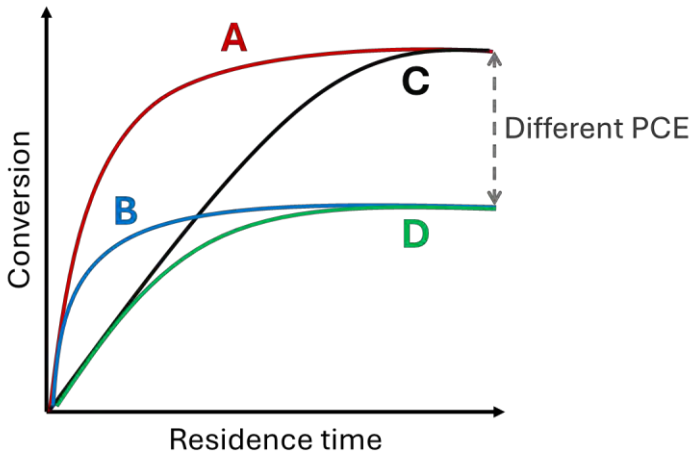

Figure 1.8. Schematic representation illustrating four cases for the evolution of the conversion vs. residence time. Cases A (red curve) and B (blue curve) each quickly reach a partial chemical equilibrium (PCE), but the conversion at the PCE is higher for case A than for case B. For cases C (black curve) and D (green curve) the conversions evolve slowly with the residence time. Hence a longer residence time is needed to reach the PCE, which is located at a higher conversion for case C compared to case D. Based on ref. 69.

1.7 Chemical interactions

As discussed in section 1.6, the introduction of a catalyst or packing inside a plasma results in various physical effects that can influence the outcome (e.g., conversion, product yield) of the reaction. Likewise, chemical effects are also possible, as species can be exchanged between the plasma and the surface, allowing gas and surface reaction pathways to interact. Hence, a rational design of plasma-catalytic systems also requires a good understanding of the chemical interactions between the plasma and the catalyst.

The following subsections will therefore discuss various chemical effects that may play a role in plasma catalysis, based on insights from both experiments and modeling. Section 1.7.1 illustrates how reactive plasma species can improve reactant activation on the catalyst surface, which enhances conversion within specific temperature ranges. Additionally, this effect is compared for endothermic and exothermic reactions. Next, section 1.7.2 illustrates how plasma-catalyst synergy can alter the trends in catalyst reactivity relative to thermal catalysis, while section 1.7.3 discusses the difference between vibrationally excited molecules and radicals in inducing plasma-catalyst synergy.

Next, Section 1.7.4 elaborates on experimental methods developed to quantify plasma-catalyst interactions and to measure plasma-induced surface heating. Section 1.7.5 illustrates how plasma-catalyst synergy can influence the product selectivities based on examples from plasma-catalytic CO_2 hydrogenation.

Section 1.7 is derived from the following publication:

Loenders, B.; Michiels, R.; Bogaerts, A. Is a Catalyst Always Beneficial in Plasma Catalysis? Insights from the Many Physical and Chemical Interactions. *J. Energy Chem.* **2023**, *85*, 501–533. DOI: 10.1016/j.jechem.2023.06.016

Section 1.7.6 discusses how a plasma typically contains a wide variety of radicals, which can strongly affect the product distribution, as well as the optimal choice of catalyst. Next, section 1.7.7 explains how these radicals can react with adsorbates via Eley-Rideal (E-R) reactions, which are likely important in plasma catalysis, although much is still unknown about the associated kinetics. Finally, section 1.7.8 underlines why a detailed understanding of the physical plasma-catalyst interactions is important for optimizing the chemical interactions, which depend on the flux of plasma species to the surface and thus the contact between the plasma and the catalyst.

1.7.1 Temperature dependence of plasma-catalyst synergy

Experimental studies on plasma-catalytic DRM[70] and steam reforming of CH_4 (SRM)[61] as well as NH_3 synthesis[71] have observed the occurrence of plasma-catalyst synergy to be temperature dependent. In other words, synergy only occurs at sufficiently high temperatures, similar to how a catalyst requires elevated temperatures to become active for thermal catalysis. This indicates that reactive plasma species may participate in the catalyst surface chemistry, enhancing specific surface reactions. As such the reaction rates on the surface are enhanced, but only if the surface reaction steps that are not directly affected by the plasma are thermally active, i.e. if the temperature is high enough.[71,72] Section 1.7.1.1 illustrates this for two endothermic reactions, namely DRM and SRM, while section 1.7.1.2 discusses the effect for NH_3 synthesis as an example of an exothermic reaction. Next, section 1.7.1.3 provides a general comparison of the temperature dependance of plasma-catalyst synergy for both endothermic and exothermic reactions.

1.7.1.1 Plasma-catalyst synergy in DRM and SRM

Kim *et al*.[70] observed a temperature dependence of plasma-catalyst synergy for DRM. The authors compared DRM in a DBD without catalyst (empty or packed with Al_2O_3) to thermal and plasma catalysis with a Ni/Al_2O_3 catalyst, at different temperatures. A schematic presentation of their results is shown in Figure 1.9. They found that plasma alone or with only an Al_2O_3 packing (blue curve) gave significant CH_4 conversions at low temperatures (< 600 K), while the conversion diminished at higher temperatures. Thermal catalysis (grey curve), on the other hand, naturally showed an opposite trend, i.e., the conversion rose with temperature due to the catalyst becoming thermally active. For plasma catalysis (red curve) the CH_4 conversion was similar to that of the plasma without catalyst at low temperatures (< 600 K), while at higher temperatures it outperformed thermal catalysis. Thus, synergy is only observed at temperatures where the catalyst also becomes active for thermal catalysis, clearly indicating the involvement of surface reactions. Because of this temperature dependency and the fact that plasma alone gave negligible conversion at high temperatures (≥ 700 K), the authors attributed the observed synergy to vibrationally excited CH_4. This would lower the activation barrier for the presumed rate-limiting step, i.e., CH_4 dissociative adsorption, and thus enhance the surface reaction rates.[70]

Similar behavior was also observed for SRM by Nozaki *et al.*[61] In that study, the CH_4 conversion in a DBD packed with a Ni/SiO_2 catalyst exceeded the combined conversions of the empty DBD and thermal catalysis at temperatures between 673 – 873 K. Moreover, CH_4 conversions beyond the thermodynamic equilibrium could be reached, indicating that plasma-enhancement of the surface reactions does not only improve the kinetics, but can also circumvent thermodynamic limitations to some extent.[61]

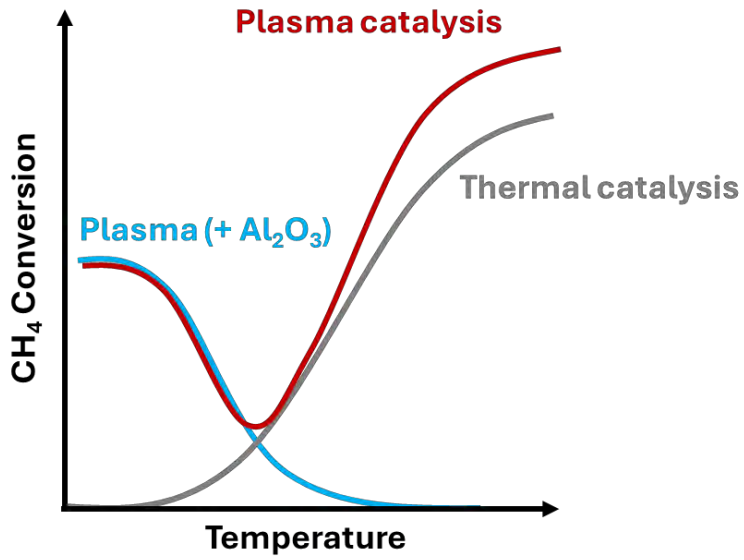

Figure 1.9. Schematic representation of the evolution of the CH_4 conversion in DRM with temperature for plasma alone or with Al_2O_3 packing (blue curve), thermal catalysis (grey curve) and plasma catalysis (red curve). Based on ref. 70.

Hence, these studies demonstrate that plasma can facilitate CH_4 activation on the catalyst surface, possibly by destabilizing the C-H bonds through vibrational excitation. The latter is further supported by the results of molecular beam studies, which show that vibrational excitation of the asymmetric C-H stretch mode in CH_4 enhances its dissociative adsorption.[73,74] However, this plasma-catalyst synergy only becomes effective above a certain temperature.

1.7.1.2 Plasma-catalyst synergy in NH_3 synthesis

To further elucidate the mechanisms behind plasma-catalyst synergy, studies of more straightforward reaction systems, such as plasma-catalytic NH_3 synthesis, can also be useful. Both experimental[71] and modeling[72] studies on plasma-catalytic NH_3 synthesis have demonstrated that plasma-catalyst synergy only occurs past a certain temperature threshold, like in DRM and SRM. However, unlike DRM and SRM, NH_3 synthesis is

exothermic and thus equilibrium-limited at high temperatures. While plasma-catalyst synergy can also push the NH_3 concentrations beyond the equilibrium composition, the exothermicity of the reaction eventually leads to a drop of the NH_3 concentrations at higher temperatures.[71,72] This behavior was clarified via modeling by Mehta *et al.*,[72] who illustrated the effect of plasma-enhanced N_2 dissociative adsorption (e.g., due to N_2 vibrational excitation or dissociation in the plasma) on the surface kinetics. The authors illustrated that at low temperatures (< 400 K), plasma-enhanced N_2 activation has no effect, as the reaction becomes rate-limited by the subsequent reaction steps, i.e., NH_x* hydrogenation and NH_3 desorption. Yet, as the temperature rises these reactions become thermally activated, allowing plasma-enhanced N_2 dissociation to improved NH_3 formation rates and concentrations. The faster NH_3 formation rate also causes an imbalance between NH_3 formation and destruction, explaining why the NH_3 concentrations can exceed the thermodynamic equilibrium. However, as the temperature rises further, the catalytic pathways for NH_3 destruction also become more active, causing the NH_3 concentration to reach a maximum and subsequently decline.[72]

As discussed in section 1.6.2, the presence of metal nanoparticles on the support material can alter the discharge behavior of the plasma, thus possibly leading to a change in conversion. It is therefore noteworthy that on top of the qualitative agreement between experimental[71] and modeling results,[72] there is also direct evidence of plasma-enhanced surface reactions.[75,76] More specifically, Barboun *et al.*[75] demonstrated the formation of surface-bound NH_x* on Ni/γ-Al_2O_3 that was sequentially treated with N_2 and H_2 plasmas to exclude the formation of NH_x radicals in the plasma. The formation of surface-bound NH_x* could indeed be attributed to plasma catalysis, as subsequent N_2 and H_2 exposure under thermal conditions without plasma did not form these species. In a follow-up work,[76] SiO_2-supported Fe, Ni, Co and Pt catalysts were treated with a N_2 plasma, followed by temperature programmed reaction with H_2 gas to eliminate the possibility of gas-phase NH_3 synthesis. Using this method, NH_3 production via thermal

hydrogenation of surface-bound N* was indeed observed. However, if the catalyst was not treated with N_2 plasma, but instead exposed to N_2 at 200 °C, no NH_3 could be formed. Hence, this proves that the plasma was essential in forming the adsorbed N*. These studies thus provide clear evidence that plasma enhances activation of N_2 on the catalysts surface.

In summary, plasma can facilitate N_2 dissociation on the catalyst surface, leading to enhanced NH_3 concentrations in the gas-phase, which can even exceed the thermodynamic equilibrium. Yet, a certain light-off temperature is still required to activate the subsequent surface reaction steps, while too high temperatures cause the NH_3 concentration to revert to the equilibrium composition.

1.7.1.3 Plasma-catalyst synergy: endothermic vs. exothermic reactions

As mentioned above, both DRM and SRM are endothermic reactions and thus equilibrium-limited at low temperatures, while NH_3 synthesis is exothermic and becomes limited by the thermodynamic equilibrium at high temperatures. As such, plasma-catalyst synergy follows a different temperature dependence for these reactions. Mehta *et al.*[77] reviewed the potential of plasma catalysis for DRM and NH_3 synthesis, as examples of processes that operate in different limiting regimes.

Figure 1.10 illustrates the effect of plasma-enhancement of the reactant activation step (i.e., dissociative adsorption) on the conversion for endothermic and exothermic reactions, for which this step is rate-limiting. For the purpose of this discussion, we define plasma-enhancement as the destabilization of the reactant through vibrational excitation or dissociation in the plasma, leading to more facile reactant activation on the surface. Note that Figure 1.10 does not include any conversion that takes place in the gas phase or any alteration of other surface reaction steps.

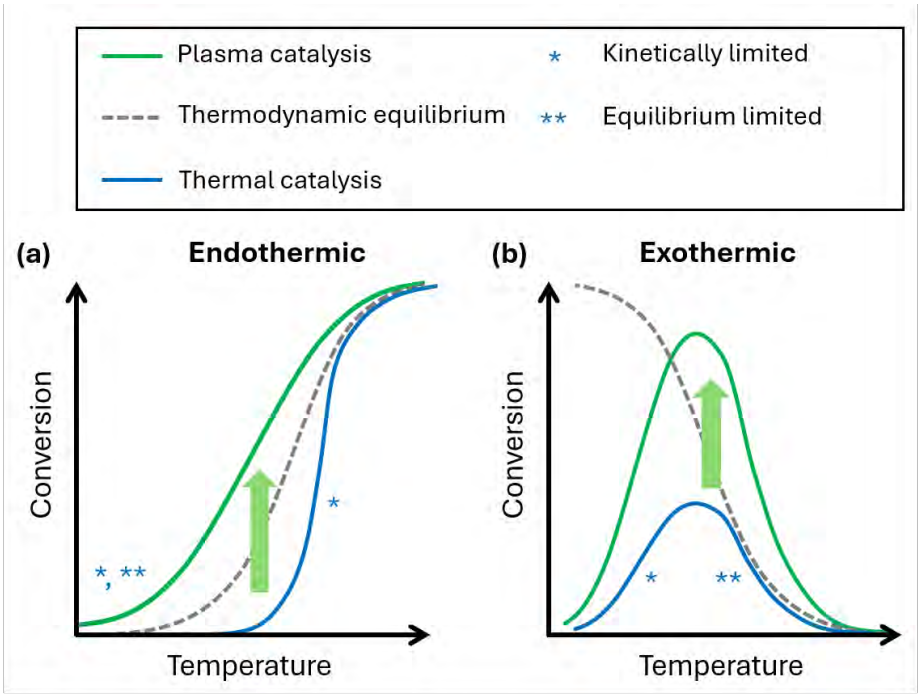

Figure 1.10. Schematic representation of the effect of plasma-enhanced reactant activation for (a) endothermic and (b) exothermic reactions that are rate-limited by this reaction step.[39]

Figure 1.10 (a) shows how endothermic reactions are affected by plasma-enhanced reactant activation. Since endothermic reactions are both kinetically and equilibrium-limited at low temperatures, enhanced conversions occur exclusively at temperatures below which the catalyst becomes active for thermal catalysis. At temperatures above the equilibrium-limited regime, plasma-enhancement has limited potential, although it can still be useful to activate catalysts that are strongly kinetically limited by reactant activation. Such catalysts require high temperatures to become catalytically active and thus both the thermal and plasma catalysis curves in Figure 1.10 (a) will be shifted to the right. Less active catalysts in terms of conversion might be chosen if they offer advantages with respect to product selectivity. For endothermic reactions, higher temperatures will result in increased conversion, yet plasma-enhancement will also become redundant, as

the equilibrium and kinetic limitations applicable to thermal catalysis will disappear. As such, the optimal operating temperature for plasma catalysis will be lower than for thermal catalysis.

The effect of plasma-enhanced reactant activation on exothermic reactions is displayed in Figure 1.10 (b) and is explained in more detail in section 1.7.1.2, where the work by Mehta *et al.*[72] on plasma-catalytic NH_3 synthesis was discussed. Exothermic reactions exhibit an optimal operating temperature, due to the kinetic and equilibrium limitations at low and high temperatures, respectively. Strong plasma-enhancement improves the conversions in both the kinetically and equilibrium-limited regime. This enables conversions closer to the equilibrium composition at low temperatures, while it allows conversions beyond the thermodynamic equilibrium at higher temperatures (see Figure 1.10 (b)). This departure from thermodynamic equilibrium is the result of plasma selectively enhancing the forward reaction rates (e.g. reactant activation). At equilibrium the forward and reverse reaction rates are equal. By promoting the forward rates relative to the reverse rates this balance is disrupted, and the gas composition shifts beyond the values that correspond to the thermodynamic equilibrium. Nevertheless, an optimal temperature will still exist where the conversion reaches a maximum. Contrary to endothermic reactions, the maximum conversion for plasma-enhanced exothermic reactions corresponds to the temperature at which plasma-enhancement has the strongest impact.

Note that the discussion above features reactions that are endergonic in part of the temperature range. However, some reactions are never limited by the equilibrium, i.e., when the reactants are not the thermodynamically favored products at any temperature. Nevertheless, the equilibrium composition can still change with temperature, meaning that depending on the temperature different products will be favored. An example of this is the partial oxidation of CH_4 (POX), which favors a mixture of non-combusted CH_4 and

complete oxidation products (H_2O, CO_2) at low temperatures (< 900 K) or syngas (CO/H_2) at high temperatures (> 900 K).[78,79] For such processes, plasma-enhancement can aid in circumventing the kinetic limitations, allowing the reaction to occur at lower temperatures and enabling the formation of products that are thermodynamically favored in the low temperature range. On the other hand, it might also shift the temperature at which transition to a different equilibrium composition occurs, i.e., by destabilizing molecules that would otherwise be thermodynamically favored at that temperature.

In conclusion, plasma can facilitate reactant activation on the catalyst surface, which can enhance the conversion for specific temperature ranges, depending on whether the reaction is endothermic or exothermic. For both types of reactions, a certain light-off temperature must first be exceeded to thermally activate surface reaction steps that are not directly affected by the plasma, before plasma-catalyst synergy is observed. For endothermic reactions (like DRM and SRM), plasma catalysis can subsequently circumvent the kinetic and equilibrium limitations that exist at low temperatures, yet becomes redundant at (very) high temperatures. For exothermic reactions (like NH_3 synthesis) plasma-catalyst synergy can (partially) lift the kinetic limitation at low temperatures and the equilibrium limitations at higher temperatures, although the conversion will eventually revert to the thermodynamic equilibrium if the temperature rises further.

1.7.2 Effect of plasma-catalyst synergy on trends in catalyst reactivity

The following section starts with a brief explanation of two important concepts that govern the trends in catalyst reactivity for thermal catalysis, namely scaling relations and the volcano curve (section 1.7.2.1). Next, section 1.7.2.2 explains how these trends are affected when the reactant activation step is enhanced by plasma, and section 1.7.2.3 illustrates this for the specific case of CH_4 conversion. Lastly, section 1.7.2.4 discusses

how the choice of catalyst affects the possibility of reaching product concentrations beyond the thermodynamic equilibrium.

1.7.2.1 Scaling relations and the volcano curve

An important concept in thermal catalysis is the existence of scaling relations, i.e., correlations between the adsorption energies of surface intermediates that bind to the surface through the same atom(s). For example, CH_x* species (with x = 0-3) bind to the catalyst surface via their C atom. Consequently, there exists a linear correlation (i.e., a scaling relation) between the adsorption energies of different CH_x* species (e.g., CH_3* and CH_2*) for a range of catalyst surfaces. These scaling relations exist not only for the adsorbate energies, but also for the energies of the surface transition states. Consequently, they determine the activation barriers and reaction energies of the reactions on the catalyst surface.[80]

Due to scaling between the adsorbate and transition state energies of the different reaction steps, it is generally not possible to independently vary the activation barrier (and rate constant) of a single reaction step. As such, these scaling relations often result in volcano behavior: plotting the catalyst activity vs. the binding strength of a specific adsorbate results in a curve with a maximum, usually for catalysts with intermediate binding strength. This optimum at intermediate binding strength results from a monotonic rise in the rate of reactant activation and a decline in that of product desorption with growing binding strength.[80] Since the binding strength of different transition metals depends on their reactivity, and hence their position in the periodic table, the same metals (e.g., Ni, Pt, Pd, Ir, Rh, Ru) are often located near the optimum in the volcano curve. The volcano behavior is schematically represented in Figure 1.11. While strongly binding catalysts can easily break the bonds in the reactant molecules, the formation of new bonds and product desorption from the surface is difficult. Weakly binding catalysts, on the other hand, allow for easy desorption, but struggle with

breaking bonds. Consequently, the highest reactions rates are typically achieved at intermediate binding strengths, for catalysts that have a balanced reactivity towards both reactant activation and product desorption.

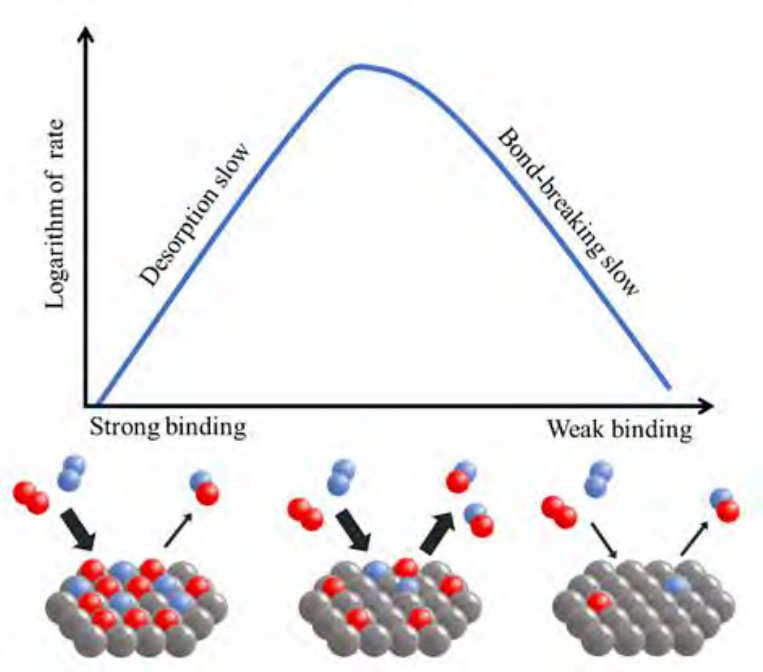

Figure 1.11. Schematic representation of volcano behavior: on strongly binding catalysts, reactant activation is facile and desorption slow, while on weakly binding catalysts, bond-breaking is difficult and desorption easy. Consequently, the optimal catalyst and highest rate are located at intermediate binding strength.[39]

1.7.2.2 Change of the volcano curve due to plasma-enhancement

As discussed in section 1.7.1, various experimental works[61,70,71] have observed a temperature dependence in the occurrence of plasma-catalyst synergy, which indicates that catalyst surface reactions play a role in the chemistry. Indeed, even when vibrational excitation lowers the barrier for reactant dissociation on the surface, a certain temperature will still be required to surpass the remaining part of the barrier. Alternatively, if reactant activation on the surface is strongly enhanced or even omitted

due to gas-phase dissociation, a subsequent surface reaction becomes rate-limiting. In this case, the new rate-limiting step needs to become thermally activated for plasma-enhancement to be effective.[72]

Since the rate-limiting reaction step changes for different catalysts, a shift of the rate-limiting step due to plasma-enhancement can also alter the optimal catalyst material. This was illustrated in a computational study by Mehta *et al.*[81] using a microkinetic model for NH_3 synthesis in which the barrier for N_2 dissociative adsorption was lowered by vibrational excitation. The authors demonstrated that enhanced N_2 dissociation can improve the rates of NH_3 synthesis, but only for catalysts that are rate-limited by N_2 dissociation. This is the case for catalysts that bind N* weakly or intermediately, such as Ru, Rh, Co, Ni, Pt and Pd, while strongly binding catalysts, like Fe, do not benefit from vibrationally excited N_2. For some of the intermediately binding catalysts (Ru and Rh), the enhancement of the N_2 dissociation step causes subsequent reaction steps to become rate-limiting. Therefore, these catalysts do not benefit further from the plasma-enhancement, and the optimum of the volcano curve shifts towards more weakly binding catalysts.[81] This is schematically presented in Figure 1.12: plasma-enhancement by vibrational excitation improves the rates for weakly and intermediately binding metals, causing a shift of the volcano maximum to more weakly binding catalysts.

The authors also support their findings with experimental results. However, it is worth mentioning that the difference in performance between the catalyst in the experiments is less extreme than predicted by the model when viewed logarithmically. This indicates that other effects, like Eley-Rideal reactions (see section 1.7.7) likely also play a role. Yet, the conclusion of this study is still important, as it illustrates how plasma catalysis can be used to circumvent the scaling relations for bond dissociation normally present in thermal catalysis, by weakening (or breaking) bonds in the plasma.[81] Similar results have

also been reported by other microkinetic studies for NH_3 synthesis,[72,82] N_2 oxidation,[30,83] non-oxidative coupling of CH_4,[84] CO_2 hydrogenation[85] and CH_4 partial oxidation.[86]

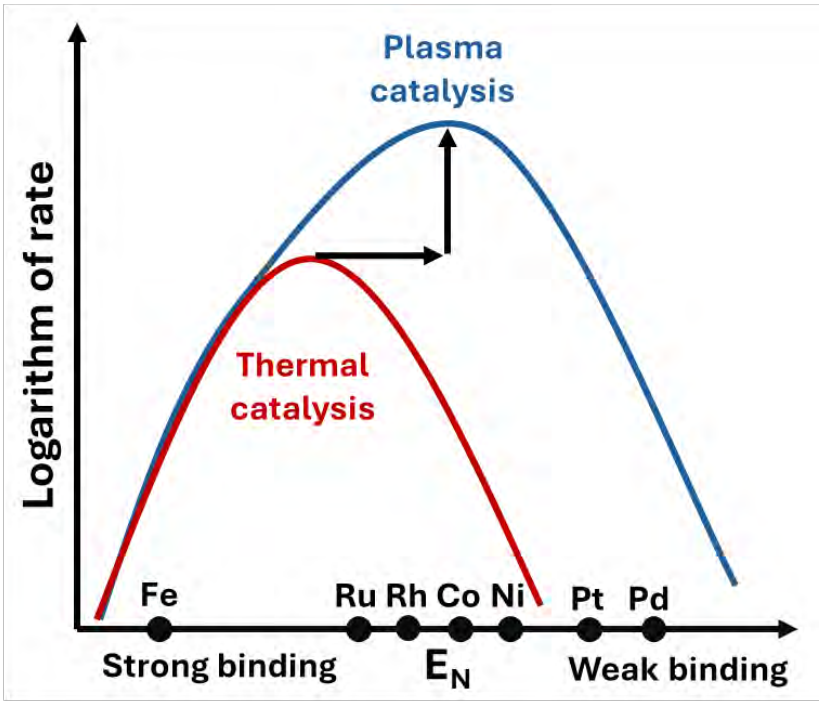

Figure 1.12. Schematic representation of the effect of N_2 vibrational excitation on the rates of NH_3 synthesis (plasma catalysis, blue curve), compared to those of thermal catalysis (red curve). The lower (or more negative) the value of E_N, the stronger the catalyst binds to N. Based on ref. 81.*

Hence, by improving the initial reactant activation step on the catalyst surface, plasma can enhance the rates on intermediately and weakly binding catalysts, which are rate-limited by this reaction step. Moreover, the enhanced reactant activation can also shift the optimum in the rate volcano to more weakly binding metals if subsequent reaction steps are easier on these catalysts.[81]

1.7.2.3 Effect of plasma-catalyst synergy on the volcano curve for CH_4 conversion

Nevertheless, it is important to keep in mind that plasma-enhancement does not necessarily shift the top of the volcano curve for all reactions. For NH_3 synthesis, the enhanced N_2 activation causes a subsequent reaction step to become rate-limiting. Because the new rate-limiting step, i.e., NH_x* hydrogenation, occurs more easily on more weakly binding catalysts, the maximum in the volcano curve will shift in that direction. However, for reactions where the new rate-limiting step does not happen more easily on the more weakly binding catalysts, a change of the optimal catalyst will not occur. This might, for example, be expected for DRM or SRM to produce syngas (CO/H_2).

Figure 1.13 illustrates the reaction and activation energies for C-H bond scission in CH_x (x = 4-2) on both Cu(211) and Ni(211) surfaces. The effect of plasma-enhanced CH_4 activation via vibrational excitation (grey arrows) and dissociation (black arrows) in the plasma is schematically represented. Although vibrationally excited CH_4 can undergo dissociative adsorption with a lower activation barrier compared to ground-state CH_4, the barrier is typically not lowered by the total energy difference between these two states. Instead, the barrier will be lowered by the energy difference multiplied with an efficiency factor between 0 and 1, as indicated by the dotted lines in Figure 1.13. Next to vibrational excitation, a molecule can also be dissociated in the plasma (black arrows), e.g., via electron impact dissociation. However, this requires a much higher energy compared to vibrational excitation and is thus less energy efficient. Yet, some dissociation in the plasma is unavoidable due to the lower threshold energies for electron impact dissociation, compared to those for electron impact ionization,[43] which is required to form and sustain the plasma.

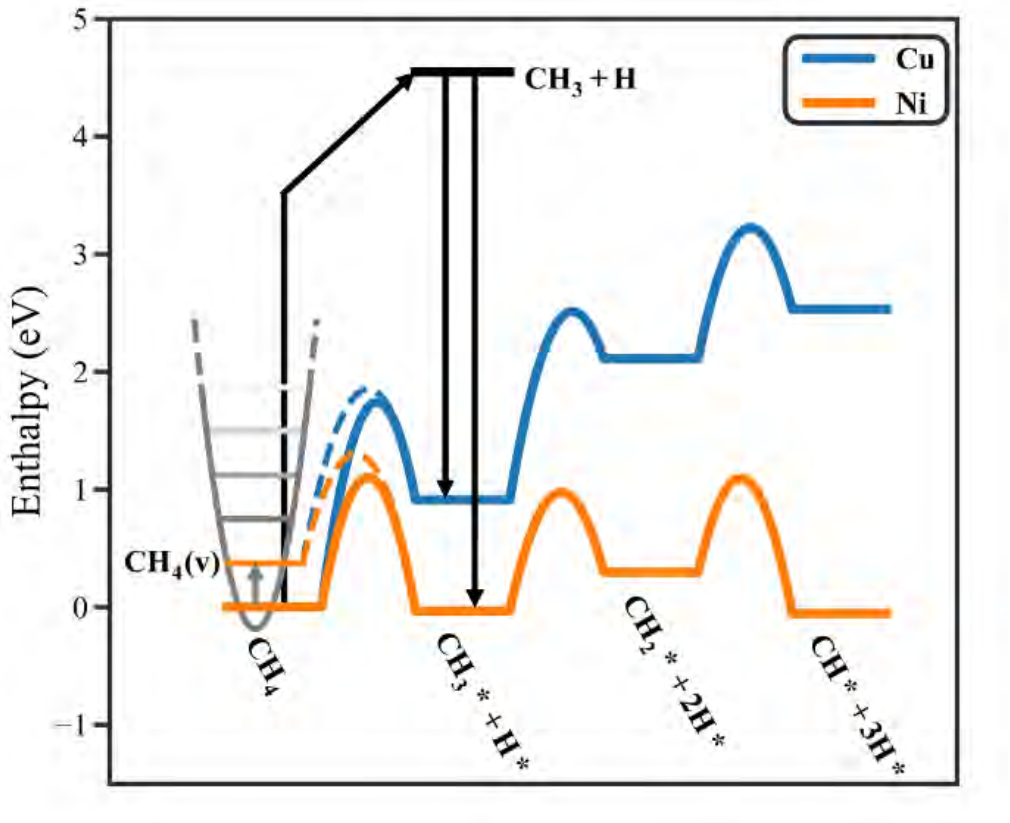

Figure 1.13. Reaction and activation enthalpies of C-H bond scission in CH_x (x = 4-2) on Cu(211) and Ni(211) surfaces. The effects of vibrational excitation and dissociation in the plasma are schematically represented with grey and black arrows, respectively. Based on data taken from the CatApp database[87] *and the NIST chemistry webbook.*[9]

As can be seen in Figure 1.13, thermal dissociative adsorption of CH_4 is much easier on Ni(211) compared to Cu(211). Indeed, Ni-based catalysts are widely used for DRM and SRM in thermal catalysis, due to their high catalytic activity for these reactions (and low price compared to Rh, Ru, Pt and Pd).[12,88] If the initial dissociation step is enhanced or omitted, because of the presence of radicals (dissociation in the plasma; black arrows in Figure 1.13), subsequent C-H bond scission steps remain. Just like the dissociation of CH_4, the CH_3* and CH_2* dissociation steps exhibit higher barriers on Cu(211), due to the

weaker binding (i.e., more noble) character of this metal. As such, it is expected that these or other bond-breaking steps will become rate-limiting on weaker binding catalysts when CH_4 dissociation is enhanced, disabling a (further) shift of the volcano maximum to lower binding strengths. This is important to consider for DRM and SRM.

The reasoning above is supported by the work of Engelmann *et al.*,[84] who constructed a microkinetic model to study the effect of vibrational excitation on CH_4 non-oxidative coupling. They found that the maximum of the CH_4 consumption volcano remains around approximately the same CH_3* binding strength if CH_4 activation is enhanced by vibrational excitation. Consequently, the intermediately binding metals, located near the volcano summit (such as Pt, Rh and Pd), still outperform the weakly binding metals (e.g., Cu, Au and Ag). Moreover, like NH_3 synthesis, the most strongly binding metals do not benefit from vibrational excitation at all, as these are rate-limited by difficult product desorption and surface poisoning.[84]

However, it is important to stress that the situation changes when plasma-produced radicals are also accounted for. Indeed, the rate volcano will change if the catalyst is in contact with complex mixtures that contain a wide variety of radicals, as will be discussed in section 1.7.6. Radicals are not only formed in the plasma through electron impact dissociation of the reactants, but subsequent gas-phase reactions also form a wide variety of other radicals. In contrast to vibrational excitation or gas-phase dissociation of the reactants, these secondary radicals can enhance other (difficult) surface reaction steps, next to the initial reactant activation step. In that case, the rates will rise considerably on the weakly binding metals (even for CH_4 conversion), and consequently, the maximum in the volcano curve will shift to the most weakly binding catalysts.[84]

Most remarkably, Engelmann *et al.*[84] also found that even though the top of the CH_4 consumption volcano does not shift much, vibrational excitation can strongly affect production rates of the individual products. Indeed, they found that the main product on

the intermediately binding catalysts (e.g., Pt, Rh and Pd) changed from C_2H_2 for thermal catalysis, to C_2H_4 when CH_4 activation is enhanced by vibrational excitation. Similarly, the main product on the most weakly binding metal (Ag) had shifted from C_2H_4 to C_2H_6. These changes in product selectivity are a consequence of the higher CH_2* and especially CH_3* coverages when CH_4 is vibrationally excited. This, in turn, is the result from the improved CH_4 dissociative adsorption on intermediately and weakly binding catalysts, in combination with their inability to further dehydrogenate these species. As such, CH_4 vibrational excitation selectively improves the production rates of C_2H_4 and C_2H_6. Hence, this study illustrates how plasma catalysis can be used to not only improve the overall reaction rate, but also to tune the product selectivity.[84]

In conclusion, enhanced reactant activation by plasma does not shift the maximum in the volcano curve to more weakly binding catalysts if the subsequent reaction steps do not happen more easily on these catalysts, as illustrated here for CH_4 conversion. In that case, plasma catalysis will mainly improve the rates for the intermediately binding catalysts near the optimum for thermal catalysis, unless additional surface reaction steps can be avoided. This might be possible due to the presence of specific radicals produced by the rich plasma chemistry, as will be discussed further in section 1.7.6. Nevertheless, while facilitating the reactant activation step does not shift the optimal catalyst in terms of CH_4 consumption, it can still be used to tune the product selectivities on the different catalysts.[84]

1.7.2.4 How the choice of catalyst affects beyond-equilibrium behavior: effect of reverse reactions

As explained in section 1.7.1, plasma-enhanced reactant activation can lead to product concentrations that exceed the thermodynamic equilibrium, because of the improved forward reaction rates. However, the product formation rates are also affected differently by plasma-enhancement depending on the catalyst, as discussed in section 1.7.2.2.

Therefore, the same applies to the possibility of achieving product concentrations beyond the thermodynamic equilibrium, as was demonstrated computationally for NH_3 synthesis by Mehta *et al*.[72] Since strongly binding catalysts do not benefit from enhanced reactant dissociation, neither can these achieve product concentrations that exceed the equilibrium composition. Weakly and intermediately binding catalysts, on the other hand, are affected by plasma-enhanced reactant activation and can thus reach product concentrations beyond the equilibrium limit. However, for exothermic reactions, like NH_3 synthesis, intermediately binding catalysts (that are optimal for thermal catalysis) revert the product concentrations to the equilibrium composition at lower temperatures. This is due to the higher catalytic activity of the intermediately binding catalysts in thermal catalysis, meaning that these catalyze both the forward and reverse reactions at a higher rate.[72]

This highlights another aspect that should be paid attention to when selecting a catalyst material, namely that thermally active catalysts are also better at destroying the products. Of course, this is mainly relevant when operating in the equilibrium-limited regime, where the products are thermodynamically unfavored. However, some products are never present in significant amounts at thermodynamic equilibrium, regardless of the temperature. This is, for example, the case for CH_3OH and other oxygenates at ambient pressure.[22] Consequently, the catalyst will stimulate the destruction of these molecules once the associated surface pathways become thermally active. As this is obviously undesired, (very) high temperatures should be avoided when aiming for these products.

Hence, when selecting an optimal catalyst for plasma catalysis, attention should be paid to the operating temperature, as catalysts that are more optimal for thermal catalysis will also catalyze the reverse reaction more efficiently. Consequently, these catalysts will

revert the gas mixture to the equilibrium composition at lower temperatures compared to more weakly binding catalysts that are less active in thermal catalysis.

1.7.3 The role of plasma species in plasma catalysis: vibrational excitation vs. radicals

As is shown in Figure 1.13, plasma can enhance reactant activation by weakening molecular bonds, thus lowering the barrier for dissociative adsorption. Alternatively, molecular bonds can be broken in the plasma, e.g., by electron impact dissociation, followed by adsorption of the formed radicals. As such, different mechanisms are possible in plasma catalysis, depending on which species are involved in the gas and surface reactions. In this framework, Rouwenhorst *et al.*[89] proposed four different mechanisms for plasma-catalytic NH_3 synthesis: (1) plasma-phase NH_3 synthesis, (2) surface-enhanced plasma-driven NH_3 synthesis, (3) plasma-enhanced semi-catalytic NH_3 synthesis, and (4) plasma-enhanced catalytic NH_3 synthesis. These mechanisms are schematically represented in Figure 1.14 (a), (b), (c) and (d), respectively.

The first mechanism involves the breaking of chemical bonds in the plasma, with the subsequent reactions occurring entirely in the gas phase (Figure 1.14 (a)). In the second mechanism, the bonds in both N_2 and H_2 are broken in the plasma, whereafter the formed radicals adsorb and react on the catalyst surface (Figure 1.14 (b)). In the third mechanism, the N_2 bond is broken in the plasma, while H_2 dissociation and the subsequent reactions occur on the surface (Figure 1.14 (c)). Lastly, in the fourth mechanism, all reactions occur on the catalyst surface, but N_2 is vibrationally excited prior to dissociating on the surface (Figure 1.14 (d)).[89]

In the same work, Rouwenhorst *et al.* compared Cs-, K- and Mg-promoted, as well as unpromoted Ru/γ-Al_2O_3 catalysts for plasma-catalytic NH_3 synthesis. The authors observed plasma-enhancement of the NH_3 synthesis rates and, interestingly, found that

the catalysts showed the same trend in reactivity as for thermal catalysis. As alkali and alkaline-earth promotors are used in thermal catalysis to improve the dissociative adsorption of N_2, this observation pointed to N_2 dissociation occurring on the catalyst. Therefore, the authors attributed the plasma-enhancement to vibrational excitation, in accordance with the mechanism for plasma-enhanced catalytic NH_3 synthesis.[89]

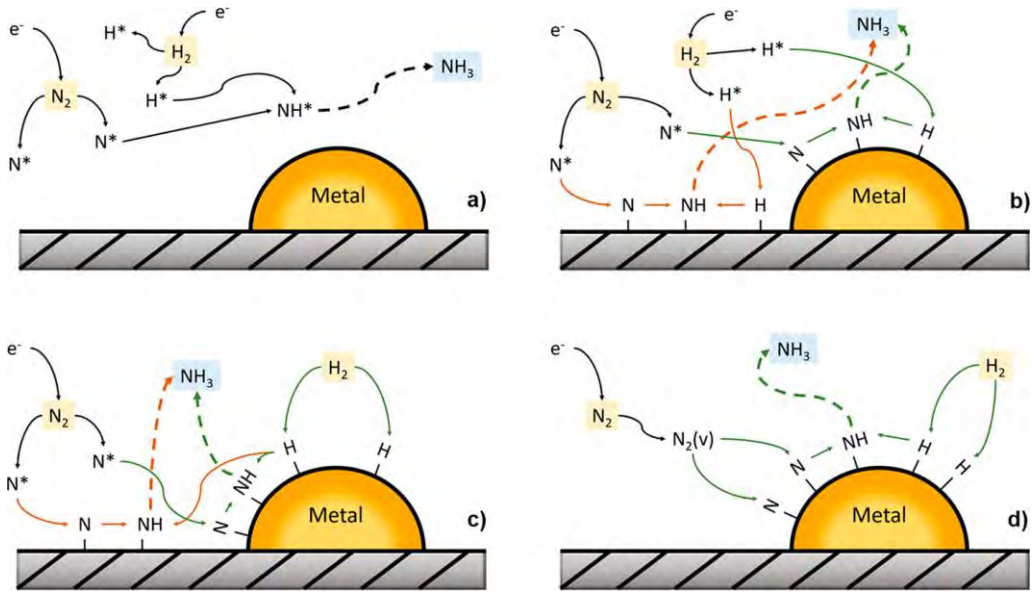

Figure 1.14. Schematic representation of different reaction mechanisms for plasma-catalytic NH_3 synthesis, namely: plasma-phase NH_3 synthesis (a), surface-enhanced plasma-driven NH_3 synthesis (b), plasma-enhanced semi-catalytic NH_3 synthesis (c), and plasma-enhanced catalytic NH_3 synthesis (d). Reactions relevant for the mechanism are depicted with full arrows, while the subsequent reaction to NH_3 is depicted with a dashed arrow. Reproduced from ref. 89. CC BY NC ND 4.0

However, in a follow-up work[71] the same authors found that plasma-catalytic NH_3 synthesis instead occurred via a radical-based mechanism in at least part of the temperature range investigated. This is illustrated in Figure 1.15, which displays the NH_3 concentration over a temperature range of 50-500 °C for an empty DBD and a DBD packed with MgO, Ru/MgO and Ru-K/MgO. As can be seen in Figure 1.15, the curves of the Ru/MgO and Ru-K/MgO catalysts start to deviate from those of the empty and MgO-

packed DBD around 125-175 °C, and synergy occurs at higher temperatures. Yet, in the temperature range between 200-300 °C, the unpromoted and K-promoted Ru/MgO catalysts show the same performance, thus indicating that N_2 dissociation does not happen on the catalyst. Hence, this points towards a radical-based mechanism. At temperatures above 300 °C, the activities of the catalysts start to deviate, indicating that enhancement by vibrational excitation also becomes important.[71] We can thus conclude that plasma-enhancement can happen both via radicals and vibrational excitation. Moreover, the dominant mechanism may vary depending on the temperature.

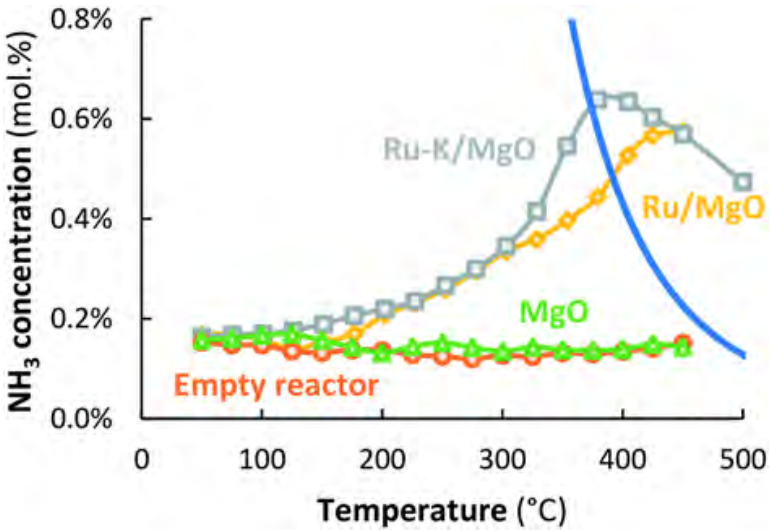

Figure 1.15. Activity for plasma-catalytic NH_3 synthesis at different temperatures for the empty reactor (orange circles) and the reactor packed with MgO (green triangles), Ru/MgO (yellow diamonds), and Ru–K/MgO (grey squares). Reaction conditions: total flow rate of 20 mL min^{-1}, 1:1 H_2/N_2 feed mixture, 130 mg catalyst loading and a plasma power of 3.8 W (SIE = 11.4 kJ L^{-1}). Reproduced from ref. 71 with permission from the Royal Society of Chemistry. CC BY 3.0

A temperature dependence of the mechanism for plasma-enhancement (i.e., radicals vs. vibrational excitation) is consistent with the idea that vibrational excitation only partly lowers the barrier for reactant dissociation. This is also depicted in Figure 1.13 for CH_4, i.e., vibrational excitation only lowers the barrier for dissociative adsorption, so a certain

temperature is still required to surpass the remaining part of the activation barrier. For plasma-enhancement by radicals, the dissociation occurs in the plasma and the radicals can adsorb onto the surface without having to surpass an enthalpy barrier. For the radical-based mechanism, the rate will thus depend on the radical density and on how facile the subsequent surface reactions can occur at the specified temperature. As such, we can interpret the results in Figure 1.15 as follows. Plasma-enhancement becomes effective around 125-175 °C, when the NH_x* hydrogenation and NH_3 desorption steps become thermally active. Up to 300 °C, plasma-enhancement is driven by radicals, which can adsorb and form surface-bound N* and H*, regardless of temperature. At temperatures above 300 °C, the dissociation of vibrationally excited N_2 becomes possible, further enhancing NH_3 formation.

This reasoning is also supported by kinetic modeling results from Ma *et al.*[83] for plasma-catalytic N_2 oxidation on Pt(211) and Au(211) surfaces. Their model showed that both Pt and Au benefit from the presence of radicals, while vibrational excitation only has an appreciable effect on Pt. Indeed, Pt, as an intermediately binding catalyst, has lower barriers for N_2 (and O_2) dissociation (2.55 and 0.17 eV, resp.) compared to the more weakly binding Au (6.52 and 1.45 eV, resp.). The combination of the already lower barriers on Pt with vibrational excitation could result in significant rates on this catalyst ($\approx 10^{-2}$ s^{-1}), while the rate on Au remained low ($< 10^{-15}$ s^{-1}) in the absence of radicals. Therefore, vibrational excitation and radicals gave comparable rates on Pt at high temperature (1000 K), while at low temperature (625 K) the radical-based mechanism resulted in the highest rates. On Au, on the other hand, the radical-based mechanism remained dominant in the entire temperature range between 625-1000 K. In addition, the model showed that due to the stronger binding character of Pt, relative to Au, Pt also required higher temperatures for the desorption step to become thermally active. Consequently, Au outperformed Pt at low temperature (300 K) in the presence of

radicals, while Pt performed better than Au at high temperature (900 K) in the presence of vibrationally excited molecules.[83]

To summarize, plasma-enhancement by vibrational excitation is expected to be mainly relevant for intermediately binding catalysts at high temperature, while radicals are more important for intermediately binding catalysts at intermediate temperatures or for weakly binding catalysts in the entire temperature range. The observation that vibrational excitation has a negligible effect compared to plasma radicals at typical DBD temperatures (400-500 K) is also supported by other microkinetic modeling studies.[84–86] Of course, this will also depend on the vibrational temperature and the radical densities in the plasma.

1.7.4 Quantifying plasma-catalyst interactions

Due to the different possible mechanisms in plasma catalysis, as well as the complex plasma chemistry that occurs in tandem with the modified surface processes, a direct comparison of different catalysts is cumbersome. Kinetic studies that present methods for quantifying plasma-catalyst interactions can therefore aid in the comparison of catalyst materials and provide fundamental insight into the mechanisms of plasma catalysis. For example, Sheng *et al.*[90] determined activation barriers for DRM in thermal catalysis, as well as plasma catalysis operated at two different frequencies (12 and 100 kHz). These authors observed a strong decrease in the activation barrier for plasma catalysis at 100 kHz (44.7 kJ/mol) compared to thermal catalysis (91.2 kJ/mol) and plasma catalysis at 12 kHz (83.2 kJ/mol), which was attributed to accumulation of vibrationally excited species and their interaction with the catalyst.[90] Hence, apparent activation barriers might be used as a measure for the synergistic effect between plasma and catalyst. In this regard, modified Arrhenius equations have been developed that enable calculation of apparent activation barriers for plasma-catalytic reactions on specific catalysts.[89,91,92] In some studies[91,92] a modified Arrhenius behavior was reported in which

the logarithm of the corrected reaction rate coefficient follows a linear correlation with the inverse of the specific energy input (SEI). A correction for the contribution of gas-phase reactions was applied by subtracting reactant consumption rates measured in a support-packed DBD from those of the plasma-catalytic case. Using this method, a strong reduction in apparent activation barriers was observed for plasma-catalytic DRM[92] and CO_2 hydrogenation,[91] relative to thermal catalysis (i.e., from 73.5 kJ mol^{-1} to 6.1-18.6 kJ mol^{-1} and from 68-113 kJ mol^{-1} to 21-43 kJ mol^{-1} for DRM and CO_2 hydrogenation, respectively). In a different study,[89] a modified Arrhenius equation was developed based on activity (i.e., amount of product formed per unit of time and amount of catalyst) divided by SEI. The logarithm of this quantity was observed to scale linearly with the inverse of temperature, and apparent activation barriers between 20-40 kJ mol^{-1} were determined for plasma-catalytic NH_3 synthesis on different catalysts (compared to 60-115 kJ mol^{-1} for thermal catalysis).[89] The presence of the SEI in both abovementioned equations illustrates the dependency of plasma-catalyst synergy on plasma species (like vibrationally excited molecules and radicals), as low SEI's produce less plasma species and thus enhance the surface reactions less efficiently.

However, a higher SEI can also result in stronger plasma-induced heating,[93] which could be responsible for the improved catalytic rates. While some plasma catalysis studies have reported that the effect of plasma-induced heating was not substantial enough to cause the observed synergy, this conclusion was often based on indirect measurements or estimations.[70,89,94] Nevertheless, recently, some experimental methods have been developed for direct, in situ measurement of the catalyst surface temperature. Moreover, these techniques do not require the insertion of, e.g., a thermocouple into the discharge region, and thus do not affect the plasma.[34,95,96]

Gibson *et al.*[95] constructed an experimental setup for in situ X-ray absorption of plasma-catalytic CH_4 partial oxidation with Pd/Al_2O_3 and found that the temperature of the

catalyst could be determined from the mean squared thermal disorder parameter, which corresponds to a change in the amplitude of oscillations of the extended X-ray adsorption fine structure of the catalyst. Parastaev *et al.*[96] developed a method for in situ measurement of the catalyst surface temperature based on thermally induced changes in absorption intensity of the 420 nm band of rutile TiO_2. Most recently, Van Turnhout *et al.*[34] developed a method to measure surface temperatures based on a downward shift of the band at 1965.9 cm^{-1} of $BaTiO_3$, which was added as an internal standard to the support. While in ref. 96 plasma-induced heating was reported to be negligible, refs. 95 and 34 reported surface temperatures up to 207 °C and 150 °C, respectively. Yet, these temperatures were still insufficient to thermally activate the catalysts. As such, these studies support the idea that plasma-enhancement of catalytic reactions is due to reactive plasma species, and not due to surface heating. Moreover, plasma-induced heating would not explain the beyond-equilibrium conversions observed for exothermic reactions, such as NH_3 synthesis, that are equilibrium-limited at higher temperatures.[71]

Hence, both experimental kinetic studies, as well as direct measurements of the surface temperature in plasma catalysis experiments indicate that plasma-catalyst synergy occurs due to interactions of reactive plasma species with the catalysts surface. Moreover, kinetic studies provide methods to directly compare the performance of different catalysts, i.e., by determining apparent activation barriers from modified Arrhenius equations, while direct measurements of the catalyst temperature are necessary to correct for plasma-induced surface heating.

1.7.5 Tailoring the selectivities towards oxygenates

A fundamental understanding of the mechanisms by which plasma catalysis alters the product selectivities for different catalysts is particularly important when aiming for products that are not thermodynamically favored, like CH_3OH and other oxygenates. Indeed, the conversion of greenhouse gases (i.e., CO_2 and/or CH_4) into oxygenates is

thermodynamically disfavored due to the higher stability of CH_4/CO_2 at low temperatures (< 900 K) and CO/H_2 at high temperatures (> 900 K) (also see section 1.2, Figure 1.1 (b)).[22]

The role of plasma in plasma catalysis is to activate thermodynamically stable reactants, such as CO_2 and CH_4, by converting these into highly energetic (and thus thermodynamically unstable) plasma species, like radicals, ions, and vibrationally and electronically excited species. Next, the catalyst should facilitate the reaction pathways that form the desired end-compounds from these plasma species. However, if CH_3OH (or another oxygenate) is the desired product, the catalyst should be inactive for any subsequent reaction steps that convert CH_3OH into more thermodynamically stable products. As discussed above, syngas (CO/H_2), CH_4 (for CO_2 hydrogenation) or CO_2 (for POX) can be competing products that are thermodynamically favored over CH_3OH. Moreover, the catalyst should also avoid back-reactions of the formed plasma species or oxygenate intermediates into the reactants (CO_2 and/or CH_4). As such, a good understanding of the influence of different catalysts on the surface reaction pathways is of great importance.

This section therefore aims to provide insight into the effect of the catalyst material on the product selectivities, with a focus on oxygenate production, based on results from plasma-catalytic CO_2 hydrogenation. The following subsections will first discuss observations from plasma-catalytic CO_2 hydrogenation on Cu and Ni, and link these to insights in catalyst selectivity from thermal-catalytic CO hydrogenation (section 1.7.5.1) Next, section 1.7.5.2, presents the hydrogenation of plasma-produced CO as an important pathway for plasma-catalytic CO2 hydrogenation. Lastly, section 1.7.5.3 discusses other potential pathways for plasma-catalytic CO_2 hydrogenation.

1.7.5.1 The role of the catalyst in tuning the selectivity

As discussed in section 1.7.1, the mechanism by which plasma catalysis improves the conversion depends on temperature. Similarly, any synergistic effects on the selectivities and yields may be influenced by the reaction temperature. This was, for example, observed in experiments on plasma-catalytic CO_2 hydrogenation by Eliason *et al.*[97] The authors studied the temperature dependence of the CH_3OH yield for thermal and in-plasma catalysis with a $CuO/ZnO/Al_2O_3$ catalyst, as well as for an empty DBD. They found that for both thermal and plasma catalysis the curve of the CH_3OH yield showed a maximum. Yet, for plasma catalysis this maximum was located at a lower temperature compared to thermal catalysis. Consequently, the catalyst combined with a DBD plasma gave higher CH_3OH yields below approximately 170 °C, while thermal catalysis performed better at higher temperatures. DBD plasma without catalyst, on the other hand, gave a negligible CH_3OH yield over the entire temperature range (80-250 °C), showing that the catalyst was essential for CH_3OH formation.[97]

The drop in the plasma-catalytic CH_3OH yield towards higher temperatures could be attributed to competitive formation of CH_3OH and CH_4. Indeed, like the CH_3OH yield, its selectivity also showed a maximum between 80-100 °C and subsequently declined at higher temperatures. This decline was accompanied by a rise in CH_4 selectivity. Hence, these results indicate that DBD plasma can enhance both the formation of CH_3OH and CH_4 when combined with $CuO/ZnO/Al_2O_3$, albeit in different temperature ranges.[97]

The role of the catalyst in tuning product selectivity for plasma-catalytic CO_2 hydrogenation was also illustrated by Ahmad *et al.*[98] They found that at 150 °C a DBD plasma without catalyst mainly produced CO (75-80% selectivity), while the presence of a Ni/Al_2O_3 catalyst in a post-plasma, thermal and in-plasma catalysis setup gave high CH_4 selectivities (> 90%). This clearly demonstrates that the Ni/Al_2O_3 catalyst was essential in achieving high CH_4 selectivity. Moreover, only the in-plasma catalysis setup showed

significantly enhanced CO_2 conversion, illustrating a synergistic effect between the plasma and catalyst. However, if the temperature was raised to 400 °C, the synergy disappeared and a similar conversion was attained for both thermal and in-plasma catalysis.[98]

In the abovementioned works, the role of the catalyst in steering the selectivities towards CH_3OH or CH_4 seems to correspond well with observations from thermal-catalytic CO hydrogenation. Indeed, it is known that for thermal-catalytic CO hydrogenation weakly binding catalysts, like Cu, favor CH_3OH production, while more strongly binding catalysts, like Ni, Rh, Ru and Ir, are selective towards CH_4.[26,99,100] This is because the weakly binding catalysts are unable to break the C-O bond and therefore cannot form CH_4, thus forming CH_3OH instead. The more strongly binding catalysts, on the other hand, can more easily break bonds and thus form CH_4 and H_2O.[26,99,100]

In conclusion, the choice of catalyst can be used to steer the product selectivities of plasma-catalytic CO_2 hydrogenation, with a Cu-based catalyst enabling CH_3OH formation, while Ni preferentially forms CH_4. These observations correspond well with insights from thermal-catalytic CO hydrogenation, for which weakly binding catalysts (e.g., Cu) selectively produce CH_3OH, as these are unable to break the strong C-O bond, while strongly binding catalysts (e.g., Ni) can break the C-O bond and form CH_4. However, other factors, like temperature, also play a role in tuning the selectivities, as illustrated by ref. 97.

1.7.5.2 Hydrogenation of plasma-produced CO as a mechanism for plasma-catalytic CO_2 hydrogenation

In both works on plasma-catalytic CO_2 hydrogenation discussed in the previous section (1.7.5.1), CO is observed as the main C-based product for plasma-only conditions.[97,98] As such, it is likely that part of the CH_3OH and CH_4 produced by plasma catalysis can be

attributed to CO_2 dissociation in the plasma, followed by CO hydrogenation reactions on the catalyst surface. This conclusion is also supported by experimental[91,96,101] and modeling studies.[85]

For example, Parastaev *et al.*[101] used isotopic labelling in combination with temperature programmed reaction and found that pre-adsorbed $^{13}CO_2$ did not form $^{13}CH_4$ at temperatures below 100 °C, while formation of $^{12}CH_4$ from $^{12}CO_2$ in the gas phase did happen at lower temperatures. However, CH_4 formation only occurred when a $Co/CeZrO_4$ or $Cu/CeZrO_4$ catalyst was present in the DBD and not for the empty or $CeZrO_4$-packed reactor. Hence, this study shows that at temperatures below 100 °C, gas-phase CO_2 was converted into CO, which adsorbed and formed CH_4 on the catalyst. In a follow-up study,[96] the same authors provided further support for this hypothesis, based on the presence of surface carbonyl (CO*) groups observed with in situ diffuse reflectance infrared Fourier transform spectroscopy (DRIFTS). In addition, Xu *et al*.[91] also found that CO was a key intermediate in plasma-catalytic CO_2 hydrogenation over Ru/MgAl-LDH catalysts, based on combined in situ DRIFTS and mass spectrometry (MS) analysis. These authors proposed a mechanism in which CO_2 dissociates partly in the gas phase and partly on the surface, followed by reaction of the formed CO on the surface to produce CH_4 via CHO*, COH* and CH_xO* intermediates. Furthermore, in a microkinetic modeling study by Michiels *et al.*,[85] hydrogenation of plasma-produced CO on Cu(111) was found to be one of the pathways that lead to enhanced CH_3OH production for plasma catalysis, relative to thermal catalysis. Hence, these studies illustrate that CO, which can be formed from dissociation of CO_2 in the plasma, is an important intermediate in plasma-catalytic CO_2 hydrogenation to CH_3OH and CH_4.

The high selectivity towards CH_4 observed for strongly binding catalysts, like Ni,[98] Co[96,101] and Ru,[91] and the formation of CH_3OH on weakly binding catalysts, like Cu,[97] is also consistent with the trends in selectivity for CO hydrogenation. However, in ref. 97 CH_4

became favored over CH_3OH at higher temperatures, while in ref. 101 $Cu/CeZrO_4$ formed CH_4 and CO as the main products. Yet, CH_4 formation on $Cu/CeZrO_4$ happened with lower selectivity and required higher temperatures (> 350 °C) compared to the more strongly binding $Co/CeZrO_4$ catalyst, consistent with the trends in catalyst reactivity for CO_2 methanation.[101] Additionally, the plasma-catalytic CO hydrogenation to CH_4 on $Co/CeZrO_4$ observed in refs. 96,101 is not possible at ambient temperature in thermal catalysis. Moreover, thermal-catalytic CO hydrogenation to CH_3OH also requires both high temperatures (200-300 °C) and pressures (30-120 atm) to kinetically activate the reaction and drive the equilibrium composition towards CH_3OH, respectively.[22,100] Hence, this illustrates that plasma does not only facilitate CO_2 hydrogenation by dissociating CO_2 in the gas phase, but also enhances subsequent hydrogenation of the formed CO by adsorbed H* radicals on the catalyst surface. As such, plasma enables the formation of CH_4 on both weakly and strongly binding catalysts, as well as the formation of CH_3OH on weakly binding catalysts under conditions for which the catalysts are inactive for thermal-catalytic CO/CO_2 hydrogenation.

In the case of CH_4 formation, the plasma-enhancement may be attributed to vibrational excitation or electron impact dissociation of CO, which facilitates breaking of the C-O bond. Notably, in ref. 96 it is suggested that adsorbed CO* dissociates on the catalyst due to electrons impacting the surface. Additionally, the plasma might also enable any formed CH_3OH to undergo consecutive reactions, e.g., due to reaction with radicals or by electron impact processes, which may limit the CH_3OH yield and lead to CH_4 formation.

To summarize, plasma can dissociate CO_2 into CO, which can subsequently be hydrogenated on the catalyst to either CH_3OH or CH_4. Moreover, this catalytic CO hydrogenation pathway is also facilitated by plasma-catalyst synergy. This allows us to understand how the choice of catalyst affects the selectivities in plasma-catalytic CO_2 hydrogenation. While weakly binding catalysts form CH_3OH in thermal catalysis, plasma

catalysis can enhance both the surface hydrogenation steps, and to some extent the dissociation of the C-O bond, thus enabling both CH_3OH and CH_4 production on these catalysts at ambient conditions. The more strongly binding catalysts, on the other hand, remain selective to CH_4, while plasma-catalyst synergy only enhances the production rates.

1.7.5.3 Other pathways for plasma-catalytic CO_2 hydrogenation

Finally, other pathways for plasma-catalytic CO_2 hydrogenation have also been reported. For example, in ref. 91 the calcination temperature of the catalyst was found to affect the mechanism of plasma-catalytic CO_2 hydrogenation. Next to the CO hydrogenation pathway, an additional surface pathway was reported for the catalyst calcined at high temperature (600 °C). In this pathway, CO_2 reacts with surface OH groups to form carbonate and bicarbonate species that subsequently react to HCOO* (formate), which forms CH_4 after multiple hydrogenation steps.[91] The modeling results presented in ref. 85 also showed additional pathways through which plasma-catalytic CH_3OH production could occur, next to CO hydrogenation. The HCOO* pathway, starting from CO_2 and adsorbed H*, was found to be the most important route for CH_3OH formation. This pathway was enhanced due to higher H* coverages, resulting from the presence of H radicals formed by the plasma. In addition, the model also predicted some surface HCOO* formation to occur through reaction between adsorbed O* radicals and CHO*. Note that CHO* is the first intermediate in the CO* hydrogenation route. Additionally, vibrational excitation of CO_2 was found to reinforce the impact of plasma-generated radicals, by lowering the activation barrier of the reaction between gas-phase CO_2 and surface H* to HCOO*.[85] The lower activation barriers for HCOO* production from vibrationally excited CO_2 were implemented based on the observations by Quan *et al*.[102] These authors found that vibrational excitation of the CO_2 bending mode facilitates the Eley-Rideal (E-R) type reaction between CO_2 and adsorbed H* to produce surface HCOO*

on Cu(111) and Cu(100) surfaces. Their findings were based on both molecular beam experiments and density functional theory (DFT) calculations. Interestingly, these results illustrate that vibrational excitation can also enhance associative reactions to activate gas molecules on the surface and not only dissociative adsorption.[102] Furthermore, Kim *et al*.[103] demonstrated both experimentally and computationally that CO_2 hydrogenation on a Pd_2Ga/SiO_2 catalyst happens via reaction between vibrationally excited CO_2 and adsorbed H* to form HCOO*, which subsequently decomposes to CO*. In addition to the gas-phase dissociation of CO_2, followed by subsequent hydrogenation of adsorbed CO*, and conversion of CO_2 on the surface via the HCOO* route, the surface-catalyzed reverse water-gas shift (RWGS) reaction via a carboxyl intermediate (COOH*) has also been proposed as a possible pathway in plasma-catalytic CO_2 hydrogenation.[104]

Hence, next to hydrogenation of plasma-produced CO (discussed in section 1.7.5.2) there exist several other pathways through which plasma-catalytic CO_2 hydrogenation can occur, such as the RWGS reaction and variations on the CHOO* route. These pathways may benefit from enhanced H* coverages due to adsorption of plasma-produced radicals. In addition, vibrationally excited CO_2 can also improve the E-R reaction between gas-phase CO_2 and adsorbed H*.

1.7.6 Complex mixtures of radicals

As already discussed in section 1.7.3, plasma can enhance catalytic reactions by lowering the barrier for reactant activation on the surface (e.g., due to vibrational excitation) or by dissociating the molecules in the plasma to form radicals. However, radicals produced via electron impact dissociation will also participate in further gas-phase reactions, resulting in a wide distribution of radicals and stable intermediates that is characteristic of a plasma. In principle, all these species can adsorb and participate in the catalyst surface chemistry. This might allow to bypass several difficult surface reactions or enable

new surface pathways that are not active in thermal catalysis. The optimal catalyst then becomes dependent on the plasma composition.

Using microkinetic modeling, Engelmann *et al.*[84] demonstrated that for catalysts exposed to radical densities representative of a CH_4 DBD plasma, the highest production rates can be achieved on the most weakly binding metals (such as, Ag, Au and Cu). Hence, the volcano maximum shifts entirely to the catalysts with the weakest binding strengths due to the strongly improved turnover frequencies (TOFs) on these catalysts, when exposed to radicals. This is because the rates on the surface are no longer limited by bond-scission. Indeed, the radicals and intermediates in the gas-phase (e.g., H_2, CH_x (x = 0-4) and $C2H_x$ (x = 1-6)) can simply adsorb onto the surface and undergo C-C coupling or hydrogenation to form stable products. As such, a lower binding strength results in higher rates, as it allows for facile recombination of the adsorbed radicals, as well as easy desorption of the products.[84]

However, it should be noted that while the most weakly binding catalysts give the highest rates in the presence of gas-phase radicals, they do not necessarily give a good selectivity for the desired product(s). Instead, the selectivities on these weakly binding catalysts will be strongly determined by the composition of the plasma, as well as the activation barriers for the different recombination processes relative to each other. For some reactions, further bond-scission in the radicals might be needed to attain the desired products. For example, CO formation from CH_4 in DRM and SRM requires that all four C-H bonds in CH_4 are broken. For such cases, a more strongly binding catalyst might be more desirable. Yet, this would also require higher operating temperatures to thermally activate the remaining bond scission steps on the surface, as well as product desorption from the catalyst.

Nevertheless, as mentioned above, the plasma composition will strongly affect the dominant reaction pathways on the surface. Moreover, these surface reactions can in

turn produce new molecules and therefore alter the gas composition as well. Thus, to obtain more insight in the combined plasma-catalyst chemistry, models must be developed that couple the reactions on the catalyst surface to those in the plasma. Maitre *et al.*[105] developed such a coupled model for plasma-catalytic CH_4 non-oxidative coupling over a Ni(111) surface. Interestingly, these authors found that plasma catalysis could briefly achieve improved turnover frequencies compared to plasma alone and thermal catalysis. Yet, this synergy was only temporal, and at steady-state plasma without catalyst outperformed plasma catalysis at all temperatures investigated (300-600 K). The model showed that H radicals produced in the plasma absorbed and saturated the surface, enabling quick hydrogenation of surface-bound CH_3* back to CH_4.[105]

Similarly, adsorption and recombination of CH_3 and H radicals back to CH_4 was also observed in the aforementioned study by Engelmann *et al.*[84] Like the other radical recombination reactions on the catalyst surface, back-reaction to CH_4 occurs more easily on the most weakly-binding metals. This is also schematically presented in Figure 1.16, which shows that the barrier for recombination of CH_3* and H* to CH_4 is lower on Cu(211) than on Ni(211). Moreover, on Cu(211) the activation barrier for CH_3*+H* recombination is also lower compared to that of CH_3* dissociation, while on Ni(211) the barriers of both reactions are similar. Hence, Cu will mainly recombine CH_3* and H*, while on Ni both reactions are expected to compete. As such, a large fraction of plasma-produced CH_3 and H radicals that diffuse to the surface possibly do not contribute to product formation, but instead recombine again into the reactants.

In summary, plasmas are complex mixtures of different reactive species and thus typically contain a wide variety of radicals. Consequently, adsorption and subsequent reaction of these radicals on the catalyst allows to circumvent additional surface reactions next to the initial reactant activation step. As such, the surface reactions strongly depend on the

densities of the radicals in the plasma. This is especially true for the most weakly binding catalysts (e.g., Cu, Ag, Au) which can recombine the radicals very efficiently. However, this does not mean that these weakly binding catalysts are necessarily the most optimal catalysts, as they can also induce back-reactions due to fast recombination of radicals to the reactants. As such, a thorough understanding of the effect of different radicals on the surface pathways is crucial, so that the gas mixture and plasma conditions can be chosen to maximize the formation of desired products and avoid unwanted back- and side-reactions.

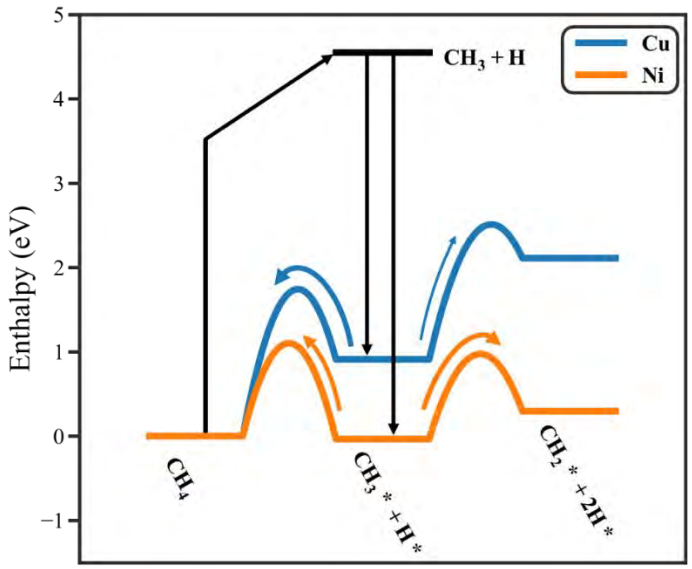

Figure 1.16. Reaction energy diagram of C-H bond scission in CH_4 and CH_3 on Cu(211) and Ni(211) surfaces. Based on data from the CatApp database[87] and the NIST chemistry webbook.[9] The black arrows represent dissociation of CH_4 into CH_3 and H radicals by the plasma and their subsequent adsorption onto the catalyst. The adsorbed CH_3* and H* can then recombine back to CH_4 or dissociate further to form CH_2* + 2H*. On Cu(211), the activation barrier for recombination of these adsorbates is clearly lower compared to that of CH_3* dissociation, while on Ni(211) the barriers of both reactions are similar. As indicated by the weight of the blue (Cu) and orange (Ni) arrows, recombination will be the main reaction on Cu, while on Ni both recombination and further dissociation can occur.*

1.7.7 Eley-Rideal (E-R) reactions involving radicals

In addition to adsorption of radicals from the plasma and subsequent surface reaction via a Langmuir-Hinshelwood (L-H) type mechanism, the highly reactive radicals may directly react with pre-adsorbed surface species via E-R type reactions.

In this thesis, we will use the term "Eley-Rideal" to refer to a reaction between a surface adsorbate and an impinging gas species. Note, however, that the correct name for this type of reaction should actually be Langmuir-Rideal reaction, as Langmuir was the first to describe this mechanism, while Eley and Rideal studied the reaction between a physisorbed and a chemisorbed species.[106] However, in literature the name "Eley-Rideal" is typically used to refer to the reaction between a gas and an adsorbed species, hence we will keep referring to this reaction as the Eley-Rideal (E-R) mechanism.

Engelmann *et al.*[82] used a microkinetic model for NH_3 synthesis to illustrate the potential effect of E-R reactions involving radicals. Their model showed that if plasma radicals can directly react with surface adsorbates with no enthalpic activation barrier, the volcano behavior of the catalyst activities disappears entirely. While weakly binding catalysts (e.g., Cu, Au and Ag) can quickly adsorb radicals and let them recombine via L-H reactions, coupling between surface adsorbates this way is difficult on strongly binding catalysts (such as Fe and Ru). This leads to high surface coverages on the more strongly binding metals, poisoning the surface. However, facile E-R reactions with radicals would allow for high reaction rates, even on catalysts that are strongly covered by adsorbates. This was found to result in similar reaction rates on weakly and strongly binding metals exposed to radicals.[82] This prediction was supported by the experimental work of Gorbanev *et al.*,[107] who observed that different Al_2O_3-supported transition metal catalysts gave a similar performance in plasma-catalytic NH_3 synthesis. Moreover, the same behavior was also observed in other experiments.[48,81,108,109] Similarly, modeling

work by Hong *et al.*[110] and van 't Veer *et al.*[111] also indicated that E-R reactions may play an important role in plasma-catalytic NH_3 synthesis.

Hence, E-R reactions may also have a significant impact on the plasma-catalytic conversion of CH_4 and CO_2. Indeed, E-R reactions between H (or D) atoms and various C- or O-containing adsorbates (e.g., CO*, CHO*, HCOO*, O*, OD*, CD_3* and cyclo-hexane) have been observed experimentally by impinging H or D radicals on pre-covered transition metal surfaces, although at temperatures and pressures well below ambient conditions.[112–114] However, there is still much uncertainty around the kinetics and products of most E-R reactions involving polyatomic radicals or adsorbates, especially at conditions relevant for plasma catalysis. Some studies have proposed that CH_3OH formation in plasma catalysis may be partly attributed to E-R reactions, like $CH_3(g) + O^* \rightarrow CH_3O^*$, and $CH_3O^* + H(g) \rightarrow CH_3OH(g)$.[79,86,115] Still, it is important to consider that other products could result from the same reactant species and may even be more important. For example, radicals impinging on large poly-atomic adsorbates might be more tended to react with the top part of the adsorbate, if the surface-bound atom is difficult to reach due to steric effects. For example, it has been experimentally shown that impinging D atoms can abstract H atoms from cyclohexane adsorbed on Cu(111).[112]

Furthermore, Michiels *et al*.[116] studied E-R reactions between an impinging H atom and various adsorbates (CH_x, NH_x, OH_x and CO), by constructing potential energy surfaces (PES) using DFT calculations. They found adsorption to be more probable than reaction via a hot atom mechanism, which in turn is more probable than E-R reactions. Moreover, adsorbates that are more sterically hindered were found to be less likely to react via the E-R mechanism. The authors also reported that the probability of the E-R reactions rises with the surface coverage for monoatomic adsorbates. Yet, for polyatomic adsorbates the effect of coverage depends on the adsorbate, and for some adsorbates the total

reaction probability even declines with rising coverage. Lastly, their results indicated that the E-R probability may vary depending on the choice of transition metal (e.g., weakly or strongly binding).[116]

To conclude, E-R reactions between gas-phase radicals and adsorbates are likely important in plasma catalysis, and may partly explain the similar reactivity for vastly different catalysts, as observed experimentally.[48,81,107–109] Yet, currently not much is known about these reactions, and kinetic models of plasma-catalytic systems often make assumptions that overestimate their importance.[116] Therefore, more fundamental research on the kinetics and product distribution of E-R reactions involving radicals is required to implement these reactions into microkinetic models in a more reliable way.

1.7.8 Radicals reaching the catalyst surface

Whether or not radicals and other plasma species can partake in the catalyst surface chemistry of course depends on the flux of these species to the surface. On one hand, this depends on the distance between the plasma and the catalyst, which for a packed-bed DBD depends on the discharge type (i.e., localized microdischarges between the packing beads or surface discharges spread over the surface of the beads). In addition, the local electric field and electron density determine the occurrence of electron impact processes, and consequently also the densities of different plasma species. As discussed in section 1.6, the discharge behavior can be strongly influenced by, among others, the properties (e.g., dielectric constant,[23,40,41,49–51,69] pore diameter,[57] bead size[50,51]) of the packing material, the size of the discharge gap,[49,51,69] the presence of metal nanoparticles[40,45–47] and the amount of metal loading.[46,47] On the other hand, the lifetime of the plasma species will determine whether they can survive long enough to travel from the bulk plasma to the surface, or inside the pores of the support where catalyst nanoparticles may be deposited, as discussed in section 1.6.4.

This aspect was considered by Jiang *et al.*,[94] who studied CH_4 partial oxidation to oxygenates using an experimental setup with a Fe/γ-Al_2O_3 catalyst placed downstream of a plasma jet at either 5 or 30 mm distance. This enabled to distinguish the effect of short-lived species, like radicals, and long-lived plasma produced species, respectively. Only at the shortest distance, enhanced CH_3OH and CO_2 production were observed. The authors postulated that even for a plasma that is in direct contact with the catalyst, plasma-species should have a sufficiently long lifetime to traverse the plasma sheath and diffuse from the bulk of the plasma to the catalyst surface. Based on measurements with molecular beam mass spectroscopy and estimates of the lifetimes of different radical species, the authors subsequently proposed that CH_3OO was responsible for the synergistic effect of plasma catalysis on CH_3OH production.[94]

Moreover, the situation is even more complex for a DBD plasma due to the periodic occurrence of short-lived microdischarges. As such, the operating conditions of the DBD should be tuned to optimize the production and number densities of specific species in the gas-phase. This was illustrated by Sheng *et al.*,[90] who found that applying a high-frequency (100 kHz) DBD plasma leads to a strong plasma-catalyst interaction for high-temperature (400-700 °C) plasma-catalytic DRM over a La-modified Ni/Al_2O_3 catalyst. On the other hand, only a weak plasma-catalyst interaction was observed when a low frequency (12 kHz) was used. The effect was attributed to accumulation of vibrationally excited CH_4 due to the more frequent pulses for the 100 kHz DBD. Hence, this study demonstrates the importance of tuning the operating conditions of the power source to improve the formation of specific plasma species.[90]

However, in general more research is needed to identify which plasma species can effectively reach the surface for different reactions and conditions. Indeed, further development of plasma catalysis not only requires a good understanding of the chemical plasma-catalyst interactions, i.e., how the plasma species can alter the surface kinetics

and pathways. Thorough knowledge of the physical effects, as discussed in section 1.6, is also needed, as these will govern the contact between the plasma and the catalyst and thus determine which chemical interactions may occur.

1.7.9 Electric fields and charge accumulation

Due to the high velocity of the electrons relative to the heavy gas particles, electrons will accumulate on the surface of a solid that is in contact with the plasma. This results in a negative surface charge and hence a local electric field near the surface. The presence of surface charges and local electric fields may affect the adsorption and reaction energies of gas species on the (catalyst) surface, thus altering the surface kinetics.[27] Bal *et al.*[117] developed a method to study the effect of additional negative surface charges using DFT modelling and applied it to CO_2 adsorption and dissociation on Al_2O_3-supported single metal catalysts. They found that addition of an excess electron improved both the adsorption and dissociation of CO_2 on M/Al_2O_3 (with M = Ti, Ni or Cu). The effect is most pronounced for Cu, followed by Ni and then Ti, hence more weakly binding metals benefit more from the presence of excess negative charges. The bonding between CO_2 and the metal happens due to overlap of the CO_2 antibonding π^* orbitals with the metal *d* orbitals. The lower the energy of the metal *d* states, the more difficult they overlap with the CO_2 π^* states. Surface charging improves the overlap between the metal *d* and CO_2 π^* states, thus lowering the energy of the M-CO_2 bonding states relative to the Fermi-level.[117]

Similarly, Jafarzadeh *et al.*[118] studied how surface charging affects CO_2 activation on TiO_2-supported Cu_5 and Ni_5 clusters, using DFT simulations. The authors found that the presence of negative surface charges led to stabilization of the adsorbed CO_2* molecule, as well as more energetically favorable CO_2 dissociation on the surface. However, in this case the effect was more pronounced for Ni, compared to Cu. Yet, this may be due to a change of the CO_2 adsorption site, when going from the neutral to the charged Cu_5/TiO_5

structure.[118] In a follow-up work, Jafarzadeh *et al*.[119] studied CO_2 adsorption on Cu (111), (211), (110) and (001) facets in the presence of both an electric field and surface charges. The authors found that application of an external electric field resulted in significantly stronger CO_2 adsorption on all facets, but the effect was stronger on the more rough surfaces (i.e., with lower coordinated sites). Moreover, the effect was further increased in the presence of excess electrons combined with the electric field. Yet, in the absence of an electric field the excess electrons had no significant effect.[119]

Kim *et al*.[120] used temperature programmed desorption to study how plasma exposure affects the desorption of CO from Pt nanoparticles. Their results showed a reduction in the apparent CO binding energy by up to 0.3 eV, which correlated linearly with the plasma density. The authors proposed that this effect results from surface charging by the plasma and the resulting electric fields. They supported this hypothesis with DFT calculations of CO adsorption on Pt(111) and (211) surfaces. Their DFT results indicated that the Pt(211) facets were much more sensitive to surface charging and electric fields, resulting in a strong decrease in the CO binding energy (i.e., causing more facile desorption). The Pt(111) sites, however, were less strongly affected and showed even slightly stronger CO binding in the presence of an excess electron.[120]

Zhang *et al*.[121] studied CO_2 adsorption on Al_2O_3-supported Ni clusters in the presence of electric fields with different strengths, using DFT modelling. They found that negative electric fields stabilized adsorbed CO_2*, while positive electric fields led to destabilization. They also found that CO_2 preferentially adsorbs on the metal-support interface, rather than on the Ni-cluster itself, although the adsorption energy on the metal cluster is more strongly affected by the electric field.[121]

To summarize, the presence of surface charges and local electric fields enhances the adsorption and dissociation of CO_2 on transition metal catalysts.[117–119,121] The effect of surface charges appears to be stronger on more weakly binding metals, provided that

the preferential adsorption site does not change due to the surface charging.[117] Additionally, more rough surfaces (i.e., with less coordinated sites) are affected more strongly by the presence of an electric field or excess surface charges.[119,120] While the adsorption of CO_2 is enhanced in the presence of negative surface charges or electric fields, this will not be the case for all molecules, e.g., adsorbed CO* is destabilized by these effects, resulting in more facile desorption.[120]

1.8 The aim of this thesis

The general aim of this thesis is to improve our understanding of the chemical interactions in plasma catalysis, by modeling reaction kinetics in the plasma and on the catalyst surface. This way, we can observe how the adsorption of reactive plasma species alters the surface chemistry of the catalyst and conversely, how the desorption of surface species affects the plasma kinetics. The obtained insights can be used in the selection of better catalysts for GHG conversion, and aid in further advancing our fundamental knowledge on this topic.

In Chapter 3, we study the influence of vibrationally excited molecules, as well as radicals and stable intermediates, on the surface kinetics of CH_4 partial oxidation with a Pt(111) catalyst. We compare how these species affect the reaction rates and product selectivities relative to each other and to thermal catalysis. Moreover, we vary the partial pressures of various radicals and intermediates in the plasma to better understand their individual effect on the surface kinetics and pathways.

Next, in Chapter 4, we investigate the gas phase chemistry of C_2H_6 dry reforming in a DBD plasma. We discuss the main reaction pathways that form C_1-C_4 hydrocarbons, syngas (CO/H_2), and various oxygenates. Additionally, we examine how changing the plasma power affects the conversions of CO_2 and C_2H_6, as well as the product selectivities.

In Chapter 5 we study plasma-catalytic DRM at DBD conditions. We first investigate the hydrogenation of plasma-produced CO on different transition metals as a potential pathway for CH_3OH production, using a descriptor-based microkinetic surface model. Next, we use a coupled plasma-surface kinetics model to illustrate that the presence of transition metal catalysts can also negatively influence DRM at conditions typical for a DBD plasma.

Finally, in Chapter 6 we examine how the presence of transition metal (Ag, Cu, Pd and Rh) and glass surfaces in the afterglow of a low-pressure CO_2 plasma affects CO_2 splitting. First, we study the importance of Eley-Rideal reactions for recombining plasma species on the catalyst surface. Next, we compare the performance of the different transition metals and glass over a broad temperature range (500-1100 K) to illustrate that the optimal catalyst depends on the temperature of the reaction. Lastly, we discuss the effect of pressure and gas flow rate on the CO_2 conversion.

Chapter 2.

Methodology

2.1 0D Microkinetic modeling

In this thesis, (micro)kinetic modeling is used to study the chemical interactions between plasma and catalysts. As discussed in sections 1.5-1.7, plasma catalysis encompasses a variety of physical and chemical interactions that can occur between the plasma and the catalyst, leading to a complex network of effects. Computational modeling is a powerful tool in this regard, as it enables us to study different interactions separately, thus isolating their effects.

This chapter discusses the use of 0D (micro)kinetic modeling to describe the chemistry in the plasma and on the catalyst surface, as well as the interaction between both. Microkinetic modeling numerically describes the reaction rates and changes in the species concentrations (or alternatively their number densities, partial pressures, surface coverages, etc.). The prefix micro- means that the individual reaction steps are considered separately, rather than the total net reaction. Hence, each reaction step has its own rate and rate coefficient. Note however, that for simplicity this prefix is often dropped. Hence, we will use kinetic and microkinetic modeling interchangeably.

In 0D (i.e., short for zero-dimensional) models, a homogenous system is assumed, meaning that no spatial gradients of the species concentrations, temperature, power density, etc. are considered. An advantage of this approach is that 0D models are not very computationally demanding and can therefore handle large sets of species and chemical reactions. However, a disadvantage is that they cannot describe (complex) spatial phenomena, such as fluid dynamics.

2.2 Reactor models

In 0D kinetic modeling, reactors are often treated using one of the three theoretical approaches presented in Figure 2.1., namely as a batch reactor (a), continuous stirred tank reactor (b) or plug-flow reactor (c). A batch reactor is a closed reactor system which does not exchange any mass (i.e., molecules) with the surrounding environment. If the reaction is considered to occur isobaric, the reactor is allowed to expand or contract to keep the pressure constant. Perfect mixing is assumed inside the reactor, resulting in a homogenous distribution of species, in accordance with the 0D approach. A continuous stirred tank reactor (CSTR), presented in Figure 2.1 (b), also assumes perfect mixing inside the reactor, but with a constant feed of reactants entering and a flow of products leaving the reactor. The composition of this outflow is the same as that inside the reactor, while the composition of the feed is different.

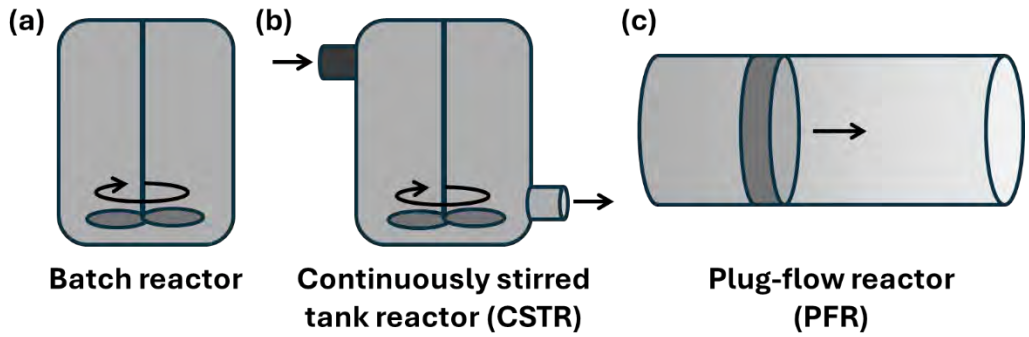

Figure 2.1. Schematic representation of three common reactor models: (a) batch reactor, (b) continuous stirred tank reactor and (c) plug-flow reactor.

Lastly, a plug flow reactor (PFR), shown in Figure 2.1 (c), consists of a cylindric tube through which the reaction mixture flows while it reacts. Hence, the composition of the reaction mixture changes with the axial position (along the direction of the flow), while the concentrations are assumed to be constant in the radial direction (perpendicular to the flow). As such, a PFR approach is in essence one dimensional (1D). However, if a small

gas volume is considered that moves through the PFR at a velocity equal to the flow rate, its position in the reactor can be determined from the time spent in the reactor. Assuming that back-mixing of the gas and diffusion along the axial direction are negligible, the gas volume moving through the PFR can be described as a (0D) batch reactor. Since this approach relates a point in time to a position in one dimension, it is referred to as a quasi-1D model. Alternatively, a PFR can also be approximated by multiple CSTR's in series.[122]

Note that in the discussion above, 0D (and 1D) refer to zero (or one) spatial dimensions (i.e., time is not considered a dimension here). This is the common terminology in plasma modeling. Batch reactors are normally solved time-dependently, while PFR reactors can be solved as function of the position in the reactor using the quasi-1D approach described above. CSTRs can be solved time-dependently, i.e., like a batch reactor but with addition of the flow-terms corresponding to the in- and outflow (see Eq. 2.1 and Eq. 2.2, in the next section). Yet, in textbooks CSTRs are typically solved at steady state, in which case the dependency on time disappears completely (also see Eq. 2.3 and Eq. 2.4).[122] The reactor can then be described using a system of algebraic equations, rather than differential equations, as will be discussed in the next section. Hence, if time is also considered as a dimension, only a CSTR model should be called 0D, while a batch reactor and PFR model should be called 1D.

2.3 Species balance equations

The kinetic model describes the evolution of the species number densities n_s (i.e., the number of particles per unit of volume) by solving a balance equation that results from the conservation of mass:

$$\frac{\partial n_s}{\partial t} = \sum_i \left(c_{s,i}^R - c_{s,i}^L\right) r_i + f_{in} - f_{out} \qquad \text{Eq. 2.1}$$

Eq. 2.1 describes the evolution of the number density n_s of a species *s* with the time *t*. The first term on the right corresponds with the change in number density due to reactions. Inside the sum, $c_{s,i}^R$ and $c_{s,i}^L$ are the stoichiometric coefficients of species *s* in reaction *i* on the right (R) and left (L) side of the reaction equation, thus corresponding to formation or loss of the species, respectively. The difference between the stoichiometric coefficients is multiplied by the reaction rate r_i, to get the net rate of formation or loss of the species in reaction *i*. Subsequently, the sum is taken over all reactions to get the net change in n_s due to reactions. The second and third terms on the right side of Eq. 2.1 correspond to the flow entering and leaving the reactor, respectively. Note that f_{in} and f_{out} are equal to zero for a batch reactor, and thus also for a quasi-1D model.

For the surface chemistry, the concentration of a species *s* on the surface is typically expressed as its fractional coverage θ_s, i.e., the number of surface sites occupied by the species divided by the total number of surface sites. We here denote surface coverages as θ, consistent with literature.[80,123] Similar to Eq. 2.1 for the gas species number density, the evolution of the fractional coverage with time can be described by a balance equation:

$$\frac{\partial \theta_s}{\partial t} = \sum_i \left(c_{s,i}^R - c_{s,i}^L\right) r_i \qquad \text{Eq. 2.2}$$

Here we assume a fixed bed reactor, meaning that the catalyst remains stationary in the reactor volume. As there are no catalytic sites entering or leaving the reactor, the flow terms are omitted. Exchange of mass between the surface and the gas phase occurs through adsorption and desorption which are included in the reactions term.

In a time-dependent model, the system of ordinary differential equations (ODE's) acquired from Eq. 2.1 and Eq. 2.2 for the different gas and surface species included in the model are solved numerically by a so-called ODE-solver algorithm. This way, the number

densities and coverages that correspond to different values of the time *t* are acquired. Alternatively, for long timespans the system will eventually reach a steady state, meaning that the number densities and surface coverages will become constant with time. Hence, if only the solution at steady state is of interest, Eq. 2.1 and Eq. 2.2 become equal to zero:

$$\frac{\partial n_s}{\partial t} = \sum_i \left(c_{s,i}^R - c_{s,i}^L\right) r_i + f_{in} - f_{out} = 0 \qquad \text{Eq. 2.3}$$

$$\frac{\partial \theta_s}{\partial t} = \sum_i \left(c_{s,i}^R - c_{s,i}^L\right) r_i = 0 \qquad \text{Eq. 2.4}$$

As such, the system of ODE's simplifies to as system of nonlinear equations, which can be solved numerically, using a root-finding algorithm.

Note that we treat the catalyst as a surface, and thus we express the concentrations of the adsorbed species as fractional coverages, i.e. the fraction of the surface sites occupied by the adsorbate. In reality, a catalyst exhibits of course a three-dimensional structure (e.g., particles), rather than a "flat" two-dimensional surface. Hence, the approach presented here assumes that the bulk of the catalyst material does not undergo any changes during the reaction.

Nevertheless, it is noteworthy that plasma can induce morphological changes in the catalyst (e.g., by etching or sputtering), thus altering the dispersion of the catalyst, and hence the number and type (i.e., facets) of surface sites.[37,38] Moreover, plasma can also affect the oxidation state of the catalyst resulting in, e.g., the formation of metal oxides on metals exposed to an O_2 plasma.[37,38,124,125] Nevertheless, these effects are thus not considered in our surface models. In principle, it could be possible to empirically determine the rate at which the number and type of surface sites change. These processes could then be included in kinetic models by changing the volumetric site densities of different site types with time. However, this is outside the scope of this thesis. Lastly, note that effects such as etching, sputtering, oxidation and surface coking

will affect the reactivity of the catalysts and may lead to its deactivation, hence determining the lifetime of the catalyst. Some experimental studies[35,65,126] on plasma-catalytic DRM have reported a drop in the activity of the catalyst over the course of hours due to surface coking, i.e. leading to catalyst deactivation. However, not all catalysts are equally susceptible to coking, hence not all catalysts show an observable decline in their activity during the first hours on stream.[65] Alternatively, some studies observe a change in the catalysts' selectivity towards specific end-compounds during the first hours on stream, such as a rise of the C_2H_2 selectivity,[127] or a switch in selectivity from CH_3OH to CH_3COOH.[128] Such effects may possibly indicate changes in the catalyst oxidation state, morphology, etc.

2.4 Reaction rates

The reaction rates r_i for gas reactions, used in Eq. 2.1, are calculated from the rate coefficients of the reaction k_i, the species densities n_s of the reactants and their corresponding stoichiometric coefficients $c_{s,i}^L$:

$$r_i = k_i \prod_{s,gas} (n_s)^{c_{s,i}^L} \qquad \text{Eq. 2.5}$$

A similar expression is used for the rates (i.e., turnover frequencies) of surface reactions:

$$r_i = k_i \prod_{s} (a_s)^{c_{s,i}^L} \qquad \text{Eq. 2.6}$$

This expression uses the activities a_s of the reactants, which correspond to the fractional coverages θ_s for surface species and the partial pressures divided by the reference pressure p_s/p_{ref} for gas species. Note that p_{ref} is typically equal to 1 bar, so that the activities of the gas species correspond to their partial pressures in bar. However, we treat all gas species as ideal gases, so that partial pressures can be converted to number

densities and vice versa, using the ideal gas law. Hence, the values used in Eq. 2.6 are not the “real” activities, as these would also consider deviations from ideal behavior.

Lastly, it is important to note that if surface reactions are included in the source terms of gas species in Eq. 2.1 (e.g., for adsorption or desorption), their rates should be multiplied by the volumetric site density (i.e., the number of surface sites divided by the gas volume).

2.5 Rate coefficients of gas reactions

Expressions for the rate coefficients k_i between heavy gas species are mostly acquired from literature or databases.[129,130] The errors reported in literature for these rate coefficients typically vary between a factor 1.1 to 10, with errors of a factor 2 to 5 being quite common.[131–138] Since models describing the plasma kinetics (such as those presented in Chapters 4, 5 and 6) typically contain hundreds of reactions, it is not straightforward to determine how much the uncertainties on the rate coefficients propagate to the results. Turner[139] presented a method to quantify the errors on the results of chemical kinetics models caused by the uncertainty on the rate coefficients. This method consists of applying uncertainty distributions to the rate coefficients based on their corresponding errors reported in literature. Then, a population of results is generated, by performing a large number of simulations for which the values of the rate coefficients are randomly varied based on the applied uncertainty distributions. Subsequently, the uncertainty distribution of the population of results is determined. This method was applied to a CO_2 plasma model by Berthelot *et al.*,[140] who found that the errors on the CO_2 conversion varied from 50% to 110% depending on the conditions. Hence, the errors on plasma kinetic models can be quite large, especially considering that additional errors may be introduced due to the assumption or approximation made in these models. Hence, it is important to note that the models presented in this thesis

do not aim to predict exact values but rather trends between different conditions, catalysts, etc. Note that we did not perform any analysis of the uncertainties for the models and chemistry sets in this thesis, as the method described above requires performing an extensive number of simulations (e.g., Berthelot *et al*.[140] executed simulations for 400 different input data sets), and is thus very computationally demanding.

For electron impact reactions, the rate coefficients need to be calculated from their corresponding collision cross-sections σ_i and the electron energy distribution function (EEDF), according to:[141]

$$k_i = \sqrt{\frac{2e}{m_e}} \int_0^{+\infty} \epsilon \sigma_i F_0 d\epsilon \qquad \text{Eq. 2.7}$$

In which e is the elementary charge, m_e is the electron mass, $\mathcal{E}$ is electron energy in eV, and F_0 is the isotropic part of the electron distribution function. The EEDF is determined numerically using a solver for the Boltzmann equations for electrons, such as BOLSIG+[141] or BOLOS.[142] These algorithms calculate the EEDF (and the rate coefficients for electron impact reactions) for a specified gas mixture and reduced electric field *E/N*.

The reduced electric field is related to the power density *P* in the plasma by:

$$\frac{E}{N} = \frac{1}{N} \sqrt{\frac{P}{n_e e \mu_e}} \qquad \text{Eq. 2.8}$$

In Eq. 2.8, N is the total gas species number density, n_e is the electron density and μ_e is the electron mobility, which is also calculated by the Boltzmann Solver.

2.6 Rate coefficients of surface reactions

The rate coefficients of reactions on catalyst surfaces are calculated using transition state theory (TST):

$$k_i = \frac{k_b T}{h} \exp\left(-\frac{\Delta G^{\ddagger\circ}}{RT}\right) = \frac{k_b T}{h} \exp\left(-\frac{\Delta \mathrm{H}^{\ddagger\circ}}{RT}\right) \exp\left(\frac{\Delta \mathrm{S}^{\ddagger\circ}}{R}\right) \qquad \text{Eq. 2.9}$$

In which k_b is the Boltzmann constant, T is the temperature, h is the Planck constant and $\Delta G^{\ddagger\circ}$, $\Delta H^{\ddagger\circ}$ and $\Delta S^{\ddagger\circ}$ are the standard Gibbs free energy, enthalpy and entropy differences, respectively, between the transition and the initial state. In other words, $\Delta H^{\ddagger\circ}$ is the activation enthalpy of the reaction, which can, for example, be acquired from DFT calculations. Note that at high temperatures, for which the contribution of the entropy is large, the numerical value of $\Delta G^{\ddagger\circ}$ may become negative or smaller than the reaction Gibbs free energy ΔG°_{rxn}, although this is not physically possible. Hence, the value of $\Delta G^{\ddagger\circ}$ is limited according to Eq. 2.10, below.

$$\Delta G^{\ddagger\circ} = \max\left[\left(\sum_{TS} G^{\circ}{}_s - \sum_{reactants} G^{\circ}{}_s\right), \Delta G^{\circ}{}_{rxn}, 0\right] \qquad \text{Eq. 2.10}$$

In which the part between round brackets is the difference between the Gibbs free energies $G^{\circ}{}_s$ of the transition state and the reactant species. This expression ensures that the Gibbs free energy barrier always corresponds to the difference between the maximum in the Gibbs free energy curve and the initial state. If the Gibbs free energy of the transition state drops below that of the final or the initial state due to entropic effects, the Gibbs free energy will only go uphill or downhill, respectively, when moving along the reaction coordinate. Consequently, the final or initial state will now correspond to the transition state, and the barrier will become equal to ΔG°_{rxn} or zero, respectively.

There exist different approaches for estimating the entropic part $\Delta S^{\ddagger\circ}$ of the Gibbs free energy barrier $\Delta G^{\ddagger\circ}$. One possibility is to assume that the rotational and vibrational

entropy contributions are negligible compared to the translational entropy. Hence, the entropy barrier and reaction entropy become zero for surface reactions, while the reaction entropy for simple adsorption corresponds to the loss of the total translational entropy S_{trans} of the gas molecule. By treating the transition state for adsorption as a 2D gas, i.e. with two translational degrees of freedom, the rate coefficient for adsorption becomes:[143]

$$k_{ads} = \frac{k_b T}{h} \exp\left(-\frac{\Delta \mathrm{H}^{\ddagger\circ}}{RT}\right) \exp\left(\frac{-\frac{1}{3} S_{trans}}{R}\right) \qquad \text{Eq. 2.11}$$

Alternatively, the rate coefficient of adsorption can be calculated with the Hertz-Knudsen equation, which describes the flux of particles to the surface, multiplied by an enthalpy based sticking coefficient:

$$k_{ads} = \frac{p_{ref} A_s}{\sqrt{2\pi m k_b T}} \exp\left(-\frac{\Delta \mathrm{H}^{\ddagger\circ}}{RT}\right) \qquad \text{Eq. 2.12}$$

With A_s the surface site area and m the mass of the gas species. Note that if adsorption occurs without enthalpy barrier ($\Delta H^{\ddagger\circ} = 0$) the exponent becomes unity and Eq. 2.12 corresponds simply to the flux of to the surface. As such, the effect of entropy in Eq. 2.12 is included in the flux to the surface, rather than explicitly as an exponent of $\Delta \mathrm{S}^{\ddagger\circ}$.

The rate coefficients for desorption can then be calculated using detailed balancing from the adsorption rate coefficients (Eq. 2.11 or Eq. 2.12) and the equilibrium constant K_{eq}:

$$k_{rev} = \frac{k_{for}}{K_{eq}} \Leftrightarrow k_{des} = \frac{k_{ads}}{K_{eq,ads}} \qquad \text{Eq. 2.13}$$

With k_{for} and k_{rev} the forward and reverse rate coefficients, respectively. Hence, for the adsorption reaction, these correspond to the rate coefficients of adsorption and desorption, respectively.

The equilibrium constant of a reaction is calculated according to:

$$K_{eq} = \exp\left(\frac{-\Delta G^{\circ}_{rxn}}{RT}\right) = \exp\left(\frac{-\Delta H^{\circ}_{rxn}}{RT}\right)\exp\left(\frac{\Delta S^{\circ}_{rxn}}{R}\right) \qquad \text{Eq. 2.14}$$

In Eq. 2.14, ΔG°_{rxn}, ΔH°_{rxn} and ΔS°_{rxn} are the standard reaction Gibbs free energy, enthalpy and entropy, respectively. The Gibbs free reaction energy is defined as the difference between the standard Gibbs free energies of the products and the reactants:

$$\Delta G^{o}_{rxn} = \sum_{products} G^{o}_{s} - \sum_{reactants} G^{o}_{s} \qquad \text{Eq. 2.15}$$

Note that if only the translational entropy is accounted for, ΔS°_{ads} equals $-S_{trans}$ for adsorption reactions. However, rather than only considering the translational entropy in Eq. 2.9 and Eq. 2.14, a more accurate approach is to also account for the electronic, vibrational and rotational entropy, as well as for the temperature dependence of the enthalpy. For surface species, the entropy and enthalpy can be calculated temperature dependently using the harmonic oscillator approximation by treating all degrees of freedom as vibrational modes. The enthalpy $H(T)$ of a surface species is then given by:[144]

$$\frac{H(T)}{N_A} = E_{pot} + \Delta E_{ZPE} + \sum_{i}^{3N} \frac{\epsilon_i}{e^{\epsilon_i/k_bT} - 1} \qquad \text{Eq. 2.16}$$

In which N_A is the Avogadro constant, E_{pot} is the potential energy of the species, ΔE_{ZPE} is the zero-point energy correction, and ϵ_i the vibrational energy level. The zero-point energy correction is calculated as:

$$\Delta E_{ZPE} = \frac{1}{2}\sum_{i} \epsilon_i \qquad \text{Eq. 2.17}$$

The entropy $S(T)$ calculated using the harmonic oscillator approximation is equal to:[144]

$$\frac{S(T)}{N_A} = k_b \sum_{i}^{3N} \left[\frac{\epsilon_i}{k_bT(e^{\epsilon_i/k_bT} - 1)} - \ln\left(1 - e^{-\epsilon_i/k_bT}\right)\right] \qquad \text{Eq. 2.18}$$

For gas species, the temperature-dependent enthalpy and entropy can be calculated from polynomials, like the Shomate equations[145] or the NASA polynomials,[16,146] when these are available. Alternatively, the temperature-dependent entropy and enthalpy can be calculated using the ideal gas approximation. The gas enthalpy is then calculated as:[144]

$$\frac{H(T)}{N_A} = E_{pot} + \Delta E_{ZPE} + \left(\frac{5}{2} + n_{rot}\frac{1}{2}\right)k_b T + \sum_i^{3N} \frac{\epsilon_i}{e^{\epsilon_i/k_b T} - 1} \qquad \text{Eq. 2.19}$$

In which n_{rot} is the number of rotational degrees of freedom. In the ideal gas approximation, the translational component of the gas species entropy is given by the Sackur-Tetrode equation:[143,144]

$$\frac{S_{trans}}{N_A} = k_b \left\{ \ln\left[\left(\frac{2\pi m k_b T}{h^2}\right)^{3/2} \frac{k_b T}{p_{ref}} \right] + \frac{5}{2} \right\} \qquad \text{Eq. 2.20}$$

This equation is also used to calculate the translational entropy S_{trans} of the gas species in the rate coefficient (Eq. 2.11) and the equilibrium constant (Eq. 2.14) of adsorption. The rotational entropy S_{rot} of an ideal gas is calculated according to Eq. 2.21 and Eq. 2.22 for linear and nonlinear molecules, respectively:[144]

$$\frac{S_{rot}}{N_A} = k_b \left[\ln\left(\frac{8\pi^2 I k_b T}{\sigma h^2} \right) + 1 \right] \qquad \text{Eq. 2.21}$$

$$\frac{S_{rot}}{N_A} = k_b \left\{ \ln\left[\frac{\sqrt{\pi I_A I_B I_C}}{\sigma} \left(\frac{8\pi^2 k_b T}{h^2}\right)^{3/2} \right] + \frac{3}{2} \right\} \qquad \text{Eq. 2.22}$$

In which I are the moments of inertia (i.e., two degenerate moments for linear molecules or three separate moments I_A, I_B and I_C for nonlinear molecules), and σ is the symmetry number of the molecule. Lastly, the vibrational entropy of the ideal gas is calculated according to Eq. 2.18, and electronic entropy is given by:

$$S_{elec} = k_b \ln(2 \times (total\ spin) + 1) \qquad \text{Eq. 2.23}$$

The total entropy of the gas species is then acquired by taking the sum of the translational, rotational, vibrational and electronic components:

$$S(T) = S_{trans} + S_{rot} + S_{vib} + S_{elec} \quad \text{Eq. 2.24}$$

In the subsequent chapters, microkinetic models are used to study the chemical interactions between the plasma and a catalyst. In Chapter 3, we use a pure surface microkinetic model that simulates the surface kinetics for a fixed gas composition. In Chapter 4, we use a pure plasma kinetics model that simulates the gas phase chemistry in absence of a catalyst. Next, in Chapters 5 and 6 we use coupled plasma-surface models that incorporate both the kinetics in the gas phase as well as on the surface, to study in-plasma catalysis and post-plasma catalysis, respectively.

Chapter 3.

Plasma-catalytic partial oxidation of methane on Pt(111): a microkinetic study of the role of different plasma species

The results presented in this chapter are published in:

Loenders, B.; Engelmann, Y.; Bogaerts, A. Plasma-Catalytic Partial Oxidation of Methane on Pt(111): A Microkinetic Study on the Role of Different Plasma Species. *J. Phys. Chem. C* **2021**, *125*, 2966–2983. DOI: 10.1021/acs.jpcc.0c09849

3.1 Introduction

In this chapter, we investigate the effect of different plasma species on the surface kinetics and pathways of plasma-catalytic POX of CH_4 on a Pt(111) catalyst, using a surface microkinetic model. POX of CH_4 into liquid chemicals (e.g., CH_3OH) is particularly interesting for valorization of the many natural gas reserves that are situated in remote locations. Indeed, on-site conversion of CH_4 into liquid chemicals, which are easier to transport over large distances, makes extracting these remote natural gas deposits more economically viable.[147,148] However, the production of liquid oxygenates via POX of CH_4 requires breaking the strong C-H bond in CH_4, while avoiding over-oxidation to CO or CO_2, in other words, without breaking all C-H bonds in the CH_4 molecule.[149,150] In classical thermal catalysis, the POX of CH_4 has therefore been mainly studied for syngas production at high temperatures (800-1300 K; see section 1.2, R1.9) with transition metal catalysts, like Ru, Rh, Ni and Pt.[78]

Indeed, based on theoretic studies, CH_3OH formation is instead expected to occur more easily on the most weakly binding (i.e., noble) metals, while CH_4 activation is also more difficult on these metals.[151,152] Nevertheless, adsorbed O* atoms can assist in dehydrogenation reactions on weakly binding metals (Cu, Ag and Au), thus facilitating both CH_4 activation, as well as subsequent CH_x* dehydrogenation steps.[151,153] As such, O* atoms can both improve the turnover frequencies for CH_4 consumption, but also lower the selectivity towards oxygenates for POX of CH_4 on weakly binding metals. Nevertheless, if the catalyst is combined with a plasma, the activation of CH_4 can occur in the gas phase, thus omitting the difficult CH_4 dissociation on the catalyst surface.

Numerical modeling studies[154–157] of CH_4 POX in a DBD plasma without catalyst show that CH_4 is dissociated in the plasma to form CH_3, which serves as a precursor for oxygenates. This CH_3 subsequently recombines with O_2 to produce CH_3OO, which is a key

intermediate in oxygenate formation.[154,157] Alternatively, three-body recombination between CH_3 and OH radicals has also been reported as an important mechanism for CH_3OH formation.[156] However, further oxidation of the oxygenates or excessive dissociation of CH_4 to CH_2, CH or C, lead to over-oxidation and the formation of CO and CO_2.[154,155,157]

In any case, the various plasma species can adsorb on the catalyst and partake in surface reactions, thus altering the surface kinetics and pathways. Indeed, Gibson *et al.*[95] investigated plasma-catalytic CH_4 oxidation with a Pd/Al_2O_3 catalyst and found that the plasma did not induce significant structural changes in the catalyst, nor sufficient heating to thermally activate the catalyst. Hence, this indicates a mechanism in which CH_4 is preactivated in the plasma, enabling the catalytic reactions to occur at reduced temperature compared to thermal catalysis.[95]

Additionally, a few other mechanistic studies on plasma-catalytic POX of CH_4 are available in literature.[158–160] Both Knoll *et al.*[158] and Zhang *et al.*[160] used DRIFTS to study the mechanism of CH_4 oxidation by an Ar/O_2 atmospheric pressure plasma jet (APPJ) in the presence of a Ni on Al_2O_3/SiO_2 catalyst, and found that CO_2 is formed by oxidation of adsorbed CO* on the catalyst. This shows that Ni catalysts promote over-oxidation by oxidizing CO to CO_2. Stere *et al.*[159] used *in situ* DRIFTS analysis to investigate plasma-catalytic CH_4 oxidation with a Pd/Al_2O_3 catalyst. They observed significant formation of HCOO* on the catalyst, which was found to be correlated to the production of CO_2. However, the authors also suggested that CO and CO_2 formation occur via different routes, due to their different formation profiles as a function of time.[159]

In this chapter, we present results from microkinetic modeling to illustrate how plasma species, such as vibrationally excited molecules, radicals and stable intermediates, affect the catalyst surface chemistry for the POX of CH_4. Transition metals from group VIIIb are known to be good catalysts for thermal POX of CH_4 to syngas at high temperature.[78,161]

Therefore, we investigated whether such transitions metals would also be suitable catalysts for oxygenate production via low-temperature POX of CH_4 in the presence of reactive plasma species. We chose Pt(111) as the catalyst since this is among the most noble transition metals in group VIIIb and can thus be expected to be the more suitable catalyst for oxygenate formation.[152] Moreover, Pt has been well studied for CH_4 POX to syngas in thermal catalysis. Hence, both DFT data[162,163] that are required as input by the model, and microkinetic modeling studies,[164–167] which can serve as a benchmark, are available in literature.

3.2 Methods

We constructed a mean field microkinetic model to simulate POX of CH_4 on Pt(111), as explained in Chapter 2. For every surface species the time-evolution of its fractional coverage θ_s is described using Eq. 2.2 (see section 2.3), which balances the different gain and loss terms. The net reactions rates are calculated as the difference between the forward and reverse reactions rates, which in turn are calculated according to Eq. 2.6 (see section 2.4). The activities a_s of the reactants in Eq. 2.6 correspond to the fractional coverages for surface species and the partial pressures in bar for gas species (i.e., p_{ref} = 1 bar). The rate coefficients k_i in Eq. 2.6 are calculated with transition state theory, i.e. according to Eq. 2.9 from section 2.6. The entropy differences are calculated based on the translational entropy, as this typically has the largest contribution to the total entropy.[80] The translational entropy S_{trans} of the gas species is calculated using the Sackur-Tetrode equation (Eq. 2.20, section 2.6). We assume that gas species lose all their translational entropy upon adsorption onto the surface, so that the reaction entropy $\Delta S°_{rxn}$ is equal to $-S_{trans}$ for adsorption processes and Eley-Rideal (E-R) reactions. Additionally, for dissociative adsorption and E-R reactions, the transition state is assumed to have lost all its translational entropy, hence $\Delta S^{\ddagger}_{ads}$ is equal to $-S_{trans}$. For molecular and radical adsorption, on the other hand, the transition state is considered a

2D gas, so that $\Delta S^{\ddagger}_{ads}$ becomes equal to -1/3S_{trans} for these processes (see section 2.6). Finally, $\Delta S°_{rxn}$ and $\Delta S^{\ddagger}°$ are considered equal to zero for Langmuir-Hinshelwood (L-H) reactions, i.e., the entropies of the surface species are assumed to be negligible.

A full list of all reactions included in the model alongside the thermodynamic data can be found in Appendix A1, Table A1.1. The effect of vibrationally excited CH_4 and O_2 is implemented by lowering the enthalpy barriers of their respective dissociative adsorption reactions, and the E-R reactions between gaseous CH_4 and surface-bound O* or OH*:

$$CH_{4_{(g)}} + O^* \rightarrow CH_3^* + OH^* \qquad \text{R3.1}$$

$$CH_{4_{(g)}} + OH^* \rightarrow CH_3^* + H_2O^* \qquad \text{R3.2}$$

A detailed description of the mathematical implementation of vibrational excitation in our model can be found in Appendix A1, section A1.2.

The model solves the species balance equations at steady state (see section 2.3, Eq. 2.4), to obtain the coverages at steady state. These can then be inserted back into the rate equations to obtain the steady state reaction rates. Unless noted otherwise, the calculations are executed for a temperature of 500 K, a total pressure of 1 bar and zero conversion. To compare the product formation rate and product distributions between different conditions, we calculate the steady state TOFs and selectivities.

The steady state TOF of a gas species s_g is calculated as:

$$TOF(s_g) = \sum_i (c_{s,i}^R - c_{s,i}^L) r_i \qquad \text{Eq. 3.1}$$

With r_i expressed in s^{-1}, as acquired from Eq. 2.6. The selectivity of a carbon-containing product $s_{g,C}$ is calculated as the percentage of the total sum of the TOFs of all formed

carbon-containing products, taking into account the number of carbon atoms in each product species (N_C):

$$Selectivity(s_{g,C}) = \frac{max[N_c \times TOF(s_{g,C}), 0]}{\sum_{s_{g,C}} max[N_c \times TOF(s_{g,C}), 0]} \times 100\% \qquad \text{Eq. 3.2}$$

Note that at non-zero conversion conditions, some products may be consumed as intermediates, resulting in negative TOFs. Naturally these negative TOFs are not considered in calculating the selectivities. Additionally, in the presence of radicals, CH_4 can have a positive (i.e., formation) TOF due to recombination of radicals on the surface back to CH_4. Yet, we do not include CH_4 in the calculation of the selectivities, as the radicals that form CH_4 on the surface would normally originate from CH_4 dissociation in the plasma.

3.3 Results and discussion

In the following sections, we solve the model for various cases. We start by solving the model for thermal catalysis, without including any plasma effects. These results will then serve as a benchmark to evaluate the plasma effects. Next, we modify the model to include either vibrational excitation or the presence of plasma-generated radicals and stable intermediates. The results of these plasma-specific cases are then compared to those of thermal catalysis. For consistency between the different cases, all simulations are performed at a temperature of 500 K and a total pressure of 1 bar, unless noted otherwise. We chose these conditions as they are representative of a DBD plasma. Additionally, the radical partial pressures that we use in the plasma simulations are based on calculations by De Bie *et al*.[157] for a CH_4/O_2 (70/30) gas mixture. Therefore, we also use this CH_4/O_2 ratio in our simulations. Note that this is close to the stoichiometric CH_4/O_2 ratio of 2/1 for POX to CH_3OH.

3.3.1 Thermal catalysis

As discussed in the introduction to this chapter, the thermal-catalytic POX of CH_4 on Pt has been mainly investigated for syngas production at high temperatures (800-1300 K).[19,164–168] Only a few studies have investigated potential pathways for oxygenate formation via POX of CH_4 on Pt.[151,152,162] We start by solving the model for thermal catalysis to reveal the most important reaction pathways for POX of CH_4 on a Pt(111) surface at steady state.

The overall pathways for the main products are shown in Figure 3.1 (a). Gaseous CH_4 dissociatively adsorbs onto the surface, forming CH_3* and H*. CH_3* is further dehydrogenated to CH_2*, which in turn forms CH*. We find that the breaking of the C-H bonds in all three steps occurs through interaction with empty surface sites, rather than with OH* or O*. Most of the CH* (90.5%) is oxidized to CHO* and subsequently decomposes to form CO*, which desorbs from the surface. A smaller fraction of CH* (9.4%) first undergoes dehydrogenation, after which the formed C* is oxidized into CO* as well. Dissociative adsorption of O_2 results in formation of surface O*. Most of the O* (79.0%) forms OH* through reaction with H* that originates from the dehydrogenation of CH_x species and CHO*, while the oxidation of CH* to CHO* is responsible for 18.0% of the total O* consumption. The OH* species abstract H from other OH* to form H_2O* and O*, after which the formed H_2O* desorbs as a side product.

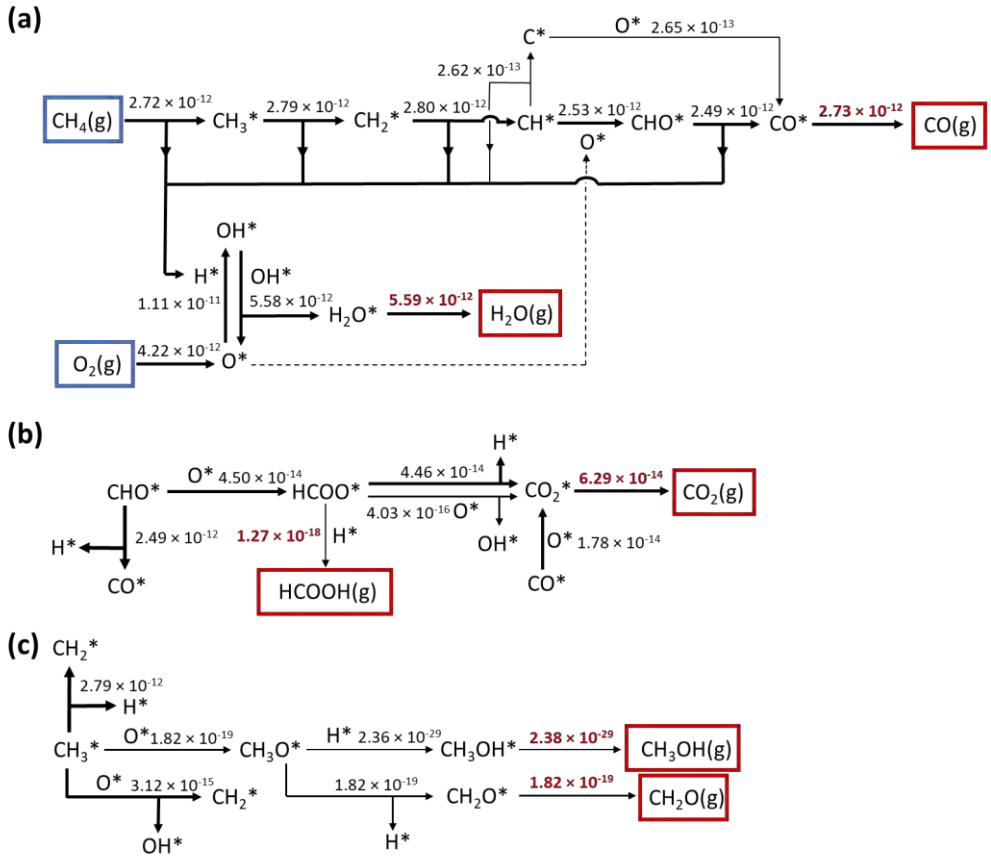

Figure 3.1. Most important reaction pathways at steady state for thermal-catalytic POX of CH_4 on Pt(111) using a CH_4/O_2 (70/30) gas mixture at 500 K and 1 bar. The values of the reaction TOFs in (s^{-1}) are displayed next to the arrows. The arrow thickness indicates the relative importance of a reaction within each separate scheme. A dotted arrow indicates the species is used as a second reactant in another reaction.

As mentioned before, we performed these calculations at 500 K, to provide a benchmark for plasma-catalytic POX of CH_4, as this is a representative temperature for a DBD plasma. Yet, as this temperature is too low for thermal-catalytic POX of CH_4, we compare the reaction pathways at 500 K from Figure 3.1 (a) with pathways calculated at 1000 K, which is a more common temperature for thermal-catalytic CH_4 POX. Additionally, we compare these results to those of earlier microkinetic studies.[164,165] The results at 1000 K and their

discussion can be found in Appendix A1, section A1.3. Note that our model only considers the reactions that occur on the Pt(111) surface, while the gas phase composition is kept constant. Hence, we do not include any gas phase reactions.

Figure 3.1 (b) represents the pathways for the formation of CO_2 and HCOOH, as well as concurrent reactions. A relatively small amount (1.8%) of the CHO* formed in the main pathway, is oxidized to HCOO* as a side reaction. Only a minor amount (0.003%) of this HCOO* undergoes hydrogenation to HCOOH, while the majority is dehydrogenated to CO_2*, either by interaction with an empty surface site (99.1%) or O* (0.9%). Another important route for the formation of CO_2* is through oxidation of CO* that is formed in the main pathway. Still, about 71.0% of CO_2* formation occurs via dehydrogenation of HCOO* by empty sites, compared to 28.4% from the oxidation of CO*. The rate of HCOOH formation in Figure 3.1 is about six orders of magnitude lower compared to that of CO desorption, which indicates that the formation of HCOOH in practice does not occur. The rate of CO_2 desorption in Figure 3.1 is roughly a factor 40 lower compared to that of CO. However, experimental and DFT results by Chin *et al.*[169] indicate that CO oxidation to CO_2 is much faster than CH_4 dissociation on Pt clusters, and because of this, only trace amounts of CO can be present in the gas phase prior to O_2 depletion. Additionally, thermodynamic equilibrium calculations show that CO_2 and H_2O are the thermodynamically favored products at 500 K.[78,170] However, the reason that the rate for desorption of CO in Figure 3.1 is higher compared to that of CO_2 is a consequence of the zero conversion conditions. Indeed, we find that the addition of even small amounts of CO (0.1-0.001%) to the gas mixture results in CO_2 becoming the main product, as CO is adsorbed and oxidized. A more in-depth discussion is provided in the Appendix A1, section A1.4.

The pathways leading to the formation of CH_3OH and CH_2O are displayed in Figure 3.1 (c). These pathways branch off from the main reaction pathway at the CH_3* species,

which can be oxidized by O* to form CH_3O*. The latter serves as a precursor for both CH_3OH and CH_2O. However, dehydrogenation of CH_3* by an empty surface site or a surface-bound O* is strongly favored over CH_3O* formation, as indicated in Figure 3.1 (c). Indeed, the TOFs of dehydrogenation by empty sites or hydrogen abstraction by O* are seven and four orders of magnitude higher, respectively, than that of CH_3O* formation. The CH_3O* species can either be hydrogenated to CH_3OH or dehydrogenated to form CH_2O, the latter being strongly favored (i.e., its rate is ten orders of magnitude higher). However, neither of these products are expected to be formed in significant amounts under these conditions, as their TOFs are several orders of magnitude lower than those of the main products, i.e., CO, CO_2 and H_2O. As mentioned earlier, this is also the case for HCOOH.

3.3.2 Plasma catalysis: effect of vibrational excitation

One of the challenges associated with POX of CH_4 is the activation of the strong C-H bond in CH_4.[150] Indeed, activation of the C-H bond has been identified as the sole kinetically relevant step for POX of CH_4 on Pt clusters, except for conditions close to O_2 depletion, where O_2 activation becomes rate-limiting.[171] Vibrational excitation of CH_4 is known to enhance its dissociative adsorption onto transition metal surfaces.[172] Thus, plasma-induced vibrational excitation can be expected to facilitate POX of CH_4 on these surfaces. In the following sections we investigate the impact of vibrational excitation on the TOFs and product selectivities of POX of CH_4 on Pt(111), and discuss the associated kinetic and mechanistic changes. We implement the effect of plasma-induced vibrational excitation by lowering the barriers of CH_4 and O_2 activation, as discussed in Appendix A1, section A1.2. We simultaneously vary the vibrational temperatures of CH_4 and O_2 between 500 and 1500 K and assume both vibrational temperatures to have the same value. Chen *et al.*[173] measured the vibrational temperature in a CH_4/N_2/He DBD plasma at 60 Torr based on the $v = 1$ peak of N_2 and observed a maximal vibrational temperature of 1350 K. We

here choose an upper limit of 1500 K, which is still in the uncertainty range of the results from Chen *et al.* [173] We choose this value as an upper limit since the vibrational temperature measured by Chen *et al.* was based on the v = 1 peak of N_2 and the vibrational temperature of CH_4 is likely lower. As a comparison, Butterworth *et al.*[174] studied the vibrational excitation of CH_4 in low pressure (25 mbar) pulsed microwave plasma and found that the vibrational and gas temperatures equilibrate around 900 K. In any case, varying the vibrational temperature in a wide range is interesting from a theoretical point of view as well.

3.3.2.1 Effect of vibrational excitation on the TOFs

Figure 3.2 illustrates the influence of vibrational excitation on the total TOF of CH_4 dissociation for a variable O_2 content (1-99%), as well as the separate TOFs of the two main CH_4 dissociation reactions. Note that typical O_2 contents in experiments are in the range of 15-50%, both for thermal catalysis[78,168] and DBD plasma,[155,175] hence more limited than the variation in Figure 3.2. As can be seen in the right panel of Figure 3.2, the TOF of CH_4 dissociation increases by several orders of magnitude, i.e. about 4 orders of magnitude at 30% O_2, upon a rise in vibrational temperature from 500 to 1500 K. Additionally, the CH_4 dissociation TOF also rises upon lower O_2 content due to the corresponding increase in the partial pressure of CH_4. Below a vibrational temperature of 1000 K, the highest CH_4 dissociation TOFs are restricted to low O_2 content. Yet, above 1000 K the highest TOFs can be found in a region that is more spread out over the different O_2 fractions. This can be linked to a change in the main mechanism of CH_4 dissociation around 1000 K. The TOFs of the main mechanisms of CH_4 dissociation can be seen in the left panels of Figure 3.2. At vibrational temperatures below 1000 K, the main mechanism for CH_4 dissociation is the dissociative adsorption on empty surface sites, while above 1000 K the dissociation of CH_4 occurs mostly through an Eley-Rideal reaction with pre-adsorbed O* (R3.1). The change in mechanism follows from a stronger rise in

the rate constant of the O* assisted CH_4 dissociation, compared to dissociative adsorption on empty sites. This is a direct result of the higher reaction barrier and Fridman-Macheret α parameter (see Appendix A1, section A1.2) of the O* assisted reaction (1.28 eV and 0.48, resp.) compared to that on empty sites (0.63 eV and 0.41, resp.). When comparing the TOFs of both reactions, we find that the O* assisted mechanism depends less on the O_2 content in the gas mixture. This is because the O* coverage varies very little with O_2 content or vibrational temperature and remains above 99.5% in the investigated range, while the fraction of free sites mainly changes with O_2 content and drops from 5.3 × 10 5 to 3.7×10^{-6}, as the O_2 content rises from 1 to 99%. As the O* assisted mechanism depends less on the fraction of free sites, i.e., it requires only one free site per molecule of CH_4, it also varies less with O_2 content. The fractional coverages of the 14 most abundant surface species, as well as the fraction of free sites, can be found in Appendix A1, section A1.5.

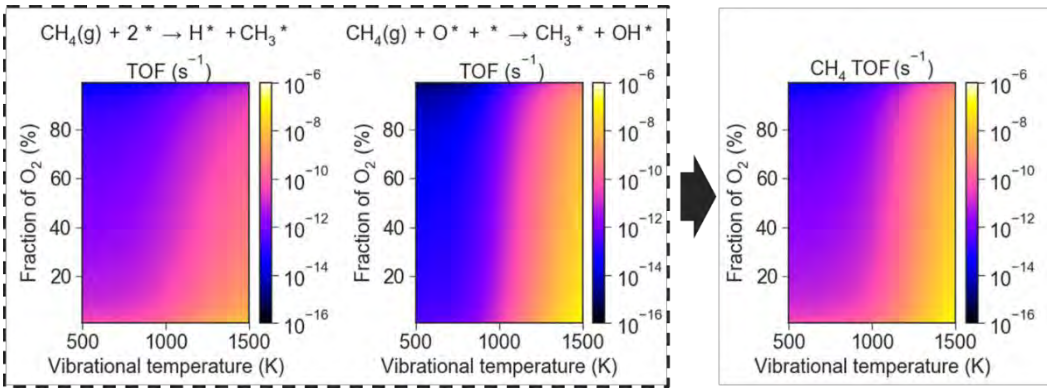

Figure 3.2. Influence of the vibrational temperature and O_2 content on the TOFs of the two main reactions for CH_4 dissociation (left panels) and on the total TOF of CH_4 dissociation (right panel), both in (s^{-1}). Calculated at steady state for a CH_4/O_2 mixture at a pressure of 1 bar and a surface temperature of 500 K. For convenience, the same scale is used for the three graphs in this figure. Note: typical O_2 fractions in experiments range from 15-50%.

Our results indicate that plasma-induced vibrational excitation shows good potential for improving the TOFs of POX of CH_4 at low temperature (500 K). The effect of vibrational

excitation on the product selectivities is discussed in the next section. Additionally, our results suggest that vibrational excitation can decrease the dependency of the TOFs on the O_2 content in the gas phase for relevant O_2 fractions (1-99%) by facilitating the O* assisted dissociation of CH_4. As a result, high TOFs become feasible even at higher O_2 fractions.

3.3.2.2 Effect of vibrational excitation on the selectivities

In the previous section we showed that vibrational excitation can enhance the TOF of CH_4 dissociation. In this section we investigate whether vibrational excitation can affect the selectivities of the products. In Figure 3.3 we illustrate how the selectivities of the oxygenates, CO_x and ethane (C_2H_6) change when varying the vibrational temperature from 500 to 1500 K for a gas mixture with variable O_2 content, i.e. 1-99% O_2. Figure 3.3 (a), (b) and (c) display the selectivities of CH_3OH, HCOOH and C_2H_6, respectively, which show a similar trend. The selectivities of these products rise strongly when increasing the vibrational temperature from 500 to 1500 K, i.e. by a factor 10^4-10^5 at 33% O_2. However, these selectivities are less dependent on the O_2 content in most of the investigated range and only show a strong decrease at high O_2 fractions. Figure 3.3 (d) and (e) display the selectivities of CH_2O and CO_2, respectively. The selectivities of both products increase only slightly with a rising vibrational temperature and instead depend stronger on the O_2 content in the gas mixture, with a higher fraction of O_2 resulting in higher selectivities towards these products. The selectivity of CO, shown in Figure 3.3 (f), changes little under the investigated conditions, but drops slightly with rising O_2 fraction or vibrational temperature. As a result, CO remains the main product under the investigated conditions.

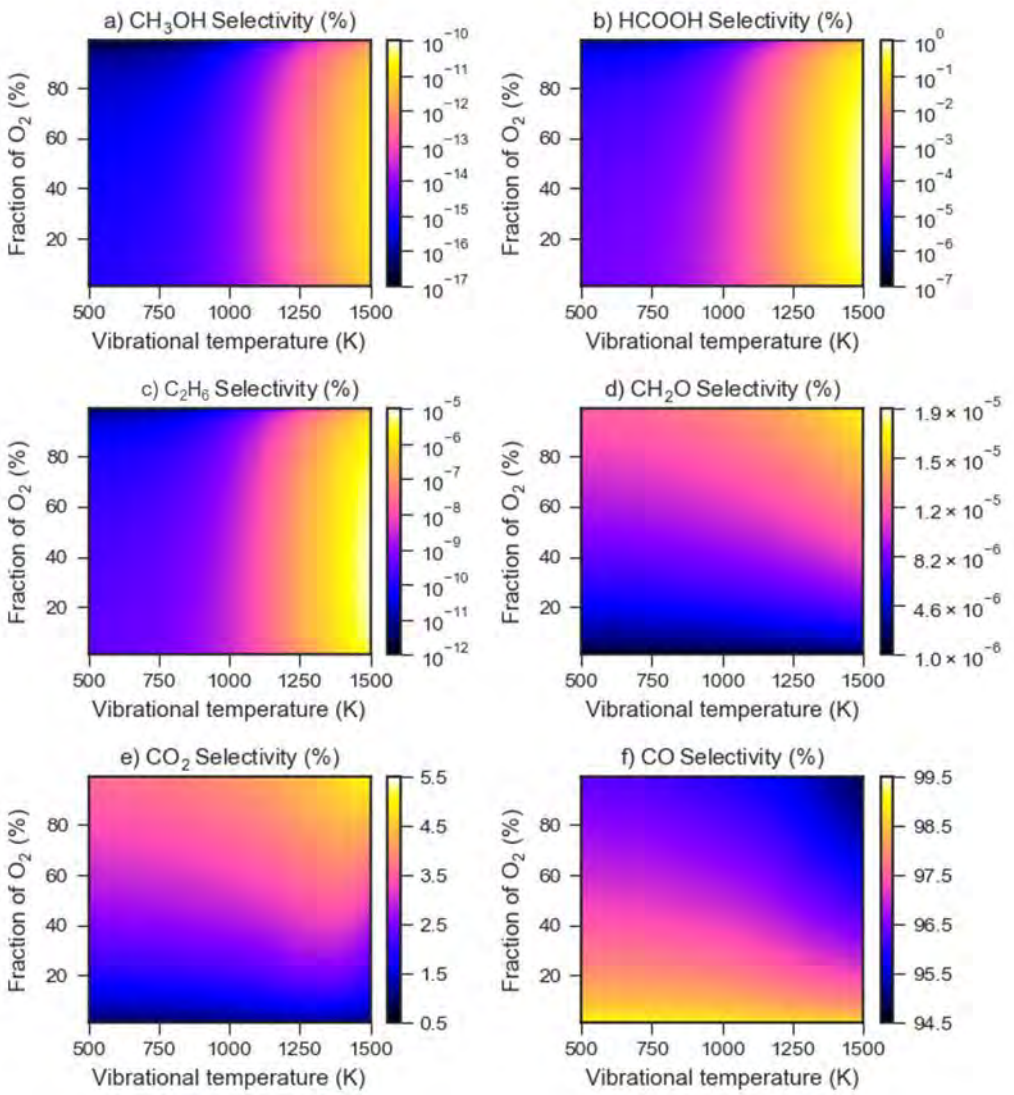

Figure 3.3. Influence of the vibrational temperature and O_2 content on the selectivities of oxygenates, CO_x and C_2H_6. Calculated at steady state for a CH_4/O_2 mixture at a pressure of 1 bar and a surface temperature of 500 K. Note that logarithmic scaling is used for CH_3OH, HCOOH and C_2H_6, while linear scaling is used for CH_2O, CO_2 and CO.

The similar trend for the selectivities of CH_3OH, HCOOH and C_2H_6, which strongly increase with rising vibrational temperature, can be explained by the enhanced dissociation of

CH_4. Vibrational excitation facilitates CH_4 dissociation, which enhances the formation of CH_x* and H*. Therefore, as the vibrational temperature rises from 500 to 1500 K, the fractional coverages of these species increase, by about a factor 10^3-10^5 at 30% O_2 (see Appendix A1, section A1.5). Higher H* coverages enhance the hydrogenation of CH_3O* and HCOO* to CH_3OH and HCOOH, respectively, resulting in higher selectivities towards these products if the vibrational temperature rises. Similarly, higher surface coverages of CH_x* enhance their coupling to form C_2 hydrocarbons. In Figure 3.3, we only show the selectivity of C_2H_6, but the selectivities of C_2H_4 and C_2H_2 show a similar trend, as shown in Appendix A1, section A1.6. While the formation of CH_x* and H* is also enhanced at high CH_4 content and thus low O_2 fractions in the gas mixture, this trend is not observed as strongly in the selectivities of CH_3OH, HCOOH and C_2 hydrocarbons. This is because lower O_2 fractions also result in higher fractions of free sites, which promote the dehydrogenation of CH_x* and CO formation according to the pathways in Figure 3.1 (a).

While vibrational excitation shows potential for improving the selectivities towards CH_3OH, HCOOH and C_2 hydrocarbons, these selectivities remain low under the investigated conditions, i.e. below 1.8×10^{-13}, 9.4×10^{-8}, 3.7×10^{-22} and 6.8×10^{-12} for CH_3OH, C_2H_6, C_2H_4 and C_2H_2, respectively. This indicates that the effect of vibrational excitation alone is not enough to make the formation of CH_3OH or C_2 hydrocarbons feasible on Pt(111). On the other hand, the selectivity towards HCOOH reaches a maximum of 0.77%, indicating that the formation of detectable amounts of HCOOH might be possible at high vibrational temperature.

As shown in Figure 3.3, the selectivities of CH_2O and CO_2 are not affected much by vibrational excitation and are instead more strongly dependent on the O_2 content in the gas mixture. Both products show increased selectivities at higher O_2 content, which is a result of the lower availability of free surface sites. As less free sites are available, a slightly lower fraction of CH_3* and CHO* can be dehydrogenated by empty sites. Instead,

relatively more CH_3* and CHO* will bind to O*, forming CH_3O* and HCOO*, respectively. As can be seen from the pathways displayed in Figure 3.1, the latter two species are precursors to CH_2O and CO_2, respectively. While the selectivities towards both products thus increase upon higher O_2 fraction, they vary relatively little under the investigated conditions, i.e. from 1.2×10^{-8} to 1.7×10^{-7} and from 0.89% to 5.1% for CH_2O and CO_2, respectively. Consequently, the selectivity towards CH_2O remains too low for its formation to become feasible on Pt(111), when only considering vibrational excitation. We find that the coupling of CH_3* and O* to CH_3O* is a bottleneck for the formation of CH_2O and CH_3OH, as CH_3O* is a precursor to both these products. This reaction is strongly disfavored on Pt(111), due to its high activation barrier (2.04 eV), while the barriers for CH_3* dehydrogenation by either an empty surface site or O* are lower (0.83 and 1.62 eV, resp.).[162]

In summary, our results show that plasma-induced vibrational excitation increases the CH_4 dissociation TOF in its POX. This supports the possibility of plasma catalysis to facilitate POX of CH_4 on transition metals, like Pt, at lower temperatures than those required in traditional thermal catalysis. Additionally, we find that vibrational excitation increases the selectivities of CH_3OH, HCOOH and C_2 hydrocarbons. The lower activation barrier of CH_4 dissociation improves the formation of H* and CH_x* species at the catalyst surface, which enhances hydrogenation of CH_3O* and HCOO* and coupling of CH_x. However, we find that the selectivities towards oxygenates and C_2 hydrocarbons remain low on Pt(111), as C-H bond breaking of the surface-bound intermediates is too strongly favored on this catalyst and the effect of vibrational excitation alone cannot counteract this.

3.3.3 Plasma catalysis: effect of radicals and stable intermediates

Radicals and stable intermediates formed in the plasma are implemented in the model by setting a non-zero partial pressure for these species. The base case assumes partial

pressures based on species densities calculated by De Bie *et al.*,[157] for a DBD plasma at a CH_4/O_2 (70/30) inlet gas mixture. These species densities are converted to partial pressures using the ideal gas law and normalized to a total pressure of 1 bar. The resulting partial pressures are listed in Table 3.1. To study the impact of different species on the surface chemistry, their partial pressures are varied in a wide range. Ions are not considered in our model as they generally have lower densities compared to the radicals, indicating that they play only a minor role in the plasma chemistry.[157] Moreover, thermodynamic data for adsorption of ions from the gas phase is not readily available.

Table 3.1. The partial pressures implemented in the model for the base case, i.e., CH_4/O_2 (70/30) inlet gas mixture. Based on species densities from De Bie et al.[157]

Reactants	**Partial pressure (bar)**
O_2	0.3
CH_4	0.7
Stable intermediates	**Partial pressure (bar)**
CO	6.91×10^{-7}
CH_3OH	2.25×10^{-7}
H_2	3.25×10^{-6}
C_2H_6	2.34×10^{-7}
C_2H_4	5.07×10^{-7}
C_2H_2	7.90×10^{-9}
H_2O	1.30×10^{-6}
CO_2	5.85×10^{-7}
CH_2O	1.98×10^{-6}
HCOOH[a]	1.98×10^{-6}

Radicals	**Partial pressure (bar)**
C	1.54×10^{-11}
CH	1.02×10^{-13}
CH_2	2.32×10^{-11}
CH_3	3.17×10^{-11}
O	2.09×10^{-7}
H	2.72×10^{-10}
OH	8.96×10^{-9}
OOH	2.62×10^{-6}
CHO	4.62×10^{-13}
CH_3OO	3.25×10^{-6}
CH_3O	9.17×10^{-8}

a) *This partial pressure was set equal to that of CH_2O, as HCOOH was not included by De Bie et al.*

We study the effect of the plasma species listed in Table 3.1, in the absence of any vibrationally excited species, to examine both effects separately. Furthermore, we find that if both effects are included in the model, the impact of vibrational excitation on the product TOFs is negligible. This is illustrated in Appendix A1, section A1.7. This indicates that for plasma catalysis with DBD plasmas, the surface chemistry is mainly governed by the plasma radicals. Similar conclusions were drawn by Engelmann *et al.*[84] for plasma-catalytic non-oxidative coupling of CH_4.

3.3.3.1 Most important reaction pathways in the presence of plasma species

Figure 3.4 illustrates the most important steady state reaction pathways on a Pt(111) surface exposed to a CH_4/O_2 (70/30) plasma, i.e. including plasma-generated radicals and intermediates. The most important surface reactions, in terms of reaction rate, are adsorption of O radicals and subsequent associative desorption of the surface-bound O* to form O_2. Approximately 96.7% of O* is formed via adsorption of O radicals from the plasma and 85.6% of O* desorbs as O_2 into the gas phase, while the rest is used in oxidation processes at the surface.

The main carbon pathway starts from adsorption and subsequent dissociation of C_2H_2 to CH*. The latter preferentially (74.2%) undergoes oxidation to CHO*, which in turn binds with O* to form HCOO*. Most of the HCOO* (92.4%) undergoes hydrogen abstraction by O* to form CO_2* and OH*, while 6.8% is hydrogenated to HCOOH. About 50.6% of the surface-bound OH* is formed from reaction between HCOO* and O*, while the remaining 49.4% is adsorbed from the plasma. Most of the OH* (80.0%) forms H_2O* and O* via a disproportionation reaction, while 19.1% reacts with CH* to form H_2O* and C*. H_2O* desorbs from the surface as a product. Surface-bound C* can either be oxidized to CO* (65.5%), undergo hydrogenation to again form CH* (19.3%), react with CO_2* to form two CO* molecules (11.6%) or bind to OH* to form COH* (3.6%). The latter decomposes into CO* and H*, forming about 9.2% of the surface-bound H*, though most H* (82.7%)

is formed by direct adsorption from the plasma. H* is mainly consumed in the hydrogenation of C* (49.8%) and the formation of HCOOH (49.7%).

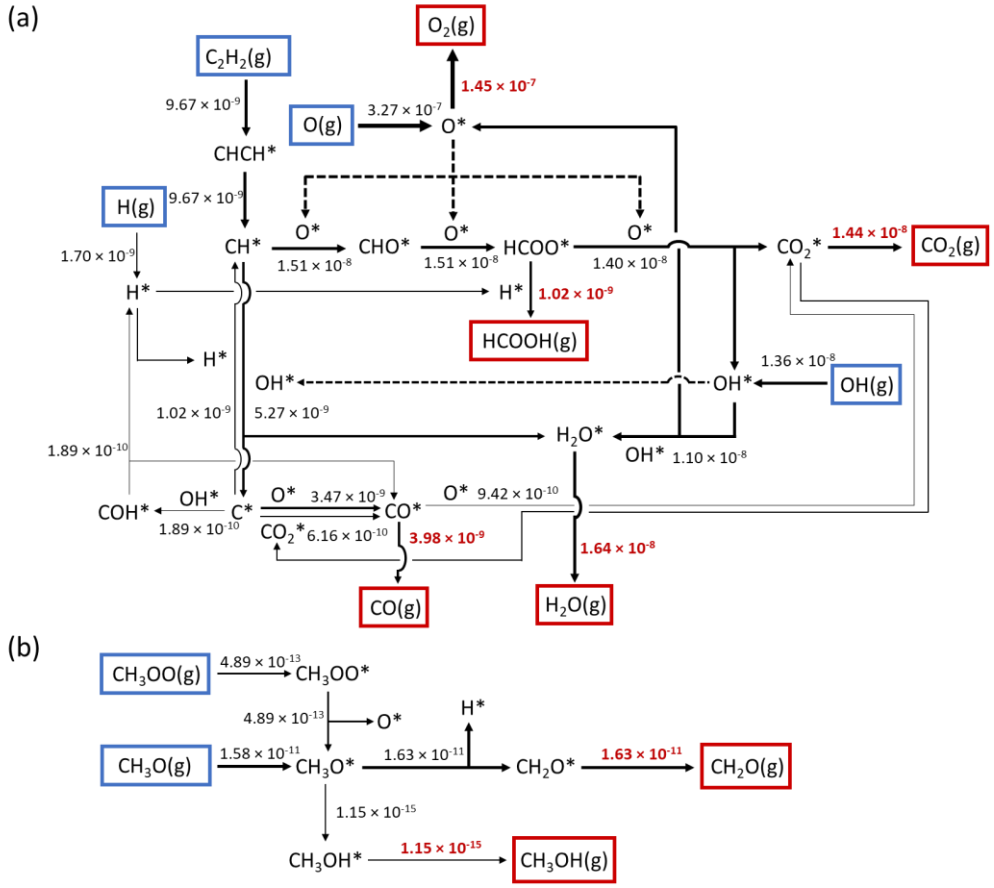

Figure 3.4. Most important reaction pathways at steady state for POX of CH_4 on a Pt(111) surface exposed to a CH_4/O_2 (70/30) DBD plasma at 500 K and 1 bar. The values of the reaction rates in (s^{-1}) are displayed next to the arrows. The arrow thickness indicates the relative importance of that reaction within each separate scheme. A dotted arrow indicates the species is used as a second reactant in another reaction.

As discussed above, various routes lead to the formation of CO*. Most of the CO* (80.9%) desorbs from the surface as a product, while a smaller amount is oxidized to CO_2* (19.1%). Thus, our results show that any CO* that reacts further is not hydrogenated to

oxygenates, but instead further oxidized to CO_2. The formation of oxygenates therefore occurs via another route than that of CO.

While our results show that some CO_2 is formed via oxidation of CO*, we do not find this to be the main pathway for CO_2 formation. Instead, we find that CO_2 is mainly formed from HCOO* in a separate pathway. Interestingly, DRIFTS results by Stere *et al*.[159] indicate that in the plasma-catalytic oxidation of CH_4 on a Pd/Al_2O_3 catalyst, CO_2 formation also occurs via HCOO*. As Pt and Pd are part of the same group in the periodic table, similarities in their surface chemistry can indeed be expected.

Note that H_2O is formed as a major product. This might be troublesome, as the presence of H_2O vapor in a DBD plasma can alter the discharge behavior, resulting in more, but less intense micro-discharges.[176] H_2O addition can also cause destabilization of the discharge, and plasma chemistry calculations revealed a drop of approximately 40% in the maximum electron density upon increasing the water content from 0 to 8% in DBD plasma.[177] Additionally, a higher H_2O concentration results in a loss of electron energy due to H_2O rotational and vibrational excitation, as is discussed in literature for He/H_2O and Ar/H_2O plasmas.[176,178] The presence of H_2O in plasma also causes quenching of the vibrational levels of CO_2, which results in less CO_2 dissociation.[179] This might lead to a higher net production of CO_2. Moreover, the presence of H_2O might also result in additional CO_2 formation in the plasma through the water-gas shift.[180] This is in line with plasma chemical kinetics simulations and experiments, which revealed that H_2O addition to a CO_2 DBD plasma causes a drop in CO_2 conversion, and the detailed chemical kinetics scheme explaining this behavior was presented in ref. [177]. Furthermore, this paper also explained the underlying chemistry why oxygenates formation was prohibited in this case. Therefore, it can be beneficial to remove H_2O from the gas phase through condensation by cooling the reactor wall. In addition, this also removes condensable oxygenates from the gas phase and limits their further oxidation.[175,180]

Figure 3.4 (b) presents the main reaction pathways for the formation of CH_3OH and CH_2O. As for the thermal-catalytic case (see Figure 3.1), CH_3O* is a key species in the formation of both CH_3OH and CH_2O. Yet, for thermal catalysis the formation of this species occurs on the catalyst surface, via O* addition to CH_3*, while Pt strongly favors CH_3* dehydrogenation instead. In the plasma case, on the other hand, CH_3O is formed in the plasma and subsequently adsorbs on the catalyst surface. As is illustrated in Figure 3.4 (b) for the plasma case, CH_3O* is either directly adsorbed from the gas phase (97.0%) or formed from adsorption of CH_3OO radicals and subsequent cleavage of the O-O bond (3.0%). The formed CH_3O* preferentially undergoes dehydrogenation to CH_2O (> 99.9%), while only a minor fraction is hydrogenated to form CH_3OH (0.007%).

In the presence of radicals, the reaction rates are generally higher compared to the thermal-catalytic case. The TOFs of CO and CO_2 have risen by about three and five orders in magnitude, respectively, compared to thermal catalysis. We find that CO_x are still the main products for the plasma case, with selectivities of 20.5% and 74.4% for CO and CO_2, respectively. However, the selectivities and TOFs of the oxygenates have strongly improved compared to the thermal-catalytic case. The calculated selectivities of CH_3OH, CH_2O and HCOOH now reach 5.9×10^{-8}, 0.084% and 5.3%, respectively, which corresponds to a rise by about ten, four and five orders of magnitude, respectively. Although CH_3OH formation still does not seem to be feasible on Pt under these conditions, a reasonable amount of HCOOH is now formed on the surface. The combination of a catalyst with plasma radicals thus shows potential for enhanced oxygenate selectivities. Additionally, tuning the partial pressures of the radicals in the plasma might further improve the formation of oxygenates. In the next section, we therefore show how different radicals affect the surface chemistry, fractional coverages and product TOFs.

3.3.3.2 The role of plasma species in the surface chemistry

As mentioned before, the reaction pathways discussed in the previous section are based on species densities calculated by De Bie *et al*.[157] (see Table 3.1), which are specific for the selected reaction conditions. In this section, we aim to gain additional understanding of how variations in the plasma composition might alter the surface chemistry by examining the influence of various plasma species on the product TOFs and surface coverages. For this purpose, we vary the partial pressures of either individual species or groups of species by a scaling factor, while keeping the partial pressures of the other species constant on the values reported in Table 3.1. The species HCOO and COOH are not included in the model by De Bie *et al*.[157] and are therefore not included in the simulations discussed below. However, a discussion of the effect of these species is included in the Appendix A1.9.

Oxidizing species

Figure 3.5 illustrates how the TOFs of CO_x, oxygenates and C_2H_6 are affected by a variation of the O partial pressure over six orders of magnitude. Next to the TOFs, the surface coverages of the most abundant surface species are also displayed. A drop in the partial pressure of O radicals results in a sudden decline of the product TOFs, combined with a strong rise in the surface C* coverage. Although our model does not contain a mechanism for cokes formation, i.e. clustering of carbonaceous species, like e.g. C*, CH*, CHCH*, high surface coverage of these species indicates that coking is likely to occur. Coking reduces the amount of available catalytic sites on the surface and thus lowers the product TOFs. Most of the TOFs in Figure 3.5 eventually stabilize upon further lowering of the O partial pressure, as OH* becomes the main oxidizing species at the surface. On the other hand, a high partial pressure of O is also disadvantageous, as O* competes with other species for free sites. If the O partial pressure is too high, O* will poison the surface, causing the TOFs to decline as well.

As can be seen in Figure 3.5, the O partial pressure can be used to tune the product selectivity between CO and CO_2. Low partial pressures of O radicals, which can be expected for plasmas with a high CH_4/O_2 ratio, favor the formation of CO. On the other hand, high O partial pressures, associated with low CH_4/O_2 ratios, give CO_2 as the main product. If the partial pressure of O is increased by about a factor 10, the faster oxidation of CO* results in net CO consumption, as plasma-produced CO adsorbs onto the surface and is oxidized to CO_2. Indeed, various experimental studies on plasma-catalytic POX of CH_4 report that transition metals (Ni,[181,182] Fe,[183] Pd[183] and Pt[184]) can catalyze the oxidation of CO to CO_2. Additionally, DRIFTS and FTIR results by Zhang *et al*.[160] for plasma-catalytic CH_4 oxidation on Ni indicate that the selectivity of CO vs. CO_2 can be tailored by adjusting the introduction of O_2 to a plasma.

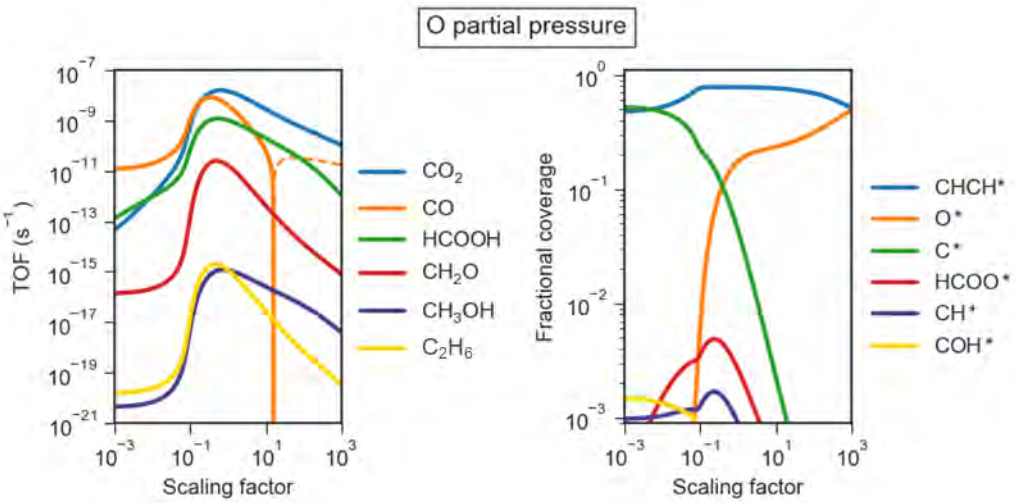

Figure 3.5. Influence of the O partial pressure on TOFs (left) and surface coverages (right). Dotted lines in the left graph indicate consumption, whereas full lines indicate production. Calculated for a temperature of 500 K and a total pressure of 1 bar. The species partial pressures used for these simulations are shown in Table 3.1, but the partial pressure of O is varied by the indicated scaling factor.

Next to O, we also examine the influence of the OH and OOH radicals as oxidizing species (see Appendix A1, section A1.8). Increasing the partial pressures of these species

enhances the formation of OH* on the surface. The formed OH* promotes dehydrogenation of CH_x, which leads to more C* and thus favors CO formation. However, a further increase in the OH and OOH partial pressures results in a higher O* coverage, due to hydrogen abstraction from OH* by another OH*. This causes a drop in the surface coverage of most of the other surface species, which results in a decline of the product TOFs. Likewise, we present the effect of the HCOO and COOH radicals on the product TOFs and surface coverages in Appendix A1, section A1.9. We conclude that HCOO and COOH mainly result in additional formation of unwanted CO_2 and CO, and their formation in the plasma should therefore be limited.

In summary, oxidative species can reduce the coverage of carbonaceous species that could cause catalyst deactivation by coking. Yet, if the partial pressures of oxidative species are too high, the surface is poisoned with O* species instead. However, due to their reactive nature, plasma radicals might be able to react with surface-bound species, such as O*, via E-R reactions with low to zero enthalpy barriers. In such case, high TOFs might be achieved even at high O* coverages. While our model does contain E-R reactions, namely R3.1 and R3.2, these reactions have higher enthalpy barriers (1.28 eV[185] and 0.50 eV[185], resp.) than what can be expected for similar reactions involving highly reactive radicals, rather than stable CH_4. In section 3.3.3.3 we therefore briefly illustrate the potential impact of E-R reactions with plasma radicals for a range of enthalpy barriers. Further, our results show that tuning the amount of O radicals against the amount of C-containing species can be used to favor the production of CO over that of CO_2.

Carbonaceous species

The influence of the strongly dehydrogenated carbonaceous species (C, CH and C_2H_2) on the TOFs and surface coverages is shown in Figure 3.6. We include C_2H_2 as well, as this is the most important species on the surface and the main source of surface carbon under

the base conditions. As is shown in Figure 3.6, high partial pressures (i.e., for scaling factors > 1) of these species lead to strong surface poisoning by CHCH* and thus a drop in the product TOFs. As mentioned before, these species can act as precursors for coking of the catalyst surface. We find that limiting the partial pressures of these carbonaceous species in the plasma has a beneficial effect on the TOFs of most products. However, low partial pressures of these species lead to adsorption and oxidation of plasma-produced CO to CO_2, as can be seen in Figure 3.6 at scaling factors < 0.58. Because less carbonaceous species are available for reaction with O*, more O* reacts with surface-bound CO*. Simultaneously, less CO* can be formed through the pathways in Figure 3.4, as these pathways go via C*, leading to a net adsorption of plasma-produced CO.

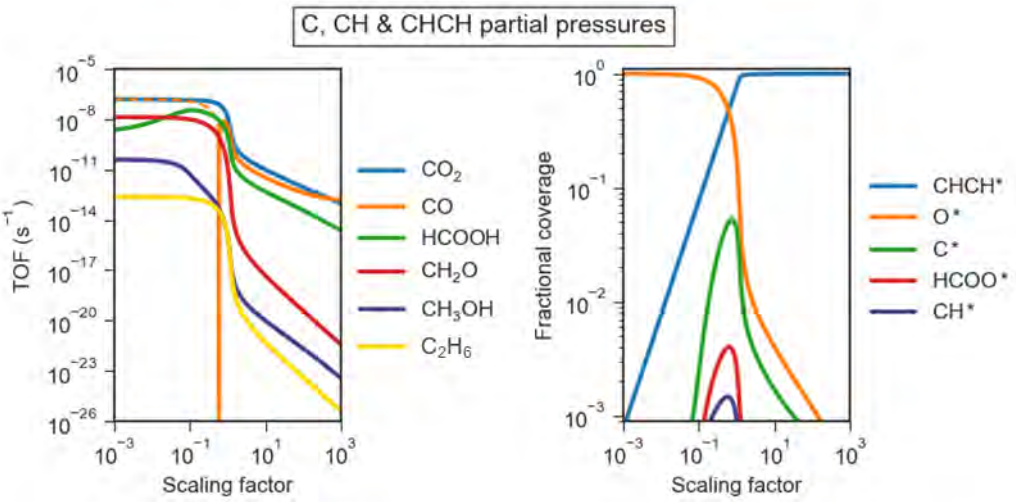

Figure 3.6. Influence of the C, CH and C_2H_2 partial pressures on TOFs (left) and surface coverages (right). Dotted lines in the left graph indicate consumption, whereas full lines indicate production. Calculated for a temperature of 500 K and a total pressure of 1 bar. The species partial pressures used for these simulations are shown in Table 3.1, but the partial pressures of C, CH and C_2H_2 are simultaneously varied by the indicated scaling factor.

Furthermore, the simultaneous drop in the C, CH and C_2H_2 partial pressures initially shows a beneficial effect on HCOOH formation, but scaling the partial pressures with a factor below 10^{-1} causes the TOF of HCOOH to decline. This results from the lower

availability of CH* on the catalyst surface, as this species is required for HCOOH formation, according to the reaction pathways shown in Figure 3.4. At low partial pressures of the strongly dehydrogenated carbonaceous species (i.e., around a scaling factor of 10^{-2}), the HCOOH TOF in Figure 3.6 eventually stabilizes, as CH_3 and CH_2 radicals become the main precursor species for the formation of CH* and HCOOH. In this regime, CH_2O becomes the most important oxygenate as its formation does not occur via CH*, but through CH_3O* and CH_3OO* instead.

Figure 3.7 displays the change in TOFs and fractional surface coverages, when increasing the partial pressures of CH_3 and CH_2 up to a factor 10^4. A higher partial pressure of these more hydrogenated carbonaceous species positively affects the TOFs, especially those of C_2H_6, HCOOH and CH_3OH. The effect on the TOF of C_2H_6 is straightforward, as a higher partial pressure of CH_3 improves the CH_3* coverages and its coupling towards C_2H_6. CH_3OH and HCOOH, on the other hand, benefit from the improved hydrogenation of CH_3O* and HCOO*, respectively, because CH_3 and CH_2 provide the surface with more H* (due to catalytic dehydrogenation). Moreover, the formation of H* through dehydrogenation of CH_2* also forms CH*, which is an intermediate in the formation of HCOOH (see Figure 3.4). As can be seen in Figure 3.7, this results in HCOOH becoming the main carbon product (even slightly above CO_2) at around a scaling factor of 10^3.

These results show that Pt is potentially a good catalyst for the plasma-catalytic HCOOH synthesis under plasma conditions with abundant CH_3 and CH_2 radicals (hence high CH_4/O_2 ratio), as it can readily dehydrogenate adsorbed CH_x* radicals to form CH*, while simultaneously forming the H* required in the hydrogenation of HCOO*, later on in the reaction path. However, as can be seen in Figure 3.7, enhancing the partial pressures of CH_3 and CH_2 by more than a factor 10^3 is no longer beneficial. The surface coverages indicate strong cokes formation past this point, resulting in a decline of most of the TOFs.

Note that CH_3 and CH_2 themselves bind less strongly to the surface compared to CH and C,[185] and are less likely to act as coking precursors.

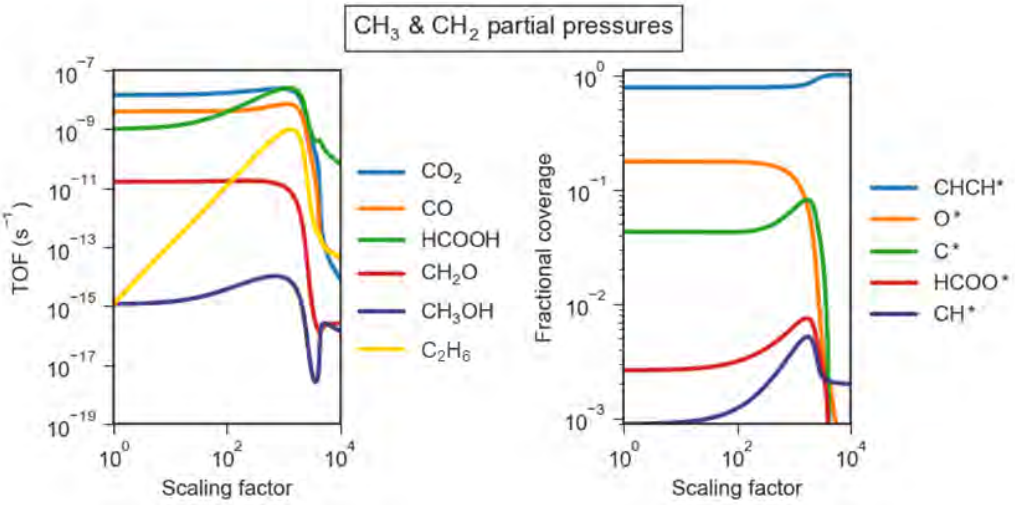

Figure 3.7. Influence of the CH_3 and CH_2 partial pressures on TOFs (left) and surface coverages (right). Calculated for a temperature of 500 K and a total pressure of 1 bar. The species partial pressures used in the simulations are shown in Table 3.1, but the partial pressures of CH_3 and CH_2 are simultaneously varied by the indicated scaling factor.

In summary, strongly dehydrogenated carbonaceous species are mainly precursors for cokes formation, and their partial pressures in the gas phase should ideally be kept low. These species also show some beneficial effect on HCOOH and CO formation at lower partial pressures. The more hydrogenated CH_2 and CH_3, generally show a more beneficial effect, enhancing the TOF of C_2H_6, HCOOH and CH_3OH at higher partial pressures, but also cause coking at very high partial pressures (i.e., above a scaling factor 10^3). The partial pressures of carbonaceous species can be expected to be higher for gas mixtures with high CH_4 content, but the ratio of less vs. more hydrogenated CH_x species might be influenced by the CH_4 fragmentation pattern through electron impact dissociation in the plasma. Nozaki *et al.*[155] simulated streamer formation in CH_4 without catalyst and showed that the fragmentation pattern depends on the reduced electric field, with

stronger reduced electric fields resulting in a larger fraction of more dehydrogenated CH_x species. Therefore, plasma characterized by weaker reduced electric fields can be expected to give less cokes formation. As discussed in the previous section, coking can also be counteracted by using high partial pressures of oxidizing radicals, e.g. O, OH and OOH, and by tuning the partial pressures of oxidizing species against those of carbonaceous species, the formation of either CO or CO_2 can be favored. Moreover, the choice of the catalyst material can also be expected to play an important role in mitigating both coking and excessive oxidation, as different transition metals have different binding strengths for O and C. It is therefore essential in plasma catalysis to carefully tune the CH_4/O_2 ratio as function of the plasma conditions and the catalyst material.

Hydrogen radicals

Figure 3.8 illustrates the influence of the H radical partial pressure on the TOFs of CO_x, the oxygenates and C_2H_6, as well as the surface coverages of the most abundant surface species. A higher partial pressure of H strongly enhances HCOOH and CH_3OH formation. This is caused by the higher availability of H* on the catalyst surface, which improves the hydrogenation of CH_3O* and HCOO* to CH_3OH and HCOOH, respectively. Upon increasing the H partial pressure by about a factor 400, a strong rise in the TOFs of CH_3OH, CH_2O and CO_2 is observed. This is attributed to the improved hydrogenation of O* to H_2O*, which readily desorbs to make more free sites available. The fraction of free sites on the surface increases from about 10^{-10} to 10^{-6} in this region. This improves the adsorption of CH_3O, which can form both CH_3OH and CH_2O (see Figure 3.4 (b)), and the adsorption of CO, which is oxidized to CO_2. At low H partial pressure ($< 3 \times 10^{-11}$ bar), the TOFs in Figure 3.8 stabilize, as OH* now becomes the main source of H*. This results from coupling between OH* and C* followed by decomposition of the formed COH* to CO* and H*.

Given the favorable effect of the H radical on the formation of oxygenates, and especially CH_3OH, it is of interest to find a way to increase the partial pressure of H in the plasma. For its POX, CH_4 serves as the source of H in the plasma and increasing the CH_4 fraction in the feed gas might thus increase the partial pressure of H radicals. As discussed above, however, high CH_4/O_2 ratios might induce coking, due to the limited availability of oxidizing species. Adding a H-containing co-reactant, such as H_2 or H_2O, might allow for more flexibility in maximizing the TOF of oxygenates, and especially CH_3OH.

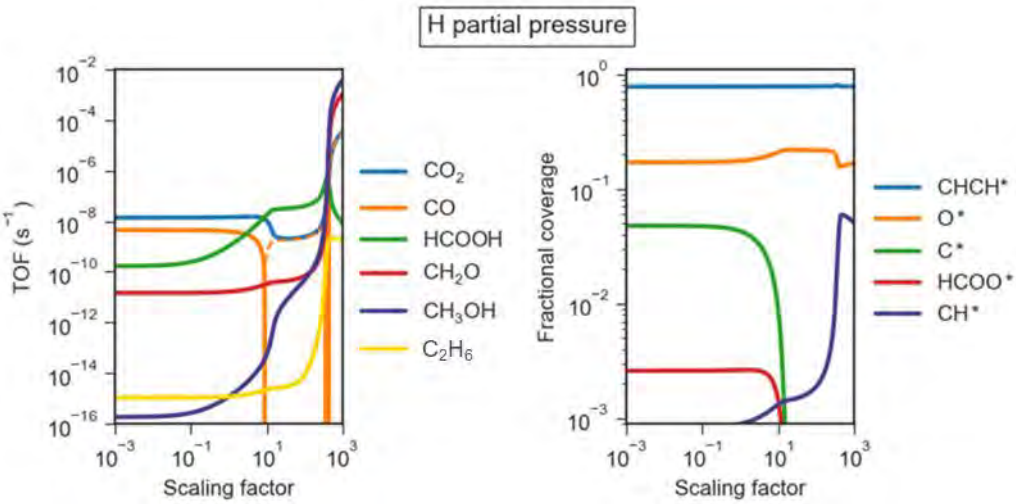

Figure 3.8. Influence of the H partial pressure on TOFs (left) and surface coverages (right). Dotted lines in the left graph indicate consumption, whereas full lines indicate production. Calculated for a temperature of 500 K and a total pressure of 1 bar. The species partial pressures used in the simulations are shown in Table 3.1, but the partial pressure of H is varied by the indicated scaling factor.

CH_3O and CH_3OO radicals

Modeling results by De Bie *et al.*[157] for plasma-only POX of CH_4 indicate that the CH_3O and CH_3OO radicals are important intermediates in the pathways leading to CH_3OH production in plasma. Our results show that for plasma catalysis these species also play an important role in the formation of CH_3OH and CH_2O at the catalyst surface, as

indicated by the pathways in Figure 3.4 (b). We are therefore interested in the influence of these species on the catalyst surface chemistry and thus examine how a variation in their partial pressures affects the TOFs and fractional coverages at the catalyst surface. The results are shown in Figure 3.9.

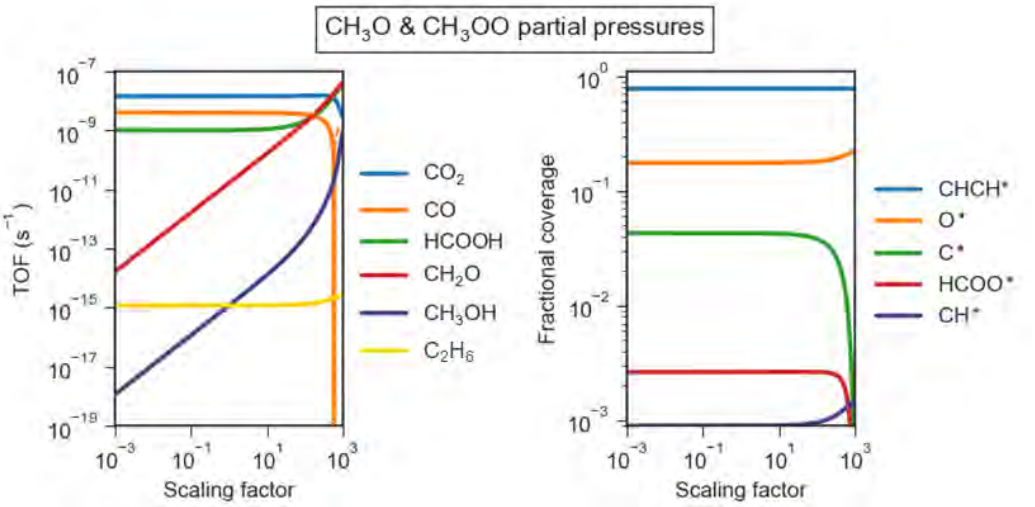

Figure 3.9. Influence of the CH_3O and CH_3OO partial pressures on TOFs (left) and surface coverages (right). Dotted lines in the left graph indicate consumption, whereas full lines indicate production. Calculated for a temperature of 500 K and a total pressure of 1 bar. The species partial pressures used in the simulations are shown in Table 3.1, but the partial pressures of CH_3O and CH_3OO are simultaneously varied by the indicated scaling factor.

As CH_3O and CH_3OO are precursors to both CH_3OH and CH_2O, the TOFs of these products strongly depend on the partial pressures of CH_3O and CH_3OO, while the TOFs of the other products are largely unaltered. Only at high partial pressures (i.e., for scaling factors $\geq 10^2$), where the adsorption and subsequent decomposition of CH_3O becomes important, the TOFs of the other products are also influenced, as can be seen in Figure 3.9. The decomposition of CH_3O^* leads not only to the formation of CH_2O^* but also provides H*. The higher availability of H* improves HCOO* hydrogenation, so that CH_2O and HCOOH eventually become the main products (even above CO and CO_2). Moreover, the rise of the CH_3OH TOF also becomes much steeper in this region, illustrating the

strong beneficial effect of both CH_3O* and H* on the CH_3OH formation. We also observe a shift in the surface coverages in Figure 3.9, as more C* is converted to CH*. The lower surface coverage of C* and preferred conversion of HCOO* to HCOOH at high CH_3O and CH_3OO partial pressures, limit the formation of undesired CO and CO_2.

We therefore find that CH_3O and CH_3OO can play an important role in enhancing the formation of oxygenates. Additionally, our results show that Pt is potentially a good catalyst for CH_2O synthesis, as CH_3O selectively decomposes to CH_2O on this catalyst. Moreover, it might be possible to vary the selectivity between CH_3OH or CH_2O by changing the catalyst material, as more noble transition metals have lower barriers for CH_3O hydrogenation and higher barriers for its dehydrogenation.[152]

Plasma-generated radicals and stable intermediates in general

In Figure 3.10, we illustrate how the TOFs and fractional coverages are affected by simultaneously lowering the partial pressures of all plasma-produced radicals and stable intermediates by a factor 10^{-6}. The product TOFs, especially those of CH_2O and CH_3OH, initially rise upon lowering the partial pressures of these plasma species, and CH_2O becomes the main product (clearly above CO and CO_2) below a scaling factor of 10^{-2}. Its TOF keeps rising upon lowering the partial pressures by a factor 10^{-3}-10^{-4}, after which all TOFs decline. The initial rise in the TOFs of CH_2O and CH_3OH results from improved adsorption of CH_3O and CH_3OO. Indeed, at high partial pressures of plasma species (i.e, corresponding to scaling factors $\geq 10^{-2}$), the adsorption of CH_3O and CH_3OO is hindered by surface poisoning by stronger binding species, such as O* and coking species. By lowering the partial pressures of all plasma species, more free sites become available, i.e. the fraction of free surface sites increases from 10^{-10} to 10^{-5} when lowering the partial pressures by a factor 10^{-6}. Moreover, the right panel of Figure 3.10 illustrates that the fractional coverages of coking precursors strongly decline as the partial pressures are lowered. The enhanced availability of free sites initially improves the adsorption of CH_3O

and CH_3OO, even though their partial pressures are lowered. As these species are precursors to CH_2O and CH_3OH, the TOFs of these products are higher (i.e., a factor ≈ 10^5 higher for a scaling factor 10^{-3}). Upon further lowering the partial pressures of the plasma species, the TOFs eventually decrease due to the lower availability of reactive plasma species in the gas phase.

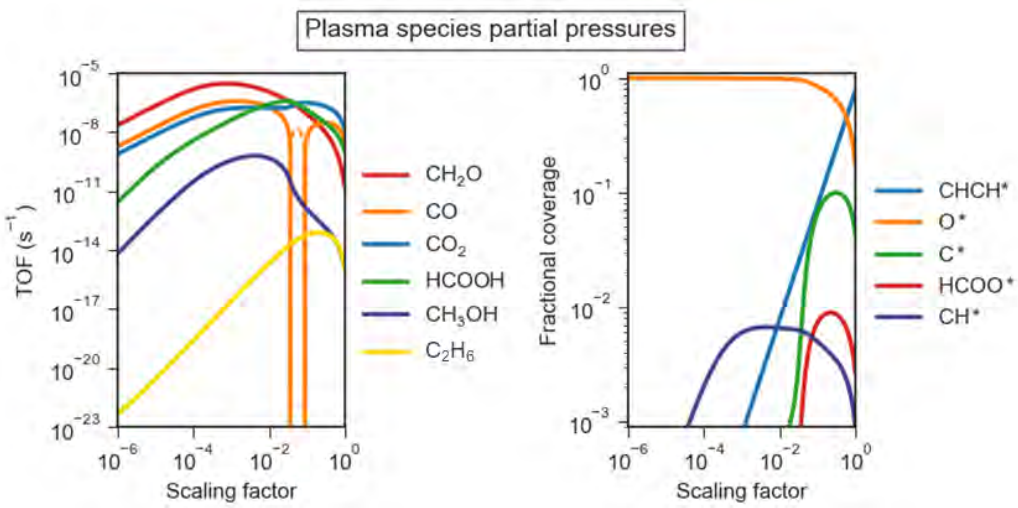

Figure 3.10. Influence of the partial pressures of all plasma-produced radicals and stable intermediates on TOFs (left) and surface coverages (right). Dotted lines in the left graph indicate consumption, whereas full lines indicate production. Calculated for a temperature of 500 K and a total pressure of 1 bar. The default values of the species partial pressures used in the simulations are shown in Table 3.1, but the partial pressures of all species, except for CH_4 and O_2, are simultaneously varied.

Our results thus show that lowering the radical densities in the plasma, up to a certain limit, is beneficial for oxygenate production, as this limits surface poisoning by strongly binding plasma species. This might be achieved by using a lower plasma power or placing a catalyst in the plasma afterglow. However, this might also change the radical distribution (in the plasma or afterglow). On the other hand, modeling of POX of CH_4 in a DBD shows that the densities of CH_3O and CH_3OO vary little between the pulses.[157]

Therefore, these species are expected to remain among the most important radicals even in the afterglow.

Figure 3.11 summarizes how the different plasma species discussed in this section affect the formation of CO_x and the oxygenates. Strongly dehydrogenated carbonaceous species, e.g. C_2H_2, CH and C, cause cokes formation on the catalyst surface and favor the production of CO over that of CO_2. O radicals, on the other hand, reduce coking but result in overoxidation to CO_2. The less strongly dehydrogenated carbonaceous species, i.e. CH_3 and CH_2, mainly favor HCOOH, but also to a lesser extent cokes formation. H enhances the formation of HCOOH and CH_3OH by improving the hydrogenation of their respective precursor species, HCOO* and CH_3O*, and it also enhances the formation of CH_2O, by the higher adsorption of CH_3O, which can form both CH_3OH and CH_2O. The CH_3O and CH_3OO radicals are the precursors to both CH_3OH and CH_2O and thus also favor the formation of these products.

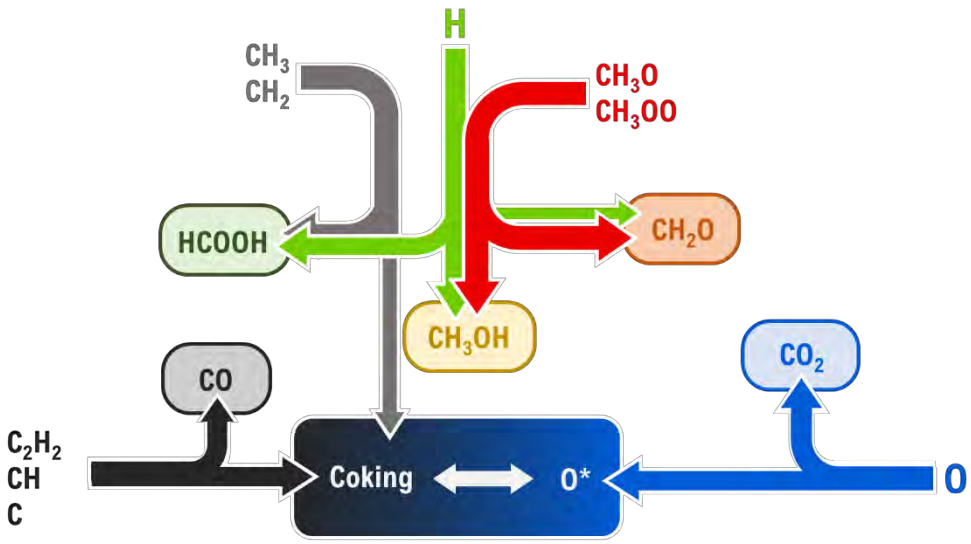

Figure 3.11. Overview of the influence of various plasma species on the formation of oxygenates and CO_x in the plasma-catalytic POX of CH_4 on Pt(111).

It should be noted that the present model focuses on the surface reactions, and the plasma chemistry is only taken as input. In Chapters 5 and 6, we combine both the plasma chemistry and catalyst surface chemistry into one model, so that the effect of the surface reactions on the gas phase composition is self-consistently accounted for.

3.3.3.3 E-R reactions involving radicals

Due to their highly reactive nature, radicals generally form strong bonds when adsorbing onto a catalyst surface. Together with the abundancy of radicals in the plasma, this can induce strong poisoning of the catalyst surface, as illustrated above. However, the high reactivity of plasma-generated radicals might also enable them to react with the surface species via E-R reactions with low to zero enthalpy barriers. Therefore, we briefly illustrate the potential effect of these ER reactions by including the following three reactions in the chemistry set:

$$CH_{3(g)} + O^* \rightarrow CH_3O^* \quad \text{R3.3}$$

$$H_{(g)} + O^* \rightarrow OH^* \quad \text{R3.4}$$

$$O_{(g)} + C^* \rightarrow CO^* \quad \text{R3.5}$$

We choose these reactions as CH_3, H and O are the main products of electron impact dissociation of CH_4 and O_2, respectively, and because O* and C* are abundant and simple surface species. To the best of our knowledge, no activation barriers have been reported for these E-R reactions. We therefore simultaneously vary the enthalpy barriers of these reactions between 0.0 and 0.75 eV. Higher enthalpy barriers show no further effect on the TOFs. For comparison, the E-R reactions that involve CH_4 (i.e., R3.1 and R3.2) have enthalpy barriers of and 1.28 eV[185] and 0.50 eV,[185] respectively. We would also like to emphasize that all ER reactions, including those with radicals, have an entropy barrier

that corresponds to the loss of all translational entropy of the corresponding radical or gas molecule, as explained in the model description.

In Figure 3.12, we illustrate the influence of these E-R reactions on the TOFs and surface coverages for the indicated range of enthalpy barriers. All the TOFs in Figure 3.12 rise upon lowering the enthalpy barriers and thus enhancing the importance of the E-R reactions. For low barriers (≤ 0.30 eV), CO becomes the main product due to the reactions of O radicals with surface C*. The TOFs of CH_2O and CH_3OH also rise strongly upon lowering the barriers, because of the enhanced formation of their precursor species, CH_3O*, through reaction between CH_3(g) and O*.

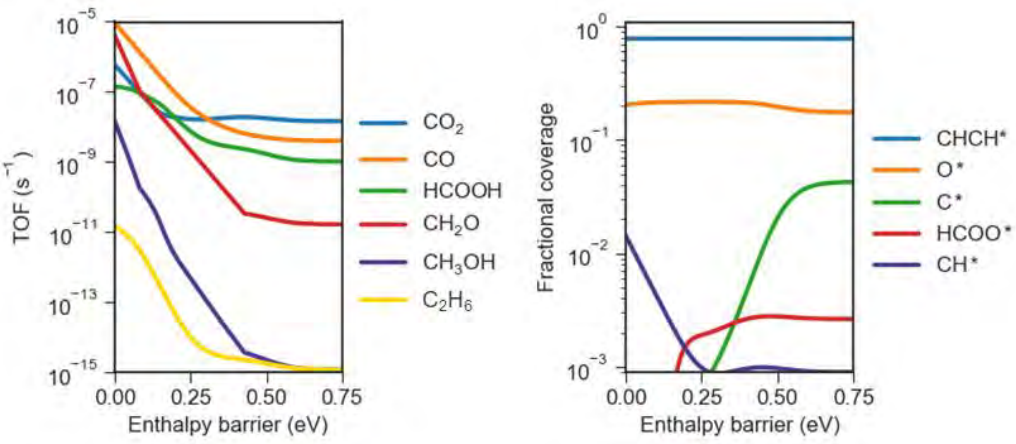

Figure 3.12. Influence of the enthalpy barriers of E-R reactions (R3.3, R3.4 and R3.5) involving radicals on the TOFs (left) and surface coverages (right). The enthalpy barriers of these E-R reactions are simultaneously varied in the simulation. Calculated for a temperature of 500 K and a total pressure of 1 bar. The values of the species partial pressures used in the simulations are shown in Table 3.1.

Note that the net rate of CH_3O and CH_3OO adsorption/desorption is set to zero if desorption of these species occurs, thus assuming that an equilibrium is reached due to accumulation of these radicals near the surface. For the lower barriers (< 0.09 eV), CH_2O becomes the second most important product, after CO. The decomposition of CH_3O* to

CH_2O* also forms H*, which enhances the formation of HCOOH and CH_3OH. Additionally, a drop in C* coverage and a rise in CH* coverage can be observed due to the improved H* formation.

In summary, our results show that E-R reactions involving radicals have a potentially strong contribution to the TOFs in plasma catalysis. Additionally, these E-R reactions might be responsible for a significant part of the oxygenate formation in plasma-catalytic POX of CH_4. We note that other E-R reactions might also be important; however, the lack of reported activation barriers currently limits the construction of an extended chemistry set with these reactions. The three E-R reactions that we considered, are aimed at illustrating the potential impact of these reactions.

3.3.4 Additional remarks and suggestions

3.3.4.1 Possible effect of C-C coupling reactions

As shown in Figure 3.5, Figure 3.6 and Figure 3.7, carbon-containing adsorbates can be present on the surface with high coverages (≈ 1). While high coverages of carbonaceous species like C*, CH* and CHCH* indicate that coking is likely to occur, our model does not explicitly capture the mechanism for coking. Additionally, C-C coupling to higher hydrocarbons might also become important under these conditions. While our model does contain some C-C coupling reactions to form C_2 hydrocarbons, C-C coupling to higher hydrocarbons is not included, mainly due to lack of availability of the required thermodynamic input data in literature. Therefore, we should remain careful with the interpretation of our results under conditions where carbonaceous species appear to poison the surface. If C-C coupling to higher hydrocarbons would be favored over cokes formation, then formation and desorption of these higher hydrocarbons might result in an improved availability of free sites and higher TOFs. However, this also depends on the barrier for desorption of the formed product. Nevertheless, we would like to emphasize

that the main focus of this study is on the formation of oxygenates under partial oxidation conditions, where oxidation reactions are the dominant mechanism.

3.3.4.2 Other catalyst materials

Our model is applied to Pt(111), but we provide here some information on how (or whether) our results might be translated to other catalyst materials, based on insights obtained from our work and literature. Microkinetic modeling of the thermal-catalytic POX of CH_4 by Yoo *et al.*[151] shows that for Pt-group metals the selectivity of CH_2O increases when going towards metals that bind O* more strongly. This was attributed to the higher O* coverages, which promote the coupling between CH_3* and O* to form CH_3O*, and the subsequent O* assisted dehydrogenation of CH_3O* to CH_2O*.[151] While for plasma conditions where CH_3O* can be formed in the plasma itself, we can expect that metals with a higher O* binding strength, such as Pd and Rh, improve the adsorption of CH_3O* and CH_3OO* to the surface, thus also enhancing CH_2O, and possibly CH_3OH formation. Yoo *et al.*[151] also found that coinage metals, such as Cu, Ag and Au, are most suitable catalysts for CH_2O and CH_3OH synthesis. The authors determined that the selectivity of CH_2O vs. CH_3OH on these catalysts was determined by competition between two reaction paths: CH_3* + O* → CH_3O* (following dehydrogenation to CH_2O*) and CH_3* + OH* → CH_3OH*.[151] For plasma catalysis we might thus also expect a change in the mechanism of CH_3OH* formation, where CH_3 and OH radicals become the main precursors for CH_3OH on the most noble metals. In this case it might be possible to steer the selectivity of CH_2O vs. CH_3OH by changing the densities of O vs OH radicals in the plasma.

Using DFT and microkinetic modeling, Studt *et al.*[186] illustrated the effect of alloying Cu with ZnO for thermal-catalytic hydrogenation of CO and CO_2. Zn results in stronger O* binding and weaker C* binding. The former enhances CO_2 hydrogenation by stabilizing the O* bound intermediates, such as HCOO*, while the latter results in more difficult

adsorption and hydrogenation of CO.[186] Applied to our results, this catalyst might also be beneficial for plasma catalysis, because stronger O* binding might result in less desorption and formation of CO_2 and more facile hydrogenation of HCOO* to HCOOH or other oxygenates, and weaker C* binding is expected to result in less adsorption and oxidation of plasma-produced CO.

Certain metal oxides, such as MoO_3 and V_2O_5, may also be suitable catalysts to produce CH_2O and CH_3OH by plasma-catalytic POX. CH_3 radicals can react with reducible metal oxides to form methoxide anions (CH_3O^-) on the surface, as was shown by Tong *et al*.[187] (Note the similarities with the Eley-Rideal reaction $CH_3 + O^* \rightarrow CH_3O^*$, discussed in section 3.3.3.3.) The reactivity of the metal oxide in this reaction depends on its reducibility, with more reducible metal oxides being more reactive. On CeO_2, the formed CH_3O^- anion reacts into a formate anion ($HCOO^-$), which produces CO and CO_2.[187] However, on MoO_3 and V_2O_5 the CH_3O^- anion can react to produce CH_2O or, in case H_2O is present, CH_3OH.[188,189] Additionally, MoO_3 and V_2O_5 are known catalysts for the selective O insertion into CH_3 in thermal-catalytic POX of CH_4 to CH_2O and CH_3OH. In this reaction NO is typically added as a radical initiator.[190] As high densities of radicals, such as CH_3, can easily be achieved in plasma, the combination of a MoO_3 or V_2O_5 catalyst with plasma also seems promising for plasma-catalytic POX of CH_4.

3.4 Conclusion

We used microkinetic modeling to investigate the influence of various plasma species on the catalyst surface chemistry for plasma-catalytic POX of CH_4 on a Pt(111) surface. We evaluated the effect of vibrationally excited CH_4 and O_2, as well as radicals and stable intermediates, and compared the results to those of thermal catalysis at the same reaction conditions.

Plasma-induced vibrational excitation of CH_4 and O_2 increases the TOF of CH_4 dissociation. Furthermore, it also shows potential for enhancing the selectivities of CH_3OH, HCOOH and C_2 hydrocarbons, but has little effect on the selectivities of CH_2O, CO and CO_2. Nevertheless, the selectivities of CH_3OH, CH_2O and C_2 hydrocarbons remain too low for their production to be feasible on Pt(111) at conditions when only vibrational excitation is considered as a plasma-effect. However, we find that for plasma-catalytic POX of CH_4 the surface chemistry is mainly governed by radicals, rather than vibrationally excited molecules.

The presence of plasma-produced radicals and stable intermediates greatly increases the TOFs of CO_x and the oxygenates, compared to thermal catalysis. Interestingly, it also enhances the selectivities of the oxygenates and we find that the production of HCOOH becomes non-negligible. Further, we examine the role of various radicals in the surface processes:

- O radicals counteract coking but also promote over-oxidation to CO_2 and their partial pressures should thus be tuned against that of carbonaceous radicals.
- Strongly dehydrogenated carbonaceous species (C_2H_2, CH, C) are found to strongly induce coking, and their formation should therefore be avoided.
- The more hydrogenated carbonaceous radicals (CH_3, CH_2) in general show a beneficial effect, as they bind less strongly to the catalyst and lead to H* formation on the surface, yet also cause coking at high partial pressures.
- H radicals appear beneficial by promoting the hydrogenation of CH_3O* and HCOO* to CH_3OH and HCOOH, respectively. Moreover, high partial pressures of H radicals can potentially form more free surface sites by removing excess O* via H_2O formation.

- CH_3O and CH_3OO radicals are important precursors to both CH_3OH and CH_2O. Increasing their partial pressures thus also strongly enhances CH_3OH and CH_2O formation.

- Lowering the radical partial pressures in general decreases surface poisoning and allows for more facile adsorption of weak-binding radicals (e.g. CH_3O and CH_3OO), which is beneficial for oxygenate formation.

Based on the effects of these radicals, we make the following suggestions on which reaction conditions should be used to favor the formation of certain products:

- The formation of undesired CO_2 is favored at low CH_4/O_2 ratios, for which high partial pressures of O radicals are expected. While such conditions should generally be avoided to limit deep oxidation, these can also be beneficial to some extent to avoid coke formation.

- The formation of CO is favored at high CH_4/O_2 ratios and might to some extent also benefit from a higher plasma power, that yields stronger CH_4 dissociation, although caution must be taken to avoid excessive carbon deposition on the surface.

- HCOOH formation benefits from the presence of CH_3 and CH_2 radicals, which are expected to be abundant in plasmas with a high CH_4/O_2 ratio and lower plasma power, avoiding complete CH_4 dissociation. An additional H source, such as H_2, might also be beneficial by improving HCOO* hydrogenation.

- The formation of CH_3OH might also benefit from a lower plasma power, resulting in lower radical densities (especially of strong binding carbonaceous species) and more free sites, which enhances CH_3O and CH_3OO adsorption. Additionally, CH_3O hydrogenation is expected to improve from using H_2 as additional H source in the plasma or a more noble catalyst.

- The formation of CH_2O is also expected to benefit from lower plasma power, for the same reason as CH_3OH. Moreover, an additional H source can also partially enhance CH_2O formation, as it can help to clear the surface from excessive O*.

Finally, we briefly illustrated the potential impact of E-R reactions that involve radicals. We find that these reactions allow to reach high TOFs (up to 10^{-5} s^{-1}), even at the high surface coverages that are relevant for plasma catalysis. Additionally, these reactions might lead to significant oxygenate production in the plasma-catalytic POX of CH_4 due to reactions such as R3.3, that result in more direct routes towards oxygenates.

Chapter 4.

Oxygenate production from plasma-activated reaction of CO_2 and ethane

The results presented in this chapter are published in:

Biswas, A. N.;‡ Winter, L. R.;‡ Loenders, B.;‡ Xie, Z.; Bogaerts, A.; Chen, J. G. Oxygenate Production from Plasma-Activated Reaction of CO_2 and Ethane. *ACS Energy Lett.* **2022**, 7, 236–241. DOI: 10.1021/acsenergylett.1c02355

‡) These authors contributed equally.

4.1 Introduction

As discussed in section 1.2, the dry reforming of CH_4 (DRM) consumes the two most important greenhouse gases, namely CO_2 and CH_4, and converts these into value-added chemicals that can be used as fuels or resources for the chemical industry.[12] Using plasma technology, DRM can produce a variety of chemicals, including syngas, C_2 and C_3 hydrocarbons, as well as oxygenates.[22,23] Moreover, converting CH_4, which is the main component of natural gas, into liquid oxygenates facilitates the valorization of the many natural gas reserves that are situated in remote locations, as discussed in section 3.1.[147,148] However, apart from CH_4, natural gas also contains significant amounts of C_2H_6 (i.e., around 10% depending on the source).[191] Hence, like DRM, the dry reforming of C_2H_6 (DRE) is a promising reaction for utilizing remote natural gas reserves, while at the same time reducing the amount of CO_2 emitted into the atmosphere.

Nevertheless, there exist only a few works that have investigated DRE with plasma (catalysis).[192,193] Zhang *et al.*[193] studied the oxidative dehydrogenation of C_2H_6 using CO_2 as an oxidant at ambient temperature and pressure using a pulsed corona discharge over different catalysts (La_2O_3, CeO_2 and Pd) on a γ-Al_2O_3 support. Yet, the authors only detected C_2H_4, C_2H_2 and syngas (CO/H_2) as products. They also found that CeO_2/γ-Al_2O_3 gave the highest C_2H_6 conversion, while Pd/γ-Al_2O_3 resulted in the highest selectivity to C_2H_4.[193] Gómez-Ramírez *et al*.[192] studied plasma-catalytic DRE in a DBD reactor packed with $BaTiO_3$ pellets, both with and without a V_2O_5/Al_2O_3 catalyst. They detected CO, H_2, H_2O, CH_4 and CH_2O as the main products, as well as small amounts of C_3 hydrocarbons. The authors reported that the presence of small amounts of the V_2O_5/Al_2O_3 catalyst significantly improved the CH_2O production, with a catalyst/$BaTiO_3$ ratio of ≈ 0.1% resulting in a threefold increase in the amount of CH_2O produced. Based on experiments with CO_2+CH_4 and CO_2+C_3H_8 as reactants, the authors also concluded that CH_4 and C_3H_8 are unlikely to be important intermediates for CH_2O formation in DRE.[192]

In this chapter, we provide insight into the gas phase chemistry of DRE in DBD plasma, based on results from chemical kinetics modeling, and we identify the main reaction pathways. Additionally, we study how the plasma power affects the conversions of CO_2 and C_2H_6, as well as the selectivities towards different products, including syngas (CO/H_2), C_1-C_4 hydrocarbons and oxygenates. We developed this model to support experiments on DRE in DBD plasma, performed at Columbia University (NY, USA), and we can explain the observed trends in conversion and product selectivities, based on insights acquired from the reaction pathways. The experimental results are presented in more detail in the original paper.[127] Indeed, this chapter focuses on the modeling results, as this is my contribution to that work.

4.2 Methods

The numerical simulations were executed using the 0D plasma chemical kinetics solver ZDPlasKin.[194] This solver calculates the number densities n_s of the species *s* as function of time, by solving the corresponding balance equations, i.e., Eq. 2.1 in section 2.3. Note that the flow terms in Eq. 2.1 are left out, as we employ the quasi-1D approach (see section 2.2 and the next paragraph). The reaction rates used in the balance equations were calculated according to Eq. 2.5, as described in section 2.4. The rate coefficients were taken from literature or, in the case of electron impact reactions, were calculated from the electron impact cross sections and the electron energy distribution function through BOLSIG+,[141] a numerical solver for the steady-state Boltzmann equation for electrons (see section 2.5).

To simulate the DBD plasma, we used the 0D DBD model developed by van 't Veer *et al*.[111,195], which was developed specifically for use in combination with the ZDPlasKin solver. In this model, the DBD reactor is treated as a plug flow reactor, meaning that the species densities only change in the axial direction and are constant along the radial

dimension (see section 2.2). Since each point along the axial dimension matches with a certain residence time, the model is solved as a function of time, i.e., without real spatial dimensions, and is thus a 0D model. However, because this time dependence is translated into a spatial dependence (along the axial direction) in the plug flow reactor, by means of the gas velocity, this model is also called a "quasi-1D model", as explained in Chapter 2. Because a DBD plasma in CO_2/C_2H_6 mixtures is filamentary, the gas molecules experience these filamentary discharges when traveling through the DBD reactor. The model simulates these filaments or microdischarges in the DBD plasma by applying periodic triangular pulses in power density. These pulses are thus characterized by a high power density and are followed by longer periods with a lower (and constant) power density, referred to as the afterglows. As such, the experimentally measured plasma power is divided over the different pulses and afterglows. For a more detailed description of the model, we refer to van 't Veer *et al*.[111,195]

The model parameters were taken to be the same as those used in the experiments to which we compare our results: the gas temperature was set to 473 K, the applied frequency to 9 kHz and the total gas flow rate to 15.8 mL min^{-1}. The plasma power was varied between 8.0 W, 10.4 W, 13.8 W and 17.9 W. The reactor volume (occupied by gas) was equal to 9.42×10^{-1} cm^3, and the length of the reactor was 8.0 cm. Simulations were performed for a 1:1 CO_2 to C_2H_6 feed gas ratio at atmospheric pressure. Although the experiments were performed in mixtures of CO_2/C_2H_6/He, the model only considered CO_2 and C_2H_6. He is an inert gas and is not expected to participate in the chemical reactions. He could only contribute by Penning ionization (i.e., reactions of metastable excited He atoms or dimers, causing ionization of CO_2 or C_2H_6, or other molecules) and charge transfer (i.e., reaction of He^+ or He^{2+} ions, again causing ionization), but this would not significantly affect the results since ion chemistry is typically of lower importance in DBD plasma. Therefore, our model of CO_2/C_2H_6 plasma can provide a good picture of the underlying chemistry.

Table 4.1 specifies the list of species included in the model. The chemistry set used for the plasma chemical kinetics modeling was compiled from reactions used in earlier modeling studies[196–199] and further extended with various neutral-neutral, ion-ion, ion-neutral, and electron-ion reactions. In addition, some electron impact cross sections and reaction rate coefficients were revised.

Table A2.1 in Appendix A2 shows the electron impact reactions for which the cross sections have been revised. Based on the work of Morillo-Candas et al.,[200] the cross sections of CO_2 electron impact dissociation from Polak and Slovetsky[44] were used, instead of the Phelps cross sections[201] that were used in earlier modeling studies.[196–199]

The cross sections for electron impact dissociation of C_2H_6 and C_3H_8 derived theoretically by Janev and Reiter[202] were found to systematically overestimate the destruction of these species. It is important to note that much of the data required to calculate these cross sections, including the threshold energies of the different dissociation channels, were unavailable, and thus, Janev and Reiter had to rely on estimates.[202]

However, we obtained a relatively good agreement with the experimental results when using the cross section for electronic excitation of C_2H_6, C_2H_4, C_3H_8, and C_3H_6 from the LXCat database[203] and assuming the corresponding excited states dissociate according to the branching ratios reported in Table A2.1. These branching ratios were chosen so that the relative importance of the different dissociation channels at high electron energies was similar to the asymptotic branching ratios estimated by Janev and Reiter,[202] while also taking into account that the excited states can only dissociate via dissociation channels with a reaction enthalpy that is lower than the excitation threshold. Table A2.2 in Appendix A2 lists the reactions used to expand the chemistry set with respect to previous modeling studies,[196–199] as well as the reactions for which different rate coefficients were used.

Table 4.1. List of the species included in the model.

Elements	Molecules	Radicals	Ions	Excited species
H	H_2	H	H^+, H^-, H_2^+, H_3^+	
C		C, C_2	C^+, C_2^+	
O	O_2, O_3	O	O^+, O^-, O_2^+, O_2^-, O_3^-, O_4^+, O_4^-	$O_2(E_1\text{-}E_2)$
C, H	CH_4, C_2H_2, C_2H_4, C_2H_6, C_3H_6, C_3H_8, C_4H_8, C_4H_{10}	CH, CH_2, CH_3, C_2H, C_2H_3, C_2H_5, C_3H_5, C_3H_7, C_4H_9	CH^+, CH_2^+, CH_2^-, CH_3^+, CH_4^+, CH_5^+, C_2H^+, $C_2H_2^+$, $C_2H_3^+$, $C_2H_4^+$, $C_2H_5^+$, $C_2H_6^+$	
C, O	CO, CO_2	C_2O	CO^+, CO_2^+, CO_3^-, CO_4^-, $C_2O_2^+$, $C_2O_3^+$, $C_2O_4^+$	$CO(E_1\text{-}E_4)$, $CO_2(V_a\text{-}V_d)$, $CO_2(V_1\text{-}V_{21})$
H, O	H_2O, H_2O_2	OH, HO_2	OH^+, OH^-, H_2O^+, H_3O^+	
C, H, O	CH_2O, HCOOH, CH_3OH, CH_3OOH, CH_2CO, CH_3CHO, C_2H_5OH, C_2H_5OOH, C_2H_5CHO, C_3H_7OH	CHO, CH_3O, CH_3O_2, CH_2OH, $HOCH_2O$, COOH, HCOO, CH_3CHOH, CH_3CO, C_2H_5O, $C_2H_5O_2$, C_2HO, C_2H_5CO, C_3H_7O, $C_3H_7O_2$	CHO^+	

As the exact microdischarge duration and number of microdischarge pulses per half cycle of the applied power are not known, values similar to those reported in literature for a CO_2 plasma were used as an approximation.[204] The microdischarge duration was set to 15.6 ns and the number of microdischarges per half cycle was varied from 200 to 447. The number of microdischarges was assumed to increase linearly with plasma power, as higher plasma powers have been reported to result in more microdischarges per half cycle.[204] Furthermore, a so-called power distribution factor (between the high-power

microdischarge pulses and the low-power afterglows in between them) of 0.3 was assumed, which lies in the range of 0.1-1 recommended by van 't Veer *et al*.[111] The microdischarge volume was estimated to be 0.047 mm^3, assuming a cylindrical shape with a length equal to the air gap between the electrodes (1.5 mm) and a filament diameter of 0.2 mm, based on Bogaerts *et al*.[205] Using these parameters, the minimum and maximum power densities, as well as the effective period over which the molecules are exposed to pulses, were calculated by the model. The obtained values are presented in Table 4.2.

Table 4.2 Calculated values of the minimum power density that is sustained in the afterglows, the maximum power density reached in the pulses, and the effective period by which molecules are exposed to pulses, for different plasma powers.

Plasma Power (W)	Minimum power density (W cm^{-3})	Maximum power density (W cm^{-3})	Effective pulse period (ms)
8.0	7.97	3.72×10^5	5.55
10.4	10.2	4.74×10^5	4.27
13.8	13.2	6.14×10^5	3.22
17.9	16.6	7.73×10^5	2.48

4.3 Results and discussion

We conducted kinetic modeling of the plasma chemistry to obtain insight into the reaction pathways of DRE in DBD plasma and explain the observed experimental trends in its product distributions. We compare the results of our simulations to the experimental results reported in ref. [127]. The model parameters were therefore set to match those of the experiments. Hence, the simulations were performed for a gas temperature of 473 K, atmospheric pressure and a flow rate of 15.8 mL min^{-1}, while the

plasma power was varied between 8.0-17.9 W. The CO_2/C_2H_6 ratio in the feed was equal to 1.

Based on the reaction rates calculated in our simulation, we identify the major reaction pathways for the formation of the main products, which include syngas (CO/H_2), hydrocarbons and oxygenates. A schematic overview of these major reaction pathways is displayed in Figure 4.1.

Electron impact dissociation of C_2H_6 results in the formation of stable molecules (C_2H_4, C_2H_2, CH_4 and H_2), as well as radicals (C_2H_5, CH_3, CH_2, C_2H_3 and H). The formed carbonaceous radicals subsequently react via recombination or disproportionation reactions to produce longer (C_3 and C_4) hydrocarbons, or CH_4. Additionally, some of the formed radicals also react back to C_2H_6. A part of the formed hydrocarbons dissociates via electron impact reactions to produce either smaller molecules (e.g., CH_4 formation from C_3H_6 or C_3H_8), or more unsaturated hydrocarbons (e.g., C_2H_2 and C_3H_6 formation from C_2H_4 and C_3H_8, respectively).

Destruction of CO_2 mainly occurs via electron impact dissociation to form CO and O, and to a lesser extent through reaction with CH_2 radicals to produce CO and CH_2O. These mechanisms together are responsible for most of the CO formation, although some CO is also produced via dehydrogenation of CHO. The latter is formed via reaction between O radicals and C_2H_4 or through dehydrogenation of CH_2O. The CHO radical plays an important role in the formation of C_2 and C_3 aldehydes, as it recombines with CH_3 and C_2H_5 radicals, to form CH_3CHO and C_2H_5CHO, respectively. However, most CHO is dehydrogenated to CO. CH_3OH is mainly produced from CH_2O via CH_3O through subsequent hydrogenation reactions, while C_2H_5OH is formed via recombination between C_2H_5 with OH or O. In the latter case, subsequent hydrogenation of the resulting C_2H_5O radical forms C_2H_5OH. A more extensive summary of the main production and destruction reactions occurring in the plasma can be found in Appendix A2, section A2.3.

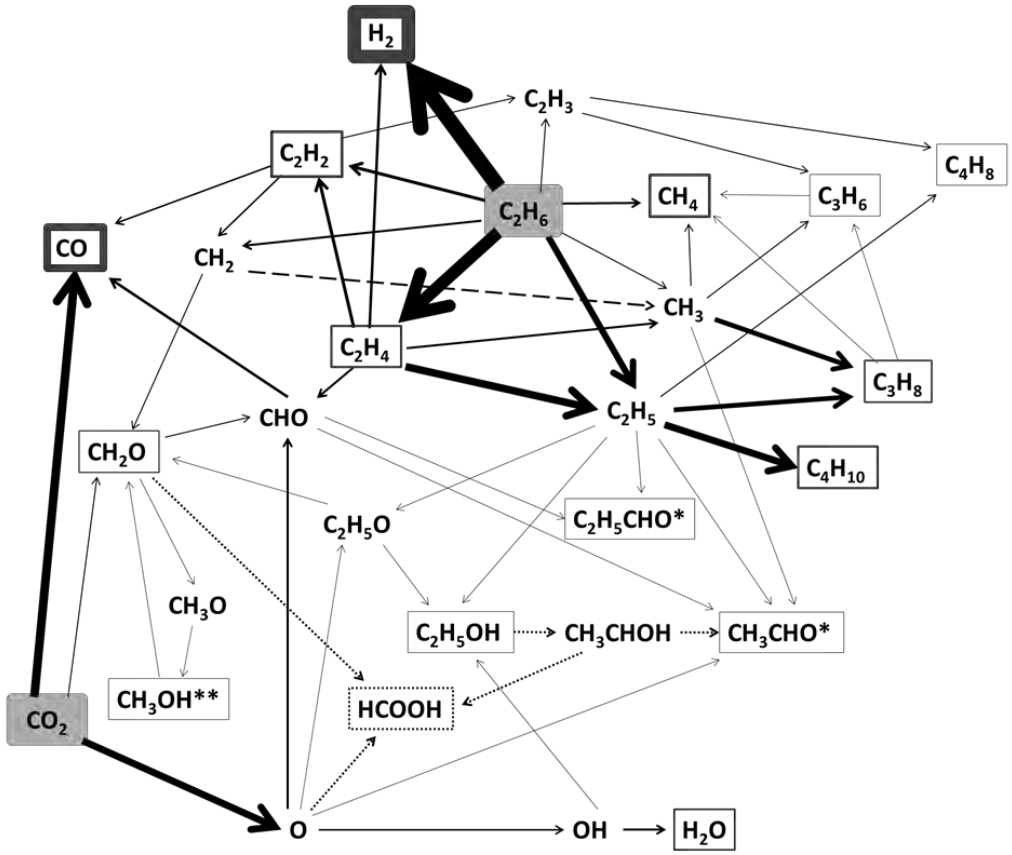

(*): These aldehydes react mainly via dehydrogenation of the formyl group, after which the formed radicals decompose into CO and an alkyl radical.
(**): CH_3OH also undergoes dehydrogenation to CH_2OH, which can be dehydrogenated to CH_2O or recombine with alkyl radicals to form alcohols.

Figure 4.1. Schematic overview of the most important reaction pathways for the main products. The thickness of the arrows and frames indicates the importance of the corresponding pathways and product densities, respectively, with exception of the dotted lines (⋯) which indicate very low rates and densities. The striped line (---) indicates an indirect pathway: $C_3H_6 + CH_2 \rightarrow C_4H_8$, followed by $C_4H_8 + H \rightarrow C_3H_6 + CH_3$.

While our model predicts direct electron impact dissociation as the main mechanism for CO_2 destruction, another possible route would be via attachment of an electron to CO_2, followed by decomposition of the CO_2^- anion to CO and O^-.[206] However, electron attachment to an isolated CO_2 molecule in the gas phase will result in a CO_2^- anion that

is excited with respect to the rovibronic ground state, which will either immediately undergo electron detachment back to CO_2 or decompose into CO and O^-.[207] While our model does not include CO_2^- explicitly as a species, it does include electron attachment to CO_2, resulting in CO and O^- formation. However, we find that this process is not as important compared to the electron impact dissociation to CO and O radical, for the conditions achieved in our DBD plasma.

To the best of our knowledge, a detailed study regarding the reaction mechanism of CO_2/C_2H_6 reforming by plasma has not been reported before. However, the dry reforming of CH_4 in a DBD plasma has been investigated using computational modeling.[58,157] Therefore, we briefly compare the results of these studies to our results for CO_2/C_2H_6 reforming. Similar to the conversion of C_2H_6 in our results, the modeling studies by Snoeckx *et al.*[58] and De Bie *et al.*[157] predict that CH_4 destruction mainly occurs through electron impact dissociation in the pulses. This results in the formation of CH_3 and other carbonaceous radicals, which recombine to form higher hydrocarbons. However, recombination between CH_3 and H radicals to form again CH_4 does also occur.[58,157] Subsequently, electron impact dissociation of the formed C_2 and C_3 hydrocarbons, and to some extend of CH_4, results in the formation of H_2.[157] This is again comparable to the case of CO_2/C_2H_6 reforming, where most H_2 is formed via the electron impact dissociation of C_2H_6. The destruction of CO_2 during CH_4 dry reforming mainly occurs through electron impact reactions in the pulses and via reaction with CH_2 radicals to form CO and CH_2O, in the afterglows. The latter reaction is responsible for most of the CH_2O formed, which is also the case for our results on CO_2/C_2H_6 reforming.[58,157]

Figure 4.2 (a) shows a good agreement for the reactant conversions between the experimental results from ref. [127] and the model. In both the experiments and the model, the C_2H_6 conversion is higher than that of CO_2. This is because the breaking of the C–H and C–C bonds in C_2H_6 is easier (i.e., resulting in higher reactions rates) than the

dissociation of the C=O double bond in CO_2. The less reactive CO_2 is primarily destructed into CO, whereas the decomposition of C_2H_6 results either directly in the formation of various hydrocarbons (C_2H_4, C_2H_2, CH_4) or radicals (e.g., H, C_2H_5, CH_3, CH_2, C_2H_3). These radicals can then again form hydrocarbons, including C_2H_6, through recombination and disproportionation reactions.

The conversions of both reactants also increase with increasing plasma power, which is the result of two effects in the model. First, an increase in peak power density in the pulse leads to a higher mean electron temperature. At higher electron temperatures, more electrons reach the threshold energy required for electron impact dissociation, which are the main reactions for C_2H_6 and CO_2 conversion. Additionally, more electrons also reach the threshold energy for electron impact ionization, which leads to higher electron densities, and thus also increases the rate of electron impact reactions. Second, the number of microdischarges should increase when increasing the plasma power, as was observed experimentally by Ozkan *et al.*[204] This was implemented in the model by linearly increasing the number of microdischarges per half cycle (i.e., more frequent pulses and afterglows), which is also found to enhance the conversion.

Figure 4.2 (b)-(d) show the selectivities calculated by the model compared to experimental results for the different plasma powers. A reasonable agreement between the experimental and modeling results is obtained for CO and C_2 hydrocarbons (Figure 4.2 (b)), CH_4, C_3, and C_4 hydrocarbons (Figure 4.2 (c)), and oxygenates (Figure 4.2 (d)). In general, the CO selectivity increases with plasma power, while the total selectivity toward hydrocarbons drops. This is because the hydrocarbon products react further into other products (e.g., oxygenates) or back to C_2H_6, while CO is relatively unreactive. Nevertheless, the selectivities of some hydrocarbons, such as CH_4, C_3H_6, and C_4H_8, show a slight increase as they may be partially formed from other hydrocarbon products.

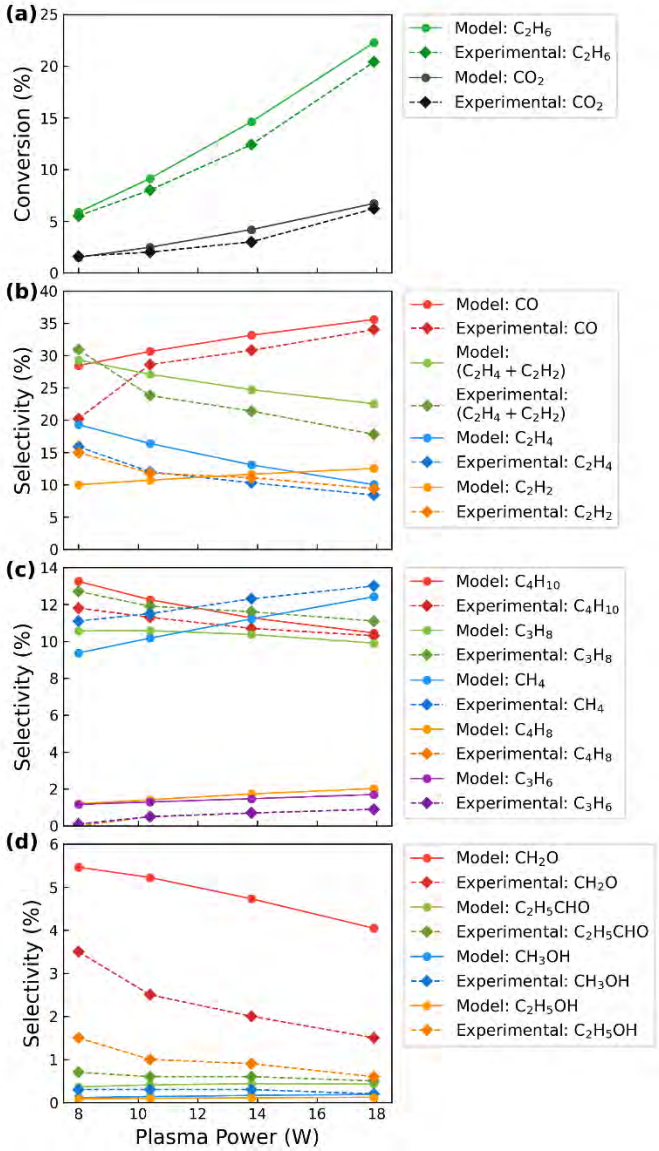

Figure 4.2. (a) Effect of plasma power on the reactant conversion of C_2H_6 and CO_2. Calculated and experimental selectivities for (b) CO and C_2 hydrocarbons, (c) CH_4, C_3, and C_4 hydrocarbons, and (d) oxygenates.

For most of the oxygenate products, the simulation results can provide a mechanistic explanation for the experimental trends. The selectivities of CH_2O and C_2H_5OH drop at

higher conversion, because as the reaction proceeds further, these oxygenates are converted into CO and other oxygenates. In contrast, the selectivities of CH_3OH and C_2H_5CHO do not decrease as much with plasma power. Although CH_3OH and C_2H_5CHO are also converted into CO, the production of these species occurs largely from other products. CH_3OH is mainly formed from CH_2O via CH_3O through subsequent hydrogenation reactions, while C_2H_5CHO is formed through the recombination of C_2H_5 and CHO. The CHO radical is formed by dehydrogenation of CH_2O or oxidation of C_2H_4. This is consistent with the results of $^{13}CO_2$ *in situ* FTIR experiments involving oxidation of ethane-derived hydrocarbons in a DBD batch reactor, which indicate that the C atoms in CO originate from CO_2, while those in CH_4 and alcohols originate from C_2H_6.[127]

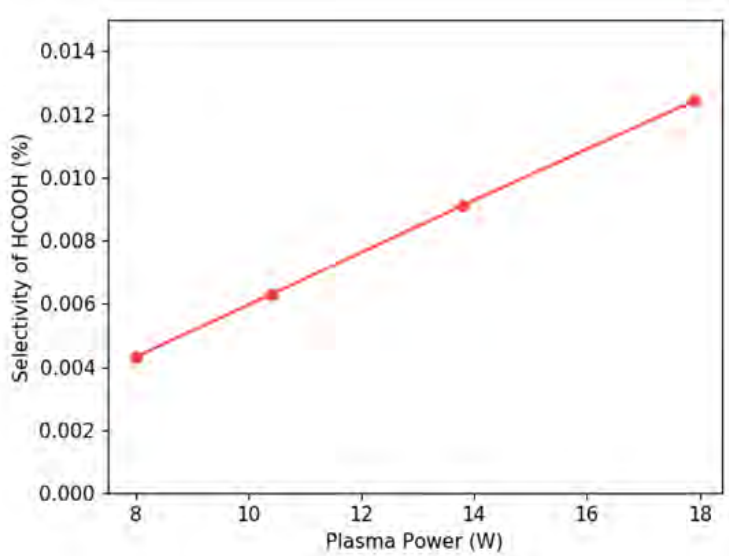

Figure 4.3. Calculated selectivity of formic acid at different plasma powers.

Furthermore, CH_2O and C_2H_5OH are also converted into HCOOH, resulting in a higher HCOOH selectivity at higher plasma powers, as can be seen in Figure 4.3. Moreover, the experimental results reported in ref. [127], also show a rise in the selectivity towards organic acids (including, acetic acid and propanoic acid) at higher plasma power. The organic acids observed in the experiments are thus likely formed from C_2 or C_3 alcohols and

aldehydes via a similar pathway, which would explain the higher selectivities measured with increasing plasma power, as well as the corresponding lower selectivities to alcohols and aldehydes at higher plasma power.

4.4 Conclusion

We used 0D kinetic modeling to study the gas phase chemistry of DRE in a DBD plasma at mild temperature (473 K), atmospheric pressure and plasma powers between 8.0-17.9 W. We identified the major reaction pathways for the formation of the main reaction products, which include syngas (CO/H_2), hydrocarbons and oxygenates. Moreover, we compared the output of our simulations with experimental data from ref. [127], and find a reasonable agreement between the results.

The conversions of CO_2 and C_2H_6 rise with plasma power due to an increase in the number and intensity of the microdischarges. Our simulations show that C_2H_6 is mainly converted via electron impact dissociation, forming H_2, hydrocarbons (C_2H_4, C_2H_2, CH_4) and radicals (e.g., H, C_2H_5, CH_3, CH_2, C_2H_3). These radicals subsequently form CH_4 and longer (C_3 and C_4) hydrocarbons via recombination or disproportionation, although some react back to C_2H_6 as well. CO_2, on the other hand, is converted to CO, mainly via electron impact dissociation, but also to a lesser extent through reaction with CH_2.

As the plasma power and the conversions rise, the selectivity towards CO increases, while the total hydrocarbon selectivity drops. This is because CO is relatively unreactive, while most hydrocarbons react further to form other products, or partly react back to C_2H_6. An exception to this are the selectivities of CH_4, C_3H_6 and C_4H_8, which slightly rise with plasma power, as these species are partly formed from other hydrocarbons products.

CH_2O is formed by the reaction between CO_2 and CH_2. Its selectivity drops at higher plasma power (and conversion) as it reacts further to form either CH_3OH by recombination with H radicals, or CHO by H abstraction. The formed CHO radicals can

recombine with CH_3 or C_2H_5 to form aldehydes (CH_3CHO and C_2H_5CHO, respectively), yet most are dehydrogenated to CO. Alternatively, CHO can be formed by oxidation of C_2H_4. The selectivity of C_2H_5OH also drops with rising plasma power, as this alcohol is directly formed from recombination between C_2H_5 and OH (or first O and then H) radicals. However, most oxygenates are formed from other products and as such their selectivities do not drop much with rising plasma power. Lastly, the selectivity of HCOOH rises with plasma power, as this product is formed by oxidation of CH_2O and C_2H_5OH. This indicates that other, longer organic acids are likely formed via oxidation of C_2 and C_3 alcohols and aldehydes, via a similar mechanism.

Hence, increasing the plasma power improves the conversion, which in turn affects the selectivities of the various products. Molecules that react further to form other products will have their selectivity reduced as the conversion rises, while the selectivities of the newly formed species improve. As such, it may be difficult to obtain high yields for some products, as this requires both a high selectivity and conversion. Plasma catalysis may be able to solve this issue, by using a catalyst that improves the selectivity towards the desired product. For example, Wang *et al.*[208] demonstrated that the choice of catalyst can be used to tune the selectivities between alcohols and organic acids in plasma-catalytic DRM.

Chapter 5.

Is a catalyst always beneficial in plasma catalysis?

The results presented in this chapter are published in:

Loenders, B.; Michiels, R.; Bogaerts, A. Is a Catalyst Always Beneficial in Plasma Catalysis? Insights from the Many Physical and Chemical Interactions. *J. Energy Chem.* **2023**, *85*, 501–533. DOI: 10.1016/j.jechem.2023.06.016

5.1 Introduction

As discussed in section 1.2, DRM is a promising technology for CCU as it simultaneously converts the two most abundant GHG's, namely CO_2 and CH_4, into value added chemicals and fuels. A particularly interesting product that can be formed from these GHG's is CH_3OH. Indeed, CH_3OH can be used both as a fuel, as well as building block for the chemical industry, and has therefore been proposed as a key compound for an anthropogenic carbon cycle.[7,14] However, CH_3OH synthesis from CO_2 and CH_4 via conventional thermal catalysis, first requires an energy-intensive conversion of the reactants to syngas (CO and H_2), followed by CH_3OH synthesis at high pressure. Fortunately, plasma-catalytic DRM can in principle produce CH_3OH at atmospheric pressure and (close to) ambient temperature, in a single reaction step.[22] Nevertheless, it is currently not yet straightforward to selectively produce the desired end-compounds using this technology, due to the high degree of complexity that arises from the many physical and chemical interactions in plasma catalysis.

In this chapter, we therefore first study plasma-catalytic CO hydrogenation as a possible pathway for CH_3OH production, by microkinetic modeling of the catalyst surface chemistry. Indeed, CO and H_2 are typically the main products of DRM, also in DBD plasmas.[23,32,33,35,36,58,65,209] Hence, hydrogenation of plasma-produced CO, e.g., by hydrogen radicals, could potentially play a role in CH_3OH production via plasma-catalytic DRM. We also refer to section 1.7.5 in the introduction to this thesis, where we discussed mechanisms for oxygenate formation in plasma-catalytic CO_2 hydrogenation, due to its similarities with DRM.

Next, we provide insights into the effect of transition metal catalysts on plasma-catalytic DRM, using a coupled plasma-surface microkinetic model. We will illustrate how the presence of a catalyst can also negatively affect the conversion and selectivity of plasma-

catalytic DRM by selectively recombining CH_3 and H radicals to CH_4 as well as O radicals and CO back to CO_2. Indeed, while the goal of plasma catalysis is to improve conversion and selectivity relative to the plasma and catalyst alone, synergy is not guaranteed, and in several experimental studies, combining the plasma with a catalyst was found to negatively impact the performance in DRM.[32–36]

5.2 Methodology

To illustrate potential pathways and trends between catalysts for CH_3OH production via plasma-catalytic DRM, we performed simulations using the descriptor-based microkinetic model CatMAP.[210] The CatMAP code calculates steady-state fractional coverages and reaction rates on a catalyst surface exposed to a fixed gas mixture. As such, we would like to emphasize that this model exclusively provides information on the catalyst surface chemistry, but does not consider any gas-phase reactions or changes to the gas composition that may occur due to surface reactions. Nevertheless, this model is useful to visualize trends in reactivity between different catalysts. This is possible due to the existence of linear scaling relations that describe the activation barriers of the reactions on different transition metals. We derived these scaling relations from DFT energies that were taken from the work of Schumann *et al*.[99] on CO hydrogenation. To include additional reactions for DRM, we extended this set with DFT results obtained by R. Michiels within our group PLASMANT, using settings that match those of Schumann *et al*. as much as possible for consistency reasons.

Nevertheless, as mentioned above, the CatMAP model does not consider any gas phase reactions or changes to the gas composition. Yet, plasmas have a very rich gas phase chemistry as a result of electron impact reactions, generating highly reactive species that subsequently react with each other or with stable gas molecules. As such, the plasma chemistry has a strong influence on the gas composition, and thus also on the surface

chemistry of a catalyst in contact with this gas mixture. In turn, the destruction and formation of gas species on the catalyst affects the gas composition, and consequently the plasma. Hence, the plasma chemistry alters the surface chemistry and vice versa. Therefore, we developed a coupled plasma and surface kinetics model, which simultaneously calculates the number densities of gas species and fractional coverages of surface species as function of time.

In the following sections, we describe the methodology for the simulations with the CatMAP code, as well as our coupled plasma-surface microkinetic model.

5.2.1 Surface kinetics simulations using the CatMAP code

The CatMAP software, developed by Medford *et al.*,[210] is a mean-field microkinetic model that calculates the reaction rates and fractional coverages at steady state for catalyst surfaces exposed to a fixed gas mixture. The model solves the species balance equations for the fractional coverages at steady state (Eq. 2.4, see section 2.3). The reaction rates in the balance equation are calculated from the fractional coverages of the surface species and the partial pressures (which are kept constant) of the gas species, according to Eq. 2.6 (see section 2.4). For more information on CatMAP, we refer to ref. [210].

While the CatMAP model does not consider any changes in the gas composition due to e.g., gas or surface reactions, it allows to clearly illustrate trends in reactivity between different transition metals. These so-called activity plots display, for example, the production or destruction rates of a specific gas species as function of two descriptors. The descriptors are variables on which other parameters in the model, in this case the adsorbate and transition state energies, are dependent.[210] The use of these descriptors is made possible due to the existence of scaling relations, i.e., correlations between the adsorption energies of surface species and those of specific descriptor adsorbates.[211,212] In our simulations the O* and CH* binding energies are used as descriptors. The binding

energies are defined as the formation energies of adsorbed O* and CH* relative to the empty slab and gaseous CO, H_2O and H_2. Note that, as long as the descriptors correlate well with the energies of the other surface species that bind to the catalyst via the O or C atom, the choice of the descriptors does not notably affect the results.

The scaling relations used in our simulations are derived from surface species energies calculated with DFT. Most of the surface species energies were taken from Schumann *et al*.[99] However, some additional species required in our DRM chemistry set, were not included in that paper, and were therefore calculated within our group by R. Michiels. More details on the DFT calculations can be found in the original publication.[39] A list of these species with their corresponding energies and frequencies can be found in Table A3.1 in Appendix A3. Note that for gas phase species (listed in Appendix A3, Table A3.2) the energies and frequencies are not calculated using DFT, but taken from the NIST chemistry webbook.[9] Additionally, Table A3.3 in Appendix A3 lists the scaling relations used in our models.

The simulations are executed at a temperature of 500 K and a total gas pressure of 1 bar, as these conditions are typical for DBD plasma. In accordance with ref. 99, we employ the approximation that H* adsorbs on a separate reservoir site, as it is assumed to have negligible interactions with the other adsorbates because of its small size.[99,213] Thus, H* can still co-adsorb even if the sites on which the larger species bind are fully covered. The Gibbs free energies of gas species are corrected using the Shomate equations. For gas species of which the Shomate parameters are not included in CatMAP by default, the parameters are taken from the NIST chemistry webbook.[9] The free energies of the surface species were corrected using the harmonic oscillator approximation, as described by Eq. 2.16 and Eq. 2.18 in section 2.6.[144] The effect of radicals and stable plasma-produced species is investigated by setting small densities of these species in the gas mixture. If a radical is not included in the gas-phase, its adsorption and desorption

reactions are removed from the chemistry set, to avoid net radical desorption from the surface due to the zero adsorption rate.

Inclusion of lateral adsorbate-adsorbate interactions is outside the scope of this study and thus not considered here. However, such interactions might destabilize adsorbates that have high fractional coverages, hence improving their reactivity and desorption. Nevertheless, while this might expand the maximum in the volcano plot towards more strongly binding catalysts, the overall trends are expected to remain the same.

5.2.2 Coupled plasma and surface kinetics simulations

Our coupled plasma-surface model uses a CSTR (see section 2.2) approach, meaning that perfect mixing is assumed in the reactor volume. As such, species densities in the plasma and surface coverages are considered uniform throughout the entire reactor. These densities and coverages change as function of time, due to chemical reactions, and because of reactants entering and products leaving the reactor.

The change in the densities of the gas species with time is described by a balance equation, i.e., by Eq. 2.1 from section 2.3. The gas flows entering and leaving the reactor (f_{in} and f_{out} in Eq. 2.1, respectively) are calculated as:

$$f_{in} = \frac{n_{s,in} v_{in}}{V_{CSTR}} \qquad \text{Eq. 5.1}$$

$$f_{out} = \frac{n_{s,out} v_{out}}{V_{CSTR}} \qquad \text{Eq. 5.2}$$

Here $n_{s,in}$ and $n_{s,out}$ are the species densities in the feed and at the outlet, respectively. The species density in the feed is equal to 7.24×10^{18} cm^{-3} for CH_4 and CO_2, and zero for all other gas species, i.e., corresponding to a 1:1 CH_4/CO_2 gas mixture at 500 K and 1 bar. Note that for simplicity the temperature of the gas, the catalyst surface and the wall are all assumed equal to 500 K, hence possible hotspots at the catalytic surface are neglected at this stage. The volumetric flow rate entering the reactor, v_{in}, is chosen as 1.79 cm^3/s

(corresponding to 107.4 mL/min for a typical DBD reactor), and the gas volume in the reactor, V_{CSTR}, is set equal to 8.85 cm^3. Note that for a CSTR, the gas mixture leaving the reactor, $n_{s,out}$, is the same as that inside the reactor (i.e., $n_{s,out} = n_s$). The volumetric flow rate exiting the reactor, v_{out}, is calculated so that the total pressure in the reactor remains constant at 1 bar (10^5 Pa):

$$v_{out} = v_{in} + \frac{V_{CSTR} k_b T}{p_{tot}} \sum_{s,gas} \sum_{i} (c_{s,i}^R - c_{s,i}^L) r_i \qquad \text{Eq. 5.3}$$

In which p_{tot} is the total pressure in the reactor and the sum denotes the change in the total number density of all gas species combined due to reactions. As such, the volumetric flow rate that leaves the reactor, v_{out}, is equal to the sum of the volumetric flow rate entering the reactor, and the change in volume that results from the reactions under the chosen conditions of pressure and temperature.

Note that the reaction rates r_i are expressed in $cm^{-3}\ s^{-1}$ for gas reactions or s^{-1} for surface (catalyst or wall) reactions. In Eq. 2.1 and Eq. 5.3, the latter are therefore converted to the corresponding change in number density per unit of time (units of $cm^{-3}\ s^{-1}$) by multiplying with their volumetric site density. We consider two types of surface sites in our model, namely sites on the catalyst surface and sites on the "non-catalytic" wall. The latter can be, e.g., the surface of the dielectric reactor wall or a dielectric packing. The number of catalytic sites per unit of gas volume is expressed as $n_{sites} \times f_{cat}$, where n_{sites} is the total volumetric site density of all (catalytic and wall) sites combined and f_{cat} is the fraction of these sites that are catalytic, i.e., transition metal sites. Conversely, the volumetric site density of non-catalytic sites is equal to $n_{sites} \times (1 - f_{cat})$.

We use an estimated value of 1.5×10^{18} cm^{-3} for n_{sites}, and the fraction of catalytic sites is set to 0.5 if a transition metal is present, or zero if this is not the case. For reference, in ref. 81 the number of catalytic (metal) sites per mass of catalyst material was determined

using CO pulse chemisorption for 5 wt.% transition metal catalysts on γ-Al_2O_3, and the measured values varied between 5-30 µmol/g (3-18 × 10^{18} sites/g). From our own observations we know that a DBD reactor with total (empty) volume of 17.7 cm^3 can hold about 12 g of γ-Al_2O_3-based catalyst pellets and that about half of the total volume of the packed reactor is occupied. As such, the gas volume, V_{CSTR}, in the reactor equals 0.5 × 17.7 cm^3 = 8.85 cm^3, as mentioned above. The parameters above correspond to volumetric site densities of 4-24 × 10^{18} cm^{-3}. In our model, we use n_{sites} = 1.5 × 10^{18} cm^{-3}, corresponding to a volumetric catalyst site density of 7.5 × 10^{17} cm^{-3} for f_{cat} = 0.5. This is a factor 5.3 to 32 lower than aforementioned values, as we assume a smaller metal loading, i.e. 1 wt.% rather than 5 wt.%, and we use the lower end of the range to avoid overestimation of the effect of the catalyst. Indeed, we expect the effect of the catalyst to be slightly overestimated in our model, as we assume perfect mixing, while this is probably not the case in reality, due to the short lifetime of the radicals. Hence, these might have reacted away before they are well mixed with the other gas species.

The change in the fractional coverages and empty site fractions on the catalyst surface and wall are described by Eq. 2.2 (section 2.3). Like the simulations with CatMAP, we employ the approximation that H* binds on a separate site type, as explained in section 5.2.1. The catalytic sites are equally distributed between normal and H reservoir sites. Also on the non-catalytic wall, two types of sites are present, namely weakly binding physisorption and strongly binding chemisorption sites. Here, we choose a fraction of 2 × 10^{-3} for chemisorption and 0.998 for physisorption sites on the wall, based on refs. [214,215].

The reaction rates used in Eq. 2.1, Eq. 2.2 and Eq. 5.3 are calculated according to Eq. 2.5 and Eq. 2.6 (see section 2.4) for gas and surface reactions, respectively. Gas species number densities (used in Eq. 2.5) are converted to partial pressures (used in Eq. 2.6) and vice versa using the ideal gas law. Note that these partial pressures need to be expressed

relative to the reference pressure of the gas (p_{ref} = 1 bar), when used in the calculation of the surface reaction rates (Eq. 2.6).

5.2.2.1 Rate coefficients of gas-phase reactions

An overview of all gas and surface species in the model can be found in Table 5.1 below. Note that we do not include any vibrationally excited molecules, as their effect is negligible compared to that of radicals at the low temperatures that are typical for a DBD reactor (~500 K), as discussed in section 1.7.3 of the introduction of this thesis. The rate coefficients, k_i, of the gas-phase reactions (with exception of electron impact reactions) are taken from literature and are listed in Table A3.4, together with the corresponding references. The rate coefficients of electron impact reactions are calculated as described in the next section.

Table 5.1. List of the gas-phase species, wall and catalyst surface species included in the model.

Gas-phase species	H_2, H, H_2O, OH, O, CO_2, CO, CH_4, CH_3, CH_2, C_2H_6, C_2H_5, CHO, CH_2O, CH_3O, CH_3OH, CH_2OH, CH_3CH_2OH, CH_3CHO, CH_3CO
Wall species (physisorbed)[a]	H^{*p}, O^{*p}, CH_3^{*p}, CH_2^{*p}, CHO^{*p}, OH^{*p}, ^{*p}
Wall species (chemisorbed)[a]	H^{*c}, O^{*c}, CH_3^{*c}, CH_2^{*c}, CHO^{*c}, OH^{*c}, ^{*c}
Catalyst surface species [a]	H^{*h}, ^{*h}, O^{*s}, OH^{*s}, CO_2^{*s}, CO^{*s}, CHO^{*s}, $CHOH^{*s}$, CH_2OH^{*s}, CH_2O^{*s}, CH_3O^{*s}, CH^{*s}, CH_2^{*s}, CH_3^{*s}, $CHCO^{*s}$, CH_2CO^{*s}, CH_3CO^{*s}, CH_3CHO^{*s}, CH_3CHOH^{*s}, $CH_3CH_2OH^{*s}$, ^{*s}

a) Superscripts p, c, h and s refer the physisorption, chemisorption, hydrogen reservoir and catalytic surface sites, respectively.

5.2.2.2 Rate coefficients of electron impact reactions

While electrons are not explicitly included as a gas-phase species, we do include electron impact dissociation reactions as a way of generating radicals. The rate coefficients of these electron impact reactions are kept constant throughout the simulation. We note that this is a clear approximation for DBD plasmas, which typically consist of

microdischarges and are hence non-uniform in both space and time. However, the goal of this study is to illustrate how the production of radicals and stable intermediates in the gas-phase can affect the surface chemistry and how the surface processes can alter the gas composition. A detailed treatment of the pulsed behavior of a DBD plasma combined with a catalyst is therefore outside the scope of this study, but will be investigated in future work.

The rate coefficients for electron impact processes are estimated as follows. First, we calculated the reduced electric field (*E/N*) at breakdown in pure CO_2 and CH_4 using the Paschen curves:[20,216]

$$\frac{E}{N} = \frac{Bk_bT}{C + \ln(p_{tot}d)} \; with \; C = lnA - ln\left(ln\left(\frac{1}{\gamma} + 1\right)\right) \qquad \text{Eq. 5.4}$$

Where *A* and *B* are experimentally determined parameters, taken from literature,[20,216] and *d* is the size of the discharge gap, assumed here to be 4.5 mm. A value of 0.1 was assumed for the secondary electron emission coefficient *γ*. Typical values of *γ* in discharges are in the range of 0.1-0.01.[20,216] Using *γ* = 0.01, however, results in a rise of only approximately 10% of the *E/N* calculated for these conditions. Using the Paschen curves, we find an *E/N* of 154 and 304 Td, for CH_4 and CO_2, respectively. We use the weighted average of these values, *E/N* = 229 Td, as a rough estimate of the electric field in the discharge for the 1:1 CH_4/CO_2 feed gas. Next, we calculate the rate coefficients of various electron impact reactions using BOLSIG+, a numerical solver for the Boltzmann equation for electrons.[141] We perform the calculation using a gas mixture containing 48.5% CO_2, 48% CH_4, 1.5% CO, 0.5% C_2H_6, 0.5% H_2O and 1.0% H_2. Small fractions of product species are included, as we also include their electron impact dissociation rate coefficients in the model. Note that the exact CH_4 and CO_2 conversions assumed for this gas mixture, and the corresponding fractions of product species, are not of great importance, as we found that the electron impact rate coefficients, calculated as

described in this section, vary only little for different compositions. As such, the rate coefficients are considered constant throughout the simulations and do not change with rising conversion. A list of the electron impact processes included in the BOLSIG+ calculations can be found in Table A3.5. We assume an electron density of 10^{14} cm^{-3}, which is in the range of typical electron densities in the microdischarge filaments of a DBD.[20] We use this value as we will first calculate the electron impact rate coefficients in the microdischarges, which we will correct afterwards to account for microdischarges only taking up a small fraction of the gas volume, as described below. Apart from the rate coefficients of the electron impact processes, BOLSIG+ also provides the reduced electron mobility, $\mu_e \times n$, as function of *E/N*. The electron mobility, μ_e, can be related to the reduced electric field through Eq. 2.8 (see section 2.5). Eq. 2.8 can be reorganized to get an expression for the power density:

$$P = E^2 n_e e \mu_e \qquad \text{Eq. 5.5}$$

If we assume all power is deposited in the discharges, we can estimate the average combined volume of the microdischarges V_{plasma}, for a plasma power of 65 W. Since only a fraction of the gas molecules in the reactor will be exposed to this power density at a given point in time, we correct the electron impact rate coefficients by multiplying with a geometrical factor V_{plasma}/V_{CSTR}. In Table A3.6, we list these corrected rate coefficients multiplied by the assumed electron density (n_e = 10^{14} cm^{-3}).

We acknowledge that calculating the electric field by taking the weighted average of electric fields at breakdown for CH_4 and CO_2 gives only a very crude estimation of *E/N*. However, we find that if the rate coefficients are calculated according to the procedure described above, their values only vary by a factor 1 to 3 when comparing rate coefficients calculated with *E/N* = 154 Td (pure CH_4), *E/N* = 304 Td (pure CO_2) and *E/N* = 229 Td (weighted average). As such, the uncertainties on these rate coefficients are within the typical range of uncertainty factors for gas-phase reactions in literature.[134]

5.2.2.3 Rate coefficients of reactions on the catalyst surface

The catalyst surface reactions included in the model are listed in Table A3.7. The rate coefficients of these reactions are calculated using transition state theory, i.e., with Eq. 2.9, as discussed in section 2.6. The enthalpy differences used in Eq. 2.9 are calculated from the species energies acquired from the scaling relations listed in Appendix A3, Table A3.3. The thermodynamic corrections on the enthalpies and entropies are calculated using the Shomate equations for gas species and the harmonic approximation (see section 2.6) for surface species, as is also the case for the CatMAP simulations, discussed in section 5.2.1.

We use Eq. 2.12 (see section 2.6) as the upper limit for the rate coefficient of adsorption. Hence, the rate of adsorption cannot exceed the gas kinetics multiplied by a sticking coefficient that depends on the activation enthalpy. The site area, A_s, in Eq. 2.12 is chosen as 10^{-15} cm^2, corresponding to a typical site density of 10^{15} cm^{-2}.[143] In the cases where the adsorption rate coefficients are calculated with Eq. 2.12, the rate coefficients of desorption are determined using detailed balancing, as described by Eq. 2.13 in section 2.6, to ensure thermodynamic consistency.

5.2.2.4 Rate coefficients of reactions on the walls

Apart from reactions on the surface of a transition metal catalyst, our model also includes radical recombination on a non-catalytic surface or the reactor walls. This way, radical loss processes to the surface are also included when no catalyst is present in the reactor. Six different types of reactions are included in the surface mechanism.[215] Radicals from the gas-phase can either reversibly adsorb on physisorption sites or irreversibly on chemisorption sites. Physisorbed species can either desorb back to the gas-phase, diffuse to an empty chemisorption site, or diffuse to an occupied chemisorption site and react via a Langmuir-Hinshelwood (L-H) mechanism. Additionally, Eley-Rideal (E-R) reactions,

in which a gas species reacts with a chemisorbed species, are also possible.[215] A full list of all wall reactions in the model can be found in Appendix A3, Table A3.8.

The rate coefficients of adsorption for both chemisorption and physisorption are described by the gas kinetics:

$$k = \frac{p_{ref} A_s}{\sqrt{2\pi m k_b T}} \qquad \text{Eq. 5.6}$$

This is identical to Eq. 2.12 (see section 2.6) without the enthalpy barrier (i.e., $\Delta H^{\ddagger}° = 0$). The site area, A_s, is considered the same for chemisorption and physisorption sites and is chosen equal to 10^{-15} cm^2. This corresponds to a surface site density of 10^{15} cm^{-2} if the surface is entirely covered with sites. Typical surface site densities are in the range of 10^{15}-10^{16} cm^{-2}.[215]

The rate coefficient for desorption from physisorption sites is given by:[215]

$$k = \nu_d \exp\left(-\frac{E_d}{RT}\right) \qquad \text{Eq. 5.7}$$

Here ν_d is the frequency factor for vibration of the physisorbed species in the direction perpendicular to the surface, and is set equal to 10^{15} s^{-1} based on ref. [215]. E_d is the activation energy for desorption. In ref. [214], a value of 51 kJ/mol is reported for E_d of O* and N* on silica, and 37 kJ/mol for that of H*. In our model we assume E_d = 50 kJ/mol for all species, except H* for which we use 40 kJ/mol.

Rate coefficients for E-R reactions between chemisorbed and gas species are calculated using the following equation:[215]

$$k = \frac{p_{ref} A_s}{\sqrt{2\pi m k_b T}} \exp\left(-\frac{E_r}{RT}\right) \qquad \text{Eq. 5.8}$$

with E_r the activation barrier for recombination. Typical values of E_r for recombination of O or N are in the range of 14-24 kJ/mol.[215] While recombination reactions in our model

occur between other species, we assume a similar value of 20 kJ/mol for E_r if recombination results in the formation of a stable gas molecule. We also consider some reactions, however, where species recombine on the wall to form a radical. In this case we assume the newly formed radical remains bound to the surface and set E_r to zero. The rate coefficient for diffusion is given by:[215,217]

$$k = \frac{\nu_D}{4} \exp\left(-\frac{E_D}{RT}\right) \qquad \text{Eq. 5.9}$$

In this expression, ν_D is the frequency of vibration of the physisorbed species parallel to the surface, which is set equal to 10^{13} s^{-1}.[214,215,217] E_D is the energy barrier for diffusion to an adjacent site and is estimated as $E_D = E_d/2$, in accordance with refs. [214,215].

Finally, the rate coefficient for L-H reactions is calculated using:

$$k = \frac{\nu_D}{4} \exp\left(-\frac{E_D + E_r}{RT}\right) = \frac{\nu_D}{4} \exp\left(-\frac{E_D}{RT}\right) \exp\left(-\frac{E_r}{RT}\right) \qquad \text{Eq. 5.10}$$

The barrier for recombination, E_r, is taken the same as for the corresponding E-R process.[215] As such, we use E_r = 20 kJ/mol in case recombination results in a stable gas molecule, or zero if a radical is formed, which is assumed to remain bound to the surface.

When using the approach discussed above, we find that the contribution of radical recombination on the non-catalytic wall or packing remains relatively small. Under the conditions studied in this work, i.e., for a temperature of 500 K and a pressure of 1 bar, these wall effects contribute only a few percents to the total radical recombination.

5.3 Results and discussion

We start this section by investigating the hydrogenation of plasma-produced CO as a potential pathway for CH_3OH formation in plasma-catalytic DRM. Hence, in section 5.3.1 we first illustrate the trends between transition metal catalysts for CH_3OH production via plasma-catalytic DRM, based on simulations with the CatMAP model. We study how the

presence of various plasma species, i.e., radicals and plasma-produced syngas (CO/H_2), affect the kinetics of CH_3OH formation on different surfaces. Additionally, we also discuss the kinetics of competing surface reactions that form other molecules. Lastly, we also provide some suggestion for the production of CH_3OH via plasma-catalytic DRM, based on our insights.

Nevertheless, the CatMAP model does not consider any gas-phase reactions or changes in the gas composition with time, and as such exclusively provides information on the catalyst surface chemistry. Therefore, we developed a coupled plasma-surface model that does include these gas-phase effects, next to the surface chemistry. In section 5.3.2, we will use our coupled plasma-surface model to illustrate that the presence of a catalyst can also negatively affect the conversion and selectivities of plasma-catalytic DRM. Indeed, experimentally studies show that the presence of transition metal catalysts not always enhances the conversion, but can also have a negative impact.[32–36] Additionally, we will discuss how the presence of different transition metal catalysts (Ag, Cu and Rh) in the plasma affects the destruction of CH_4 and CO_2, as well as the production of CO, H_2, H_2O and CH_3OH.

5.3.1 The role of CO hydrogenation in plasma-catalytic DRM

In this section, we investigate potential pathways for CH_3OH formation in plasma-catalytic DRM, using the descriptor-based microkinetic model CatMAP.[210] As discussed in section 5.2.1, this model calculates the steady state reaction rates and surface coverages at a fixed gas composition for different values of the O* and CH* binding energies. The binding energies of these species are correlated to the energies of all others surface species (including transition states) via scaling relations, and thus serve as descriptors that determine the activation barriers and rate coefficients. Hence, this enables visualization of trends in the reaction kinetics on different catalysts.

We focus on the reaction pathways and kinetics that occur due to the presence of plasma-produced syngas (CO/H_2) and small partial pressures of radicals (CH_3, H and O) in the CH_4/CO_2 gas mixture. Specifically, CH_3, H and O radicals were considered as they can be directly formed from the reactants, i.e., CH_4 and CO_2, by electron impact dissociation. Unless noted otherwise, we used a 1:1 CO_2/CH_4 gas mixture, which also contains 1.4×10^{17} cm^{-3} (0.01 bar) CO and H_2, as well as 1.4×10^{11} cm^{-3} (10^{-8} bar) CH_3, H and O radicals. For CO and H_2, we chose a number density of 1.4×10^{17} cm^{-3} as a representative value at low conversion, because the possibility of attaining high conversions will be more strongly dependent on the reaction conditions and catalyst. In addition, we chose a value of 1.4×10^{11} cm^{-3} as a typical radical density in a DBD plasma, based on ref. [157] in which radical densities between 10^{10}-10^{14} cm^{-3} were reported for CH_3, H and O. The simulations were performed for a total pressure of 1 bar and a temperature of 500 K, as these conditions are representative for a DBD plasma, commonly used for plasma catalysis.

5.3.1.1 Effect of plasma species on the catalytic formation of CH_3OH

To illustrate how the plasma-catalytic formation of CH_3OH is affected by different plasma species, i.e. radicals, as well as H_2 and CO formed in the plasma, we calculated the CH_3OH formation rates for different gas mixtures. By removing certain species from the gas mixture, we can observe their effect on the CH_3OH production pathways. We would like to emphasize that for pure CH_4/CO_2 gas mixtures, no reaction occurs at 500 K as the process is strongly equilibrium-limited by the high thermodynamic stability of CH_4 and CO_2 at this temperature.[22] This case is therefore not considered. Our results are displayed in Figure 5.1, which shows the CH_3OH production rates as function of the O* and CH* binding energies for four different gas mixtures. These binding energies are defined as the formation energies of the adsorbed species relative to the empty slab and CO, H_2O and H_2 in the gas phase. As such, lower (i.e., negative, more exothermic) binding energies

correspond to more stable, and thus more strongly bound adsorbates, while higher (or positive) binding energies correspond to more weakly bound adsorbates.

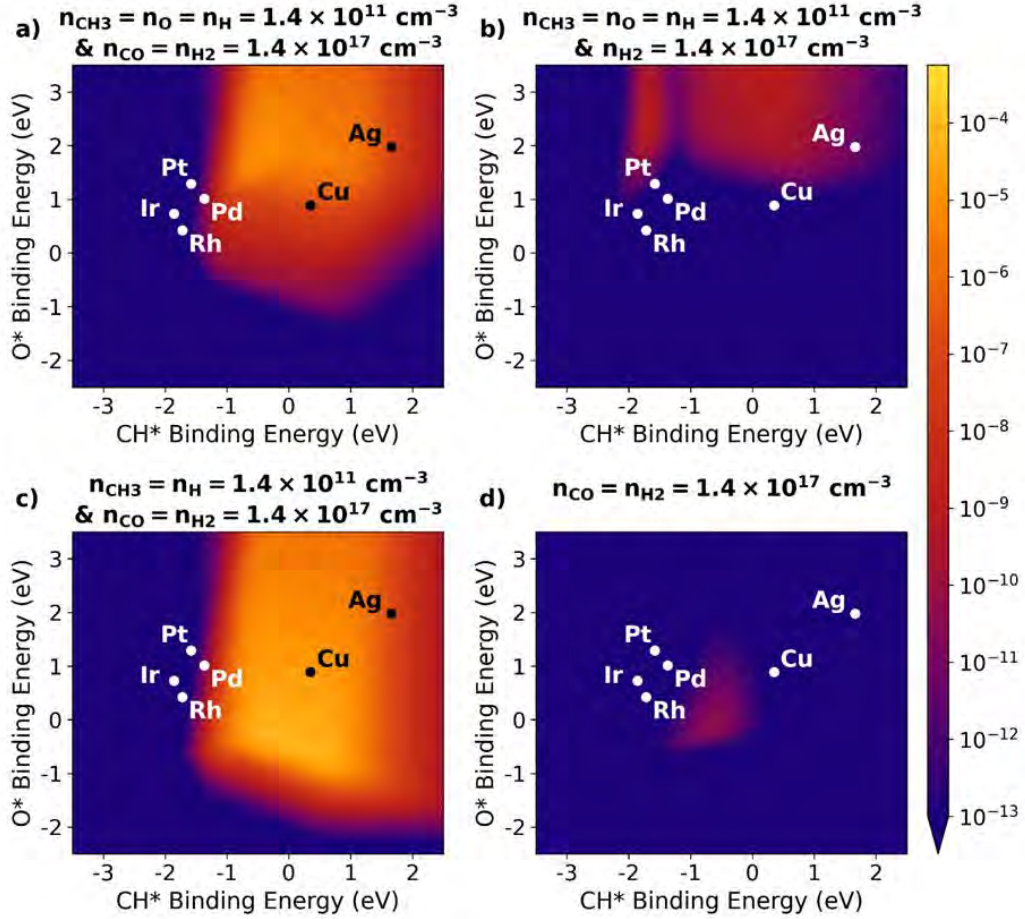

Figure 5.1. Activity plots of the CH_3OH production rates in s^{-1} on transition metal (111) surfaces exposed to a 1:1 CH_4/CO_2 gas mixture, that also contains (a) 1.4×10^{11} cm^{-3} (10^{-8} bar) of CH_3, H and O radicals and 1.4×10^{17} cm^{-3} (10^{-2} bar) of H_2 and CO, (b) 1.4×10^{11} cm^{-3} (10^{-8} bar) of CH_3, H and O radicals and 1.4×10^{17} cm^{-3} (10^{-2} bar) of H_2, but no CO, (c) 1.4×10^{11} cm^{-3} (10^{-8} bar) of CH_3 and H radicals and 1.4×10^{17} cm^{-3} (10^{-2} bar) of H_2 and CO, but no O, or (d) 1.4×10^{17} cm^{-3} (10^{-2} bar) of H_2 and CO, but no radicals. The total pressure is 1 bar and the temperature 500 K for all cases. The binding energies of O and CH* are the formation energies of the adsorbed species relative to the empty slab and CO, H_2O and H_2 in the gas phase. Low (negative) values of these binding energies represent strongly binding catalysts, while high (positive) values correspond to weakly binding catalysts.*

Figure 5.1 (a) displays the CH_3OH production rates for a gas mixture that contains plasma-produced CH_3, H and O radicals, as well as syngas (CO and H_2), next to the feed gas (CH_4 and CO_2). For this gas mixture, CH_3OH is formed through hydrogenation of CO by H radicals, which are both directly adsorbed from the plasma. The CO* hydrogenation pathway goes through CHO*, CH_2O* and CH_3O* via subsequent hydrogenation steps to eventually form CH_3OH. The best performing catalysts for this gas mixture are Cu and Ag, which can be attributed to the facile bond formation steps on these weakly binding catalysts. In addition, the rates remain negligible at strong CH* and O* binding, due to surface poisoning by CO* (which binds through carbon and thus scales with CH*) or O*, respectively.

When CO is removed from the gas mixture, the CH_3OH formation rate is much lower (see Figure 5.1 (b)). Indeed, CH_3OH formation cannot proceed through CO hydrogenation anymore, but instead happens from adsorbed CH_3*, H* and O* radicals. In the broad region at weak CH* binding, this occurs via the CH_3O* intermediate through: O* + H* → OH*, followed by CH_3* + OH* → CH_3O* + H* and subsequently CH_3O* + H* → CH_3OH. In the second, narrower region at stronger CH* binding, adsorbed CH_3* is first partly dehydrogenated to CH*, followed by coupling with OH* to form CHOH*. This species is then subsequently hydrogenated to form CH_3OH. The best catalysts for CH_3OH production via these pathways are Ag and Pt, respectively. However, comparison between Figure 5.1 (a) and (b) clearly shows that formation of CH_3OH directly from adsorbed CH_3*, O* and H* radicals is much more difficult than CO* hydrogenation by adsorbed H* radicals on the catalyst surface.

When O radicals are removed from the gas mixture (without removing CO), the CH_3OH formation rate drastically increases, and Cu becomes the best catalyst, followed by Ag (see Figure 5.1 (c)). Indeed, O* poisoning becomes (quasi) negligible in this case, as direct adsorption of O radicals is no longer possible. As such, a high density of O radicals in the

plasma is not beneficial for the surface reactions as this limits the rates on the catalyst due to poisoning. Note that also removing CH_3 radicals from the gas mixture of Figure 5.1 (c) results in essentially the same CH_3OH production rates, as CH_3* does not participate in the CO* hydrogenation pathway.

Finally, as illustrated in Figure 5.1 (d), removing all radicals from the gas mixture results in a strong reduction of the CH_3OH production rates overall. In this case, CH_3OH is formed from the small fraction of syngas that is present, through thermal catalytic CO hydrogenation. Comparing Figure 5.1 (c) and (d) illustrates how the presence of H radicals strongly increases the rate of CH_3OH production on the metals that bind CH* weakly. This is because these catalysts have more difficulty with breaking the H-H bond in H_2. However, if H radicals are present in the gas phase, this H-H bond has already been broken by the plasma. In this way, H_2 dissociation on the catalyst surface can be circumvented. Consequently, this improves the H* coverages on the weakly binding catalysts, which in turn enhances the CO* hydrogenation steps.

In conclusion, these results again demonstrate how plasma can overcome the scaling relations for bond dissociation that are normally present in thermal catalysis, by breaking or weakening bonds in the reactant molecules, as was discussed in the introduction of this thesis, section 1.7.2.2. However, as we will illustrate in the next section, CH_3OH formation from plasma-produced radicals and syngas (CO/H_2) is negligible compared to the production rates of other molecules (CH_4, CO_2, H_2O and H_2), at least for gas mixtures that are representative for CH_4/CO_2 plasmas.

5.3.1.2 Surface reactions that compete with CO hydrogenation in plasma-catalytic DRM

In section 5.3.1.1, we illustrated that plasma-produced CO and H radicals can enhance the formation of CH_3OH on the surface of weakly binding metals, like Cu and Ag. However, we find that CH_4, CO_2, H_2O and H_2 have significantly higher production rates, at least for a gas mixture representative of CH_4/CO_2 plasma, that contains CH_3, H and O radicals, as well as syngas (CO and H_2), next to the feed gas (CH_4 and CO_2). Figure 5.2 illustrates the production rates of CH_4, CO_2, H_2O and H_2 for such a gas mixture, i.e., the same gas mixture used for Figure 5.1 (a). As can be observed by comparing Figure 5.1 (a) and Figure 5.2, the CH_3OH production rates are indeed negligible compared to the high production rates of CH_4, CO_2, H_2O and H_2. A high production rate for CH_4 or CO_2 in this context means that the catalysts can efficiently recombine H and CH_3 radicals, formed in the plasma, back to CH_4, or CO and O back to CO_2. This is of course an unwanted effect and indicates that the catalyst will lower the effective plasma conversion and thus acts as an inhibitor for the overall reaction. Note that CO is oxidized to CO_2, and thus destroyed, on all catalysts for the conditions in Figure 5.2. Since the CO destruction rate matches the CO_2 production rate, it is not included in Figure 5.2.

Figure 5.2 (a) displays the rate for CH_4 production due to recombination of CH_3 and H radicals on the catalyst. This occurs most easily on catalysts that bind CH* relatively weakly or intermediately and O* weakly. i.e., specifically Cu, followed by Ag and to a lesser extent Pd. At strong CH* or O* binding the rates are limited due to surface poisoning, as is also the case for CH_3OH production (discussed in section 5.3.1.1.). This is also observed in the production rates of CO_2 and H_2O (Figure 5.2 (b) and (c), respectively). The maximum of the CH_4 production rate at intermediate CH* binding strength results from lower barriers for recombination on more weakly binding metals, while some CH* binding is required to a have sufficiently high CH_3* coverage. Indeed, CH_3* binds the

surface relatively weakly for a radical (e.g., $\Delta H_{CH3(g)\rightarrow CH3*}$ = -0.99 eV on Ag(111) in this chemistry set).[9,99]

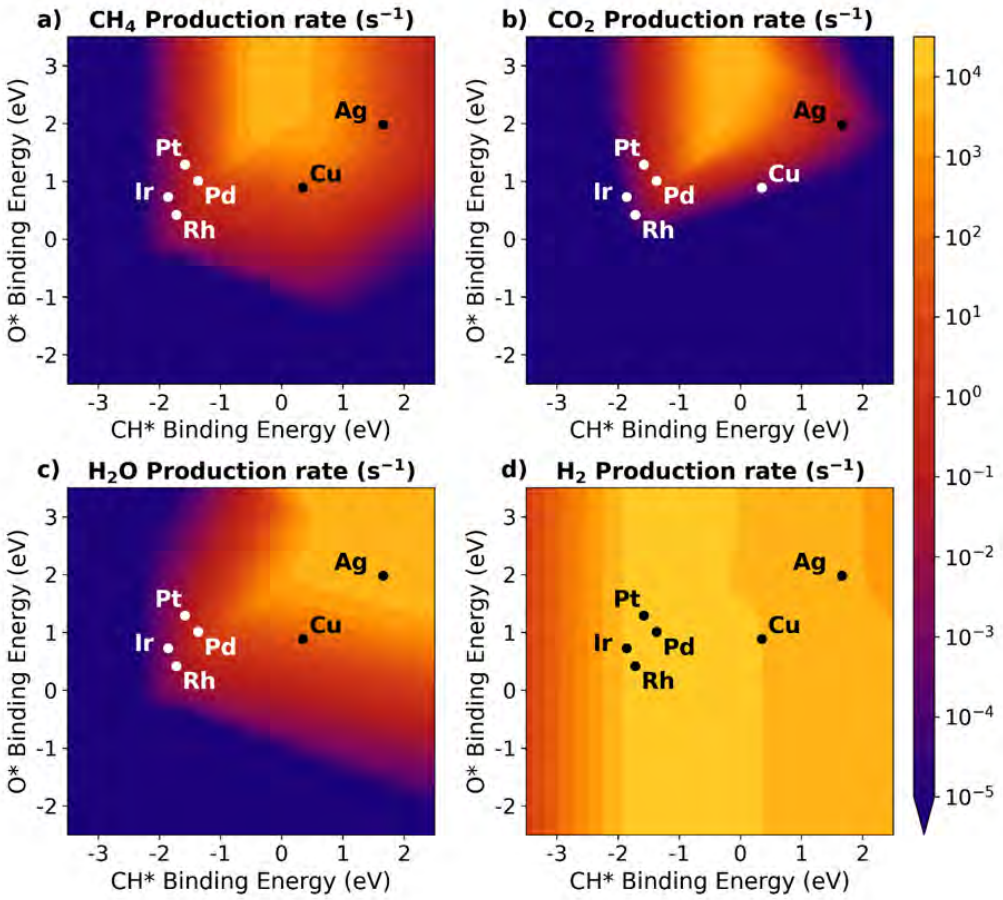

Figure 5.2. Activity plots of the production rates in s^{-1} for (a) CH_4, (b) CO_2, (c) H_2O and (d) H_2 on (111) transition metal surfaces exposed to a gas mixture containing 7.1×10^{18} cm^{-3} (0.49 bar) CO_2 and CH_4, 1.4×10^{17} cm^{-3} (0.01 bar) H_2 and CO, and 1.4×10^{11} cm^{-3} (10^{-8} bar) CH_3, H and O radicals at a temperature of 500 K. We do not plot the CO production rate, as CO is oxidized into CO_2, and thus destroyed at the catalyst surface; the CO destruction rate matches the CO_2 production rate. The binding energies of O and CH* are the formation energies of the adsorbed species relative to the empty slab and CO, H_2O and H_2 in the gas phase. Low (negative) values of these binding energies represent strongly binding catalysts, while high (positive) values correspond to weakly binding catalysts.*

The rate for CO_2 production via oxidation of plasma-produced CO by adsorbed O* radicals is shown in Figure 5.2 (b). The rate exhibits a similar trend as that for CH_4 formation, but it declines more rapidly upon going to weaker CH* or stronger O* binding. This similar trend is because sufficiently strong CH* binding is required to have a high enough coverage of CO* (which binds to the surface via the carbon atom), while bond formation is easier on the more weakly binding metals. The highest CO_2 formation rate is observed for Pd, which is in line with thermal catalytic CO oxidation, for which Pd is widely known to be a good catalyst, as it is used for this purpose in automobile exhaust catalysts.[218,219]

H_2O is formed by recombination of H* and O* radicals on the surface, with OH* as intermediate adsorbate. As presented in Figure 5.2 (c), the H_2O formation rate is the highest on Ag and (to a lesser extent) on Cu. Since both the O and H radicals bind to the surface strongly, sufficient coverages can be attained on even the most weakly binding metals. Consequently, the highest rates are observed for the most weakly binding catalysts. It is important to realize that H_2O formation competes with CO_2 formation for O*, while it competes with CH_4 and H_2 formation for H*. Similarly, CH_3OH also competes with the formation of CH_4, H_2O and H_2 for H*, and with the formation of CO_2 for CO*. Yet, CH_3OH formation is disadvantaged compared to these other reactions on all catalysts. Consequently, the adsorption of CH_3 and O on the surface is undesirable as these species can scavenge surface H* and CO* to form thermodynamically (very) stable CH_4, H_2O and CO_2 molecules. Moreover, these recombination reactions occur much more easily than CO* hydrogenation to CH_3OH.

Lastly, H_2 is formed upon recombination of two H* radicals, and this reaction occurs with the highest rate on most catalysts (except Ag), as illustrated in Figure 5.2 (d). The slight decrease of the H_2 production rate in the region around Ag, is due to competition for H* with H_2O production. Note that the uniformly high H_2 production rates are partly attributed to the assumption that H can still co-adsorb onto sites that are already

occupied by another species. As a result, H radicals in the model can still adsorb and recombine to H_2, even if the surface is poisoned by another, larger species. For more information see section 5.2.1. Note that the recombination of H radicals to H_2 on the surface will always compete for H* with CO* hydrogenation to CH_3OH. This will inevitably result in a loss of energy efficiency as a large fraction of the energy used to form H radicals in the plasma will not be directed into the formation of CH_3OH.

To summarize, while plasma-produced CO and H can enhance the formation of CH_3OH on the catalyst surface, the CH_3OH formation rate is negligible compared to the production rates of CH_4, CO_2, H_2O and H_2. Indeed, these molecules can easily be formed through recombination reactions of adsorbed radicals and CO on the catalyst. Moreover, these processes direct CO* and H*, needed for CH_3OH production, into other molecules, meaning that these plasma species will not be used efficiently. To avoid the competing formation of CH_4, H_2O and CO_2, adsorption of CH_3 and O radicals should be limited. This may be achieved by reducing their formation in the plasma. However, these radicals may be important for the gas-phase production of CH_3OH.[157] Nevertheless, if chemical effects play a dominant role in plasma catalysis, it would be more beneficial to maximize the reaction rates on the catalyst surface at the cost of those in the bulk plasma. Of course, this would only be applicable to conditions where the chemical effects positively affect the formation of the desired products.

Finally, we would briefly like to mention that although we did not consider the RWGS and HCOO* (formate) pathways in the simulation, our general conclusion would remain largely the same. Indeed, these pathways could possibly result in more facile CO* and CH_3OH formation. However, both the RWGS and HCOO* pathways depend on the presence of H* radicals on the surface. Consequently, the presence of CH_3* and O* on the surface are still undesired, as these react easily with H* to form CH_4 and H_2O,

respectively. Moreover, O radicals would still oxidize surface-bound CO*, back to CO_2 and inhibit the overall DRM reaction.

5.3.1.3 A proposed solution for CH_3OH production in DRM

As illustrated in section 5.3.1.1 (and section 1.7.5 in the introduction to this thesis), plasma-produced H radicals and CO are likely to play an important role in plasma-catalytic CH_3OH formation for DRM and CO_2 hydrogenation. Based on the trends in catalyst selectivity for CO/CO_2 hydrogenation, weakly binding catalysts (like Cu) are expected to be more suitable for CH_3OH production. As discussed in section 1.7.5, this can be attributed to the lower activity of these weakly binding catalysts for C-O bond scission, which would result in CH_4 instead of CH_3OH.[26,99,100] Indeed, Cu-based catalysts have been observed to form CH_3OH in plasma-catalytic CO_2 hydrogenation experiments.[97,104] Moreover, the hydrogenation of CO* to CH_3OH also benefits most from plasma-produced H radicals on the weakly binding Cu and Ag surfaces, as illustrated in our modeling results (section 5.3.1.1). However, this does require that high densities of CO and H radicals can be obtained in the gas phase. On the other hand, the additional presence of CH_3 and O radicals negatively affects surface pathways for plasma-catalytic CH_3OH formation, as these radicals easily recombine with H* and CO* to produce CH_4, H_2O and CO_2, as illustrated by our modeling results in section 5.3.1.2. Yet, since CH_3 and O can be formed directly from the dissociation of CH_4 and CO_2, these radicals are important plasma species in DRM.

Relatively strongly binding catalysts (e.g., Ni, Ru, Co) can hydrogenate CO_2/CO to CH_4 (as discussed in section 1.7.5) and should thus be avoided at the relatively low temperatures ($\leq$ 600 K) where CH_4 is strongly thermodynamically favored. Indeed, plasma enables CH_4 formation on these catalysts even at low temperature, as was experimentally observed for plasma-catalytic CO_2 hydrogenation with catalysts based on Ni,[98] Ru[91] and Co.[96,101] On the other hand, strongly binding metals (e.g., Ni) are still expected to be good catalysts

for DRM to syngas at high temperatures (> 600 K), as these can also more easily break the C-H bonds in CH_4. Indeed, plasma-catalyst synergy for DRM to syngas (CO/H_2) has experimentally been observed on Ni catalysts at high temperatures (600-900 K).[70] Moreover, the combination of a relatively strongly binding catalyst, like Ni, with high temperatures would also enable plasma catalysis via vibrational excitation, rather than radicals (see section 1.7.3), which is more energy efficient. Addition of specific promotors may further improve the reaction, as was illustrated by Sheng *et al*.,[220] who reported that adding a La-promotor to a Ni/Al_2O_3 catalyst enhanced the production of syngas in plasma-catalytic DRM. The La-promotor was found to enable the formation of surface carbonates from vibrationally excited CO_2, which facilitated the oxidation of CH_x* on the Ni catalyst.

Hence, we could propose a plausible solution based on a two-stage plasma reactor setup, in which a first reactor operates at high temperature, combined with a strongly binding catalyst (e.g., Ni) to enrich the gas mixture with syngas, and reduce the amount of CH_4 and CO_2. A second reactor can then be placed in series that operates at low temperature, with a more weakly binding catalyst (e.g., Cu) to form CH_3OH.

5.3.2 Insight from coupled plasma-surface simulations: effect of catalyst on DRM

Here we present the results of our coupled plasma-surface kinetics model, to explain why the presence of a transition metal catalyst in plasma-catalytic DRM can also negatively affect the chemistry. The model uses a CSTR approach, as explained in section 5.2.2, with a 1:1 CH_4/CO_2 feed mixture entering the reactor. During the simulations, the temperature and pressure are kept constant at 500 K and 1 bar, respectively, as these are typical conditions for a DBD plasma. While DRM is not possible in thermal catalysis at these conditions, as the reaction is kinetically and equilibrium-limited, the formation of

reactive plasma species (e.g., radicals) enables this reaction in plasma catalysis. Indeed, these highly reactive plasma species react further in the gas-phase, but can also adsorb and react on the catalyst surface, thus bypassing the difficult reactant activation steps present in thermal catalysis.

The surface species energies in the coupled model are described using the same scaling relations as those used in the simulations with CatMAP (see section 5.2.1). This allows us to model transition metal catalysts for which only limited reaction data is available, or even hypothetical catalysts. However, for the purpose of this study, we limit ourselves to Ag(111), Cu(111) and Rh(111) surfaces. We perform simulations for four different cases: i.e., plasma without catalyst, as well as combined with one of the abovementioned catalysts. The corresponding values of CH* and O* binding energies, used in the scaling relations, are (E_{CH*} = 1.66 eV, E_{O*} = 1.98 eV) for Ag, (E_{CH*} = 0.35 eV, E_{O*} = 0.89 eV) for Cu, and (E_{CH*} = -1.72 eV, E_{O*} = 0.42 eV) for Rh, as acquired from ref. 99 and our own DFT results (see Table A3.1 in Appendix A3). As such, we compare a set of metals for which both CH* and O* become more strongly bound when going from Ag to Cu to Rh.

In Appendix A3, Figure A3.1, we present the time-evolution of the H, CH_3, O and OH radical densities in the plasma. Initially, the radical densities increase with time, both with and without catalysts, due to electron impact dissociation in the plasma. As radical adsorption becomes significant, the radical densities for the different transition metals and the plasma-only case start to deviate, as the net adsorption rates vary with the catalyst material. This eventually causes the radical densities to stabilize at different values for different transition metals. A more detailed analysis is given in Appendix A3, section A3.8.

This demonstrates how the catalysts affect the plasma (radical) composition. In the following subsections, we will describe how the catalysts affect the destruction of the reactants (CO_2 and CH_4) and the formation of various stable molecules (CO, H_2, H_2O and

CH_3OH) at steady state, as obtained by our coupled plasma-surface kinetics model. We will compare the net production or destruction rates for the plasma without catalyst, as well as combined with the three different metals. To highlight the effect of the catalyst, distinction will be made between the total net rate, the net rate on the catalyst surface and the net rate in the plasma.

Note that while C_2H_6 is included in the gas-phase as a species representative for higher hydrocarbons, C_2H_6 formation on the catalyst surface is not included in our model as these reactions are not included in the reaction set by Schumann *et al.*,[99] which we use as input for our model, and taking the corresponding values from other studies would lead to an inconsistent reaction set. Therefore, an analysis of the effect of the catalyst on C_2H_6 production is outside the scope of this work. However, it is worth mentioning that C_2H_6 is still the second most important carbon-containing product in the gas-phase (the main carbon-containing product is CO).

5.3.2.1 CO_2 destruction at steady state

Figure 5.3 shows the net rate of CO_2 destruction for the different cases at steady state. Note that hatched bars indicate net production on the catalyst surface, instead of destruction. As can be seen in Figure 5.3, CO_2 is net produced on all catalyst surfaces due to recombination of CO* and O* on the catalyst. This is in line with our results of section 5.3.1.2, where we also discussed the production of CO_2 on the catalyst surface (see Figure 5.2). While CO_2 production on Rh happens at a rate that is many orders of magnitude lower than the other rates in Figure 5.3, CO_2 production is non-negligible on Cu (5.7×10^{15} cm^{-3} s^{-1}), and even significant (1.0×10^{17} cm^{-3} s^{-1}) on Ag surfaces. The low rate (4.7×10^{9} cm^{-3} s^{-1}) on Rh results from CO* poisoning of this catalyst at 500 K.

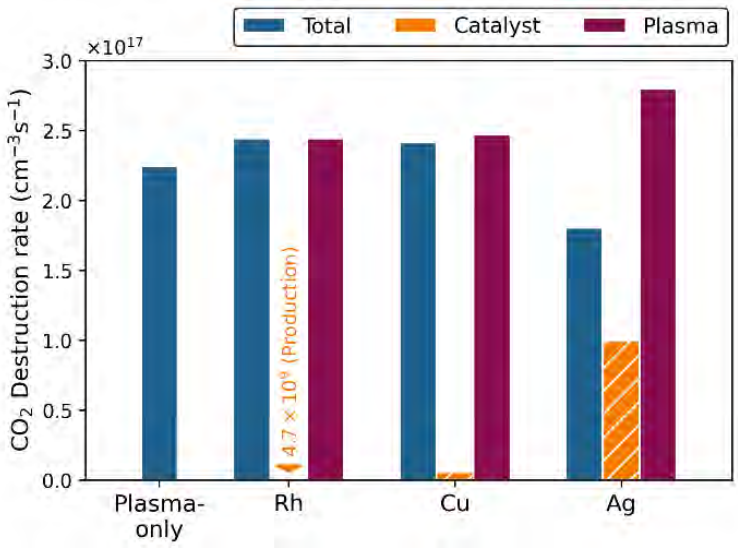

Figure 5.3. Net rates of CO_2 destruction at steady state (t = 10^6 s) for plasma without catalyst, or combined with a Rh, Cu or Ag catalyst. Distinction is made between the total rate, the rate on the catalyst surface and the rate in the plasma. Hatched bars indicate net production instead of destruction. The net (production) rate on the Rh surface is indicated by its numerical value, as it is many orders of magnitude lower compared to the other rates in the figure. Calculated for a 1:1 CH_4/CO_2 feed mixture using a total pressure of 1 bar and a temperature of 500 K.

The rate of recombination to CO_2 is indeed most notable for the Ag surface, as it is large enough to cause a clear drop in the total net destruction rate of CO_2. As such, less CO_2 is destroyed in total for the case with Ag compared to plasma without catalyst, or combined with Rh or Cu. As mentioned in previous paragraph, this is due to the quick recombination of adsorbed CO* and O*, and it is also partly responsible for the lower O (and OH) densities in the plasma, which can be observed in Figure A3.1 (c) and (d) in Appendix A3. While Ag is indeed among the better catalysts for CO_2 formation in Figure 5.2 (b), it is not the catalyst with the highest rate in this figure. However, in the coupled plasma-surface simulations, the CO and O densities in the gas phase are higher (9.7×10^{17} cm^{-3} and 2.6×10^{11} cm^{-3}, respectively, for plasma with Ag) compared to those used in the simulations with the CatMAP code (see section 5.3.1.2). This can increase the CO_2

formation rates on weaker binding catalysts, relative to the more strongly binding catalysts, as the latter are more susceptible to poisoning.

The total (and plasma) CO_2 destruction rates are slightly higher for the cases with Cu and Rh relative to the plasma without catalyst. This is due to a higher rate of $CO_2 + CH_2 \rightarrow CO + CH_2O$ in the plasma, which is caused by a higher CH_2 density in the plasma. As can be seen in Figure A3.1 (a), the H density in the plasma is strongly reduced when a transition metal is present, which results in less CH_2 recombining with H, and thus in higher CH_2 densities. This is also the case for Ag, and for this catalyst the net CO_2 destruction rate in the plasma is even higher, due to a reduction in the rate of CO_2 formation via $CO + OH \rightarrow CO_2 + H$. The latter is caused by the lower OH densities in the plasma when Ag is present, as illustrated in Figure A3.1 (d).

Nevertheless, the high net CO_2 destruction rate in the plasma in case of the Ag catalyst is largely compensated by the net CO_2 production on the Ag catalyst surface, as mentioned above, so the total net CO_2 destruction rate in the case of the Ag catalyst is clearly lower than in the plasma-only case (see Figure 5.3). Hence, our model predicts that an Ag catalyst is detrimental for the overall CO_2 conversion, compared to plasma without catalyst.

5.3.2.2 CH_4 destruction at steady state

Figure 5.4 presents the net steady state CH_4 destruction rates for the plasma-only case and the plasma combined with the three different catalysts. Similar to CO_2, CH_4 is net produced on the catalyst surfaces (as indicated by the hatched bars), through recombination of adsorbed CH_3* and H*. However, for Rh the rate of CH_4 formation on the catalyst is again extremely low (9.8×10^{12} cm^{-3} s^{-1}) due to surface poisoning, as is also the case for CO_2 formation on this metal. Among these three transition metals, the highest rate of CH_4 formation on the catalyst is now observed for Cu (3.8×10^{17} cm^{-3} s^{-1}). In fact, the fast recombination of CH_3* and H* on the Cu surface results in a clear drop in

the total net destruction rate of CH_4 compared to the other cases. Indeed, Cu was also identified as the best catalyst for radical recombination to CH_4 in the surface kinetics simulations with CatMAP, as displayed in Figure 5.2 (a). Since the Cu catalyst gives the fastest recombination of H and CH_3 radicals to CH_4, it also causes the strongest drop of the CH_3 density in the plasma, as can be seen in Figure A3.1 (b). As a result, the net destruction of CH_4 in the plasma is faster for the case with Cu, compared to that with Rh or without catalyst (see Figure 5.4), due to recombination between CH_3 and H happening now predominantly on the catalyst, causing a lower rate of the corresponding reaction in the gas phase.

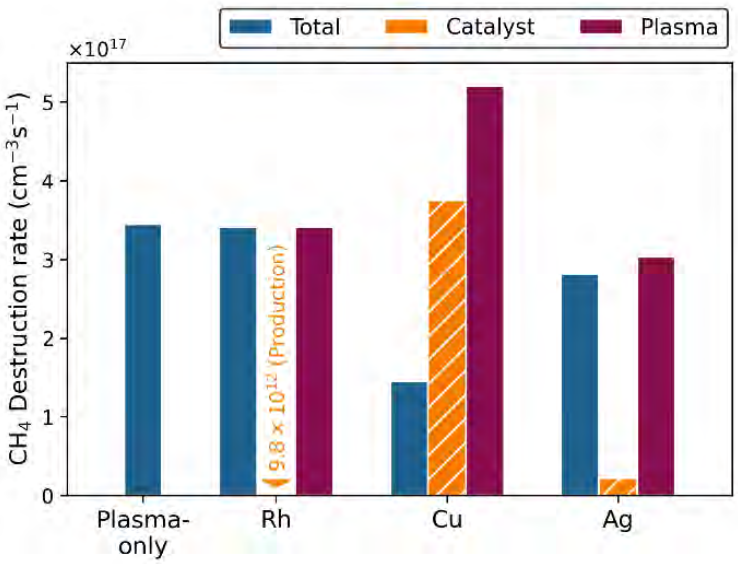

Figure 5.4 Net rates of CH_4 destruction at steady state ($t = 10^6$ s) for plasma without catalyst, or combined with a Rh, Cu or Ag catalyst. Distinction is made between the total rate, the rate on the catalyst surface and the rate in the plasma. Hatched bars indicate net production instead of destruction. The net (production) rate on the Rh surface is indicated by its numerical value, as it is many orders of magnitude lower compared to the other rates in the figure. Calculated for a 1:1 CH_4/CO_2 feed mixture using a total pressure of 1 bar and a temperature of 500 K.

For plasma combined with Ag, the total net rate of CH_4 destruction is also lowered compared to Rh and plasma-only. However, for this case the lower total CH_4 destruction

results partly from recombination reactions that form CH_4 on the catalyst, and partly from lower CH_4 destruction in the plasma. The latter is caused by lower O and OH densities in the plasma when Ag is present as a catalyst, as illustrated in Figure A3.1 (c) and (d), respectively. As shown in Figure 5.3, significant CO_2 formation occurs on the Ag surface, due to recombination of CO* and O* on this catalyst. Additionally, an even higher amount of O radicals is used on the Ag surface to form H_2O, as will be discussed in section 5.3.2.5 below. These processes in turn reduce the density of O radicals in the plasma, as illustrated in Figure A3.1 (c). Since O radicals are partly responsible for CH_4 conversion in the plasma via $CH_4 + O \rightarrow CH_3 + OH$, the drop in O density also reduces the CH_4 destruction in the plasma. Additionally, the formed OH radicals can also convert CH_4 via $CH_4 + OH \rightarrow CH_3 + H_2O$. A drop in the O radical density also causes a drop in the OH density, which is formed from O, and both effects result in less CH_4 destruction in the plasma.

To summarize, while Cu results in a high net CH_4 destruction rate (5.2×10^{17} $cm^{-3}s^{-1}$) inside the plasma, it also causes the strongest drop in the total CH_4 destruction rate compared to plasma-only, due to quick recombination of CH_3* and H*, and thus CH_4 production, on the catalyst surface. Ag, on the other hand gives a less pronounced reduction of the CH_4 destruction rate compared to plasma without catalyst, but the effect of Ag is dual, i.e. due to both recombination of CH_3 and H on the catalyst, and less destruction of CH_4 via reactions with O and OH in the plasma (due to the lower densities of the latter species). In general, however, both Ag and especially Cu catalysts seem detrimental for the overall CH_4 conversion, compared to plasma-only, as predicted by our model.

5.3.2.3 CO production at steady state

The net rates of CO production are displayed in Figure 5.5. Note that hatched bars in the figure now indicate net destruction of CO on the catalyst surface, instead of formation. CO is mainly produced directly from CO_2 via electron impact dissociation in the plasma.

However, by comparing the rates of CO production in Figure 5.5 and of CO_2 destruction in Figure 5.3, it becomes clear that CO production occurs faster and that a significant fraction of CO is not produced directly, i.e. not in a single step, from CO_2. Indeed, CO is also produced through decomposition of CH_3CO and dehydrogenation of CHO, which are formed by dehydrogenation of CH_3CHO and CH_2O, respectively. These aldehydes (CH_3CHO and CH_2O) in turn result from the oxidation of alkyl radicals (CH_3 and C_2H_5) by O, originating from CO_2.

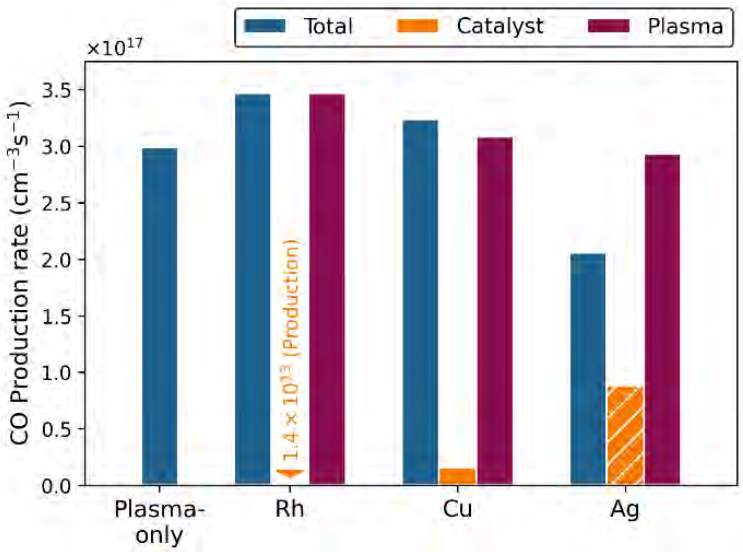

Figure 5.5. Net rates of CO production at steady state (t = 10^6 s) for plasma without catalyst, or combined with a Rh, Cu or Ag catalyst. Distinction is made between the total rate, the rate on the catalyst surface and the rate in the plasma. Hatched bars indicate net destruction instead of production. The net (production) rate on the Rh surface is indicated by its numerical value, as it is many orders of magnitude lower compared to the other rates in the figure. Calculated for a 1:1 CH_4/CO_2 feed mixture using a total pressure of 1 bar and a temperature of 500 K.

As is the case for CO_2 destruction in Figure 5.3, the CO production rate rises in the presence of Rh or Cu, compared to the plasma-only case. This can be partly attributed to the higher rate of $CO_2 + CH_2 \rightarrow CO + CH_2O$ in the plasma, as the lower H radical density (see Figure A3.1 (a) in Appendix A3) causes a rise in the density of CH_2. Yet, the rise in CO

production (Figure 5.5) is more significant compared to that of CO_2 destruction. Indeed, the drop in H density in the presence of the catalysts also suppresses hydrogenation and enhances dehydrogenation reactions. This increases the CO produced through dehydrogenation of CH_3CHO and CH_2O, as discussed above.

The rise in (total and plasma) CO production is less expressed for Cu compared to Rh. This is because Cu catalyzes recombination between CH_3* and H*, reducing the densities of CH_3 (Figure A3.1 (b)), as well as C_2H_6 and thus C_2H_5, in the plasma. Indeed, C_2H_6 is formed by recombination of CH_3, and C_2H_5 is formed by dehydrogenation of C_2H_6. Since CH_3 and C_2H_5 play an important role in the formation of aldehydes (CH_3CHO and CH_2O) and also in dehydrogenating CHO, Cu produces less CO in the plasma, and in total, compared to Rh. However, on the Cu surface, some dehydrogenation of adsorbed CHO* takes place, forming CO* which can desorb to form CO or become oxidized to CO_2. As a result of this CO formation on the catalyst, the total CO production rate is slightly higher for Cu compared to the plasma-only case. The rate of CHO* decomposition on Rh is negligible due to surface poisoning.

For Ag the total CO production rate is lower relative to the plasma only-case, due to adsorption and subsequent oxidation of CO back to CO_2, as discussed in section 5.3.2.1. This is also clear from CO being net destroyed instead of produced on the catalyst, as displayed in Figure 5.5.

5.3.2.4 H_2 production at steady state

The net rates of H_2 production for the four different cases are displayed in Figure 5.6. The H_2 production rate appears especially high on the Rh surface (2.6×10^{17} cm^{-3} s^{-1}), where recombination of adsorbed H* radicals to H_2 occurs the fastest. The fast destruction of H radicals on this catalyst, however, results in a lower H density in the plasma (see Figure A3.1 (a) in Appendix A3), which in turn reduces the rates of H_2 formation in the gas phase and causes a net destruction of H_2 in the plasma (hatched bar in Figure 5.6). However, H_2

production on the Rh catalyst is sufficiently fast to counter the net destruction of H_2 by plasma processes and leads to a total rate of H_2 production, which surpasses that of the plasma-only case. This is of course a positive effect, as H_2 is a value-added product. As discussed in section 5.2.1, H adsorbs on a separate site type in our model, as it is assumed to have negligible interactions with the larger adsorbates on the surface. This allows H radicals to adsorb and recombine on the surface, even though the catalyst is poisoned by CO*. Note that H* can still react with other adsorbates on the surface, but H* recombination to H_2 is strongly favored over CO* hydrogenation.

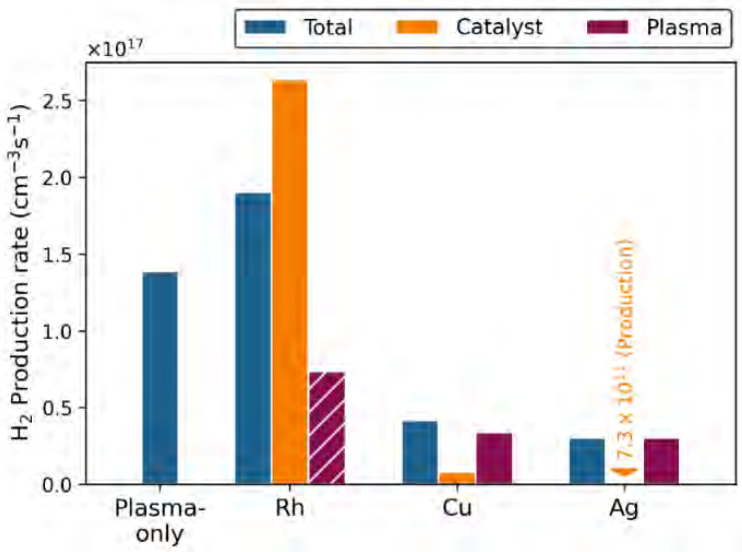

Figure 5.6. Net rates of H_2 production at steady state (t = 10^6 s) for plasma without catalyst, or combined with a Rh, Cu or Ag catalyst. Distinction is made between the total rate, the rate on the catalyst surface and the rate in the plasma. Hatched bars indicate net destruction instead of production. The net (production) rate on the Ag surface is indicated by its numerical value, as it is many orders of magnitude lower compared to the other rates in the figure. Calculated for a 1:1 CH_4/CO_2 feed mixture using a total pressure of 1 bar and a temperature of 500 K.

For the Cu and Ag catalysts, the H_2 production rate is positive in the plasma, yet clearly lower compared to the plasma-only case. This is due to the lower H densities in the plasma (see Figure A3.1 (a), due to H adsorption on these surfaces. However, on the Cu

and Ag surfaces, the adsorbed H* is mainly used to form CH_4 and H_2O, rather than recombining to H_2. As such, the H_2 production rate is low on the Cu surface (8.0×10^{15} $cm^{-3}\,s^{-1}$) and negligible on the Ag surface ($7.3 \times 10^{11}\,cm^{-3}\,s^{-1}$). Because of the this, the total net H_2 production rates are significantly lower compared to the plasma without catalyst or with Rh catalyst.

5.3.2.5 H_2O production at steady state

In this section we discuss the formation of H_2O, which is an undesired side-product of plasma-catalytic DRM. Figure 5.7 shows the net rates of H_2O production for plasma-only and the different catalysts. H_2O is produced on all catalyst surfaces, although the net rate on Rh is negligible due to surface poisoning. Yet, on Cu and Ag surfaces, non-negligible and even significant amounts of H_2O are formed, respectively, via hydrogenation of adsorbed O*, or to a lesser extent, OH* radicals. For the Cu catalyst, the formation of H_2O on the surface results in an additional amount of H_2O formed on top of the large production rate in the plasma. This increases the total rate of H_2O formation to a slightly higher value compared to the plasma-only case. For the Ag catalyst, on the other hand, formation on the catalyst surface appears by far the dominant mechanism of H_2O production. The high H_2O formation rate (1.6×10^{17} $cm^{-3}\,s^{-1}$) on the Ag surface is in agreement with the trend predicted by the surface kinetics simulation with CatMAP, as displayed in Figure 5.2 (c). The quick adsorption of O and OH radicals from the plasma and their subsequent recombination with H on the catalyst significantly reduces the O and OH densities in the plasma, as shown in Appendix A3, Figure A3.1 (c) and (d). This reduces the rates for H_2O formation in the gas phase and even causes net destruction of H_2O in the plasma.

To summarize, despite the clearly different pathways for H_2O formation for the different catalysts (i.e., Rh and Cu, vs Ag), the total net rates of H_2O production do not vary much between the different cases, and are also very similar to the plasma-only case. Indeed,

the H_2O formation is largely determined by the production of O radicals, which can either form H_2O in the plasma by abstracting H from H-containing species (e.g. CH_4) (in case of Rh and Cu), or adsorb and react with H on the catalyst surface (in case of Ag). Whether or not the latter is favored depends on the supply of H to the surface and the activation barriers for hydrogenation to OH* and H_2O on the catalyst.

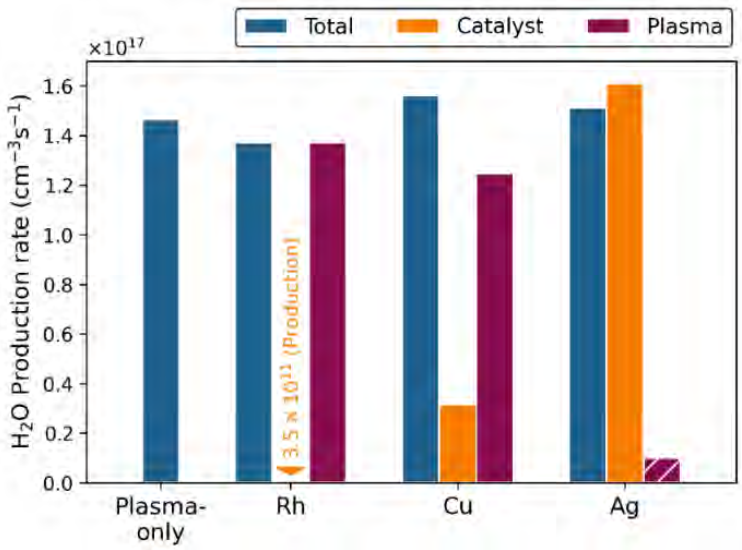

Figure 5.7. Net rates of H_2O production at steady state (t = 10^6 s) for plasma without catalyst, or combined with a Rh, Cu or Ag catalyst. Distinction is made between the total rate, the rate on the catalyst surface and the rate in the plasma. Hatched bars indicate net destruction instead of production. The net (production) rate on the Rh surface is indicated by its numerical value, as it is many orders of magnitude lower compared to the other rates in the figure. Calculated for a 1:1 CH_4/CO_2 feed mixture using a total pressure of 1 bar and a temperature of 500 K.

5.3.2.6 CH_3OH production at steady state

While typically not the main product, CH_3OH is a highly desired value-added chemical that could be formed in one step through plasma-catalytic DRM.[22] Therefore, it is especially interesting to investigate how CH_3OH formation is affected by the presence of the transition metal catalysts. Figure 5.8 displays the net production rates of CH_3OH for plasma without catalyst, as well as with Rh, Cu or Ag. Note that the vertical axis is now

logarithmically scaled, to better visualize the trends. As can be seen, most of the CH_3OH is formed in the plasma, rather than on the catalyst surface. The highest CH_3OH formation rates on the surface are observed for Cu, followed by Ag. This is in agreement with the surface kinetics simulations performed with the CatMAP code, which predict Cu and Ag as the best catalysts for CH_3OH formation on the catalyst surface (cf. Figure 5.1 (a)).

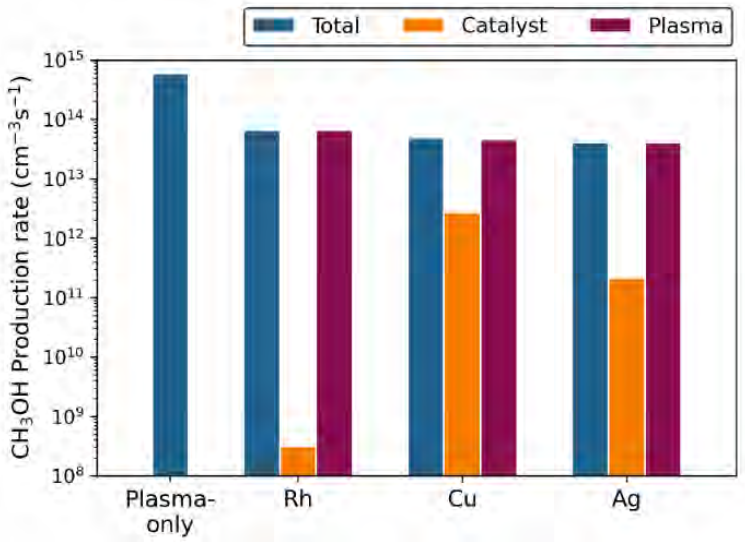

Figure 5.8. Net rates of CH_3OH production at steady state ($t = 10^6$ s) for plasma without catalyst, or combined with a Rh, Cu or Ag catalyst. Distinction is made between the total rate, the rate on the catalyst surface and the rate in the plasma. Note that the rates are logarithmically scaled. Calculated for a 1:1 CH_4/CO_2 feed mixture using a total pressure of 1 bar and a temperature of 500 K.

However, while weakly binding catalysts, like Cu and Ag, produce more CH_3OH on the catalyst, this is not reflected in the total CH_3OH production. The latter is mainly determined by the CH_3OH production in the plasma (cf. the logarithmic scale to accommodate the large difference in magnitudes). As such, the highest total net CH_3OH formation is observed for the plasma without catalyst. Plasma combined with Rh, Cu or Ag, on the other hand, produces significantly less CH_3OH compared to the plasma-only

case. The total net rate of CH_3OH production for the three catalysts is similar, although it is slightly reduced when going from Rh to Cu to Ag.

The formation of CH_3OH in the plasma-only case mainly occurs through pathways in which O radicals oxidize alkyl radicals (CH_3, C_2H_5) to form CH_2O, which subsequently reacts to form CH_2OH radicals. This species then recombines with H radicals into CH_3OH. Additionally, CH_3OH is also formed through recombination of CH_3 and OH, although to a lesser extent. When the plasma is in contact with a catalyst, however, radical adsorption and recombination on the surface causes a drop in the gas-phase densities of these species, as displayed in Figure A3.1 (a), (b) and (d) in Appendix A3 for H, CH_3 and OH radicals, respectively. The reduction of these radical densities thus lowers the CH_3OH formation rate in the plasma. As discussed above, (very) small amounts of CH_3OH can be formed on the catalyst surfaces. For Rh and Cu, this occurs through adsorption of CH_2O, followed by hydrogenation to CH_3O* and subsequently, CH_3OH. On Ag, CHO is adsorbed from the gas phase and hydrogenated to CH_2O*, followed by the same reaction steps as on Rh and Cu. Hence, while adsorbed radicals can also react on the surface to form CH_3OH, this process is not favored and instead these species rather recombine to form either CH_4, CO_2, H_2O or H_2.

In summary, while CH_3OH formation does take place at the catalyst surfaces, the rate is much lower than the CH_3OH formation rate in the plasma, and the latter is significantly reduced compared to the plasma-only case, due to adsorption of radicals at the catalyst surface, making them not available anymore for the plasma reactions producing CH_3OH.

Hence, our calculations suggest that transition metals would be detrimental for CH_3OH formation by plasma-catalytic DRM, at the conditions under study, because they mainly recombine radicals to undesired molecules (e.g., CH_4, CO_2 and H_2O). As such, these radicals are no longer available to form the desired end-compounds, like CH_3OH. Additionally, the plasma itself is already so reactive, due to the presence of the many

radicals, so that the CH_3OH formation rate is largely dominated by plasma reactions. However, at the same time, the high plasma reactivity also hinders the selective production of the targeted compounds. Thus, careful analysis is needed on how the role of the catalyst can be promoted in plasma catalysis, but also on how the adsorbed radicals can be directed into desired, rather than unwanted products.

5.4 Conclusion

We studied the hydrogenation of plasma-produced CO as a mechanism for CH_3OH production in plasma-catalytic DRM, using the descriptor-based microkinetic model CatMAP. We find that in the presence of syngas (CO/H_2) combined with CH_3, H and O radicals the formation of CH_3OH on transition metals catalysts occurs predominantly through hydrogenation of CO by H radicals. This pathway is favored over recombination of absorbed CH_3*, O* and H* radicals to CH_3OH, and thermal catalytic CO hydrogenation. The presence of H radicals enhances the hydrogenation of CO, especially on weakly binding metals. This is because these catalysts have more difficulty with breaking the H-H bond in H_2. However, if H radicals are present in the gas phase, the H-H bond has already been broken by the plasma. In this way, H_2 dissociation on the catalyst surface can be circumvented. As such, the rates of CH_3OH formation via the abovementioned mechanism are the highest on weakly binding metals, like Cu and Ag.

However, we also find that the rate of CH_3OH formation is negligible compared to the production rates of CH_4, CO_2, H_2O and H_2. Indeed, these molecules can easily be formed on the catalyst by recombination of adsorbed CH_3*, H* and O* radicals, as well as CO*. Moreover, these processes direct CO* and H*, required for CH_3OH production, into other molecules, meaning that these plasma species will not be used efficiently. Additionally, we developed a coupled plasma-surface model that allows us to study how the chemistry of the plasma and catalyst affect each other, which leads to similar conclusions.

Using our coupled plasma-surface model, we compared four different cases, namely plasma without catalyst or combined with Rh, Cu and Ag. The model reveals that the presence of transition metal catalysts in plasma-catalytic DRM, for typical DBD conditions at which the radical chemistry dominates, has mainly negative, rather than positive effects. Indeed, we find that Ag has a detrimental effect on the net CO_2 destruction rate, as the catalyst efficiently recombines CO* and O* on the surface, and thus partly counteracts the dissociation of CO_2 in the plasma. The net destruction of CH_4, on the other hand, is especially reduced by Cu, due to facile recombination of CH_3* and H* on this catalyst. Additionally, the presence of Ag also slightly reduces the net CH_4 destruction rate. On one hand, this is caused by the formation of CH_4 on the surface. On the other hand, many O and OH radicals are adsorbed and subsequently converted to CO_2 and H_2O on the Ag surface, making these radicals unavailable for CH_4 destruction reactions in the gas-phase.

Our model also predicts that CO production mainly happens in the plasma, either directly from CO_2 or via various oxidation and dehydrogenation reactions. As such, the net production of CO is negatively affected by Ag, due to CO oxidation on the surface to form again CO_2. The production of H_2 is improved by Rh, due to adsorption of H radicals on hydrogen reservoir sites and facile subsequent recombination to H_2, while other catalytic sites are poisoned. However, on Cu and Ag, the adsorbed H* is primarily used for the production of CH_4 and H_2O, respectively, resulting in a significant drop of the net H_2 production. On the other hand, H_2O, as undesired side-product, is produced at similar net rates for all cases, yet the pathways through which the H_2O is formed depend on the catalyst. For Ag, most H_2O is formed on the catalyst, while for Cu and Rh, the H_2O production mainly happens in the plasma.

Most importantly, the CH_3OH production seems to be negatively affected by the presence of transition metal catalysts for the conditions under study. While some net

CH_3OH formation occurs on the surfaces of all catalysts, the total CH_3OH production is mostly determined by plasma reactions. However, radicals that are lost from the plasma due to adsorption on the catalyst are primarily directed towards the formation of other products (i.e., CO_2, CH_4, CO, H_2 or H_2O) rather than CH_3OH. Consequently, the CH_3OH formation rate drops due to the loss of radicals from the plasma. This highlights the need to identify conditions and catalysts that can selectively produce CH_3OH from radicals and other plasma-produced species, to fully use the potential of plasma catalysis and avoid unwanted side-effects.

Hence, our model illustrates that transition metal catalysts are detrimental to the radical chemistry for plasma-catalytic DRM, due to efficient back-reactions of the radicals on the catalyst. This indicates that plasma-catalyst synergy in DRM is unlikely to happen under conditions for which radicals are the dominant species for plasma catalysis, i.e., at typical (low temperature) DBD conditions. As such, plasma-catalytic DRM may benefit more from higher reaction temperatures, at which vibrational excitation can enhance the surface reactions (see section 1.7.3). This is in agreement with the work by Kim *et al.*[70] (discussed in section 1.7.1.1), who showed that vibrationally excited CH_4 could enhance plasma-catalytic DRM at temperatures in excess of 600 K, and also with the work of Sheng *et al.*,[90,220] demonstrating the key role of vibrationally excited CO_2 and CH_4 molecules in promoting plasma-catalytic DRM. While high temperatures can also lead to increased V-T relaxation and thus less vibrationally excited species, this effect is only relevant for warm plasmas (typically with T > 3000 K), for which in-plasma catalysis is not possible.[221] Moreover, as we discussed in section 5.3.1.3, limiting the adsorption of CH_3 and O radicals, which can otherwise recombine with H* and CO*, back into CH_4 and CO_2, respectively, can also be beneficial for plasma-catalytic DRM. The formation of CH_3 and O may be limited if high conversion to CO and H_2 (which are typically the main products of plasma-catalytic DRM) can be achieved. This can subsequently also enable plasma-catalytic hydrogenation of CO and CO_2, in tandem with DRM, which would open up

additional reaction pathways, like the HCOO* and RWGS pathways. Apart from the adsorption of H radicals, these pathways can also benefit from vibrational excitation of the CO_2 bending mode (for sufficiently high temperatures), as discussed in section 1.7.5.3. Of course, the presence of a transition metal catalyst in a DBD can also modify the discharge characteristics (as discussed in section 1.6), which may (partly) counter the negative chemical interactions, but this requires further investigation.

Chapter 6.

How plasma reaction conditions affect the optimal catalyst: A microkinetic study of plasma-catalytic CO_2 splitting

The results presented in this chapter are published in:

Loenders, B.; Michiels, R.; Bogaerts, A. How Plasma Reaction Conditions Affect the Optimal Catalyst: A Microkinetic Study of Plasma-Catalytic CO_2 Splitting. *Plasma Chem. Plasma Process.* **2025**, *45*, 1849–1899. DOI: 10.1007/s11090-025-10599-4

6.1 Introduction

The goal of plasma catalysis is to achieve synergy between the plasma and catalyst, meaning that the conversion or product yield of plasma catalysis surpasses the sum of the conversions or yields of the plasma and catalyst alone.[24] Yet, the conditions that lead to plasma-catalyst synergy are usually not known *a priori,* and experimentally they have to be identified in practice through trial-and-error. Indeed, a thorough and fundamental understanding of the mechanisms responsible for synergy is still lacking, due to the highly complex nature of plasma catalysis,[39,222] as we discussed previously, in section 1.5. Moreover, there are a variety of both physical and chemical effects that may lead to plasma-catalyst synergy, as we discussed in sections 1.6 and 1.7, respectively. Finally, as demonstrated in the previous chapter, plasma-catalyst synergy is not always reached.

Hence, more fundamental research is needed to identify and understand the underlying mechanisms responsible for synergy.[27,39,222] This fundamental research can be performed by carefully designed experiments, which should ideally be executed using standardized experiment setups, or by computational models, which can be developed to focus on specific interactions. This way, plasma-catalyst interactions can be isolated as much as possible to study their individual effects and identify whether they contribute to plasma-catalyst synergy, and if so, under what circumstances.[39] Therefore, various studies have employed microkinetic modeling to investigate how reactive plasma species can affect the catalyst surface chemistry for, e.g., NH_3 synthesis,[72,81,82] N_2 oxidation,[30,83,223] non-oxidative coupling of CH_4,[84,105] CO_2 hydrogenation,[85] partial oxidation of CH_4[86] (as demonstrated in Chapter 3) and DRM (as presented in Chapter 5).[39]

These studies find that weakening reactant bonds through vibrational excitation or breaking these bonds to form radicals can enhance the product turnover frequencies,[30,72,81–86] and may even result in product concentrations that exceed the

thermodynamic equilibrium.[30,72,83] However, only moderately to weakly binding catalysts, on which bond dissociation is rate limiting, can benefit from this effect.[72,81,84] In general, the effect of plasma radicals is found to be much stronger compared to vibrational excitation,[82,84–86] especially on the most weakly binding catalysts, as these have more difficulty with dissociating the reactants.[30,83,84] However, strongly binding catalysts may also benefit from the presence of plasma radicals, if the barrier for E-R reactions between the impinging radicals and surface adsorbates is sufficiently low.[82] Yet, the presence of a catalyst in the plasma is not necessarily beneficial, as the catalyst can also lower the conversion by promoting backreactions.[39,105]

Hence, there is a need for studies that identify which combinations of reaction conditions and catalysts can achieve plasma-catalyst synergy, and which cause detrimental effects on the conversion. In this chapter, we therefore investigate how parameters like temperature, pressure and flow rate affect plasma-catalytic CO_2 splitting (R1.1) and we compare these effects for different transition metal catalysts, as well as for glass, representing the wall surface for the plasma and afterglow. For this purpose, we developed a coupled plasma-surface microkinetic model, similar to the model presented in previous chapter, but significantly improved, as it now includes a Boltzmann solver for calculating the rates of electron impact reactions in the gas (plasma) phase. This way, we simulate the formation of plasma species in the gas phase, their subsequent interaction with the catalyst surface and the resulting change in the species densities of the gas molecules.

The system under study consists of a transition metal (Ag, Cu, Pd or Rh) or glass wall surface that surrounds the afterglow of a non-thermal plasma at low pressure (0.05-10 mbar), i.e., similar to a low-pressure RF plasma, as studied in refs. 83 and 30. This way, we avoid the complexity of DBD plasmas, which are highly inhomogeneous in both space and time and sensitive to various physical effects. Due to the absence of such physical

interactions in our system, we can focus purely on the chemical effects. Moreover, our interest goes specifically towards the effect of plasma-produced radicals and ground-state molecules, as previous microkinetic models[82,84–86] (including our work presented in Chapter 3) indicate that the effect of vibrationally excited molecules remains limited, when radicals are present. Note that the plasma drives CO_2 splitting into CO and O_2, and the role of the catalyst is to maximize the recombination of O atoms from the plasma into O_2 and avoid their recombination with CO back to CO_2, which would reduce the overall CO_2 conversion. Hence, the role of the plasma is to activate CO_2 to form these O atoms, as well as CO. Indeed, the thermodynamic equilibrium of the CO_2 splitting reaction is strongly shifted towards CO_2 at the conditions under study (0.5-10 mbar and 500-1100 K), for which the maximum O_2 and CO mole fractions at the thermodynamic equilibrium reach only 1×10^{-5} and 2×10^{-5}, respectively (calculated using the algorithm described in ref. 15). Therefore, the system exceeds the thermodynamic equilibrium limit for almost all cases investigated.

We do not only consider L-H reactions between adsorbed radicals, but also E-R reactions involving impinging radicals, by postulating that a correlation exists between the activation barrier of the E-R reaction and the binding strength of the involved adsorbate to the surface. Indeed, our results suggest that E-R reactions should be important in order to explain the high recombination coefficients for O atoms on transition metal surfaces that are reported in literature (typically between 0.01-0.5).[224] Moreover, our results illustrate that the optimal catalyst for plasma-catalytic CO_2 splitting is strongly dependent on the reaction conditions, especially temperature and flow rate. As such there is no “single best catalyst”, and a single catalyst material can have beneficial or detrimental effects depending on reaction conditions.

6.2 Methods

We developed a coupled plasma-surface kinetics model, that simultaneously calculates the reaction kinetics in the gas phase (plasma and afterglow) and on the surface of the catalyst or reactor wall. This model is a significant improvement compared to our previous model (discussed in Chapter 5, section 5.2.2),[39] as it now includes a solver for the Boltzmann equation for electrons.[141,142] Thus, it enables the calculation of the electron impact rate coefficients at a specified electric field or power density. The code of our model is developed in-house using Python. For the solver of the electron Boltzmann equation, we use BOLOS, an open-source Python library developed by Luque *et al.*[142] The model simulates the reaction kinetics inside a cylindrical reactor by treating it as multiple sequential continuous stirred tank reactor (CSTR) units, that are placed in series to approach a plug flow reactor (PFR).

This approach is less computationally expensive compared to one-dimensional (or higher-dimensional) fluid models, thus allowing our model to consider a larger chemistry set. Nevertheless, this method also has some drawbacks compared to true more-dimensional models, namely that processes such as back-mixing and axial diffusion are not considered. Moreover, diffusion to the walls is treated only implicitly in our model (see section 6.2.6), as the model does not include a radial dimension. Additionally, the changes in species densities and coverages along the length of the reactor are not continuous, but occur in (albeit small) discrete steps, i.e., corresponding to the individual CSTR units. Consequently, the surface coverages in a CSTR unit will only start to evolve to steady state after the previous CSTR unit has reached steady state, as most of the radicals will not pass the previous CSTR otherwise. Hence, the separate CSTR units do not evolve to a steady state at a similar rate, but rather one-by-one. This could lead to sharp changes in surface coverages and gas species densities between consecutive

CSTR's, if one is at steady state, while the other is not yet. For this reason, we compare our results only when all CSTR units have reached steady state.

6.2.1 Reactor geometry and conditions

To study the effect of plasma-created radicals on the catalytic surface pathways, we simulate a non-thermal plasma at low pressure (0.5-10 mbar), representative of, e.g., a low-pressure RF plasma torch.[30] Although low-pressure plasmas are not so suitable for real plasma catalysis applications, as the extra cost of pumps makes it less interesting for industrial applications, these conditions allow for relatively high radical fractions in the plasma and its afterglow, while avoiding the high computational cost and complexity associated with simulating dielectric barrier discharges (DBD's), due to their inhomogeneous nature. Additionally, we can focus on the fundamental chemical interactions between the radicals and the catalyst, without the added complexity of physical interactions (e.g., alteration of the discharge behavior) that would occur in DBD's.[24,37,39]

The reactor is modelled as an initial "plasma" CSTR unit, in which power is applied, followed by multiple other CSTR units in series, i.e., representing the afterglow, thus approximating a PFR. The reactor is assumed cylindrical in shape, with a radius $R_{reactor}$ = 2.0 cm. The plasma region is modelled as a single CSTR, with a volume of 62.8 cm^3 (corresponding to a length of 5.0 cm), in which a power density of 1.59×10^6 W/m^3 is applied (corresponding to a plasma power of 100 W). The initial, "plasma" unit is followed by a region with a length of 50.0 cm in which no power is applied, to simulate the afterglow and the rest of the reactor. This zone is divided into 100 CSTR units, each with a length of 0.5 cm and a volume of 6.3 cm^3. The surface reactions and rate coefficients in the plasma region are representative for a borosilicate glass surface (see section 6.2.4), while in the rest of the reactor, either borosilicate glass or transition metal (Ag, Cu, Pd or Rh) surfaces are used.

Unless specified otherwise, the simulations are performed at a pressure of 5 mbar, and with a flow rate of 100 sccm (USA definition)[225] for pure CO_2 feed gas. One of the parameters varied is the gas (and wall) temperature, which are considered to be equal. This assumption is justified considering that heat loss of the reactor to the environment (i.e., cooling of the reactor wall) can be avoided by isolating the reactor or by placing it inside an oven. Varying the temperature between simulations allows us to study its effect on the plasma-catalyst interaction. We use temperatures in the range of 500-1100 K, considering that some heating by the plasma will be inevitable in experiments, while additional heating can be applied (e.g., by placing the reactor in an oven or preheating the feed). The typical simulation time required for the initial plasma CSTR unit is around 1-1.5 hour, while the series of subsequent afterglow CSTR units solves in a couple of hours for the 100 units combined. Hence, the simulation time for the complete reactor is in the order of hours.

A schematic overview of the model is presented in Figure 6.1. The model describes the reactor as a series of CSTR units (Figure 6.1 (a)) with an initial 'plasma' CSTR followed by 100 smaller CSTR units describing the afterglow. The walls of the plasma CSTR are made of glass, representing a low-pressure RF plasma, while the afterglow CSTRs are surrounded by a glass or catalytic metal surface. Inside a single CSTR unit, the balance of the species densities and coverages (see Chapter 2, section 2.3) is described by multiple processes (Figure 6.1 (b)), namely the flow of gas entering and leaving the CSTR, as well as the reactions in the bulk gas and on the surface. The different types of surface reactions included in the model are shown in Figure 6.1 (c). We also provide an overview of the different reactor and operating parameters in Table 6.1.

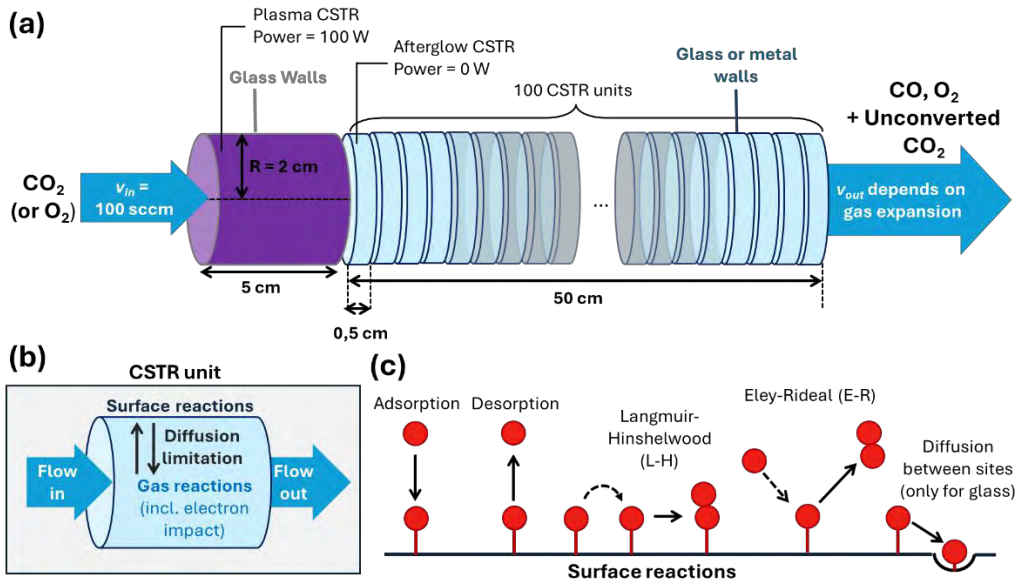

Figure 6.1. Schematic representation of the model: (a) the reactor is modelled as a series of CSTR units, (b) processes governing the species densities and coverages in a single CSTR unit, (c) the types of surface reactions in the model.

Note that at the low-pressure conditions studied in this work, the (recombination) reactions in the gas phase are slow compared to the reactions on the surface. Hence, in the afterglow where E/N = 0, the change in density of the main gas species (CO_2, CO, O and O_2) can mostly be described based on the surface chemistry alone. However, this is not the case for the plasma stage, where electron impact reactions are important, while recombination of O+O and O+CO is still determined by the surface reactions on the glass wall. Hence, coupling the gas and surface chemistry is certainly necessary for the plasma stage. Coupling between the plasma and the post-plasma stages in the model is effectively achieved by using the output of the plasma-stage as input for the afterglow. This does also mean that if the densities in the plasma can be obtained from experiments, estimation, etc. they could in principle also be used as input for the post-plasma sections instead of the calculated values. Of course, it is still valuable to model the gas phase densities in the plasma rather than having to estimate them, especially

when comparing different reaction conditions (temperature, pressure and flow rate) that affect the species densities in the plasma.

Table 6.1. List of the various reactor and operating parameters used in the model.

Reactor radius	2 cm
Length of plasma zone	5 cm
Length of afterglow zone	50 cm
Surface/Volume ratio	100 m^{-1}
Surface site density	10^{20} m^{-2}
Sites per volume	10^{22} m^{-3}
Plasma power	100 W
Power density	1.59×10^6 W/m³
Flow rate feed	100 sccm (50-200 sccm)
Pressure	5 mbar (0.5-10 mbar)
Gas temperature	500-1100 K Constant during simulation
Wall temperature	= Gas temperature

6.2.2 Species balance equations

As discussed in section 6.2.1, the reactor is divided into multiple consecutive units, which are modelled using a CSTR approach. This means that perfect mixing is assumed within each individual unit, hence the species densities and coverages in a single unit are uniform. However, we do consider mass transfer limitations due to diffusion to the reactor wall (see section 6.2.6). Each CSTR unit has a flow of gas entering and leaving the reactor (see Figure 6.1 (b)). The gas composition of the outflow equals the composition in the CSTR volume, while the mass flow rate and composition of the feed entering the

CSTR are equal to the outflow of the previous unit. Thus, the time-evolution of the species densities in a single CSTR is described using Eq. 2.1, which is discussed in section 2.3. Note that the rates of the surface reactions in Eq. 2.1 need to be multiplied by the average volumetric site density n_{sites}, i.e., the number of surface sites relative to the gas volume. The value of n_{sites} is set to 10^{22} sites m^{-3}, which corresponds to the surface over volume ratio of the tubular reactor ($2/R = 10^2$ m^{-1}) multiplied by a typical surface site density of 10^{20} sites m^{-2}.[215,217] The time-evolution of the fractional coverages (θ_s) of the surface species is described by Eq. 2.2.

The flow of the species entering and leaving the CSTR unit (f_{in} and f_{out} in Eq. 2.1, respectively) are calculated according to Eq. 5.1 and Eq. 5.2 in section 5.2.2, respectively. Here V_{CSTR} is the volume of the CSTR unit. For the first CSTR unit, $n_{s,in}$ and v_{in}, are the species densities and flow rate of the feed. For the subsequent CSTR units, $n_{s,in}$ and v_{in} match $n_{s,out}$ and v_{out} of the previous unit. Also note that the species number density in the outflow equals that in the CSTR unit, i.e., $n_s = n_{s,out}$. For each CSTR unit, the volumetric flow rate leaving the reactor, v_{out} in Eq. 5.2, is calculated as the sum of volumetric flow rate entering the reactor and the change in volume due to reactions, according to Eq. 5.3 (see section 5.2.2).

The reaction rates are calculated using Eq. 2.5 and Eq. 2.6 (see section 2.4), for gas and surface reactions, respectively. A list of the reactions with their corresponding rate coefficients is included in Appendix A4, Table A4.1. Additionally, in sections 6.2.3-6.2.6 we provide more information on the calculation of the rate coefficients for electron impact and surface reactions, respectively. The gas phase reactions, including electron impact processes, are taken from the CO_2 part of the chemistry set presented by Slaets *et al*.[226,227] for CO_2/CH_4 plasma, to which we added reactions for $CO(A^3P)$, $O(^1D)$, CO_3^- and CO_4^-. Likewise, the list of electron impact cross sections is also taken from Slaets *et al*.[226,227]

6.2.3 Solving the Boltzmann equation for electrons

To calculate the electron energy distribution function (EEDF) and the rate coefficients of the electron impact reactions, our model requires a solver for the electron Boltzmann equation. For this purpose, we use BOLOS,[142] an open-source Python library containing a Boltzmann solver, that is based on the work of Hagelaar and Pitchford.[141] This algorithm calculates the EEDF, the rate coefficients for electron impact reactions and the electron mobilities μ_e, for a specified gas mixture and reduced electric field *E/N* (i.e., ratio of electric field over gas number density, an important parameter to characterize the plasma conditions). Additionally, BOLOS requires the cross sections of the relevant electron impact processes. A list of these processes with the sources of the corresponding cross sections can be found in Table A4.2 in Appendix A4.

The reduced electric field *E/N* is related to the power density *P* in the plasma via Eq. 2.8 (see section 2.5). Hence, the model determines the value of the *E/N* that corresponds to a specified power density, by combining Eq. 2.8 with BOLOS, which relates μ_e to the *E/N*. During the numerical integration (i.e., as the code solves the system of differential equations provided by Eq. 2.1 and Eq. 2.2, the reaction rates of electron impact processes are calculated with BOLOS by solving the EEDF for the corresponding *E/N*. The *E/N* itself is calculated from Eq. 2.8 during the integration, while μ_e is kept constant. Hence, the *E/N* and corresponding electron impact reaction rates (from BOLOS) are continuously (re)calculated during the integration, while μ_e remains constant. This leads to a (small) drift of the power density *P* during the integration. After each integration period, the value of μ_e is therefore updated by iterating over Eq. 2.8 and BOLOS to acquire the values of *E/N* and μ_e that correspond to the actual set power density. The model then calculates the length of the next timestep over which is integrated, based on the deviation of the power density during the previous step, so that the deviation of the set power density remains below 1% during each integration period.

6.2.4 Rate coefficients for glass surfaces

The reactor walls in our model are either catalytic transition metals or non-catalytic borosilicate glass surfaces. While the reactions on the former are described using TST combined with DFT data, the reactions on the glass surface are treated with empirically determined expressions that are commonly used in literature, a more in dept discussion of which can be found in refs. [215], [217] and [228]. We consider the following reaction types in our model:

- Physisorption
- Chemisorption
- Desorption (of chemisorbed and physisorbed species)
- Surface diffusion from a physisorption to a chemisorption site
- Langmuir-Hinshelwood (L-H) reactions between a physisorbed and a chemisorbed species
- Eley-Rideal (E-R) reactions between a gas species and a chemisorbed or physisorbed species

Note that some recent works consider additional reactions, such as the formation of metastable chemisorption sites,[229] or O_3 formation on the surface.[230] However, we here limit ourselves to the most general and commonly used reactions for glass surfaces, because we aim to keep the chemistry on the glass surface relatively simple, as the focus of this work is on the catalysts.

As is apparent from the glass surface reactions listed above, two types of surface sites are considered, namely physisorption ($*^p$) and chemisorption ($*^c$) sites. Note that the distribution between chemisorption and physisorption sites varies widely in literature for different SiO_2-based surfaces (e.g., values between 2×10^{-3} and 0.25 are mentioned in ref. [215] for the fraction of chemisorption sites). In our model, we use a chemisorption site

fraction equal to 2×10^{-3} in accordance with ref. [215], and the remaining site fraction (0.998) consists of physisorption sites. Similarly, a large range of values are reported in literature for the recombination coefficient *γ*, i.e., the fraction of radicals that recombines at the wall surface upon collision with the wall.[224] For example, Paul *et al*.[224] reviewed *γ* values for O atom recombination on various materials and reported values between 10^{-5} and 10^{-2} for glass-based surfaces around room temperature (r.t.). Possible explanations for this large deviation include the possible role of impurities as chemisorption sites, or chemisorption sites being created as a result of ion-bombardment on the surface.[215,224]

In this regard, Booth *et al*.[28] found that for an O_2 DC glow discharge inside a pyrex tube the γ values decreased with lowering the pressure until 0.75 Torr (1.0 mbar), below which γ increased with further lowering the pressure. The authors found that below approximately 0.3 Torr, ions and fast neutrals incident on the wall have sufficient energy to clean or modify the surface, and hence attributed this effect to surface bombardment by energetic species.[28] This was further expanded upon by, Afonso *et al.*,[229] who developed a kinetic model that includes surface modification by energetic plasma species to form metastable chemisorption sites. The authors compared their modeling results to experiments to derive the values of certain surface parameters used in their model, and were also able to reproduce the experimental results.[229] However, we did not include such effect in our own model, as surface modification by the plasma is outside the scope of this study. Nevertheless, it is worth noting that surface bombardment and modification by energetic plasma species, leading to, e.g., different site types, may also occur on transition metal catalysts.[38]

Note that glass is included in our model as a non-catalytic reference surface, to compare to the catalytic transition metals. Hence, only highly reactive radicals can adsorb (physisorption or chemisorption) on glass, while dissociative adsorption of stable molecules is not considered for this surface, because of its non-catalytic nature.

In the following subsections we describe the different surface reactions and their corresponding rate coefficients. A list of the surface reactions that are included in our model for the glass surface can be found in Appendix A4, Table A4.3.

Physisorption and chemisorption

The rate coefficients for adsorption of radicals on both physisorption and chemisorption sites are described by the flux to the surface (i.e., by Eq. 5.6 from section 5.2.2.4), because radicals have 100% adsorption probability, and they are the only species considered for adsorption on the glass surface. The surface sites area, A_s, is set equal to 10^{-20} m^2, i.e., the inverse of the surface site density.

Desorption

The rate coefficient for desorption from both physisorption and chemisorption sites is given by Eq. 5.7 (see section 5.2.2.4).[28,215,228] We use a typical value of 10^{15} s^{-1} for v_d, i.e., the vibrational frequency for the movement of the adsorbate perpendicular to the surface.[215] We use a value of 0.302 eV as the activation energy for desorption, E_d, of physisorbed O, based on ref. 28, and 2.90 eV for desorption of chemisorbed O, based on ref. [217]. Note that in ref. 28, a lower value of 10^{13} s^{-1} was used for v_d, as this led to better agreement with their experimental values for the recombination coefficient γ. However, in that study the recombination of O atoms through L-H reactions was not considered in the surface chemistry. We found that using the typical value of 10^{15} s^{-1} for v_d and including L-H reactions in the chemistry set, results in γ values that are comparable to those measured in ref. 28, which was also mentioned by Viegas *et al*.[230] Hence, this justifies combining the empirically determined value for E_d from ref. 28, with the more generally used value of 10^{15} s^{-1} for v_d. However, it must be noted that Ibach *et al*.[231] pointed out that v_d should be temperature dependent. More recently, Viegas *et al.*[230] developed a model for surface recombination on a Pyrex surface in contact with an O_2 DC glow

discharge and compared their results to experimental measurements. The authors observed an exponential decrease of v_d with the wall temperature (for T_{wall} between 253 and 323 K), which they mentioned could also be explained by a variation of the activation barrier for desorption with coverage, i.e., since the coverage rises as the temperature drops.[230] Moreover, Ibach *et al*.[231] find a quadratic rather than an exponential dependency of v_d on temperature for adsorbates that have lost all three translational degrees of freedom (as is the case for activated surface diffusion), yet also predict that v_d is proportional to $\exp(\theta_{ads}/(1-\theta_{ads}))$ when lateral interactions between adsorbates are present.[231] Hence, it is more likely that the exponential decrease of v_d at lower wall temperature observed experimentally by Viegas *et al.*[230] is the result from higher coverages and lateral interactions between the adsorbates. Nevertheless, we choose to treat v_d as a constant in our model for simplicity, and due to the uncertainties associated with the temperature dependency.

Eley-Rideal reactions

The rate coefficients of E-R reactions are described by Eq. 5.8 (see section 5.2.2.4). This expression takes a similar form as that for adsorption (Eq. 5.6), but contains an exponential factor with the activation energy E_r of the reactions, i.e., representing the probability of the reaction occurring upon collision with an adsorbate.[215,217,228] As an approximation we use the same activation energy for E-R reactions involving chemisorbed or physisorbed species as the adsorbate. For recombination of two O atoms via E-R, we use E_r = 0.13 eV, which was experimentally determined for O_2 plasma in a Pyrex tube.[28] We also include an E-R reaction between gaseous CO and an adsorbed O atom, for which we use an activation energy of 0.10 eV, as experimentally determined in ref. [232] for a borosilicate glass-based heatshield coating.

Surface diffusion

The surface diffusion coefficient of a physisorbed species to a chemisorption site is calculated according to Eq. 5.9 (see section 5.2.2.4).[215,217] In which v_D is the frequency for vibration of the adsorbate in the direction parallel to the surface and E_D is the activation barrier for diffusion to an adjacent site. We use a typical value of 10^{13} s^{-1} for v_D,[214,215,217] while E_D is approximated by $E_d/2$.[214,215]

Langmuir-Hinshelwood reactions

The rate coefficient for recombination between a physisorbed and a chemisorbed O atom is described by Eq. 5.10 (see section 5.2.2.4). This expression takes a similar form as the rate coefficient for surface diffusion (Eq. 5.9), but with an additional exponential factor containing the activation energy for recombination.[215] Hence, this extra exponential factor considers the probability that recombination occurs upon diffusion of a physisorbed O atom to an occupied O chemisorption site. The values of E_r for L-H in Eq. 5.10 and E-R in Eq. 5.8 are considered to be the same.[215]

Note that some models[228–230] also consider L-H recombination between physisorbed atoms, which is assumed to occur with E_r = 0.0 eV, i.e. so that the reaction barrier becomes E_D. The assumption that the recombination between physisorbed atoms is barrierless (except for the barrier associated with diffusion) is based on the fact that physisorbed atoms only weakly interact with the surface. This reaction was studied computationally by Marinov *et al.*[228] who investigated the effect of varying its activation barrier, and compared the contribution of the reaction to the total recombination coefficient γ. Even at $E_r = 0.0$ *eV* the contribution of L-H between two physisorbed O atoms only became important below a wall temperature of 300 K, as the coverage of physisorbed atoms rises at lower temperatures.[228] Since our simulations are performed at relatively high temperatures of 500-1100 K, we do not consider this reaction here as

it is not expected to be important, and because of the uncertainties associated with its recombination barrier.

Lastly, we would like to mention that there is a lot of variation in the values of the different parameters governing the glass surface kinetics reported in literature.[215] We have therefore investigated how varying these parameters affects our results for a single set of conditions, and we discuss these results in Appendix A4, section A4.4.

6.2.5 Rate coefficients for transition metals

We consider four reaction types on the transition metal surfaces: adsorption, desorption, L-H reactions and E-R reactions. For the former three reaction types, the corresponding rate coefficients are derived from DFT energies calculated within our research group by R. Michiels. For more details regarding the DFT calculations we refer to the original publication.[233]

Because the DFT energies are calculated for pure metal (111) surface facets, without lattice defects or impurities, we consider only one site type on which species can adsorb. This is in contrast with the glass surface used in our model, for which both weak (i.e., physisorption) and strong (i.e., chemisorption) binding sites are considered, in accordance with the empirical models described in literature.[215,217] As only one site type is considered for transition metals, surface diffusion (i.e., between different site types) is not included in the model for the metal surfaces. Table 6.2 lists the reactions for which the activation barriers are calculated using DFT. Note that dissociative adsorption is considered as a two-step reaction, i.e., adsorption of O_2 or CO_2, followed by dissociation of the molecule on the surface.

Table 6.2. Reactions on the transition metal surfaces for which the activation barriers are calculated using DFT.

Adsorption	**Desorption**
$O + * \rightarrow O*$	$O* \rightarrow O + *$
$O_2 + * \rightarrow O_2*$	$O_2* \rightarrow O_2 + *$
$CO + * \rightarrow CO*$	$CO* \rightarrow CO + *$
$CO_2 + * \rightarrow CO_2*$	$CO_2* \rightarrow CO_2 + *$
Recombination	**Dissociation**
$CO* + O* \rightarrow CO_2* + *$	$CO_2* + * \rightarrow CO* + O*$
$O* + O* \rightarrow O_2* + *$	$O_2* + * \rightarrow O* + O*$

The rate coefficients for E-R reactions are not calculated via DFT, as the transition state found along the minimum energy path does not include any dynamical effects, which are considered to be important for E-R reactions.[234] Instead, we use recombination coefficients from literature to estimate the values of the associated rate coefficients, which we postulate are correlated to the O binding energy determined with DFT. In the following sections we describe how the rate coefficients for the different reaction types, and their corresponding activation and reaction energies, are calculated.

Adsorption and desorption

The rate coefficients for molecular adsorption are not described by TST, but instead by the Hertz-Knudsen equation multiplied by an enthalpy-based sticking coefficient, i.e., by Eq. 2.12 (see section 2.6).

However, we consider molecular adsorption to occur without enthalpy barrier. Since adsorption is exothermic, $\Delta H^{\ddagger\circ}$ thus equals zero so that the sticking coefficient becomes one and Eq. 2.12 becomes equal to the Hertz-Knudsen equation. The rate coefficient for

the corresponding reverse reaction, i.e., desorption, is calculated through detailed balancing with Eq. 2.13, as discussed in section 2.6. The equilibrium constant K_{eq} used for detailed balancing is calculated according to Eq. 2.14, as also discussed in section 2.6. The standard reaction Gibbs free energy, enthalpy and entropy of adsorption used in Eq. 2.14 are obtained from our DFT calculations (see below, and Table A4.4 in Appendix A4).

Langmuir-Hinshelwood reactions

The rate coefficients for reactions happening on transition metal surfaces are calculated using TST, i.e., Eq. 2.9 (see section 2.6). Using $\Delta G^{\ddagger\circ}$, $\Delta H^{\ddagger\circ}$ and $\Delta S^{\ddagger\circ}$ obtained from our DFT calculations (see below, and Table A4.4 in Appendix A4). Note again that in our model the wall temperature, $T_{wall,}$ is set equal to that of the gas, T_{gas}. The entropy of the surface species (adsorbates and transition states) is calculated using the harmonic oscillator approximation (Eq. 2.18 in section 2.6). Hence, all degrees of freedom in the surface species are treated as vibrational modes.

Reaction and activation energies

The Gibbs free activation and reaction energies are calculated according to Eq. 2.10 and Eq. 2.15, respectively, as discussed in section 2.6. The standard Gibbs free energies $G°_s$ of the individual species are calculated from the corrected species enthalpies $H_s°(T)$ and entropies $S_s°(T)$:

$$G_s^o = H_s°(T) - TS_s°(T) \qquad \text{Eq. 6.1}$$

For surface species, $H_s°(T)$ and $S_s°(T)$ are calculated from our DFT data, using the harmonic oscillator approximation (see section 2.6), i.e., using Eq. 2.16 and Eq. 2.18 for $H_s°(T)$ and $S_s°(T)$, respectively. The harmonic oscillator approximation requires the vibrational frequencies of the surface species, which are acquired from our DFT calculations and are listed in Appendix A4, Table A4.4, together with the species enthalpies.

For gas species, the enthalpy correction and entropy are calculated using the ideal gas approach, which is also described in section 2.6 (Eq. 2.19 to Eq. 2.24). The values of the parameters used in the ideal gas approximation are listed in Table A4.5 in Appendix A4 along with their corresponding sources.

Simplified expression for the rate equations

To simplify the expressions of the reaction rate coefficients used for transition metal surfaces in the model, while also including the correction on the enthalpy and entropy, we calculate the values of the rate coefficients for the temperature range 100-1200 K and fit these to a modified Arrhenius expression:

$$k = a \times T^{b} \exp\left(\frac{c}{T}\right) \qquad \text{Eq. 6.2}$$

In which a, b and c are fitting parameters. Eq. 6.2 is frequently used in literature to describe rate coefficients that have a more complex dependence on temperature than described by the simple Arrhenius equation (i.e., for which b = 0).[235,236] In this way, the loss or gain of translational and rotational degrees of freedom is better captured in the rate coefficient. See Eq. 2.20 - Eq. 2.22: when the entropy is filled into Eq. 2.9, the dependency on temperature moves outside the exponent. Moreover, in this way, the dependency on temperature in the factor $k_b T/h$ in the TST rate coefficient (see Eq. 2.9) is also included in the Arrhenius equation. Note that we only use this approach for the rate coefficients of adsorption, desorption, and L-H reactions on the transition metal surfaces. The rate coefficients acquired by fitting to Eq. 6.2 can be found in Appendix A4, Table A4.6. By fitting our calculated rate coefficients to Eq. 6.2, we acquire a simple expression that incorporates the effect of the temperature-dependent entropy and correction on the enthalpy, without the requirement to recalculate these thermodynamic quantities at each temperature. This facilitates the use of the rate coefficients calculated in this work by other researchers, especially for simulations in which the temperature is not constant.

Langmuir-Rideal reactions

There is still much uncertainty on the kinetics of various E-R reactions and their importance in plasma catalysis.[116] In kinetic models for plasma catalysis, the rate coefficients for E-R reactions are often calculated using collision theory combined with (estimated) sticking coefficients,[105,110,111,237–239] or by TST in which the enthalpy barrier is varied or assumed zero.[82,86] Using a microkinetic model for NH_3 synthesis, Engelmann *et al.*[82] illustrated that if E-R reactions would occur without enthalpy barrier, this should result in high reaction rates for all transition metal catalysts used, yielding a flat volcano curve when viewed on a logarithmic scale, in agreement with experimental data.[107] On the other hand, various experimental studies show that for O atom recombination on transition metal surfaces, most metals have indeed a high catalytic activity, although there exist clear (yet less extreme) differences between the different metals.[124,125,224,240,241] Additionally, as we will explain in the Results and Discussion section, our simulations show that the high recombination coefficients for O atoms on transition metals cannot be explained based on L-H reactions alone. Instead, we propose that at relatively low temperatures (≤ 600 K), recombination of O atoms on metal surfaces occurs through an E-R reaction between an impinging and a pre-adsorbed O atom. Only at higher temperatures, O_2 formation via L-H between adsorbed O atoms becomes relevant. Assuming that the rate coefficients for adsorption and E-R can be described by Eq. 5.6 and Eq. 5.8, respectively, the activation energy for E-R can be calculated from the recombination coefficient γ (i.e., by solving the species balance equations at steady state):

$$E_r = -RTln\left(\frac{\gamma}{2-\gamma}\right) \qquad \text{Eq. 6.3}$$

May *et al.*[125] reported values of 0.22 and 0.063 for the recombination coefficient of O at r.t. on Ag and Cu surfaces, respectively. Using Eq. 6.3, the corresponding values for the

activation energy are calculated as 5.2 and 8.5 kJ/mol (0.054 and 0.088 eV) for Ag and Cu, respectively.

To the best of our knowledge, there are no experimentally measured γ values for O recombination on Pd or Rh surfaces available in literature. Nevertheless, experimental studies[124,125,240,241] show that the activity of a metal for O atom recombination can be linked to its chemical character (i.e., noble metal or not). Hence, γ is typically the highest on Ag (~10^{-1} at r.t.), followed by Cu (~10^{-1}-10^{-2} at r.t.) and non-noble metals, like Fe (~10^{-2} at r.t.) and Ni (~10^{-2} at r.t.). Note that exceptions to this rule do exist, most notably for Au, which has a relatively low γ (~10^{-2}-10^{-3} at r.t.).[125,240,241] The observed trend appears to be the result of the formation of either bulk metal oxide or a thin oxidation layer on the surface of most metals.[124,125,240,241] Consequently, more stable metal oxides result in a lower catalytic activity (i.e., a lower γ value) of the corresponding metal. Indeed, if O binds less strongly to the metal, it will be easier to remove the O atom from the metal surface (or oxide layer) during the E-R reaction with an impinging radical from the gas phase.[241]

Hence, we assume a linear correlation between the O binding strength of the metal and its barrier for O recombination via E-R. Using the activation energies that we calculated for Ag and Cu, and the O atom adsorption energies calculated from DFT, we then estimate the values of the activation energies on Pd and Rh to be 7.6 and 9.6 kJ/mol (0.079 and 0.10 eV), respectively. At 300 K this corresponds to γ values of 0.09 and 0.04, respectively, which is in the same range as typical values for other transition metals reported in literature.[224] Note that we do not consider the formation of a bulk oxide in our simulations, however the formation of a layer of adsorbed O atoms can be seen as an initial step in oxidation of the metal.

In some of our simulations we also study the potential influences of the E-R reactions between an adsorbed CO* molecule and an incoming O atom (see section 6.3.2). Since

this requires the O atom to attack the C atom from CO* (which is directed towards the surface), the reaction must be highly entropically constrained. Therefore, we describe the rate coefficient for this reaction using TST (i.e., Eq. 2.9) and assume an entropy barrier equal to the loss of (translational) entropy of the impinging O atom. The enthalpic part of the activation barrier is assigned a value between 0 and 0.2 eV to illustrate its effect on the reaction.

6.2.6 Correction for diffusion to the wall

To consider that the loss of species at the reactor wall may be limited by their rate of diffusion to the wall, we apply a correction factor to the rates of adsorption and E-R reactions. The mean lifetime (inverse loss frequency) of a species due to wall recombination can be expressed as the sum of the mean time required for diffusion to the wall and that for reaction at the wall:[29,242]

$$\tau = \tau_{diff} + \tau_{net\ loss} \qquad \text{Eq. 6.4}$$

The mean time for diffusion to the wall τ_{diff} is calculated from the characteristic diffusion length of the reactor Λ_0 and the diffusion coefficient D:[29,242]

$$\tau_{diff} = \frac{\Lambda_0^2}{D} = \left(\frac{R_{reactor}}{2.405}\right)^2 \frac{1}{D} \qquad \text{Eq. 6.5}$$

In which $\Lambda_0 = R_{reactor}/2.405$, with $R_{reactor}$ the radius of the reactor. The diffusion coefficient of the gas species is estimated using:[29]

$$D = \frac{1}{3} l v_{th} = \frac{1}{3}\left(\frac{k_b T_{gas}}{\sqrt{2} \cdot p\pi d^2}\right)\sqrt{\frac{8 k_b T_{gas}}{\pi m}} \qquad \text{Eq. 6.6}$$

With l the mean free path, v_{th} the thermal velocity of the gas species, p the pressure, m the mass of the species and d the kinetic diameter of the molecule. The values of d for

CO_2, CO and O_2 are equal to 330 ppm, 376 ppm and 346 ppm, respectively.[243] The value for O atoms is assumed similar to that of O_2.[29]

The mean lifetime $\tau_{net\ loss}$ of gas species near the surface before consumption due to surface reactions (i.e., adsorption, E-R) is typically described by the recombination coefficient γ and the thermal velocity of the gas species. However, in our model, the recombination of gas species at the surface is not considered as a single reaction step. Instead, we use a detailed reaction mechanism in which the different surface reactions (adsorption, desorption, L-H, E-R, etc.) are included as separate reactions steps. Moreover, as long as steady state is not reached, atoms and molecules can accumulate on the surface. Hence, we calculate the mean lifetime of a gas species before it is consumed by surface reactions (when the reaction is not diffusion-limited) as:

$$\tau_{net\ loss} = \frac{n_s}{n_{sites} \sum_{i,surf} (c_{s,i}^L - c_{s,i}^R) r_i} \qquad \text{Eq. 6.7}$$

In which the numerator equals the species density, and the denominator is the source term for the net loss of the gas species *s* due to surface reactions (e.g., adsorption, E-R). We use the same notation for the overall lifetime (= inverse loss frequency), but here we also include a correction factor f_s to take the effect of diffusion into account. If the loss of a gas species at the wall is limited by diffusion, the density of this species near the wall will decrease, limiting the consumption rate at the wall surface.

By combining Eq. 6.4 and Eq. 6.7 we get:

$$\frac{n_s}{n_{sites} \sum_{i,surf} (f_s c_{s,i}^L - c_{s,i}^R) r_i} = \tau_{diff} + \frac{n_s}{n_{sites} \sum_{i,surf} (c_{s,i}^L - c_{s,i}^R) r_i} \qquad \text{Eq. 6.8}$$

Which can be rearranged into:

$$f_s = \left(\left(\frac{\tau_{diff}}{n_s} n_{sites} + \frac{1}{\sum_{i,surf} (c_{s,i}^L - c_{s,i}^R) r_i} \right)^{-1} + \sum_{i,surf} c_{s,i}^R r_i \right) \cdot \left(\sum_{i,surf} c_{s,i}^L r_i \right)^{-1} \qquad \text{Eq. 6.9}$$

The rate equations for adsorption and E-R reactions are then multiplied by the correction factor f_s of the gaseous reactant. In this way the overall loss of a gas species due to surface reactions cannot exceed the rate for diffusion of the species to the wall. Note that f_s is set to 1 if $\sum_{i,surf}(c_{s,i}^L - c_{s,i}^R) r_i$ is negative, i.e., if the gas species is net produced at the wall surface. Hence, f_s can have values between 0 and 1. As such, f_s becomes 1 if the effect of diffusion is negligible and the loss of species at the surface is not diffusion-limited. If recombination of species at the surface is fast, the rate becomes limited by diffusion to the surface and the value of f_s drops.

We find that for the conditions under study, $f_s \approx 1.0$ for loss of O atoms on the glass surface. Hence, due to the low γ values for glass, the loss of O atoms to the surface is not limited by diffusion and the O atom density can be considered uniform along the radial direction. This agrees with the work by Viegas *et al*.[244] for low-pressure DC O_2 glow discharges at 1-10 Torr (1.3-13.3 mbar), who found that the O(^{3}P) density along the radial direction has an almost flat profile, based on 1D fluid dynamics simulations. Nevertheless, we find that the effect of diffusion to the wall is relevant for the transition metals at most of the conditions under study. Indeed, transition metals typically have higher γ values for O atom recombination than glass.[224] Hence, the fast loss of O atoms to the transition metal surfaces causes the rate to become limited by diffusion to the walls. For the conditions under study, we find that the f_s values vary between 9.9×10^{-2} and 5.1×10^{-3} for Ag, 1.9×10^{-1} and 1.3×10^{-2} for Cu, 1.0 and 7.6×10^{-3} for Pd, and 1.0 and 1.5×10^{-2} for Rh.

6.3 Results and Discussion

The purpose of this study is to investigate how different transition metal catalysts affect the recombination of radicals in plasma catalysis, which can both positively or negatively impact the conversion, depending on the catalyst and conditions, like temperature, pressure, and flow rate. Our combined plasma-surface microkinetic model simulates the reaction kinetics, both in the gas phase and at the catalyst surface, for a low-pressure CO_2 discharge in a cylindrical reactor with either a glass wall or a transition metal wall that functions as the catalyst. The reactor is modelled as an initial discharge region (with glass wall) with a length of 5.0 cm, followed by a 50.0 cm long afterglow region, with a glass or transition metal wall surface.

Regarding the plasma-catalyst interactions, we focus exclusively on the exchange of radicals and ground-state molecules between the plasma and the surface. We do not consider the effect of vibrationally excited species on the surface chemistry, because of the following reasons. Multiple microkinetic models have already studied the effect of vibrational excitation on various plasma-catalytic reactions, including NH_3 synthesis,[72,81,82] CH_4 non-oxidative coupling,[84,105] CH_4 partial oxidation,[86] CO_2 hydrogenation[85] and N_2 oxidation.[30,83] In these studies, the Fridman-Macheret α model[20] is used to describe the drop in activation barrier for surface reactions involving vibrationally excited species. However, the Fridman-Macheret model is originally intended for gas phase reactions,[20] and is a rough approximation. Moreover, the aforementioned microkinetic models[30,82–86] predict that the vibrationally excited species have only a minor effect compared to plasma-produced radicals, while both result in more facile reactant activation. It should however be noted that a recent study[245] shows that the Fridman-Macheret model significantly underestimates the effect of vibrational activation on dissociative adsorption, when compared to values calculated using molecular dynamics simulations, which also illustrates the inaccuracy of the Fridman-

Macheret model. Additionally, based on the Polanyi-rules,[246] dissociative adsorption of CO_2 is expected to have high efficiencies for vibrational activation, due to its late transition state.[247] Yet, as we aim to disentangle the contributions of radicals and vibrationally excited species on the surface chemistry, and want to avoid the use of the inaccurate Fridman-Macheret model, we here focus exclusively on the effect of radicals and ground-state molecules.

Note that the model and the different components of the chemistry set could unfortunately not yet be validated with experiments, since, to the best of our knowledge, only very limited diagnostic experimental data is available for low pressure CO_2 RF discharges, on which we based our model. Moreover, the focus of this work is primarily on the interaction of the plasma species (CO, O_2 and O) with the transition metal catalysts, for which model validation against plasma diagnostic data would not be sufficient. Indeed, validation should be carried out by in-situ catalyst surface diagnostics, for which unfortunately also no experimental data could be found in literature. Hence, the reader should be aware that our model has no predictive character, but it can hopefully still provide qualitative trends, and useful insights in the underlying mechanisms, and in suitable catalysts and operating conditions. For validation of the model and chemistry set in possible future work, we suggest simulating a low-pressure CO_2 DC glow discharge, for which more detailed experimental diagnostics are available, such as the work by Morillo-Candas *et al.*[29] However, we believe it would be beneficial to first optimize and validate the chemistry for recombination of O atoms on the glass surface, by comparing simulation results of low-pressure O_2 DC glow discharges, against diagnostic experimental data, which is readily available in literature.[28,248]

In the following subsections, we will first illustrate the importance of E-R reactions for O atom recombination into O_2, as well as the potential effect of E-R reactions for CO oxidation back into CO_2. Next, we will discuss the reaction mechanisms and kinetics of

CO_2 splitting in a low-pressure plasma and its afterglow exposed to a non-catalytic (glass) or catalytic (Ag) surface, for a single set of representative conditions. This serves as a basis for the following sections in which we will discuss how different types of transition metals can both positively and negatively affect plasma-catalytic CO_2 splitting. Moreover, we will show that whether a catalyst has a positive effect on the conversion, does not only depend on the type of transition metal, but also on conditions, like temperature, pressure and flow rate. Hence, the same type of catalyst can differently affect CO_2 conversion, depending on the reaction conditions. We will end with a discussion on the optimal catalyst properties, i.e., which transition metal catalyst would be beneficial for (post-)plasma catalysis, and at which reaction conditions. We base this discussion on material characteristics of the catalysts (weakly or strongly binding) and the insights obtained by our model.

6.3.1 Importance of Eley-Rideal reactions for O atom recombination

To illustrate the importance of E-R reactions for O atom recombination, we compare the evolution of the calculated O atom fractions for chemistry sets with and without E-R reactions, for a pure O_2 plasma. Note that our model does not distinguish between “true” E-R reactions and “hot atom” reactions. In the former, a gas species collides and reacts directly with an adsorbate, while in the latter, a gas species hits the surface but does not fully adsorb and retains some of its energy, allowing it to move over the surface and react with a fully adsorbed species. Hence, in the framework of our model, E-R reactions refer to all reactions in which a gas species does not occupy a surface site prior to reaction with an adsorbate.

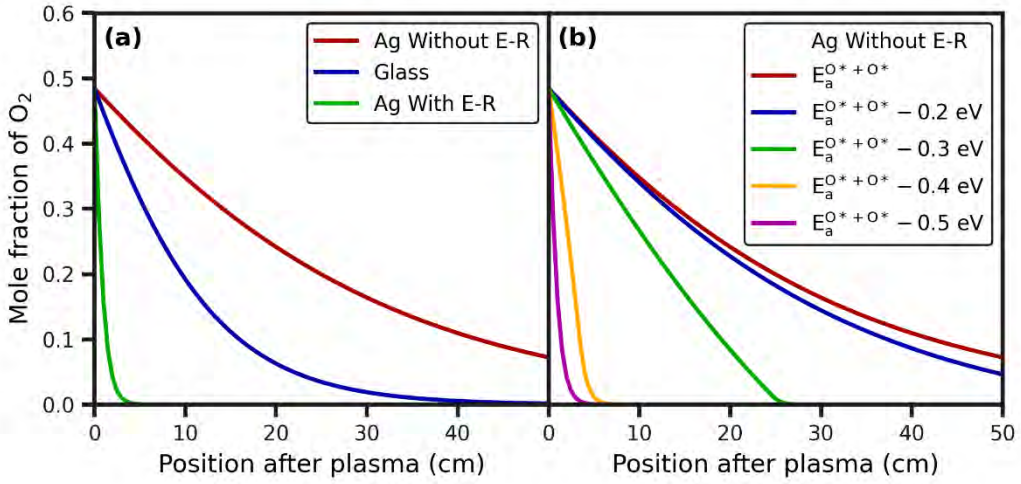

Figure 6.2. Effect of the surface chemistry on the spatial evolution of the mole fraction of O atoms in the afterglow of an O_2 plasma. In (a) three surface chemistry sets are considered: an Ag surface, both with and without E-R reactions, as well as a glass surface. In (b) the effect of lowering the activation barrier of $O^* + O^* \rightarrow O_2^* + *$ is illustrated, for the Ag surface without E-R reactions. Conditions: T = 500 K, p = 5 mbar and flow rate = 100 sccm.

Figure 6.2 (a) illustrates the importance of E-R reactions for O recombination, by comparing the evolution of the mole fraction of O atoms in the afterglow of an O_2 plasma for different surface chemistry sets. We consider three cases, namely an Ag surface with and without the inclusion of E-R reactions, as well as a glass surface. Note that we do not show the results for other transition metals, as their curves largely overlap with those of Ag. Right after the plasma, i.e., the start of the afterglow, the O atom mole fraction is slightly below 0.5, with the remaining component being mainly O_2 molecules (slightly above 0.5), hence representing a dissociation degree of 32%. As can be seen in Figure 6.2, the Ag chemistry set with E-R reactions results in the fastest drop in the fraction of O atoms, while Ag without E-R reactions shows the slowest consumption of O atoms, even compared to a glass surface. However, from literature it is clear that most transition metals, especially Ag, are highly active for O atom recombination, while glass surfaces are typically relatively inert for O atom recombination.[224] Indeed, most literature studies

report γ values above 0.1 for Ag, while γ values for glass surfaces are typically between 10^{-2}-10^{-5}.[224] As such, the fraction of O atoms in the afterglow should decline much faster for an Ag wall compared to a glass wall. Hence, E-R reactions should play an important role in O atom recombination on transition metal surfaces. Indeed, we find that when only L-H reactions are considered for O atom recombination on the Ag surface, this reaction occurs very slowly (Figure 6.2 (a)), which is not in agreement with the high recombination coefficients that are observed experimentally for this metal. We therefore suggest that a second type of surface reactions, namely E-R reactions, plays an important role in the recombination of O atoms on transition metal surfaces at 500 K.

While not shown in Figure 6.2 (a), the O* coverages on the Ag surface are very high: above 0.99 when only L-H reactions are accounted for, and between 0.77 and 0.89 when E-R reactions are also considered. Hence the rate of the L-H reaction, which has a second order dependency on the O* coverage, is not limited by the availability of adsorbed O*, but instead by the low rate coefficient (8.3×10^4 s^{-1}) of this reaction at 500 K. Note that the O* coverages are slightly lower if O atom recombination via E-R is included in the chemistry set, as this reaction removes part of the adsorbed O*.

If we calculate the γ values for the conditions used in Figure 6.2 (a), we find values of 0.44, 0.13, 0.16 and 0.10 for Ag, Cu, Pd and Rh, respectively, when E-R reactions are accounted for. When E-R are not included, however, the γ values are unrealistically low, with values in the order of magnitude of 10^{-7}-10^{-8} for Ag, 10^{-16} for Cu, 10^{-15}-10^{-16} for Pd, and 10^{-19} for Rh. For reference, the recombination coefficient γ of the glass surface in Figure 6.2 is equal to 2.0×10^{-4}.

The effect of E-R reactions is two-fold: on one hand it enables more facile production of O_2 compared to when only L-H reactions are considered, on the other hand it aids in the removal of adsorbed O* atoms from the surface. The latter results in lower O* coverages and thus less O* poisoning, which in turn improves adsorption of new O atoms from the

gas phase, due to the higher availability of free surface sites. Note that as temperature rises, the contribution of L-H reactions may increase, as traversing the activation barrier becomes easier. While not shown in Figure 6.2 (a), we find that as the temperature rises above 600-650 K, O atom recombination on transition metals via L-H reactions alone becomes sufficiently fast to reach the high recombination coefficients (i.e., 0.01-0.5) reported in literature for O_2 plasma.

Nevertheless, we must note that the high experimental recombination coefficients for O atoms on transition metals may also be caused by other effects than those of E-R reactions. For example, our model does not consider the destabilization of adsorbed O* atoms due to lateral adsorbate-adsorbate interactions, which may lower the barrier for O* atom recombination to O_2.[249–251] We therefore investigated how lowering the barrier for O* atom recombination via L-H affects our results for the Ag surface without E-R reactions. These results are displayed in Figure 6.2 (b), which shows that lowering the activation barrier by 0.2 eV has only a small effect on the O_2 mole fraction in the afterglow, while reducing the activation barrier by 0.3 eV gives O_2 mole fractions that are similar to the glass surface in Figure 6.2 (a). When the barrier is further decreased by 0.4 and 0.5 eV (Figure 6.2 (b)), the O_2 mole fraction becomes comparable to the case where E-R reactions are considered Figure 6.2 (a). Hence, if lateral adsorbate-adsorbate interactions between O* are sufficiently strong, so that the activation barrier for L-H reactions is lowered by approximately 0.4 eV, this effect may also explain the facile O* atom recombination on transition metal surfaces.

Lastly, a second effect that is not considered by our model is the formation of bulk oxides. Indeed, high surface coverages of O* atoms, i.e., similar to a thin oxide film, can initiate the formation of bulk metal oxides.[252] Moreover, oxide formation is often reported in literature for metal surfaces exposed to a flux of O atoms.[124,125,240,241] Hence, the kinetics for adsorption and recombination of O atoms on bulk metal oxides, which do not

necessarily occur via the same reaction mechanisms as on the corresponding transition metals, is likely to be important as well. This is, however, outside the scope of this work.

6.3.2 Effect of E-R reactions in plasma-catalytic CO_2 splitting

As discussed in section 6.3.1, we hypothesize that E-R reactions play an important role in the recombination of O atoms on transition metal surfaces. As O atoms are present in large amounts in CO_2 plasmas, surface recombination of O atoms into O_2 can also play an important role in plasma-catalytic CO_2 splitting. Importantly, if a catalyst surface can selectively recombine O atoms into O_2, thus avoiding that they recombine with CO back into CO_2, this could improve the overall CO_2 conversion.

To illustrate how E-R reactions can affect the recombination of O atoms in CO_2 splitting, we simulated a CO_2 plasma afterglow in contact with a Rh surface, again using different surface chemistry sets. These results are presented in Figure 6.3, which shows the mole fractions of O atoms (a), O_2 (b), and CO (c) as function of position in the afterglow. Right after the plasma, i.e., the start of the afterglow, the O, O_2 and CO mole fractions are about 0.022, 0.0035 and 0.028, respectively, while the majority of the mixture is CO_2 with a mole fraction of 0.95. This corresponds to a dissociation degree of 2.9% for CO_2, and particle densities of 1.6×10^{15}, 2.3×10^{14}, 2.0×10^{15} and 6.9×10^{16} cm^{-3} for O, O_2, CO and CO_2, respectively. These mole fractions are calculated with our model for T = 500 K, p = 5 mbar, a mass flow rate of 100 sccm, and a plasma power of 100 W (corresponding to an SEI of 13.9 eV/molecule). For comparison, Rond *et al.*[253] investigated CO_2 splitting in a RF plasma torch for pressures ranging from 1 to 2 mbar, mass flow rates between 100 and 300 sccm, plasma powers between 80 and 160 W, and SEI's between 6.1 and 18.2 eV/molecule. These authors report CO_2 dissociation degrees between 2% and 13%, and CO and O densities ranging from 2×10^{14} to 8×10^{14} cm^{-3}.[253] Note that the dissociation degree is naturally larger at lower pressures. Hence, our calculated mole fractions are indeed representative for a low-pressure CO_2 RF plasma.

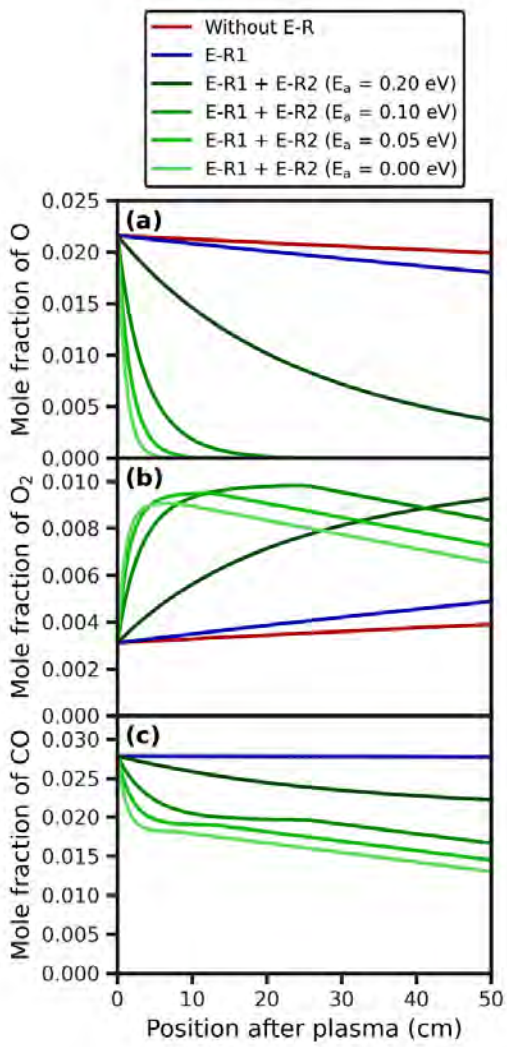

Figure 6.3. Effect of E-R reactions on the spatial evolution of the mole fractions of O atoms (a), O_2 molecules (b), and CO molecules (c) for a CO_2 plasma afterglow in contact with a Rh surface. Two E-R reactions are considered: $O + O^* \rightarrow O_2 + *$ (E-R1) and $O + CO^* \rightarrow CO_2 + *$ (E-R2). The base chemistry set, without E-R reactions (red line), is expanded with E-R1 (blue line), or both E-R1 and E-R2 (green lines). The activation enthalpy (E_a) of E-R2 is varied from 0.00 to 0.20 eV (light to dark green). Conditions: T = 500 K, p = 5 mbar and flow rate = 100 sccm.

The red curves in Figure 6.3 represent the results for a chemistry set in which only adsorption, desorption and L-H reactions are possible on the surface. For the blue curves,

an additional (E-R) reaction is included, namely O + O* → O_2 + *, to which we refer as E-R1. As can be seen in Figure 6.3 (a), the possibility for O atoms to recombine into O_2 via E-R1 results in a slight drop of the O mole fraction, yet the recombination of O atoms on the Rh surface remains quite slow. Indeed, the O mole fraction near the outlet is still about 83% of the value in the plasma for the blue curve. The slight drop in the O mole fraction is accompanied by a small rise in the mole fraction of O_2; see Figure 6.3 (b), red and blue curves.

The reason that O recombination is slow on Rh for a CO_2 plasma, even if E-R1 is accounted for, is due to the strong CO binding on this transition metal. As E-R1 results in the facile removal of O* from the surface, it lowers the O* coverage and thus enhances the fraction of free sites. Yet, on Rh these free sites are rapidly occupied by CO* molecules, as these bind strongly to the surface. This consequently leads to CO* poisoning of the surface, which keeps the catalyst activity low. Note that this is mainly a problem for strong binding catalysts at relatively low temperature (500 K), as CO desorption will improve at higher temperatures (see section 6.3.4 for the effect of temperature for different transition metals).

This effect raises the question whether adsorbed CO* molecules can also efficiently react with incoming O atoms via an E-R reaction, as this would significantly improve the activity of strong binding catalysts. Nevertheless, to the best of our knowledge, there are no rate coefficients available for this reaction on transition metal surfaces. Yet, we can expect that the E-R reaction of O with adsorbed CO* is more difficult than with O*, as the former requires the O atom to attack the C of CO*, which is directed to the surface and thus shielded by the rest of the CO* molecule.

To illustrate the potential effect of the reaction O + CO* → CO_2 + *, we include it in the simulations for Figure 6.3 (green curves), in which this reaction is labeled as E-R2. As discussed in the subsection on Eley-Rideal reactions in section 6.2.5, we set the entropy

barrier of this reaction equal to the loss of the translational entropy of the incoming O atom, due to the high constraints associated with attacking the C of CO*. The enthalpy of activation is varied from 0.00 to 0.20 eV (corresponding to the light to dark green curves, respectively). In this way, we illustrate the potential effect of E-R2 on the O and O_2 fractions, depending on how facile the reaction can occur.

As shown in Figure 6.3 (a), the recombination of O atoms improves when E-R2 is allowed to occur in addition to E-R1. As is evident from the green curves, a lower activation barrier for E-R2 further enhances the recombination of O atoms on the surface and thus reduces the O fraction in the afterglow. Interestingly, the faster drop of the O atom fraction in Figure 6.3 (a) also corresponds to a faster rise of the O_2 fraction in Figure 6.3 (b). This is caused by the improved removal of CO* molecules from the surface as the barrier for E-R2 drops, and thus the recombination of CO* with O becomes easier. As this reduces the CO* poisoning of the surface, it leads to more free sites on which O atoms can adsorb, which in turn enhances the recombination of O with O* to O_2 (i.e., E-R1). Hence, allowing O atoms to recombine with adsorbed CO* can also improve the recombination between O and O*, by lowering surface poisoning. Nevertheless, the maximum O_2 fraction in Figure 6.3 (b) becomes slightly lower upon lowering the activation energy for E-R2, due to more O atoms recombining with CO*, rather than with O*. This is also visible in Figure 6.3 (c), as the curves that correspond to the lowest barriers for E-R2 result in the lowest CO mole fractions. Note that the red and blue curves in Figure 6.3 (c) overlap, as no CO is consumed on the Rh surface when E-R2 is not considered.

Additionally, the maxima in the O_2 curves (Figure 6.3 (b)) are followed by a consistent drop of the O_2 fraction. This is because thermal-catalytic CO oxidation (i.e., oxidation by O* originating from the dissociative adsorption of O_2), becomes the main surface reaction when O atoms start to get depleted. Indeed, with less remaining plasma-

produced O atoms or other plasma species, thermal catalysis becomes the dominant reaction mechanism. This can also be observed in Figure 6.3 (c), as the CO mole fraction seems to briefly stabilize when the O atoms in the gas drop, followed by a linear decline of the CO mole fraction once the O atoms approach depletion and thermal catalysis becomes the dominant mechanism for CO oxidation. Note, however, that thermal catalytic CO oxidation in Figure 6.3 is only possible due to a small amount of remaining O atoms in the gas phase, which avoids that the Rh surface becomes fully poisoned by O* (from O_2) or CO*. If the O atoms are fully depleted, the Rh surface only becomes active for thermal catalytic CO oxidation at temperatures above 900 K, as we will discuss in section 6.3.4.4.

As CO oxidation produces CO_2, the mole fraction of CO_2 behaves opposite to that of CO, i.e., the CO_2 mole fraction rises as that of CO drops and vice versa, and is therefore not included in Figure 6.3. Since CO_2 is thermodynamically favored over CO and O_2 at the conditions of temperature and pressure under study (500 K, 5 mbar), the Rh surface will catalyze the oxidation of CO to CO_2 which consumes the O_2 formed in the first part of the reactor. This illustrates that the presence of a catalyst material in plasma catalysis (either in- or post-plasma) does not necessarily have a positive effect on the CO_2 conversion, but that the effect of the catalyst can differ, depending on the reaction conditions and the stage of the reaction.

To gain a better understanding of whether a catalyst will have a positive or negative effect on the global reaction, we will study how different transition metal catalysts (Ag, Cu, Pd and Rh) perform relative to each other and a glass surface, for different conditions of temperature, pressure and residence time in the next sections. Note that due to the uncertainty (i.e., lack of a rate coefficient) for the E-R reaction between O and CO* (E-R2), we will exclude this reaction from the chemistry sets of the transition metals in this chapter. This choice is justified, as this reaction is likely difficult because the O atom

would have to attack the C atom of CO*, which is directed towards the surface. Also, it will mainly have an impact on conditions that are sensitive to CO* poisoning, namely for catalysts that bind CO* strongly (i.e., Pd and Rh) at low temperature (500 K). However, we do include the recombination of O atoms through E-R (E-R1) in all subsequent simulations, as we illustrated the importance of this reaction in section 6.3.1.

6.3.3 The mechanism of low-pressure plasma-catalytic CO_2 splitting

In this section, we provide insight into the reaction kinetics of CO_2 splitting in a low-pressure plasma and its afterglow exposed to a non-catalytic (glass) or catalytic (Ag) surface, for a single set of (representative) conditions (namely 1100 K, 5 mbar and 100 sccm). Hence, we first discuss the reaction mechanisms at play, providing a basis for the next sections where we discuss how different reaction parameters (catalyst, temperature, pressure and flow rate) affect the kinetics and thus the product yield.

Figure 6.4 shows the main loss and formation reactions of CO_2 (a), O atoms (b), CO (c) and O_2 (d) in the plasma (first CSTR unit). Destruction of CO_2 happens predominantly via electron impact dissociation into CO and O(^{1}D), and to a lesser extent via dissociative attachment, as well as dissociation upon collision with CO(A^3P). The main mechanism for CO_2 formation (i.e., backreactions) is via an E-R reaction between CO and a chemisorbed O atom (O*) (Figure 6.4 (a)). Likewise, chemisorption is the main loss reaction for O atoms in the plasma, next to electron impact excitation to O(^{1}D) and the E-R reaction with a chemisorbed O* atom to form O_2 (Figure 6.4 (b)). Note, however, that most of the O(^{1}D) formed via electron impact dissociation of CO_2 or excitation of ground-state O, undergoes de-excitation by collisions with CO_2 to again form ground-state O atoms. This is also the main reaction for the formation of ground-state O atoms. Other important O formation reactions are electron detachment from O^- and CO_2 dissociation upon collision with CO(A^3P). The main loss reactions of CO (Figure 6.4 (c)) are the back-reaction to CO_2 via E-R with a chemisorbed O* atom, as well as electron impact excitation to CO(A^3P).

The main formation process of CO is electron impact dissociation of CO_2, followed by dissociative attachment of CO_2, de-excitation of $CO(A^3P)$, as well as, CO_2 dissociation upon collision with $CO(A^3P)$. Lastly, O_2 is formed via E-R between gaseous and chemisorbed O atoms, while a small amount of the formed O_2 is destroyed via electron impact dissociation (Figure 6.4 (d)).

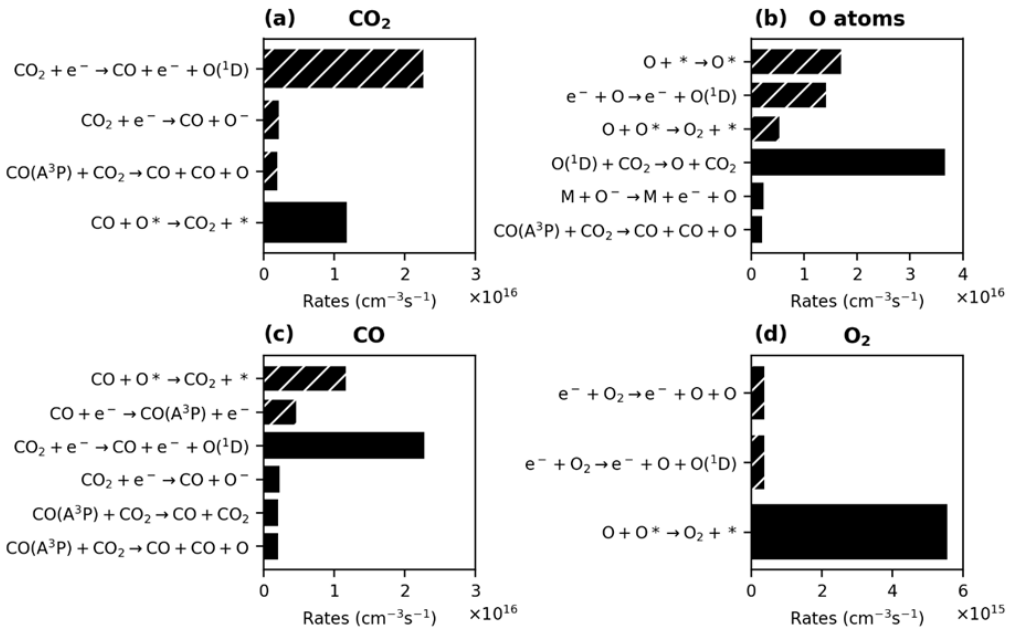

Figure 6.4. The main loss (hatched bars) and formation (full bars) reactions and their corresponding rates for CO_2 (a), O atoms (b), CO (c) , and O_2 (d) in the plasma. Conditions: T = 1100 K, p = 5 mbar and flow rate = 100 sccm.

To summarize, CO_2 dissociates in the plasma, which occurs predominantly via electron impact dissociation to CO and $O(^1D)$. The latter species de-excites to form ground-state O atoms, which adsorb on the chemisorption sites of the glass surface that encloses the plasma. The chemisorbed O* atoms are then either converted back to CO_2 via an E-R reaction with an impinging CO molecule, or they form O_2 via E-R with an impinging O atom.

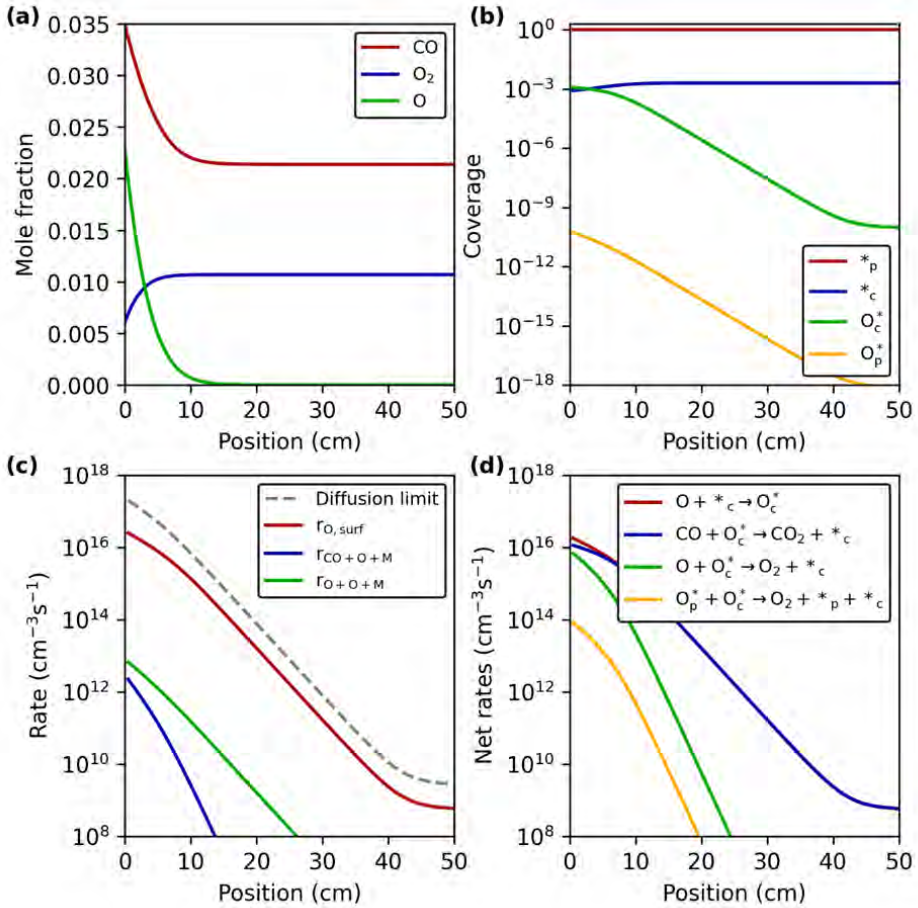

Figure 6.5. Mole fractions (a), fractional surface coverages (b), O atom loss rates (c), and net surface rates (d) of a CO_2 plasma afterglow in contact with a glass surface. $*_p$, $*_c$, $O*_p$ and $O*_c$ in (b) and (d) represent empty surface sites for physisorption/chemisorption, and physisorbed/chemisorbed O atoms, respectively. Conditions: T = 1100 K, p = 5 mbar and flow rate = 100 sccm.

Figure 6.5 presents the calculated mole fractions of gas species (a), fractional surface coverages (b), O atom loss rates (c) and net surface rates (d) for a CO_2 plasma afterglow in contact with a (non-catalytic) glass surface. Figure 6.5 (a) displays the mole fractions of the main gas species except for CO_2, which makes up most of the gas phase. As can be seen, the mole fraction of O drops in the afterglow, as O atoms chemisorb on the glass

surface and recombine with incoming CO molecules or other O atoms to form CO_2 or O_2, respectively. Consequently, the CO fraction drops as well, and the O_2 fraction rises, until the O atoms are depleted.

While the chemisorption sites are initially mostly covered with O* atoms, the depletion of O atoms in the gas phase causes a similar decline in the coverage of chemisorbed O* atoms (O^*_c; Figure 6.5 (b)). Note that the fraction of physisorbed O atoms (O^*_p) is extremely low (10^{-8}-10^{-18}) and the physisorption sites are almost empty. This is due to the high temperature (1100 K) considered here, as desorption of the weakly bound physisorbed O* atoms occurs very easily. However, even at 500 K most of the physisorption sites are still empty.

Figure 6.5 (c) displays the total net loss rate of O atoms on the glass surface (red curve), as well as the maximum rate for diffusion of O atoms from the bulk gas to the reactor walls (dashed grey line). As can be seen, the net loss rate for O atoms on the surface is well below the diffusion limit, hence the loss of O atoms is not limited by diffusion. Note that at the low-pressure conditions used in this work (0.5-10 mbar) the loss of O atoms due to gas reactions is negligible compared to recombination on the surface. To illustrate this, the rates of three-body recombination of O atoms, with either O or CO, to O_2 and CO_2 are also plotted in Figure 6.5 (c).

Finally, the net rates of the main surface reactions are plotted in Figure 6.5 (d). The main surface pathways on the glass surface involve chemisorption of O atoms, followed by their recombination with either incoming CO or O atoms, via E-R reactions. Right after the plasma, when a significant amount of O is still present in the gas phase, the rates of the E-R reactions that form CO_2 and O_2 are similar (although the latter is slightly lower), but the rate of the E-R reaction with O atoms drops faster as a function of position in the afterglow, due to O atom depletion. In contrast, the rate of the L-H reaction between physisorbed and chemisorbed O* atoms is about two orders of magnitude lower

compared to that of the E-R reactions, due to the low coverage (10^{-8}-10^{-18}) of physisorbed O atoms. The rates of E-R reactions with physisorbed O atoms are even lower and therefore not shown in Figure 6.5 (d). The rates of all surface reactions drop as the O atoms in the gas phase become depleted.

In analogy with Figure 6.5, Figure 6.6 illustrates the calculated mole fractions of gas species (a), fractional surface coverages (b), O atom loss rates (c) and net surface rates (d) for a CO_2 plasma afterglow in contact with a (catalytic) Ag surface. The mole fraction of O atoms now drops much more rapidly at the start of the afterglow, as compared to the glass surface (Figure 6.5 (a)), which coincides with a rise of the O_2 fraction; see Figure 6.6 (a). Following the depletion of the O atoms, the fractions of both CO and O_2 decrease slowly when moving along the afterglow, due to thermal catalytic CO oxidation.

The coverages on the Ag surface remain relatively stable throughout the afterglow, although the O* coverage shows a drop near the start of the afterglow due to fast depletion of the O atoms in the gas phase (Figure 6.6 (b)). However, this drop of the coverage remains limited, as adsorbed O* is formed via adsorption and subsequent dissociation of O_2, once O in the gas phase is depleted. Also note that the majority of the surface is empty, which is a consequence of the high temperature and the weakly binding character of Ag. However, the surface coverages for the other, more strongly binding metals considered in this work are clearly higher. For reference, the O* coverages are between 0.39 and 0.98 for Cu, between 0.026 and 0.47 for Pd, and above 0.98 for Rh, when using the same reaction conditions as those in Figure 6.6.

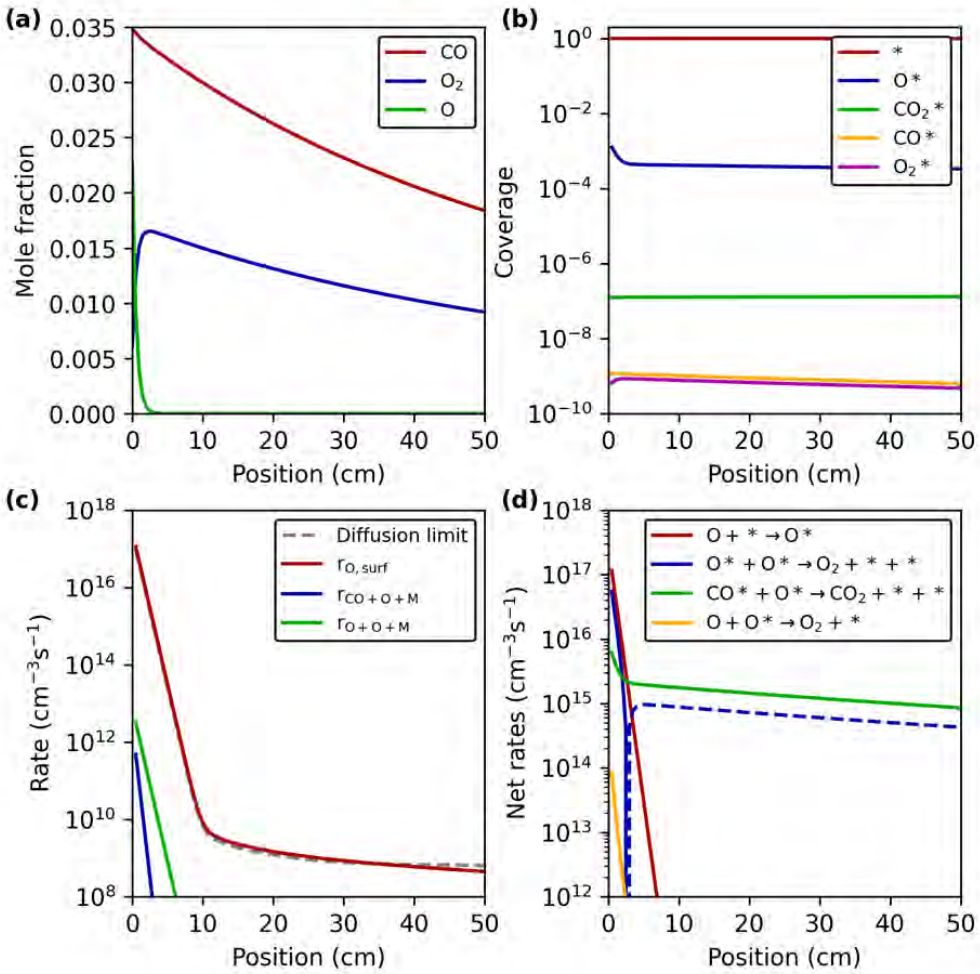

Figure 6.6. Mole fractions (a), fractional surface coverages (b), O atom loss rates (c), and net surface rates (d) of a CO_2 plasma afterglow in contact with an Ag surface. The dashed line in (d) indicates a negative rate. Conditions: T = 1100 K, p = 5 mbar and flow rate = 100 sccm.

As can be seen in Figure 6.6 (c), the net loss rate of O atoms on the surface becomes limited by diffusion in this case, due to the fast recombination of O atoms on the Ag surface, i.e. the red and the dashed grey curves overlap. Also note again that due to the low-pressure conditions O atom recombination in the gas phase is substantially slower compared to on the surface.

Finally, Figure 6.6 (d) shows the net rates of the reactions on the Ag surface. Near the start of the afterglow, when O atoms are still present in the gas phase, the main surface pathway is O atom adsorption and recombination to O_2 via L-H (hence, between adsorbed O*). Recombination between adsorbed O* and CO* into CO_2 is not favored, due to the low CO* coverage ($\approx 10^{-9}$) at 1100 K. However, as the temperature decreases, the contribution of CO_2 formation, relative to O_2 formation will increase. Likewise, the contribution of O_2 formation via E-R (hence, with incoming O atoms) is negligible for Ag at 1100 K, but will be more important for more strongly binding catalysts and lower temperatures; see next sections. Hence, at high temperatures, the rate of the L-H reaction exceeds that of the E-R reactions, despite the lower O* coverages at high temperatures, as the rate coefficient of the L-H reaction rises more strongly with temperature between 500-1100 K relative to that of the E-R reaction. Importantly, following the depletion of the O atoms in the gas phase, the rate of O adsorption drops and O_2* starts dissociating into O* instead. This is indicated by the dashed blue line in Figure 6.6 (d), which represents a negative value for this rate (i.e., the reaction proceeds to the left). The O* formed by dissociation of O_2* subsequently oxidizes adsorbed CO* into CO_2 (green line). To summarize, O atoms adsorb on the Ag surface and recombine via a L-H reaction to form O_2. However, once the O atoms in the gas phase are depleted, thermal catalytic CO oxidation will occur, which again forms CO_2, thereby reducing the overall CO_2 conversion.

Note that the enthalpy correction and entropy of the surface species are calculated using the harmonic oscillator approximation, as discussed in section 6.2.5. To investigate the impact of this assumption, we also simulated the conditions used in Figure 6.6 with the free translator approximation, in which surface species are assumed to retain two translational degrees of freedom (i.e., free translation over the surface along two dimensions). We find that if the free translator approximation is used, the rate of thermal-catalytic CO oxidation rises, due to stronger increase in entropy upon

dissociation of O_2* into O*, which enhances the dissociation rate. This results in a faster drop of the O_2 and CO mole fractions in the plasma, compared to when the harmonic oscillator approximation is used. A detailed discussion of these results is presented in section A4.8 of Appendix A4.

6.3.4 Effect of temperature on plasma-catalytic CO_2 splitting

In this section we will demonstrate how the optimal catalyst for plasma-catalytic CO_2 splitting is affected by the temperature. We consider L-H reactions, as well as O atom recombination via E-R, which has been shown to be important (see section 6.3.1), but not the E-R reaction between O atoms and adsorbed CO*, for the reasons explained above.

Figure 6.7 shows the mole fractions of O_2 and CO in the afterglow of a CO_2 plasma at 500, 800 and 1100 K, and for different transition metal and glass walls. Note that the mole fraction of O atoms in the gas phase is approximately equal to $n_{CO} - 2n_{O2}$ (due to the stoichiometry of CO_2 splitting into CO + O, with the O atoms partially recombining into ½ O_2), while the remaining part of the gas mixture consists mainly of CO_2. Other plasma species, like ions, electronically excited species, C atoms and O_3, occur only in small amounts and are therefore not relevant for further discussion. The role of the catalyst is thus to reduce recombination between CO and O back to CO_2, by enhancing the recombination of O atoms to O_2.

Note that we compare plasma catalysis with transition metal catalysts, to a plasma and afterglow that are in contact with a glass surface (i.e., the walls of the glass tube surrounding the RF plasma). The latter serves as a reference case for the plasma (afterglow) without catalyst. This is because at the low pressures under study (0.5-10 mbar) the recombination of the plasma species occurs predominantly at the reactor walls, as recombination in the gas phase is very slow. Hence, the formation of O_2 and CO_2

and consumption of O atoms in the bulk gas of the afterglow is negligible compared to the reactions on the surface (except for Pd and Rh at 500 K, which are strongly poisoned, see section 6.3.4.4). For reference, if we use the same conditions as in Figure 6.7 and neglect surface reactions, the O atom mole fraction drops only slightly: from 3.38×10^{-2} in the plasma to 3.02×10^{-2} at the end of the afterglow at 500 K, and from 5.54×10^{-2} to 5.48×10^{-2} at 1100 K. At 500 K, about 94% of the O atoms that recombine in the bulk gas during their residence time form O_2, while at 1100 K this is about 50%. Hence, at the low-pressure conditions studied in this work, recombination reactions in the gas phase are too slow and therefore not important.

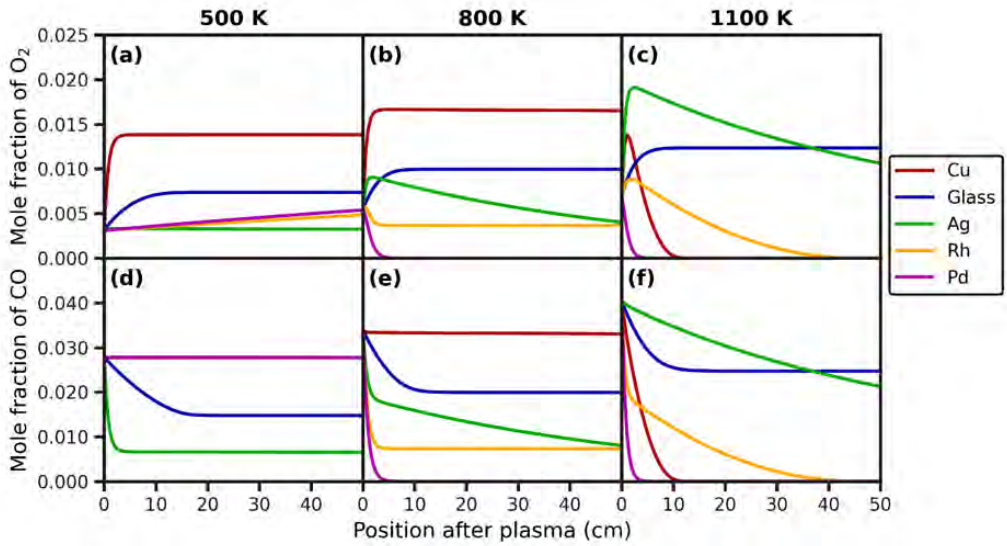

Figure 6.7. Evolution of the mole fractions of O_2 (a, b, c) and CO (d, e, f) with position in the afterglow of a CO_2 plasma. The results are plotted for different wall surfaces (transition metals and glass) and temperatures, i.e., 500 K (a,d), 800 K (b, e) and 1100 K (c, f). Other conditions: p = 5 mbar and flow rate = 100 sccm.

6.3.4.1 Cu surface

As can be seen in Figure 6.7 (a) and (b), for 500 and 800 K, respectively, Cu gives the highest O_2 fraction of all studied materials, while at 1100 K, Cu performs significantly worse compared to most other materials (see Figure 6.7 (c)). Indeed, at 1100 K the O_2 mole fraction quickly drops in the afterglow, while at lower temperatures the O_2 fraction for the Cu surface initially rises with position and then stays more or less constant (or declines only very slightly). Evidently, the initial rise in O_2 fraction can be explained by the recombination of O atoms on the surface to form O_2. At 500 K (Figure 6.7 (a)) the O_2 fraction for Cu remains stable after depletion of the O atoms in the gas phase, as the surface is not thermally active yet. For 800 K (Figure 6.7 (b)) the Cu surface starts to become slightly thermally active for CO oxidation, resulting in a very slow decline, which is however difficult to notice in (Figure 6.7 (b). As the temperature increases further to 1100 K (Figure 6.7 (c)), the Cu surface becomes fully thermally active, resulting in a quick consumption of the O_2 molecules in the afterglow. These effects are also visible in the mole fractions of CO. Figure 6.7 (d) and (e) show that the CO fraction at 500 and 800 K remains fairly stable, as almost no CO* is oxidized by adsorbed O* radicals or O_2. Note that the curves for Cu and Pd in Figure 6.7 (d) overlap. At 1100 K, the higher temperature causes the Cu surface to become fully active for thermal catalysis, resulting in a steep drop of the CO* fraction directly after the plasma, as illustrated in Figure 6.7 (f).

6.3.4.2 Glass surface

The O_2 fraction for the glass surface at 500 and 800 K (Figure 6.7 (a) and (b), respectively) behaves similarly to that of Cu, i.e., the O_2 fraction initially rises due to O atom recombination and remains constant once the O atoms are depleted. However, the glass surface is not active in thermal catalysis (i.e. in the absence of O atoms) and will thus not become thermally active at higher temperatures. Hence, even at 1100 K the O_2 fraction in the gas phase will initially increase and subsequently remain constant; see Figure 6.7

(c). Contrary to Cu, however, the glass surface also facilitates recombination between CO and adsorbed O* radicals, even at temperatures between 500-800 K. This results in an initial drop of the CO fraction for the glass surface at all temperatures studied (see Figure 6.7 (d), (e) and (f)).

6.3.4.3 Ag surface

While Cu is the best performing catalyst at 500 K for producing both O_2 and CO in the CO_2 plasma afterglow, but one of the worst performing at 1100 K, this trend is reversed for Ag. Indeed, Ag gives the lowest O_2 fractions at 500 K (Figure 6.7 (a)), yet has the highest O_2 fractions at 1100 K in most of the plasma afterglow (Figure 6.7 (c)), compared to the other materials. Only glass outperforms Ag at 1100 K near the end of the reactor.

While Ag and Cu are both relatively weakly binding catalysts, Ag is still more weakly binding compared to Cu. Hence the breaking of bonds between adsorbates and the Ag surface and the formation of new bonds between these adsorbates is easier on Ag. Consequently, the Ag surface can more easily form bonds between adsorbed O* atoms and CO* molecules via L-H reactions, which is favored over O atom recombination into O_2 at 500 K, as can be seen in Figure 6.7 (a) and (d). Almost no O atom recombination into O_2 occurs for Ag at 500 K, as the O_2 fraction in Figure 6.7 (a) remains constant throughout the entire afterglow. On the other hand, the CO fraction shows a steep decline for Ag, near the start of the afterglow, and remains constant once the O atoms are depleted, as shown in Figure 6.7 (d). Indeed, Ag is a weakly binding catalyst and thus requires high temperatures to be able to break the bond in O_2. Therefore, Ag requires the presence of O atoms to be able to oxidize CO at 500 K, just like it needs high temperatures (≥ 650 K) to become active for thermal-catalytic CO oxidation.

However, as the temperature increases, the Ag surface becomes more selective towards O_2, and less towards the back-reaction into CO_2. Indeed, by comparing Figure 6.7 (a), (b) and (c) it is clear that the maximum in the curve of the O_2 mole fraction for Ag becomes

strongly enhanced at higher temperatures. This is due to the more facile desorption of CO molecules and thus lower CO* coverages with rising temperature. Hence, less O* will recombine with CO* and more will recombine with other O atoms, via either L-H or E-R reactions, as the temperature increases. Moreover, since Ag is more weakly binding than Cu, Ag allows for easier CO* desorption, and has more difficulty breaking the O_2 bond. Thus, at high temperature Ag will be more selective towards O_2 formation and less active for thermal-catalytic CO oxidation compared to other metals, as can be seen at 1100 K in Figure 6.7 (c). At both 800 and 1100 K (Figure 6.7 (b) and (c)), the curve of the O_2 fraction for Ag shows a clear maximum due to the initial recombination of O atoms into O_2, followed by O_2 consumption via thermal-catalytic CO oxidation. Based on the O_2 fraction at the maximum, Ag is the best performing catalyst at 1100 K, however thermal catalysis (oxidation of CO into CO_2) causes the O_2 and CO fractions to drop later in the reactor. This illustrates the importance of controlling thermal-catalytic back-reactions that occur in combination with plasma-catalytic CO_2 splitting. This may be possible by limiting the catalytic region in the reactor, or by changing the residence time.

6.3.4.4 Rh and Pd surfaces

The results for Rh and Pd at 500 K are similar to each other, i.e., the O_2 fractions for both catalysts rise slowly throughout the reactor due to recombination of O atoms, as shown in Figure 6.7 (a). Likewise, the CO fractions of Rh and Pd remain quasi constant at 500 K and the curves for both catalysts overlap, as illustrated in Figure 6.7 (d). As we explained in section 6.3.2, the low activity and slow O atom recombination is due to CO* poisoning of these catalysts at 500 K. Whether these results are accurate or not depends on the possibility for O atoms to recombine with adsorbed CO* via an E-R reaction, as also discussed in section 6.3.2. If that reaction is sufficiently easy, CO* poisoning would be avoided, and O atom recombination would be much faster. Nevertheless, at higher temperatures CO* poisoning disappears, regardless of whether E-R between O atoms

and CO* is considered, as CO* gains sufficient energy to desorb. Indeed, Pd is highly active for thermal-catalytic CO oxidation at 800 and 1100 K, causing an immediate drop of both the O_2 and CO fractions at the start of the afterglow (Figure 6.7 (b,e) and (c,f), respectively).

At 800 K, the Rh surface also catalyzes CO oxidation, causing a drop in the mole fractions of O_2 and CO, see Figure 6.7 (b) and (e). However, in contrast with the Pd surface, Rh is not active for thermal catalysis at 800 K, and the consumption of O_2 and CO stops once the O atoms in the gas phase are depleted. This can be explained by the removal of adsorbed O* by incident O atoms via E-R, which opens up free sites on which CO can adsorb. Once the O atoms are depleted, however, the surface is poisoned by adsorbed O*, formed by O_2 dissociative adsorption. This stops further CO oxidation. At 1100 K, Rh behaves similar to Ag, i.e., initially the O_2 fraction rises due to O atom recombination, followed by O_2 consumption through thermal-catalytic CO oxidation (Figure 6.7 (c)). However, in contrast with Ag, the Rh surface recombines less O atoms into O_2 and is more selective towards CO oxidation by O atoms. Hence, the maximum in the O_2 fraction is lower and the initial drop in the CO fraction is steeper for Rh compared to Ag (see Figure 6.7 (c) and (f) for O_2 and CO, respectively).

6.3.4.5 Energy efficiency

The energy efficiency η is a measure of how efficiently the energy is used compared to the standard reaction enthalpy. The energy efficiency is calculated according to:[14]

$$\eta(\%) = \frac{X_{CO_2}(\%) \times \Delta H°_{298K}(kJ/mol)}{SEI(kJ/mol)} \qquad \text{Eq. 6.10}$$

With X_{CO2} the CO_2 conversion, $\Delta H°_{298K}$ the standard reaction enthalpy at 298 K (283 kJ/mol for CO_2 splitting) and SEI the specific energy input. Note that Eq. 6.10 is only valid following the depletion of the O atoms in the gas phase, when CO_2, CO and O_2 are the only relevant gas components. Since all simulations in Figure 6.7 are executed at the

same SEI (13.9 eV/molecule = 1.34×10^3 kJ/mol), η follows the same trend as the O_2 and CO mole fractions after depletion of the O atoms (i.e., η drops towards the end of the reactor, if the catalyst is thermally active). The point at which the O atoms are depleted is typically at the maximum in the O_2 curve when the surface is thermally active, or after the mole fractions stabilize when it is not thermally active. Hence, at 500 K the highest energy efficiency is reached by Cu, for which η_{max} = 0.59%, followed by glass with η_{max} = 0.31%. η_{max} here refers to the maximum energy efficiency reached for the surface after depletion of the O atoms. The lowest value at 500 K is attained by Ag for which η_{max} = 0.14%. For Pd and Rh, the O atoms do not become fully depleted in the reactor at this temperature. At 800 K, Cu is still the best performing catalyst, reaching a maximum value of η_{max} = 0.71%, followed by glass (η_{max} = 0.42%) and Ag (η_{max} = 0.38 %). Rh reaches a value of η_{max} = 0.16%, while for Pd the energy efficiency approaches zero as depletion of the O atoms occurs simultaneously with CO and O_2 consumption by thermal catalysis. This is also the case for Pd at 1100 K. For the other surfaces, the values of η_{max} at 1100 K equal 0.82%, 0.53%, 0.37% and 0.36% for Ag, glass, Cu and Rh, respectively.

Note that the energy efficiencies reported above are quite low. Yet, we did not include vibration excitation into our model (except as an energy loss process in the calculation of the EEDF). Hence, our model does not consider processes such as vibrational ladder climbing, or enhanced CO_2 dissociation (neither on the surface, nor in the gas phase). As such, dissociation of CO_2 in the plasma occurs via electron impact dissociation (i.e., via excitation to a dissociative level), which requires more energy than the bond dissociation energy in CO_2.[254] If vibrational ladder climbing is considered, the energy efficiency, CO_2 conversion, and the mole fractions of CO and O_2 may improve. However, the predicted trends between the different surface in the afterglow region are expected to remain unchanged.

Note that overall, the energy efficiency in plasma catalysis is quite low, certainly with DBD plasmas (in contrast to warm plasmas, like (gliding) arc and microwave plasmas). Hence, the energy efficiency and/or the selectivity towards higher-value compounds will need to be significantly improved, before plasma catalysis can become industrially relevant.

6.3.4.6 Summary

In summary, the optimal catalyst depends both on its activity for O atom recombination into O_2, as well as for thermal catalytic CO oxidation into CO_2. Indeed, Cu performs well at 500 and 800 K, as it selectively recombines O atoms into O_2 via E-R reactions, and thus avoids recombination of O atoms with CO back to CO_2. Yet, at 1100 K Cu is active for thermal catalytic CO oxidation, causing a drop in the CO and O_2 mole fractions.

Conversely, Ag performs very bad at 500 K, as its weakly binding character enables facile recombination between adsorbed O* atoms and CO* to form CO_2 via the L-H mechanism. Yet, at 1100 K Ag performs very well compared to the other catalysts, as less CO* remains adsorbed on the surface to recombine with O*, and the difficult dissociation of O_2 on Ag results in a relatively low rate for thermal catalytic CO oxidation.

Pd is very active for thermal catalytic CO oxidation at 800 and 1100 K, but at 500 K it is poisoned by CO*, and thus performs bad for plasma-catalytic CO_2 splitting. Rh is fairly inactive for both O atom recombination into O_2, as well as thermal catalytic CO oxidation. Consequently, Rh generally performs moderately.

Lastly, the glass surface gives moderate to good results (especially at 1100 K) as it is not active for thermal catalytic CO oxidation, and only aids in recombination of O atoms with other O atoms or CO.

6.3.5 The optimal catalyst depends on temperature and residence time

As discussed previously, the best catalyst in terms of O_2 formation can change depending on the position in the reactor. Hence, we can compare catalyst performance based on the O_2 and CO fractions at the reactor outlet, but this is dependent on our choice of reaction conditions and reactor dimensions. As such, the potential of the catalyst for plasma-catalytic CO_2 splitting can also be expressed by the maximum O_2 fraction attained in the reactor. Indeed, the drop in the O_2 fraction due to thermal catalytic CO oxidation may be avoided by limiting the catalytic bed length (or catalytically active region of the reactor wall) or altering the residence time in the catalytic bed. To compare the performance of the different catalyst materials (or glass surface) as a function of temperature, we therefore compare both the O_2 mole fraction at the outlet, as well as the maximum O_2 fraction in the reactor, which are displayed in Figure 6.8 (a) and (b), respectively.

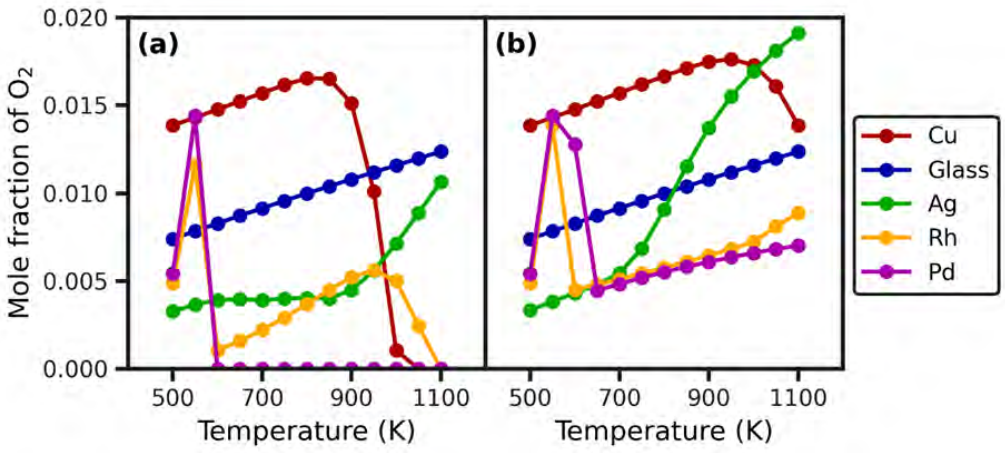

Figure 6.8. Influence of temperature on the O_2 mole fraction at the reactor outlet (a) and at its maximum in the reactor (b), for the different transition metals and the glass surface. Other conditions: p = 5 mbar and flow rate = 100 sccm.

6.3.5.1 Cu surface

By looking at the curves for Cu in Figure 6.8, it becomes clear that Cu is the best performing catalyst at low and intermediate temperatures (500-850 K), both based on the outlet and maximum O_2 fractions. However, the outlet O_2 fraction (Figure 6.8 (a)) rapidly drops above 900 K, as the Cu surface becomes active for thermal-catalytic CO oxidation, while the decline of the maximum O_2 fraction (Figure 6.8 (b)) occurs more slowly. Moreover, the highest O_2 fraction in Figure 6.8 (b) occurs at a higher temperature (950 K) compared to Figure 6.8 (a) (800 K). This indicates that there is still potential for further optimization of the O_2 fraction, and thus CO_2 conversion, at the reactor outlet, by shortening the catalytic region, or reducing the gas residence time (by a shorter catalyst bed or higher flow rates), when working at temperatures above 800 K.

6.3.5.2 Glass surface

As observed in Figure 6.8, the outlet (a) and maximum (b) O_2 fractions for the glass surface are the same, as glass is not active for thermal catalysis, and thus will not consume O_2 for CO oxidation, regardless of temperature. As such, glass is the best performing surface for CO_2 splitting at high temperatures (≥ 900 K), when looking at the outlet O_2 fraction in Figure 6.8 (a), because the transition metal catalysts will all give rise to thermal-catalytic CO oxidation to CO_2, to some extent. However, when looking at the maximum achievable O_2 fractions in Figure 6.8 (b), the glass surface is outperformed by different transition metals at all temperatures, most notably by Ag at high temperatures (≥ 900 K).

6.3.5.3 Ag surface

While Ag results in the highest maximum O_2 fractions (0.018-0.019) at 1050 - 1100 K, it is one of the worst performing materials below 700 K, as it selectively recombines O atoms with CO back to CO_2. Above 700 K, O atom recombination into O_2 also becomes relevant for the Ag surface, which can be observed from the increase in the maximum

achievable O_2 fraction in Figure 6.8 (b). However, the O_2 fraction at the outlet (Figure 6.8 (a)) remains more or less constant for the Ag surface between 700 and 900 K, as O_2 formation by O atom recombination is compensated for by subsequent thermal-catalytic CO oxidation. Note that Ag, being a weakly binding catalyst, can readily catalyze the formation of new bonds (i.e., the formation of CO_2* from adsorbed CO* and O*) at low temperatures, while it struggles with breaking bonds in molecules, i.e., O_2* dissociation. Hence, when Ag becomes active for thermal catalysis around 700 K, this is the result of the O_2 dissociation step becoming active, while recombination of CO* and O* already occurs at a lower temperature, as O atoms are provided by the plasma. Above 900 K, the O_2 fraction at the reactor outlet also rises (Figure 6.8 (a)), as more O_2 is formed near the start of the afterglow than can be consumed by thermal-catalytic back-reactions in the rest of the reactor. Note that this of course depends on the reactor dimensions. Based on the maximum achievable O_2 fraction in Figure 6.8 (b), Ag becomes the best performing catalyst above 900 K, outperforming both Cu and glass. As discussed previously, higher temperatures strongly reduce the amount of adsorbed CO* on the weakly binding Ag catalyst, which results in less CO oxidation by adsorbed O atoms. Consequently, more O atoms will recombine with each other into O_2, through E-R or L-H reactions, upon rising temperature.

6.3.5.4 Rh and Pd surfaces

The Rh and Pd surfaces behave similarly below 600 K, as also discussed in section 6.3.4.4. At 500 K, the reactions on both Rh and Pd are strongly limited by CO* poisoning, making the recombination of O atoms into O_2 very slow, as was also visible in Figure 6.7 (a). Hence, Figure 6.8 (a) and (b) show the same values at 500 K for both the O_2 fraction at the maximum and at the reactor outlet, as the O_2 fraction in the afterglow is still rising with the position in the reactor. At slightly higher temperature (550 K) the O_2 fractions for both Rh and Pd show a peak in Figure 6.8 (a) and (b). This is due to a drop in CO*

poisoning by the easier CO* desorption at higher temperature. Consequently, more O atoms can adsorb and recombine into O_2 via E-R. However, as the temperature further rises, the O_2 fraction drops as CO oxidation becomes feasible, which can be seen for both the outlet and maximum O_2 fractions in Figure 6.8 (a) and (b), respectively. Indeed, Rh and Pd are relatively strongly binding catalysts that struggle with bond formation reactions between adsorbates (L-H mechanism), as these catalysts themselves form strong bonds with the adsorbates.

Yet above 600 K the temperature is sufficiently high for CO* and O* to associate into CO_2*, meaning that CO oxidation by adsorbed O atoms or through thermal catalysis can occur. For Pd, the outlet O_2 fraction (Figure 6.8 (a)) is near zero for temperatures ≥ 600 K, as Pd is a very good catalyst for CO oxidation and will thus quickly revert the gas composition to the thermodynamic equilibrium (≈ 100% CO_2). Indeed, Pd is used as an exhaust catalyst for CO oxidation in the automotive industry.[218,219] For Rh, the outlet O_2 fractions at temperatures ≥ 600 K are larger than for Pd. Indeed, at intermediate temperatures (600-950 K) the Rh surface can only oxidize CO in the presence of O atoms, as shown in Figure 6.7 (b). This is because the O atoms free up a part of the surface by removing O* via an E-R reaction, thus allowing for adsorption and oxidation of CO. As the temperature rises from 600 to 950 K, the outlet O_2 fraction in Figure 6.8 (a) increases, as CO* desorbs more easily, and thus less CO oxidation will occur. Above 950 K, the outlet O_2 fraction drops as the rate of thermal-catalytic CO oxidation by O_2 increases. When looking at the maximum achievable O_2 fractions (Figure 6.8 (b)), the results for Pd and Rh are almost identical in the temperature range between 650 to 900 K, as the maximum O_2 fraction is at the start of the afterglow. Indeed, as the reaction proceeds, O_2 will be consumed by CO oxidation. However, at temperatures above 900 K, the maximum O_2 fraction for Rh increases slightly relative to that of Pd, as the Rh surface becomes more notably active for O atom recombination into O_2.

6.3.5.5 Summary

There is still potential for improving the CO and O_2 yields at the outlet by avoiding thermal catalytic CO oxidation, which could be achieved by tuning the residence time or limiting the length of the catalyst bed. Especially for Ag above 600 K, there is a clear difference between the maximum and outlet O_2 fractions, due to thermal catalytic CO oxidation (by O_2) after the O atoms in the gas phase are depleted. Based on the maximum O_2 fraction in the reactor, Ag could become the best performing catalyst above 1000 K, while for our current set of reaction parameters the glass surface gives the highest outlet O_2 fraction. Nevertheless, below 950 K the best performing catalyst is always Cu, both based on the maximum and outlet O_2 fractions. Pd is by far the worst performing catalyst at temperatures above 600 K, both based on the maximum and outlet O_2 fractions, while Rh performs slightly better. However, both Rh and Pd show a narrow spike in maximum and outlet O_2 fraction around 550 K.

6.3.6 Effect of pressure on plasma-catalytic CO_2 splitting

In this section, we illustrate how plasma-catalytic CO_2 splitting is affected by the gas pressure. As we find that the effect of pressure is similar for all surfaces and temperatures under study, we discuss the results of one transition metal as a general example. We choose the Cu surface at 1100 K, as the evolution of the O_2 and CO mole fractions with position in the afterglow is the clearest (i.e., steepest) for this catalyst. Figure 6.9 (a) and (b) therefore display the evolution of the O_2 and CO mole fractions, respectively, with position in the afterglow for the aforementioned conditions (Cu, 1100 K), and pressures varying from 0.5 to 10.0 mbar. Additionally, we list the mole fractions of the main gas species at the end of the plasma (i.e., the first point in Figure 6.9) in Table 6.3 for the different pressures.

As can be seen in Figure 6.9, lower pressures result in higher maximum O_2 and CO fractions, while their subsequent decline due to thermal-catalytic back-reactions is slower, thus resulting in higher O_2 and CO mole fractions in the entire afterglow.

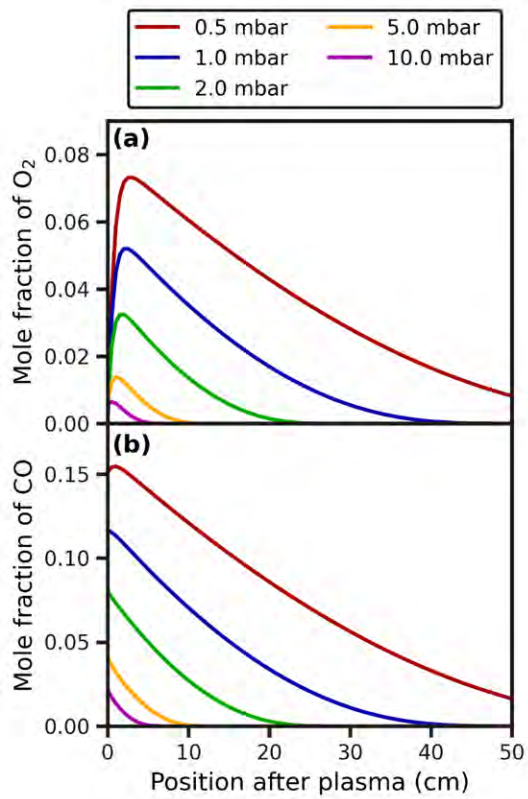

Figure 6.9. Effect of pressure on the spatial evolution of the O_2 (a) and CO (b) mole fractions in the afterglow for a Cu surface. Other conditions: T = 1100 K and flow rate = 100 sccm.

The reason for this is twofold: first, higher pressures result in a different EEDF, because there are more electron-neutral collisions, leading to lower electron energies and thus less electron impact ionization. Indeed, we find that the electron density in the plasma region is lower at 10.0 mbar ($n_e = 2.6 \times 10^{10}$ cm^{-3}), compared to 0.5 mbar ($n_e = 2.5 \times 10^{11}$ cm^{-3}). Hence, the lower electron energy and density at higher pressure hinder the formation of O atoms via electron impact dissociation of CO_2. Consequently, the O and

CO densities do not rise proportionally with increasing pressure, resulting in lower O and CO fractions at the end of the plasma for higher pressures, as can be seen in Table 6.3. Thus, due to the lower mole fraction of O atoms available for recombination, a lower fraction of O_2 is formed.

Table 6.3. Mole fractions of the main gas species at the end of the plasma for different pressures at 1100 K and 100 sccm.

Pressure (mbar)	O_2 Mole fraction	CO Mole fraction	O Mole fraction	CO_2 Mole fraction
0.5	1.9×10^{-3}	1.5×10^{-1}	1.5×10^{-1}	6.9×10^{-1}
1.0	3.4×10^{-3}	1.2×10^{-1}	1.1×10^{-1}	7.7×10^{-1}
2.0	5.7×10^{-3}	8.0×10^{-2}	6.9×10^{-2}	8.5×10^{-1}
5.0	7.0×10^{-3}	4.0×10^{-2}	2.6×10^{-2}	9.3×10^{-1}
10.0	5.7×10^{-3}	2.1×10^{-2}	9.9×10^{-3}	9.6×10^{-1}

In addition, less of the available O atoms will recombine into O_2 at higher pressures and more will react back to CO_2. Indeed, while the CO mole fraction in the plasma is lower at higher pressures, i.e. 0.021 at 10 mbar vs. 0.15 at 0.5 mbar, this is not the case for the CO number density, which equals 1.4×10^{15} cm^{-3} at 10 mbar vs. 5.0×10^{14} cm^{-3} at 0.5 mbar. Hence, the CO density rises with pressure, albeit by a lower factor than the pressure itself. The higher CO density at higher pressures enhances the CO adsorption and oxidation on the catalyst surface, which results in more O atoms reacting back to CO_2. This is also visible in Figure 6.9 (a), in which the initial rise in O_2 fraction becomes smaller upon rising pressure.

Since the results shown in Figure 6.9 are all calculated using the same SEI, the highest energy efficiency is again reached for the conditions that coincide with the highest O_2 mole fractions. Hence, the lowest pressure (0.5 mbar) results in the highest energy

efficiency (η_{max} = 3.3%), while the highest pressure (10.0 mbar) reaches a maximal energy efficiency of only 0.039%.

In summary, our results show that plasma-catalytic CO_2 splitting would benefit from operating at lower pressures, at least within the pressure range under study (0.5 to 10 mbar). This effect is partly due to the physical changes in the plasma (lower electron energy and density at higher pressure) and partly due to catalytic effects (CO oxidation at the catalyst surface). The use of lower gas pressures enhances the O_2 mole fraction and consequently allows for more facile tuning of residence time and length of the catalyst bed, as higher O_2 fractions will be available in a broader region of the reactor. Note, however, that for temperatures at which the catalyst is not thermally active, the O_2 fraction will stop changing when the O atoms in the afterglow are depleted, regardless of the pressure used. Also note that for all pressures in Figure 6.9, the simulations are performed with a flow rate of 100 sccm and a plasma power of 100 W, and thus all correspond to the same specific energy input (SEI), namely 13.9 eV/molecule. Finally, it should be kept in mind that in practice, plasma catalysis is more feasible at atmospheric pressure. However, our results are useful to obtain better insights in the current limitations, and how to overcome them, by tuning various operating conditions.

6.3.7 Effect of flow rate on plasma-catalytic CO_2 splitting

To illustrate the influence of the flow rate in plasma-catalytic CO_2 splitting, we plot the O_2 and CO mole fractions in the afterglow, in Figure 6.10 (a) and (b), respectively, at different flow rates and for both Ag and glass surfaces. Hence, we show results for a (thermally active) catalytic surface (Ag), and a non-catalytic surface (glass). Additionally, we list the mole fractions of the main gas species at the end of the plasma in Table 6.4 for the different flow rates.

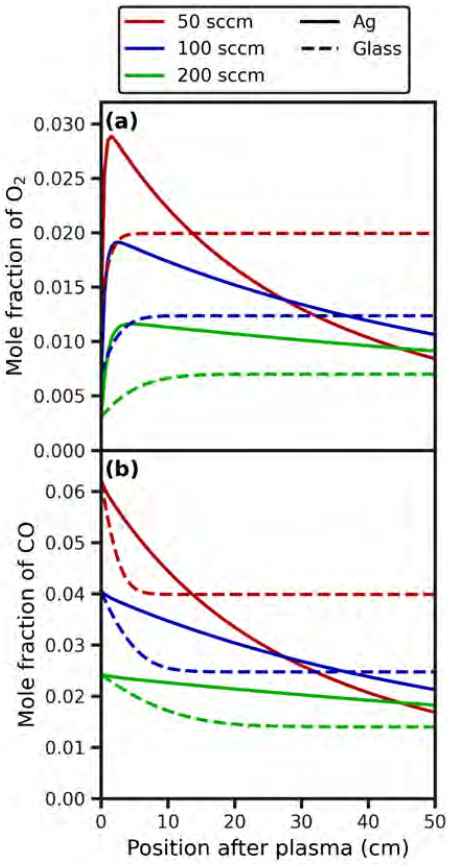

Figure 6.10. Effect of the flow rate on the spatial evolution of the O_2 (a) and CO (b) mole fractions in the afterglow, for Ag (full lines) and glass (dashed lines) surfaces. Other conditions: T = 1100 K and p = 5 mbar.

In case of the Ag surface, the effect of lowering the flow rate is two-fold: on one hand, the maximum O_2 fraction (Figure 6.10 (a)) increases, but on the other hand, the subsequent drop in O_2 fraction occurs much faster. Indeed, by lowering the flow rate, the residence time becomes longer, and the SEI rises. Consequently, more CO_2 molecules dissociate in the plasma, resulting in more O atoms which recombine into O_2, thus leading to higher maximum O_2 fractions, as can be seen in Table 6.4. However, the formed O_2 molecules also take longer to travel through the reactor at lower flow rates, resulting

in more O_2 consumption by thermal-catalytic CO oxidation, and thus, a steeper decline of the O_2 fraction with the position in the afterglow.

Likewise, the CO mole fractions (Figure 6.10 (b)) at the start of the afterglow are higher for lower flow rates, but also drop more quickly with position in the reactor. This second effect does not occur on the glass surface, because it is not catalytically active. Hence, lower flow rates are always beneficial in the case of the non-catalytic glass surface, while for the catalytic Ag surface the effect can be either positive or negative, depending on the position in the reactor.

Table 6.4. Mole fractions of the main gas species at the end of the plasma for different flow rates at 1100 K and 5 mbar.

Flow rate (sccm)	**O_2 Mole fraction**	**CO Mole fraction**	**O Mole fraction**	**CO_2 Mole fraction**
50	1.3×10^{-2}	6.2×10^{-2}	3.5×10^{-2}	8.9×10^{-1}
100	7.0×10^{-3}	4.0×10^{-2}	2.6×10^{-2}	9.3×10^{-1}
200	3.1×10^{-3}	2.4×10^{-2}	1.8×10^{-2}	9.5×10^{-1}

As such, the length of the post-plasma-catalytic bed should ideally be tuned against the flow rate, if the surface is catalytic and thermally active at the operating temperature. Indeed, by limiting the catalytic region to the space in the reactor where O_2 formation occurs, the subsequent destruction of O_2 (and CO) by thermal catalytic CO oxidation can be avoided. In this case, the maximum O_2 fraction would also be the outlet O_2 fraction, and the use of Ag and low flow rates would be favored over a glass surface and high flow rates. As can be seen in Figure 6.10, the maximum O_2 fraction for Ag exceeds that of glass at all flow rates, and the highest maximum is attained for the lowest flow rate. However, when comparing the O_2 and CO fractions at the outlet (50 cm) in Figure 6.10 (a) and (b), the Ag surface only outperforms the glass surface at the highest flow rate (200 sccm). At lower flow rates, the O_2 and CO fractions for the Ag surface drop below that for glass,

due to the enhanced O_2 and CO consumption. Hence, the best catalyst material for attaining high O_2 and CO fractions (and thus a high CO_2 conversion) can differ depending on the flow rate. Moreover, for thermally active catalysts, such as Ag in Figure 6.10, there exists an optimum between high and low flow rates, as the highest outlet O_2 and CO fractions for Ag are attained at 100 sccm, while both 50 and 200 sccm result in less O_2 and CO at the outlet.

As discussed above, the SEI differs for the three flow rates, and hence the trends in energy efficiency between the different flow rates do not necessarily match those of the O_2 mole fraction. In fact, the highest energy efficiencies are now obtained with the highest flow rate and thus the lowest SEI. Indeed, η_{max} reaches values of 0.99% and 0.60% at 200 sccm, 0.82% and 0.52% at 100 sccm, and 0.62% and 0.43% at 50 sccm, for Ag and glass, respectively. As such, when viewed from an energy efficiency-based perspective, lower flow rates and SEI's would be favored. Yet, simultaneously this also lowers the maximum attainable conversion (and O_2 mole fraction), meaning that a balance between energy efficiency and conversion, should be maintained. Nevertheless, as higher flow rates reduce the loss of CO and O_2 by thermal catalytic back-reactions, the drop in energy efficiency from the maximum to the outlet also become smaller. Hence, for Ag at 50 sccm the energy efficiency drops from η_{max} = 0.62% to η_{outlet} = 0.17%, while at 200 sccm η_{max} = 0.99% to η_{outlet} = 0.78%. In this regard, higher flow rates can significantly reduce the loss in energy efficiency towards the outlet.

Finally, we consider how the effect of the flow rate translates to other catalyst materials and conditions. If the catalyst surface is not thermally active at the operating temperature, the gas composition will stop changing once the radicals in the afterglow are depleted. Consequently, the CO_2 dissociation in the plasma, and thus also the formation of O_2 and CO, will always rise upon lowering the flow rate (as explained above, hence independent of the surface material after the plasma), while no subsequent

thermal-catalytic back-reactions occur. Hence, under these conditions, a lower flow rate will always result in higher O_2 and CO fractions, and thus a higher CO_2 conversion, at the reactor outlet. This is always the case for glass, but also for transition metals that are not thermally active at the operating temperature. For example, in Figure 6.7 (b) the O_2 fraction for the Rh surface at 800 K stabilizes at a non-zero value after depletion of the O atoms in the plasma, and similarly, the O_2 content for Cu at 800 K drops only very slowly. Hence, the net O_2 formation for Rh and Cu surfaces at 800 K will mainly benefit from a lower flow rate, as this will primarily enhance the number of O atoms formed in the plasma. However, if the catalyst is thermally active at the operating temperature, the initial rise in O_2 fraction is followed by a drop due to thermal-catalytic CO oxidation. Consequently, there is an optimal flow rate that balances the effects of the higher CO_2 dissociation at lower flow rates against the reduced O_2 consumption at higher flow rates. Note that for some catalysts the consumption of O_2 occurs directly at the start of the afterglow, before depletion of the O atoms. In this case, the maximum O_2 fraction coincides with that in the plasma and will thus rise for lower flow rates, while the subsequent decline of the O_2 fraction will still become more rapid upon lower flow rate.

In summary, lower flow rates, and thus higher SEI's, result in more CO_2 dissociation in the plasma, but also increase the residence time in the catalyst bed. If the catalyst is thermally active for CO oxidation, the longer residence time causes more CO and O_2 to react back to CO_2. Hence, the optimal flow rate depends on the catalyst and its activity for CO oxidation.

6.3.8 Discussion of the optimal catalyst properties

Finally, in this section, we discuss which properties should be targeted when searching for the optimal catalyst for plasma-catalytic CO_2 splitting, based on our modeling insights. For the conditions under study, the role of the plasma is to activate the CO_2 molecules, i.e., by electron impact dissociation. Hence, the plasma causes a departure from the

thermodynamic equilibrium composition (which favors CO_2 at these conditions) resulting in the formation of O atoms and CO molecules. The role of the catalyst is then to minimize the recombination of O with CO back into CO_2, by maximizing the recombination of O atoms into O_2. However, the catalyst should not be (too) active for thermal catalysis under the envisioned reaction conditions, as this will cause a return to the thermodynamic equilibrium composition (i.e., pure CO_2), due to thermal catalytic CO oxidation.

To avoid backreactions to CO_2, the catalyst should preferentially have a high activation barrier for recombination between adsorbed CO* and O*, while a low CO* coverage and thus a low CO* binding strength is also preferred. However, in practice the adsorption energies of adsorbates and the activation barriers for reactions between adsorbates cannot be varied independently. This is due to existence of Brønsted-Evans-Polanyi (BEP) relations, i.e. correlations between reaction and activation energies, as well as linear scaling relations between the binding strength of different adsorbates, in heterogenous catalysis.[255,256] Therefore, catalysts that bind adsorbates weakly have lower activation barriers for their desorption and recombination reactions. As such, low CO* binding strengths result in lower barriers for CO_2 formation, but also more facile CO* desorption. Hence, there should exist an optimal CO* binding strength at which these conflicting effects are balanced. Our model predicts that for the system and conditions under study, the catalysts that bind CO* weakly, i.e. Ag and Cu ($\Delta H°_{CO(g)\rightarrow CO*}$ = -0.17 eV and -0.61 eV, respectively), generally perform better than catalysts that bind CO* strongly, i.e. Pd and Rh ($\Delta H°_{CO(g)\rightarrow CO*}$ = -1.76 eV and -1.74 eV, respectively). Indeed, adsorbed CO* can only be removed from the surface via desorption or recombination to CO_2. If both are difficult, the surface will become poisoned by CO*, which we find to be the case for Pd and Rh at 500 K and 5 mbar. Thus, our model reveals that the optimal catalyst binds CO* weakly, i.e., has a larger, less negative CO adsorption enthalpy, to allow for facile CO* desorption.

However, a weak CO* binding not only promotes desorption, but also recombination of CO* with O* to form CO_2. To compensate for this effect and retain a sufficiently high activation barrier for CO_2 formation, a catalyst that binds O* strongly might be desired. Indeed, stronger O* binding stabilizes adsorbed O* atoms, and thus results in higher activation barriers for reactions involving O*, such as the reaction with CO* to form CO_2. In other words, if the catalyst binds both O* and CO* weakly, they are not stabilized as much and the barrier for CO_2 formation will be low. This is the case for Ag, which binds both CO* and O* weakly ($\Delta H°_{CO(g)\rightarrow CO*}$ = -0.17 eV and $\Delta H°_{0.5O2(g)\rightarrow O*}$ = -0.64 eV). Indeed, Ag efficiently catalyzes the recombination of O* and CO* to CO_2 at relatively low temperatures (500-700 K). Nevertheless, as the temperature rises, the contribution of CO* desorption relative to recombination increases, as desorption is an entropically driven process, and Ag becomes a good catalyst for O* recombination to O_2. Cu, on the other hand, binds CO* relatively weakly ($\Delta H°_{CO(g)\rightarrow CO*}$ = -0.61 eV), but O* quite strongly ($\Delta H°_{0.5O2(g)\rightarrow O*}$ = -1.78 eV). Indeed, the O* binding strength of Cu lays in between Pd ($\Delta H°_{0.5O2(g)\rightarrow O*}$ = -1.47 eV), and Rh ($\Delta H°_{0.5O2(g)\rightarrow O*}$ = -2.19 eV). While the weak CO* binding of Cu improves CO* desorption, the relatively strong O* binding increases the activation barrier for recombination between O* and CO*, thus limiting CO_2 formation. However, the stronger O* binding also results in more difficult recombination of O* atoms to O_2 and more facile dissociation of O_2 to O* atoms, as the catalyst stabilizes the surface bound O* more strongly. Yet, the activation barrier for O atom recombination via E-R does not increase much with rising O* binding strength, so that O_2 formation via E-R remains facile as long as O atoms are present in the gas phase. As such, we find that Cu is a good catalyst for O atom recombination at temperatures between 500 and 900 K. Yet, at higher temperatures, Cu starts to dissociate the formed O_2 and becomes active for thermal catalytic CO oxidation to CO_2. It is important to note that stronger O* binding results in more facile O_2 dissociation and hence in a lower temperature needed for thermal catalytic CO oxidation by O_2, that is, as long as O_2 dissociation is the rate-limiting

step. Because of this, Ag becomes a better catalyst for O recombination to O_2 than Cu at high temperatures (≥ 1000 K).

As discussed in section 6.3.2, it may be possible that CO_2 can also be formed by E-R reactions between adsorbed CO* and an impinging O atom from the gas phase. While we did not consider this reaction in the rest of the paper, due to its many uncertainties, we would like to note that the reaction would benefit from high CO* coverages. Thus, to counteract it, high O* and low CO* coverages would be needed, which means that catalysts that bind O* strongly and CO* weakly are still preferred.

To conclude, catalysts that bind CO* weakly are expected to be promising candidates for plasma-catalytic CO_2 splitting, while the optimal O* binding strength may vary depending on the temperature. Overall, materials that bind O* strongly, such as Cu, are expected to be better at lower temperatures, yet might more quickly become active for thermal catalytic CO oxidation as the temperature rises. Higher temperatures might therefore require catalysts that bind O* more weakly, such as Ag.

6.4 Conclusion

We developed a coupled plasma-surface microkinetic model with a Boltzmann solver to study the interaction of plasma-produced radicals and molecules with a transition metal or glass surface placed in the afterglow of a low-pressure CO_2 discharge. We consider four transition metals, namely Ag, Cu, Pd and Rh, as well as glass, which represents the glass tube surrounding the plasma/afterglow, and we compare their effect on the reaction kinetics for plasma-catalytic CO_2 splitting. Moreover, we used DFT to calculate the reaction barriers on the transition metal catalysts and we combine these with TST to acquire surface rate coefficients that are used as input for our model. Although our model could not yet be validated against experimental data, and thus cannot make

quantitative predictions, it can still provide qualitative trends, insights and comparisons on the influence of the different catalysts and reactions conditions.

We do not only consider adsorption of radicals on the surface followed by L-H reactions, but also their recombination via E-R reactions. Indeed, based on simulations for a pure O_2 plasma, we suggest that E-R reactions play an important role in O atom recombination on transition metal surfaces, as the high recombination coefficients that are reported in literature for transition metals cannot be explained by our model based on L-H reactions alone, at least for temperatures ≤ 600 K.

In plasma-catalytic CO_2 splitting, recombination of O atoms via E-R results in O_2 formation and creates free surface sites, enabling some CO to adsorb next to O atoms. Consequently, some recombination of O and CO back to CO_2 also occurs. However, transition metals also become active for thermal catalytic CO oxidation by the formed O_2 if the temperature is sufficiently high, resulting in a subsequent decline of the O_2 and CO mole fractions, and thus also of the CO_2 conversion, as well as a maximum in the evolution of the O_2 mole fraction vs. position in the reactor. Moreover, the temperature at which a catalyst becomes active for thermal catalytic back-reactions depends strongly on the type of metal. Hence, the optimal catalyst depends strongly on the operating temperature. In other words, there is no single best catalyst, but rather an optimal catalyst for specific reaction conditions.

Although this conclusion seems evident, many experimental studies on plasma catalysis compare different catalysts for only a single set of reaction conditions, rather than evaluating their performance over a range of temperatures, residence times or SEI's.[32,35,36,65,104,128,257,258] However, this only gives a limited view of their potential, since the trend between catalysts may change depending on the reaction conditions, as we illustrated in this chapter.

We find that Cu is the best catalyst up to 900-1000 K, as this relatively weakly binding metal can easily recombine O atoms into O_2 via E-R at 500-900 K, thus avoiding their recombination with CO into CO_2 again, and leading to a higher CO yield and CO_2 conversion. Yet, Cu becomes thermally active for CO oxidation into CO_2 above 900 K.

The Ag surface, on the other hand, performs very badly at 500-600 K, as its very weakly binding character results in low barriers ($\Delta H^{\ddagger\circ}$ = 0.06 eV) for recombination between adsorbed O* and CO* via L-H, causing most O atoms to react with CO to again form CO_2. However, as the temperature rises, less CO* remains adsorbed on the surface, causing more O atoms to recombine into O_2 and leading to higher maximum O_2 and CO mole fractions in the reactor, and a higher CO_2 conversion. Hence, Ag is the optimal catalyst at very high temperatures (> 1000 K), provided that the length of the catalytic zone is limited to avoid thermal catalytic back-reactions after the O atoms in the gas phase are consumed.

Both Pd and Rh are poisoned by CO* at 500 K, but Pd becomes highly thermally active for CO oxidation at higher temperatures, making it detrimental for CO_2 splitting. Rh, on the other hand, is neither very efficient at recombining O atoms into O_2 or in thermal catalytic CO oxidation.

Next to temperature, we studied the effect of the gas pressure and flow rate, which determines the residence time of the gas in the catalytic bed. We find that plasma-catalytic CO_2 splitting benefits strongly from lower gas pressures, due to more CO_2 dissociation in the plasma and slower thermal catalytic back-reactions in the afterglow. However, this is not beneficial for practical applications, and therefore, plasma catalysis is typically performed at atmospheric pressure, which might thus limit the achievable CO_2 conversion.

Additionally, lower flow rates result in more CO_2 conversion in the plasma, but also cause more thermal catalytic back-reactions in the reactor due to the longer residence time. Hence, under conditions where transition metals are thermally active, the flow rate should be optimized against the length of the catalyst bed to avoid thermal catalytic CO oxidation after depletion of the O atoms in the gas phase, while still achieving sufficient CO_2 dissociation in the plasma. Indeed, if the flow rate is too low, thermal catalysis may consume a large amount of CO and O_2, and the use of a non-catalytic surface (e.g., glass) would be favored instead.

To conclude, this study illustrates how the performance of different transition metals for plasma catalytic CO_2 splitting can change depending on the reaction conditions, and we also compare their performance with a glass tube surrounding the afterglow. Overall, the optimal catalyst depends both on its activity for O atom recombination into O_2, thus avoiding their recombination with CO back into CO_2, as well as its activity for thermal catalytic CO oxidation into CO_2, and the performance thereof is temperature dependent. Moreover, if the catalyst is active for thermal catalytic CO oxidation, this back-reaction can be avoided by optimizing the flow rate or the length of the catalytic bed. These findings should be considered when comparing different catalysts experimentally.

Chapter 7.

Overall conclusions and future outlook

This thesis investigates the use of plasma catalysis for greenhouse gas (GHG) conversion through computational simulation of the reaction kinetics. In the introduction (Chapter 1), we illustrated the complexity of plasma catalysis resulting from the different interactions that occur between the plasma and the catalyst. Subsequently, we explained the main equations and assumptions that form the basis of the kinetic models used throughout this thesis. In the following chapters, we discussed various reactions that convert CH_4, CO_2 or both into value-added chemicals, including CH_4 partial oxidation (Chapter 3), dry reforming of C_2H_6 (Chapter 4), dry reforming of CH_4 (Chapter 5), and CO_2 splitting (Chapter 6).

In the introduction we covered various physical and chemical effects that happen due to interaction between the plasma and the catalyst. Physical effects are mostly related to changes in the discharge behavior due to introduction of a catalyst or support packing into the plasma. Indeed, the discharge behavior is influenced by various properties of the catalyst and reactor setup, among others the dielectric constant of the packing,[40,41] the dimensions of the packing beads[50] and discharge gap,[49] as well as the type and amount of the catalyst nanoparticles loaded on the support.[40,46,47] By altering the discharge type from localized microdischarges to surface discharges, the aforementioned parameters determine the contact between the plasma and the catalyst. Moreover, they also affect the electric field and thus the electron temperature, the plasma chemistry, as well as the position of the partial chemical equilibrium. Hence, different packings evolve to other partial chemical equilibria at different rates and thus perform differently depending on the gas residence time.[69] Additionally, other material properties like porosity can be used to tune the contact between the plasma and the catalyst.[57] Hence, comparison between different support packings and catalysts in experimental studies is far from straightforward. This stresses the need for standardized experimental setups and elaborate documentation of packing properties, to disentangle the various effects and make progress in this promising research field.

In addition to the complex interplay of physical effects, plasma catalysis encompasses many chemical interactions as well. For example, the plasma can weaken or break bonds in the reactants (i.e., via vibrational excitation or radicals, respectively) and thus facilitate the dissociation of the reactant molecules on the catalyst. Moreover, other surface reaction steps can be enhanced by radical adsorption or E-R reactions, depending on the number densities of the involved radicals near the catalyst surface. Hence, these chemical effects can enhance the reaction rates and consequently the product concentrations in the gas-phase, which can even reach values beyond the thermodynamic equilibrium.[72] As such, plasma catalysis enables to circumvent the scaling relation for bond dissociation that are normally present in thermal catalysis.[81]

This thesis focusses predominantly on these chemical interactions, specifically for plasma catalysis for GHG conversion into value-added chemicals. In Chapter 3, we studied how vibrationally excited CH_4 and O_2, as well as radicals and stable intermediates from the plasma, affect the surface chemistry of CH_4 partial oxidation on a Pt(111) surface. While both vibrational excitation and radicals enhance the turnover frequencies of this reaction, the effect of the latter clearly dominates. By varying the number densities of the different radicals and stable intermediates independently, we could pinpoint their influence on the reaction pathways and turnover frequencies of various products. We found that strongly dehydrogenated carbonaceous species (C, CH, C_2H_2) induce coking, while O radicals counteract coking but promote overoxidation to CO_2. Hence, the formation of both types of species should be balanced against each other, and strong dehydrogenation of carbonaceous species should be avoided. However, the presence of moderate amounts of less strongly dehydrogenated species (CH_3, CH_2) is beneficial as these bind the surface less strongly and give rise to H* formation. Yet, these species also cause surface coking when present in large amounts. High densities of H radicals are beneficial as these promote the final hydrogenation steps in the formation of CH_3OH and HCOOH on Pt(111). CH_3O and CH_3OO are identified as important precursors in the

formation of CH_3OH and CH_2O, and hence their presence improves the production of these oxygenates. Nevertheless, we also found that high radical densities in general lead to surface poisoning. As such, lowering the radical densities in general can improve the adsorption of more weakly binding radicals, like CH_3O and CH_3OO, which is beneficial to the formation of oxygenates.

In Chapter 4, we investigated the gas phase chemistry of C_2H_6 dry reforming in a DBD plasma using a 0D chemical kinetics model, to support the experimental work performed at Columbia University (NY, USA). Our simulations show that C_1-C_4 hydrocarbons and H_2 are produced through electron impact dissociation of C_2H_6, either directly or through recombination or disproportionation of the formed radicals. CO, on the other hand, is mainly produced through electron impact dissociation of CO_2. The conversion of both reactants, as well as the CO selectivity, rises with increasing plasma power, while the total hydrocarbon selectivity declines as these molecules partly react back to C_2H_6 at higher conversions.

Regarding oxygenates, we found that CH_2O is formed by reaction between CO_2 and a CH_2 radical. Its selectivity declines with rising plasma power and conversion, as it is either hydrogenated to CH_3OH, or dehydrogenated to CHO. The latter radical is also formed through oxidation of C_2H_4 by O, and it can recombine with CH_3 or C_2H_5 to form aldehydes (CH_3CHO and C_2H_5CHO, respectively). Since CH_3OH, CH_3CHO and C_2H_5CHO are formed from other products, their selectivities do not drop much with rising plasma power (and thus conversion). C_2H_5OH, however, is directly formed from recombination between C_2H_5 and OH (or first O and then H) radicals. Consequently, its selectivity drops with rising plasma power. Finally, the HCOOH selectivity rises with plasma power, as it is formed by oxidation of CH_2O and C_2H_5OH, thus indicating that longer acids are likely formed via oxidation of C_2 and C_3 alcohols and aldehydes, via a similar mechanism. Since the selectivity of some products declines with rising plasma power and conversion, it might

be difficult to achieve high yields for these species. Combining the plasma with a catalyst, might provide a solution to this issue, by improving the selectivity of these species at high conversion. Our predicted trends in reactant conversion and product selectivities align well with the experimental trends, and our simulations are useful to explain the mechanisms behinds these trends, to steer the experiments towards improved performance.

In Chapter 5, we first studied hydrogenation of plasma-produced CO on the catalyst as a mechanism for CH_3OH production in plasma-catalytic DRM. Using descriptor-based microkinetic modeling, we found that in the presence of syngas (CO/H_2), as well as CH_3, H and O radicals, CH_3OH is mainly formed through hydrogenation of CO by H radicals, which happens most easily on weakly binding metals, like Cu and Ag. Yet, we also found that the rate of CH_3OH formation is negligible compared to those of CH_4, CO_2, H_2O and H_2. Hence, the CO molecules and CH_3, H and O radicals produced in the plasma preferentially recombine to other, more stable molecules, meaning that the plasma species are not used efficiently.

Therefore, we subsequently developed a coupled plasma-surface model, which combines the surface kinetics model of Chapter 3 with a plasma kinetics model as presented in Chapter 4. Using this coupled model, we investigate plasma-catalytic DRM at DBD conditions, for four different cases, namely plasma without catalyst or combined with Rh, Cu and Ag. By comparing these results, we found that the combination of plasma with transition metals has mainly negative effects. Indeed, Ag efficiently recombines adsorbed CO* and O* back to CO_2, while Cu and to a lesser extent also Ag recombine CH_3* and H* back to CH_4, thus lowering the net conversion of CO_2 and CH_4, respectively. Moreover, both Ag and Cu use adsorbed H* atoms to form CH_4 and H_2O, thus reducing the net formation of H_2. Only Rh improves the formation of H_2, under the condition that the small H atoms can still adsorb while the surface is poisoned by larger species. Lastly,

our model suggests that the net CH_3OH production is negatively affected by the presence of transition metals for the conditions under study, as radicals that are lost from the plasma through adsorption on the catalyst are primarily directed towards the formation of other products (i.e., CO_2, CH_4, CO, H_2 or H_2O).

In Chapter 6, we studied the interaction of plasma species with a transition metal (Ag, Cu, Pd or Rh) or glass surface placed inside the afterglow of a low-pressure CO_2 discharge, by developing an improved coupled plasma-surface model with respect to Chapter 5, namely by integrating a Boltzmann solver for the electron impact reactions. We found that E-R reactions are likely important for O atom recombination on transition metals at temperatures ≤ 600 K, as L-H reactions alone cannot explain the high recombination coefficients (0.01-0.5) reported in literature. Our results show that O atom recombination via E-R not only facilitates O_2 formation, but due to removal of adsorbed O*, also enables adsorption and subsequent oxidation of CO on the catalyst. Moreover, at sufficiently high temperatures, transition metals become active for thermal catalytic CO oxidation, which converts CO and O_2 back to CO_2.

We found that Cu performs well for plasma-catalytic CO_2 splitting below 900-1000 K, as it efficiently recombines O atoms into O_2 at 500-900 K. Yet, it becomes thermally active for CO oxidation above 900 K, causing a strong drop in the net CO_2 conversion. Conversely, Ag performs badly at 500-600 K, as it recombines CO* with O* back to CO_2. Yet, with rising temperature the CO* coverage drops and Ag becomes the best catalyst for O atom recombination into O_2 above 1000 K. Pd is highly thermally active for CO oxidation above 500 K, making this catalyst detrimental for CO_2 splitting. Rh is neither very efficient at recombining O atoms into O_2 nor in thermal catalytic CO oxidation. Moreover, the optimal catalyst depends not only on temperature, but also on other operating parameters, like pressure and residence time.

Hence, this complex interplay makes comparison between different catalysts in experiments far from straightforward. Moreover, not only can the optimal catalyst change depending on the reaction conditions, but on top of this, physical effects add another layer of complexity. As such, a thorough understanding of the individual chemical and physical interactions in plasma catalysis is essential to further develop this technology. This is especially so, since the combination of plasma with a catalyst does not necessarily result in synergy, but can also negatively impact the conversion and product selectivity.

Future research should therefore focus on experimentally validating the various microkinetic modeling studies that have investigated the chemical interactions between plasma species (e.g., vibrationally excited molecules, radicals, stable intermediates) and transition metal catalysts. The insights provided by these experiments can then be used to update the models and *vice versa*. This requires carefully designed experiments that attempt to limit any physical interactions as much as possible, while covering a broad range of reaction conditions (e.g., temperature, pressure, plasma power, flow rate, gas mixture). Once extensive fundamental knowledge regarding these chemical interactions is achieved, it should be combined with existing insights into the physical effects to optimize reaction systems in which both types of interactions occur simultaneously.

Lastly, we would like to note that although the methods and models presented in this thesis are applied to CO_2 and CH_4 conversion, they can also be used to study plasma catalysis for other reactions, such as ammonia synthesis, nitrogen oxidation and VOC abatement, among others, provided that the data (i.e., enthalpy barriers and reaction rate coefficients) required to compile a chemistry set are available, of course. Hence, it would be interesting for future research to use the same modelling and experimental setup to study different reactions and validate the model for each of these separately. In this way, broad fundamental insights into the behavior of different reactions types (e.g.,

exothermic vs. endothermic) for a wide range of reaction conditions may be achieved, forming a solid foundation for further development of the plasma catalysis research field.

Indeed, most plasma catalysis applications are still in the early stages of development,[24] and a strong fundamental basis is needed to efficiently optimize experimental setups at laboratory conditions. Once the most favorable conditions at laboratory scale are identified, a scale-up to industrial level can be considered. For packed-bed DBD reactors, scale-up may be achieved by operating multiple DBD reactors parallel to each other, as is done, for example, in industrial ozone production.[20] Hence, the product yields and energy efficiencies obtained at laboratory scale can provide reliable estimates for those at industrial scale. To judge the economic validity of the process at industrial scale, techno-economic assessment (TEA) should be performed. A TEA also analyzes the main costs and revenues of the process and can thus serve as a guideline for development at laboratory scale, by identifying the main economic bottlenecks for scale-up. In this context, Lamberts-Van Assche *et al*.[259] performed a TEA for CO_2 splitting and DRM in a packed-bed DBD, based on earlier experimental results obtained in our group, by Uytdenhouwen *et al.*[69], and suggested that future experimental work should aim to improve the (low) energy efficiency (see also Chapter 6), as energy is a major cost factor, while revenues may be improved by targeting higher-value products. Hence, a TEA can identify *which* aspects of the experiments should be improved to make a plasma-catalytic process economically viable, while a thorough fundamental basis is needed to know *how* to improve these.

Appendix

A1. Appendix to Chapter 3

A1.1. The chemistry set and corresponding thermodynamic data

Table A1.1. List of reactions included in the model, for both thermal and plasma catalysis (plasma reactions listed separately), with the corresponding activation and reaction enthalpies on Pt(111) ($\Delta H^{\ddagger\circ}$ and ΔH°_{rxn}, respectively) and their associated references.[a)]

N°	Dissociative adsorption / Associative desorption	$\Delta H^{\ddagger\circ}$ (eV)	Ref.	ΔH°_{rxn} (eV)	Ref.
1	$CH_4(g) + 2* \rightleftharpoons CH_3* + H*$	0.63	185	-0.28	185
2	$O_2(g) + 2* \rightleftharpoons 2O*$	-0.07[a)]	260	-1.89[a)]	260
3	$H_2(g) + 2* \rightleftharpoons 2H*$	0.19	185	-0.67	185
4	$C_2H_6(g) + 2* \rightleftharpoons 2CH_3*$	1.09[b)]	261	-0.30[c)]	185
5	$HCOOH(g) + 2* \rightleftharpoons H* + COOH*$	0.22	262	-0.84	262
6	$HCOOH(g) + 2* \rightleftharpoons HCOO* + H*$	0.25[d)]	262	-0.45[e)]	
N°	**Molecular adsorption / desorption**	**$\Delta H^{\ddagger\circ}$ (eV)[f)]**	**Ref.**	**ΔH°_{rxn} (eV)**	**Ref.**
7	$C_2H_4(g) + * \rightleftharpoons CH_2CH_2*$	0.00	-	-1.51	185
8	$C_2H_2(g) + * \rightleftharpoons CHCH*$	0.00	-	-2.87	185
9	$CO(g) + * \rightleftharpoons CO*$	0.00	-	-1.41	263
10	$CO_2(g) + * \rightleftharpoons CO_2*$	0.00	-	-0.03	264
11	$H_2O(g) + * \rightleftharpoons H_2O*$	0.00	-	-0.22	263
12	$CH_3OH(g) + * \rightleftharpoons CH_3OH*$	0.00	-	-0.34	162
13	$CH_2O(g) + * \rightleftharpoons CH_2O*$	0.00	-	-0.50	265
N°	**Eley-Rideal reactions**	**$\Delta H^{\ddagger\circ}$ (eV)**	**Ref.**	**ΔH°_{rxn} (eV)**	**Ref.**
14	$CH_4(g) + OH* + * \rightleftharpoons CH_3* + H_2O*$	0.50	162	-0.86	162
15	$CH_4(g) + O* + * \rightleftharpoons CH_3* + OH*$	1.28	162	-0.13	162

N°	Langmuir-Hinshelwood reactions	$\Delta H^{\ddagger\circ}$ (eV)	Ref.	ΔH°_{rxn} (eV)	Ref.
16	$CH_3^* + * \rightleftharpoons CH_2^* + H^*$	0.83	[185]	0.07	[185]
17	$CH_2^* + * \rightleftharpoons CH^* + H^*$	0.17	[185]	-0.65	[185]
18	$CH^* + * \rightleftharpoons C^* + H^*$	1.29	[185]	0.47	[185]
19	$CH_3^* + O^* \rightleftharpoons CH_2^* + OH^*$	1.62	[162]	0.22	[162]
20	$CH_2^* + O^* \rightleftharpoons CH^* + OH^*$	1.44	[162]	-0.50	[162]
21	$CH^* + O^* \rightleftharpoons C^* + OH^*$	2.13	[162]	0.62	[162]
22	$CH_3^* + OH^* \rightleftharpoons CH_2^* + H_2O^*$	1.07	[162]	-0.51	[162]
23	$CH_2^* + OH^* \rightleftharpoons CH^* + H_2O^*$	0.31	[162]	-1.23[g)]	[162]
24	$CH^* + OH^* \rightleftharpoons C^* + H_2O^*$	0.77	[162]	-0.11[g)]	[162]
25	$CH_3^* + O^* \rightleftharpoons CH_3O^* + *$	2.04	[162]	0.34	[162]
26	$CH_2^* + O^* \rightleftharpoons CH_2O^* + *$	2.18	[162]	-0.29	[162]
27	$CH^* + O^* \rightleftharpoons CHO^* + *$	1.69	[162]	-0.42	[162]
28	$C^* + O^* \rightleftharpoons CO^* + *$	1.92	[162]	-1.84	[162]
29	$CH_3^* + OH^* \rightleftharpoons CH_3OH^* + *$	2.02	[162]	-0.18	[162]
30	$CH_2^* + OH^* \rightleftharpoons CH_2OH^* + *$	1.05	[162]	-0.75	[162]
31	$CH^* + OH^* \rightleftharpoons CHOH^* + *$	1.17	[162]	-0.42	[162]
32	$C^* + OH^* \rightleftharpoons COH^* + *$	1.08	[162]	-1.47	[162]
33	$CH_3OH^* + * \rightleftharpoons CH_2OH^* + H^*$	0.77	[162]	-0.50[g)]	[162]
34	$CH_2OH^* + * \rightleftharpoons CHOH^* + H^*$	0.63	[162]	-0.32[g)]	[162]
35	$CHOH^* + * \rightleftharpoons COH^* + H^*$	0.62	[162]	-0.58[g)]	[162]
36	$CH_3OH^* + * \rightleftharpoons CH_3O^* + H^*$	0.80	[162]	0.37[g)]	[162]
37	$CH_2OH^* + * \rightleftharpoons CH_2O^* + H^*$	0.99	[162]	0.31[g)]	[162]
38	$CHOH^* + * \rightleftharpoons CHO^* + H^*$	0.54	[162]	-0.15[g)]	[162]
39	$COH^* + * \rightleftharpoons CO^* + H^*$	0.84	[162]	-0.52	[162]
40	$CH_3O^* + * \rightleftharpoons CH_2O^* + H^*$	0.24	[162]	-0.56[g)]	[162]
41	$CH_2O^* + * \rightleftharpoons CHO^* + H^*$	0.14	[162]	-0.78[g)]	[162]
42	$CHO^* + * \rightleftharpoons CO^* + H^*$	0.36	[162]	-0.95	[162]

43	$2CH_2^* \rightleftharpoons CH_2CH_2^* + *$	1.59	[185]	-0.63	[185]
44	$2CH^* \rightleftharpoons CHCH^* + *$	1.78	[185]	0.71	[185]
45	$O^* + H^* \rightleftharpoons OH^* + *$	1.09	[264]	0.15	[264]
46	$OH^* + H^* \rightleftharpoons H_2O^* + *$	0.20	[264]	-0.58[g)]	[264]
47	$OH^* + OH^* \rightleftharpoons H_2O^* + H^*$	0.00	[264]	-0.73[g)]	[264]
48	$CO^* + O^* \rightleftharpoons CO_2^* + *$	1.07	[264]	0.14	[264]
49	$C^* + CO2^* \rightleftharpoons CO^* + CO^*$	0.00	[165]	-1.98[e)]	-
50	$CO^* + OH^* \rightleftharpoons COOH^* + *$	0.46	[264]	-0.24	[264]
51	$COOH^* + * \rightleftharpoons CO_2^* + H^*$	0.85	[264]	0.23[g)]	[264]
52	$COOH^* + O^* \rightleftharpoons CO_2^* + OH^*$	0.47	[264]	0.38[g)]	[264]
53	$COOH^* + OH^* \rightleftharpoons CO_2^* + H_2O^*$	0.10	[264]	-0.35	[264]
54	$CHO^* + O^* \rightleftharpoons CHOO^* + *$	1.03	[264]	-0.65	[264]
55	$HCOO^* + * \rightleftharpoons CO_2^* + H^*$	1.04	[264]	-0.16[g)]	[264]
56	$HCOO^* + O^* \rightleftharpoons CO_2^* + OH^*$	1.74	[264]	-0.01[g)]	[264]
57	$HCOO^* + OH^* \rightleftharpoons CO_2^* + H_2O^*$	1.01	[264]	-0.74	[264]
Specific plasma reactions					
N°	**Radical adsorption / desorption**	**$\Delta H^{\ddagger\circ}$ (eV)[f)]**	**Ref.**	**$\Delta H°_{rxn}$ (eV)**	**Ref.**
58	$CH_3(g) + * \rightleftharpoons CH_3^*$	0.00	-	-2.16	[185]
59	$CH_2(g) + * \rightleftharpoons CH_2^*$	0.00	-	-4.12	[185]
60	$CH(g) + * \rightleftharpoons CH^*$	0.00	-	-7.31	[185]
61	$C(g) + * \rightleftharpoons C^*$	0.00	-	-7.05	[185]
62	$O(g) + * \rightleftharpoons O^*$	0.00	-	-3.93	[264]
63	$H(g) + * \rightleftharpoons H^*$	0.00	-	-2.74	[264]
64	$OH(g) + * \rightleftharpoons OH^*$	0.00	-	-2.44	[264]
65	$CH_3O(g) + * \rightleftharpoons CH_3O^*$	0.00	-	-1.43[h)]	[266]
66	$CHO(g) + * \rightleftharpoons CHO^*$	0.00	-	-2.66	[264]
67	$OOH(g) + * \rightleftharpoons OOH^*$	0.00	-	-1.06	[267]
68	$CH_3OO(g) + * \rightleftharpoons CH_3OO^*$	0.00	-	-1.06[i)]	-

69	COOH(g) + * ⇌ COOH* [j]	0.00	-	-2.59	[264]
70	HCOO(g) + * ⇌ HCOO* [j]	0.00	-	-2.42	[264]
N°	**Langmuir-Hinshelwood reactions**	**$\Delta H^{\ddagger\circ}$ (eV)**	**Ref.**	**ΔH°_{rxn} (eV)**	**Ref.**
71	OOH* + * ⇌ OH* + O*	0.14	[267]	-1.25	[268]
72	CH_3OO* + * ⇌ CH_3O* + O*	0.14 [i]	-	-1.25 [i]	-
N°	**Eley-Rideal reactions** [k]	**$\Delta H^{\ddagger\circ}$ (eV)** [k]	**Ref.**	**ΔH°_{rxn} (eV)**	**Ref.**
73	CH_3(g) + O* ⇌ CH_3O*	-	-	-1.82 [e]	-
74	H(g) + O* ⇌ OH*	-	-	-2.59 [e]	-
75	O(g) + C* ⇌ CO*	-	-	-5.77 [e]	-

a) *Empty surface sites are denoted by '*'. However, not all species adsorb on the same type of site. The '*' thus represents the fraction of the empty surface, rather than the fraction of a specific type of sites.*

b) *For convenience, the data for molecular adsorption of O_2 and dissociation of O_2*, reported in ref. [260], are combined in one dissociative adsorption reaction. Because the enthalpy barrier for dissociation is lower than the adsorption enthalpy, the resulting enthalpy of activation has a negative value. This is not a problem as long as the total Gibbs free energy barrier is positive, which is the case for all temperatures above 81 K. The reaction enthalpy is calculated as the sum of the reaction enthalpies of the adsorption of O_2 and the dissociation of O_2*.*

c) *Calculated using Brønsted-Evans-Polanyi relation for C-C cleavage from ref. [261].*

d) *The reaction enthalpy is calculated from the enthalpies of the other reactions reported in ref. [185].*

e) *Recalculated from the enthalpy of the reverse reaction from ref. [262] and the reaction enthalpy used in our model.*

f) *The reaction enthalpy is calculated based on those of other reactions included in the chemistry set to ensure thermodynamic consistency.*

g) *Molecular and radical adsorption processes are assumed to occur without enthalpy barrier.*

h) *The reaction enthalpies are changed by 0.01 eV to ensure thermodynamic consistency.*

i) *Calculated using scaling relation from ref. [266] and the OH adsorption enthalpy.*

j) *As no data is available for CH_3OO, the data of OOH is used as an approximation.*

k) *Adsorption of COOH and HCOO are only included in the simulations that investigate the effect of these particular species.*

l) *These reactions are only included when explicitly mentioned and their enthalpy barriers are varied during the simulation.*

As indicated in Table A1.1, we combine the data for O_2 adsorption and O_2* dissociation from ref. [260] into one dissociative adsorption reaction, as this is more convenient for the implementation of O_2 vibrational excitation. The limit for lowering the Gibbs free energy barrier of this combined reaction due to vibrational excitation is set to 0.56 eV, which is the enthalpy barrier for dissociation of adsorbed O_2* reported in ref. [260]. Thus, the Gibbs free energy is reduced by αE_v if $\alpha E_v < 0.56$ eV or by 0.56 eV if $\alpha E_v \geq 0.56$ eV. The value of the Fridman-Macheret α parameter (see next section) is calculated using the forward (0.56 eV)[260] and reverse (1.82 eV)[260] barriers for the dissociation of adsorbed O_2* (i.e. α = 0.24). If the calculated Gibbs free energy barrier is smaller than the barrier for O_2 adsorption (corresponding to the loss of 1/3 of the translational entropy), the latter is used instead. This is done to make sure there is always a non-zero barrier for this process. Using the approximations above, O_2 is assumed to either immediately dissociate after adsorption, before thermalization of T_{vib} with the surface can occur, or to desorb back to the gas phase.

A1.2. The effect of vibrational excitation

The effect of vibrationally excited CH_4 and O_2 is accounted for by modifying the enthalpy barrier of their dissociative adsorption processes and the E-R reactions between gaseous CH_4 and surface-bound OH* or O* (see Table A1.1., reactions 14 and 15). The forward rate coefficient of a reaction starting from a vibrationally excited CH_4 or O_2 molecule with vibrational level v is calculated according to:[84]

$$k_{f,v} = \frac{k_b T}{h} \exp\left(\frac{\Delta S^{\ddagger\circ}}{R}\right) \exp\left(-\frac{\Delta H^{\ddagger\circ} - \alpha E_v}{RT}\right) = k_f \exp\left(\frac{\alpha E_v}{RT}\right) \qquad \text{Eq. A1.1}$$

If $\Delta H^{\ddagger\circ} > \alpha E_v$,

and:

$$k_{f,\nu} = \frac{k_b T}{h} \exp\left(\frac{\Delta S^{\ddagger}}{R}\right) = k_f \exp\left(\frac{\Delta H^{\ddagger}}{RT}\right) \qquad \text{Eq. A1.2}$$

If $\Delta H^{\ddagger\circ} \leq \alpha E_v$.

Where E_v is the energy of the vibrational level v and α is the parameter of the Fridman-Macheret model, which denotes how efficiently the energy of a certain vibrational excitation can lower the energy barrier:[20]

$$\alpha = \frac{\Delta H_f^{\ddagger\circ}}{\Delta H_f^{\ddagger\circ} + \Delta H_r^{\ddagger\circ}} \qquad \text{Eq. A1.3}$$

With $\Delta H_f^{\ddagger\circ}$ and $\Delta H_r^{\ddagger\circ}$ the activation enthalpies of the reaction in the forward and reverse direction, respectively. The Fridman-Macheret model is supported by the high efficiency factors that are observed for strong endothermic reactions, whose activation barriers are close to the reaction enthalpy, and the low efficiency factors associated with strong exothermic reactions, which generally have low activation barriers.[20]

The energy levels of the vibrational overtones are estimated using the harmonic approximation. For CH_4 only the symmetric (ν_1) and asymmetric (ν_3) stretch modes are considered, as the bending modes (ν_2 and ν_4) are less effective in breaking the C-H bond.[269] Additionally, we assume that the dissociation barrier is influenced by the total energy $E_{v,stretch}$ allocated in all stretch modes, i.e. we use $E_v = E_{v,stretch}$ in Eq. A1.1 and Eq. A1.2. The population of the vibrational levels is assumed to follow a Boltzmann distribution:[174,269]

$$P(\nu) = \frac{g(\nu) \cdot \exp\left(\frac{-E_\nu}{k_b T_{vib}}\right)}{\sum_{\nu'=0}^{\nu_{max}} g(\nu') \cdot \exp\left(\frac{-E_{\nu\prime}}{k_b T_{vib}}\right)} \qquad \text{Eq. A1.4}$$

Where $P(v)$ is the fractional population of a vibrational level v with energy E_v and degeneracy $g(v)$ at a vibrational temperature T_{vib}. The denominator gives the total partition sum over all levels that are considered, i.e. from the ground level to v_{max}. For O_2, which has only one vibrational mode, the level degeneracy $g(v)$ is always equal to one and E_v is equal to the energy of the vibrational state. However, the situation is more complicated for CH_4 which has one symmetric stretch (v_1), two doubly degenerate bending (v_2), three triply asymmetric stretch (v_3) and three triply degenerate bending modes (v_4). The population of a vibrational state (v_1, v_2, v_3, v_4) for which the vibrational quantum numbers v_i of the four fundamental modes are specified can be calculated as described by Butterworth *et al.*:[174]

$$P(\nu_1, \nu_2, \nu_3, \nu_4) = \prod_{i=1,2,3,4} \frac{g_i(\nu_i) \cdot \exp\left(\frac{-E_i}{k_b T_{vib}}\right)}{Q_i(T_{vib})} \qquad \text{Eq. A1.5}$$

Where $g_i(v_i)$ is the level degeneracy per mode, E_i is the level energy per mode and $Q_i(T_{vib})$ is the mode partition sum. As discussed above, we make the approximation that the dissociation barrier is affected by the total energy allocated to the stretch modes of a given vibrational state, but not by the energy allocated to the bending modes. Under these conditions, all vibrational states (ν_1, ν_2, ν_3, ν_4) for which $\nu_1 + \nu_3 = \nu_{stretch}$ and ν_2, $\nu_4 \in [0, +\infty[$ experience the same modified rate constant for dissociation (see Eq. A1.1 and Eq. A1.2). Additionally, the frequencies of the symmetric (ν_1) and asymmetric (ν_3) stretch modes are relatively close (2916 cm^{-1} and 3019 cm^{-1}, respectively).[269] Therefore, we treat the one ν_1 and the three ν_3 modes as four modes with the same vibrational frequency.[174] This frequency is set equal to the weighted average of the vibrational frequencies of these modes (2993 cm^{-1}). The combined population density $P_{comb}(v_{stretch})$ for all states which experience the same modified rate constant is then calculated as:

$$P_{comb}(\nu_{stretch}) = \frac{g_{stretch}(\nu_{stretch}) \cdot \exp\left(\frac{-E_{\nu,stretch}}{k_b T_{vib}}\right)}{\sum_{\nu'_{stretch}=0}^{\nu_{max}} g_{stretch}(\nu'_{stretch}) \cdot \exp\left(\frac{-E_{\nu',stretch}}{k_b T_{vib}}\right)} \quad \text{Eq. A1.6}$$

Where $g_{stretch}(\nu_{stretch})$ is the level degeneracy for the stretch modes when these are considered together and $E_{\nu,stretch}$ is the total energy allocated in the stretch modes. We calculate $g_{stretch}(\nu_{stretch})$ as the number of ways that $\nu_{stretch}$ number of vibrational quanta can be distributed over the four stretch modes:

$$g_{stretch}(\nu_{stretch}) = \binom{3+\nu_{stretch}}{\nu_{stretch}} = \frac{(3+\nu_{stretch})!}{\nu_{stretch}!\,3!} \quad \text{Eq. A1.7}$$

From the modified rate constant and the populations, the total modified forward rate constant k_f' for all vibrational levels is calculated as:

$$k_f{}' = \sum_{\nu} k_{f,\nu} P(\nu) \quad \text{Eq. A1.8}$$

With $\nu = \nu_{stretch}$ and $P(\nu) = P_{comb}(\nu_{stretch})$ in the case of CH_4.

Because the harmonic approximation does not account for the decrease in energy difference between vibrational levels upon increasing level, we use a cut-off for the number of levels included in the model. For CH_4, the first 12 vibrationally excited levels are included ($\nu_{max} = 12$), as the 12th level has an energy roughly equal to the C-H bond energy in CH_4. In the case of O_2, the first 26 vibrationally excited levels are considered ($\nu_{max} = 26$), as the energy of the 26th level is closest to the bond energy in O_2.

Note that the Fridman-Macheret α model (i.e., Eq. A1.1) is only approximate as it introduces fundamental errors against thermodynamics. When vibrational excitation by the plasma is negligible, the gas and vibrational temperatures are in thermal equilibrium, i.e. $T_{gas} = T_{vib}$, and the rate coefficient for dissociative adsorption should become equal to k_f (i.e., the unmodified rate coefficient). However, Eq. A1.1 is only equal to k_f for $E_v = 0$, i.e., when the molecule is in its vibrational ground state, and this means that k_f' in Eq.

A1.8 only becomes equal to k_f if all molecules are in the vibrational ground state. This is of course not physical, because at thermal equilibrium the population of the vibrational levels should follow a Boltzmann distribution at T_{gas}.

Moreover, the Fridman-Macheret α model is based on Polanyi's rules, which state that vibrational energy is more efficient in traversing "late" reaction barriers. The α parameter in the Fridman-Macheret model estimates this efficiency and hence the lateness of the reaction barrier from the ratio between the forward and reverse barriers (see Eq. A1.3). However, it is not guaranteed that the ratio between the barriers is related to the position of the transition state. Moreover, depending on the reaction, different vibrational modes can have significantly different reactivities. Yet, the Fridman-Macheret model only contains one efficiency factor α and hence does not consider mode specificity. Furthermore, the Fridman-Macheret model assumes that the efficiency of the vibrational modes in traversing the reaction barrier is independent of other degrees of freedom (DOF's). Yet, in practice different DOF's (e.g., vibrational, rotational, translational) can interact, which can result in enhanced efficiencies if multiple DOF's are excited simultanously.[270]

Recently, Gerrits *et al*.[270] developed a model that improves upon the Fridman-Macheret approach. This new model calculates the vibrational efficacy η^{fit}, which replaces α in Eq. A1.1. The method relies on the forward activation barrier of the reaction $\Delta H_f^{\ddagger\circ}$, the ratio of the length of the dissociating bond between the transition state and the reactant ($R_{\ddagger}/R_{gas}$) and the sudden vector projection (SVP) approach. The ratio ($R_{\ddagger}/R_{gas}$) serves as an indicator of the "lateness" of the activation barriers, while the SVP approach calculates the overlap between the vibrational modes of the gas phase reactant and the reaction coordinate at the transition state. Hence, the SVP approach is used to incorporate a measure of vibrational mode specificity for polyatomic molecules.

The vibrational efficacies can then be calculated as:

$$\eta^{fit} = a_1 \Delta H_f^{\ddagger\circ} \left(\frac{R_{\ddagger}}{R_{gas}} \right) \mathrm{erf}\big(a_2 (SVP + a_3)\big) \qquad \text{Eq. A1.9}$$

In which erf is the error function and a_1, a_2 and a_3 are parameters determined by fitting to vibrational efficacies acquired from molecular dynamics (MD) simulations. This method was found to agree significantly better to vibrational efficacies calculated with MD (R^2 = 0.52) than the Fridman-Macheret approach does (R^2 = -0.35).[270] Therefore, more recent works within our research group,[271] use the approach of Gerrits *et al*. However, this method was not yet developed when we published the research presented in Chapter 3, and therefore we still used the Fridman-Macheret approach in this work.

A1.3. Comparison of the thermal-catalytic pathways with literature

Figure 3.1 (a) in section 3.3.1 describes the overall reaction pathways towards the main products for thermal-catalytic POX of CH_4 at 500 K using a 70/30 CH_4/O_2 mixture. These calculations are performed at 500 K, so that the results can serve as a benchmark for the plasma case, which are simulated at conditions relevant for a DBD. In this section, we compare the reaction pathways from Figure 3.1 (a) to pathways calculated for a temperature that is relevant for thermal-catalytic POX of CH_4, i.e. 1000 K. These pathways are displayed in Figure A1.1. Additionally, we also compare our results to earlier microkinetic studies by Aghalayam *et al.*[164] and Mhadeshwar *et al.*[165] The results of Aghalayam *et al.* are calculated at 800 K and for a mixture of 10% CH_4 in air.[164] Those of Mhadeshwar *et al.* are calculated at 1123 K and for a mixture of 2% CH_4, 1.8% O_2 and 96.2% N_2.[165]

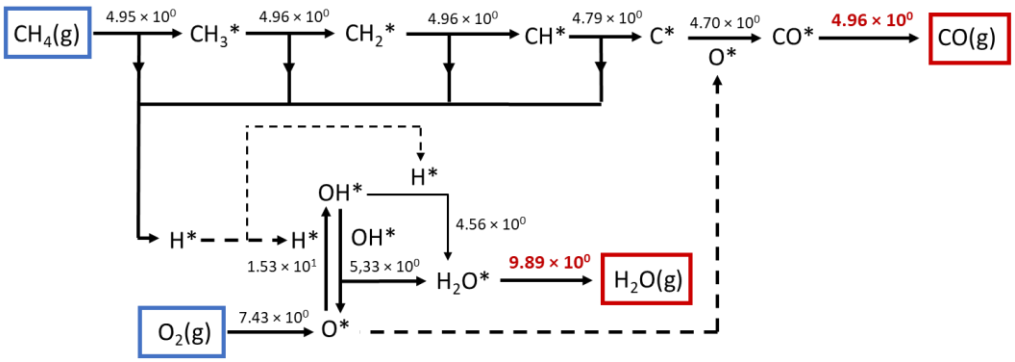

Figure A1.1 Most important reaction pathways at steady state for thermal-catalytic POX of CH_4 on Pt(111) using a CH_4/O_2 (70/30) gas mixture at 1000 K and 1 bar. The values of the reaction TOFs in (s^{-1}) are displayed next to the arrows. The arrow thickness indicates the relative importance of a reaction. A dotted arrow indicates the species is used as a second reactant in another reaction.

The reaction pathways at 500 K (Figure 3.1 (a) in Chapter 3) and at 1000 K (Figure A1.1) are largely similar. Under both conditions, the activation of CH_4 occurs through dissociative adsorption on empty sites, followed by dehydrogenation of CH_3* and CH_2* by empty surface sites. In contrast, the models by Aghalayam *et al.*[164] and Mhadeshwar *et al.*[165] predict that CH_x* dehydrogenation occurs mainly via an O* assisted route. However, these models are based on the less accurate bond order conservation theory, which predicts lower activation barriers for the O* assisted route, while various DFT studies found that for Pt the O* assisted route has higher barriers.[153,162,272] At 1000 K, CH* is dehydrogenated through interaction with an empty site and the formed C* is subsequently oxidized to CO*. Aghalayam *et al.*[164] and Mhadeshwar *et al.*[165] instead reported that CH* mainly reacts with O* to form CO* and H* via a direct route. At 500 K, we find that CH* dissociation and subsequent C* oxidation is only a secondary route, as CH* mainly (90.5%) reacts with O* to form CHO*. This is likely a result of the higher O* coverage at this temperature. The formed CHO* subsequently decomposes to CO* and H*. Note that this route is similar to the one reported by Aghalayam *et al.*[164] and Mhadeshwar *et al.*[165] as the formation of CO* from CH* occurs through interaction between CH* and O* and does not go via C*. Aghalayam *et al.*[164] and Mhadeshwar *et*

al.[165] both reported that CO* is further oxidized to CO_2*. As is discussed in the next section, we find that the importance of this reaction depends on the presence of small amounts of CO in the gas phase and on the temperature. In accordance with Mhadeshwar *et al.,*[165] we find that H_2O* is formed through disproportionation of two OH* species. Yet, at 1000 K, we find that the hydrogenation of OH* is only slightly less important (46.1%) for the formation of H_2O* than the disproportionation of OH* species, which forms 53.8% of H_2O*.

A1.4. Effect of CO on CO_2 selectivity in thermal POX of CH_4

There exists a discussion in literature about whether syngas formation via POX of CH_4 in thermal catalysis occurs via a direct or an indirect mechanism. The direct mechanism claims that CO and H_2 are mainly formed directly from CH_4 and O_2. The indirect mechanism assumes that two zones are present in the reactor: an oxidation zone at the start of the reactor and a successive reforming zone. In the oxidation zone, O_2 is consumed in the total oxidation of CH_4, to primarily form CO_2 and H_2O. In the subsequent reforming zone, where O_2 has been depleted, the formed CO_2 and H_2O react with the remaining CH_4 via dry and steam reforming, respectively, to form syngas.[168] Based on whether a direct, indirect or intermediate mechanism occurs, we can thus expect either syngas, complete oxidation products or a mixture of both, as the main products in the presence of O_2. The more recent studies on thermal-catalytic POX of CH_4 on Pt seem to support either the indirect[164,165,169] or intermediate mechanism.[19,166,168] However, at the relatively low temperature of 500 K of our simulations, H_2O and CO_2 are the thermodynamically favored products according to thermodynamic equilibrium calculations. We could thus expect the formation of CO_2 to be favored over that of CO. The fact that our model does not predict this, however, can be attributed to the zero conversion conditions.

Figure A1.2 illustrates that the presence of small fractions of CO (0.1-0.001%) in a CH_4/O_2 gas mixture causes CO_2 to become the main product at temperatures below 1000 K. This shows that the formation of CO_2 in the thermal POX of CH_4 depends on the presence of small quantities of CO in the gas phase. High CO content and low temperature favor CO_2, while low CO content and high temperature favor CO. Note that other products, e.g. H_2, H_2O and CO_2, will also form and accumulate in the gas phase, which will further influence the selectivities towards CO and CO_2. To make more accurate predictions on which product is favored under the different reaction conditions, a reactor model is required that considers the change in gas phase composition, based on product formation.

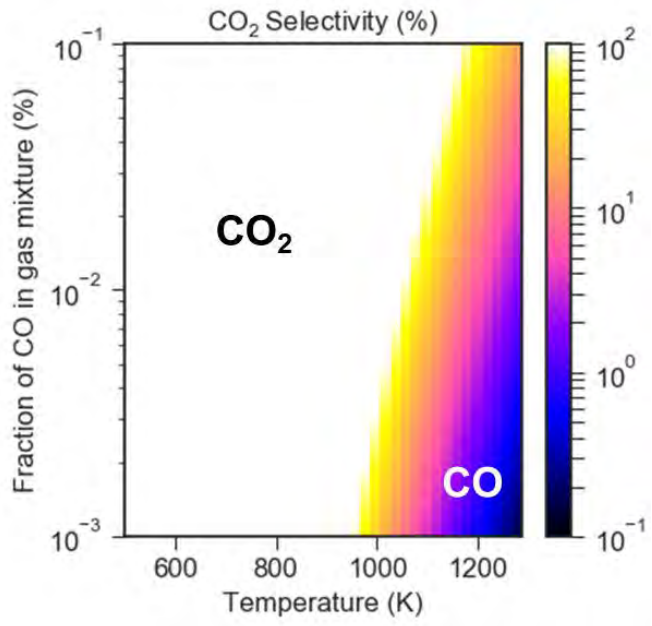

Figure A1.2. The influence of small fractions of CO in a CH_4/O_2 (70/30) gas mixture and of temperature on the CO_2 selectivity in (%) for thermal-catalytic POX of CH_4 on Pt(111). Calculated at steady-state and for a total pressure of 1 bar.

A1.5. Influence of vibrational excitation on the surface coverages

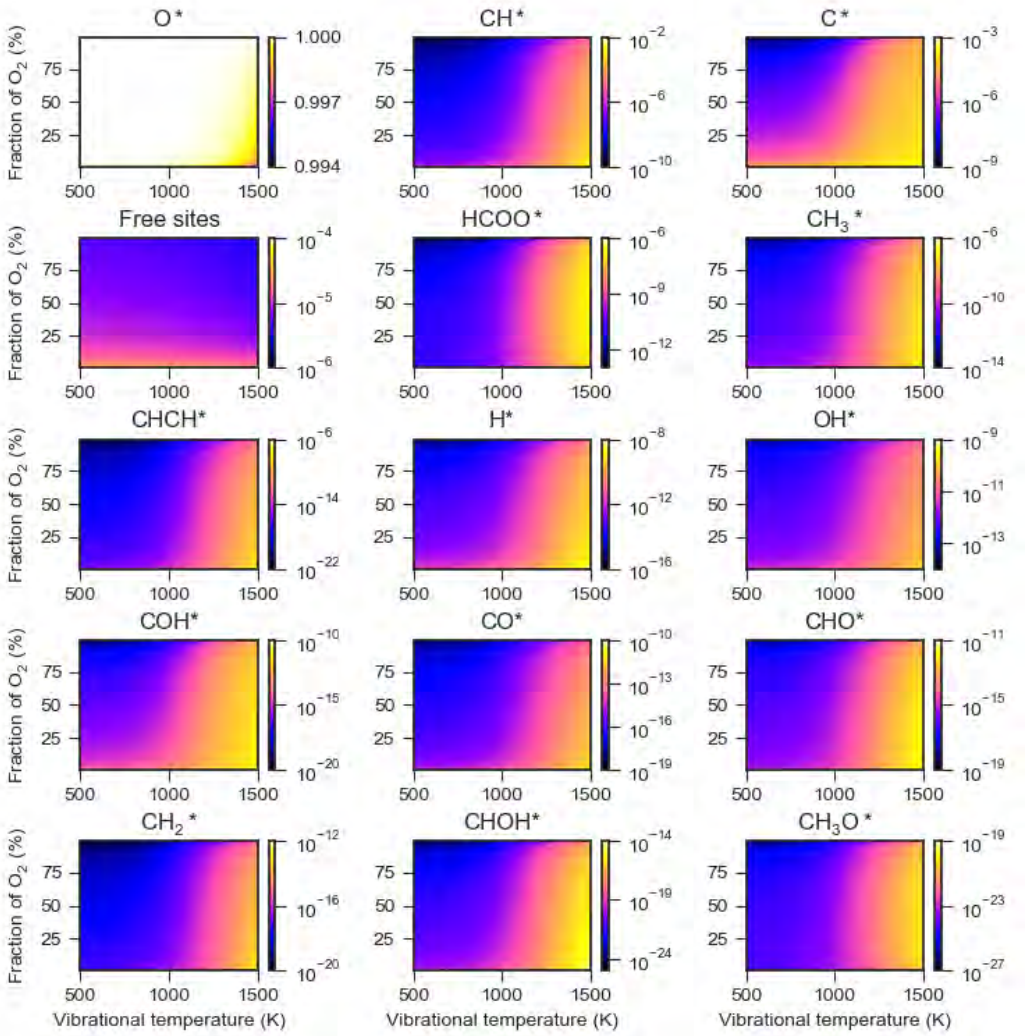

Figure A1.3. Influence of the vibrational temperature and O_2 content on the fractional coverages of the 14 most abundant surface species, as well as the fraction of free sites. Calculated at steady state for a CH_4/O_2 mixture at a pressure of 1 bar and a surface temperature of 500 K. Note that linear scaling is used for the O coverage, while logarithmic scaling is used for the other surface coverages.*

Figure A1.3 shows the surface coverages of the 14 most abundant surface species, as well of the fraction of free sites, when varying the vibrational temperature between 500 and 1500 K and the O_2 content between 1 and 99%. O* species cover almost the whole surface for the entire range of investigated conditions, but its coverage decreases slightly when lowering the O_2 content or increasing the vibrational temperature. The fraction of free sites mainly depends on the O_2 content in the gas mixture and increases upon decreasing O_2 fraction. The coverages of the other species increase with rising vibrational temperature, while many also show some dependency on the O_2 fraction.

A1.6. Influence of vibrational excitation on the selectivities of C_2H_4 and C_2H_2

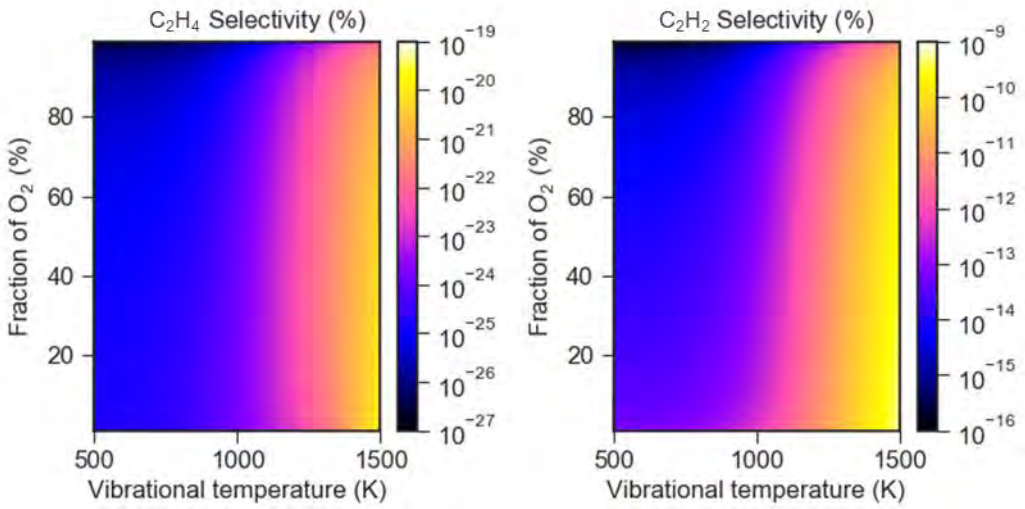

Figure A1.4. Influence of the vibrational temperature and O_2 content on the selectivities of C_2H_4 and C_2H_2. Calculated at steady state for a CH_4/O_2 mixture at a pressure of 1 bar and a surface temperature of 500 K.

A1.7. Effect of vibrational excitation in the presence of radicals

Figure A1.5 illustrates the effect of the vibrational temperature of CH_4 and O_2 on the TOFs of the products and reactants, when radicals are present in the gas phase. All TOFs, except that of CH_4 dissociation, remain constant as the vibrational temperature rises from 500 to 1500 K. This indicates that in the presence of radicals, vibrational excitation of CH_4 and O_2 has only a negligible effect on the surface chemistry, and consequently that the surface chemistry is mainly governed by the plasma radicals. While the TOF of CH_4 dissociation does change when the vibrational temperature rises above 1000 K, this does not affect the TOFs of any other reactants or products. Below 1160 K, CH_4 is net formed at the surface, as its dissociation products from the plasma, i.e. CH_3* and H*, adsorb onto the surface and recombine to form CH_4. At higher temperatures, the dissociation of vibrationally excited CH_4 becomes more important, resulting in a net consumption of CH_4 at the surface. Note that the CH_4 dissociation TOFs at the catalyst surface are low for these conditions. Therefore, CH_4 conversion will mainly occur in the plasma, resulting in the formation of reactive radicals that react much faster at the surface.

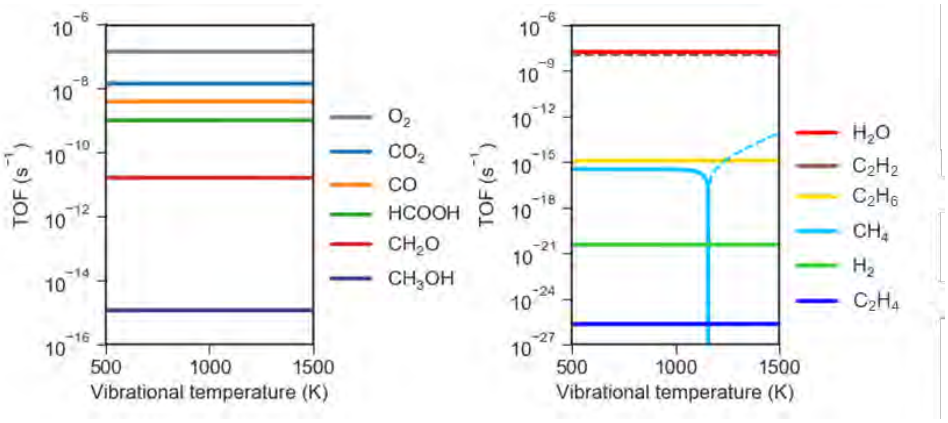

Figure A1.5. Effect of the vibrational temperature on the TOFs of products and reactants when radicals are present in the gas phase. Dotted lines indicate consumption, whereas full lines indicate production. Calculated for a temperature of 500 K and a total pressure of 1 bar. The partial pressures used in the simulations are listed in section 3.3.3, Table 3.1.

A1.8. Effect of OH and OOH radicals on TOFs and surface coverages

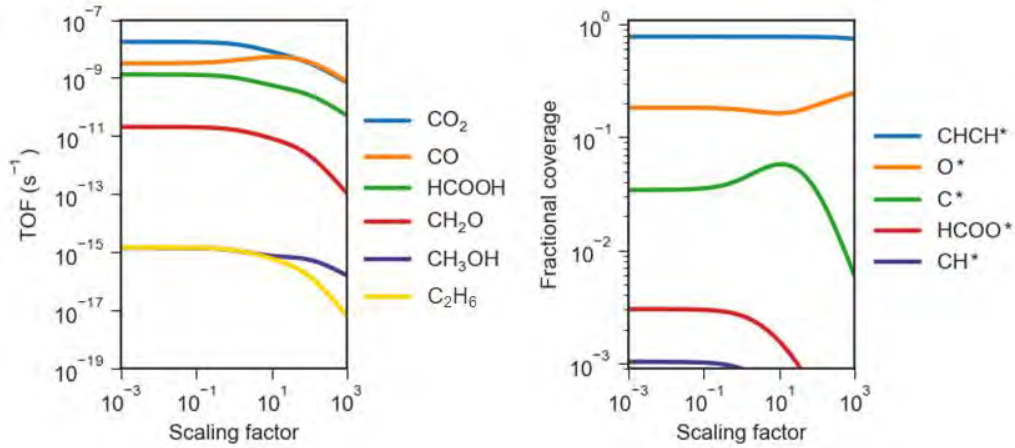

Figure A1.6. Influence of the OH and OOH partial pressures on TOFs (left) and surface coverages (right). Calculated for a temperature of 500 K and a total pressure of 1 bar. The species partial pressures used in the simulations are listed in section 3.3.3, Table 3.1, but the partial pressures of OH and OOH are varied by the indicated scaling factor.

A1.9. Effect of HCOO and COOH radicals on TOFs and surface coverages

As mentioned before, we estimated the partial pressures of the various plasma species based on the densities calculated by De Bie *et al.*[157] (see Table 3.1 in section 3.3.3). However, the model by De Bie *et al.* does not include HCOO and COOH radicals. Yet, these species might also have an important influence on the surface chemistry. In this section, we therefore briefly discuss their potential effect. To investigate this, we include the adsorption and desorption of these species in the chemistry set and choose a low value of 10^{-13} bar for their partial pressures, so that these radicals do not influence the rest of the surface chemistry. We then separately increase their partial pressures by up to a factor 10^{6}, i.e. up to a maximum partial pressure of 10^{-7} bar.

The resulting variations in TOFs and surface coverages are displayed in Figure A1.7 and Figure A1.8 for HCOO and COOH, respectively. Enhanced adsorption of HCOO leads to a higher formation of CO_2 and HCOOH, according to the pathways in Figure 3.4 of section 3.3.3.1. The higher CO_2* formation enhances CO production via the reverse Boudouard reaction, while the higher consumption of H* upon hydrogenation of HCOO* hampers CH_3OH formation. A higher partial pressure of COOH also favors the production of CO_2 through hydrogen abstraction from the adsorbed COOH* by O*. This also leads to a higher TOF of CO, caused by the reverse Boudouard reaction. Thus, HCOO and COOH radicals mainly result in additional formation of unwanted CO_2 and CO, and their formation in the plasma should therefore be limited. On the other hand, the formation of HCOO in the plasma might be beneficial if HCOOH is the desired product.

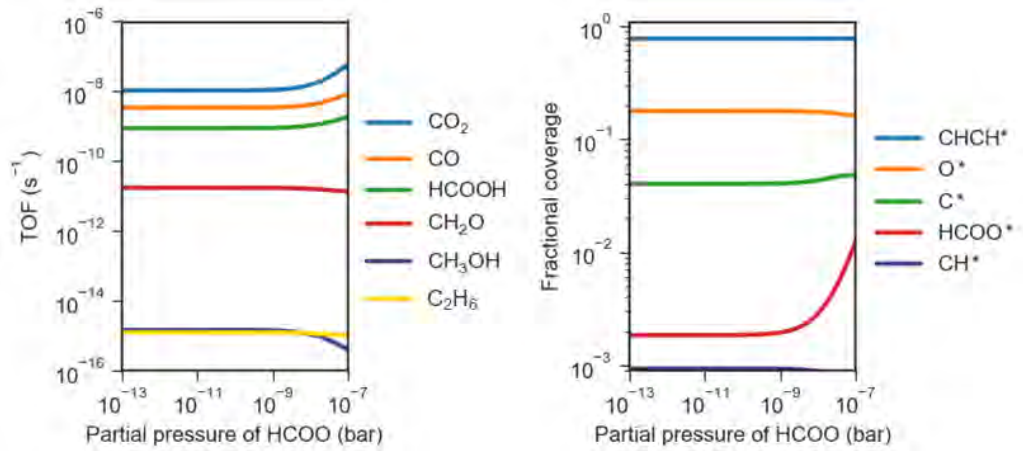

Figure A1.7. Influence of the HCOO partial pressure on TOFs (left) and surface coverages (right). Calculated for a temperature of 500 K and a total pressure of 1 bar. The partial pressure of HCOO is varied throughout the simulation, the partial pressure of COOH is kept constant at 10^{-13} bar. The other partial pressures are listed in section 3.3.3, Table 3.1.

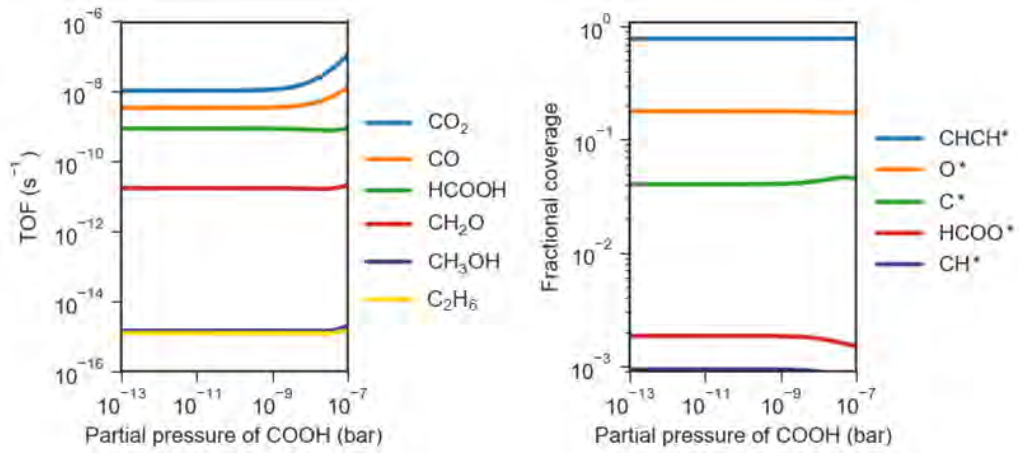

Figure A1.8. Influence of the COOH partial pressure on TOFs (left) and surface coverages (right). Calculated for a temperature of 500 K and a total pressure of 1 bar. The partial pressure of COOH is varied throughout the simulation, the partial pressure of HCOO is kept constant at 10^{-13} bar, and the other partial pressures are listed in section 3.3.3, Table 3.1.

A2. Appendix to Chapter 4

A2.1. Revised electron impact cross sections

Table A2.1. Overview of the electron impact processes for which the cross sections have been revised as compared to earlier modeling studies from our research group.[196–199] *For the electron impact dissociation reactions of C_2H_6, C_2H_4, C_3H_8, and C_3H_6, the cross sections for excitation to the indicated electronically excited states were used and the excited states were assumed to dissociate according to the indicated branching ratios.*

Reaction			Ref.
$CO_2 + e^- \rightarrow CO + O + e^-$			44
$CO_2 + e^- \rightarrow CO(E_1) + O + e^-$			44
Reaction	**Branching Ratio**	**From excited state**	**Ref.**
$C_2H_6 + e^- \rightarrow C_2H_4 + H_2 + e^-$	0.46	$C_2H_6(E_1)$, $C_2H_6(E_2)$	203,273
$C_2H_6 + e^- \rightarrow C_2H_5 + H + e^-$	0.24	$C_2H_6(E_1)$, $C_2H_6(E_2)$	203,273
$C_2H_6 + e^- \rightarrow C_2H_2 + 2H_2 + e^-$	0.11	$C_2H_6(E_1)$, $C_2H_6(E_2)$	203,273
$C_2H_6 + e^- \rightarrow CH_3 + CH_3 + e^-$	0.08	$C_2H_6(E_1)$, $C_2H_6(E_2)$	203,273
$C_2H_6 + e^- \rightarrow CH_4 + CH_2 + e^-$	0.07	$C_2H_6(E_1)$, $C_2H_6(E_2)$	203,273
$C_2H_6 + e^- \rightarrow C_2H_3 + H_2 + H + e^-$	0.04	$C_2H_6(E_1)$, $C_2H_6(E_2)$	203,273
$C_2H_4 + e^- \rightarrow C_2H_2 + H_2 + e^-$	1.00	$C_2H_4(E_1)$	203,274
$C_2H_4 + e^- \rightarrow C_2H_2 + H_2 + e^-$	0.30	$C_2H_4(E_2)$	203,274
$C_2H_4 + e^- \rightarrow C_2H_3 + H_2 + e^-$	0.40	$C_2H_4(E_2)$	203,274
$C_2H_4 + e^- \rightarrow C_2H_2 + 2H + e^-$	0.20	$C_2H_4(E_2)$	203,274
$C_2H_4 + e^- \rightarrow CH_4 + C + e^-$	0.10	$C_2H_4(E_2)$	203,274
$C_2H_4 + e^- \rightarrow C_2H + H_2 + H + e^-$	0.40	$C_2H_4(E_3)$	203,274
$C_2H_4 + e^- \rightarrow CH_3 + CH + e^-$	0.30	$C_2H_4(E_3)$	203,274
$C_2H_4 + e^- \rightarrow 2CH_2 + e^-$	0.30	$C_2H_4(E_3)$	203,274
$C_3H_8 + e^- \rightarrow C_3H_6 + H_2 + e^-$	0.34	$C_3H_8(E_1)$, $C_3H_8(E_2)$	275
$C_3H_8 + e^- \rightarrow C_2H_4 + CH_4 + e^-$	0.30	$C_3H_8(E_1)$, $C_3H_8(E_2)$	275

$C_3H_8 + e^- \rightarrow C_3H_7 + H + e^-$	0.22	$C_3H_8(E_1)$, $C_3H_8(E_2)$	[275]
$C_3H_8 + e^- \rightarrow C_2H_5 + CH_3 + e^-$	0.04	$C_3H_8(E_1)$, $C_3H_8(E_2)$	[275]
$C_3H_8 + e^- \rightarrow C_2H_6 + CH_2 + e^-$	0.03	$C_3H_8(E_1)$, $C_3H_8(E_2)$	[275]
$C_3H_6 + e^- \rightarrow C_2H_2 + CH_4 + e^-$	0.42	$C_3H_6(E_1)$	[276,277]
$C_3H_6 + e^- \rightarrow C_2H_2 + CH_4 + e^-$	0.22	$C_3H_6(E_2)$	[276,277]
$C_3H_6 + e^- \rightarrow C_3H_5 + H + e^-$	0.25	$C_3H_6(E_2)$	[276,277]
$C_3H_6 + e^- \rightarrow C_2H_4 + CH_2 + e^-$	0.06	$C_3H_6(E_2)$	[276,277]
$C_3H_6 + e^- \rightarrow C_2H_3 + CH_3 + e^-$	0.06	$C_3H_6(E_2)$	[276,277]

A2.2. Updated rate coefficients as compared to earlier work[196–199]

Table A2.2. Overview of the neutral-neutral, ion-ion, ion-neutral, and electron-ion reactions that were added to the chemistry set or for which different rate coefficients were used compared to earlier modeling studies.[196–199] *For each reaction we list the corresponding rate coefficients and the references from which these were adopted. The units of the rate coefficients are in s^{-1} and cm^3 s^{-1} for first and second order reactions, respectively. In the expressions of the rate constants T_g denotes the gas temperature in K, T_e denotes the average electron temperature in K, and R denotes the ideal gas constant in J $mole^{-1}$ K^{-1}. The units of the activation barriers match those of the denominator (i.e., J $mole^{-1}$ for RT_g, or K for T_g) so that the exponent itself is unitless.*

Neutral-neutral reactions		
Reaction	**Rate coefficient**	**Ref.**
$C_2H_4 + O \rightarrow C_2H_3 + OH$	$1.33 \times 10^{-12} \left(\frac{T_g}{298}\right)^{1.91} exp\left(\frac{-1.56 \times 10^4}{RT_g}\right)$	[278]
$C_2H_4 + O \rightarrow CHO + CH_3$	$1.50 \times 10^{-12} \left(\frac{T_g}{298}\right)^{1.55} exp\left(\frac{-1.788 \times 10^3}{RT_g}\right)$	[134]
$C_2H_4 + O \rightarrow CH_3CO + H$	$9.11 \times 10^{-13} \left(\frac{T_g}{298}\right)^{-0.48} exp\left(\frac{-8.192 \times 10^3}{RT_g}\right)$	[279]
$C_2H_4 + O \rightarrow CH_2O + CH_2$	$8.08 \times 10^{-13} \left(\frac{T_g}{298}\right)^{1.99} exp\left(\frac{-1.20 \times 10^4}{RT_g}\right)$	[279]
$C_2H_4 + O \rightarrow CH_2CO + H_2$	3.82×10^{-14}	[280]

$C_2H_4 + O_2 \rightarrow C_2H_3 + HO_2$	$7.01 \times 10^{-11} exp\left(\frac{-2.41 \times 10^5}{RT_g}\right)$	134
$C_2H_4 + OH \rightarrow C_2H_3 + H_2O$	$2.29 \times 10^{-13} \left(\frac{T_g}{298}\right)^{2.74} exp\left(\frac{-9.271 \times 10^3}{RT_g}\right)$	281
$C_2H_4 + H \rightarrow C_2H_5$	$1.25 \times 10^{-11} \left(\frac{T_g}{298}\right)^{1.07} exp\left(\frac{-6.067 \times 10^3}{RT_g}\right)$	282
$C_2H_4 \rightarrow C_2H_3 + H$	$2.0 \times 10^{16} exp\left(\frac{-4.61 \times 10^5}{RT_g}\right)$	283
$C_2H_4 \rightarrow C_2H_2 + H_2$	$9.75 \times 10^{13} \left(\frac{T_g}{298}\right)^{0.44} exp\left(\frac{-3.72 \times 10^5}{RT_g}\right)$	134
$CH_3 + C_2H_5 \rightarrow C_3H_8$	5.60×10^{-11}	133
$CH_3 + C_2H_5 \rightarrow C_2H_4 + CH_4$	$1.88 \times 10^{-12} \left(\frac{T_g}{298}\right)^{-0.50}$	134
$C_2H_5 + C_2H_3 \rightarrow C_2H_6 + C_2H_2$	$0.37 \times (6.50 \times 10^{-11})$	284,285
$C_2H_5 + H \rightarrow C_2H_6$	1.66×10^{-10}	286
$C_2H_5 \rightarrow C_2H_4 + H$	$6.86 \times 10^{12} \left(\frac{T_g}{298}\right)^{0.95} exp\left(\frac{-1.55 \times 10^5}{RT_g}\right)$	282
$CH_3 + C_2H_3 \rightarrow C_3H_5 + H$	$2.59 \times 10^{-9} \left(\frac{T_g}{298}\right)^{-1.25} exp\left(\frac{-3.21 \times 10^4}{RT_g}\right)$	287
$CH_3 + C_2H_3 \rightarrow C_3H_6$	1.20×10^{-10}	285
$C_2H_3 + H \rightarrow C_2H_4$	2.01×10^{-10}	288
$C_2H_3 \rightarrow C_2H_2 + H$	$2.0 \times 10^{14} exp\left(\frac{-1.66 \times 10^5}{RT_g}\right)$	132
$C_2H_3 + H \rightarrow C_2H_2 + H_2$	3.32×10^{-11}	289
$C_2H_3 + OH \rightarrow CH_3CHO$	5.00×10^{-11}	134
$C_2H_3 + OH \rightarrow CH_3CO + H$	$2.92 \times 10^{-11} \left(\frac{T_g}{298}\right)^{-1.01} exp\left(\frac{-1.621 \times 10^3}{RT_g}\right)$	290
$C_2H_3 + OH \rightarrow CH_3 + CHO$	$2.88 \times 10^{-10} \left(\frac{T_g}{298}\right)^{-1.85} exp\left(\frac{-4.166 \times 10^3}{RT_g}\right)$	290
$C_2H_3 + OH \rightarrow CH_2CO + H_2$	$2.22 \times 10^{-12} \left(\frac{T_g}{298}\right)^{-1.52} exp\left(\frac{-3.018 \times 10^3}{RT_g}\right)$	290

$C_2H_2 + H \rightarrow C_2H_3$	$9.13 \times 10^{-12} exp\left(\frac{-1.01 \times 10^4}{RT_g}\right)$	289
$C_2H_2 \rightarrow C_2H + H$	$2.63 \times 10^{15} exp\left(\frac{-5.19 \times 10^5}{RT_g}\right)$	134
$2CH_3 \rightarrow C_2H_6$	$4.08 \times 10^{-11} \left(\frac{T_g}{298}\right)^{-0.40}$	289
$CH_3 + H \rightarrow CH_4$	3.50×10^{-10}	133
$CH_3 + CH_3CO \rightarrow C_2H_6 + CO$	$0.38 \times (1.43 \times 10^{-10})$	291
$CH_3 \rightarrow CH_2 + H$	$1.90 \times 10^{16} \left(\frac{T_g}{298}\right)^{0.09} exp\left(\frac{-4.59 \times 10^5}{RT_g}\right)$	292
$CH_4 \rightarrow CH_3 + H$	$3.72 \times 10^{15} exp\left(\frac{-4.34 \times 10^5}{RT_g}\right)$	134
$C_2H_6 \rightarrow 2CH_3$	$1.54 \times 10^{18} \left(\frac{T_g}{298}\right)^{-1.24} exp\left(\frac{-3.80 \times 10^5}{RT_g}\right)$	133
$CH + CH \rightarrow C_2H_2$	1.99×10^{-10}	293
$CH + H_2 \rightarrow CH_3$	$2.01 \times 10^{-10} \left(\frac{T_g}{298}\right)^{0.15}$	294
$C_3H_8 \rightarrow C_2H_5 + CH_3$	$2.78 \times 10^{18} \left(\frac{T_g}{298}\right)^{-1.80} exp\left(\frac{-3.71 \times 10^5}{RT_g}\right)$	138
$C_3H_7 + H \rightarrow C_3H_8$	6.00×10^{-11}	295
$C_3H_6 + H \rightarrow C_3H_7$	$6.64 \times 10^{-12} exp\left(\frac{-1.10 \times 10^4}{RT_g}\right)$	289
$C_3H_5 + H \rightarrow C_3H_6$	$2.64 \times 10^{-10} \left(\frac{T_g}{298}\right)^{0.18} exp\left(\frac{5.24 \times 10^2}{RT_g}\right)$	296
$CH + C_2H_5 \rightarrow C_3H_5 + H$	$3.8 \times 10^{-8} T_g^{-0.859} exp\left(\frac{-33.5}{T_g}\right)$	297
$2C_2H_5 \rightarrow C_4H_{10}$	1.66×10^{-11}	289
$C_4H_{10} \rightarrow C_3H_7 + CH_3$	$2.00 \times 10^{16} exp\left(\frac{-3.40 \times 10^5}{RT_g}\right)$	289
$C_4H_{10} \rightarrow C_2H_5 + C_2H_5$	$2.00 \times 10^{16} exp\left(\frac{-3.40 \times 10^5}{RT_g}\right)$	289

$C_2H_6 + C_4H_9 \rightarrow C_4H_{10} + C_2H_5$	$8.30 \times 10^{-13} exp\left(\frac{-6.28 \times 10^4}{RT_g}\right)$	298
$C_4H_{10} + O \rightarrow C_4H_9 + OH$	$7.06 \times 10^{-12} \left(\frac{T_g}{298}\right)^{2.40} exp\left(\frac{-2.30 \times 10^4}{RT_g}\right)$	299
$C_4H_{10} + OH \rightarrow C_4H_9 + H_2O$	$1.31 \times 10^{-12} \left(\frac{T_g}{298}\right)^{1.73} exp\left(\frac{-3.151 \times 10^3}{RT_g}\right)$	300
$C_4H_{10} \rightarrow C_4H_9 + H$	$1.58 \times 10^{16} exp\left(\frac{-4.10 \times 10^5}{RT_g}\right)$	283
$C_4H_{10} + HO_2 \rightarrow C_4H_9 + H_2O_2$	$1.86 \times 10^{-11} exp\left(\frac{-8.11 \times 10^4}{RT_g}\right)$	301
$C_4H_{10} + H \rightarrow C_4H_9 + H_2$	$3.05 \times 10^{-12} \left(\frac{T_g}{298}\right)^{2.54} exp\left(\frac{-2.92 \times 10^4}{RT_g}\right)$	302
$C_4H_{10} + CH_3 \rightarrow C_4H_9 + CH_4$	$3.01 \times 10^{-15} \left(\frac{T_g}{298}\right)^{3.65} exp\left(\frac{-3.03 \times 10^4}{RT_g}\right)$	302
$C_4H_9 \rightarrow C_4H_8 + H$	$1.10 \times 10^{13} \left(\frac{T_g}{298}\right)^{0.25} exp\left(\frac{-1.49 \times 10^5}{RT_g}\right)$	282
$C_4H_9 \rightarrow C_2H_4 + C_2H_5$	$3.70 \times 10^{13} exp\left(\frac{-1.20 \times 10^5}{RT_g}\right)$	289
$C_4H_9 \rightarrow C_3H_6 + CH_3$	$1.26 \times 10^{12} exp\left(\frac{-1.13 \times 10^5}{RT_g}\right)$	303
$C_4H_9 + O_2 \rightarrow C_4H_8 + HO_2$	4.48×10^{-13}	304
$C_2H_4 + C_2H_5 \rightarrow C_4H_8 + H$	8.63×10^{-17}	305
$C_2H_3 + C_2H_5 \rightarrow C_4H_8$	6.50×10^{-11}	285
$C_3H_5 + CH_3 \rightarrow C_4H_8$	$2.72 \times 10^{-11} \left(\frac{T_g}{298}\right)^{-0.32} exp\left(\frac{5.49 \times 10^2}{RT_g}\right)$	137
$2C_4H_9 \rightarrow C_4H_{10} + C_4H_8$	$6.61 \times 10^{-10} exp\left(\frac{-5.438 \times 10^3}{RT_g}\right)$	303
$CH_3 + C_4H_9 \rightarrow CH_4 + C_4H_8$	2.46×10^{-11}	306
$2C_2H_4 \rightarrow C_4H_8$	$6.96 \times 10^{-14} exp\left(\frac{-1.50 \times 10^5}{RT_g}\right)$	307

$C_3H_6 + CH_2 \rightarrow C_4H_8$	$1.35 \times 10^{-11} \left(\frac{T_g}{298}\right)^{-0.15} exp\left(\frac{-1.18 \times 10^{1}}{RT_g}\right)$	308
$C_4H_8 + H \rightarrow C_4H_9$	$7.59 \times 10^{-12} \left(\frac{T_g}{298}\right)^{0.51} exp\left(\frac{-1.10 \times 10^{4}}{RT_g}\right)$	282
$C_4H_8 + H \rightarrow C_2H_4 + C_2H_5$	$5.71 \times 10^{-11} exp\left(\frac{-1.64 \times 10^{4}}{RT_g}\right)$	309
$C_4H_8 + H \rightarrow C_3H_6 + CH_3$	$6.53 \times 10^{-11} exp\left(\frac{-9.578 \times 10^{3}}{RT_g}\right)$	309
$CHO + H \rightarrow CH_2O$	$7.77 \times 10^{-14} exp\left(\frac{1.90 \times 10^{4}}{RT_g}\right)$	310
$CH_2OH \rightarrow CH_2O + H$	$1.16 \times 10^{17} \left(\frac{T_g}{298}\right)^{-7.11} exp\left(\frac{-1.84 \times 10^{5}}{RT_g}\right)$	311
$CH_3O \rightarrow CH_2O + H$	$1.69 \times 10^{14} \left(\frac{T_g}{298}\right)^{-0.39} exp\left(\frac{-1.10 \times 10^{5}}{RT_g}\right)$	282
$CH_3 + OH \rightarrow CH_3OH$	1.00×10^{-10}	133
$CH_3 + CO \rightarrow CH_3CO$	$8.40 \times 10^{-13} exp\left(\frac{-2.88 \times 10^{4}}{RT_g}\right)$	133
$CH_2O + O_2 \rightarrow CHO + HO_2$	$3.40 \times 10^{-11} exp\left(\frac{-1.63 \times 10^{5}}{RT_g}\right)$	134
$H + CH_3CHO \rightarrow CH_3CO + H_2$	$6.64 \times 10^{-11} exp\left(\frac{-1.76 \times 10^{4}}{RT_g}\right)$	289
$CH_3CO + H \rightarrow CH_3CHO$	$1.50 \times 10^{-10} \left(\frac{T_g}{298}\right)^{0.16}$	290
$C_2H_5 + O_2 \rightarrow CH_3CHO + OH$	$1.0 \times 10^{-13} exp\left(\frac{-2.87 \times 10^{4}}{RT_g}\right)$	134
$CH_3CHO + H \rightarrow CO + H_2 + CH_3$	$4.88 \times 10^{-13} \left(\frac{T_g}{298}\right)^{2.75} exp\left(\frac{-4.041 \times 10^{3}}{RT_g}\right)$	312
$CH_3CHO + O_2 \rightarrow CH_3CO + HO_2$	$5.0 \times 10^{-11} exp\left(\frac{-1.64 \times 10^{5}}{RT_g}\right)$	132
$CH_3CHO + C_2H_3 \rightarrow C_2H_4 + CH_3CO$	$1.35 \times 10^{-13} exp\left(\frac{-1.54 \times 10^{4}}{RT_g}\right)$	313

$CH + H_2O \rightarrow CH_2OH$	$9.48 \times 10^{-12} exp\left(\frac{3.159 \times 10^3}{RT_g}\right)$	314
$CH_3CO + O_2 \rightarrow CO_2 + CH_3O$	$7.37 \times 10^{-14} exp\left(\frac{4.506 \times 10^3}{RT_g}\right)$	315
$CH_3O + H \rightarrow CH_3OH$	$1.59 \times 10^{-10} \left(\frac{T_g}{298}\right)^{0.24} exp\left(\frac{2.17 \times 10^2}{RT_g}\right)$	316
$CH_3O + HO_2 \rightarrow CH_3OH + O_2$	4.70×10^{-11}	317
$CO + CH_3O \rightarrow CH_2O + CHO$	3.26×10^{-33}	318
$CH_3CHO + H \rightarrow CH_4 + CHO$	8.80×10^{-14}	319
$CHO + H \rightarrow O + CH_2$	$6.61 \times 10^{-11} exp\left(\frac{-4.29 \times 10^5}{RT_g}\right)$	320
$CHO \rightarrow CO + H$	$2.0 \times 10^5 exp\left(\frac{-1.10 \times 10^5}{RT_g}\right)$	321
$CH_3 + CHO \rightarrow CH_3CHO$	3.01×10^{-11}	134
$CH_3 + O_2 \rightarrow CH_2O + OH$	$2.81 \times 10^{-13} exp\left(\frac{-4.14 \times 10^4}{RT_g}\right)$	129,322
$CH_3 + OH \rightarrow CH_2O + H_2$	$2.59 \times 10^{-13} \left(\frac{T_g}{298}\right)^{-0.53} exp\left(\frac{-4.52 \times 10^4}{RT_g}\right)$	323
$CH_3O + CH_3CO \rightarrow CH_2O + CH_3CHO$	1.0×10^{-11}	134
$CH_3O_2 + HO_2 \rightarrow CH_2O + H_2O + O_2$	$1.60 \times 10^{-15} exp\left(\frac{-1.44 \times 10^4}{RT_g}\right)$	324
$CH_3O_2 + CH_2OH \rightarrow CH_2O + CH_3OOH$	$4.75 \times 10^{-18} \left(\frac{T_g}{298}\right)^{2.69} exp\left(\frac{-1.43 \times 10^4}{RT_g}\right)$	325
$CH_3O_2 \rightarrow CH_2O + OH$	$5.86 \times 10^{10} \left(\frac{T_g}{298}\right)^{2.98} exp\left(\frac{-1.63 \times 10^5}{RT_g}\right)$	326
$C_3H_5 + O_2 \rightarrow CH_2O + C_2H_2 + OH$	$3.37 \times 10^{-10} \left(\frac{T_g}{298}\right)^{-2.70} exp\left(\frac{-1.05 \times 10^5}{RT_g}\right)$	327
$CH_3OH + OH \rightarrow CH_2O + H_2O + H$	$1.10 \times 10^{-12} \left(\frac{T_g}{298}\right)^{1.44} exp\left(\frac{-4.74 \times 10^2}{RT_g}\right)$	328

$CH_2O + H \rightarrow CH_2OH$	$2.41 \times 10^{-13} \left(\frac{T_g}{298}\right)^{-1.40} exp\left(\frac{-2.17 \times 10^4}{RT_g}\right)$	311
$CH_2O + H \rightarrow CH_3O$	$3.99 \times 10^{-11} exp\left(\frac{-1.72 \times 10^4}{RT_g}\right)$	282
$HCOOH \rightarrow CO + H_2O$	$9.12 \times 10^{12} exp\left(\frac{-2.52 \times 10^5}{RT_g}\right)$	329
$CH_2OH + HO_2 \rightarrow HCOOH + H_2O$	$1.18 \times 10^{-11} \left(\frac{T_g}{298}\right)^{0.12} exp\left(\frac{-1.9 \times 10^3}{RT_g}\right)$	330
$CH_3CHOH + O \rightarrow HCOOH + CH_3$	$3.90 \times 10^{-10} \left(\frac{T_g}{298}\right)^{0.18} exp\left(\frac{-4.07}{RT_g}\right)$	331
$CH_3O_2 + CH_2OH \rightarrow HCOOH + CH_3OH$	$2.34 \times 10^{-17} \left(\frac{T_g}{298}\right)^{2.74} exp\left(\frac{1.49 \times 10^4}{RT_g}\right)$	325
$CO + H_2O \rightarrow HCOOH$	$5.11 \times 10^{-15} \left(\frac{T_g}{298}\right)^{3.10} exp\left(\frac{-2.43 \times 10^5}{RT_g}\right)$	332
$CH_2O + OH \rightarrow HCOOH + H$	2.01×10^{-13}	333
$HCOOH \rightarrow CO_2 + H_2$	$4.46 \times 10^{13} exp\left(\frac{-2.86 \times 10^5}{RT_g}\right)$	334
$HCOOH + OH \rightarrow H_2O + HCOO$	$2.26 \times 10^{-14} exp\left(\frac{-6.535 \times 10^3}{RT_g}\right)$	335
$HCOOH + OH \rightarrow COOH + H_2O$	$9.85 \times 10^{-13} exp\left(\frac{-8.614 \times 10^3}{RT_g}\right)$	335
$CO + H_2O_2 \rightarrow COOH + OH$	$9.60 \times 10^{-14} \left(\frac{T_g}{298}\right)^{2.09} exp\left(\frac{-2.28 \times 10^4}{RT_g}\right)$	336
$CO + OH \rightarrow COOH$	$9.34 \times 10^{-13} \left(\frac{T_g}{298}\right)^{-3.5} exp\left(\frac{-5.478 \times 10^3}{RT_g}\right)$	337
$COOH + O_2 \rightarrow CO_2 + HO_2$	2.09×10^{-12}	338
$COOH \rightarrow CO + OH$	$29.85 \left(\frac{T_g}{298}\right)^{0.13} exp\left(\frac{-1.53 \times 10^5}{RT_g}\right)$	339
$COOH \rightarrow CO_2 + H$	$1.25 \times 10^2 \left(\frac{T_g}{298}\right)^{0.41} exp\left(\frac{-1.48 \times 10^5}{RT_g}\right)$	339
$COOH + O \rightarrow CO_2 + OH$	1.44×10^{-11}	340

$COOH + OH \rightarrow CO_2 + H_2O$	1.03×10^{-11}	341
$HCOO \rightarrow CO + OH$	$1.21 \times 10^{14} \left(\frac{T_g}{298}\right)^{0.53} exp\left(\frac{-1.42 \times 10^5}{RT_g}\right)$	342
$HCOO \rightarrow CO_2 + H$	$1.0 \times 10^{13} \left(\frac{T_g}{298}\right)^{0.31} exp\left(\frac{-1.38 \times 10^5}{RT_g}\right)$	342
$CH_3O_2 + CH_2OH \rightarrow CH_3O + HOCH_2O$	$1.67 \times 10^{-13} \left(\frac{T_g}{298}\right)^{0.89} exp\left(\frac{1.04 \times 10^4}{RT_g}\right)$	325
$CH_2O + OH \rightarrow HOCH_2O$	$1.13 \times 10^{-13} \left(\frac{T_g}{298}\right)^{1.63} exp\left(\frac{-1.79 \times 10^4}{RT_g}\right)$	343
$HOCH_2O \rightarrow HCOOH + H$	$1.0 \times 10^{14} exp\left(\frac{-6.24 \times 10^4}{RT_g}\right)$	344
$O_2 + HOCH_2O \rightarrow HCOOH + HO_2$	3.50×10^{-14}	345
$CH_2CO + CH_2 \rightarrow C_2H_4 + CO$	2.09×10^{-10}	346
$CH_2CO + H \rightarrow CH_3CO$	$2.66 \times 10^{-11} exp\left(\frac{-6.279 \times 10^3}{RT_g}\right)$	347
$CH_2CO + OH \rightarrow CH_2O + CHO$	4.65×10^{-11}	348
$CH_2CO + CH_3 \rightarrow CO + C_2H_5$	$9.54 \times 10^{-14} \left(\frac{T_g}{298}\right)^{2.29} exp\left(\frac{-4.45 \times 10^4}{RT_g}\right)$	349
$CH_2CO + CH_2 \rightarrow CH_3 + C_2HO$	1.0×10^{-17}	350
$CH_2CO + O \rightarrow C_2HO + OH$	$3.11 \times 10^{-10} exp\left(\frac{-6.98 \times 10^4}{RT_g}\right)$	351
$CH_2CO + CH_3 \rightarrow CH_4 + C_2HO$	$5.94 \times 10^{-14} \left(\frac{T_g}{298}\right)^{3.38} exp\left(\frac{-4.40 \times 10^4}{RT_g}\right)$	349
$2CH_3CO \rightarrow CH_3CHO + CH_2CO$	1.49×10^{-11}	352
$CH_3 + CH_3CO \rightarrow CH_4 + CH_2CO$	1.01×10^{-11}	352
$CH_3CHO \rightarrow CH_2CO + H_2$	$3.0 \times 10^{14} exp\left(\frac{-3.51 \times 10^5}{RT_g}\right)$	353
$CH_3CO \rightarrow CH_2CO + H$	$6.54 \times 10^{-4} \left(\frac{T_g}{298}\right)^{-4.34} exp\left(\frac{-1.94 \times 10^5}{RT_g}\right)$	354

$OH + C_2HO \rightarrow CH_2CO + O$	$1.76 \times 10^{-13} \left(\frac{T_g}{298}\right)^{1.99} exp\left(\frac{-4.72 \times 10^4}{RT_g}\right)$	351
$C_2H_5O + H \rightarrow C_2H_5OH$	$8.32 \times 10^{-11} \left(\frac{T_g}{298}\right)^{0.89} exp\left(\frac{-54.04}{RT_g}\right)$	355
$CH_3 + CH_2OH \rightarrow C_2H_5OH$	2.01×10^{-11}	136
$C_2H_5 + OH \rightarrow C_2H_5OH$	1.28×10^{-10}	356
$C_2H_5O + C_2H_6 \rightarrow C_2H_5OH + C_2H_5$	$4.0 \times 10^{-13} exp\left(\frac{-2.968 \times 10^4}{RT_g}\right)$ Rate Coefficient taken from: $CH_3O + C_2H_6 \rightarrow CH_3OH + C_2H_5$	134
$C_2H_5O + CHO \rightarrow C_2H_5OH + CO$	1.50×10^{-10} Rate Coefficient taken from: $CH_3O + CHO \rightarrow CH_3OH + CO$	134
$C_2H_5O \rightarrow CH_2O + CH_3$	$1.0 \times 10^{15} exp\left(\frac{-9.06 \times 10^4}{RT_g}\right)$	357
$C_2H_5OH + H \rightarrow C_2H_5 + H_2O$	$9.80 \times 10^{-13} exp\left(\frac{-1.45 \times 10^4}{RT_g}\right)$	358
$C_2H_5OH + OH \rightarrow C_2H_5O + H_2O$	$1.67 \times 10^{-14} \left(\frac{T_g}{298}\right)^{3.15} exp\left(\frac{2.380 \times 10^3}{RT_g}\right)$	359
$C_2H_5OH \rightarrow C_2H_4 + H_2O$	$6.91 \times 10^{16} \left(\frac{T_g}{298}\right)^{-3.68} exp\left(\frac{-2.96 \times 10^5}{RT_g}\right)$	360
$C_2H_5OH \rightarrow CH_3 + CH_2OH$	$7.91 \times 10^{24} \left(\frac{T_g}{298}\right)^{-10.59} exp\left(\frac{-4.22 \times 10^5}{RT_g}\right)$	360
$C_2H_5OH \rightarrow C_2H_5 + OH$	$1.34 \times 10^{17} \left(\frac{T_g}{298}\right)^{-2.16} exp\left(\frac{-4.04 \times 10^5}{RT_g}\right)$	135
$C_2H_5OH \rightarrow C_2H_5O + H$	$1.53 \times 10^{16} \left(\frac{T_g}{298}\right)^{0.31} exp\left(\frac{-4.24 \times 10^5}{RT_g}\right)$	355
$C_2H_5OH \rightarrow CH_3CHOH + H$	$1.57 \times 10^{16} \left(\frac{T_g}{298}\right)^{-0.28} exp\left(\frac{-3.93 \times 10^5}{RT_g}\right)$	355
$C_2H_5OH + H \rightarrow CH_3CHOH + H_2$	$1.64 \times 10^{-11} \left(\frac{T_g}{298}\right)^{-0.33} exp\left(\frac{-2.25 \times 10^4}{RT_g}\right)$	359

$C_2H_5OH + OH \rightarrow CH_3CHOH + H_2O$	$1.38 \times 10^{-12} \left(\frac{T_g}{298}\right)^{1.13} exp\left(\frac{1.903 \times 10^3}{RT_g}\right)$	359
$C_2H_5OH + HO_2 \rightarrow CH_3CHOH + H_2O_2$	$3.09 \times 10^{-10} \left(\frac{T_g}{298}\right)^{-1.81} exp\left(\frac{-6.89 \times 10^4}{RT_g}\right)$	359
$C_2H_5OH + CH_3 \rightarrow CH_4 + CH_3CHOH$	$8.87 \times 10^{-15} \left(\frac{T_g}{298}\right)^{3.37} exp\left(\frac{-3.29 \times 10^4}{RT_g}\right)$	359
$C_2H_5OH + O \rightarrow CH_3CHOH + OH$	1.03×10^{-13}	361
$C_2H_5O \rightarrow CH_3CHO + H$	$1.07 \times 10^{14} \left(\frac{T_g}{298}\right)^{-0.69} exp\left(\frac{-9.30 \times 10^4}{RT_g}\right)$	282
$C_2H_5O + C_2H_5O_2 \rightarrow CH_3CHO + C_2H_5OOH$	1.54×10^{-11}	362
$C_2H_5O + H \rightarrow CH_3 + CH_2OH$	$1.23 \times 10^{-10} \left(\frac{T_g}{298}\right)^{0.70} exp\left(\frac{-1.447 \times 10^3}{RT_g}\right)$	355
$C_2H_5O + H \rightarrow C_2H_5 + OH$	$1.25 \times 10^{-12} \left(\frac{T_g}{298}\right)^{1.27} exp\left(\frac{-1.305 \times 10^3}{RT_g}\right)$	355
$C_2H_5O + H \rightarrow CH_3CHO + H_2$	$8.69 \times 10^{-12} \left(\frac{T_g}{298}\right)^{1.15} exp\left(\frac{-2.819 \times 10^3}{RT_g}\right)$	355
$C_2H_5O + H \rightarrow C_2H_4 + H_2O$	$9.69 \times 10^{-12} \left(\frac{T_g}{298}\right)^{-0.81} exp\left(\frac{-2.985 \times 10^3}{RT_g}\right)$	355
$C_2H_5O + H \rightarrow CH_2O + CH_4$	$3.88 \times 10^{-16} \left(\frac{T_g}{298}\right)^{2.21} exp\left(\frac{7.52 \times 10^2}{RT_g}\right)$	355
$CH_3CHO + H \rightarrow C_2H_5O$	$1.33 \times 10^{-11} exp\left(\frac{-2.68 \times 10^4}{RT_g}\right)$	282
$CH_2O + CH_3 \rightarrow C_2H_5O$	$4.98 \times 10^{-13} exp\left(\frac{-2.65 \times 10^4}{RT_g}\right)$	282
$C_2H_5 + O_2 \rightarrow C_2H_5O + O$	$6.14 \times 10^{-12} \left(\frac{T_g}{298}\right)^{-0.20} exp\left(\frac{-1.17 \times 10^5}{RT_g}\right)$	363
$C_2H_5 + HO_2 \rightarrow C_2H_5O + OH$	4.98×10^{-11}	363
$C_2H_5O_2 + O_3 \rightarrow C_2H_5O + 2O_2$	9.27×10^{-18}	364

$2C_2H_5O_2 \rightarrow CH_3CHO + C_2H_5O + HO_2$	$1.21 \times 10^{-15} exp\left(\frac{-0.07}{RT_g}\right)$	365
$C_2H_5O_2 \rightarrow C_2H_5O + O$	$1.78 \times 10^{15} \left(\frac{T_g}{298}\right)^{-0.09} exp\left(\frac{-2.58 \times 10^5}{RT_g}\right)$	366
$C_2H_5 + O \rightarrow C_2H_5O$	$6.31 \times 10^{-11} \left(\frac{T_g}{298}\right)^{0.03} exp\left(\frac{1.648 \times 10^3}{RT_g}\right)$	367
$C_2H_5 + O_3 \rightarrow C_2H_5O + O_2$	3.32×10^{-14}	368
$C_2H_5OOH \rightarrow C_2H_5O + OH$	$4.0 \times 10^{15} exp\left(\frac{-1.80 \times 10^5}{RT_g}\right)$	133
$CH_3CHOH + O_2 \rightarrow CH_3CHO + HO_2$	1.90×10^{-11}	369
$CH_3CHOH + O \rightarrow CH_3CHO + OH$	3.16×10^{-10}	370
$CH_3CHOH + H \rightarrow CH_3CHO + H_2$	3.32×10^{-11}	370
$CH_3CHOH + H \rightarrow CH_3 + CH_2OH$	$8.99 \times 10^{-10} \left(\frac{T_g}{298}\right)^{-0.89} exp\left(\frac{-1.21 \times 10^4}{RT_g}\right)$	355
$CH_3CHOH + H \rightarrow C_2H_5O + H$	$9.31 \times 10^{-16} \left(\frac{T_g}{298}\right)^{2.94} exp\left(\frac{-3.55 \times 10^4}{RT_g}\right)$	355
$CH_3CHOH + H \rightarrow C_2H_5 + OH$	$3.55 \times 10^{-11} \left(\frac{T_g}{298}\right)^{-0.83} exp\left(\frac{-2.01 \times 10^4}{RT_g}\right)$	355
$CH_3CHOH + H \rightarrow C_2H_4 + H_2O$	$2.63 \times 10^{-10} \left(\frac{T_g}{298}\right)^{-3.02} exp\left(\frac{-1.19 \times 10^4}{RT_g}\right)$	355
$CH_3CHOH + H \rightarrow CH_2O + CH_4$	$8.73 \times 10^{-17} \left(\frac{T_g}{298}\right)^{2.10} exp\left(\frac{-8.90 \times 10^2}{RT_g}\right)$	355
$CH_3CHOH + H \rightarrow C_2H_5OH$	$8.43 \times 10^{-11} \left(\frac{T_g}{298}\right)^{0.06} exp\left(\frac{-1.829 \times 10^3}{RT_g}\right)$	355
$CH_3CHOH \rightarrow CH_3CHO + H$	$1.20 \times 10^{15} \left(\frac{T_g}{298}\right)^{-5.19} exp\left(\frac{-1.49 \times 10^5}{RT_g}\right)$	371
$CH_3CHOH \rightarrow CH_2O + CH_3$	$1.49 \times 10^{13} \left(\frac{T_g}{298}\right)^{-3.59} exp\left(\frac{-1.45 \times 10^5}{RT_g}\right)$	371
$C_2H_5O \rightarrow CH_3CHOH$	$1.87 \left(\frac{T_g}{298}\right)^{12.40} exp\left(\frac{-1.77 \times 10^4}{RT_g}\right)$	372

$CH_3CHO + H \rightarrow CH_3CHOH$	$8.02 \times 10^{-13} \left(\frac{T_g}{298}\right)^{2.20} exp\left(\frac{-3.14 \times 10^4}{RT_g}\right)$	312
$CH_3CHO + HO_2 \rightarrow CH_3CHOH + O_2$	$4.19 \times 10^{-10} \left(\frac{T_g}{298}\right)^{-1.80} exp\left(\frac{-1.09 \times 10^5}{RT_g}\right)$	373
$C_3H_7O \rightarrow C_2H_5CHO + H$	$6.38 \times 10^{12} \left(\frac{T_g}{298}\right)^{0.75} exp\left(\frac{-8.81 \times 10^4}{RT_g}\right)$	282
$C_3H_7O \rightarrow CH_2O + C_2H_5$	$2.36 \times 10^{15} \left(\frac{T_g}{298}\right)^{-2.45} exp\left(\frac{-7.10 \times 10^4}{RT_g}\right)$	282
$C_3H_7O + O_2 \rightarrow C_2H_5CHO + HO_2$	$1.40 \times 10^{-14} exp\left(\frac{-9.15 \times 10^2}{RT_g}\right)$	374
$C_3H_7 + HO_2 \rightarrow OH + C_3H_7O$	4.00×10^{-11}	138
$C_2H_5CHO + H \rightarrow C_3H_7O$	$6.64 \times 10^{-12} exp\left(\frac{-2.62 \times 10^4}{RT_g}\right)$	282
$CH_2O + C_2H_5 \rightarrow C_3H_7O$	$1.66 \times 10^{-13} exp\left(\frac{-1.46 \times 10^4}{RT_g}\right)$	282
$C_3H_7 + OH \rightarrow C_3H_7OH$	4.00×10^{-11}	138
$CH_2OH + C_2H_5 \rightarrow C_3H_7OH$	2.01×10^{-11}	136
$C_3H_7OH + OH \rightarrow H_2O + C_3H_7O$	$3.23 \times 10^{-14} exp\left(\frac{4.008 \times 10^3}{RT_g}\right)$	375
$C_3H_7OH \rightarrow C_2H_5 + CH_2OH$	$2.70 \times 10^{16} exp\left(\frac{-3.47 \times 10^5}{RT_g}\right)$	376
$C_3H_7OH \rightarrow C_3H_6 + H_2O$	$3.95 \times 10^{13} \left(\frac{T_g}{298}\right)^{0.50} exp\left(\frac{-2.51 \times 10^5}{RT_g}\right)$	377
$C_3H_7 + O_2 \rightarrow C_3H_7O_2$	$1.15 \times 10^{-12} \left(\frac{T_g}{298}\right)^{0.50} exp\left(\frac{4.656 \times 10^3}{RT_g}\right)$	378
$C_3H_6 + HO_2 \rightarrow C_3H_7O_2$	$9.62 \times 10^{-17} \left(\frac{T_g}{298}\right)^{3.27} exp\left(\frac{-4.10 \times 10^4}{RT_g}\right)$	379
$C_3H_7O_2 \rightarrow C_3H_7 + O_2$	$7.46 \times 10^{21} \left(\frac{T_g}{298}\right)^{-12.51} exp\left(\frac{-1.77 \times 10^5}{RT_g}\right)$	380
$C_3H_7O_2 \rightarrow C_2H_5CHO + OH$	$1.74 \times 10^{11} \left(\frac{T_g}{298}\right)^{2.31} exp\left(\frac{1.54 \times 10^5}{RT_g}\right)$	326

$C_3H_7O_2 \rightarrow C_3H_6 + HO_2$	$6.06 \times 10^{20} \left(\frac{T_g}{298}\right)^{-13.03} exp\left(\frac{-1.76 \times 10^5}{RT_g}\right)$	380
$C_2H_5CO \rightarrow C_2H_5 + CO$	$2.09 \times 10^{13} exp\left(\frac{-6.15 \times 10^4}{RT_g}\right)$	381
$CH_2CO \rightarrow CO + CH_2$	$3.00 \times 10^{14} exp\left(\frac{-2.97 \times 10^5}{RT_g}\right)$	289
$C_2H_5 + O_2 \rightarrow C_2H_5O_2$	$1.09 \times 10^{-7} \left(\frac{T_g}{298}\right)^{-10.30} exp\left(\frac{-2.54 \times 10^4}{RT_g}\right)$	363
$C_2H_5O_2 \rightarrow C_2H_5 + O_2$	$5.30 \times 10^{15} \left(\frac{T_g}{298}\right)^{-0.83} exp\left(\frac{-1.43 \times 10^5}{RT_g}\right)$	382
$C_2H_5O_2 \rightarrow CH_3CHO + OH$	$7.27 \times 10^{10} \left(\frac{T_g}{298}\right)^{2.63} exp\left(\frac{-1.55 \times 10^5}{RT_g}\right)$	326
$C_3H_7 + O_2 \rightarrow C_2H_5CHO + OH$	1.83×10^{-16}	383
$C_2H_5 + CHO \rightarrow C_2H_5CHO$	3.01×10^{-11}	134
$CO + C_2H_5 \rightarrow C_2H_5CO$	$2.51 \times 10^{-13} exp\left(\frac{-2.01 \times 10^4}{RT_g}\right)$	134
$C_2H_5CHO + O \rightarrow OH + C_2H_5CO$	$9.43 \times 10^{-12} exp\left(\frac{6.452 \times 10^3}{RT_g}\right)$	384
$C_2H_5CHO + O_2 \rightarrow HO_2 + C_2H_5CO$	5.65×10^{-23}	385
$C_2H_5CHO + OH \rightarrow H_2O + C_2H_5CO$	1.85×10^{-11}	386
$C_2H_5CHO + HO_2 \rightarrow H_2O_2 + C_2H_5CO$	2.52×10^{-15}	387
$C_2H_5CHO + C_2H_5 \rightarrow C_2H_6 + C_2H_5CO$	$8.32 \times 10^{-14} exp\left(\frac{-2.63 \times 10^4}{RT_g}\right)$	129,388

Ion-ion reactions

Reaction	Rate coefficient	Ref.
$H^- + CHO^+ \rightarrow 2H + CO$	$3.76 \times 10^{-8} \left(\frac{T_g}{300}\right)^{-0.50}$	130
$H^- + CHO^+ \rightarrow H + CHO$	$3.76 \times 10^{-8} \left(\frac{T_g}{300}\right)^{-0.50}$	130
$O^- + CHO^+ \rightarrow O + H + CO$	$3.76 \times 10^{-8} \left(\frac{T_g}{300}\right)^{-0.50}$	130

$O^- + CHO^+ \rightarrow O + CHO$	$3.76 \times 10^{-8} \left(\frac{T_g}{300}\right)^{-0.50}$	130
$O_2^- + CHO^+ \rightarrow O_2 + H + CO$	$3.76 \times 10^{-8} \left(\frac{T_g}{300}\right)^{-0.50}$	130
$O_2^- + CHO^+ \rightarrow O_2 + CHO$	$3.76 \times 10^{-8} \left(\frac{T_g}{300}\right)^{-0.50}$	130
$OH^- + CHO^+ \rightarrow OH + H + CO$	$3.76 \times 10^{-8} \left(\frac{T_g}{300}\right)^{-0.50}$	130
$OH^- + CHO^+ \rightarrow OH + CHO$	$3.76 \times 10^{-8} \left(\frac{T_g}{300}\right)^{-0.50}$	130
$O^- + C^+ \rightarrow C + O$	$7.51 \times 10^{-8} \left(\frac{T_g}{300}\right)^{-0.50}$	130
$O^- + C_2H_2^+ \rightarrow O + C_2H_2$	$7.51 \times 10^{-8} \left(\frac{T_g}{300}\right)^{-0.50}$	130
$O^- + C_2H_3^+ \rightarrow O + C_2H_3$	$7.51 \times 10^{-8} \left(\frac{T_g}{300}\right)^{-0.50}$	130
$O^- + CH_3^+ \rightarrow O + CH_3$	$7.51 \times 10^{-8} \left(\frac{T_g}{300}\right)^{-0.50}$	130
$O_2^- + C^+ \rightarrow C + O_2$	$7.51 \times 10^{-8} \left(\frac{T_g}{300}\right)^{-0.50}$	130
$O_2^- + C_2H_2^+ \rightarrow O_2 + C_2H_2$	$7.51 \times 10^{-8} \left(\frac{T_g}{300}\right)^{-0.50}$	130
$O_2^- + C_2H_3^+ \rightarrow O_2 + C_2H_3$	$7.51 \times 10^{-8} \left(\frac{T_g}{300}\right)^{-0.50}$	130
$O_2^- + CH_3^+ \rightarrow O_2 + CH_3$	$7.51 \times 10^{-8} \left(\frac{T_g}{300}\right)^{-0.50}$	130
$OH^- + C_2H_2^+ \rightarrow OH + C_2H_2$	$7.51 \times 10^{-8} \left(\frac{T_g}{300}\right)^{-0.50}$	130
$OH^- + C_2H_3^+ \rightarrow OH + C_2H_3$	$7.51 \times 10^{-8} \left(\frac{T_g}{300}\right)^{-0.50}$	130
$OH^- + CH_3^+ \rightarrow OH + CH_3$	$7.51 \times 10^{-8} \left(\frac{T_g}{300}\right)^{-0.50}$	130
$H^- + C_2H_2^+ \rightarrow H + C_2H_2$	$7.51 \times 10^{-8} \left(\frac{T_g}{300}\right)^{-0.50}$	130

$H^- + C_2H_3^+ \rightarrow H + C_2H_3$	$7.51 \times 10^{-8} \left(\frac{T_g}{300}\right)^{-0.50}$	130
$H^- + CH_3^+ \rightarrow H + CH_3$	$7.51 \times 10^{-8} \left(\frac{T_g}{300}\right)^{-0.50}$	130
$H^- + H_3O^+ \rightarrow 2H + H_2O$	$7.51 \times 10^{-8} \left(\frac{T_g}{300}\right)^{-0.50}$	130

Ion-neutral reactions

Reaction	**Rate coefficient**	**Ref.**
$O^- + O_2 \rightarrow O_2^- + O$	7.30×10^{-10}	130
$CH_2 + O^- \rightarrow CH_2O + e^-$	5.00×10^{-10}	130
$CH + O^- \rightarrow CHO + e^-$	5.00×10^{-10}	130
$C^+ + C_3H_6 \rightarrow C_2H_2^+ + C_2H_4$	3.00×10^{-10}	130
$C^+ + C_3H_6 \rightarrow C_2H_3^+ + C_2H_3$	6.00×10^{-10}	130
$H_3^+ + C_2H_5OH \rightarrow C_2H_3^+ + H_2O + 2H_2$	$4.00 \times 10^{-10} \left(\frac{T_g}{300}\right)^{-0.50}$	130
$H_3^+ + C_3H_6 \rightarrow C_2H_3^+ + CH_4 + H_2$	9.00×10^{-10}	130
$H_3^+ + CH_3CHO \rightarrow C_2H_3^+ + H_2 + H_2O$	$8.97 \times 10^{-10} \left(\frac{T_g}{300}\right)^{-0.50}$	130
$C^+ + CH_3OH \rightarrow CHO + CH_3^+$	$2.08 \times 10^{-9} \left(\frac{T_g}{300}\right)^{-0.50}$	130
$CH^+ + CH_3OH \rightarrow CH_2O + CH_3^+$	$1.45 \times 10^{-9} \left(\frac{T_g}{300}\right)^{-0.50}$	130
$CH^+ + CH_2O \rightarrow CO + CH_3^+$	$9.60 \times 10^{-10} \left(\frac{T_g}{300}\right)^{-0.50}$	130
$CH_2^+ + CHO \rightarrow CO + CH_3^+$	$4.50 \times 10^{-10} \left(\frac{T_g}{300}\right)^{-0.50}$	130
$H^+ + CH_3OH \rightarrow CH_3^+ + H_2O$	$5.90 \times 10^{-10} \left(\frac{T_g}{300}\right)^{-0.50}$	130
$H_3^+ + C_2H_5OH \rightarrow CH_3^+ + CH_4 + H_2O$	$1.50 \times 10^{-9} \left(\frac{T_g}{300}\right)^{-0.50}$	130
$H_3^+ + CH_3CHO \rightarrow CH_3^+ + CH_3OH$	$1.45 \times 10^{-9} \left(\frac{T_g}{300}\right)^{-0.50}$	130

$H_3^+ + CH_3OH \rightarrow CH_3^+ + H_2O + H_2$	$3.71 \times 10^{-9} \left(\frac{T_g}{300}\right)^{-0.50}$	130
$C^+ + CHO \rightarrow CHO^+ + C$	$4.80 \times 10^{-10} \left(\frac{T_g}{300}\right)^{-0.50}$	130
$C_2^+ + CHO \rightarrow CHO^+ + C_2$	$3.80 \times 10^{-10} \left(\frac{T_g}{300}\right)^{-0.50}$	130
$C_2H_2^+ + CHO \rightarrow CHO^+ + C_2H_2$	$5.00 \times 10^{-10} \left(\frac{T_g}{300}\right)^{-0.50}$	130
$CH^+ + CHO \rightarrow CHO^+ + CH$	$4.60 \times 10^{-10} \left(\frac{T_g}{300}\right)^{-0.50}$	130
$CH_3^+ + CHO \rightarrow CH_3 + CHO^+$	$4.40 \times 10^{-10} \left(\frac{T_g}{300}\right)^{-0.50}$	130
$CO^+ + CHO \rightarrow CO + CHO^+$	$7.40 \times 10^{-10} \left(\frac{T_g}{300}\right)^{-0.50}$	130
$H^+ + CHO \rightarrow CHO^+ + H$	$9.40 \times 10^{-10} \left(\frac{T_g}{300}\right)^{-0.50}$	130
$H_2^+ + CHO \rightarrow CHO^+ + H_2$	$1.00 \times 10^{-9} \left(\frac{T_g}{300}\right)^{-0.50}$	130
$H_2O^+ + CHO \rightarrow CHO^+ + H_2O$	$2.80 \times 10^{-10} \left(\frac{T_g}{300}\right)^{-0.50}$	130
$CHO + O_2^+ \rightarrow CHO^+ + O_2$	$3.60 \times 10^{-10} \left(\frac{T_g}{300}\right)^{-0.50}$	130
$O^+ + CHO \rightarrow CHO^+ + O$	$4.30 \times 10^{-10} \left(\frac{T_g}{300}\right)^{-0.50}$	130
$OH^+ + CHO \rightarrow OH + CHO^+$	$2.80 \times 10^{-10} \left(\frac{T_g}{300}\right)^{-0.50}$	130
$C^+ + CH_2O \rightarrow CHO^+ + CH$	$7.80 \times 10^{-10} \left(\frac{T_g}{300}\right)^{-0.50}$	130
$C^+ + H_2O \rightarrow CHO^+ + H$	$9.00 \times 10^{-10} \left(\frac{T_g}{300}\right)^{-0.50}$	130
$C_2H + CO^+ \rightarrow CHO^+ + C_2$	3.90×10^{-10}	130
$C + H_3O^+ \rightarrow CHO^+ + H_2$	1.00×10^{-11}	130
$CH^+ + CO_2 \rightarrow CHO^+ + CO$	1.60×10^{-9}	130

$CH^+ + CH_2O \rightarrow CHO^+ CH_2$	$9.60 \times 10^{-10} \left(\frac{T_g}{300}\right)^{-0.50}$	130
$CH^+ + H_2O \rightarrow CHO^+ + H_2$	$2.90 \times 10^{-9} \left(\frac{T_g}{300}\right)^{-0.50}$	130
$CH^+ + O_2 \rightarrow CHO^+ + O$	9.70×10^{-10}	130
$CH_2^+ + CH_2O \rightarrow CHO^+ + CH_3$	$2.81 \times 10^{-9} \left(\frac{T_g}{300}\right)^{-0.50}$	130
$CH_2^+ + O_2 \rightarrow CHO^+ + OH$	9.10×10^{-10}	130
$CH_2^+ + O \rightarrow CHO^+ + H$	7.50×10^{-10}	130
$CH_2 + CO^+ \rightarrow CHO^+ + CH$	4.30×10^{-10}	130
$CH_3^+ + CH_2O \rightarrow CHO^+ + CH_4$	$1.60 \times 10^{-9} \left(\frac{T_g}{300}\right)^{-0.50}$	130
$CH_3^+ + O \rightarrow CHO^+ + H_2$	4.00×10^{-10}	130
$CH_4^+ + CO \rightarrow CHO^+ + CH_3$	1.40×10^{-9}	130
$CH_4 + CO^+ \rightarrow CHO^+ + CH_3$	4.55×10^{-10}	130
$CH_5^+ + CO \rightarrow CHO^+ + CH_4$	1.00×10^{-9}	130
$CH + CO^+ \rightarrow CHO^+ + C$	$3.20 \times 10^{-10} \left(\frac{T_g}{300}\right)^{-0.50}$	130
$CH + O_2^+ \rightarrow CHO^+ + O$	$3.10 \times 10^{-10} \left(\frac{T_g}{300}\right)^{-0.50}$	130
$CO^+ + CH_2O \rightarrow CHO^+ + CHO$	$1.65 \times 10^{-9} \left(\frac{T_g}{300}\right)^{-0.50}$	130
$H^+ + CH_3OH \rightarrow CHO^+ + 2H_2$	$8.85 \times 10^{-10} \left(\frac{T_g}{300}\right)^{-0.50}$	130
$H^+ + CO_2 \rightarrow CHO^+ + O$	3.50×10^{-9}	130
$H^+ + CH_2O \rightarrow CHO^+ + H_2$	$3.57 \times 10^{-9} \left(\frac{T_g}{300}\right)^{-0.50}$	130
$H_2^+ + CO \rightarrow CHO^+ + H$	2.16×10^{-9}	130
$H_2^+ + CH_2O \rightarrow CHO^+ + H_2 + H$	$1.40 \times 10^{-9} \left(\frac{T_g}{300}\right)^{-0.50}$	130
$H_2 + CO^+ \rightarrow CHO^+ + H$	7.50×10^{-10}	130

$CH_2O + O_2^+ \rightarrow O_2 + CHO^+ + H$	$2.30 \times 10^{-10} \left(\frac{T_g}{300}\right)^{-0.50}$	130
$H_2O^+ + CO \rightarrow CHO^+ + OH$	5.00×10^{-10}	130
$H_2O + CO^+ \rightarrow CHO^+ + OH$	$8.84 \times 10^{-10} \left(\frac{T_g}{300}\right)^{-0.50}$	130
$H_3^+ + CO \rightarrow CHO^+ + H_2$	$1.36 \times 10^{-9} \left(\frac{T_g}{300}\right)^{-0.14} exp\left(\frac{3.40}{T_g}\right)$	130
$H + CO_2^+ \rightarrow CHO^+ + O$	2.90×10^{-10}	130
$O^+ + CH_2O \rightarrow CHO^+ + OH$	$1.40 \times 10^{-9} \left(\frac{T_g}{300}\right)^{-0.50}$	130
$C_2H_2 + O_2^+ \rightarrow CHO^+ + H + CO$	6.50×10^{-11}	130
$O + C_2H^+ \rightarrow CHO^+ + C$	3.30×10^{-10}	130
$O + C_2H_2^+ \rightarrow CHO^+ + CH$	8.50×10^{-11}	130
$O + C_2H_4^+ \rightarrow CHO^+ + CH_3$	8.40×10^{-11}	130
$OH^+ + CO \rightarrow CHO^+ + O$	1.05×10^{-9}	130
$OH + CO^+ \rightarrow CHO^+ + O$	$3.10 \times 10^{-10} \left(\frac{T_g}{300}\right)^{-0.50}$	130
$C_2 + CHO^+ \rightarrow CO + C_2H^+$	8.30×10^{-10}	130
$C_2H_2 + CHO^+ \rightarrow C_2H_3^+ + CO$	1.40×10^{-9}	130
$C_2H_3 + CHO^+ \rightarrow C_2H_4^+ + CO$	$1.40 \times 10^{-9} \left(\frac{T_g}{300}\right)^{-0.50}$	130
$C_2H_4 + CHO^+ \rightarrow C_2H_5^+ + CO$	1.40×10^{-9}	130
$C_2H + CHO^+ \rightarrow C_2H_2^+ + CO$	7.80×10^{-10}	130
$C + CHO^+ \rightarrow CH^+ + CO$	1.10×10^{-9}	130
$CH_2 + CHO^+ \rightarrow CO + CH_3^+$	8.60×10^{-10}	130
$CH + CHO^+ \rightarrow CO + CH_2^+$	$6.30 \times 10^{-10} \left(\frac{T_g}{300}\right)^{-0.50}$	130
$H_2O + CHO^+ \rightarrow CO + H_3O^+$	$2.50 \times 10^{-9} \left(\frac{T_g}{300}\right)^{-0.50}$	130
$CHO^+ + C_2H_5 \rightarrow C_2H_6^+ + CO$	1.40×10^{-9}	130

$OH + CHO^+ \rightarrow CO + H_2O^+$	$6.20 \times 10^{-10} \left(\frac{T_g}{300}\right)^{-0.50}$	130

Electron-ion dissociative recombination		
Reaction	**Rate coefficient**	**Ref.**
$CHO^+ + e^- \rightarrow H + CO$	$0.88 \times 2.4 \times 10^{-7} \left(\frac{T_e}{300}\right)^{-0.69}$	389,390
$CHO^+ + e^- \rightarrow C + OH$	$0.06 \times 2.4 \times 10^{-7} \left(\frac{T_e}{300}\right)^{-0.69}$	389,390
$CHO^+ + e^- \rightarrow CH + O$	$0.06 \times 2.4 \times 10^{-7} \left(\frac{T_e}{300}\right)^{-0.69}$	389,390

A2.3. Main species production and destruction reactions

We provide here the main (production and destruction) reactions occurring in the plasma for the most important molecules, as well as some radicals. As a DBD consists of filaments, the chemistry is clearly different in these filaments (called pulses; characterized by higher plasma power) compared to the space in between filaments (called afterglows; characterized by lower plasma power). Note that we always performed simulations with the entire chemistry set, i.e., we did not apply any form of model reduction.

A2.3.1. C_2H_6

Destruction

Destruction of C_2H_6 occurs mainly through electron impact dissociation in the pulses:

$$C_2H_6 + e^- \rightarrow C_2H_4 + H_2 + e^- \quad \text{RA2.1}$$

$$C_2H_6 + e^- \rightarrow C_2H_5 + H + e^- \quad \text{RA2.2}$$

$$C_2H_6 + e^- \rightarrow C_2H_2 + 2H_2 + e^-$$ RA2.3

$$C_2H_6 + e^- \rightarrow 2CH_3 + e^-$$ RA2.4

$$C_2H_6 + e^- \rightarrow CH_4 + CH_2 + e^-$$ RA2.5

$$C_2H_6 + e^- \rightarrow C_2H_3 + H_2 + H + e^-$$ RA2.6

With (preset) branching ratios for electron impact dissociation of (0.46, 0.24, 0.11, 0.08, 0.07 and 0.04), respectively.

A smaller, but still relevant amount of C_2H_6 destruction occurs in the afterglows through reactions with radicals:

$$C_2H_6 + OH \rightarrow C_2H_5 + H_2O$$ RA2.7

$$C_2H_6 + O \rightarrow C_2H_5 + OH$$ RA2.8

$$C_2H_6 + H \rightarrow C_2H_5 + H_2$$ RA2.9

The rates of (RA2.1-RA2.9) decrease at higher C_2H_6 conversions, as less C_2H_6 is available and as a higher fraction of the OH, O and H radicals will react away with the formed products.

Production

Production of C_2H_6 occurs mainly in the afterglows through recombination and disproportionation reactions with radicals:

$$C_2H_5 + H \rightarrow C_2H_6$$ RA2.10

$$2CH_3 \rightarrow C_2H_6$$ RA2.11

$$2C_2H_5 \rightarrow C_2H_4 + C_2H_6$$ RA2.12

$$C_2H_5 + CHO \rightarrow C_2H_6 + CO$$ RA2.13

At low conversions, destruction reactions are more important in the afterglows, while at high conversions, the productions reactions become more important in the afterglows.

A2.3.2. CO_2

Destruction

Destruction of CO_2 occurs mainly in the pulses by electron impact dissociation:

$$CO_2 + e^- \rightarrow CO + O + e^- \quad \text{RA2.14}$$

And to some extent in the afterglows through:

$$CH_2 + CO_2 \rightarrow CH_2O + CO \quad \text{RA2.15}$$

Under the investigated conditions and at the calculated CO_2 conversions, the formation of CO_2 is not important relative to its destruction.

A2.3.3. CO

Production

The production of CO occurs both in the pulses and in the afterglows. The most important reaction in the pulses is electron impact dissociation of CO_2 (RA2.14):

$$CO_2 + e^- \rightarrow CO + O + e^- \quad \text{RA2.14}$$

The most important reactions for production of CO in the afterglows are:

$$CH_2 + CO_2 \rightarrow CH_2O + CO \quad \text{RA2.15}$$

$$C_2H_5 + CHO \rightarrow C_2H_6 + CO \quad \text{RA2.16}$$

$$C_2H_2 + O \rightarrow CH_2 + CO \quad \text{RA2.17}$$

$$C_2H_5CO \rightarrow C_2H_5 + CO \quad \text{RA2.18}$$

Destruction

Destruction of CO occurs mainly in the afterglows through reaction:

$$C_2H_5 + CO \rightarrow C_2H_5CO \quad \text{RA2.19}$$

And to a lesser extent through:

$$CH_3 + CO \rightarrow CH_3CO \quad \text{RA2.20}$$

However, most of the C_2H_5CO is formed through reaction RA2.18 and decomposes back to CO via RA2.19. As a result, the net reaction does not contribute as much to the formation of CO, compared to the other formation reactions listed.

A2.3.4. C_2H_4

Production

Formation of C_2H_4 occurs mainly through electron impact dissociation of C_2H_6 in the pulse:

$$C_2H_6 + e^- \rightarrow C_2H_4 + H_2 + e^- \quad \text{RA2.1}$$

And also to some extent by disproportionation of C_2H_x radicals in the afterglows:

$$C_2H_5 + C_2H_3 \rightarrow C_2H_4 + C_2H_2 \quad \text{RA2.21}$$

$$C_2H_5 + C_2H_5 \rightarrow C_2H_4 + C_2H_4 \quad \text{RA2.22}$$

Destruction:

Destruction of C_2H_4 in the pulses happens through electron impact dissociation:

$$C_2H_4 + e^- \rightarrow C_2H_2 + H_2 + e^- \quad \text{RA2.23}$$

$$C_2H_4 + e^- \rightarrow C_2H_3 + H + e^- \quad \text{RA2.24}$$

$$C_2H_4 + e^- \rightarrow C_2H_2 + 2H + e^- \quad \text{RA2.25}$$

And by recombination and oxidation reactions in the afterglows:

$$C_2H_4 + H \rightarrow C_2H_5 \quad \text{RA2.26}$$

$$C_2H_4 + O \rightarrow CH_3 + CHO \quad \text{RA2.27}$$

A2.3.5. C_2H_2

Production

C_2H_2 is mainly formed in the pulses through electron impact reaction of C_2H_6 and C_2H_4:

$$C_2H_6 + e^- \rightarrow C_2H_2 + 2H_2 + e^- \quad \text{RA2.3}$$

$$C_2H_4 + e^- \rightarrow C_2H_2 + H_2 + e^- \quad \text{RA2.23}$$

And to a lesser extent also through disproportionation and electron-ion recombination reactions in the afterglows:

$$C_2H_5 + C_2H_3 \rightarrow C_2H_4 + C_2H_2 \quad \text{RA2.21}$$

$$CH_3 + C_2H_3 \rightarrow CH_4 + C_2H_2 \quad \text{RA2.28}$$

$$e^- + C_2H_4^+ \rightarrow C_2H_2 + 2H \quad \text{RA2.29}$$

Destruction

Destruction of C_2H_2 occurs in the afterglows through oxidation and recombination:

$$C_2H_2 + O \rightarrow CH_2 + CO \quad \text{RA2.17}$$

$$C_2H_2 + H \rightarrow C_2H_3 \quad \text{RA2.30}$$

A2.3.6. CH_4

Production

Production of CH_4 occurs through electron impact dissociation of higher hydrocarbons in the pulses:

$$C_2H_6 + e^- \rightarrow CH_4 + CH_2 + e^- \quad \text{RA2.5}$$

$$C_3H_8 + e^- \rightarrow C_2H_4 + CH_4 + e^- \quad \text{RA2.31}$$

$$C_3H_6 + e^- \rightarrow C_2H_2 + CH_4 + e^- \quad \text{RA2.32}$$

As well as through recombination and disproportionation reactions between radicals in the afterglows:

$$CH_3 + H \rightarrow CH_4 \quad \text{RA2.33}$$

$$CH_3 + CHO \rightarrow CH_4 + CO \quad \text{RA2.34}$$

Destruction

Destruction of CH_4 occurs mainly through electron impact reactions in the pulses:

$$CH_4 + e^- \rightarrow CH_3 + H + e^- \quad \text{RA2.35}$$

$$CH_4 + e^- \rightarrow CH_2 + H_2 + e^- \quad \text{RA2.36}$$

A2.3.7. C_3H_8

Production

C_3H_8 is produced through recombination of radicals in the afterglows:

$$CH_3 + C_2H_5 \rightarrow C_3H_8 \quad \text{RA2.37}$$

Destruction

Destruction happens through electron impact reactions in the pulses:

$$C_3H_8 + e^- \rightarrow C_3H_6 + H_2 + e^- \quad \text{RA2.38}$$

$$C_3H_8 + e^- \rightarrow C_2H_4 + CH_4 + e^- \quad \text{RA2.39}$$

$$C_3H_8 + e^- \rightarrow C_3H_7 + H + e^- \quad \text{RA2.40}$$

A2.3.8. C_4H_{10}

Production

C_4H_{10} is formed through recombination in the afterglows:

$$C_2H_5 + C_2H_5 \rightarrow C_4H_{10} \quad \text{RA2.41}$$

Destruction

Electron impact reactions of C_4 hydrocarbons are not included in the model (no cross sections are available), and as a result there are no important destruction reactions for this product.

A2.3.9. C_3H_6

Production

The formation of C_3H_6 occurs through electron impact dissociation of C_3H_8 in the pulses, and reactions between radicals in the afterglows:

$$C_3H_8 + e^- \rightarrow C_3H_6 + H_2 + e^- \quad \text{RA2.38}$$

$$CH_3 + C_2H_3 \rightarrow C_3H_6 \quad \text{RA2.42}$$

$$C_4H_8 + H \rightarrow C_3H_6 + CH_3 \quad \text{RA2.43}$$

Destruction

Destruction occurs by electron impact dissociation in the pulses and recombination with CH_2 radicals in the afterglows:

$$C_3H_6 + e^- \rightarrow C_2H_2 + CH_4 + e^- \quad \text{RA2.44}$$

$$C_3H_6 + e^- \rightarrow C_3H_5 + H + e^- \quad \text{RA2.45}$$

$$C_3H_6 + CH_2 \rightarrow C_4H_8 \quad \text{RA2.46}$$

A2.3.10. C_4H_8

Production

Production of C_4H_8 occurs through recombination reactions in the afterglows:

$$C_3H_6 + CH_2 \rightarrow C_4H_8 \quad \text{RA2.46}$$

$$C_2H_5 + C_2H_3 \rightarrow C_4H_8 \quad \text{RA2.47}$$

Where RA2.46 becomes more important at higher conversions.

Destruction

Destruction of C_4H_8 occurs in the afterglows (as no electron impact reactions could be included for C_4 hydrocarbons) through:

$$C_4H_8 + H \rightarrow C_3H_6 + CH_3 \quad \text{RA2.48}$$

$$C_4H_8 + H \rightarrow C_2H_4 + C_2H_5 \quad \text{RA2.49}$$

A2.3.11. CH_2O

Production

Formation of CH_2O happens in the afterglows through:

$$CH_2 + CO_2 \rightarrow CH_2O + CO \quad \text{RA2.15}$$

$$C_2H_5 + O \rightarrow CH_3 + CH_2O \quad \text{RA2.50}$$

$$C_2H_5O \rightarrow CH_3 + CH_2O \quad \text{RA2.51}$$

$$C_3H_7O \rightarrow C_2H_5 + CH_2O \quad \text{RA2.52}$$

RA2.50 and RA2.51 are more important at low conversion, while RA2.52 becomes more important at higher conversions. However, RA2.52 is largely counteracted by its reverse reaction (RA2.54, see below) so that the net rate is not important.

Destruction

The destruction of CH_2O occurs in the afterglows by the following reactions:

$$CH_2O + H \rightarrow CH_3O \quad \text{RA2.53}$$

$$CH_2O + C_2H_5 \rightarrow C_3H_7O \quad \text{RA2.54}$$

$$CH_2O + H \rightarrow CHO + H_2 \quad \text{RA2.55}$$

$$CH_2O + O \rightarrow CHO + OH \quad \text{RA2.56}$$

$$CH_2O + OH \rightarrow CHO + H_2O \quad \text{RA2.57}$$

Note that reactions RA2.52 and RA2.54 largely cancel each other out especially at higher conversions.

A2.3.12. CH_3CHO

Production

Production of CH_3CHO (acetaldehyde) occurs in the afterglows through oxidation of C_2H_5 radicals or by recombination between CH_3 and CHO radicals:

$$C_2H_5 + O \rightarrow CH_3CHO + H \quad \text{RA2.58}$$

$$CH_3 + CHO \rightarrow CH_3CHO \quad \text{RA2.59}$$

Destruction

Destruction also occurs in the afterglows through reaction with H, O and OH radicals:

$$H + CH_3CHO \rightarrow H_2 + CH_3CO \quad \text{RA2.60}$$

$$H + CH_3CHO \rightarrow H_2 + CH_3 + CO \quad \text{RA2.61}$$

$$O + CH_3CHO \rightarrow OH + CH_3CO \quad \text{RA2.62}$$

$$OH + CH_3CHO \rightarrow H_2O + CH_3CO \quad \text{RA2.63}$$

CH_3CO primarily decomposes into CO and CH_3:

$$CH_3CO \rightarrow CH_3 + CO \quad \text{RA2.64}$$

A2.3.13. C_2H_5CHO

C_2H_5CHO (propanal) is formed in the afterglows via recombination:

$$C_2H_5 + CHO \rightarrow C_2H_5CHO \quad \text{RA2.65}$$

Destruction also happens in the afterglows by:

$$C_2H_5CHO + O \rightarrow C_2H_5CO + OH \quad \text{RA2.66}$$

$$C_2H_5CHO + OH \rightarrow C_2H_5CO + H_2O \quad \text{RA2.67}$$

A2.3.14. CH_3OH

Production

Production of CH_3OH happens in the afterglows by:

$$CH_3 + OH \rightarrow CH_3OH \quad \text{RA2.68}$$

$$CH_3O + H \rightarrow CH_3OH \quad \text{RA2.69}$$

$$CH_3O + C_2H_6 \rightarrow CH_3OH + C_2H_5 \quad \text{RA2.70}$$

$$CH_3O + CHO \rightarrow CH_3OH + CO \quad \text{RA2.71}$$

$$CH_3O + CH_2O \rightarrow CH_3OH + CHO \quad \text{RA2.72}$$

The importance of R14.1 relative to the total production decreases at higher conversions, while that of R14.4 and R14.5 increases with conversion.

Destruction

Destruction of CH_3OH occurs in the afterglows by:

$$CH_3OH + O \rightarrow OH + CH_2OH \quad \text{RA2.73}$$

$$CH_3OH + O \rightarrow OH + CH_3O \quad \text{RA2.74}$$

$$CH_3OH + OH \rightarrow H_2O + CH_3O \quad \text{RA2.75}$$

$$CH_3OH + OH \rightarrow CH_2O + H_2O + H \quad \text{RA2.76}$$

$$H + CH_3OH \rightarrow CH_2OH + H_2 \quad \text{RA2.77}$$

Most CH_3O reacts to form CH_2O, CH_2OH reacts to form alcohols or formaldehyde:

$$CH_3O + CH_3 \rightarrow CH_2O + CH_4 \quad \text{RA2.78}$$

$$CH_3O + C_2H_5 \rightarrow CH_2O + C_2H_6 \quad \text{RA2.79}$$

$$CH_2OH + C_2H_5 \rightarrow C_3H_7OH \quad \text{RA2.80}$$

$$CH_2OH + CH_3 \rightarrow C_2H_5OH \quad \text{RA2.81}$$

$$CH_2OH + CHO \rightarrow CH_3OH + CO \quad \text{RA2.82}$$

$$CH_2OH + CHO \rightarrow 2CH_2O \quad \text{RA2.83}$$

A2.3.15. C_2H_5OH

Production

Production happens in the afterglows through:

$$C_2H_5 + OH \rightarrow C_2H_5OH \quad \text{RA2.84}$$

$$C_2H_5O + H \rightarrow C_2H_5OH \quad \text{RA2.85}$$

$$C_2H_5O + CHO \rightarrow C_2H_5OH + CO \quad \text{RA2.86}$$

$$C_2H_5O + C_2H_6 \rightarrow C_2H_5OH + C_2H_5 \quad \text{RA2.87}$$

the C_2H_5O radical is formed by recombination of C_2H_5 and O:

$$C_2H_5 + O \rightarrow C_2H_5O \quad \text{RA2.88}$$

Destruction

Destruction of C_2H_5OH occurs in the afterglows by:

$$C_2H_5OH + H \rightarrow C_2H_5 + H_2O \quad \text{RA2.89}$$

$$C_2H_5OH + H \rightarrow CH_3CHOH + H_2 \quad \text{RA2.90}$$

$$C_2H_5OH + O \rightarrow CH_3CHOH + OH \quad \text{RA2.91}$$

$$C_2H_5OH + OH \rightarrow CH_3CHOH + H_2O \quad \text{RA2.92}$$

A2.3.16. HCOOH

Production

HCOOH (formic acid) is formed through oxidation reactions in the afterglows:

$$CH_2O + OH \rightarrow HCOOH + H \quad \text{RA2.93}$$

$$CH_3CHOH + O \rightarrow HCOOH + CH_3 \quad \text{RA2.94}$$

Destruction

The rate of destruction is much less important compared to that of production under the conditions investigated and at the conversion reached during the residence time.

A2.3.17. CHO radicals

Production

The CHO radical is formed in the afterglows by:

$$C_2H_4 + O \rightarrow CH_3 + CHO \quad \text{RA2.27}$$

$$CH_2O + O \rightarrow CHO + OH \quad \text{RA2.56}$$

Destruction

Destruction mainly happens through:

$$C_2H_5 + CHO \rightarrow C_2H_6 + CO \quad \text{RA2.13}$$

$$CH_3 + CHO \rightarrow CH_4 + CO \quad \text{RA2.34}$$

A2.3.18. CH_3CHOH radicals

Production

This radical is mainly formed from C_2H_5OH in the afterglows:

$$C_2H_5OH + H \rightarrow CH_3CHOH + H_2 \quad \text{RA2.90}$$

$$C_2H_5OH + O \rightarrow CH_3CHOH + OH \quad \text{RA2.91}$$

$$C_2H_5OH + OH \rightarrow CH_3CHOH + H_2O \quad \text{RA2.92}$$

Destruction

The radical is oxidized in the afterglows to form HCOOH and CH_3CHO:

$$CH_3CHOH + O \rightarrow HCOOH + CH_3 \quad \text{RA2.94}$$

$$CH_3CHOH + O \rightarrow CH_3CHO + OH \quad \text{RA2.95}$$

A3. Appendix to Chapter 5

A3.1. Surface and gas-phase species energies and frequencies

The surface species energies and vibrational frequencies calculated by DFT within our group (by R. Michiels) are listed in Table A3.1; for the energies and frequencies of other surface species used in the models, we refer to ref. 99. The adsorbate and transition state energies are given relative to the empty (111) slab and CO, H_2O and H_2 in the gas-phase. In accordance with ref. 99, we use 12 cm^{-1} as a lower limit for the vibrational frequencies and smaller frequencies are replaced with this value. The energies and vibrational frequencies of gas species are listed in Table A3.2. These energies are not calculated with DFT, but instead we use the experimental enthalpies of formation, which are taken from the NIST chemistry webbook.[9] The zero-point energy (ZPE) and thermodynamic contribution are subtracted from these enthalpies of formation to give the "uncorrected" enthalpies at 0 K. The thermodynamic contribution is estimated from the heat capacity as c_p(300 K) × 300 K, with c_p(300 K) the heat capacity at 300 K.[26] The acquired energies are subsequently recalculated as the formation enthalpies relative to gaseous CO, H_2O and H_2. Note that the energies in Table A3.2 are only given without the ZPE and thermodynamic contributions, as the "uncorrected" energies are required as input for CatMAP. However, in both CatMAP and our coupled plasma-surface model, the ZPE and thermodynamic contributions are added again to these "uncorrected" energies during the simulations. The vibrational frequencies of the gas species are taken from ref. [391].

Table A3.1. Energies and vibrational frequencies of surface species on various transition metal (111) surfaces. The energies are calculated as the formation energy of the surface species relative to the empty (111) slab and CO, H_2O and H_2 in the gas-phase. The DFT data was calculated by R. Michiels, for more details see the original publication.[39]

Species [a]	**Surface**	**Energy (eV)**	**Vibrational frequencies (cm^{-1})** [b]
O^{*s}	Rh	0.42	314.0, 314.0, 461.0
O^{*s}	Ag	1.98	-
O^{*s}	Cu	0.89	-
O^{*s}	Pd	1.01	-
O^{*s}	Pt	1.29	-
O^{*s}	Ir	0.73	-
CO_2^{*s}	Rh	-0.85	12.0, 12.0, 12.0, 37.0, 45.0, 610.0, 620.0, 1311.0, 2343.0
CO_2^{*s}	Ag	-0.82	-
CO_2^{*s}	Cu	-0.83	-
CO_2^{*s}	Pd	-0.84	-
CO_2^{*s}	Pt	-0.85	-
CO_2^{*s}	Ir	-0.85	-
$O\text{-}CO^{*s}$	Rh	0.14	55.0, 117.0, 257.0, 274.0, 383.0, 432.0, 564.0, 1889
$O\text{-}CO^{*s}$	Ag	2.12	-
$O\text{-}CO^{*s}$	Cu	1.02	-
$O\text{-}CO^{*s}$	Pd	0.92	-
$O\text{-}CO^{*s}$	Pt	1.06	-
$O\text{-}CO^{*s}$	Ir	0.13	-
$H\text{-}H^{*h}$	Rh	0.03	85.0, 204.0, 311.0, 1767.0, 1932.0
$H\text{-}H^{*h}$	Ag	1.83	-
$H\text{-}H^{*h}$	Cu	0.98	-
$H\text{-}H^{*h}$	Pd	0.14	-
$H\text{-}H^{*h}$	Pt	0.25	-

H-H*[h]	Ir	0.11	-
O-H*[s]	Rh	1.42	111.0, 270.0, 423.0, 459.0, 938.0
O-H*[s]	Ag	3.22	-
O-H*[s]	Cu	2.03	-
O-H*[s]	Pd	1.87	-
O-H*[s]	Pt	2.11	-
O-H*[s]	Ir	1.85	-

a) Species containing a hyphen (-) denote transition states.

b) The vibrational frequencies of the species on Rh are used for all descriptor values.

Table A3.2. Gas-phase species energies and vibrational frequencies.

Species	**Energy (eV)**	**Vibrational frequencies (cm^{-1})**
H_2	0.00	4401.2
H_2O	0.00	3657.0, 1595.0, 3756.0
CH_4	-2.77	2917.0, 1534.0, 1534.0, 3019.0, 3019.0, 3019.0, 1306.0, 1306.0, 1306.0
CO	0.00	2169.8
CO_2	-0.33	1333.0, 2349.0, 667.0, 667.0
CH_2O	-0.28	2782.0, 1746.0, 1500.0, 1167.0, 2843.0, 1249.0
CH_3OH	-1.51	3681.0, 3000.0, 2844.0, 1477.0, 1455.0, 1345.0, 1060.0, 1033.0, 2960.0, 1477.0, 1165.0, 200.0
CH_3CHO	-2.74	3014.0, 2923.0, 2716.0, 1743.0, 1433.0, 1395.0, 1352.0, 1114.0, 867.0, 509.0, 2964.0, 1431.0, 1102.0, 764.0, 150.0
CH_3CH_2OH	-3.71	3652.9, 2984.1, 2939.2, 2899.6, 1490.2, 1463.5, 1411.7, 1371.4, 1256.3, 1090.7, 1027.7, 887.6, 416.5, 2991.4, 2909.6, 1445.8, 1274.8, 1161.0, 811.8, 251.0, 200.0
O	5.32	-
H	2.38	-
CH_3	-0.29	3004.4, 606.5, 3160.8, 3160.8, 1396.0, 1396.0
CH_2	2.39	2805.9, 963.1, 3190.0
OH	3.07	3737.8
CHO	1.56	2434.5, 1868.2, 1080.8

A3.2. Scaling relations describing the surface species energies

Table A3.3. Scaling relations that describe the surface species binding energies as function of the binding energies of CH and O* (E_{CH*} and E_{O*}, respectively). All energies are expressed in eV. The binding energies are defined as the formation energies of the adsorbed species relative to the empty (111) slab and CO, H_2O and H_2 in the gas-phase.*

Surface species	**Scaling relation for surface species energy (eV)**
H^{*h}	$0.2157 \times E_{CH*} + 0.0208$
CH_2CO^{*s}	$0.3840 \times E_{CH*} - 2.0507$
CH_2OH^{*s}	$0.4036 \times E_{CH*} - 0.7973$
CH_2O^{*s}	$0.0299 \times E_{CH*} + 0.1287 \times E_{O*} - 0.8431$
CH_2^{*s}	$0.5987 \times E_{CH*} - 0.6190$
$CH_3CH_2OH^{*s}$	$0.0953 \times E_{O*} - 4.247$
CH_3CHOH^{*s}	$0.3899 \times E_{CH*} - 3.0096$
CH_3CHO^{*s}	$0.1068 \times E_{O*} - 3.2775$
CH_3CO^{*s}	$0.4514 \times E_{CH*} - 2.7583$
CH_3O^{*s}	$0.3151 \times E_{O*} - 1.5419$
CH_3^{*s}	$0.2981 \times E_{CH*} - 1.7338$
$CHCO^{*s}$	$0.4047 \times E_{CH*} - 1.6985$
$CHOH^{*s}$	$0.62583 \times E_{CH*} - 0.0469$
CHO^{*s}	$0.4721 \times E_{CH*} - 0.1194$
CH^{*s}	E_{CH*}
CO_2^{*s}	$0.0086 \times E_{CH*} - 0.8335$
CO^{*s}	$0.5075 \times E_{CH*} - 0.8177$
OH^{*s}	$0.3089 \times E_{O*} + 0.2447$
O^{*s}	E_{O*}
$H\text{-}H^{*h}$	$0.4627 \times E_{CH*} + 0.9053$
$CH\text{-}CO^{*s}$	$1.0504 \times E_{CH*} - 0.0304$
$CH\text{-}H^{*s}$	$1.1198 \times E_{CH*} + 0.5586$

CH-OH*^{s}	$0.8717 \times E_{CH^*} + 0.2692 \times E_{O^*} + 0.9914$
CH_2-H*^{s}	$0.7830 \times E_{CH^*} - 0.1068$
CH_3-CO*^{s}	$0.4927 \times E_{CH^*} - 1.3135$
CH_3-H*^{s}	$0.4721 \times E_{CH^*} - 1.1043$
CH_3-OH*^{s}	$0.1327 \times E_{CH^*} + 0.1939 \times E_{O^*} + 0.0450$
CH_3CHO-H*^{s}	$0.3742 \times E_{CH^*} + 0.0096 \times E_{O^*} - 2.2066$
CH_3CHOH-H *^{s}	$0.4713 \times E_{CH^*} + 0.0211 \times E_{O^*} - 2.5172$
CH_3O-H*^{s}	$0.1085 \times E_{CH^*} + 0.1585 \times E_{O^*} - 0.5971$
H-CH_2CO*^{s}	$0.4969 \times E_{CH^*} - 1.2740$
H-CH_2OH*^{s}	$0.4492 \times E_{CH^*} - 0.1866$
H-CH_2O*^{s}	$0.1947 \times E_{CH^*} + 0.1673 \times E_{O^*} - 0.3649$
H-CH_3CO*^{s}	$0.4777 \times E_{CH^*} + 0.0303 \times E_{O^*} - 2.1454$
H-CHCO*^{s}	$0.6542 \times E_{CH^*} - 0.8822$
H-CHOH*^{s}	$0.6167 \times E_{CH^*} + 0.6003$
H-CHO*^{s}	$0.4828 \times E_{CH^*} + 0.0401 \times E_{O^*} + 0.2964$
H-CO*^{s}	$0.5341 \times E_{CH^*} + 0.1823$
H-OH*^{s}	$0.1497 \times E_{CH^*} + 0.2144 \times E_{O^*} + 0.9553$
HCO-H*^{s}	$0.6838 \times E_{CH^*} + 0.5385$
O-CO*^{s}	$0.2986 \times E_{CH^*} + 0.5883 \times E_{O^*} + 0.5036$
O-H*^{s}	$0.1603 \times E_{CH^*} + 0.7434 \times E_{O^*} + 1.4210$

A3.3. Rate coefficients of gas-phase reactions

Table A3.4 lists the gas-phase reactions and corresponding rate coefficients used in the coupled plasma-surface model, with exception of the electron impact dissociation reactions, which are listed in Table A3.6. Some of the rate coefficients for the dissociation and recombination reactions in Table A3.4 are given as fall-off expressions of the form:[131]

$$k = \frac{k_0 M k_\infty}{k_0 M + k_\infty} F \qquad \text{Eq. A3.1}$$

$$\log(F) = \frac{\log(F_c)}{1 + \left[\frac{\log(k_0 M / k_\infty)}{N}\right]^2} \qquad \text{Eq. A3.2}$$

$$N = 0.75\text{-}1.27\log(F_c) \qquad \text{Eq. A3.3}$$

In which k_0 and k_∞ are the low- and high-pressure limit rate coefficients, respectively, F_c is the centered broadening factor and M is the density of neutral gas species, equal to 1.449×10^{19} cm^{-3} at 500 K. Expressions for k_0, k_∞ and F_c are listed in Table A3.4.

Table A3.4. List of gas-phase reactions included in the coupled plasma-surface model with the corresponding rate coefficient expressions and references. For each reaction we list the corresponding rate coefficients and the references from which these were adopted. In the expressions of the rate constants T denotes the gas temperature in K, R denotes the ideal gas constant in J mole^{-1} K^{-1} and N_A is Avogadro's number. The units of the activation barriers match those of the denominator (i.e., J mole^{-1} for RT, or K for T), so that the exponent itself is unitless.

Reaction	Rate coefficient [a, b]	Ref.
H + OH → H_2 + O	$4.1\times10^{-12}\left(\frac{T}{300}\right)\exp\left(\frac{-3.50\times10^{3}}{T}\right)$	392
H + OH→ H_2O	$6.7\times10^{-31}\left(\frac{T}{300}\right)^{-2.0}\times M$	392
OH + OH → H_2O + O	$1.02\times10^{-12}\left(\frac{T}{300}\right)^{1.4}\exp\left(\frac{2.0\times10^{2}}{T}\right)$	134
OH → O + H	$4.7\times10^{-8}\left(\frac{T}{300}\right)^{-1.0}\exp\left(\frac{-5.0830\times10^{4}}{T}\right)\times M$	392

$H_2 + OH \rightarrow H + H_2O$	$3.6\times10^{-16}T^{1.52}\exp\left(\frac{-1.74\times10^{3}}{T}\right)$	131
$H_2O + O \rightarrow OH + OH$	$7.6\times10^{-15}T^{1.3}\exp\left(\frac{-8.6\times10^{3}}{T}\right)$	134
$H + H_2O \rightarrow H_2 + OH$	$7.5\times10^{-16}T^{1.6}\exp\left(\frac{-9.03\times10^{3}}{T}\right)$	131
$O + H \rightarrow OH$	$4.33\times10^{-32}\left(\frac{T}{300}\right)^{-1}\times M$	134
$H_2 + O \rightarrow H + OH$	$9\times10^{-12}\left(\frac{T}{300}\right)\exp\left(\frac{-4.480\times10^{3}}{T}\right)$	392
$H + H \rightarrow H_2$	$1.8\times10^{-30}T^{-1}\times M$	392
$CO + O \rightarrow CO_2$	$2.79\times10^{-29}T^{-1.5}\exp\left(\frac{-2.52\times10^{3}}{T}\right)\times M$	393
$CH_4 + H \rightarrow CH_3 + H_2$	$6.4\times10^{-18}T^{2.11}\exp\left(\frac{-3.9\times10^{3}}{T}\right)$	394
$CH_3 + H_2 \rightarrow CH_4 + H$	$6.62\times10^{-20}T^{2.24}\exp\left(\frac{-3.22\times10^{3}}{T}\right)$	394
$CH_3 + H \rightarrow CH_2 + H_2$	$2.1\times10^{-8}T^{-0.56}\exp\left(\frac{-8.0\times10^{3}}{T}\right)$	131
$CH_3 + H \rightarrow CH_4$	$k_0 = 1.7\times10^{-24}T^{-1.8}$ $k_\infty = 3.5\times10^{-10}$ $F_c = 6.3\times10^{-1}\exp\left(\frac{-T}{3.3150\times10^{3}}\right)$ $+3.7\times10^{-1}\exp\left(\frac{-T}{6.10\times10^{1}}\right)$	131 c
$CH_2 + H_2 \rightarrow CH_3 + H$	$7.32\times10^{-19}T^{2.3}\exp\left(\frac{-3.6990\times10^{3}}{T}\right)$	395
$CH_3 + CH_4 \rightarrow C_2H_6 + H$	$\frac{8\times10^{13}}{N_A}\exp\left(\frac{-1.6736\times10^{5}}{RT}\right)$	396
$CH_3 + CH_4 \rightarrow C_2H_5 + H_2$	$\frac{1\times10^{13}}{N_A}\exp\left(\frac{-9.6232\times10^{4}}{RT}\right)$	396

$CH_2 + CH_4 \rightarrow CH_3 + CH_3$	$7.14\times10^{-12}\exp\left(\frac{-4.199\times10^{4}}{RT}\right)$	397
$CH_3 + CH_3 \rightarrow C_2H_6$	$k_0 = 3.5\times10^{-7}T^{-7}\exp\left(\frac{-1.39\times10^{3}}{T}\right)$ $k_\infty = 6\times10^{-11}$ $F_c = 3.8\times10^{-1}\exp\left(\frac{-T}{7.3\times10^{1}}\right)$ $+6.2\times10^{-1}\exp\left(\frac{-T}{1.18\times10^{3}}\right)$	131 c
$CH_3 + CH_3 \rightarrow C_2H_5 + H$	$9\times10^{-11}\exp\left(\frac{-8.08\times10^{3}}{T}\right)$	131
$CH_3 + CH_3 \rightarrow CH_2 + CH_4$	$5.6\times10^{-17}T^{1.34}\exp\left(\frac{-6.791\times10^{4}}{RT}\right)$	398
$CH_3 \rightarrow CH_2 + H$	$1.7\times10^{-8}\exp\left(\frac{-4.560\times10^{4}}{T}\right)\times M$	131
$C_2H_6 + H \rightarrow C_2H_5 + H_2$	$1.63\times10^{-10}\exp\left(\frac{-4.640\times10^{3}}{T}\right)$	131
$C_2H_5 + H_2 \rightarrow C_2H_6 + H$	$5.1\times10^{-24}T^{3.6}\exp\left(\frac{-4.253\times10^{3}}{T}\right)$	131
$C_2H_5 + H \rightarrow CH_3 + CH_3$	7×10^{-11}	131
$C_2H_5 + H \rightarrow C_2H_6$	$\frac{6\times10^{-11}}{1+10^{-1.915+2.69\times10^{-3}T-2.35\times10^{-7}T^{2}}}$	134
$C_2H_6 + CH_3 \rightarrow C_2H_5 + CH_4$	$9.3\times10^{-14}\exp\left(\frac{-4.740\times10^{3}}{T}\right)$ $+1.4\times10^{-9}\exp\left(\frac{-1.120\times10^{4}}{T}\right)$	131
$C_2H_6 + CH_2 \rightarrow C_2H_5 + CH_3$	$\frac{6.5\times10^{12}}{N_A}\exp\left(\frac{-3.31\times10^{4}}{RT}\right)$	397
$C_2H_5 + CH_4 \rightarrow C_2H_6 + CH_3$	$1.43\times10^{-25}T^{4.14}\exp\left(\frac{-6.322\times10^{3}}{T}\right)$	134
$C_2H_5 + CH_3 \rightarrow C_2H_6 + CH_2$	$3\times10^{-44}T^{9.0956}$	399

$CO_2 + H \rightarrow CO + OH$	$4.7\times10^{-10}\exp\left(\frac{-1.3915\times10^{4}}{T}\right)$	131
$CO + H \rightarrow CHO$	$2\times10^{-35}T^{0.2}\times M$	131
$CO + OH \rightarrow CO_2 + H$	$\frac{3.3\times10^{6}}{N_A}T^{1.55}\exp\left(\frac{4.02\times10^{2}}{T}\right)$	400
$CH_4 + O \rightarrow CH_3 + OH$	$7.3\times10^{-19}T^{2.5}\exp\left(\frac{-3.310\times10^{3}}{T}\right)$	131
$CH_3 + O \rightarrow H + CH_2O$	$0.8\times1.4\times10^{-10}$	131
$CH_3 + O \rightarrow CO + H_2 + H$	$0.2\times1.4\times10^{-10}$	131
$CH_2 + O \rightarrow CO + H + H$	$0.6\times3.4\times10^{-10}\exp\left(\frac{-2.7\times10^{2}}{T}\right)$	131
$CH_2 + O \rightarrow CO + H_2$	$0.4\times3.4\times10^{-10}\exp\left(\frac{-2.7\times10^{2}}{T}\right)$	131
$CH_3 + CO \rightarrow CH_3CO$	$k_0 = 1.6\times10^{-37}T^{1.05}\exp\left(\frac{-1.3\times10^{3}}{T}\right)$ $k_\infty = 3.1\times10^{-16}T^{1.05}\exp\left(\frac{-2.85\times10^{3}}{T}\right)$ $F_c = 5\times10^{-1}$	131 c
$CH_2 + CO_2 \rightarrow CO + CH_2O$	3.9×10^{-14}	134
$CH_4 + OH \rightarrow CH_3 + H_2O$	$1.66\times10^{-18}T^{2.182}\exp\left(\frac{-1.231\times10^{3}}{T}\right)$	401
$CH_3 + OH \rightarrow CH_3OH$	$k_0 = 1.06\times10^{-10}T^{-6.21}\exp\left(\frac{-6.71\times10^{2}}{T}\right)$ $k_\infty = 7.2\times10^{-9}T^{-0.79}$ $F_c = 7.5\times10^{-1}\exp\left(\frac{-T}{2.1\times10^{2}}\right)$ $+2.5\times10^{-1}\exp\left(\frac{-T}{1.434\times10^{3}}\right)$	131 c
$CH_3 + OH \rightarrow CH_2 + H_2O$	$\frac{k}{M}$ $k_0 = 1.8\times10^{-8}T^{-0.91}\exp\left(\frac{-2.75\times10^{2}}{T}\right)$	131 c

	$k_\infty = 6.4\times10^{-8}T^{5.8}\exp\left(\frac{4.85\times10^{2}}{T}\right)$ $F_c = 6.64\times10^{-1}\exp\left(\frac{-T}{3.569\times10^{3}}\right)$ $+3.36\times10^{-1}\exp\left(\frac{-T}{1.08\times10^{2}}\right)$ $+\exp\left(\frac{-3.24\times10^{3}}{T}\right)$	
$CH_3 + OH \rightarrow CH_2OH + H$	$1.2\times10^{-12}\exp\left(\frac{-2.76\times10^{3}}{T}\right)$	131
$CH_3 + OH \rightarrow CH_3O + H$	$2\times10^{-14}\exp\left(\frac{-6.99\times10^{3}}{T}\right)$	131
$CH_3 + OH \rightarrow H_2 + CH_2O$	$5.3\times10^{-15}\exp\left(\frac{-2.53\times10^{3}}{T}\right)$	131
$CH_3 + OH \rightarrow CH_4 + O$	$1.16\times10^{-19}T^{2.2}\exp\left(\frac{-2.24\times10^{3}}{T}\right)$	402
$CH_3 + H_2O \rightarrow CH_4 + OH$	$8\times10^{-22}T^{2.9}\exp\left(\frac{-7.48\times10^{3}}{T}\right)$	403
$CH_2 + OH \rightarrow H + CH_2O$	5×10^{-11}	134
$CH_2 + H_2O \rightarrow CH_3 + OH$	1×10^{-16}	134
$CH_3O + CO \rightarrow CH_3 + CO_2$	$2.6\times10^{-11}\exp\left(\frac{-5.94\times10^{3}}{T}\right)$	134
$H + CHO \rightarrow CO + H_2$	1.5×10^{-10}	131
$H + CHO \rightarrow CH_2 + O$	$\frac{3.981\times10^{13}}{N_A}\exp\left(\frac{-4.29\times10^{5}}{RT}\right)$	320
$H_2 + CHO \rightarrow H + CH_2O$	$3\times10^{-18}T^{2}\exp\left(\frac{-8.972\times10^{3}}{T}\right)$	134
$H + CH_2O \rightarrow H_2 + CHO$	$3.34\times10^{-23}T^{-3.81}\exp\left(\frac{-2.02\times10^{2}}{T}\right)$	131
$H + CH_2O \rightarrow CH_3O$	$\frac{2.4\times10^{13}}{N_A}\exp\left(\frac{-1.72\times10^{4}}{T}\right)$	282
$CH_3O + H \rightarrow H_2 + CH_2O$	3.3×10^{-11}	134

$CH_3O + H \rightarrow CH_3OH$	$3.4\times10^{-10}\left(\frac{T}{300}\right)^{0.33}$	404
$CH_3O + H_2 \rightarrow CH_3OH + H$	$1.7\times10^{-15}\left(\frac{T}{300}\right)^{4}\exp\left(\frac{-2.47\times10^{3}}{T}\right)$	405
$CH_2OH + H \rightarrow H_2 + CH_2O$	1×10^{-11}	136
$CH_2OH + H \rightarrow CH_3 + OH$	1.6×10^{-10}	136
$CH_2OH + H_2 \rightarrow CH_3OH + H$	$1.12\times10^{-18}T^{2}\exp\left(\frac{-6.722\times10^{3}}{T}\right)$	136
$CH_3OH + H \rightarrow CH_2OH + H_2$	$5.7\times10^{-15}T^{1.24}\exp\left(\frac{-2.26\times10^{3}}{T}\right)$	131
$CH_3OH + H \rightarrow CH_3 + H_2O$	1.9×10^{-28}	406
$CHO + OH \rightarrow CO + H_2O$	1.8×10^{-10}	131
$H_2O + CHO \rightarrow CH_2O + OH$	$3.9\times10^{-16}T^{1.35}\exp\left(\frac{-1.3146\times10^{4}}{T}\right)$	134
$CH_2O + OH \rightarrow H_2O + CHO$	$2.31\times10^{-11}\exp\left(\frac{-3.04\times10^{2}}{T}\right)$	131
$CH_3O + OH \rightarrow H_2O + CH_2O$	3×10^{-11}	134
$CH_2OH + OH \rightarrow H_2O + CH_2O$	4×10^{-11}	136
$CH_2OH + H_2O \rightarrow CH_3OH + OH$	$4.2\times10^{-14}\left(\frac{T}{300}\right)^{3.0}\exp\left(\frac{-10440}{T}\right)$	405
$CH_3OH + OH \rightarrow H + H_2O + CH_2O$	$2.96\times10^{-16}T^{1.4434}\exp\left(\frac{-5.7\times10^{1}}{T}\right)$	328
$CHO + O \rightarrow CO + OH$	5×10^{-11}	134
$CHO + O \rightarrow CO_2 + H$	5×10^{-11}	134
$CH_2O + O \rightarrow CHO + OH$	$6.9\times10^{-13}T^{0.57}\exp\left(\frac{-1.39\times10^{3}}{T}\right)$	131
$CH_3O + O \rightarrow CH_2O + OH$	$0.25\times2.5\times10^{-11}$	131
$CH_3OH + O \rightarrow CH_2OH + OH$	$4.1\times10^{-11}\exp\left(\frac{-2.67\times10^{3}}{T}\right)$	131
$CH_4 + CHO \rightarrow CH_3 + CH_2O$	$1.21\times10^{-20}T^{2.85}\exp\left(\frac{-1.133\times10^{4}}{T}\right)$	134

$CH_3 + CHO \rightarrow CH_4 + CO$	2×10^{-10}	134
$CH_3 + CHO \rightarrow CH_3CHO$	3×10^{-11}	134
$CH_2 + CHO \rightarrow CH_3 + CO$	3×10^{-11}	134
$CH_3 + CH_2O \rightarrow CH_4 + CHO$	$5.3\times10^{-23}T^{3.36}\exp\left(\frac{-2.17\times10^{3}}{T}\right)$	131
$CH_2 + CH_2O \rightarrow CH_3 + CHO$	1×10^{-14}	134
$CH_3O + CH_4 \rightarrow CH_3 + CH_3OH$	$2.6\times10^{-13}\exp\left(\frac{-4.45\times10^{3}}{T}\right)$	134
$CH_3 + CH_3O \rightarrow CH_4 + CH_2O$	4×10^{-11}	134
$CH_2 + CH_3O \rightarrow CH_3 + CH_2O$	3×10^{-11}	134
$CH_2OH + CH_4 \rightarrow CH_3 + CH_3OH$	$3.6\times10^{-23}T^{3.1}\exp\left(\frac{-8.166\times10^{3}}{T}\right)$	136
$CH_2OH + CH_3 \rightarrow CH_3CH_2OH$	2×10^{-11}	136
$CH_2OH + CH_3 \rightarrow CH_4 + CH_2O$	4×10^{-12}	136
$CH_2 + CH_2OH \rightarrow CH_3 + CH_2O$	2×10^{-12}	136
$CH_3 + CH_3OH \rightarrow CH_2OH + CH_4$	$0.33\times5\times10^{-23}T^{3.45}\exp\left(\frac{-4.02\times10^{3}}{T}\right)$	131
$CH_3 + CH_3OH \rightarrow CH_3O + CH_4$	$0.67\times5\times10^{-23}T^{3.45}\exp\left(\frac{-4.02\times10^{3}}{T}\right)$	131
$CH_2 + CH_3OH \rightarrow CH_2OH + CH_3$	$5.3\times10^{-23}T^{3.2}\exp\left(\frac{-3.609\times10^{3}}{T}\right)$	136
$CH_2 + CH_3OH \rightarrow CH_3 + CH_3O$	$2.4\times10^{-23}T^{3.1}\exp\left(\frac{-3.49\times10^{3}}{T}\right)$	136
$CHO + CHO \rightarrow CO + CH_2O$	$0.853\times5\times10^{-11}$	131
$CHO + CHO \rightarrow CO + CO + H_2$	$0.147\times5\times10^{-11}$	131
$CH_3O + CHO \rightarrow CH_3OH + CO$	1.5×10^{-10}	134
$CH_2OH + CHO \rightarrow CH_3OH + CO$	2×10^{-10}	136
$CH_2OH + CHO \rightarrow CH_2O + CH_2O$	3×10^{-10}	136
$CH_3OH + CHO \rightarrow CH_2OH + CH_2O$	$1.6\times10^{-20}T^{2.9}\exp\left(\frac{-6.596\times10^{3}}{T}\right)$	136

$CH_3OH + CHO \rightarrow CH_3O + CH_2O$	$1.6\times10^{-22}T^{2.9}\exp\left(\frac{-6.596\times10^{3}}{T}\right)$	136
$CH_3O + CH_2O \rightarrow CH_3OH + CHO$	$1.7\times10^{-13}\exp\left(\frac{-1.5\times10^{3}}{T}\right)$	134
$CH_2OH + CH_2O \rightarrow CH_3OH + CHO$	$9.1\times10^{-21}T^{2.8}\exp\left(\frac{-2.95\times10^{3}}{T}\right)$	136
$CH_3O + CH_3O \rightarrow CH_3OH + CH_2O$	1×10^{-10}	134
$CH_2OH + CH_3O \rightarrow CH_3OH + CH_2O$	4×10^{-11}	136
$CH_3O + CH_3OH \rightarrow CH_2OH + CH_3OH$	$5\times10^{-13}\exp\left(\frac{-2.05\times10^{3}}{T}\right)$	136
$CH_2OH + CH_2OH \rightarrow CH_3OH + CH_2O$	8×10^{-12}	136
$CH_2OH + CH_3OH \rightarrow CH_3O + CH_3OH$	$1.3\times10^{-14}\exp\left(\frac{-6.07\times10^{3}}{T}\right)$	136
$C_2H_6 + OH \rightarrow C_2H_5 + H_2O$	$1.52\times10^{-17}T^{2}\exp\left(\frac{-5\times10^{2}}{T}\right)$	131
$C_2H_5 + OH \rightarrow C_2H_6 + O$	$1.7\times10^{-40}T^{8.8}\exp\left(\frac{-2.5\times10^{2}}{T}\right)$	402
$C_2H_5 + H_2O \rightarrow C_2H_6 + OH$	$5.6\times10^{-18}T^{1.44}\exp\left(\frac{-1.015\times10^{4}}{T}\right)$	134
$C_2H_6 + O \rightarrow C_2H_5 + OH$	$3\times10^{-19}T^{2.8}\exp\left(\frac{-2.92\times10^{3}}{T}\right)$	131
$C_2H_5 + O \rightarrow CH_3CHO + H$	$0.4\times2.2\times10^{-10}$	131
$C_2H_5 + O \rightarrow CH_3 + CH_2O$	$0.3\times2.2\times10^{-10}$	131
$C_2H_6 + CHO \rightarrow C_2H_5 + CH_2O$	$7.8\times10^{-20}T^{2.72}\exp\left(\frac{-9.176\times10^{3}}{T}\right)$	134
$C_2H_6 + CH_3O \rightarrow C_2H_5 + CH_3OH$	$4\times10^{-13}\exp\left(\frac{-3.57\times10^{3}}{T}\right)$	134
$C_2H_6 + CH_2OH \rightarrow C_2H_5 + CH_3OH$	$3.3\times10^{-22}T^{2.95}\exp\left(\frac{-7.033\times10^{3}}{T}\right)$	136
$C_2H_5 + CHO \rightarrow C_2H_6 + CO$	2×10^{-10}	134

$C_2H_5 + CH_2O \rightarrow C_2H_6 + CHO$	$9.2\times10^{-21}T^{2.81}\exp\left(\frac{-2.95\times10^{3}}{T}\right)$	134
$C_2H_5 + CH_3O \rightarrow C_2H_6 + CH_2O$	4×10^{-11}	134
$C_2H_5 + CH_2OH \rightarrow C_2H_6 + CH_2O$	4×10^{-12}	136
$C_2H_5 + CH_3OH \rightarrow C_2H_6 + CH_2OH$	$5.3\times10^{-23}T^{3.2}\exp\left(\frac{-4.61\times10^{3}}{T}\right)$	136
$C_2H_5 + CH_3OH \rightarrow C_2H_6 + CH_3O$	$2.4\times10^{-23}T^{3.1}\exp\left(\frac{-4.5\times10^{3}}{T}\right)$	136
$CH_3CO + H \rightarrow CH_3 + CHO$	$0.65\times\frac{2\times10^{13}}{N_A}$	289,407
$CH_3CO + H \rightarrow CH_3CHO$	$6.02\times10^{-11}T^{0.16}$	290
$CH_3CO + H_2 \rightarrow CH_3CHO + H$	$6.8\times10^{-18}T^{1.82}\exp\left(\frac{-8.862\times10^{3}}{T}\right)$	134
$CH_3CHO + H \rightarrow CH_3CO + H_2$	$2.18\times10^{-19}T^{2.58}\exp\left(\frac{-6.14\times10^{2}}{T}\right)$	312
$CH_3CH_2OH + H \rightarrow C_2H_5 + H_2O$	$\frac{5.9\times10^{11}}{N_A}\exp\left(\frac{-1.44\times10^{4}}{RT}\right)$	408
$CH_3CHO + OH \rightarrow CH_3CO + H_2O$	$0.93\times4.8\times10^{-16}T^{1.35}\exp\left(\frac{7.92\times10^{2}}{T}\right)$	131
$CH_3CO + O \rightarrow CH_3 + CO_2$	$0.75\times3.5\times10^{-10}$	131
$CH_3CHO + O \rightarrow CH_3CO + OH$	$\frac{5\times10^{12}}{N_A}\exp\left(\frac{-7.5\times10^{3}}{RT}\right)$	289
$CH_3CO + CH_4 \rightarrow CH_3 + CH_3CHO$	$3.6\times10^{-21}T^{2.88}\exp\left(\frac{-1.08\times10^{4}}{T}\right)$	134
$CH_3 + CH_3CHO \rightarrow CH_3CO + CH_4$	$0.993\times5.8\times10^{-32}T^{6.21}\exp\left(\frac{-8.2\times10^{2}}{T}\right)$	131
$CH_3 + CH_3CHO \rightarrow CH_3 + CH_4 + CO$	$\frac{6.31\times10^{12}}{N_A}T^{0.5}\exp\left(\frac{-4.48\times10^{4}}{RT}\right)$	409
$C_2H_6 + CH_3CO \rightarrow C_2H_5 + CH_3CHO$	$3\times10^{-20}T^{2.75}\exp\left(\frac{-8.82\times10^{3}}{T}\right)$	134
$C_2H_5 + CH_3CHO \rightarrow C_2H_6 + CH_3CO$	$\frac{1.26\times10^{12}}{N_A}\exp\left(\frac{-3.56\times10^{4}}{RT}\right)$	410

$CH_3CO + CHO \rightarrow CH_3CHO + CO$	1.5×10^{-11}	134
$CH_3CO + CH_2O \rightarrow CH_3CHO + CHO$	$3\times10^{-13}\exp\left(\frac{-6.5\times10^{3}}{T}\right)$	134
$CH_3CO + CH_3O \rightarrow CH_3CHO + CH_2O$	1×10^{-11}	134
$CH_3CO + CH_3OH \rightarrow CH_3CHO + CH_2OH$	$8.06\times10^{-21}T^{2.99}\exp\left(\frac{-6.21\times10^{3}}{T}\right)$	136
$CH_3CHO + CH_3O \rightarrow CH_3CO + CH_3OH$	$\frac{1.69\times10^{5}}{N_A}T^{2.04}\exp\left(\frac{-9.84\times10^{3}}{RT}\right) + \frac{9.62\times10^{3}}{N_A}T^{2.5}\exp\left(\frac{-6.65\times10^{2}}{RT}\right)$	411
$CHO \rightarrow CO + H$	$6.6\times10^{-11}\exp\left(\frac{-7.82\times10^{3}}{T}\right)\times M$	131
$CH_2O \rightarrow H + CHO$	$8.09\times10^{-9}\exp\left(\frac{-3.805\times10^{4}}{T}\right)\times M$	131
$CH_2O \rightarrow CO + H_2$	$4.7\times10^{-9}\exp\left(\frac{-3.211\times10^{4}}{T}\right)\times M$	131
$CH_3O \rightarrow H + CH_2O$	$6.8\times10^{13}\exp\left(\frac{-1.317\times10^{4}}{T}\right)$	131
$CH_2OH \rightarrow H + CH_2O$	$k_0 = \frac{6.01\times10^{33}}{N_A}T^{-5.39}\exp\left(\frac{-1.51\times10^{5}}{RT}\right)$ $k_\infty = 2.8\times10^{14}T^{-0.73}\exp\left(\frac{-1.37\times10^{5}}{RT}\right)$ $F_c = 4\times10^{-2}\exp\left(\frac{-T}{6.76\times10^{1}}\right) + 9.6\times10^{-1}\exp\left(\frac{-T}{1.855\times10^{3}}\right) + \exp\left(\frac{-7.543\times10^{3}}{T}\right)$	412 c
$CH_3OH \rightarrow CH_3 + OH$	$0.8\times k$ $k_0 = 1.1\times10^{-7}\exp\left(\frac{-3.308\times10^{4}}{T}\right)$	131,413 c

	$k_\infty = 2.5\times10^{19}T^{-0.94}\exp\left(\frac{-4.703\times10^4}{T}\right)$ $F_c = 1.8\times10^{-1}\exp\left(\frac{-T}{2\times10^2}\right)$ $+8.2\times10^{-1}\exp\left(\frac{-T}{1.438\times10^3}\right)$	
$CH_3OH \rightarrow CH_2 + H_2O$	$0.15\times k$ $k_0 = 1.1\times10^{-7}\exp\left(\frac{-3.308\times10^4}{T}\right)$ $k_\infty = 2.5\times10^{19}T^{-0.94}\exp\left(\frac{-4.703\times10^4}{T}\right)$ $F_c = 1.8\times10^{-1}\exp\left(\frac{-T}{2\times10^2}\right)$ $+8.2\times10^{-1}\exp\left(\frac{-T}{1.438\times10^3}\right)$	131,413 c
$CH_3OH \rightarrow CH_2OH + H$	$1.64\times10^7T^{2.55}\exp\left(\frac{-3.85\times10^5}{RT}\right)$	414
$CH_3CO \rightarrow CH_3 + CO$	$k_0 = 1\times10^{-8}\exp\left(\frac{-7.08\times10^3}{T}\right)$ $k_\infty = 2\times10^{13}\exp\left(\frac{-8.63\times10^3}{T}\right)$ $F_c = 5\times10^{-1}$	131 c
$CH_3CHO \rightarrow CH_3CO + H$	$5\times10^{14}\exp\left(\frac{-3.68\times10^5}{RT}\right)$	353
$CH_3CHO \rightarrow CH_4 + CO$	$1\times10^{15}\exp\left(\frac{-3.56\times10^5}{RT}\right)$	353
$CH_3CHO \rightarrow CH_3 + CHO$	$2.1\times10^{16}\exp\left(\frac{-4.1135\times10^4}{T}\right)$	131
$CH_3CH_2OH \rightarrow CH_2OH + CH_3$	$k_0 = \frac{2.88\times10^{85}}{N_A}T^{-18.9}\exp\left(\frac{-5.532\times10^4}{T}\right)$ $k_\infty = 5.94\times10^{23}T^{-1.68}\exp\left(\frac{-4.588\times10^4}{T}\right)$ $F_c = 5\times10^{-1}\exp\left(\frac{-T}{2\times10^2}\right)$	415 c

	$+5\times10^{-1}\exp\left(\frac{-T}{8.9\times10^{2}}\right)$ $+\exp\left(\frac{-4.6\times10^{3}}{T}\right)$	
$C_2H_6 + H \rightarrow CH_3 + CH_4$	$K_{eq} \times k_{rev}$	[d]
$C_2H_5 + H_2 \rightarrow CH_3 + CH_4$	$K_{eq} \times k_{rev}$	[d]
$CH_2 + H \rightarrow CH_3$	$K_{eq} \times k_{rev}$	[d]
$H + CH_2O \rightarrow CH_3 + O$	$K_{eq} \times k_{rev}$	[d]
$CO + H_2 \rightarrow CH_2 + O$	$K_{eq} \times k_{rev}$	[d]
$CO + CH_2O \rightarrow CH_2 + CO_2$	$K_{eq} \times k_{rev}$	[d]
$CH_3O + H \rightarrow CH_3 + OH$	$K_{eq} \times k_{rev}$	[d]
$H_2 + CH_2O \rightarrow CH_3 + OH$	$K_{eq} \times k_{rev}$	[d]
$H + CH_2O \rightarrow CH_2 + OH$	$K_{eq} \times k_{rev}$	[d]
$CH_3 + CO_2 \rightarrow CH_3O + CO$	$K_{eq} \times k_{rev}$	[d]
$CO + H_2 \rightarrow H + CHO$	$K_{eq} \times k_{rev}$	[d]
$CH_2 + O \rightarrow H + CHO$	$K_{eq} \times k_{rev}$	[d]
$H_2 + CH_2O \rightarrow CH_3O + H$	$K_{eq} \times k_{rev}$	[d]
$CH_3OH \rightarrow CH_3O + H$	$K_{eq} \times k_{rev}$	[d]
$CH_3OH + H \rightarrow CH_3O + H_2$	$K_{eq} \times k_{rev}$	[d]
$H_2 + CH_2O \rightarrow CH_2OH + H$	$K_{eq} \times k_{rev}$	[d]
$CH_3 + H_2O \rightarrow CH_3OH + H$	$K_{eq} \times k_{rev}$	[d]
$CO + H_2O \rightarrow CHO + OH$	$K_{eq} \times k_{rev}$	[d]
$H_2O + CH_2O \rightarrow CH_3O + OH$	$K_{eq} \times k_{rev}$	[d]
$H_2O + CH_2O \rightarrow CH_2OH + OH$	$K_{eq} \times k_{rev}$	[d]
$CH_3OH + OH \rightarrow CH_2OH + H_2O$	$K_{eq} \times k_{rev}$	[d]
$CO + OH \rightarrow CHO + O$	$K_{eq} \times k_{rev}$	[d]
$CO_2 + H \rightarrow CHO + O$	$K_{eq} \times k_{rev}$	[d]
$CHO + OH \rightarrow CH_2O + O$	$K_{eq} \times k_{rev}$	[d]
$CH_2O + OH \rightarrow CH_3O + O$	$K_{eq} \times k_{rev}$	[d]

$CH_2OH + OH \rightarrow CH_3OH + O$	$K_{eq} \times k_{rev}$	[d]
$CH_4 + CO \rightarrow CH_3 + CHO$	$K_{eq} \times k_{rev}$	[d]
$CH_3 + CO \rightarrow CH_2 + CHO$	$K_{eq} \times k_{rev}$	[d]
$CH_3 + CHO \rightarrow CH_2 + CH_2O$	$K_{eq} \times k_{rev}$	[d]
$CH_4 + CH_2O \rightarrow CH_3 + CH_3O$	$K_{eq} \times k_{rev}$	[d]
$CH_3 + CH_2O \rightarrow CH_2 + CH_3O$	$K_{eq} \times k_{rev}$	[d]
$CH_4 + CH_2O \rightarrow CH_2OH + CH_3$	$K_{eq} \times k_{rev}$	[d]
$CH_3 + CH_2O \rightarrow CH_2 + CH_2OH$	$K_{eq} \times k_{rev}$	[d]
$CH_2OH + CH_3 \rightarrow CH_2 + CH_3OH$	$K_{eq} \times k_{rev}$	[d]
$CH_3 + CH_3O \rightarrow CH_2 + CH_3OH$	$K_{eq} \times k_{rev}$	[d]
$CO + CH_2O \rightarrow CHO + CHO$	$K_{eq} \times k_{rev}$	[d]
$CH_3OH + CO \rightarrow CH_3O + CHO$	$K_{eq} \times k_{rev}$	[d]
$CH_3OH + CO \rightarrow CH_2OH + CHO$	$K_{eq} \times k_{rev}$	[d]
$CH_2O + CH_2O \rightarrow CH_2OH + CHO$	$K_{eq} \times k_{rev}$	[d]
$CH_3OH + CH_2O \rightarrow CH_3O + CH_3O$	$K_{eq} \times k_{rev}$	[d]
$CH_3OH + CH_2O \rightarrow CH_2OH + CH_3O$	$K_{eq} \times k_{rev}$	[d]
$CH_3OH + CH_2O \rightarrow CH_2OH + CH_2OH$	$K_{eq} \times k_{rev}$	[d]
$CH_3CHO + H \rightarrow C_2H_5 + O$	$K_{eq} \times k_{rev}$	[d]
$CH_3 + CH_2O \rightarrow C_2H_5 + O$	$K_{eq} \times k_{rev}$	[d]
$C_2H_6 + CO \rightarrow C_2H_5 + CHO$	$K_{eq} \times k_{rev}$	[d]
$C_2H_6 + CH_2O \rightarrow C_2H_5 + CH_3O$	$K_{eq} \times k_{rev}$	[d]
$C_2H_6 + CH_2O \rightarrow C_2H_5 + CH_2OH$	$K_{eq} \times k_{rev}$	[d]
$CH_3 + CHO \rightarrow CH_3CO + H$	$K_{eq} \times k_{rev}$	[d]
$C_2H_5 + H_2O \rightarrow CH_3CH_2OH + H$	$K_{eq} \times k_{rev}$	[d]
$CH_3CO + H_2O \rightarrow CH_3CHO + OH$	$K_{eq} \times k_{rev}$	[d]
$CH_3 + CO_2 \rightarrow CH_3CO + O$	$K_{eq} \times k_{rev}$	[d]
$CH_3CO + OH \rightarrow CH_3CHO + O$	$K_{eq} \times k_{rev}$	[d]

$CH_3CHO + CO \rightarrow CH_3CO + CHO$	$K_{eq} \times k_{rev}$	d
$CH_3CHO + CHO \rightarrow CH_3CO + CH_2O$	$K_{eq} \times k_{rev}$	d
$CH_3CHO + CH_2O \rightarrow CH_3CO + CH_3O$	$K_{eq} \times k_{rev}$	d
$CH_2OH + CH_3CHO \rightarrow CH_3CO + CH_3OH$	$K_{eq} \times k_{rev}$	d
$CH_3CO + CH_3OH \rightarrow CH_3CHO + CH_3O$	$K_{eq} \times k_{rev}$	d
$H + CHO \rightarrow CH_2O$	$K_{eq} \times k_{rev}$	d
$CO + H_2 \rightarrow CH_2O$	$K_{eq} \times k_{rev}$	d
$H + CH_2O \rightarrow CH_2OH$	$K_{eq} \times k_{rev}$	d
$CH_2 + H_2O \rightarrow CH_3OH$	$K_{eq} \times k_{rev}$	d
$CH_2OH + H \rightarrow CH_3OH$	$K_{eq} \times k_{rev}$	d
$CH_4 + CO \rightarrow CH_3CHO$	$K_{eq} \times k_{rev}$	d

a) *Units are s^{-1}, $cm^3\ s^{-1}$ or $cm^6\ s^{-1}$ for unimolecular, bimolecular or trimolecular reactions, respectively.*

b) *$N_A = 6.02214076 \times 10^{23}\ mol^{-1}$, $R = 8.314462618\ J\ mol^{-1}\ K^{-1}$, $M = 1.449 \times 10^{19}\ cm^{-3}$.*

c) *Fall-off expressions, see Eq. A3.1, Eq. A3.2 and Eq. A3.3.*

d) *Rate coefficient calculated from the equilibrium constants and the rate coefficient of the reverse reaction. Equilibrium constants are calculated from the data in ref. 16.*

A3.4. Electron impact processes included in the Bolsig+ calculations

Table A3.5. List of electron impact processes used in the calculation of the electron impact dissociation rate coefficients and electron mobilities with BOLSIG+.

Electron impact process	**Reference**
$CH_4 + e^- \rightarrow CH_4^+ + 2e^-$	[43]
$CH_4 + e^- \rightarrow CH_3^+ + H + 2e^-$	[43]
$CH_4 + e^- \rightarrow CH_2^+ + H_2 + 2e^-$	[43]
$CH_4 + e^- \rightarrow CH_2^+ + 2H + 2e^-$	[43]
$CH_4 + e^- \rightarrow CH^+ + H_2 + H + 2e^-$	[43]
$CH_4 + e^- \rightarrow CH_3 + H + e^-$	[43]
$CH_4 + e^- \rightarrow CH_2 + H_2 + e^-$	[43]
$CH_4 + e^- \rightarrow CH_2 + 2H + e^-$	[43]
$CH_4 + e^- \rightarrow CH + H_2 + H + e^-$	[43]
$CH_4 + e^- \rightarrow C + H_2 + 2H + e^-$	[43]
$CH_4 + e^- \rightarrow C + 2H_2 + e^-$	[43]
$CH_4 + e^- \rightarrow CH_4 + e^-$ (elastic)	[42]
$CH_4 + e^- \rightarrow CH_4(v_{1,3}) + e^-$	[42]
$CH_4 + e^- \rightarrow CH_4(v_{2,4}) + e^-$	[42]
$CH_4 + e^- \rightarrow CH_2^- + H_2$	[42]
$CH_4 + e^- \rightarrow CH_3 + H^-$	[42]
$CO_2 + e^- \rightarrow CO_2^+ + 2e^-$	[42]
$CO_2 + e^- \rightarrow CO + O(1D) + e^-$	[44]
$CO_2 + e^- \rightarrow CO(a3P) + O + e^-$	[44]
$CO_2 + e^- \rightarrow CO_2 + e^-$ (effective)	[42]
$CO_2 + e^- \rightarrow CO_2(v_{010}) + e^-$	[42]
$CO_2 + e^- \rightarrow CO_2(v_{020}) + e^-$	[42]
$CO_2 + e^- \rightarrow CO_2(v_{100}) + e^-$	[42]

$CO_2 + e^- \rightarrow CO_2(v_{030+110}) + e^-$	42
$CO_2 + e^- \rightarrow CO_2(v_{001}) + e^-$	42
$CO_2 + e^- \rightarrow CO_2(v_{040+120+011}) + e^-$	42
$CO_2 + e^- \rightarrow CO_2(X, v_{020}) + e^-$	42
$CO_2 + e^- \rightarrow CO_2(X, v_{050+210+130+021+101}) + e^-$	42
$CO_2 + e^- \rightarrow CO_2(X, v_{300}) + e^-$	42
$CO_2 + e^- \rightarrow CO_2(X, v_{060+220+140}) + e^-$	42
$CO_2 + e^- \rightarrow CO_2(X, v_{0n0+n00}) + e^-$	42
$CO_2 + e^- \rightarrow CO_2(E1) + e^-$	42
$CO_2 + e^- \rightarrow CO_2(E2) + e^-$	42
$CO_2 + e^- \rightarrow CO + O^-$	416
$CO + e^- \rightarrow CO^+ + 2e^-$	42
$CO + e^- \rightarrow C + O + e^-$	42
$CO + e^- \rightarrow CO + e^-$ (elastic)	42
$CO + e^- \rightarrow CO(v_x) + e^-$ (with x = 1-10)	42
$CO + e^- \rightarrow CO(a3P) + e^-$	42
$CO + e^- \rightarrow CO(a'3Su+) + e^-$	42
$CO + e^- \rightarrow CO(A1P) + e^-$	42
$CO + e^- \rightarrow CO(b3Su+) + e^-$	42
$CO + e^- \rightarrow CO(B1Su+) + e^-$	42
$CO + e^- \rightarrow CO(C1Su+) + e^-$	42
$CO + e^- \rightarrow CO(E1P) + e^-$	42
$CO + e^- \rightarrow C + O^-$	42
$C_2H_6 + e^- \rightarrow C_2H_6^+ + 2e^-$	43
$C_2H_6 + e^- \rightarrow C_2H_5^+ + H + 2e^-$	43
$C_2H_6 + e^- \rightarrow C_2H_4^+ + H_2 + 2e^-$	43
$C_2H_6 + e^- \rightarrow C_2H_3^+ + H_2 + H + 2e^-$	43
$C_2H_6 + e^- \rightarrow C_2H_2^+ + 2H_2 + 2e^-$	43

$C_2H_6 + e^- \rightarrow C_2H_2^+ + H_2 + 2H + 2e^-$	43
$C_2H_6 + e^- \rightarrow C_2H_4 + H_2^+ + 2e^-$	43
$C_2H_6 + e^- \rightarrow CH_3^+ + CH_3 + 2e^-$	43
$C_2H_6 + e^- \rightarrow C_2H_5 + H + e^-$	43,202
$C_2H_6 + e^- \rightarrow C_2H_4 + H_2 + e^-$	43,202
$C_2H_6 + e^- \rightarrow C_2H_3 + H_2 + H + e^-$	43,202
$C_2H_6 + e^- \rightarrow C_2H_2 + 2H_2 + e^-$	43,202
$C_2H_6 + e^- \rightarrow CH_4 + CH_2 + e^-$	43,202
$C_2H_6 + e^- \rightarrow 2CH_3 + e^-$	43,202
$C_2H_6 + e^- \rightarrow C_2H_6 + e^-$ (elastic)	203
$C_2H_6 + e^- \rightarrow C_2H_6(v_{1,3}) + e^-$	203
$C_2H_6 + e^- \rightarrow C_2H_6(v_{2,4}) + e^-$	203
$C_2H_6 + e^- \rightarrow C_2H_6(E1) + e^-$	203
$C_2H_6 + e^- \rightarrow C_2H_6(E2) + e^-$	203
$H_2 + e^- \rightarrow H_2^+ + 2e^-$	42
$H_2 + e^- \rightarrow H + H^+ + 2e^-$	417
$H_2 + e^- \rightarrow 2H + e^-$	417
$H_2 + e^- \rightarrow H_2 + e^-$ (elastic)	42
$H_2 + e^- \rightarrow H_2(v_x) + e^-$ (with x = 1-3)	42
$H_2 + e^- \rightarrow H_2(b3Su) + e^-$	42
$H_2 + e^- \rightarrow H_2(B1Su) + e^-$	42
$H_2 + e^- \rightarrow H_2(c3Pu) + e^-$	42
$H_2 + e^- \rightarrow H_2(a3Sg) + e^-$	42
$H_2 + e^- \rightarrow H_2(C1Pu) + e^-$	42
$H_2 + e^- \rightarrow H_2(E1Sg, F1Sg) + e^-$	42
$H_2 + e^- \rightarrow H_2(e3Su) + e^-$	42
$H_2 + e^- \rightarrow H_2(B'1Su) + e^-$	42
$H_2 + e^- \rightarrow H_2(D1Pu) + e^-$	42

$H_2 + e^- \rightarrow H_2(B''1Su) + e^-$	42
$H_2 + e^- \rightarrow H_2(D'1Pu) + e^-$	42
$H_2 + e^- \rightarrow H + H^-$	417
$H_2O + e^- \rightarrow H_2O^+ + 2e^-$	418,419
$H_2O + e^- \rightarrow H + OH^+ + 2e^-$	418,419
$H_2O + e^- \rightarrow H_2 + O^+ + 2e^-$	418,419
$H_2O + e^- \rightarrow H_2^+ + O + 2e^-$	418,419
$H_2O + e^- \rightarrow H^+ + OH + 2e^-$	418,419
$H_2O + e^- \rightarrow H + OH + e^-$	420
$H_2O + e^- \rightarrow H_2O + e^-$ (elastic)	203
$H_2O + e^- \rightarrow H_2O(rot) + e^-$	418
$H_2O + e^- \rightarrow H_2O(\nu_{010}) + e^-$	418
$H_2O + e^- \rightarrow H_2O(\nu_{100+001}) + e^-$	418
$H_2O + e^- \rightarrow H + OH^-$	418,419
$H_2O + e^- \rightarrow H_2 + O^-$	418,420
$H_2O + e^- \rightarrow H^- + OH$	418,420

A3.5. Electron impact dissociation rate coefficients

Table A3.6. Electron impact dissociation reactions included in the coupled plasma-surface model and the corresponding calculated rate coefficients multiplied with the electron density ($n_e = 10^{14}$ cm^{-3}).

Reaction	**$k \times n_e$ (s^{-1})**
$CH_4 + e^- \rightarrow CH_3 + H + e^-$	4.1×10^{-2}
$CH_4 + e^- \rightarrow CH_2 + H_2 + e^-$	9.2×10^{-3}
$CH_4 + e^- \rightarrow CH_2 + 2H + e^-$	6.9×10^{-4}
$CO_2 + e^- \rightarrow CO + O + e^-$	4.4×10^{-2}
$H_2O + e^- \rightarrow H + OH + e^-$	8.2×10^{-2}
$H_2 + e^- \rightarrow 2H + e^-$	9.3×10^{-2}
$C_2H_6 + e^- \rightarrow C_2H_5 + H + e^-$	1.1×10^{-2}
$C_2H_6 + e^- \rightarrow CH_2 + CH_4 + e^-$	4.1×10^{-3}
$C_2H_6 + e^- \rightarrow 2CH_3 + e$	5.9×10^{-3}

Table A3.6. Electron impact dissociation reactions included in the coupled plasma-surface model and the corresponding calculated rate coefficients multiplied with the electron density (ne = 1014 cm-3).Table A3.6 lists the rate coefficients (multiplied by the electron density) that are used in the model. As discussed in section 5.2.2.2, these rate coefficients are estimates of the time- and space-averaged rate coefficients inside the reactor. Hence, the actual rate coefficients of electron impact reactions inside the microdischarges (which are both short-lived and compact), are much higher. Multiplying the rate coefficients in Table A3.6 with the number densities of CO_2 and CH_4 in the feed ($n = 7.24 \times 10^{19}$ cm^{-3} for both) gives total electron impact dissociation rates of 3.19×10^{17} and 3.69×10^{17} cm^{-3} s^{-1} for CO_2 and CH_4, respectively. This is in the same order of magnitude as the net CO_2 and CH_4 destruction rates presented in Figure 5.3 and Figure 5.4 (i.e., 2.23×10^{17} and 3.45×10^{17} cm^{-3} s^{-1}, respectively) for the plasma-only case.

Indeed, electron impact dissociation is the main driving force behind the conversion of these molecules. Using these rate coefficients, we obtain CO_2 and CH_4 conversions of 15.3% and 23.5%, respectively, for the plasma-only case with the reaction conditions used in our model. This is in agreement with experimental conversions (6-13% and 13-24% for CO_2 and CH_4, respectively) for DRM in a DBD using similar reaction conditions.[421]

A3.6. Catalyst surface reactions

Table A3.7. List of catalyst surface reactions included in the CatMAP and coupled plasma-surface models.

Reaction[a, b]	**Transition state**
$CH_4 + *^s + *^h \rightleftharpoons CH_3*^s + H*^h$	$CH_3\text{-}H*^s + *^h$
$CH_3*^s + *^h \rightleftharpoons CH_2*^s + H*^h$	$CH_2\text{-}H*^s + *^h$
$CH_2*^s + *^h \rightleftharpoons CH*^s + H*^h$	$CH\text{-}H*^s + *^h$
$CO_2 + *^s \rightleftharpoons CO_2*^s$	-[c]
$CO_2*^s + *^s \rightleftharpoons CO*^s + O*^s$	$O\text{-}CO*^s + *^s$
$CO + *^s \rightleftharpoons CO*^s$	-[c]
$H_2 + *^h + *^h \rightleftharpoons H*^h + H*^h$	$H\text{-}H*^h + *^h$
$O*^s + H*^h \rightleftharpoons OH*^s + *^h$	$O\text{-}H*^s + *^h$
$OH*^s + H*^h \rightleftharpoons H_2O + *^s + *^h$	$H\text{-}OH*^s + *^h$
$H + *^h \rightleftharpoons H*^h$	-[c]
$O + *^s \rightleftharpoons O*^s$	-[c]
$CH_3 + *^s \rightleftharpoons CH_3*^s$	-[c]
$CH_2 + *^s \rightleftharpoons CH_2*^s$	-[c, d]
$OH + *^s \rightleftharpoons OH*^s$	-[c, d]
$CHO + *^s \rightleftharpoons CHO*^s$	-[c, d]
$CO*^s + H*^h \rightleftharpoons CHO*^s + *^h$	$H\text{-}CO*^s + *^h$
$CHO*^s + H*^h \rightleftharpoons CHOH*^s + *^h$	$HCO\text{-}H*^s + *^h$

$CHOH^{*s} + *^{s} \rightleftharpoons CH^{*s} + OH^{*s}$	$CH\text{-}OH^{*s} + *^{s}$
$CH^{*s} + CO^{*s} \rightleftharpoons CHCO^{*s} + *^{s}$	$CH\text{-}CO^{*s} + *^{s}$
$CHCO^{*s} + H^{*h} \rightleftharpoons CH_2CO^{*s} + *^{h}$	$H\text{-}CHCO^{*s} + *^{h}$
$CH_2CO^{*s} + H^{*h} \rightleftharpoons CH_3CO^{*s} + *^{h}$	$H\text{-}CH_2CO^{*s} + *^{h}$
$CH_3CO^{*s} + H^{*h} \rightleftharpoons CH_3CHO^{*s} + *^{h}$	$H\text{-}CH_3CO^{*s} + *^{h}$
$CH_3CHO^{*s} \rightleftharpoons CH_3CHO + *^{s}$	-[c]
$CH_3CHO^{*s} + H^{*h} \rightleftharpoons CH_3CHOH^{*s} + *^{h}$	$CH_3CHO\text{-}H^{*s} + *^{h}$
$CH_3CHOH^{*s} + H^{*h} \rightleftharpoons CH_3CH_2OH^{*s} + *^{h}$	$CH_3CHOH\text{-}H^{*s} + *^{h}$
$CH_3CH_2OH^{*s} \rightleftharpoons CH_3CH_2OH + *^{s}$	-[c]
$CHO^{*s} + H^{*h} \rightleftharpoons CH_2O^{*s} + *^{h}$	$H\text{-}CHO^{*s} + *^{h}$
$CH_2O^{*s} \rightleftharpoons CH_2O + *^{s}$	-[c, d]
$CH_2O^{*s} + H^{*h} \rightleftharpoons CH_3O^{*s} + *^{h}$	$H\text{-}CH_2O^{*s} + *^{h}$
$CH_3O^{*s} + H^{*h} \rightleftharpoons CH_3OH + *^{s} + *^{h}$	$CH_3O\text{-}H^{*s} + *^{h}$
$CHOH^{*s} + H^{*h} \rightleftharpoons CH_2OH^{*s} + *^{h}$	$H\text{-}CHOH^{*s} + *^{h}$
$CH_2OH^{*s} + H^{*h} \rightleftharpoons CH_3OH + *^{s} + *^{h}$	$H\text{-}CH_2OH^{*s} + *^{h}$
$CH_3O^{*s} + *^{s} + H^{*h} \rightleftharpoons CH_3{}^{*s} + OH^{*s} + *^{h}$	$CH_3\text{-}OH^{*s} + *^{s} + *^{h}$
$CH_3{}^{*s} + CO^{*s} \rightleftharpoons CH_3CO^{*s} + *^{s}$	$CH_3\text{-}CO^{*s} + *^{s}$

a) *All reactions on the transition metal surfaces are included in both the forward and reverse direction.*

b) *Superscripts h and s denote hydrogen reservoir and catalytic surface sites, respectively.*

c) *Molecular and radical adsorption/desorption reactions are considered to occur without additional energy barrier. For these cases the enthalpy and Gibbs free energy barriers are determined by the reaction enthalpy and Gibbs free energy, respectively.*

d) *These adsorption/desorption reactions are only included in the coupled plasma-surface simulations and not in the simulations with the CatMAP model.*

A3.7. Reactions on the non-catalytic wall

Table A3.8. List of reactions that occur on the non-catalytic wall included in the coupled plasma-surface model.

Physisorption [a]	**Desorption** [a]
$H + *^{p} \rightarrow H*^{p}$	$H*^{p} \rightarrow H + *^{p}$
$O + *^{p} \rightarrow O*^{p}$	$O*^{p} \rightarrow O + *^{p}$
$CH_3 + *^{p} \rightarrow CH_3*^{p}$	$CH_3*^{p} \rightarrow CH_3 + *^{p}$
$CH_2 + *^{p} \rightarrow CH_2*^{p}$	$CH_2*^{p} \rightarrow CH_2 + *^{p}$
$CHO + *^{p} \rightarrow CHO*^{p}$	$CHO*^{p} \rightarrow CHO + *^{p}$
$OH + *^{p} \rightarrow OH*^{p}$	$OH*^{p} \rightarrow OH + *^{p}$
Chemisorption [a]	**Surface diffusion** [a]
$H + *^{c} \rightarrow H*^{c}$	$H*^{p} + *^{c} \rightarrow H*^{c} + *^{p}$
$O + *^{c} \rightarrow O*^{c}$	$O*^{p} + *^{c} \rightarrow O*^{c} + *^{p}$
$CH_3 + *^{c} \rightarrow CH_3*^{c}$	$CH_3*^{p} + *^{c} \rightarrow CH_3*^{c} + *^{p}$
$CH_2 + *^{c} \rightarrow CH_2*^{c}$	$CH_2*^{p} + *^{c} \rightarrow CH_2*^{c} + *^{p}$
$CHO + *^{c} \rightarrow CHO*^{c}$	$CHO*^{p} + *^{c} \rightarrow CHO*^{c} + *^{p}$
$OH + *^{c} \rightarrow OH*^{c}$	$OH*^{p} + *^{c} \rightarrow OH*^{c} + *^{p}$
Eley-Rideal [a]	**Langmuir-Hinshelwood** [a]
$H + H*^{c} \rightarrow H_2 + *^{c}$	$H*^{p} + H*^{c} \rightarrow H_2 + *^{p} + *^{c}$
$H + CH_3*^{c} \rightarrow CH_4 + *^{c}$	$H*^{p} + CH_3*^{c} \rightarrow CH_4 + *^{p} + *^{c}$
$H + CHO*^{c} \rightarrow CH_2O + *^{c}$	$H*^{p} + CHO*^{c} \rightarrow CH_2O + *^{p} + *^{c}$
$H + OH*^{c} \rightarrow H_2O + *^{c}$	$H*^{p} + OH*^{c} \rightarrow H_2O + *^{p} + *^{c}$
$H + O*^{c} \rightarrow OH*^{c}$	$H*^{p} + O*^{c} \rightarrow OH*^{c} + *^{p}$
$H + CH_2*^{c} \rightarrow CH_3*^{c}$	$H*^{p} + CH_2*^{c} \rightarrow CH_3*^{c} + *^{p}$
$CH_3 + H*^{c} \rightarrow CH_4 + *^{c}$	$CH_3*^{p} + H*^{c} \rightarrow CH_4 + *^{p} + *^{c}$
$CHO + H*^{c} \rightarrow CH_2O + *^{c}$	$CHO*^{p} + H*^{c} \rightarrow CH_2O + *^{p} + *^{c}$
$OH + H*^{c} \rightarrow H_2O + *^{c}$	$OH*^{p} + H*^{c} \rightarrow H_2O + *^{p} + *^{c}$

$O + H^{*c} \rightarrow OH^{*c}$	$O^{*p} + H^{*c} \rightarrow OH^{*c} + *^{p}$
$CH_2 + H^{*c} \rightarrow CH_3^{*c}$	$CH_2^{*p} + H^{*c} \rightarrow CH_3^{*c} + *^{p}$
$CO + O^{*c} \rightarrow CO_2 + *^{c}$	

a) Superscripts c and p denote chemisorption and physisorption sites, respectively.

A3.8. Evolution of radicals with operating time

Figure A3.1 illustrates the evolution of the H, CH_3, O and OH radical densities in the plasma following the start of the reaction process. We call this "operating time", to make clear that this is not the residence time of the gas in the plasma. The latter is determined by the gas flow rate and length of the plasma in the reactor, while the operating time is the time as function of which the gas densities and surface coverages in the CSTR reactor change (see section 2.3). This corresponds to the time that evolves following the start of an experiment, i.e. after turning on the plasma and gas flow. Our current model does not yet consider the filamentary character of a DBD, i.e., occurrence of microdischarge pulses that cause temporal and spatial nonuniformities. Nevertheless, the time evolution of the radicals can still provide useful insight in the interactions between the plasma species and the catalyst, both at short and long timescales. Note that both the horizontal and vertical axes in Figure A3.1 are logarithmically scaled.

Initially, the radical densities clearly increase for all cases, due to electron impact dissociation of the reactant molecules (for the formation of H, CH_3 and O) and subsequent gas-phase reactions (in which also OH is formed). At this timescale, the radical densities are not yet affected by the presence of a transition metal surface and the density curves overlap. At longer timescales, the effect of radical adsorption on the catalyst surface becomes relevant. As a result, the radical densities for the cases without and with different catalysts start to deviate. This occurs between 10^{-8}-10^{-7} s for H radicals

(Figure A3.1 (a)) and around 10^{-6} s for CH_3, O and OH radicals (Figure A3.1 (b), (c) and (d), respectively).

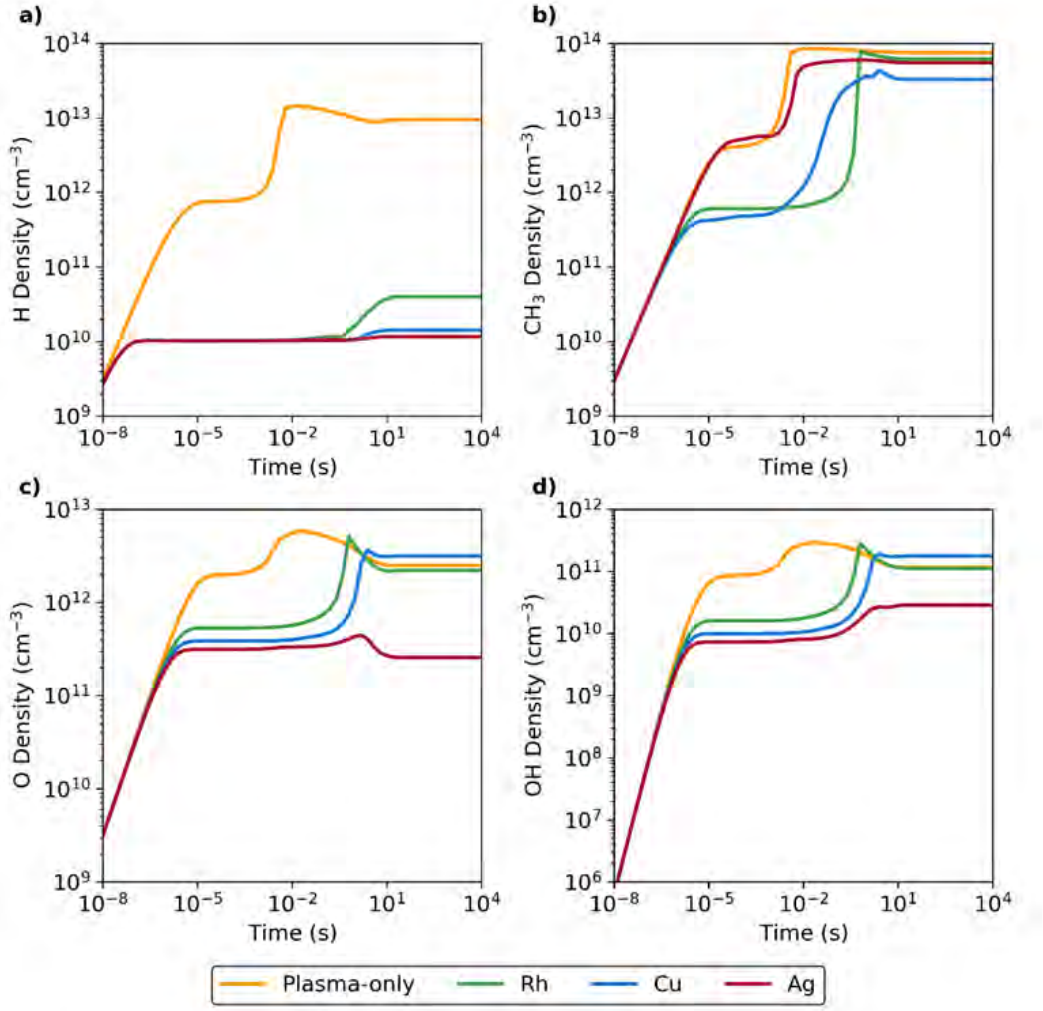

Figure A3.1. Evolution of the (a) H, (b) CH_3, (c) O and (d) OH radical densities with operating time for four different cases, i.e., plasma without catalyst, and plasma combined with a Rh, Cu or Ag catalyst. Calculated for a total pressure of 1 bar and a temperature of 500 K.

For the cases with transition metals, most of the radical densities in Figure A3.1 show a temporary region of stability. During this period, radical production is partly

compensated for by adsorption of radicals on the transition metal surface. Consequently, the densities of these radicals remain constant as a function of time, and are in general significantly lower when a catalyst is present compared to the plasma-only case. However, exceptions also occur, as can be seen in Figure A3.1 (b) for the CH_3 radicals, when the plasma is combined with Ag. Due to the low adsorption enthalpy of CH_3 on Ag, the density curve for this radical is quite similar to that of the plasma without catalyst. Note that for the plasma-only case, radicals can still recombine on a "non-catalytic" surface, which represents the surface of the reactor wall or a silica packing. However, due to the low densities of chemisorption sites on such a surface and the facile desorption of species from physisorption sites, the rates of radical recombination are typically much lower on the wall compared to on a transition metal surface. Still, exceptions on this do occur when the catalyst is poisoned or for species that bind the transition metal very weakly (like CH_3 on Ag, as explained above).

At timescales of 0.1-1 s, the surfaces of the Cu and Rh catalysts start to become saturated. Due to the drop in the free surface site fractions on these catalysts, less radicals can adsorb on their surfaces and the radical densities in the plasma rise. This is especially visible for CH_3, O and OH in Figure A3.1 (b), (c) and (d), respectively, for the cases with Cu and Rh. The rise in CH_3 density starts earlier for the case with Cu, i.e., around 10^{-3}-10^{-2} s. At timescales of 1-10 s, there is again a period of stabilization, and the system typically reaches steady state between 10^{2}-10^{3} s. Depending on the rates of radical recombination on the catalyst surface, the steady-state radical densities can be lower than those in the plasma without catalyst. This is most clear for the H radical densities displayed in Figure A3.1 (a). The CH_3 densities in Figure A3.1 (b) show slightly reduced steady-state values for Rh and Ag, compared to plasma without catalyst, while the drop is more significant for Cu. The O and OH densities, on the other hand, are significantly lowered for the case with Ag, as displayed in Figure A3.1 (c) and (d), respectively. For the cases with Rh and Cu, the O and OH densities at steady state are relatively close to those

of plasma without catalyst. Note that in the case of Cu, the O and OH densities are slightly higher compared to the plasma-only case, even though these radicals also adsorb on Cu. The reason for this is unclear, but the effect appears to result from a drop in the densities of many other gas species that would otherwise react with O radicals in the gas-phase. As OH is primarily formed from reaction between O and CH_4 or C_2H_6 in the plasma, the densities of O and OH are coupled.

For the plasma combined with Rh, the radical densities in Figure A3.1 (b), (c) and (d) are quite similar to those of the plasma-only case. This is caused by CO* poisoning of the Rh surface at steady state, resulting in partial deactivation of the catalyst. We found this also to be the case for Pt, Pd and Ir, which are not included in Figure A3.1. Note that inclusion of lateral interactions between adsorbed CO* might result in partial re-activation of these catalysts. Such interactions are currently not included in our model, as the effect is outside the scope of this study. However, we do expect the global trends to remain valid, i.e., in which the more strongly binding metals are at least partly deactivated due to more difficult desorption. Also note that H radical adsorption and recombination is not affected by the CO* poisoning of the Rh surface, which is a consequence of the separate adsorption site for H* used in our model. In other words, it results from the assumed negligible interactions between the small H atoms and larger adsorbates. For more information, see section 5.2.1.

A4. Appendix to chapter 6

A4.1. Rate coefficients used in the model

Table A4.1 lists the gas phase reactions included in the model, along with their rate coefficients. Some of these rate coefficients are calculated from the rate coefficients of the corresponding reverse reaction and the equilibrium constant via detailed balancing. The equilibrium constant used for detailed balancing is calculated according to:

$$K_{eq} = \exp\left(-\frac{\Delta G}{R_{gas}T_{gas}}\right) \cdot \left(\frac{p_{ref}}{R_{gas}T_{gas}}\right)^{\Sigma c^{R} - \Sigma c^{L}} \qquad \text{Eq. A4.1}$$

With p_{ref} = 10^5 Pa (1 bar) and c^R and c^L are the stoichiometry coefficients of the products and the reactants, respectively. The second factor in Eq. A4.1 is required to keep the units of K_{eq} consistent with those of the rate coefficients. The Gibbs free energy ΔG is calculated using the NASA Polynomials.[16,146]

Table A4.1. List of gas phase reactions included in the model, with their corresponding rate coefficients. For each reaction we list the corresponding rate coefficients and the references from which these were adopted. In the expressions of the rate constants T_{gas} denotes the gas temperature in K, T_e denotes the average electron temperature in K, and N_A denotes Avogadro's number. The units of the activation barriers match those of the denominator (i.e., K for T_{gas}) so that the exponent itself is unitless.

Reaction	**Rate coefficient[a]**	**Ref.**
$e^- + O \rightarrow e^- + e^- + O^+$	*f(σ)*	42
$e^- + O^- \rightarrow e^- + e^- + O$	*f(σ)*	275
$e^- + O_2 \rightarrow e^- + e^- + O_2^+$	*f(σ)*	42
$e^- + O_2 \rightarrow e^- + e^- + O + O^+$	*f(σ)*	417
$e^- + O_2 \rightarrow e^- + O + O$	*f(σ)*	42
$e^- + O_2 \rightarrow e^- + O + O(1D)$	*f(σ)*	42
$e^- + O \rightarrow e^- + O(1D)$	*f(σ)*	42

$e^- + O_2 \rightarrow O + O^-$	$f(\sigma)$	[42]
$e^- + O_3 \rightarrow O + O_2^-$	$f(\sigma)$	[275]
$e^- + O_3 \rightarrow O_2 + O^-$	$f(\sigma)$	[275]
$CO_2 + e^- \rightarrow CO_2^+ + e^- + e^-$	$f(\sigma)$	[42]
$CO_2 + e^- \rightarrow CO(a3P) + O + e^-$	$f(\sigma)$	[44]
$CO_2 + e^- \rightarrow CO + O(1D) + e^-$	$f(\sigma)$	[44]
$CO_2 + e^- \rightarrow CO + O^-$	$f(\sigma)$	[416]
$CO + e^- \rightarrow CO^+ + e^- + e^-$	$f(\sigma)$	[42]
$CO + e^- \rightarrow CO(a3P) + e^-$	$f(\sigma)$	[42]
$CO + e^- \rightarrow C + O^-$	$f(\sigma)$	[42]
$CO + e^- \rightarrow C + O + e^-$	$f(\sigma)$	[42]
$C + e^- \rightarrow C^+ + e^- + e^-$	$f(\sigma)$	[275]
$M + e^- + O \rightarrow M + O^-$	1×10^{-31}	[392,422]
$M + e^- + O_2 \rightarrow M + O_2^-$	1×10^{-31}	[392,422]
$e^- + e^- + O^+ \rightarrow e^- + O$	$7 \times 10^{-20} \cdot \left(\frac{3.0 \times 10^2}{T_e}\right)^{4.5}$	[392]
$M + e^- + O^+ \rightarrow M + O$	$6 \times 10^{-27} \cdot \left(\frac{3.0 \times 10^2}{T_e}\right)^{1.5}$	[392,422]
$e^- + e^- + O_2^+ \rightarrow e^- + O_2$	$1 \times 10^{-19} \cdot \left(\frac{3.0 \times 10^2}{T_e}\right)^{4.5}$	[422]
$M + e^- + O_2^+ \rightarrow M + O_2$	$6 \times 10^{-27} \cdot \left(\frac{3.0 \times 10^2}{T_e}\right)^{1.5}$	[392,422]
$e^- + O_2^+ \rightarrow O + O$	$2.7 \times 10^{-7} \cdot \left(\frac{3.0 \times 10^2}{T_e}\right)^{0.7}$	[392]
$M + O + O \rightarrow M + O_2$	$5.2 \times 10^{-35} \cdot \exp\left(\frac{9 \times 10^2}{T_{gas}}\right)$	[134]
$O + O \rightarrow e^- + O_2^+$	$\frac{1.12 \times 10^{13}}{N_A} \cdot \exp\left(\frac{-8.06 \times 10^4}{T_{gas}}\right)$	[423]
$O + O^- \rightarrow e^- + O_2$	2.3×10^{-10}	[424]

$M + O + O^+ \rightarrow M + O_2^+$	1×10^{-29}	392,422
$O + O_2^- \rightarrow O_2 + O^-$	3.3×10^{-10}	392,422
$O + O_2^- \rightarrow e^- + O_3$	1.5×10^{-10}	392,422
$O + O_3 \rightarrow O_2 + O_2$	$8 \times 10^{-12} \cdot \exp\left(\frac{-2.060 \times 10^3}{T_{gas}}\right)$	425
$M + O + O_2 \rightarrow M + O_3$	$5.4 \times 10^{-34} \cdot \left(\frac{3.0 \times 10^2}{T_{gas}}\right)^{1.9}$	392
$O_2 + O^+ \rightarrow O + O_2^+$	$2 \times 10^{-11} \cdot \left(\frac{3.0 \times 10^2}{T_{gas}}\right)^{0.5}$	392
$O_3 + O^+ \rightarrow O_2 + O_2^+$	1×10^{-10}	392,422
$O^- + O^+ \rightarrow O + O$	$2 \times 10^{-7} \cdot \left(\frac{3.0 \times 10^2}{T_{gas}}\right)^{0.5}$	422
$O_2^- + O^+ \rightarrow O + O_2$	$2 \times 10^{-7} \cdot \left(\frac{3.0 \times 10^2}{T_{gas}}\right)^{0.5}$	422
$M + O_2^- + O^+ \rightarrow M + O + O_2$	$2 \times 10^{-25} \cdot \left(\frac{3.0 \times 10^2}{T_{gas}}\right)^{2.5}$	422
$M + O^- + O^+ \rightarrow M + O + O$	$2 \times 10^{-25} \cdot \left(\frac{3.0 \times 10^2}{T_{gas}}\right)^{2.5}$	422
$M + O_2^- + O^+ \rightarrow M + O_3$	$2 \times 10^{-25} \cdot \left(\frac{3.0 \times 10^2}{T_{gas}}\right)^{2.5}$	422
$M + O^- + O^+ \rightarrow M + O_2$	$2 \times 10^{-25} \cdot \left(\frac{3.0 \times 10^2}{T_{gas}}\right)^{2.5}$	422
$O_2^+ + O^- \rightarrow O + O + O$	1×10^{-7}	422
$O_2^+ + O^- \rightarrow O + O_2$	$2 \times 10^{-7} \cdot \left(\frac{3.0 \times 10^2}{T_{gas}}\right)^{0.5}$	422
$O_2 + O^- \rightarrow e^- + O_3$	5×10^{-15}	392,422
$O_3 + O^- \rightarrow e^- + O_2 + O_2$	3×10^{-10}	392,426
$M + O^- \rightarrow M + e^- + O$	$6.9 \times 10^{-10} \cdot \left(\frac{3.0 \times 10^2}{T_{gas}}\right)^{-0.5}$	427

$M + O_2^+ + O^- \rightarrow M + O + O_2$	$2 \times 10^{-25} \cdot \left(\frac{3.0 \times 10^2}{T_{gas}}\right)^{2.5}$	422
$M + O_2^+ + O^- \rightarrow M + O_3$	$2 \times 10^{-25} \cdot \left(\frac{3.0 \times 10^2}{T_{gas}}\right)^{2.5}$	422
$O_2 + O_2 \rightarrow O + O_3$	$2 \times 10^{-11} \cdot \exp\left(\frac{-4.980 \times 10^4}{T_{gas}}\right)$	392
$M + O_2 \rightarrow M + O + O$	$3 \times 10^{-6} \cdot T_{gas}^{-1} \cdot \exp\left(\frac{-5.938 \times 10^4}{T_{gas}}\right)$	134
$M + O_2^- + O_2^+ \rightarrow M + O_2 + O_2$	$2 \times 10^{-25} \cdot \left(\frac{3.0 \times 10^2}{T_{gas}}\right)^{2.5}$	422
$O_2^- + O_2^+ \rightarrow O + O + O_2$	1×10^{-7}	422
$O_2^- + O_2^+ \rightarrow O_2 + O_2$	$2 \times 10^{-7} \cdot \left(\frac{3.0 \times 10^2}{T_{gas}}\right)^{0.5}$	422,428
$M + O_2^- \rightarrow M + e^- + O_2$	$2 \times 10^{-10} \cdot \left(\frac{3.0 \times 10^2}{T_{gas}}\right)^{-0.5}$	427
$M + O_3 \rightarrow M + O + O_2$	$6.6 \times 10^{-10} \cdot \exp\left(\frac{-1.160 \times 10^4}{T_{gas}}\right)$	392
$CO^+ + e^- \rightarrow C + O$	$6.8 \times 10^{-7} \cdot \left(\frac{T_e}{3.0 \times 10^2}\right)^{-0.4}$	429
$CO_2^+ + e^- \rightarrow CO + O$	$0.5 \cdot 3.4 \times 10^{-6} \cdot \left(\frac{T_e}{3.0 \times 10^2}\right)^{-0.4}$	429
$CO_2^+ + e^- \rightarrow C + O_2$	$0.5 \cdot 3.4 \times 10^{-6} \cdot \left(\frac{T_e}{3.0 \times 10^2}\right)^{-0.4}$	429
$CO + O \rightarrow CO_2^+ + e^-$	$\frac{1.12 \times 10^{13}}{N_A} \cdot \exp\left(\frac{-8.06 \times 10^4}{T_{gas}}\right)$	430 b
$C + O_2 \rightarrow CO_2^+ + e^-$	$\frac{1.12 \times 10^{13}}{N_A} \cdot \exp\left(\frac{-8.06 \times 10^4}{T_{gas}}\right)$	430 b
$C + O \rightarrow CO^+ + e^-$	$\frac{5.28 \times 10^{12}}{N_A} \cdot \exp\left(\frac{-3.2 \times 10^4}{T_{gas}}\right)$	423,430
$CO^+ + e^- + e^- \rightarrow CO + e^-$	$1 \times 10^{-19} \cdot \left(\frac{3.0 \times 10^2}{T_e}\right)^{4.5}$	422 c

$M + CO^+ + e^- \rightarrow M + CO$	$6 \times 10^{-27} \cdot \left(\frac{3.0 \times 10^2}{T_e}\right)^{1.5}$	422 d
$CO_2^+ + e^- + e^- \rightarrow CO_2 + e^-$	$1 \times 10^{-19} \cdot \left(\frac{3.0 \times 10^2}{T_e}\right)^{4.5}$	422 c
$M + CO_2^+ + e^- \rightarrow M + CO_2$	$6 \times 10^{-27} \cdot \left(\frac{3.0 \times 10^2}{T_e}\right)^{1.5}$	422 d
$M + C + O \rightarrow M + CO$	$9.1 \times 10^{-22} \cdot T_{gas}^{-3.08} \cdot \exp\left(\frac{-2.114 \times 10^3}{T_{gas}}\right)$	429
$C + O_2 \rightarrow CO + O$	$\frac{1.2 \times 10^{14}}{N_A} \cdot \exp\left(\frac{-2.01 \times 10^3}{T_{gas}}\right)$	431
$M + C + O^+ \rightarrow M + CO^+$	$1 \times 10^{-19} \cdot T_{gas}^{-3.08} \cdot \exp\left(\frac{-2.114 \times 10^3}{T_{gas}}\right)$	432
$C + O_2^+ \rightarrow CO^+ + O$	5.2×10^{-11}	433
$C + O_2^+ \rightarrow C^+ + O_2$	5.2×10^{-11}	433
$C + O^- \rightarrow CO + e^-$	5×10^{-10}	433
$M + C^+ + O \rightarrow M + CO^+$	$1 \times 10^{-19} \cdot T_{gas}^{-3.08} \cdot \exp\left(\frac{-2.114 \times 10^3}{T_{gas}}\right)$	432
$C^+ + O_2 \rightarrow CO + O^+$	$6.2 \times 10^{-1} \cdot 9.9 \times 10^{-10}$	434
$C^+ + O_2 \rightarrow CO^+ + O$	$3.8 \times 10^{-1} \cdot 9.9 \times 10^{-10}$	434
$CO_2 + O \rightarrow CO + O_2$	$\frac{1.7 \times 10^{13}}{N_A} \cdot \exp\left(\frac{-2.65 \times 10^4}{T_{gas}}\right)$	429
$CO_2 + O^+ \rightarrow CO_2^+ + O$	$0.5 \cdot 9 \times 10^{-10}$	434
$CO_2 + O^+ \rightarrow CO + O_2^+$	$0.5 \cdot 9 \times 10^{-10}$	434
$M + CO + O \rightarrow M + CO_2$	$8.3 \times 10^{-34} \cdot \exp\left(\frac{-1.51 \times 10^3}{T_{gas}}\right)$	134
$CO + O_2 \rightarrow CO_2 + O$	$4.2 \times 10^{-12} \cdot \exp\left(\frac{-2.4 \times 10^4}{T_{gas}}\right)$	134
$CO + O_3 \rightarrow CO_2 + O_2$	4×10^{-25}	435
$CO + O^+ \rightarrow CO^+ + O$	$2 \times 10^{-11} \cdot \left(\frac{T_{gas}}{5 \times 10^3}\right)^{0.5} \cdot \exp\left(\frac{-4.58 \times 10^3}{T_{gas}}\right)$	432

$CO + O^- \rightarrow CO_2 + e^-$	$6 \times 10^{-10} \cdot \left(\frac{T_{gas}}{3 \times 10^2}\right)^{-0.39}$	436
$CO_2^+ + O \rightarrow CO_2 + O^+$	$0.37 \cdot 2.6 \times 10^{-10}$	434
$CO_2^+ + O \rightarrow CO + O_2^+$	$0.63 \cdot 2.6 \times 10^{-10}$	434
$CO_2^+ + O_2 \rightarrow CO_2 + O_2^+$	5.3×10^{-11}	436
$CO^+ + O \rightarrow CO + O+$	1.4×10^{-10}	437
$CO^+ + O_2 \rightarrow CO + O_2^+$	1.2×10^{-10}	438
$C + CO_2 \rightarrow CO + CO$	1×10^{-15}	439
$CO_2 + C^+ \rightarrow CO + CO^+$	1.1×10^{-9}	440
$C + CO^+ \rightarrow CO + C^+$	1.1×10^{-10}	433
$M + CO_2 \rightarrow M + CO + O$	$\frac{3.65 \times 10^{14}}{N_A} \cdot \exp\left(\frac{-5.2525 \times 10^4}{T_{gas}}\right)$	441
$CO_2 + CO^+ \rightarrow CO + CO_2^+$	1×10^{-9}	438
$M + CO \rightarrow M + C + O$	$1.46 \times 10^6 \cdot T_{gas}^{-3.52} \cdot \exp\left(\frac{-1.287 \times 10^5}{T_{gas}}\right)$	429
$CO(a3P) + O_2 \rightarrow CO + O_2$	5.0×10^{-11}	442
$CO(a3P) + O_2 \rightarrow CO + O + O$	5.0×10^{-11}	442
$CO(a3P) + O_2 \rightarrow CO_2 + O$	3.0×10^{-11}	442
$CO(a3P) + CO \rightarrow CO + CO$	1.4×10^{-10}	442
$CO(a3P) + CO \rightarrow CO_2 + C$	1.4×10^{-12}	442
$CO(a3P) + CO_2 \rightarrow CO + CO_2$	1.5×10^{-11}	442
$CO(a3P) + CO_2 \rightarrow CO + CO + O$	1.5×10^{-11}	442
$O + O(1D) \rightarrow O + O$	8.0×10^{-12}	443
$CO + O(1D) \rightarrow CO + O$	8.0×10^{-11}	444
$O_2 + O(1D) \rightarrow O_2 + O$	$0.312 \times 10^{-10} \cdot \exp\left(\frac{7.00 \times 10^1}{T_{gas}}\right)$	445
$CO_2 + O(1D) \rightarrow CO_2 + O$	$0.74 \times 10^{-10} \cdot \exp\left(\frac{1.33 \times 10^2}{T_{gas}}\right)$	445
$CO_2^+ + CO_3^- \rightarrow CO_2 + CO_2 + O$	5.0×10^{-7}	446
$CO + CO_3^- \rightarrow CO_2 + CO_2 + e^-$	5.0×10^{-13}	447

$CO_4^- + O \rightarrow CO_3^- + O_2$	$0.333 \cdot 1.4 \times 10^{-10}$	434
$CO_3^- + O_2^+ \rightarrow CO_2 + O + O_2$	3.0×10^{-7}	446
$CO_3^- + O \rightarrow CO_2 + O_2^-$	8.0×10^{-11}	447
$M + CO_2 + O^- \rightarrow M + CO_3^-$	9.0×10^{-29}	447
$M + CO_2 + O_2^- \rightarrow M + CO_4^-$	4.7×10^{-29}	434
$CO_4^- + O \rightarrow CO_2 + O_2 + O^-$	$0.333 \cdot 1.4 \times 10^{-10}$	434
$CO_4^- + O_2^+ \rightarrow CO_2 + O_2 + O_2$	3.0×10^{-7}	446
$CO_2^+ + CO_4^- \rightarrow CO_2 + CO_2 + O_2$	5.0×10^{-7}	446
$CO + O \rightarrow C + O_2$	$k_{rev} \cdot K_{eq}$	e
$CO_2 + O_2 \rightarrow CO + O_3$	$k_{rev} \cdot K_{eq}$	e
$CO + CO \rightarrow C + CO_2$	$k_{rev} \cdot K_{eq}$	e
$CO_2 + O + O_2 \rightarrow CO_3^- + O_2^+$	$k_{rev} \cdot K_{eq}$	e
$CO_2 + O_2^- \rightarrow CO_3^- + O$	$k_{rev} \cdot K_{eq}$	e
$M + CO_3^- \rightarrow M + CO_2 + O^-$	$k_{rev} \cdot K_{eq}$	e

a) Units are s^{-1}, $cm^3\ s^{-1}$ or $cm^6\ s^{-1}$ for unimolecular, bimolecular or trimolecular gas phase reactions, respectively.

b) Estimated: equal to $O + O \rightarrow O_2^+ + e^-$

c) Estimated: equal to $A^+ + e^- + e^- \rightarrow A + e^-$

d) Estimated: equal to $A^+ + e^- + M \rightarrow A + M$

e) Calculated via detailed balancing.

A4.2. Electron impact reactions included in the model

Table A4.2. List of the electron impact reactions included in the calculation of the electron energy distribution function.

Electron impact reaction	**Ref.**
$C + e^- \rightarrow C^+ + e^- + e^-$	275
$C + e^- \rightarrow C + e^-$ (effective)	275
$C + e^- \rightarrow C(1D) + e^-$	275
$C + e^- \rightarrow C(1S) + e^-$	275
$CO + e^- \rightarrow CO + e^-$ (elastic)	42
$CO + e^- \rightarrow CO(v_n) + e^-$ (with n = 1-10)	42
$CO + e^- \rightarrow CO(a3P) + e^-$	42
$CO + e^- \rightarrow CO(a'3Su+) + e^-$	42
$CO + e^- \rightarrow CO(A1P) + e^-$	42
$CO + e^- \rightarrow CO(b3Su+) + e^-$	42
$CO + e^- \rightarrow CO(B1Su+) + e^-$	42
$CO + e^- \rightarrow CO(C1Su+) + e^-$	42
$CO + e^- \rightarrow CO(E1P) + e^-$	42
$CO + e^- \rightarrow C + O + e^-$	42
$CO + e^- \rightarrow C + O^-$	42
$CO + e^- \rightarrow CO^+ + e^- + e^-$	42
$CO_2 + e^- \rightarrow CO_2(v_{010}) + e^-$	42
$CO_2 + e^- \rightarrow CO_2(v_{020}) + e^-$	42
$CO_2 + e^- \rightarrow CO_2(v_{100}) + e^-$	42
$CO_2 + e^- \rightarrow CO_2(v_{030+110}) + e^-$	42
$CO_2 + e^- \rightarrow CO_2(v_{001}) + e^-$	42
$CO_2 + e^- \rightarrow CO_2(v_{040+120+011}) + e^-$	42
$CO_2 + e^- \rightarrow CO_2(X,v_{200}) + e^-$	42
$CO_2 + e^- \rightarrow CO_2(X,v_{050+210+130+021+101}) + e^-$	42

$CO_2 + e^- \rightarrow CO_2(X,v_{300}) + e^-$	42
$CO_2 + e^- \rightarrow CO_2(X,v_{060+220+140}) + e^-$	42
$CO_2 + e^- \rightarrow CO_2(X,v_{0n0+n00}) + e^-$	42
$CO_2 + e^- \rightarrow CO_2(E1) + e^-$	42
$CO_2 + e^- \rightarrow CO_2(E2) + e^-$	42
$CO_2 + e^- \rightarrow CO_2 + e^-$ (effective)	42
$CO_2 + e^- \rightarrow CO + O(1D) + e^-$	44
$CO_2 + e^- \rightarrow CO(a3P) + O + e^-$	44
$CO_2 + e^- \rightarrow CO_2^+ + e^- + e^-$	42
$CO_2 + e^- \rightarrow CO + O^-$	416
$O + e^- \rightarrow O + e^-$ (elastic)	42
$O + e^- \rightarrow O(1D) + e^-$	42
$O + e^- \rightarrow O(1S) + e^-$	42
$O + e^- \rightarrow O(4S0) + e^-$	42
$O + e^- \rightarrow O(2D0) + e^-$	42
$O + e^- \rightarrow O(2P0) + e^-$	42
$O + e^- \rightarrow O(3P0) + e^-$	42
$O + e^- \rightarrow O^+ + e^- + e^-$	42
$O_2 + e^- \rightarrow O_2(v_n) + e^-$ (n = 1-4)	42
$O_2 + e^- \rightarrow O_2(a1Dg) + e^-$	42
$O_2 + e^- \rightarrow O_2(b1Sg+) + e^-$	42
$O_2 + e^- \rightarrow O_2(A3Su+, C3Du, c1Su-) + e^-$	42
$O_2 + e^- \rightarrow O_2(9.97eV) + e^-$	42
$O_2 + e^- \rightarrow O_2(14.7eV) + e^-$	42
$O_2 + e^- \rightarrow O_2 + e^-$ (effective)	42
$O_2 + e^- \rightarrow O_2^+ + e^- + e^-$	42
$O_2 + e^- \rightarrow O + O^+ + e^- + e^-$	417
$O_2 + e^- \rightarrow O + O^-$	42

$O_2 + e^- \rightarrow O + O + e^-$	42
$O_2 + e^- \rightarrow O + O(1D) + e^-$	42
$O_3 + e^- \rightarrow O_3 + e^-$ (effective)	275
$O_3 + e^- \rightarrow O + O_2^-$	275
$O_3 + e^- \rightarrow O_2 + O^-$	275
$O^- + e^- \rightarrow O + e^- + e^-$	275

A4.3. Surface reactions on glass

Table A4.3. List of the surface reactions included in the model for glass.

Reaction[a,b]
$O + *^p \rightarrow O*^p$
$O + *^c \rightarrow O*^c$
$O*^p + *^c \rightarrow *^p + O*^c$
$O*^p \rightarrow O + *^p$
$O*^c \rightarrow O + *^c$
$O*^p + O*^c \rightarrow O_2 + *^p + *^c$
$O + O*^p \rightarrow O_2 + *^p$
$O + O*^c \rightarrow O_2 + *^c$
$CO + O*^p \rightarrow CO_2 + *^p$
$CO + O*^c \rightarrow CO_2 + *^c$

a) Superscripts p and c refer to physisorption and chemisorption sites, respectively.

b) For the corresponding rate coefficients, see sections 6.2.4 and 6.2.6 in Chapter 6.

A4.4. Effect of varying the parameters governing the glass surface kinetics

In this section we illustrate the possible impact of uncertainties regarding the main parameters that govern the glass surface kinetics. We therefore vary the values of these parameters and observe how the CO and O_2 mole fractions are affected for a CO_2 plasma afterglow at 500 K, 5 mbar and a flow rate of 100 sccm. We study the following parameters: the fraction of chemisorption sites f_c, the pre-exponential factor for desorption v_d, and the activation barriers for recombination to O_2 and CO_2 ($E_{r,\,O+O}$ and $E_{r,\,CO+O}$, respectively).

Figure A4.1 shows the effect of varying the fraction of chemisorption sites f_c. The default value used in Chapter 6 is f_c = 0.002, so we study here the effect of both increasing and reducing f_c by a factor 10. As can be seen, this causes a strong change in the time required for the O_2 and CO mole fractions to stabilize (which happens when the O atoms in the gas phase are depleted). Indeed, the recombination of O atoms on the glass surface occurs predominantly via an E-R reaction between a chemisorbed O* atom and an impinging O atom or CO molecule from the gas phase, forming O_2 or CO_2, respectively. Hence, the larger f_c, the faster recombination occurs. Note that the O_2 and CO mole fractions stabilize at a lower value for a higher value of f_c. While the rate for recombination between CO and O* is higher than that for O + O*, the ratio between both does not change when f_c is altered. Nevertheless, the effect of the fastest reaction (CO+O*) on the mole fractions becomes more pronounced as both rates are increased by the same factor. Also note that large variations in f_c have only a moderate effect on the CO density in the plasma (i.e., at 0 cm) as the CO fraction roughly doubles when f_c drops from 0.02 to 0.002 and the effect is even smaller when f_c drops further from 0.002 to 0.0002.

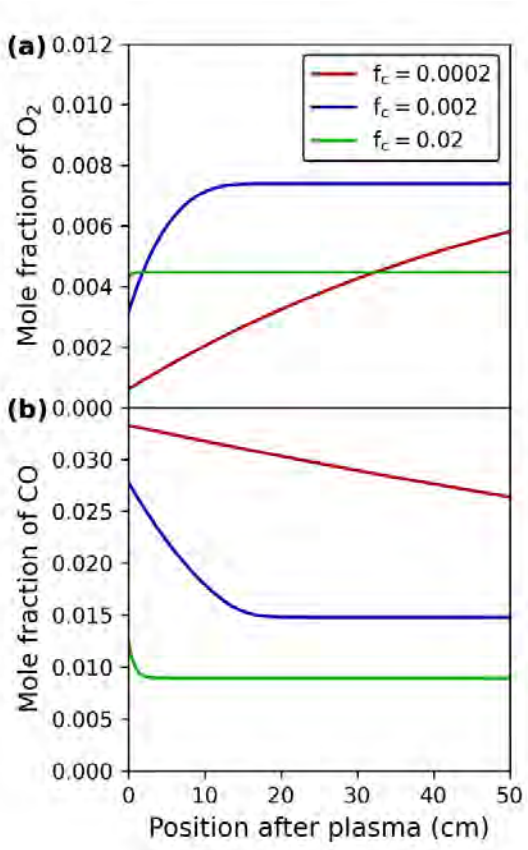

Figure A4.1. Effect of varying the fraction of chemisorption sites f_c on the mole fractions of O_2 (a) and CO (b). The default value in the model is f_c = 0.002. Conditions: T = 500 K, p = 5 mbar and flow rate = 100 sccm.

The effect of varying the pre-exponential factor for desorption v_d is illustrated in Figure A4.2. When the default value of v_d is lowered by a factor 10, i.e., from 10^{15} to 10^{14} s^{-1}, the O_2 and CO mole fractions stabilize at slightly higher values. Lowering the pre-exponential factor results in lower rates for desorption from both physisorption and chemisorption sites, but the latter are already largely occupied when v_d = 10^{15} s^{-1}. Hence, lowering v_d from 10^{15} to 10^{14} s^{-1} mainly enhances the coverage of physisorbed O* atoms, which improves the formation of O_2 via the L-H reaction between physisorbed and chemisorbed O* atoms. Since more O atoms recombine to O_2, the mole fraction of CO also stabilizes

at a higher value, as less O atoms will be available to recombine with CO to CO_2. When v_d is set to 10^{16} s^{-1}, recombination of O atoms on the surface becomes very slow, as is apparent from the slow evolution of the O_2 and CO mole fractions in the afterglow. This is because desorption from chemisorption sites becomes significant for this value of v_d, thus lowering the coverage of chemisorbed O* atoms, which indicates that a value of 10^{16} s^{-1} for v_d is not realistic.

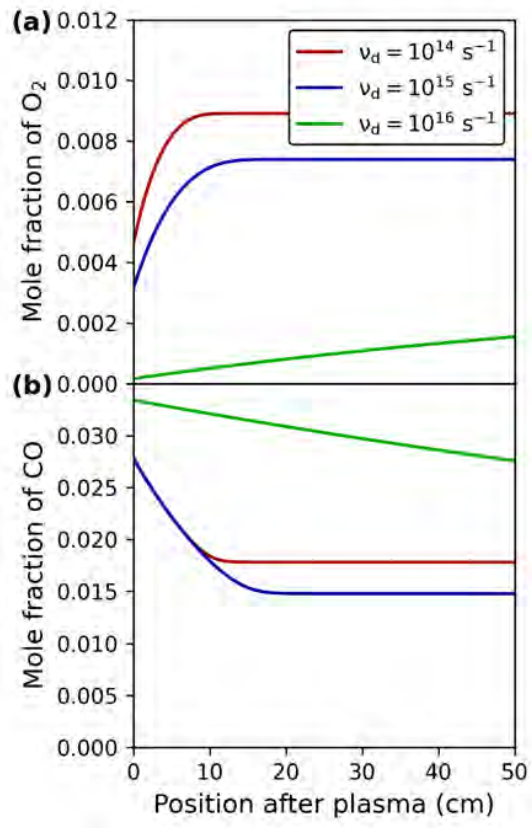

Figure A4.2. Effect of varying the pre-exponential factor for desorption v_d on the mole fractions of O_2 (a) and CO (b). The default value in the model is $v_d = 10^{15}$ s^{-1}. Conditions: T = 500 K, p = 5 mbar and flow rate = 100 sccm.

Figure A4.3 illustrates the effect of varying the activation barrier for recombination between two O atoms $E_{r,O+O}$ by a factor 3/2. Naturally, a lower activation barrier improves

the reaction rate for O+O recombination, and thus also the O_2 (and CO) mole fractions. When $E_{r,O+O}$ is increased by a factor 3/2, i.e., from 0.13 to 0.20 eV, the O_2 and CO mole fractions at the end of the afterglow are approximately halved. Conversely, when $E_{r,O+O}$ is lowered from 0.13 to 0.087 eV, the O_2 and CO mole fractions at the end of the afterglow rise by approximately 40%. Note that while the O atom fraction in the plasma (at 0 cm) clearly depends on the value of $E_{r,O+O}$, the CO mole fraction in the plasma does not change significantly when $E_{r,O+O}$ is altered.

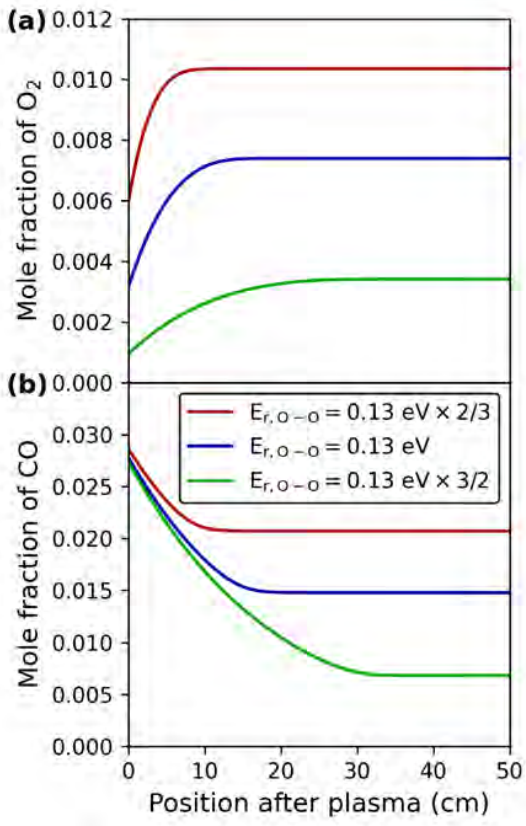

Figure A4.3. Effect of varying the activation barrier for recombination between O atoms $E_{r,O+O}$ on the mole fractions of O_2 (a) and CO (b). The default value in the model is $E_{r,O+O}$ = 0.13 eV. Conditions: T = 500 K, p = 5 mbar and flow rate = 100 sccm.

Lastly, Figure A4.4 illustrates the effect of varying the activation barrier for recombination between CO and an adsorbed O* atom. Increasing this activation barrier lowers the rate of the backreaction to CO_2 and thus enhances the O_2 and CO mole fractions. When the value of $E_{r,CO+O}$ is increased by a factor 3/2, i.e., from 0.104 to 0.156 eV, the O_2 and CO mole fractions near the end of the afterglow are enhanced by approximately 55%. Lowering the activation barrier from 0.104 to 0.069 eV reduces the O_2 and CO mole fractions at the end of the afterglow by approximately 35%.

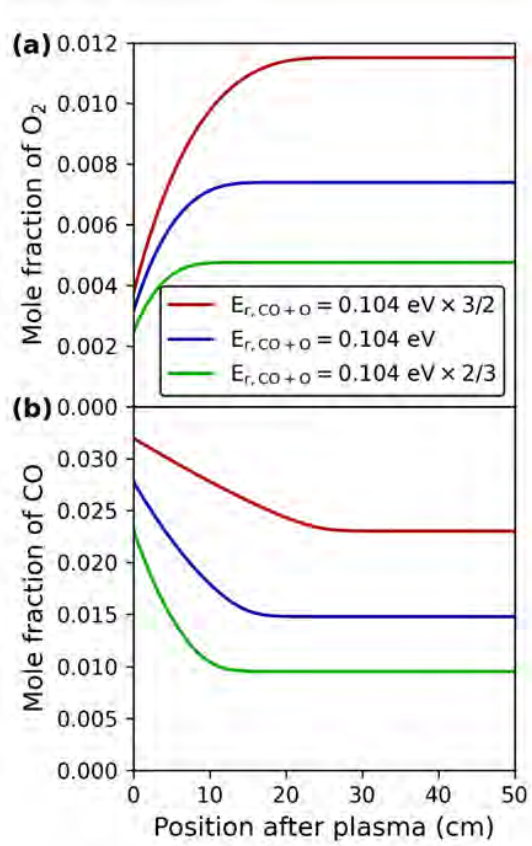

Figure A4.4. Effect of varying the activation barrier for recombination between CO and an adsorbed O atom $E_{r,CO+O}$ on the mole fractions of O_2 (a) and CO (b). The default value in the model is $E_{r,CO+O}$ = 0.104 eV. Conditions: T = 500 K, p = 5 mbar and flow rate = 100 sccm.*

Hence, the height of the activation barriers for the recombination reactions has a significant impact on the mole fractions of O_2 and CO, and thus on the CO_2 conversion. Whether most of the O* adsorbed atoms will recombine with impinging O atoms to form O_2, or with CO to form CO_2, eventually depends on the height of the activation barriers of both reactions relative to each other.

A4.5. DFT energies and vibrational frequencies

Table A4.4. DFT energies and vibrational frequencies of the species involved in reactions on the transition metal surfaces. The energies are calculated as the formation energy of the species relative to CO and O_2 in the gas phase, and the empty slab. The DFT data was calculated by R. Michiels, for more details see the original publication.[233]

Species	**Surface**	**Energy (eV)**	**Frequencies (cm^{-1})[a]**
CO_2	-	-3.02	[667.0, 667.0, 1333.0, 2349.0][b, 391]
CO	-	0.0	[2143.2] [b, 391]
O_2	-	0.0	[1556.4] [b, 391]
O	-	2.88	[]
*	All	0.0	[]
CO_2*	Ag(111)	-3.21	[50.0, 50.0, 50.0, 50.0, 51.0, 595.8, 610.3, 1298.5, 2305.2]
	Cu(111)	-3.21	[50.0, 50.0, 50.0, 50.0, 50.9, 596.9, 611.0, 1298.3, 2303.5]
	Pd(111)	-3.24	[50.0, 50.0, 50.0, 50.0, 55.1, 592.9, 611.0, 1297.2, 2299.4]
	Rh(111)	-3.24	[50.0, 50.0, 50.0, 50.0, 55.1, 589.0, 608.7, 1296.7, 2298.7]
CO*	Ag(111)	-0.17	[50.0, 50.0, 116.9, 116.9, 137.1, 2035.0]
	Cu(111)	-0.61	[50.0, 50.0, 257.3, 257.4, 296.0, 2002.1]
	Pd(111)	-1.76	[146.5, 147.2, 298.4, 322.6, 323.2, 1749.9]
	Rh(111)	-1.74	[50.0, 50.0, 386.0, 386.0, 430.3, 1966.0]
O_2*	Ag(111)	-0.36	[50.0, 81.8, 85.2, 145.5, 271.6, 1056.2]
	Cu(111)	-1.05	[108.7, 165.4, 192.2, 328.5, 365.7, 626.6]
	Pd(111)	-1.06	[125.3, 191.9, 281.5, 320.2, 414.3, 805.8]
	Rh(111)	-1.69	[138.5, 207.7, 269.3, 361.6, 442.4, 648.8]
O*	Ag(111)	-0.64	[311.1, 311.1, 322.1]
	Cu(111)	-1.78	[370.5, 370.5, 407.2]

	Pd(111)	-1.47	[361.5, 361.5, 398.2]
	Rh(111)	-2.19	[340.8, 340.9, 443.9]
O-O*	Ag(111)	0.40	[69.6, 148.6, 200.4, 259.1, 292. 3]
	Cu(111)	-1.03	[71.1, 268.1, 293.3, 375.8, 406.2]
	Pd(111)	-0.48	[63.3, 152.1, 348.5, 422.8, 537.9]
	Rh(111)	-1.60	[124.2, 221.1, 253.6, 438.9, 526.2]
O-CO*	Ag(111)	-0.75	[50.0, 96.9, 161.7, 225.1, 264.3, 304.3, 418.8, 1955.4]
	Cu(111)	-1.80	[50.0, 77.6, 211.2, 297.2, 325.5, 364.0, 519.3, 1930.3]
	Pd(111)	-1.78	[50.0, 113.1, 246.6, 309.2, 358.3, 361.5, 500.0, 1951.9]
	Rh(111)	-2.59	[56.8, 124.9, 272.6, 278.4, 379.0, 436.3, 568.7, 1874.0]

a) A cut-off of 50.0 cm^{-1} was used as lower boundary for the vibrational frequencies.

b) For gas molecules experimental frequencies taken from the NIST Computational Chemistry Comparison and Benchmark Database[391] were used.

A4.6. Parameters used in the ideal gas approximation

Table A4.5. Parameters used in the ideal gas approximation for calculating the enthalpy correction and entropy of gas molecules.

Species	**Geometry**	**I_{rot} (amu Å^2)[391]**	**Mass (amu)[9]**	**Symmetry number**	**Spin multiplicity**
O_2	Linear	11.72561	31.9988	2	1
O	Monoatomic	0.0	15.9994	1	1
CO_2	Linear	43.20143	44.0095	2	0
CO	Linear	8.768466	28.0101	1	0

A4.7. Parameters used in the modified Arrhenius expression of the surface rate coefficients as a function of temperature

Table A4.6. List of the parameters acquired by fitting the calculated values of the rate coefficients for surface reactions to a modified Arrhenius expression.

Surface	Reaction	a[a]	b	c
Ag(111)	O + * → O*	9.094×10^{-14}	5.000×10^{-1}	9.388×10^{-7}
Ag(111)	O* → O + *	1.387×10^{16}	-5.959×10^{-1}	-4.052×10^{4}
Ag(111)	O_2 + * → O_2*	6.431×10^{-14}	5.000×10^{-1}	2.871×10^{-6}
Ag(111)	O_2* → O_2 + *	1.167×10^{20}	-2.011	-4.442×10^{3}
Ag(111)	CO_2 + * → CO_2*	5.483×10^{-14}	5.000×10^{-1}	-6.286×10^{-6}
Ag(111)	CO_2* → CO_2 + *	8.318×10^{18}	-2.086	-2.350×10^{3}
Ag(111)	CO + * → CO*	6.873×10^{-14}	5.000×10^{-1}	5.979×10^{-6}
Ag(111)	CO* → CO + *	1.180×10^{19}	-1.933	-1.991×10^{3}
Ag(111)	O_2* + * → O* + O*	4.372×10^{12}	4.897×10^{-1}	-1.910×10^{4}
Ag(111)	O* + O* → O_2* + *	6.869×10^{10}	4.670×10^{-1}	-8.263×10^{3}
Ag(111)	CO_2* + * → CO* + O*	1.350×10^{12}	-7.697×10^{-2}	-7.121×10^{2}
Ag(111)	CO* + O* → CO_2* + *	5.859×10^{8}	9.106×10^{-1}	-2.723×10^{4}
Cu(111)	O + * → O*	9.094×10^{-14}	5.000×10^{-1}	1.587×10^{-5}
Cu(111)	O* → O + *	6.182×10^{15}	-4.112×10^{-1}	-5.361×10^{4}
Cu(111)	O_2 + * → O_2*	6.431×10^{-14}	5.000×10^{-1}	-2.305×10^{-5}
Cu(111)	O_2* → O_2 + *	1.705×10^{21}	-1.969	-1.257×10^{4}
Cu(111)	CO_2 + * → CO_2*	5.483×10^{-14}	5.000×10^{-1}	4.972×10^{-7}
Cu(111)	CO_2* → CO_2 + *	8.325×10^{18}	-2.086	-2.350×10^{3}
Cu(111)	CO + * → CO*	6.873×10^{-14}	5.000×10^{-1}	1.360×10^{-5}
Cu(111)	CO* → CO + *	1.762×10^{19}	-1.676	-6.924×10^{3}
Cu(111)	O_2* + * → O* + O*	6.720×10^{12}	3.619×10^{-1}	-2.902×10^{4}
Cu(111)	O* + O* → O_2* + *	6.683×10^{12}	3.377×10^{-2}	-1.349×10^{2}

Cu(111)	$CO_2^* + * \rightarrow CO^* + O^*$	2.921×10^{12}	8.546×10^{-2}	-6.746×10^{3}
Cu(111)	$CO^* + O^* \rightarrow CO_2^* + *$	1.237×10^{9}	6.955×10^{-1}	-1.523×10^{4}
Pd(111)	$O + * \rightarrow O^*$	9.094×10^{-14}	5.000×10^{-1}	1.587×10^{-5}
Pd(111)	$O^* \rightarrow O + *$	6.780×10^{15}	-4.325×10^{-1}	-5.003×10^{4}
Pd(111)	$O_2 + * \rightarrow O_2^*$	6.431×10^{-14}	5.000×10^{-1}	-2.305×10^{-5}
Pd(111)	$O_2^* \rightarrow O_2 + *$	7.679×10^{20}	-1.734	-1.245×10^{4}
Pd(111)	$CO_2 + * \rightarrow CO_2^*$	5.483×10^{-14}	5.000×10^{-1}	4.972×10^{-7}
Pd(111)	$CO_2^* \rightarrow CO_2 + *$	9.148×10^{18}	-2.089	-2.705×10^{3}
Pd(111)	$CO + * \rightarrow CO^*$	6.873×10^{-14}	5.000×10^{-1}	1.360×10^{-5}
Pd(111)	$CO^* \rightarrow CO + *$	9.200×10^{19}	-1.555	-2.033×10^{4}
Pd(111)	$O_2^* + * \rightarrow O^* + O^*$	6.369×10^{12}	3.718×10^{-1}	-2.827×10^{4}
Pd(111)	$O^* + O^* \rightarrow O_2^* + *$	2.371×10^{12}	3.206×10^{-1}	-6.419×10^{3}
Pd(111)	$CO_2^* + * \rightarrow CO^* + O^*$	1.354×10^{13}	1.305×10^{-1}	-1.686×10^{4}
Pd(111)	$CO^* + O^* \rightarrow CO_2^* + *$	1.100×10^{9}	6.379×10^{-1}	-1.587×10^{4}
Rh(111)	$O + * \rightarrow O^*$	9.094×10^{-14}	5.000×10^{-1}	1.587×10^{-5}
Rh(111)	$O^* \rightarrow O + *$	6.488×10^{15}	-4.281×10^{-1}	-5.838×10^{4}
Rh(111)	$O_2 + * \rightarrow O_2^*$	6.431×10^{-14}	5.000×10^{-1}	-2.305×10^{-5}
Rh(111)	$O_2^* \rightarrow O_2 + *$	1.236×10^{21}	-1.780	-1.983×10^{4}
Rh(111)	$CO_2 + * \rightarrow CO_2^*$	5.483×10^{-14}	5.000×10^{-1}	4.972×10^{-7}
Rh(111)	$CO_2^* \rightarrow CO_2 + *$	9.403×10^{18}	-2.094	-2.710×10^{3}
Rh(111)	$CO + * \rightarrow CO^*$	6.873×10^{-14}	5.000×10^{-1}	1.360×10^{-5}
Rh(111)	$CO^* \rightarrow CO + *$	6.015×10^{18}	-1.381	-1.981×10^{4}
Rh(111)	$O_2^* + * \rightarrow O^* + O^*$	2.587×10^{12}	3.890×10^{-1}	-3.196×10^{4}
Rh(111)	$O^* + O^* \rightarrow O_2^* + *$	1.693×10^{12}	2.839×10^{-1}	-7.974×10^{2}
Rh(111)	$CO_2^* + * \rightarrow CO^* + O^*$	1.189×10^{12}	1.892×10^{-1}	-1.535×10^{4}
Rh(111)	$CO^* + O^* \rightarrow CO_2^* + *$	1.587×10^{9}	5.136×10^{-1}	-6.536×10^{3}

a) Units are $cm^3\ s^{-1}$ for adsorption reactions and s^{-1} for other surface reactions.

A4.8. Effect of the free translator vs. harmonic oscillator approximation on the kinetics of plasma-catalytic CO_2 splitting

As discussed in section 6.2.5, we use the harmonic oscillator approximation[144] to calculate the entropy of the surface species, as well as their change in enthalpy with temperature. The harmonic oscillator approximation treats all degrees of freedom of the surface species as vibrational modes, corresponding to an adsorbate that oscillates within a surface site. Naturally, this results in a relatively low estimate of the adsorbate entropies. Another limiting case is the free translator approximation in which the surface species are assumed to retain two translational degrees of freedom, i.e. corresponding to an adsorbate that moves freely on the surface. Consequently, this approximation results in a larger estimate of the adsorbate entropies, and thus more stable surface species (i.e., lower Gibbs free energies) especially at high temperature.

To illustrate the effect of using the free translator approximation, we here discuss the results for plasma-catalytic CO_2 splitting with an Ag catalyst at 1100 K, 5 mbar and a flow rate of 100 sccm, i.e., the same conditions as used in Figure 6.6 in section 6.3.3. To calculate the enthalpy correction and entropy using the free translation approximation, the two vibrational modes with the lowest vibrational frequencies of each surface species were replaced by translational modes. The contribution of the two translational modes to the enthalpy correction and entropy were calculated as two-third of the total translational contribution used in the ideal gas approximation[144] (i.e., which accounts for three translational degrees of freedom). Note that the contribution of the remaining vibrational modes to the enthalpy correction and entropy were still included in the total enthalpy correction and entropy.

Figure A4.5 shows the calculated mole fractions of gas species (a), fractional surface coverages (b), O atom loss rates (c) and net surface rates (d) for a CO_2 plasma afterglow

in contact with a catalytic Ag surface, when the free translator approximation is used. For comparison, Figure 6.6 in section 6.3.3 shows the results of the corresponding simulation when the harmonic oscillator approximation is used. As can be seen in Figure A4.5 (a), the decline of the CO and O_2 mole fractions following the depletion of the O atoms in the gas phase is much faster when the free translator approximation is used, compared to the harmonic oscillator approximation (Figure 6.6 (a) in section 6.3.3). Indeed, the free translator approximation results in higher adsorbate entropies, and thus more stable surface species (i.e., lower Gibbs free energies of formation), especially at high temperature. This makes desorption of the adsorbed molecules more difficult and enhances the dissociation of adsorbates on the surface, as dissociation results in a net gain of two translational degrees of freedom. Consequently, the thermal catalytic oxidation of CO is enhanced, as its rate-determining step on Ag, namely O_2* dissociation, becomes easier.

The effect of the more difficult desorption and easier dissociation on the surface can also be observed in the surface coverages in Figure A4.5 (b). Indeed, the surface coverages increase upon switching from the harmonic oscillator to the free translator approximation (Figure 6.6 (b) in section 6.3.3 and Figure A4.5 (b), respectively). Especially the coverage of O* rises strongly and O* even covers most of the surface before depletion of the O atoms in the gas phase.

While the use of the free translator approximation significantly affects the surface kinetics, the flux and net consumption of O atoms on the surface remain largely the same compared to the harmonic oscillator approximation (Figure A4.5 (c) and Figure 6.6 (c), respectively). In both cases most O atom recombination occurs almost exclusively via surface reactions and the loss of O atoms at the surface is limited by diffusion to the surface.

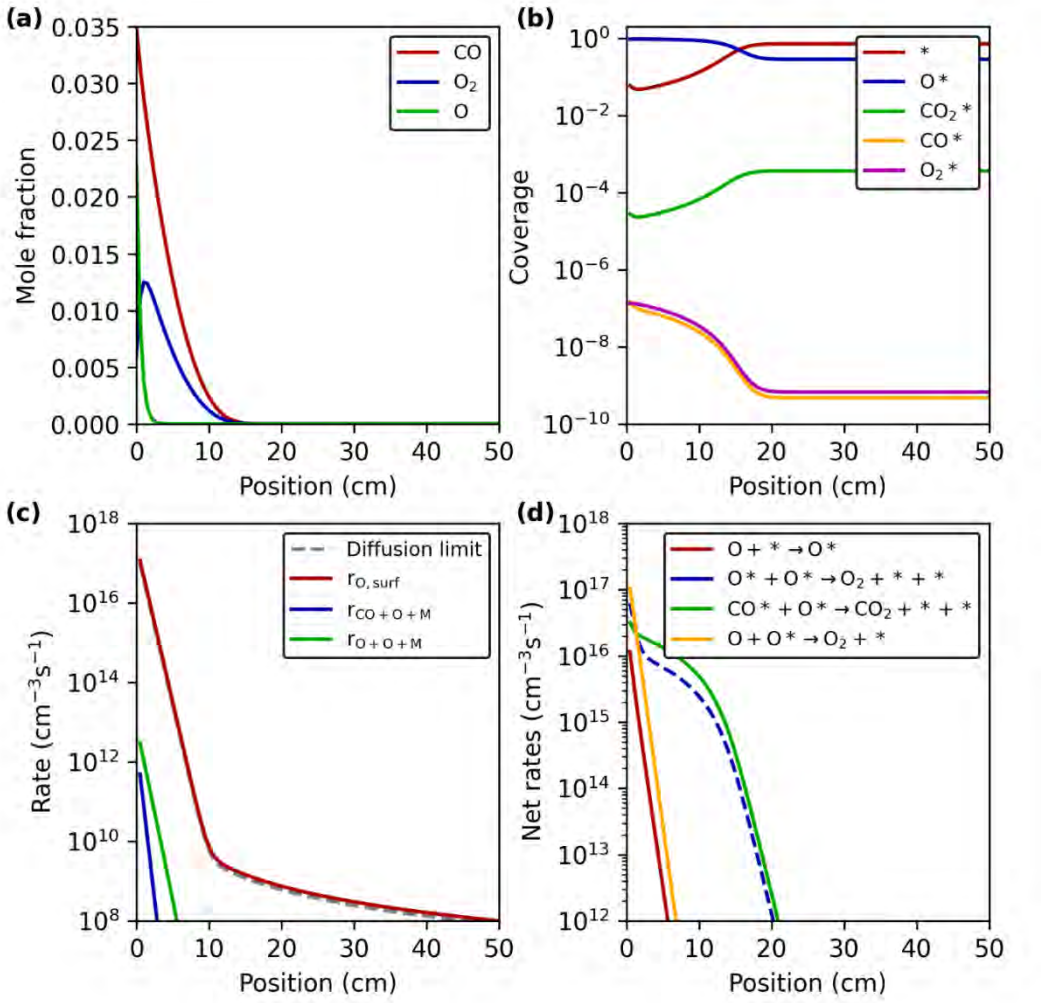

Figure A4.5. Mole fractions (a), fractional surface coverages (b), O atom loss rates (c), and net surface rates (d) of a CO_2 plasma afterglow in contact with an Ag surface, when using the free translator approximation to calculate the enthalpy corrections and entropies of the surface species. The dashed line in (d) indicates a negative net rate, corresponding to the reverse reaction, i.e., dissociation of O_2. Conditions: T = 1100 K, p = 5 mbar and flow rate = 100 sccm.*

Figure A4.5 (d) illustrates the net reaction rates for loss of O atoms on the Ag surface. Note that in line with Figure 6.6 (d) in section 6.3.3, the dashed (blue) line of O*+O* recombination indicates a negative net rate, and thus corresponds to the reverse

reaction, i.e., dissociation of O_2*. Interestingly, due to the more facile dissociation of O_2* with the free translator approximation, it becomes easier for O_2, which is formed at the surface, to re-adsorb and dissociate into O* than for O atoms to diffuse to the surface and adsorb. Instead, the O atoms that reach the surface will now react with O* via an E-R reaction to form O_2, of which a fraction adsorbs and dissociates again to form adsorbed O*. This arises from the diffusion limitation between the bulk gas and the surface, which limits the loss rate of O atoms to the surface. Because O_2 is formed at the surface, its adsorption rate is not limited by diffusion to the surface. Hence, despite resulting in higher O* coverages, the free translator approximation reduces the net rate of O* recombination via the L-H reaction, as this results in a larger entropy loss (i.e., corresponding to two translational degrees of freedom) upon going from two adsorbates (O*+O*) to one (O_2*). The rate of the E-R reaction, however, is increased due to the higher O* coverages and E-R becomes the main process for O atom recombination (Figure A4.5 (d)). However, the rate coefficient used for the E-R reaction (Eq. 5.8 (see section 5.2.2.4)) only includes an enthalpy barrier in the sticking coefficient, while the pre-exponential factor (i.e., the Hertz-Knudsen equation) only accounts for the loss of one translational degree of freedom of the impinging atom. Hence, any loss of entropy of the adsorbate between the initial and transition state is not considered.

Finally, the rates of O_2* dissociation and recombination between O* and CO* to form CO_2* are initially higher when the free translation approximation is used (Figure A4.5 (d)), compared to when the harmonic oscillator approximation is used Figure 6.6 (d) in section 6.3.3), as is also evident from the evolution of the O_2 and CO mole fractions in panel (a) of both figures. However, due to the faster decline of the mole fractions of these gas species in Figure A4.5 (a), the rates of O_2* dissociation and CO*+O* recombination in Figure A4.5 (d) also drop rapidly, around 15 cm after the plasma.

To conclude, the use of the free translator approximation results in easier O_2* dissociation, and thus faster thermal-catalytic CO* oxidation to CO_2*, which gives rise to a quick drop of the CO* and O_2* mole fractions after depletion of O atoms in the gas phase.

References

(1) *Statistical Review of World Energy*. Energy Institute. **2024**. https://www.energyinst.org/statistical-review.

(2) Richie, H.; Rosado, P. *Energy Mix*. Our World in Data. **2020**. https://ourworldindata.org/energy-mix.

(3) *The Future of Petrochemicals*. International Energy Agency. **2018**. https://www.iea.org/reports/the-future-of-petrochemicals.

(4) Lan, X.; Tans, P.; Thoning, K. W. Trends in Globally-Averaged CO_2 Determined from NOAA Global Monitoring Laboratory Measurements. DOI: 10.15138/9N0H-ZH07.

(5) *IPCC, 2001: Climate Change 2001: The Scientific Basis. Contribution of Working Group I to the Third Assessment Report of the Intergovernmental Panel on Climate Change*; Houghton, J. T., Ding, Y., Griggs, D. J., Noguer, M., van der Linden, P. J., Dai, X., Maskell, K., Johnson, C. A., Eds.; Cambridge University Press: Cambridge, United Kingdom and New York, NY, USA, 2001.

(6) Climate Change 2023: Synthesis Report. Contribution of Working Groups I, II and III to the Sixth Assessment Report of the Intergovernmental Panel on Climate Change; Lee, H., Romero, J., Eds.; IPCC: Geneva, Switzerland, 2023; pp 35–115. DOI: 10.59327/IPCC/AR6-9789291691647.

(7) Goeppert, A.; Czaun, M.; Jones, J.-P.; Prakash, G. K. S.; Olah, G. A. Recycling of Carbon Dioxide to Methanol and Derived Products – Closing the Loop. *Chem. Soc. Rev.* **2014**, *43*, 7995–8048. DOI: 10.1039/C4CS00122B.

(8) Hepburn, C.; Adlen, E.; Beddington, J.; Carter, E. A.; Fuss, S.; Mac Dowell, N.; Minx,

J. C.; Smith, P.; Williams, C. K. The Technological and Economic Prospects for CO_2 Utilization and Removal. *Nature* **2019**, *575*, 87–97. DOI: 10.1038/s41586-019-1681-6.

(9) *NIST Chemistry WebBook, NIST Standard Reference Database Number 69*; Linstrom, P. J., Mallard, W. G., Eds.; National Institute of Standards and Technology: Gaithersburg MD, 20899. DOI: 10.18434/T4D303.

(10) Aramouni, N. A. K.; Touma, J. G.; Tarboush, B. A.; Zeaiter, J.; Ahmad, M. N. Catalyst Design for Dry Reforming of Methane: Analysis Review. *Renewable Sustainable Energy Rev.* **2018**, *82*, 2570–2585. DOI: 10.1016/j.rser.2017.09.076.

(11) Liu, G.; Hagelin-Weaver, H.; Welt, B. A Concise Review of Catalytic Synthesis of Methanol from Synthesis Gas. *Waste* **2023**, *1*, 228–248. DOI: 10.3390/waste1010015.

(12) Pakhare, D.; Spivey, J. A Review of Dry (CO_2) Reforming of Methane over Noble Metal Catalysts. *Chem. Soc. Rev.* **2014**, *43*, 7813–7837. DOI: 10.1039/C3CS60395D.

(13) Zhai, P.; Li, Y.; Wang, M.; Liu, J.; Cao, Z.; Zhang, J.; Xu, Y.; Liu, X.; Li, Y.-W.; Zhu, Q.; Xiao, D.; Wen, X.-D.; Ma, D. Development of Direct Conversion of Syngas to Unsaturated Hydrocarbons Based on Fischer-Tropsch Route. *Chem* **2021**, *7*, 3027–3051. DOI: 10.1016/j.chempr.2021.08.019.

(14) Snoeckx, R.; Bogaerts, A. Plasma Technology – a Novel Solution for CO_2 Conversion? *Chem. Soc. Rev.* **2017**, *46*, 5805–5863. DOI: 10.1039/c6cs00066e.

(15) Biondo, O.; Hughes, A.; van de Steeg, A.; Maerivoet, S.; Loenders, B.; van Rooij, G.; Bogaerts, A. Power Concentration Determined by Thermodynamic Properties in Complex Gas Mixtures: The Case of Plasma-Based Dry Reforming of Methane.

Plasma Sources Sci. Technol. **2023**, *32*, 045001. DOI: 10.1088/1361-6595/acc6ec.

(16) McBride, B. J.; Zehe, M. J.; Gordon, S. *NASA Glenn Coefficients for Calculating Thermodynamic Properties of Individual Species*; 2002. https://ntrs.nasa.gov/search.jsp?R=20020085330 2020-05-03T03:42:36+00:00Z.

(17) Lan, X.; Thoning, K. W.; Dlugokencky, E. J. *Trends in globally-averaged CH_4, N_2O, and SF_6 determined from NOAA Global Monitoring Laboratory measurements.* National Oceanic and Atmospheric Administration. DOI: 10.15138/P8XG-AA10.

(18) Forster, P., T. Storelvmo, K. Armour, W. C.; J.-L. Dufresne, D. Frame, D.J. Lunt, T. Mauritsen, M. D. P.; M. Watanabe, M. Wild, and H. Z. The Earth's Energy Budget, Climate Feedbacks and Climate Sensitivity. In *Climate Change 2021 – The Physical Science Basis*; Cambridge University Press, 2023; pp 923–1054. DOI: 10.1017/9781009157896.009.

(19) Bitsch-Larsen, A.; Horn, R.; Schmidt, L. D. Catalytic Partial Oxidation of Methane on Rhodium and Platinum: Spatial Profiles at Elevated Pressure. *Appl. Catal. A* **2008**, *348*, 165–172. DOI: 10.1016/j.apcata.2008.06.036.

(20) Fridman, A. *Plasma Chemistry*; Cambridge University Press: New York, 2008.

(21) Boulos, M. I.; Fauchais, P.; Pfender, E. *Thermal Plasmas: Fundamentals and Applications*; Springer New York: New York, NY, 1994. DOI: 10.1007/978-1-4899-1337-1.

(22) Liu, S.; Winter, L. R.; Chen, J. G. Review of Plasma-Assisted Catalysis for Selective Generation of Oxygenates from CO_2 and CH_4. *ACS Catal.* **2020**, *10*, 2855–2871. DOI: 10.1021/acscatal.9b04811.

(23) Michielsen, I.; Uytdenhouwen, Y.; Bogaerts, A.; Meynen, V. Altering Conversion and Product Selectivity of Dry Reforming of Methane in a Dielectric Barrier

Discharge by Changing the Dielectric Packing Material. *Catalysts* **2019**, *9*, 51. DOI: 10.3390/catal9010051.

(24) Bogaerts, A.; Tu, X.; Whitehead, J. C.; Centi, G.; Lefferts, L.; Guaitella, O.; Azzolina-Jury, F.; Kim, H.-H.; Murphy, A. B.; Schneider, W. F.; Nozaki, T.; Hicks, J. C.; Rousseau, A.; Thevenet, F.; Khacef, A.; Carreon, M. The 2020 Plasma Catalysis Roadmap. *J. Phys. D: Appl. Phys.* **2020**, *53*, 443001. DOI: 10.1088/1361-6463/ab9048.

(25) Catalyst. In *The IUPAC Compendium of Chemical Terminology*; International Union of Pure and Applied Chemistry (IUPAC): Research Triangle Park, NC, 2025. DOI: 10.1351/goldbook.C00876.

(26) Medford, A. J.; Lausche, A. C.; Abild-Pedersen, F.; Temel, B.; Schjødt, N. C.; Nørskov, J. K.; Studt, F. Activity and Selectivity Trends in Synthesis Gas Conversion to Higher Alcohols. *Top. Catal.* **2014**, *57*, 135–142. DOI: 10.1007/s11244-013-0169-0.

(27) Bogaerts, A.; Neyts, E. C.; Guaitella, O.; Murphy, A. B. Foundations of Plasma Catalysis for Environmental Applications. *Plasma Sources Sci. Technol.* **2022**, *31*, 053002. DOI: 10.1088/1361-6595/ac5f8e.

(28) Booth, J. P.; Guaitella, O.; Chatterjee, A.; Drag, C.; Guerra, V.; Lopaev, D.; Zyryanov, S.; Rakhimova, T.; Voloshin, D.; Mankelevich, Y. Oxygen (^{3}P) Atom Recombination on a Pyrex Surface in an O_2 Plasma. *Plasma Sources Sci. Technol.* **2019**, *28*, 055005. DOI: 10.1088/1361-6595/ab13e8.

(29) Morillo-Candas, A. S.; Drag, C.; Booth, J.-P.; Dias, T. C.; Guerra, V.; Guaitella, O. Oxygen Atom Kinetics in CO_2 Plasmas Ignited in a DC Glow Discharge. *Plasma Sources Sci. Technol.* **2019**, *28*, 075010. DOI: 10.1088/1361-6595/ab2b84.

(30) Ma, H.; Sharma, R. K.; Welzel, S.; van de Sanden, M. C. M.; Tsampas, M. N.; Schneider, W. F. Observation and Rationalization of Nitrogen Oxidation Enabled Only by Coupled Plasma and Catalyst. *Nat. Commun.* **2022**, *13*, 402. DOI: 10.1038/s41467-021-27912-2.

(31) Peeters, F.; Butterworth, T. Electrical Diagnostics of Dielectric Barrier Discharges. In *Atmospheric Pressure Plasma - from Diagnostics to Applications*; IntechOpen, 2019. DOI: 10.5772/intechopen.80433.

(32) Andersen, J. A.; Christensen, J. M.; Østberg, M.; Bogaerts, A.; Jensen, A. D. Plasma-Catalytic Dry Reforming of Methane: Screening of Catalytic Materials in a Coaxial Packed-Bed DBD Reactor. *Chem. Eng. J.* **2020**, *397*, 125519. DOI: 10.1016/j.cej.2020.125519.

(33) Sentek, J.; Krawczyk, K.; Młotek, M.; Kalczewska, M.; Kroker, T.; Kolb, T.; Schenk, A.; Gericke, K.-H.; Schmidt-Szałowski, K. Plasma-Catalytic Methane Conversion with Carbon Dioxide in Dielectric Barrier Discharges. *Appl. Catal. B Environ.* **2010**, *94*, 19–26. DOI: 10.1016/j.apcatb.2009.10.016.

(34) Van Turnhout, J.; Aceto, D.; Travert, A.; Bazin, P.; Thibault-Starzyk, F.; Bogaerts, A.; Azzolina-Jury, F. Observation of Surface Species in Plasma-Catalytic Dry Reforming of Methane in a Novel Atmospheric Pressure Dielectric Barrier Discharge in Situ IR Cell. *Catal. Sci. Technol.* **2022**, *12*, 6676–6686. DOI: 10.1039/D2CY00311B.

(35) Wang, A.; Harrhy, J. H.; Meng, S.; He, P.; Liu, L.; Song, H. Nonthermal Plasma-Catalytic Conversion of Biogas to Liquid Chemicals with Low Coke Formation. *Energy Convers. Manag.* **2019**, *191*, 93–101. DOI: 10.1016/j.enconman.2019.04.026.

(36) Wang, L.; Yi, Y.; Wu, C.; Guo, H.; Tu, X. One-Step Reforming of CO_2 and CH_4 into

High-Value Liquid Chemicals and Fuels at Room Temperature by Plasma-Driven Catalysis. *Angew. Chem., Int. Ed.* **2017**, *56*, 13679–13683. DOI: 10.1002/anie.201707131.

(37) Neyts, E. C.; Bogaerts, A. Understanding Plasma Catalysis through Modelling and Simulation—a Review. *J. Phys. D: Appl. Phys.* **2014**, *47*, 224010. DOI: 10.1088/0022-3727/47/22/224010.

(38) Neyts, E. C.; Ostrikov, K. K.; Sunkara, M. K.; Bogaerts, A. Plasma Catalysis: Synergistic Effects at the Nanoscale. *Chem. Rev.* **2015**, *115*, 13408–13446. DOI: 10.1021/acs.chemrev.5b00362.

(39) Loenders, B.; Michiels, R.; Bogaerts, A. Is a Catalyst Always Beneficial in Plasma Catalysis? Insights from the Many Physical and Chemical Interactions. *J. Energy Chem.* **2023**, *85*, 501–533. DOI: 10.1016/j.jechem.2023.06.016.

(40) Kim, H.; Teramoto, Y.; Ogata, A. Time-Resolved Imaging of Positive Pulsed Corona-Induced Surface Streamers on TiO_2 and γ-Al_2O_3-Supported Ag Catalysts. *J. Phys. D: Appl. Phys.* **2016**, *49*, 415204. DOI: 10.1088/0022-3727/49/41/415204.

(41) Wang, W.; Kim, H.-H.; Van Laer, K.; Bogaerts, A. Streamer Propagation in a Packed Bed Plasma Reactor for Plasma Catalysis Applications. *Chem. Eng. J.* **2018**, *334*, 2467–2479. DOI: 10.1016/j.cej.2017.11.139.

(42) *Obtained from LXCAT (IST-Lisbon database)*. www.lxcat.net.

(43) Reiter, D.; Janev, R. K. Hydrocarbon Collision Cross Sections for Magnetic Fusion: The Methane, Ethane and Propane Families. *Contrib. to Plasma Phys.* **2010**, *50*, 986–1013. DOI: 10.1002/ctpp.201000090.

(44) Polak, L. S.; Slovetsky, D. I. Electron Impact Induced Electronic Excitation and Molecular Dissociation. *Int. J. Radiat. Phys. Chem.* **1976**, *8*, 257–282. DOI:

10.1016/0020-7055(76)90070-X.

(45) Tu, X.; Gallon, H. J.; Twigg, M. V.; Gorry, P. A.; Whitehead, J. C. Dry Reforming of Methane over a Ni/Al2O3 Catalyst in a Coaxial Dielectric Barrier Discharge Reactor. *J. Phys. D: Appl. Phys.* **2011**, *44*, 274007. DOI: 10.1088/0022-3727/44/27/274007.

(46) Kim, H.-H.; Kim, J.-H.; Ogata, A. Microscopic Observation of Discharge Plasma on the Surface of Zeolites Supported Metal Nanoparticles. *J. Phys. D: Appl. Phys.* **2009**, *42*, 135210. DOI: 10.1088/0022-3727/42/13/135210.

(47) Kim, H.-H.; Ogata, A. Nonthermal Plasma Activates Catalyst: From Current Understanding and Future Prospects. *Eur. Phys. J. Appl. Phys.* **2011**, *55*, 13806. DOI: 10.1051/epjap/2011100444.

(48) Ndayirinde, C.; Gorbanev, Y.; Ciocarlan, R.-G.; De Meyer, R.; Smets, A.; Vlasov, E.; Bals, S.; Cool, P.; Bogaerts, A. Plasma-Catalytic Ammonia Synthesis: Packed Catalysts Act as Plasma Modifiers. *Catal. Today* **2023**, *419*, 114156. DOI: 10.1016/j.cattod.2023.114156.

(49) Van Laer, K.; Bogaerts, A. Influence of Gap Size and Dielectric Constant of the Packing Material on the Plasma Behaviour in a Packed Bed DBD Reactor: A Fluid Modelling Study. *Plasma Process. Polym.* **2017**, *14*, 1600129. DOI: 10.1002/ppap.201600129.

(50) Van Laer, K.; Bogaerts, A. How Bead Size and Dielectric Constant Affect the Plasma Behaviour in a Packed Bed Plasma Reactor: A Modelling Study. *Plasma Sources Sci. Technol.* **2017**, *26*, 085007. DOI: 10.1088/1361-6595/aa7c59.

(51) Uytdenhouwen, Y.; Van Alphen, S.; Michielsen, I.; Meynen, V.; Cool, P.; Bogaerts, A. A Packed-Bed DBD Micro Plasma Reactor for CO_2 Dissociation: Does Size

Matter? *Chem. Eng. J.* **2018**, *348*, 557–568. DOI: 10.1016/j.cej.2018.04.210.

(52) Butterworth, T.; Elder, R.; Allen, R. Effects of Particle Size on CO_2 Reduction and Discharge Characteristics in a Packed Bed Plasma Reactor. *Chem. Eng. J.* **2016**, *293*, 55–67. DOI: 10.1016/j.cej.2016.02.047.

(53) Chen, H. L.; Lee, H. M.; Chen, S. H.; Chang, M. B. Review of Packed-Bed Plasma Reactor for Ozone Generation and Air Pollution Control. *Ind. Eng. Chem. Res.* **2008**, *47*, 2122–2130. DOI: 10.1021/ie071411s.

(54) Veerapandian, S.; Leys, C.; De Geyter, N.; Morent, R. Abatement of VOCs Using Packed Bed Non-Thermal Plasma Reactors: A Review. *Catalysts* **2017**, *7*, 113. DOI: 10.3390/catal7040113.

(55) Ogata, A.; Einaga, H.; Kabashima, H.; Futamura, S.; Kushiyama, S.; Kim, H.-H. Effective Combination of Nonthermal Plasma and Catalysts for Decomposition of Benzene in Air. *Appl. Catal. B Environ.* **2003**, *46*, 87–95. DOI: 10.1016/S0926-3373(03)00180-2.

(56) Ogata, A.; Shintani, N.; Mizuno, K.; Kushiyama, S.; Yamamoto, T. Decomposition of Benzene Using a Nonthermal Plasma Reactor Packed with Ferroelectric Pellets. *IEEE Trans. Ind. Appl.* **1999**, *35*, 753–759. DOI: 10.1109/28.777181.

(57) Zhang, Q. Z.; Bogaerts, A. Propagation of a Plasma Streamer in Catalyst Pores. *Plasma Sources Sci. Technol.* **2018**, *27*, 35009. DOI: 10.1088/1361-6595/aab47a.

(58) Snoeckx, R.; Aerts, R.; Tu, X.; Bogaerts, A. Plasma-Based Dry Reforming: A Computational Study Ranging from the Nanoseconds to Seconds Time Scale. *J. Phys. Chem. C* **2013**, *117*, 4957–4970. DOI: 10.1021/jp311912b.

(59) Zhang, Y.-R.; Van Laer, K.; Neyts, E. C.; Bogaerts, A. Can Plasma Be Formed in Catalyst Pores? A Modeling Investigation. *Appl. Catal. B Environ.* **2016**, *185*, 56–

67. DOI: 10.1016/j.apcatb.2015.12.009.

(60) Kim, H.-H.; Teramoto, Y.; Negishi, N.; Ogata, A. A Multidisciplinary Approach to Understand the Interactions of Nonthermal Plasma and Catalyst: A Review. *Catal. Today* **2015**, *256*, 13–22. DOI: 10.1016/j.cattod.2015.04.009.

(61) Nozaki, T.; Muto, N.; Kado, S.; Okazaki, K. Dissociation of Vibrationally Excited Methane on Ni Catalyst Part 1. Application to Methane Steam Reforming. *Catal. Today* **2004**, *89*, 57–65. DOI: 10.1016/j.cattod.2003.11.040.

(62) Khoja, A. H.; Tahir, M.; Saidina Amin, N. A. Process Optimization of DBD Plasma Dry Reforming of Methane over Ni/La_2O_3-$MgAl_2O_4$ Using Multiple Response Surface Methodology. *Int. J. Hydrogen Energy* **2019**, *44*, 11774–11787. DOI: 10.1016/j.ijhydene.2019.03.059.

(63) Mikhail, M.; Da Costa, P.; Amouroux, J.; Cavadias, S.; Tatoulian, M.; Gálvez, M. E.; Ognier, S. Tailoring Physicochemical and Electrical Properties of Ni/CeZrO<sub>X<\sub> Doped Catalysts for High Efficiency of Plasma Catalytic CO<sub>2<\sub> Methanation. *Appl. Catal. B Environ.* **2021**, *294*, 120233. DOI: 10.1016/j.apcatb.2021.120233.

(64) Ray, D.; Chawdhury, P.; Subrahmanyam, C. Promising Utilization of CO_2 for Syngas Production over Mg^{2+}- and Ce^{2+}-Promoted Ni/γ-Al_2O_3 Assisted by Nonthermal Plasma. *ACS Omega* **2020**, *5*, 14040–14050. DOI: 10.1021/acsomega.0c01442.

(65) Mei, D.; Sun, M.; Liu, S.; Zhang, P.; Fang, Z.; Tu, X. Plasma-Enabled Catalytic Dry Reforming of CH_4 into Syngas, Hydrocarbons and Oxygenates: Insight into the Active Metals of γ-Al_2O_3 Supported Catalysts. *J. CO2 Util.* **2023**, *67*, 102307. DOI: 10.1016/j.jcou.2022.102307.

(66) Dębek, R.; Azzolina-Jury, F.; Travert, A.; Maugé, F. A Review on Plasma-Catalytic

Methanation of Carbon Dioxide – Looking for an Efficient Catalyst. *Renewable Sustainable Energy Rev.* **2019**, *116*, 109427. DOI: 10.1016/j.rser.2019.109427.

(67) Gao, X.; Wang, Z.; Huang, Q.; Jiang, M.; Askari, S.; Dewangan, N.; Kawi, S. State-of-Art Modifications of Heterogeneous Catalysts for CO_2 Methanation – Active Sites, Surface Basicity and Oxygen Defects. *Catal. Today* **2022**, *402*, 88–103. DOI: 10.1016/j.cattod.2022.03.017.

(68) Chung, W. C.; Chang, M. B. Review of Catalysis and Plasma Performance on Dry Reforming of CH₄ and Possible Synergistic Effects. *Renewable Sustainable Energy Rev.* **2016**, *62*, 13–31. DOI: 10.1016/j.rser.2016.04.007.

(69) Uytdenhouwen, Y.; Bal, K. M.; Michielsen, I.; Neyts, E. C.; Meynen, V.; Cool, P.; Bogaerts, A. How Process Parameters and Packing Materials Tune Chemical Equilibrium and Kinetics in Plasma-Based CO2 Conversion. *Chem. Eng. J.* **2019**, *372*, 1253–1264. DOI: 10.1016/j.cej.2019.05.008.

(70) Kim, J.; Abbott, M. S.; Go, D. B.; Hicks, J. C. Enhancing C–H Bond Activation of Methane via Temperature-Controlled, Catalyst–Plasma Interactions. *ACS Energy Lett.* **2016**, *1*, 94–99. DOI: 10.1021/acsenergylett.6b00051.

(71) Rouwenhorst, K. H. R.; Burbach, H. G. B.; Vogel, D. W.; Núñez Paulí, J.; Geerdink, B.; Lefferts, L. Plasma-Catalytic Ammonia Synthesis beyond Thermal Equilibrium on Ru-Based Catalysts in Non-Thermal Plasma. *Catal. Sci. Technol.* **2021**, *11*, 2834–2843. DOI: 10.1039/d0cy02189j.

(72) Mehta, P.; Barboun, P. M.; Engelmann, Y.; Go, D. B.; Bogaerts, A.; Schneider, W. F.; Hicks, J. C. Plasma-Catalytic Ammonia Synthesis beyond the Equilibrium Limit. *ACS Catal.* **2020**, *10*, 6726–6734. DOI: 10.1021/acscatal.0c00684.

(73) Dombrowski, E.; Peterson, E.; Del Sesto, D.; Utz, A. L. Precursor-Mediated

Reactivity of Vibrationally Hot Molecules: Methane Activation on Ir(111). *Catal. Today* **2015**, *244*, 10–18. DOI: 10.1016/j.cattod.2014.10.025.

(74) Smith, R. R.; Killelea, D. R.; DelSesto, D. F.; Utz, A. L. Preference for Vibrational over Translational Energy in a Gas-Surface Reaction. *Science (80-.).* **2004**, *304*, 992–995. DOI: 10.1126/science.1096309.

(75) Barboun, P. M.; Daemen, L. L.; Waitt, C.; Wu, Z.; Schneider, W. F.; Hicks, J. C. Inelastic Neutron Scattering Observation of Plasma-Promoted Nitrogen Reduction Intermediates on Ni/γ-Al_2O_3. *ACS Energy Lett.* **2021**, *6*, 2048–2053. DOI: 10.1021/acsenergylett.1c00643.

(76) Barboun, P. M.; Otor, H. O.; Ma, H.; Goswami, A.; Schneider, W. F.; Hicks, J. C. Plasma-Catalyst Reactivity Control of Surface Nitrogen Species through Plasma-Temperature-Programmed Hydrogenation to Ammonia. *ACS Sustain. Chem. Eng.* **2022**, *10*, 15741–15748. DOI: 10.1021/acssuschemeng.2c04217.

(77) Mehta, P.; Barboun, P.; Go, D. B.; Hicks, J. C.; Schneider, W. F. Catalysis Enabled by Plasma Activation of Strong Chemical Bonds: A Review. *ACS Energy Lett.* **2019**, *4*, 1115–1133. DOI: 10.1021/acsenergylett.9b00263.

(78) Enger, B. C.; Lødeng, R.; Holmen, A. A Review of Catalytic Partial Oxidation of Methane to Synthesis Gas with Emphasis on Reaction Mechanisms over Transition Metal Catalysts. *Appl. Catal. A* **2008**, *346*, 1–27. DOI: 10.1016/j.apcata.2008.05.018.

(79) Yi, Y.; Li, S.; Cui, Z.; Hao, Y.; Zhang, Y.; Wang, L.; Liu, P.; Tu, X.; Xu, X.; Guo, H.; Bogaerts, A. Selective Oxidation of CH_4 to CH_3OH through Plasma Catalysis: Insights from Catalyst Characterization and Chemical Kinetics Modelling. *Appl. Catal. B Environ.* **2021**, *296*, 120384. DOI: 10.1016/j.apcatb.2021.120384.

(80) Nørskov, J. K.; Studt, F.; Abild-Pedersen, F.; Bligaard, T. *Fundamental Concepts in Heterogeneous Catalysis*; John Wiley & Sons, Inc.: Hoboken, New Jersey, 2014.

(81) Mehta, P.; Barboun, P.; Herrera, F. A.; Kim, J.; Rumbach, P.; Go, D. B.; Hicks, J. C.; Schneider, W. F. Overcoming Ammonia Synthesis Scaling Relations with Plasma-Enabled Catalysis. *Nat. Catal.* **2018**, *1*, 269–275. DOI: 10.1038/s41929-018-0045-1.

(82) Engelmann, Y.; Van'T Veer, K.; Gorbanev, Y.; Neyts, E. C.; Schneider, W. F.; Bogaerts, A. Plasma Catalysis for Ammonia Synthesis: A Microkinetic Modeling Study on the Contributions of Eley-Rideal Reactions. *ACS Sustain. Chem. Eng.* **2021**, *9*, 13151–13163. DOI: 10.1021/acssuschemeng.1c02713.

(83) Ma, H.; Schneider, W. F. Plasma-Catalyst Modeling for Materials Selection: Challenges and Opportunities in Nitrogen Oxidation. *J. Phys. D: Appl. Phys.* **2021**, *54*, 454004. DOI: 10.1088/1361-6463/ac1bd1.

(84) Engelmann, Y.; Mehta, P.; Neyts, E. C.; Schneider, W. F.; Bogaerts, A. Predicted Influence of Plasma Activation on Nonoxidative Coupling of Methane on Transition Metal Catalysts. *ACS Sustain. Chem. Eng.* **2020**, *8*, 6043–6054. DOI: 10.1021/acssuschemeng.0c00906.

(85) Michiels, R.; Engelmann, Y.; Bogaerts, A. Plasma Catalysis for CO_2 Hydrogenation: Unlocking New Pathways toward CH_3OH. *J. Phys. Chem. C* **2020**, *124*, 25859–25872. DOI: 10.1021/acs.jpcc.0c07632.

(86) Loenders, B.; Engelmann, Y.; Bogaerts, A. Plasma-Catalytic Partial Oxidation of Methane on Pt(111): A Microkinetic Study on the Role of Different Plasma Species. *J. Phys. Chem. C* **2021**, *125*, 2966–2983. DOI: 10.1021/acs.jpcc.0c09849.

(87) Hummelshøj, J. S.; Abild-Pedersen, F.; Studt, F.; Bligaard, T.; Nørskov, J. K. CatApp:

A Web Application for Surface Chemistry and Heterogeneous Catalysis. *Angew. Chemie* **2012**, *124*, 278–280. DOI: 10.1002/ange.201107947.

(88) Meloni, E.; Martino, M.; Palma, V. A Short Review on Ni Based Catalysts and Related Engineering Issues for Methane Steam Reforming. *Catalysts* **2020**, *10*, 352. DOI: 10.3390/catal10030352.

(89) Rouwenhorst, K. H. R.; Kim, H. H.; Lefferts, L. Vibrationally Excited Activation of N_2 in Plasma-Enhanced Catalytic Ammonia Synthesis: A Kinetic Analysis. *ACS Sustain. Chem. Eng.* **2019**, *7*, 17515–17522. DOI: 10.1021/acssuschemeng.9b04997.

(90) Sheng, Z.; Watanabe, Y.; Kim, H.-H.; Yao, S.; Nozaki, T. Plasma-Enabled Mode-Selective Activation of CH_4 for Dry Reforming: First Touch on the Kinetic Analysis. *Chem. Eng. J.* **2020**, *399*, 125751. DOI: 10.1016/j.cej.2020.125751.

(91) Xu, S.; Chansai, S.; Shao, Y.; Xu, S.; Wang, Y. chi; Haigh, S.; Mu, Y.; Jiao, Y.; Stere, C. E.; Chen, H.; Fan, X.; Hardacre, C. Mechanistic Study of Non-Thermal Plasma Assisted CO_2 Hydrogenation over Ru Supported on MgAl Layered Double Hydroxide. *Appl. Catal. B Environ.* **2020**, *268*, 118752. DOI: 10.1016/j.apcatb.2020.118752.

(92) Kim, J.; Go, D. B.; Hicks, J. C. Synergistic Effects of Plasma–Catalyst Interactions for CH_4 Activation. *Phys. Chem. Chem. Phys.* **2017**, *19*, 13010–13021. DOI: 10.1039/C7CP01322A.

(93) Jidenko, N.; Bourgeois, E.; Borra, J.-P. Temperature Profiles in Filamentary Dielectric Barrier Discharges at Atmospheric Pressure. *J. Phys. D: Appl. Phys.* **2010**, *43*, 295203. DOI: 10.1088/0022-3727/43/29/295203.

(94) Jiang, J.; Bruggeman, P. J. Investigation of the Mechanisms Underpinning Plasma-

Catalyst Interaction for the Conversion of Methane to Oxygenates. *Plasma Chem. Plasma Process.* **2022**, *42*, 689–707. DOI: 10.1007/s11090-022-10251-5.

(95) Gibson, E. K.; Stere, C. E.; Curran-McAteer, B.; Jones, W.; Cibin, G.; Gianolio, D.; Goguet, A.; Wells, P. P.; Catlow, C. R. A.; Collier, P.; Hinde, P.; Hardacre, C. Probing the Role of a Non-Thermal Plasma (NTP) in the Hybrid NTP Catalytic Oxidation of Methane. *Angew. Chem., Int. Ed.* **2017**, *56*, 9351–9355. DOI: 10.1002/anie.201703550.

(96) Parastaev, A.; Kosinov, N.; Hensen, E. J. M. Mechanistic Study of Catalytic CO_2 Hydrogenation in a Plasma by Operando DRIFT Spectroscopy. *J. Phys. D: Appl. Phys.* **2021**, *54*, 264004. DOI: 10.1088/1361-6463/abeb96.

(97) Eliasson, B.; Kogelschatz, U.; Xue, B.; Zhou, L.-M. Hydrogenation of Carbon Dioxide to Methanol with a Discharge-Activated Catalyst. *Ind. Eng. Chem. Res.* **1998**, *37*, 3350–3357. DOI: 10.1021/ie9709401.

(98) Ahmad, F.; Lovell, E. C.; Masood, H.; Cullen, P. J.; Ostrikov, K. K.; Scott, J. A.; Amal, R. Low-Temperature CO_2 Methanation: Synergistic Effects in Plasma-Ni Hybrid Catalytic System. *ACS Sustain. Chem. Eng.* **2020**, *8*, 1888–1898. DOI: 10.1021/acssuschemeng.9b06180.

(99) Schumann, J.; Medford, A. J.; Yoo, J. S.; Zhao, Z.-J.; Bothra, P.; Cao, A.; Studt, F.; Abild-Pedersen, F.; Nørskov, J. K. Selectivity of Synthesis Gas Conversion to C_{2+} Oxygenates on Fcc(111) Transition-Metal Surfaces. *ACS Catal.* **2018**, *8*, 3447–3453. DOI: 10.1021/acscatal.8b00201.

(100) Elnabawy, A. O.; Schumann, J.; Bothra, P.; Cao, A.; Nørskov, J. K. The Challenge of CO Hydrogenation to Methanol: Fundamental Limitations Imposed by Linear Scaling Relations. *Top. Catal.* **2020**, *63*, 635–648. DOI: 10.1007/s11244-020-01283-2.

(101) Parastaev, A.; Hoeben, W. F. L. M.; van Heesch, B. E. J. M.; Kosinov, N.; Hensen, E. J. M. Temperature-Programmed Plasma Surface Reaction: An Approach to Determine Plasma-Catalytic Performance. *Appl. Catal. B Environ.* **2018**, *239*, 168–177. DOI: 10.1016/j.apcatb.2018.08.011.

(102) Quan, J.; Muttaqien, F.; Kondo, T.; Kozarashi, T.; Mogi, T.; Imabayashi, T.; Hamamoto, Y.; Inagaki, K.; Hamada, I.; Morikawa, Y.; Nakamura, J. Vibration-Driven Reaction of CO_2 on Cu Surfaces via Eley–Rideal-Type Mechanism. *Nat. Chem.* **2019**, *11*, 722–729. DOI: 10.1038/s41557-019-0282-1.

(103) Kim, D.-Y.; Ham, H.; Chen, X.; Liu, S.; Xu, H.; Lu, B.; Furukawa, S.; Kim, H.-H.; Takakusagi, S.; Sasaki, K.; Nozaki, T. Cooperative Catalysis of Vibrationally Excited CO_2 and Alloy Catalyst Breaks the Thermodynamic Equilibrium Limitation. *J. Am. Chem. Soc.* **2022**, *144*, 14140–14149. DOI: 10.1021/jacs.2c03764.

(104) Wang, L.; Yi, Y.; Guo, H.; Tu, X. Atmospheric Pressure and Room Temperature Synthesis of Methanol through Plasma-Catalytic Hydrogenation of CO_2. *ACS Catal.* **2018**, *8*, 90–100. DOI: 10.1021/acscatal.7b02733.

(105) Maitre, P.-A.; Bieniek, M. S.; Kechagiopoulos, P. N. Plasma-Catalysis of Nonoxidative Methane Coupling: A Dynamic Investigation of Plasma and Surface Microkinetics over Ni(111). *J. Phys. Chem. C* **2022**, *126*, 19987–20003. DOI: 10.1021/acs.jpcc.2c03503.

(106) Prins, R. Eley–Rideal, the Other Mechanism. *Top. Catal.* **2018**, *61*, 714–721. DOI: 10.1007/s11244-018-0948-8.

(107) Gorbanev, Y.; Engelmann, Y.; van't Veer, K.; Vlasov, E.; Ndayirinde, C.; Yi, Y.; Bals, S.; Bogaerts, A. Al_2O_3-Supported Transition Metals for Plasma-Catalytic NH_3 Synthesis in a DBD Plasma: Metal Activity and Insights into Mechanisms. *Catalysts* **2021**, *11*, 1230. DOI: 10.3390/catal11101230.

(108) Wang, Y.; Craven, M.; Yu, X.; Ding, J.; Bryant, P.; Huang, J.; Tu, X. Plasma-Enhanced Catalytic Synthesis of Ammonia over a Ni/Al_2O_3 Catalyst at Near-Room Temperature: Insights into the Importance of the Catalyst Surface on the Reaction Mechanism. *ACS Catal.* **2019**, *9*, 10780–10793. DOI: 10.1021/acscatal.9b02538.

(109) Shah, J.; Gorky, F.; Psarras, P.; Seong, B.; Gómez-Gualdrón, D. A.; Carreon, M. L. Enhancement of the Yield of Ammonia by Hydrogen-Sink Effect during Plasma Catalysis. *ChemCatChem* **2020**, *12*, 1200–1211. DOI: 10.1002/cctc.201901769.

(110) Hong, J.; Pancheshnyi, S.; Tam, E.; Lowke, J. J.; Prawer, S.; Murphy, A. B. Kinetic Modelling of NH_3 Production in N_2–H_2 Non-Equilibrium Atmospheric-Pressure Plasma Catalysis. *J. Phys. D: Appl. Phys.* **2017**, *50*, 154005. DOI: 10.1088/1361-6463/aa6229.

(111) van 't Veer, K.; Engelmann, Y.; Reniers, F.; Bogaerts, A. Plasma-Catalytic Ammonia Synthesis in a DBD Plasma: Role of Microdischarges and Their Afterglows. *J. Phys. Chem. C* **2020**, *124*, 22871–22883. DOI: 10.1021/acs.jpcc.0c05110.

(112) Xi, M.; Bent, B. E. Reaction of Deuterium Atoms with Cyclohexane on Copper (111): Hydrogen Abstraction Reactions by Eley-Rideal Mechanisms. *J. Phys. Chem.* **1993**, *97*, 4167–4172. DOI: 10.1021/j100118a037.

(113) Weinberg, W. H. Eley−Rideal Surface Chemistry: Direct Reactivity of Gas Phase Atomic Hydrogen with Adsorbed Species. *Acc. Chem. Res.* **1996**, *29*, 479–487. DOI: 10.1021/ar9500980.

(114) Rettner, C. T.; Auerbach, D. J.; Lee, J. Dynamics of the Formation of CD_4 from the Direct Reaction of Incident D Atoms with CD_3/Cu(111). *J. Chem. Phys.* **1996**, *105*, 10115–10122. DOI: 10.1063/1.472840.

(115) Du, J.; Zong, L.; Zhang, S.; Gao, Y.; Dou, L.; Pan, J.; Shao, T. Numerical Investigation on the Heterogeneous Pulsed Dielectric Barrier Discharge Plasma Catalysis for CO2 Hydrogenation at Atmospheric Pressure: Effects of Ni and Cu Catalysts on the Selectivity Conversions to CH4 and CH3OH. *Plasma Process. Polym.* **2022**, *19*, 2100111. DOI: 10.1002/ppap.202100111.

(116) Michiels, R.; Gerrits, N.; Neyts, E.; Bogaerts, A. Plasma Catalysis Modeling: How Ideal Is Atomic Hydrogen for Eley–Rideal? *J. Phys. Chem. C* **2024**, *128*, 11196–11209. DOI: 10.1021/acs.jpcc.4c02193.

(117) Bal, K. M.; Huygh, S.; Bogaerts, A.; Neyts, E. C. Effect of Plasma-Induced Surface Charging on Catalytic Processes: Application to CO_2 Activation. *Plasma Sources Sci. Technol.* **2018**, *27*, 024001. DOI: 10.1088/1361-6595/aaa868.

(118) Jafarzadeh, A.; Bal, K. M.; Bogaerts, A.; Neyts, E. C. CO_2 Activation on TiO_2-Supported Cu_5 and Ni_5 Nanoclusters: Effect of Plasma-Induced Surface Charging. *J. Phys. Chem. C* **2019**, *123*, 6516–6525. DOI: 10.1021/acs.jpcc.8b11816.

(119) Jafarzadeh, A.; Bal, K. M.; Bogaerts, A.; Neyts, E. C. Activation of CO2 on Copper Surfaces: The Synergy between Electric Field, Surface Morphology, and Excess Electrons. *J. Phys. Chem. C* **2020**, *124*, 6747–6755. DOI: 10.1021/acs.jpcc.0c00778.

(120) Kim, M.; Biswas, S.; Barraza Alvarez, I.; Christopher, P.; Wong, B. M.; Mangolini, L. Nonthermal Plasma Activation of Adsorbates: The Case of CO on Pt. *JACS Au* **2024**, *4*, 2979–2988. DOI: 10.1021/jacsau.4c00309.

(121) Zhang, Y.-J.; Lv, C.-Q.; Liu, J.-H.; Wang, G.-C. Theoretical Study on the Activation of CO_2 at the Ni/Al_2O_3 Interface under External Electric Field. *Langmuir* **2025**, *41*, 15384–15396. DOI: 10.1021/acs.langmuir.5c01029.

(122) *Reactor Design for Chemical Engineers*; J. M. Winterbottom, M. K., Ed.; Stanley Thornes (Publisers) Ltd: Cheltenham, 1999.

(123) Filot, I. A. W. *Introduction to Microkinetic Modeling*; Eindhoven University of Technology: Eindhoven, 2018.

(124) Cauquot, P.; Cavadias, S.; Amouroux, J. Thermal Energy Accommodation from Oxygen Atoms Recombination on Metallic Surfaces. *J. Thermophys. Heat Transf.* **1998**, *12*, 206–213. DOI: 10.2514/2.6323.

(125) May, J. W.; Linnett, J. W. Recombination of Atoms at Surfaces. An Effusion Method Applied to Oxygen Atom Recombination. *J. Catal.* **1967**, *7*, 324–341. DOI: 10.1016/0021-9517(67)90161-3.

(126) Diao, Y.; Zhang, X.; Liu, Y.; Chen, B.; Wu, G.; Shi, C. Plasma-Assisted Dry Reforming of Methane over Mo_2C-Ni/Al_2O_3 Catalysts: Effects of β-Mo_2C Promoter. *Appl. Catal. B Environ.* **2022**, *301*, 120779. DOI: 10.1016/j.apcatb.2021.120779.

(127) Biswas, A. N.; Winter, L. R.; Loenders, B.; Xie, Z.; Bogaerts, A.; Chen, J. G. Oxygenate Production from Plasma-Activated Reaction of CO_2 and Ethane. *ACS Energy Lett.* **2022**, *7*, 236–241. DOI: 10.1021/acsenergylett.1c02355.

(128) Li, J.; Dou, L.; Gao, Y.; Hei, X.; Yu, F.; Shao, T. Revealing the Active Sites of the Structured Ni-Based Catalysts for One-Step CO_2/CH_4 Conversion into Oxygenates by Plasma-Catalysis. *J. CO2 Util.* **2021**, *52*, 101675. DOI: 10.1016/j.jcou.2021.101675.

(129) Manion, J. A.; Huie, R. E.; Levin, R. D.; Jr., D. R. B.; Orkin, V. L.; Tsang, W.; McGivern, W. S.; Hudgens, J. W.; Knyazev, V. D.; Atkinson, D. B.; Chai, E.; Tereza, A. M.; Lin, C.-Y.; Allison, T. C.; Mallard, W. G.; Westley, F.; Herron, J. T.; Hampson, R. F.; Frizzell, D. H. *NIST Chemical Kinetics Database, NIST Standard Reference*

Database 17, Version 7.0 (Web Version), Release 1.6.8, Data version 2015.09, National Institute of Standards and Technology, Gaithersburg, Maryland, 20899-8320. https://kinetics.nist.gov/.

(130) McElroy, D.; Walsh, C.; Markwick, A. J.; Cordiner, M. A.; Smith, K.; Millar, T. J. The UMIST Database for Astrochemistry 2012. *Astron. Astrophys.* **2013**, *550*, A36. DOI: 10.1051/0004-6361/201220465.

(131) Baulch, D. L.; Bowman, C. T.; Cobos, C. J.; Cox, R. A.; Just, T.; Kerr, J. A.; Pilling, M. J.; Stocker, D.; Troe, J.; Tsang, W.; Walker, R. W.; Warnatz, J. Evaluated Kinetic Data for Combustion Modeling: Supplement II. *J. Phys. Chem. Ref. Data* **2005**, *34*, 757–1397. DOI: 10.1063/1.1748524.

(132) Baulch, D. L.; Cobos, C. J.; Cox, R. A.; Esser, C.; Frank, P.; Just, T.; Kerr, J. A.; Pilling, M. J.; Troe, J.; Walker, R. W.; Warnatz, J. Evaluated Kinetic Data for Combustion Modelling. *J. Phys. Chem. Ref. Data* **1992**, *21*, 411–734. DOI: 10.1063/1.555908.

(133) Baulch, D. L.; Cobos, C. J.; Cox, R. A.; Frank, P.; Hayman, G.; Just, T.; Kerr, J. A.; Murrells, T.; Pilling, M. J.; Troe, J.; Walker, R. W.; Warnatz, J. Evaluated Kinetic Data for Combustion Modeling. Supplement I. *J. Phys. Chem. Ref. Data* **1994**, *23*, 847–848. DOI: 10.1063/1.555953.

(134) Tsang, W.; Hampson, R. F. Chemical Kinetic Data Base for Combustion Chemistry. Part I. Methane and Related Compounds. *J. Phys. Chem. Ref. Data* **1986**, *15*, 1087–1279. DOI: 10.1063/1.555759.

(135) Tsang, W. Energy Transfer Effects during the Multichannel Decomposition of Ethanol. *Int. J. Chem. Kinet.* **2004**, *36*, 456–465. DOI: 10.1002/kin.20015.

(136) Tsang, W. Chemical Kinetic Data Base for Combustion Chemistry. Part 2. Methanol. *J. Phys. Chem. Ref. Data* **1987**, *16*, 471–508. DOI: 10.1063/1.555802.

(137) Tsang, W. Chemical Kinetic Data Base for Combustion Chemistry Part V. Propene. *J. Phys. Chem. Ref. Data* **1991**, *20*, 221–273. DOI: 10.1063/1.555880.

(138) Tsang, W. Chemical Kinetic Data Base for Combustion Chemistry. Part 3: Propane. *J. Phys. Chem. Ref. Data* **1988**, *17*, 887–951. DOI: 10.1063/1.555806.

(139) Turner, M. M. Uncertainty and Error in Complex Plasma Chemistry Models. *Plasma Sources Sci. Technol.* **2015**, *24*, 035027. DOI: 10.1088/0963-0252/24/3/035027.

(140) Berthelot, A.; Bogaerts, A. Modeling of CO_2 Plasma: Effect of Uncertainties in the Plasma Chemistry. *Plasma Sources Sci. Technol.* **2017**, *26*, 115002. DOI: 10.1088/1361-6595/aa8ffb.

(141) Hagelaar, G. J. M.; Pitchford, L. C. Solving the Boltzmann Equation to Obtain Electron Transport Coefficients and Rate Coefficients for Fluid Models. *Plasma Sources Sci. Technol.* **2005**, *14*, 722–733. DOI: 10.1088/0963-0252/14/4/011.

(142) Luque, A. *BOLOS: An open source solver for the Boltzmann equation*. https://github.com/aluque/bolos (accessed 2024-08-27).

(143) Campbell, C. T.; Sprowl, L. H.; Árnadóttir, L. Equilibrium Constants and Rate Constants for Adsorbates: Two-Dimensional (2D) Ideal Gas, 2D Ideal Lattice Gas, and Ideal Hindered Translator Models. *J. Phys. Chem. C* **2016**, *120*, 10283–10297. DOI: 10.1021/acs.jpcc.6b00975.

(144) Larsen, A. H.; Mortensen, J. J.; Blomqvist, J.; Castelli, I. E.; Christensen, R.; Dułak, M.; Friis, J.; Groves, M. N.; Hammer, B.; Hargus, C.; Hermes, E. D.; Jennings, P. C.; Jensen, P. B.; Kermode, J.; Kitchin, J. R.; Kolsbjerg, E. L.; Kubal, J.; Kaasbjerg, K.; Lysgaard, S.; Bergmann Maronsson, J.; Maxson, T.; Olsen, T.; Pastewka, L.; Peterson, A.; Rostgaard, C.; Schiøtz, J.; Schütt, O.; Strange, M.; Thygesen, K. S.;

Vegge, T.; Vilhelmsen, L.; Walter, M.; Zeng, Z.; Jacobsen, K. W. The Atomic Simulation Environment—a Python Library for Working with Atoms. *J. Phys. Condens. Matter* **2017**, *29*, 273002. DOI: 10.1088/1361-648X/aa680e.

(145) Shomate, C. H. A Method for Evaluating and Correlating Thermodynamic Data. *J. Phys. Chem.* **1954**, *58*, 368–372. DOI: 10.1021/j150514a018.

(146) Burcat, a; Branko, R. *Third Millennium Ideal Gas and Condensed Phase Thermochemical Database for Combustion with Updates from Active Thermochemical Tables*; 2005.

(147) Schwach, P.; Pan, X.; Bao, X. Direct Conversion of Methane to Value-Added Chemicals over Heterogeneous Catalysts: Challenges and Prospects. *Chem. Rev.* **2017**, *117*, 8497–8520. DOI: 10.1021/acs.chemrev.6b00715.

(148) Olivos-Suarez, A. I.; Szécsényi, À.; Hensen, E. J. M.; Ruiz-Martinez, J.; Pidko, E. A.; Gascon, J. Strategies for the Direct Catalytic Valorization of Methane Using Heterogeneous Catalysis: Challenges and Opportunities. *ACS Catal.* **2016**, *6*, 2965–2981. DOI: 10.1021/acscatal.6b00428.

(149) Dinh, K. T.; Sullivan, M. M.; Serna, P.; Meyer, R. J.; Dincă, M.; Román-Leshkov, Y. Viewpoint on the Partial Oxidation of Methane to Methanol Using Cu- and Fe-Exchanged Zeolites. *ACS Catal.* **2018**, *8*, 8306–8313. DOI: 10.1021/acscatal.8b01180.

(150) Karakaya, C.; Kee, R. J. Progress in the Direct Catalytic Conversion of Methane to Fuels and Chemicals. *Prog. Energy Combust. Sci.* **2016**, *55*, 60–97. DOI: 10.1016/j.pecs.2016.04.003.

(151) Yoo, J. S.; Schumann, J.; Studt, F.; Abild-Pedersen, F.; Nørskov, J. K. Theoretical Investigation of Methane Oxidation on Pd(111) and Other Metallic Surfaces. *J.*

Phys. Chem. C **2018**, *122*, 16023–16032. DOI: 10.1021/acs.jpcc.8b02142.

(152) Olivera, P. P.; Patrito, E. M.; Sellers, H. Direct Synthesis of Methanol over Metallic Catalysts. *Surf. Sci.* **1995**, *327*, 330–357. DOI: 10.1016/0039-6028(94)00847-7.

(153) Xing, B.; Pang, X.-Y.; Wang, G.-C. C–H Bond Activation of Methane on Clean and Oxygen Pre-Covered Metals: A Systematic Theoretical Study. *J. Catal.* **2011**, *282*, 74–82. DOI: 10.1016/j.jcat.2011.05.027.

(154) Goujard, V.; Nozaki, T.; Yuzawa, S.; Ağiral, A.; Okazaki, K. Plasma-Assisted Partial Oxidation of Methane at Low Temperatures: Numerical Analysis of Gas-Phase Chemical Mechanism. *J. Phys. D: Appl. Phys.* **2011**, *44*, 274011. DOI: 10.1088/0022-3727/44/27/274011.

(155) Nozaki, T.; Hattori, A.; Okazaki, K. Partial Oxidation of Methane Using a Microscale Non-Equilibrium Plasma Reactor. *Catal. Today* **2004**, *98*, 607–616. DOI: 10.1016/j.cattod.2004.09.053.

(156) Qian, M.; Zhong, W.; Kang, J.; Liu, S.; Ren, C.; Zhang, J.; Wang, D. Global Modeling on Partial Oxidation of Methane to Oxygenates and Syngas in Non-Equilibrium Plasma. *Jpn. J. Appl. Phys.* **2020**, *59*, 066003. DOI: 10.35848/1347-4065/ab91cd.

(157) De Bie, C.; van Dijk, J.; Bogaerts, A. The Dominant Pathways for the Conversion of Methane into Oxygenates and Syngas in an Atmospheric Pressure Dielectric Barrier Discharge. *J. Phys. Chem. C* **2015**, *119*, 22331–22350. DOI: 10.1021/acs.jpcc.5b06515.

(158) Knoll, A. J.; Zhang, S.; Lai, M.; Luan, P.; Oehrlein, G. S. Infrared Studies of Gas Phase and Surface Processes of the Enhancement of Catalytic Methane Decomposition by Low Temperature Plasma. *J. Phys. D: Appl. Phys.* **2019**, *52*, 225201. DOI: 10.1088/1361-6463/ab0c66.

(159) Stere, C.; Chansai, S.; Gholami, R.; Wangkawong, K.; Singhania, A.; Goguet, A.; Inceesungvorn, B.; Hardacre, C. A Design of a Fixed Bed Plasma DRIFTS Cell for Studying the NTP-Assisted Heterogeneously Catalysed Reactions. *Catal. Sci. Technol.* **2020**, *10*, 1458–1466. DOI: 10.1039/D0CY00036A.

(160) Zhang, S.; Li, Y.; Knoll, A.; Oehrlein, G. S. Mechanistic Aspects of Plasma-Enhanced Catalytic Methane Decomposition by Time-Resolved Operando Diffuse Reflectance Infrared Fourier Transform Spectroscopy. *J. Phys. D: Appl. Phys.* **2020**, *53*, 215201. DOI: 10.1088/1361-6463/ab795b.

(161) York, A. P. E.; Xiao, T.; Green, M. L. H. Brief Overview of the Partial Oxidation of Methane to Synthesis Gas. *Top. Catal.* **2003**, *22*, 345–358. DOI: 10.1023/A:1023552709642.

(162) Chen, Y.; Vlachos, D. G. Density Functional Theory Study of Methane Oxidation and Reforming on Pt(111) and Pt(211). *Ind. Eng. Chem. Res.* **2012**, *51*, 12244−12252. DOI: 10.1021/ie301792g.

(163) Wang, R.; Chen, J.; Zhao, W.; Wen, J.; Li, H.; Li, L.; Ran, J. Mechanism of the Catalytic Oxidation of Methane on Pt(1 1 1) Surfaces in Moist Environment: A Density Functional Theory Study. *Appl. Surf. Sci.* **2019**, *471*, 566–586. DOI: 10.1016/j.apsusc.2018.12.055.

(164) Aghalayam, P.; Park, Y. K.; Fernandes, N.; Papavassiliou, V.; Mhadeshwar, A. B.; Vlachos, D. G. A C1 Mechanism for Methane Oxidation on Platinum. *J. Catal.* **2003**, *213*, 23–38. DOI: 10.1016/S0021-9517(02)00045-3.

(165) Mhadeshwar, A. B.; Vlachos, D. G. A Catalytic Reaction Mechanism for Methane Partial Oxidation at Short Contact Times, Reforming, and Combustion, and for Oxygenate Decomposition and Oxidation on Platinum. *Ind. Eng. Chem. Res.* **2007**, *46*, 5310–5324. DOI: 10.1021/ie070322c.

(166) Korup, O.; Goldsmith, C. F.; Weinberg, G.; Geske, M.; Kandemir, T.; Schlögl, R.; Horn, R. Catalytic Partial Oxidation of Methane on Platinum Investigated by Spatial Reactor Profiles, Spatially Resolved Spectroscopy, and Microkinetic Modeling. *J. Catal.* **2013**, *297*, 1–16. DOI: 10.1016/j.jcat.2012.08.022.

(167) Kraus, P.; Lindstedt, R. P. Microkinetic Mechanisms for Partial Oxidation of Methane over Platinum and Rhodium. *J. Phys. Chem. C* **2017**, *121*, 9442–9453. DOI: 10.1021/acs.jpcc.7b02397.

(168) Horn, R.; Williams, K.; Degenstein, N.; Bitsch-Larsen, A.; Dalle Nogare, D.; Tupy, S.; Schmidt, L. Methane Catalytic Partial Oxidation on Autothermal Rh and Pt Foam Catalysts: Oxidation and Reforming Zones, Transport Effects, and Approach to Thermodynamic Equilibrium. *J. Catal.* **2007**, *249*, 380–393. DOI: 10.1016/j.jcat.2007.05.011.

(169) Chin, Y.-H. C.; Buda, C.; Neurock, M.; Iglesia, E. Selectivity of Chemisorbed Oxygen in C–H Bond Activation and CO Oxidation and Kinetic Consequences for CH_4–O_2 Catalysis on Pt and Rh Clusters. *J. Catal.* **2011**, *283*, 10–24. DOI: 10.1016/j.jcat.2011.06.011.

(170) Nozaki, T.; Ağıral, A.; Yuzawa, S.; Gardeniers, J. G. E. H.; Okazaki, K. A Single Step Methane Conversion into Synthetic Fuels Using Microplasma Reactor. *Chem. Eng. J.* **2011**, *166*, 288–293. DOI: 10.1016/j.cej.2010.08.001.

(171) Chin, Y.-H.; Buda, C.; Neurock, M.; Iglesia, E. Reactivity of Chemisorbed Oxygen Atoms and Their Catalytic Consequences during CH_4 –O_2 Catalysis on Supported Pt Clusters. *J. Am. Chem. Soc.* **2011**, *133*, 15958–15978. DOI: 10.1021/ja202411v.

(172) Maitre, P.-A.; Bieniek, M. S.; Kechagiopoulos, P. N. Plasma-Enhanced Catalysis for the Upgrading of Methane: A Review of Modelling and Simulation Methods. *React. Chem. Eng.* **2020**, *5*, 814–837. DOI: 10.1039/D0RE00024H.

(173) Chen, T. Y.; Rousso, A. C.; Wu, S.; Goldberg, B. M.; van der Meiden, H.; Ju, Y.; Kolemen, E. Time-Resolved Characterization of Plasma Properties in a CH_4/He Nanosecond-Pulsed Dielectric Barrier Discharge. *J. Phys. D: Appl. Phys.* **2019**, *52*, 18LT02. DOI: 10.1088/1361-6463/ab0598.

(174) Butterworth, T.; van de Steeg, A.; van den Bekerom, D.; Minea, T.; Righart, T.; Ong, Q.; van Rooij, G. Plasma Induced Vibrational Excitation of CH_4 —a Window to Its Mode Selective Processing. *Plasma Sources Sci. Technol.* **2020**, *29*, 095007. DOI: 10.1088/1361-6595/aba1c9.

(175) Larkin, D. W.; Lobban, L. L.; Mallinson, R. G. The Direct Partial Oxidation of Methane to Organic Oxygenates Using a Dielectric Barrier Discharge Reactor as a Catalytic Reactor Analog. *Catal. Today* **2001**, *71*, 199–210. DOI: 10.1016/S0920-5861(01)00430-8.

(176) Du, Y.; Nayak, G.; Oinuma, G.; Peng, Z.; Bruggeman, P. J. Effect of Water Vapor on Plasma Morphology, OH and H_2O_2 Production in He and Ar Atmospheric Pressure Dielectric Barrier Discharges. *J. Phys. D: Appl. Phys.* **2017**, *50*, 145201. DOI: 10.1088/1361-6463/aa5e7d.

(177) Snoeckx, R.; Ozkan, A.; Reniers, F.; Bogaerts, A. The Quest for Value-Added Products from Carbon Dioxide and Water in a Dielectric Barrier Discharge: A Chemical Kinetics Study. *ChemSusChem* **2017**, *10*, 409–424. DOI: 10.1002/cssc.201601234.

(178) Vasko, C. A.; Liu, D. X.; van Veldhuizen, E. M.; Iza, F.; Bruggeman, P. J. Hydrogen Peroxide Production in an Atmospheric Pressure RF Glow Discharge: Comparison of Models and Experiments. *Plasma Chem. Plasma Process.* **2014**, *34*, 1081–1099. DOI: 10.1007/s11090-014-9559-8.

(179) Nunnally, T.; Gutsol, K.; Rabinovich, A.; Fridman, A.; Gutsol, A.; Kemoun, A.

Dissociation of CO_2 in a Low Current Gliding Arc Plasmatron. *J. Phys. D: Appl. Phys.* **2011**, *44*, 274009. DOI: 10.1088/0022-3727/44/27/274009.

(180) Larkin, D. W.; Zhou, L.; Lobban, L. L.; Mallinson, R. G. Product Selectivity Control and Organic Oxygenate Pathways from Partial Oxidation of Methane in a Silent Electric Discharge Reactor. *Ind. Eng. Chem. Res.* **2001**, *40*, 5496–5506. DOI: 10.1021/ie010298h.

(181) Pietruszka, B.; Anklam, K.; Heintze, M. Plasma-Assisted Partial Oxidation of Methane to Synthesis Gas in a Dielectric Barrier Discharge. *Appl. Catal. A* **2004**, *261*, 19–24. DOI: 10.1016/j.apcata.2003.10.027.

(182) Heintze, M.; Pietruszka, B. Plasma Catalytic Conversion of Methane into Syngas: The Combined Effect of Discharge Activation and Catalysis. *Catal. Today* **2004**, *89*, 21–25. DOI: 10.1016/j.cattod.2003.11.006.

(183) Jurković, D. L.; Puliyalil, H.; Pohar, A.; Likozar, B. Plasma-Activated Methane Partial Oxidation Reaction to Oxygenate Platform Chemicals over Fe, Mo, Pd and Zeolite Catalysts. *Int. J. Energy Res.* **2019**, *43*, 8085–8099. DOI: 10.1002/er.4806.

(184) Indarto, A.; Lee, H.; Choi, J.-W.; Song, H. K. Partial Oxidation of Methane with Yttria-Stabilized Zirconia Catalyst in a Dielectric Barrier Discharge. *Energy Sources, Part A* **2008**, *30*, 1628–1636. DOI: 10.1080/15567030701268385.

(185) Chen, Y.; Vlachos, D. G. Hydrogenation of Ethylene and Dehydrogenation and Hydrogenolysis of Ethane on Pt(111) and Pt(211): A Density Functional Theory Study. *J. Phys. Chem. C* **2010**, *114*, 4973–4982. DOI: 10.1021/jp909163z.

(186) Studt, F.; Behrens, M.; Kunkes, E. L.; Thomas, N.; Zander, S.; Tarasov, A.; Schumann, J.; Frei, E.; Varley, J. B.; Abild-Pedersen, F.; Nørskov, J. K.; Schlögl, R. The Mechanism of CO and CO_2 Hydrogenation to Methanol over Cu-Based

Catalysts. *ChemCatChem* **2015**, *7*, 1105–1111. DOI: 10.1002/cctc.201500123.

(187) Tong, Y.; Lunsford, J. H. Mechanistic and Kinetic Studies of the Reactions of Gas-Phase Methyl Radicals with Metal Oxides. *J. Am. Chem. Soc.* **1991**, *113*, 4741–4746. DOI: 10.1021/ja00013a005.

(188) Pak, S.; Smith, C. E.; Rosynek, M. P.; Lunsford, J. H. Conversion of Methyl Radicals to Methanol and Formaldehyde over Vanadium Oxide Catalysts. *J. Catal.* **1997**, *165*, 73–79. DOI: 10.1021/j100096a025.

(189) Pak, S.; Rosynek, M. P.; Lunsford, J. H. Conversion of Methyl Radicals to Methanol and Formaldehyde over Molybdenum Oxide Catalysts. *J. Phys. Chem.* **1994**, *98*, 11786–11790. DOI: 10.1021/j100096a025.

(190) Alvarez-Galvan, M. C.; Mota, N.; Ojeda, M.; Rojas, S.; Navarro, R. M.; Fierro, J. L. G. Direct Methane Conversion Routes to Chemicals and Fuels. *Catal. Today* **2011**, *171*, 15–23. DOI: 10.1016/j.cattod.2011.02.028.

(191) Mimura, N.; Takahara, I.; Inaba, M.; Okamoto, M.; Murata, K. High-Performance Cr/H-ZSM-5 Catalysts for Oxidative Dehydrogenation of Ethane to Ethylene with CO_2 as an Oxidant. *Catal. Commun.* **2002**, *3*, 257–262. DOI: 10.1016/S1566-7367(02)00117-6.

(192) Gómez-Ramírez, A.; Rico, V. J.; Cotrino, J.; González-Elipe, A. R.; Lambert, R. M. Low Temperature Production of Formaldehyde from Carbon Dioxide and Ethane by Plasma-Assisted Catalysis in a Ferroelectrically Moderated Dielectric Barrier Discharge Reactor. *ACS Catal.* **2014**, *4*, 402–408. DOI: 10.1021/cs4008528.

(193) Zhang, X.; Zhu, A.; Li, X.; Gong, W. Oxidative Dehydrogenation of Ethane with CO2 over Catalyst under Pulse Corona Plasma. *Catal. Today* **2004**, *89*, 97–102. DOI: 10.1016/j.cattod.2003.11.015.

(194) Pancheshnyi, S.; Eismann, B.; Hagelaar, G. J. M.; Pitchford, L. C. Computer Code ZDPlasKin. (University of Toulouse, LAPLACE, CNRS-UPS-INP, Toulouse, France)., LAPLACE, CNRS-UPS-INP, Toulouse, France). 2008. http://www.zdplaskin.laplace.univ-tlse.fr.

(195) van 't Veer, K.; Reniers, F.; Bogaerts, A. Zero-Dimensional Modeling of Unpacked and Packed Bed Dielectric Barrier Discharges: The Role of Vibrational Kinetics in Ammonia Synthesis. *Plasma Sources Sci. Technol.* **2020**, *29*, 045020. DOI: 10.1088/1361-6595/ab7a8a.

(196) Vermeiren, V.; Bogaerts, A. Plasma-Based CO_2 Conversion: To Quench or Not to Quench? *J. Phys. Chem. C* **2020**, *124*, 18401–18415. DOI: 10.1021/acs.jpcc.0c04257.

(197) Cleiren, E.; Heijkers, S.; Ramakers, M.; Bogaerts, A. Dry Reforming of Methane in a Gliding Arc Plasmatron: Towards a Better Understanding of the Plasma Chemistry. *ChemSusChem* **2017**, *10*, 4025–4036. DOI: 10.1002/cssc.201701274.

(198) Slaets, J.; Aghaei, M.; Ceulemans, S.; Van Alphen, S.; Bogaerts, A. CO_2 and CH_4 Conversion in "Real" Gas Mixtures in a Gliding Arc Plasmatron: How Do N_2 and O_2 Affect the Performance? *Green Chem.* **2020**, *22*, 1366–1377. DOI: 10.1039/C9GC03743H.

(199) Heijkers, S.; Aghaei, M.; Bogaerts, A. Plasma-Based CH_4 Conversion into Higher Hydrocarbons and H_2 : Modeling to Reveal the Reaction Mechanisms of Different Plasma Sources. *J. Phys. Chem. C* **2020**, *124*, 7016–7030. DOI: 10.1021/acs.jpcc.0c00082.

(200) Morillo-Candas, A. S.; Silva, T.; Klarenaar, B. L. M.; Grofulović, M.; Guerra, V.; Guaitella, O. Electron Impact Dissociation of CO_2. *Plasma Sources Sci. Technol.* **2020**, *29*, 01LT01. DOI: 10.1088/1361-6595/ab6075.

(201) Hake, R. D.; Phelps, A. V. Momentum-Transfer and Inelastic-Collision Cross Sections for Electrons in O_2, CO, and CO_2. *Phys. Rev.* **1967**, *158*, 70–84. DOI: 10.1103/PhysRev.158.70.

(202) Janev, R. K.; Reiter, D. Collision Processes of $C_{2,3}H_y$ and $C_{2,3}H_y^+$ Hydrocarbons with Electrons and Protons. *Phys. Plasmas* **2004**, *11*, 780–829. DOI: 10.1063/1.1630794.

(203) *Obtained from LXCAT (Hayashi database)*. www.lxcat.net.

(204) Ozkan, A.; Dufour, T.; Silva, T.; Britun, N.; Snyders, R.; Bogaerts, A.; Reniers, F. The Influence of Power and Frequency on the Filamentary Behavior of a Flowing DBD—Application to the Splitting of CO_2. *Plasma Sources Sci. Technol.* **2016**, *25*, 025013. DOI: 10.1088/0963-0252/25/2/025013.

(205) Bogaerts, A.; Wang, W.; Berthelot, A.; Guerra, V. Modeling Plasma-Based CO_2 Conversion: Crucial Role of the Dissociation Cross Section. *Plasma Sources Sci. Technol.* **2016**, *25*, 055016. DOI: 10.1088/0963-0252/25/5/055016.

(206) Wang, J.; Liu, C.; Eliassion, B. Density Functional Theory Study of Synthesis of Oxygenates and Higher Hydrocarbons from Methane and Carbon Dioxide Using Cold Plasmas. *Energy Fuels* **2004**, *18*, 148–153. DOI: 10.1021/ef0300949.

(207) Knapp, M.; Echt, O.; Kreisle, D.; Märk, T. D.; Recknagel, E. Formation of Long-Lived CO_2^-, N_2O^-, and Their Dimer Anions, by Electron Attachment to van Der Waals Clusters. *Chem. Phys. Lett.* **1986**, *126*, 225–231. DOI: 10.1016/S0009-2614(86)80074-4.

(208) Wang, Y.; Fan, L.; Xu, H.; Du, X.; Xiao, H.; Qian, J.; Zhu, Y.; Tu, X.; Wang, L. Insight into the Synthesis of Alcohols and Acids in Plasma-Driven Conversion of CO_2 and CH_4 over Copper-Based Catalysts. *Appl. Catal. B Environ.* **2022**, *315*, 121583. DOI:

10.1016/j.apcatb.2022.121583.

(209) Vakili, R.; Gholami, R.; Stere, C. E.; Chansai, S.; Chen, H.; Holmes, S. M.; Jiao, Y.; Hardacre, C.; Fan, X. Plasma-Assisted Catalytic Dry Reforming of Methane (DRM) over Metal-Organic Frameworks (MOFs)-Based Catalysts. *Appl. Catal. B Environ.* **2020**, *260*, 118195. DOI: 10.1016/j.apcatb.2019.118195.

(210) Medford, A. J.; Shi, C.; Hoffmann, M. J.; Lausche, A. C.; Fitzgibbon, S. R.; Bligaard, T.; Nørskov, J. K. CatMAP: A Software Package for Descriptor-Based Microkinetic Mapping of Catalytic Trends. *Catal. Letters* **2015**, *145*, 794–807. DOI: 10.1007/s10562-015-1495-6.

(211) Abild-Pedersen, F.; Greeley, J.; Studt, F.; Rossmeisl, J.; Munter, T. R.; Moses, P. G.; Skúlason, E.; Bligaard, T.; Nørskov, J. K. Scaling Properties of Adsorption Energies for Hydrogen-Containing Molecules on Transition-Metal Surfaces. *Phys. Rev. Lett.* **2007**, *99*, 016105. DOI: 10.1103/PhysRevLett.99.016105.

(212) Wang, S.; Temel, B.; Shen, J.; Jones, G.; Grabow, L. C.; Studt, F.; Bligaard, T.; Abild-Pedersen, F.; Christensen, C. H.; Nørskov, J. K. Universal Brønsted-Evans-Polanyi Relations for C–C, C–O, C–N, N–O, N–N, and O–O Dissociation Reactions. *Catal. Letters* **2011**, *141*, 370–373. DOI: 10.1007/s10562-010-0477-y.

(213) Lausche, A. C.; Medford, A. J.; Khan, T. S.; Xu, Y.; Bligaard, T.; Abild-Pedersen, F.; Nørskov, J. K.; Studt, F. On the Effect of Coverage-Dependent Adsorbate–Adsorbate Interactions for CO Methanation on Transition Metal Surfaces. *J. Catal.* **2013**, *307*, 275–282. DOI: 10.1016/j.jcat.2013.08.002.

(214) Kim, Y. C.; Boudart, M. Recombination of O, N, and H Atoms on Silica: Kinetics and Mechanism. *Langmuir* **1991**, *7*, 2999–3005. DOI: 10.1021/la00060a016.

(215) Guerra, V. Analytical Model of Heterogeneous Atomic Recombination on

Silicalike Surfaces. *IEEE Trans. Plasma Sci.* **2007**, *35*, 1397–1412. DOI: 10.1109/TPS.2007.902028.

(216) Heylen, A. E. D. Ionization Coefficients and Sparking Voltages from Methane to Butane. *Int. J. Electron.* **1975**, *39*, 653–660. DOI: 10.1080/00207217508920532.

(217) Afonina, N. E.; Gromov, V. G.; Kovalev, V. L. Investigation of the Influence of Different Heterogeneous Recombination Mechanisms on the Heat Fluxes to a Catalytic Surface in Dissociated Carbon Dioxide. *Fluid Dyn.* **2002**, *37*, 117–125.

(218) Falsig, H.; Hvolbæk, B.; Kristensen, I. S.; Jiang, T.; Bligaard, T.; Christensen, C. H.; Nørskov, J. K. Trends in the Catalytic CO Oxidation Activity of Nanoparticles. *Angew. Chem., Int. Ed.* **2008**, *47*, 4835–4839. DOI: 10.1002/anie.200801479.

(219) Kummer, J. T. Use of Noble Metals in Automobile Exhaust Catalysts. *J. Phys. Chem.* **1986**, *90*, 4747–4752. DOI: 10.1021/j100411a008.

(220) Sheng, Z.; Kim, H.-H.; Yao, S.; Nozaki, T. Plasma-Chemical Promotion of Catalysis for CH_4 Dry Reforming: Unveiling Plasma-Enabled Reaction Mechanisms. *Phys. Chem. Chem. Phys.* **2020**, *22*, 19349–19358. DOI: 10.1039/D0CP03127E.

(221) Bogaerts, A.; Centi, G. Plasma Technology for CO_2 Conversion: A Personal Perspective on Prospects and Gaps. *Front. Energy Res.* **2020**, *8*, 1–23. DOI: 10.3389/fenrg.2020.00111.

(222) Lefferts, L. Leveraging Expertise in Thermal Catalysis to Understand Plasma Catalysis. *Angew. Chem., Int. Ed.* **2024**, *63*. DOI: 10.1002/anie.202305322.

(223) Eshtehardi, H. A.; Van ‘t Veer, K.; Delplancke, M.-P.; Reniers, F.; Bogaerts, A. Postplasma Catalytic Model for NO Production: Revealing the Underlying Mechanisms to Improve the Process Efficiency. *ACS Sustain. Chem. Eng.* **2023**, *11*, 1720–1733. DOI: 10.1021/acssuschemeng.2c05665.

(224) Paul, D.; Mozetic, M.; Zaplotnik, R.; Primc, G.; Đonlagić, D.; Vesel, A. A Review of Recombination Coefficients of Neutral Oxygen Atoms for Various Materials. *Materials (Basel).* **2023**, *16*, 1774. DOI: 10.3390/ma16051774.

(225) Wanten, B.; Vertongen, R.; De Meyer, R.; Bogaerts, A. Plasma-Based CO_2 Conversion: How to Correctly Analyze the Performance? *J. Energy Chem.* **2023**, *86*, 180–196. DOI: 10.1016/j.jechem.2023.07.005.

(226) Slaets, J.; Loenders, B.; Bogaerts, A. Plasma-Based Dry Reforming of CH_4: Plasma Effects vs. Thermal Conversion. *Fuel* **2024**, *360*, 130650. DOI: 10.1016/j.fuel.2023.130650.

(227) Slaets, J.; Morais, E.; Bogaerts, A. Afterglow Quenching in Plasma-Based Dry Reforming of Methane: A Detailed Analysis of the Post-Plasma Chemistry via Kinetic Modelling. *RSC Sustain.* **2025**, *3*, 1477–1493. DOI: 10.1039/d4su00676c.

(228) Marinov, D.; Teixeira, C.; Guerra, V. Deterministic and Monte Carlo Methods for Simulation of Plasma-surface Interactions. *Plasma Process. Polym.* **2017**, *14*, 1–18. DOI: 10.1002/ppap.201600175.

(229) Afonso, J.; Vialetto, L.; Guerra, V.; Viegas, P. Plasma-Induced Reversible Surface Modification and Its Impact on Oxygen Heterogeneous Recombination. *J. Phys. D: Appl. Phys.* **2024**, *57*, 04LT01. DOI: 10.1088/1361-6463/ad039b.

(230) Viegas, P.; Silveira, J.; Cunha Dias, T.; Guaitella, O.; Sofía Morillo Candás, A.; Guerra, V. Surface Recombination in Pyrex in Oxygen DC Glow Discharges: Mesoscopic Modelling and Comparison with Experiments. *Plasma Sources Sci. Technol.* **2024**, *33*, 055003. DOI: 10.1088/1361-6595/ad4055.

(231) Ibach, H.; Erley, W.; Wagner, H. The Preexponential Factor in Desorption — CO on Ni(111). *Surf. Sci.* **1980**, *92*, 29–42. DOI: 10.1016/0039-6028(80)90240-X.

(232) Afonina, N. E.; Gromov, V. G.; Kovalev, V. L. Modeling of the Catalytic Properties of High-Temperature Surface Insulation in a Dissociated Carbon Dioxide — Nitrogen Mixture. *Fluid Dyn.* **2000**, *35*, 87–94. DOI: 10.1007/BF02698792.

(233) Loenders, B.; Michiels, R.; Bogaerts, A. How Plasma Reaction Conditions Affect the Optimal Catalyst: A Microkinetic Study of Plasma-Catalytic CO_2 Splitting. *Plasma Chem. Plasma Process.* **2025**, *45*, 1849–1899. DOI: 10.1007/s11090-025-10599-4.

(234) Jiang, B.; Guo, H. Dynamics in Reactions on Metal Surfaces: A Theoretical Perspective. *J. Chem. Phys.* **2019**, *150*, 1–16. DOI: 10.1063/1.5096869.

(235) Chung, Y.; Green, W. H. New Modified Arrhenius Equation to Describe the Temperature Dependence of Liquid Phase Reaction Rates. *Chem. Eng. J.* **2025**, *516*, 163300. DOI: 10.1016/j.cej.2025.163300.

(236) Modified Arrhenius Equation. In *The IUPAC Compendium of Chemical Terminology*; International Union of Pure and Applied Chemistry (IUPAC): Research Triangle Park, NC, 2014. DOI: 10.1351/goldbook.M03963.

(237) Carrasco, E.; Jiménez-Redondo, M.; Tanarro, I.; Herrero, V. J. Neutral and Ion Chemistry in Low Pressure Dc Plasmas of H_2/N_2 Mixtures: Routes for the Efficient Production of NH_3 and NH_4^+. *Phys. Chem. Chem. Phys.* **2011**, *13*, 19561–19572. DOI: 10.1039/c1cp22284h.

(238) Chen, Z.; Koel, B. E.; Sundaresan, S. Plasma-Assisted Catalysis for Ammonia Synthesis in a Dielectric Barrier Discharge Reactor: Key Surface Reaction Steps and Potential Causes of Low Energy Yield. *J. Phys. D: Appl. Phys.* **2022**, *55*, 055202. DOI: 10.1088/1361-6463/ac2f12.

(239) Jiménez-Redondo, M.; Chatain, A.; Guaitella, O.; Cernogora, G.; Carrasco, N.;

Alves, L. L.; Marques, L. N_2 –H_2 Capacitively Coupled Radio-Frequency Discharges at Low Pressure: II. Modeling Results: The Relevance of Plasma-Surface Interaction. *Plasma Sources Sci. Technol.* **2020**, *29*, 085023. DOI: 10.1088/1361-6595/ab9b1b.

(240) Melin, G. A.; Madix, R. J. Energy Accommodation during Oxygen Atom Recombination on Metal Surfaces. *Trans. Faraday Soc.* **1971**, *67*, 198–211. DOI: 10.1039/tf9716700198.

(241) Greaves, J. C.; Linnett, J. W. The Recombination of Oxygen Atoms at Surfaces. *Trans. Faraday Soc.* **1958**, *54*, 1323–1330. DOI: 10.1039/tf9585401323.

(242) Chantry, P. J. A Simple Formula for Diffusion Calculations Involving Wall Reflection and Low Density. *J. Appl. Phys.* **1987**, *62*, 1141–1148. DOI: 10.1063/1.339662.

(243) Mehio, N.; Dai, S.; Jiang, D. E. Quantum Mechanical Basis for Kinetic Diameters of Small Gaseous Molecules. *J. Phys. Chem. A* **2014**, *118*, 1150–1154. DOI: 10.1021/jp412588f.

(244) Viegas, P.; Dias, T. C.; Fromentin, C.; Chukalovsky, A.; Mankelevich, Y.; Proshina, O.; Rakhimova, T.; Guerra, V.; Voloshin, D. Comparison between 1D Radial and 0D Global Models for Low-Pressure Oxygen DC Glow Discharges. *Plasma Sources Sci. Technol.* **2023**, *32*, 024002. DOI: 10.1088/1361-6595/acbb9c.

(245) Gerrits, N.; Bogaerts, A. Vibrationally Excited Molecule-Metal Surface Reactions in Heterogeneous and Plasma Catalysis : Going beyond the Fridman-Macheret α Model. *EES Catal.* Submitted.

(246) Polanyi, J. C. Concepts in Reaction Dynamics. *Acc. Chem. Res.* **1972**, *5*, 161–168.

(247) Yin, R.; Guo, H. Multidimensional Dynamics of CO_2 Dissociative Chemisorption on Cu(110). *J. Phys. Chem. C* **2024**, *128*, 9483–9491. DOI: 10.1021/acs.jpcc.4c00850.

(248) Booth, J.-P.; Chatterjee, A.; Guaitella, O.; Sousa, J. S.; Lopaev, D.; Zyryanov, S.; Rakhimova, T.; Voloshin, D.; Mankelevich, Y.; de Oliveira, N.; Nahon, L. Determination of Absolute O(3 P) and O 2 (a 1 Δ g) Densities and Kinetics in Fully Modulated O 2 Dc Glow Discharges from the O 2 (X 3 Σ g −) Afterglow Recovery Dynamics. *Plasma Sources Sci. Technol.* **2020**, *29*, 115009. DOI: 10.1088/1361-6595/abb5e7.

(249) Wu, C.; Schmidt, D. J.; Wolverton, C.; Schneider, W. F. Accurate Coverage-Dependence Incorporated into First-Principles Kinetic Models: Catalytic NO Oxidation on Pt (111). *J. Catal.* **2012**, *286*, 88–94. DOI: 10.1016/j.jcat.2011.10.020.

(250) Hoffmann, M. J.; Medford, A. J.; Bligaard, T. Framework for Scalable Adsorbate–Adsorbate Interaction Models. *J. Phys. Chem. C* **2016**, *120*, 13087–13094. DOI: 10.1021/acs.jpcc.6b03375.

(251) Grabow, L. C.; Hvolbæk, B.; Nørskov, J. K. Understanding Trends in Catalytic Activity: The Effect of Adsorbate–Adsorbate Interactions for CO Oxidation Over Transition Metals. *Top. Catal.* **2010**, *53*, 298–310. DOI: 10.1007/s11244-010-9455-2.

(252) Montemore, M. M.; van Spronsen, M. A.; Madix, R. J.; Friend, C. M. O2 Activation by Metal Surfaces: Implications for Bonding and Reactivity on Heterogeneous Catalysts. *Chem. Rev.* **2018**, *118*, 2816–2862. DOI: 10.1021/acs.chemrev.7b00217.

(253) Rond, C.; Bultel, A.; Boubert, P.; Chéron, B. G. Spectroscopic Measurements of Nonequilibrium CO_2 Plasma in RF Torch. *Chem. Phys.* **2008**, *354*, 16–26. DOI: 10.1016/j.chemphys.2008.09.006.

(254) Bogaerts, A.; Neyts, E. C. Plasma Technology: An Emerging Technology for Energy

Storage. *ACS Energy Lett.* **2018**, *3*, 1013–1027. DOI: 10.1021/acsenergylett.8b00184.

(255) Vojvodic, A.; Nørskov, J. K. New Design Paradigm for Heterogeneous Catalysts. *Natl. Sci. Rev.* **2015**, *2*, 140–143. DOI: 10.1093/nsr/nwv023.

(256) Evans, M. G.; Polanyi, M. Inertia and Driving Force of Chemical Reactions. *Trans. Faraday Soc.* **1938**, *34*, 11–24. DOI: 10.1039/tf9383400011.

(257) Zeng, Y.; Zhu, X.; Mei, D.; Ashford, B.; Tu, X. Plasma-Catalytic Dry Reforming of Methane over γ-Al_2O_3 Supported Metal Catalysts. *Catal. Today* **2015**, *256*, 80–87. DOI: 10.1016/j.cattod.2015.02.007.

(258) Zeng, Y. X.; Wang, L.; Wu, C. F.; Wang, J. Q.; Shen, B. X.; Tu, X. Low Temperature Reforming of Biogas over K-, Mg- and Ce-Promoted Ni/Al_2O_3 Catalysts for the Production of Hydrogen Rich Syngas: Understanding the Plasma-Catalytic Synergy. *Appl. Catal. B Environ.* **2018**, *224*, 469–478. DOI: 10.1016/j.apcatb.2017.10.017.

(259) Lamberts-Van Assche, H.; Thomassen, G.; Compernolle, T. The Early-Stage Design of Plasma for the Conversion of CO_2 to Chemicals: A Prospective Techno-Economic Assessment. *J. CO2 Util.* **2022**, *64*, 102156. DOI: 10.1016/j.jcou.2022.102156.

(260) Yang, Z.; Wang, J.; Yu, X. Density Functional Theory Studies on the Adsorption, Diffusion and Dissociation of O_2 on Pt(111). *Phys. Lett. A* **2010**, *374*, 4713–4717. DOI: 10.1016/j.physleta.2010.09.049.

(261) Sutton, J. E.; Vlachos, D. G. Effect of Errors in Linear Scaling Relations and Brønsted–Evans–Polanyi Relations on Activity and Selectivity Maps. *J. Catal.* **2016**, *338*, 273–283. DOI: 10.1016/j.jcat.2016.03.013.

(262) Yoo, J. S.; Abild-Pedersen, F.; Nørskov, J. K.; Studt, F. Theoretical Analysis of Transition-Metal Catalysts for Formic Acid Decomposition. *ACS Catal.* **2014**, *4*, 1226–1233. DOI: 10.1021/cs400664z.

(263) Wellendorff, J.; Silbaugh, T. L.; Garcia-Pintos, D.; Nørskov, J. K.; Bligaard, T.; Studt, F.; Campbell, C. T. A Benchmark Database for Adsorption Bond Energies to Transition Metal Surfaces and Comparison to Selected DFT Functionals. *Surf. Sci.* **2015**, *640*, 36–44. DOI: 10.1016/j.susc.2015.03.023.

(264) Stamatakis, M.; Chen, Y.; Vlachos, D. G. First-Principles-Based Kinetic Monte Carlo Simulation of the Structure Sensitivity of the Water–Gas Shift Reaction on Platinum Surfaces. *J. Phys. Chem. C* **2011**, *115*, 24750–24762. DOI: 10.1021/jp2071869.

(265) Greeley, J.; Mavrikakis, M. A First-Principles Study of Methanol Decomposition on Pt(111). *J. Am. Chem. Soc.* **2002**, *124*, 7193–7201. DOI: 10.1021/ja017818k.

(266) Calle-Vallejo, F.; Loffreda, D.; Koper, M. T. M.; Sautet, P. Introducing Structural Sensitivity into Adsorption–Energy Scaling Relations by Means of Coordination Numbers. *Nat. Chem.* **2015**, *7*, 403–410. DOI: 10.1038/nchem.2226.

(267) Yu, T. H.; Hofmann, T.; Sha, Y.; Merinov, B. V.; Myers, D. J.; Heske, C.; Goddard, W. A. Finding Correlations of the Oxygen Reduction Reaction Activity of Transition Metal Catalysts with Parameters Obtained from Quantum Mechanics. *J. Phys. Chem. C* **2013**, *117*, 26598–26607. DOI: 10.1021/jp4071554.

(268) Todorovic, R.; Meyer, R. J. A Comparative Density Functional Theory Study of the Direct Synthesis of H_2O_2 on Pd, Pt and Au Surfaces. *Catal. Today* **2011**, *160*, 242–248. DOI: 10.1016/j.cattod.2010.07.011.

(269) Juurlink, L. B. F.; Killelea, D. R.; Utz, A. L. State-Resolved Probes of Methane

Dissociation Dynamics. *Prog. Surf. Sci.* **2009**, *84*, 69–134. DOI: 10.1016/j.progsurf.2009.01.001.

(270) Gerrits, N.; Bogaerts, A. Vibrationally Excited Molecule-Metal Surface Reactions in Heterogeneous and Plasma Catalysis: Going beyond the Fridman-Macheret α Model. *EES Catal.* **2025**, *3*, 733–742. DOI: 10.1039/d5ey00062a.

(271) Li, S.; Luo, S.; Liu, R.; Cui, Z.; Yi, Y.; Neyts, E. C.; Bogaerts, A.; Gerrits, N. Plasma-Assisted CH_4 Activation on Cu/CeO_2 Catalysts: Insights into the Effect of Catalyst Surface and Vibrational Excitation. *Phys. Chem. Chem. Phys.* **2026**, *28*, 4753–4763. DOI: 10.1039/D5CP03569D.

(272) Yoo, J. S.; Khan, T. S.; Abild-Pedersen, F.; Nørskov, J. K.; Studt, F. On the Role of the Surface Oxygen Species during A–H (A = C, N, O) Bond Activation: A Density Functional Theory Study. *Chem. Commun.* **2015**, *51*, 2621–2624. DOI: 10.1039/C4CC08658A.

(273) Hayashi, M. Electron Collision Cross-Sections for Molecules Determined from Beam and Swarm Data. In *Swarm Studies and Inelastic Electron-Molecule Collisions*; Springer New York: New York, NY, 1987; pp 167–187. DOI: 10.1007/978-1-4612-4662-6_33.

(274) Hayashi, M. Electron Collision Cross-Sections Determined from Beam and Swarm Data by Boltzmann Analysis; 1990; Vol. 220, pp 333–340. DOI: 10.1007/978-1-4615-3780-9_21.

(275) *Obtained from LXCAT (Morgan database)*. www.lxcat.net.

(276) *Obtained from LXCAT (Puech database)*. www.lxcat.net.

(277) Fresnet, F.; Pasquiers, S.; Postel, C.; Puech, V. Dynamics and Breakdown Delay Times in Neon-Ethene and Neon-Propene Photo-Triggered Discharges. *J. Phys. D:*

Appl. Phys. **2002**, *35*, 882–890. DOI: 10.1088/0022-3727/35/9/308.

(278) Mahmud, K.; Marshall, P.; Fontijn, A. A High-Temperature Photochemistry Kinetics Study of the Reaction of Oxygen(3P) Atoms with Ethylene from 290 to 1510 K. *J. Phys. Chem.* **1987**, *91*, 1568–1573. DOI: 10.1021/j100290a056.

(279) Li, X.; Jasper, A. W.; Zádor, J.; Miller, J. A.; Klippenstein, S. J. Theoretical Kinetics of O + C2H4. *Proc. Combust. Inst.* **2017**, *36*, 219–227. DOI: 10.1016/j.proci.2016.06.053.

(280) Pruss, F. J.; Slagle, I. R.; Gutman, D. Determination of Branching Ratios for the Reaction of Oxygen Atoms with Ethylene. *J. Phys. Chem.* **1974**, *78*, 663–665. DOI: 10.1021/j100600a003.

(281) Vasu, S. S.; Hong, Z.; Davidson, D. F.; Hanson, R. K.; Golden, D. M. Shock Tube/Laser Absorption Measurements of the Reaction Rates of OH with Ethylene and Propene. *J. Phys. Chem. A* **2010**, *114*, 11529–11537. DOI: 10.1021/jp106049s.

(282) Curran, H. J. Rate Constant Estimation for C1 to C4 Alkyl and Alkoxyl Radical Decomposition. *Int. J. Chem. Kinet.* **2006**, *38*, 250–275. DOI: 10.1002/kin.20153.

(283) Dean, A. M. Predictions of Pressure and Temperature Effects upon Radical Addition and Recombination Reactions. *J. Phys. Chem.* **1985**, *89*, 4600–4608. DOI: 10.1021/j100267a038.

(284) Ibuki, T.; Takezaki, Y. The Reaction of Hydrogen Atoms with Acetylene. *Bull. Chem. Soc. Jpn.* **1975**, *48*, 769–773.

(285) Laufer, A. H.; Fahr, A. Reactions and Kinetics of Unsaturated C2 Hydrocarbon Radicals. *Chem. Rev.* **2004**, *104*, 2813–2832. DOI: 10.1021/cr030039x.

(286) Sillesen, A.; Ratajczak, E.; Pagsberg, P. Kinetics of the Reactions H + C2H4 → C2H5,

H + C2H5 → 2CH3 and CH3 + C2H5 → Products Studied by Pulse Radiolysis Combined with Infrared Diode Laser Spectroscopy. *Chem. Phys. Lett.* **1993**, *201*, 171–177. DOI: 10.1016/0009-2614(93)85052-P.

(287) Blanquart, G.; Pepiot-Desjardins, P.; Pitsch, H. Chemical Mechanism for High Temperature Combustion of Engine Relevant Fuels with Emphasis on Soot Precursors. *Combust. Flame* **2009**, *156*, 588–607. DOI: 10.1016/j.combustflame.2008.12.007.

(288) Fahr, A.; Laufer, A.; Klein, R.; Braun, W. Reaction Rate Determinations of Vinyl Radical Reactions with Vinyl, Methyl, and Hydrogen Atoms. *J. Phys. Chem.* **1991**, *95*, 3218–3224. DOI: 10.1021/j100161a047.

(289) Warnatz, J. Rate Coefficients in the C/H/O System. In *Combustion Chemistry*; Springer New York: New York, NY, 1984; pp 197–360. DOI: 10.1007/978-1-4684-0186-8_5.

(290) Knyazev, V. D. Kinetics and Mechanism of the Reaction of Recombination of Vinyl and Hydroxyl Radicals. *Chem. Phys. Lett.* **2017**, *685*, 165–170. DOI: 10.1016/j.cplett.2017.07.040.

(291) Adachi, H.; Basco, N.; James, D. G. L. The Acetyl Radicals CH3CO· and CD3CO· Studied by Flash Photolysis and Kinetic Spectroscopy. *Int. J. Chem. Kinet.* **1981**, *13*, 1251–1276. DOI: 10.1002/kin.550131206.

(292) Su, J. Z.; Teitelbaum, H. The Rate of Methyl Radical Decomposition at High Temperatures and Pressures. *Int. J. Chem. Kinet.* **1994**, *26*, 159–169. DOI: 10.1002/kin.550260116.

(293) Braun, W.; McNesby, J. R.; Bass, A. M. Flash Photolysis of Methane in the Vacuum Ultraviolet. II. Absolute Rate Constants for Reactions of CH with Methane,

Hydrogen, and Nitrogen. *J. Chem. Phys.* **1967**, *46*, 2071–2080. DOI: 10.1063/1.1841003.

(294) Fulle, D.; Hippler, H. The Temperature and Pressure Dependence of the Reaction CH+H2⇔CH3⇔CH2+H. *J. Chem. Phys.* **1997**, *106*, 8691–8698. DOI: 10.1063/1.473930.

(295) Gregory P. Smith; Golden, D. M.; Frenklach, M.; Moriarty, N. W.; Eiteneer, B.; Goldenberg, M.; Bowman, C. T.; Hanson, R. K.; Song, S.; Gardiner, W. C.; Lissianski, J. V. V.; Qin, Z. *GRI-MECH 3.0*. http://www.me.berkeley.edu/gri_mech/.

(296) Harding, L. B.; Klippenstein, S. J.; Georgievskii, Y. On the Combination Reactions of Hydrogen Atoms with Resonance-Stabilized Hydrocarbon Radicals. *J. Phys. Chem. A* **2007**, *111*, 3789–3801. DOI: 10.1021/jp0682309.

(297) Canosa, A.; Sims, I. R.; Travers, D.; Smith, I. W. M.; Rowe, B. R. Reactions of the Methylidine Radical with CH_4, C_2H_2, C_2H_4, C_2H_6, and but-1-Ene Studied between 23 and 295 K with a CRESU Apparatus. *Astron. Astrophys* **1997**, *323*, 644–651.

(298) Lin, M. C.; Back, M. H. THE THERMAL DECOMPOSITION OF ETHANE: PART III. SECONDARY REACTIONS. *Can. J. Chem.* **1966**, *44*, 2369–2380. DOI: 10.1139/v66-358.

(299) Cohen, N.; Westberg, K. R. The Use of Transition-State Theory to Extrapolate Rate Coefficients for Reactions of O Atoms with Alkanes. *Int. J. Chem. Kinet.* **1986**, *18*, 99–140. DOI: 10.1002/kin.550180109.

(300) Droege, A. T.; Tully, F. P. Hydrogen Atom Abstraction from Alkanes by Hydroxyl. 5. n-Butane. *J. Phys. Chem.* **1986**, *90*, 5937–5941. DOI: 10.1021/j100280a096.

(301) Pitz, W. J.; Westbrook, C. K. Chemical Kinetics of the High Pressure Oxidation of N-Butane and Its Relation to Engine Knock. *Combust. Flame* **1986**, *63*, 113–133.

DOI: 10.1016/0010-2180(86)90115-X.

(302) Manion, J. A.; Sheen, D. A.; Awan, I. A. Evaluated Kinetics of the Reactions of H and CH3 with N-Alkanes: Experiments with n-Butane and a Combustion Model Reaction Network Analysis. *J. Phys. Chem. A* **2015**, *119*, 7637–7658. DOI: 10.1021/acs.jpca.5b01004.

(303) Kerr, J. A.; Trotman-Dickenson, A. F. 323. The Reactions of Alkyl Radicals. Part III. n-Butyl Radicals from the Photolysis of n-Valeraldehyde. *J. Chem. Soc.* **1960**, 1602–1608. DOI: 10.1039/jr9600001602.

(304) Baker, R. R.; Baldwin, R. R.; Fuller, A. R.; Walker, R. W. Addition of N-C4H10 and C4H8 to Slowly Reacting Mixtures of Hydrogen and Oxygen at 480°C. Part 1.—Formation of Hydrocarbon Products. *J. Chem. Soc. Faraday Trans. 1 Phys. Chem. Condens. Phases* **1975**, *71*, 736–755. DOI: 10.1039/f19757100736.

(305) MacKenzie, A. L.; Pacey, P. D.; Wimalasena, J. H. Radical Addition, Decomposition, and Isomerization Reactions in the Pyrolysis of Ethane and Ethylene. *Can. J. Chem.* **1984**, *62*, 1325–1328. DOI: 10.1139/v84-222.

(306) Thynne, J. C. J. Reactions of Alkyl Radicals. Part 1.—Methyl Radical Photosensitized Decomposition of Ethyl Formate. *Trans. Faraday Soc.* **1962**, *58*, 676–684. DOI: 10.1039/TF9625800676.

(307) Silcocks, C. G.; A, P. R. S. L. The Kinetics of the Thermal Decomposition and Polymerization of Ethane and Ethylene. *Proc. R. Soc. London. Ser. A. Math. Phys. Sci.* **1956**, *233*, 465–479. DOI: 10.1098/rspa.1956.0004.

(308) Polino, D.; Klippenstein, S. J.; Harding, L. B.; Georgievskii, Y. Predictive Theory for the Addition and Insertion Kinetics of 1CH2 Reacting with Unsaturated Hydrocarbons. *J. Phys. Chem. A* **2013**, *117*, 12677–12692. DOI:

10.1021/jp406246y.

(309) Manion, J. A.; Awan, I. A. Evaluated Kinetics of Terminal and Non-Terminal Addition of Hydrogen Atoms to 1-Alkenes: A Shock Tube Study of H + 1-Butene. *J. Phys. Chem. A* **2015**, *119*, 429–441. DOI: 10.1021/jp5110856.

(310) Tsuboi, T.; Katoh, M.; Kikuchi, S.; Hashimoto, K. Thermal Decomposition of Methanol behind Shock Waves. *Jpn. J. Appl. Phys.* **1981**, *20*, 985–992.

(311) Xu, Z. F.; Raghunath, P.; Lin, M. C. Ab Initio Chemical Kinetics for the CH3 + O(3P) Reaction and Related Isomerization–Decomposition of CH3O and CH2OH Radicals. *J. Phys. Chem. A* **2015**, *119*, 7404–7417. DOI: 10.1021/acs.jpca.5b00553.

(312) Sivaramakrishnan, R.; Michael, J. V.; Klippenstein, S. J. Direct Observation of Roaming Radicals in the Thermal Decomposition of Acetaldehyde. *J. Phys. Chem. A* **2010**, *114*, 755–764. DOI: 10.1021/jp906918z.

(313) Scherzer, K.; Löser, U.; Stiller, W. BSBL-Rechnungen Zu Wasserstoffabspaltungsreaktionen (Durch Alkenylradikale; Vinylradikale. *Zeitschrift für Chemie* **1987**, *27*, 300–301. DOI: 10.1002/zfch.19870270815.

(314) Zabarnick, S.; Fleming, J. W.; Lin, M. C. Temperature Dependence of CH Radical Reactions with H2O and CH2O. *Symp. Combust.* **1988**, *21*, 713–719. DOI: 10.1016/S0082-0784(88)80303-5.

(315) Hoare, D. E.; Whytock, D. A. Photooxidation of Acetone Vapor. *Can. J. Chem.* **1967**, *45*, 865–872. DOI: 10.1139/v67-144.

(316) Jasper, A. W.; Klippenstein, S. J.; Harding, L. B.; Ruscic, B. Kinetics of the Reaction of Methyl Radical with Hydroxyl Radical and Methanol Decomposition †. *J. Phys. Chem. A* **2007**, *111*, 3932–3950. DOI: 10.1021/jp067585p.

(317) Assaf, E.; Schoemaecker, C.; Vereecken, L.; Fittschen, C. The Reaction of Fluorine Atoms with Methanol: Yield of CH3O/CH2OH and Rate Constant of the Reactions CH3O + CH3O and CH3O + HO2. *Phys. Chem. Chem. Phys.* **2018**, *20*, 10660–10670. DOI: 10.1039/c7cp05770a.

(318) Wang, B.; Hou, H.; Gu, Y. Ab Initio/Density Functional Theory and Multichannel RRKM Calculations for the CH3O + CO Reaction. *J. Phys. Chem. A* **1999**, *103*, 8021–8029. DOI: 10.1021/jp991203g.

(319) Lambert, R. M.; Christie, M. I.; Linnett, J. W. A Novel Reaction of Hydrogen Atoms. *Chem. Commun.* **1967**, No. 8, 388–389. DOI: 10.1039/c19670000388.

(320) Tsuboi, T.; Hashimoto, K. Shock Tube Study on Homogeneous Thermal Oxidation of Methanol. *Combust. Flame* **1981**, *42*, 61–76. DOI: 10.1016/0010-2180(81)90142-5.

(321) Trenwith, A. B. 847. The Thermal Decomposition of Acetaldehyde: The Formation of Hydrogen. *J. Chem. Soc.* **1963**, 4426–4430. DOI: 10.1039/jr9630004426.

(322) Teitel'boim, M. A.; Romanovich, L. B.; Vedeneev, B. I. Calculation, Based on RRKM Theory, of Certain Channels of Interaction of Methyl Radical with Oxygen. *Kinet. Catal.* **1973**, *19*, 1131–1136.

(323) Dean, A. M.; Westmoreland, P. R. Bimolecular QRRK Analysis of Methyl Radical Reactions. *Int. J. Chem. Kinet.* **1987**, *19*, 207–228. DOI: 10.1002/kin.550190305.

(324) Elrod, M. J.; Ranschaert, D. L.; Schneider, N. J. Direct Kinetics Study of the Temperature Dependence of the CH2O Branching Channel for the CH3O2 + HO2 Reaction. *Int. J. Chem. Kinet.* **2001**, *33*, 363–376. DOI: 10.1002/kin.1030.

(325) Zhao, Z.; Song, J.; Su, B.; Wang, X.; Li, Z. Mechanistic Study of the Reactions of Methyl Peroxy Radical with Methanol or Hydroxyl Methyl Radical. *J. Phys. Chem.*

A **2018**, *122*, 5078–5088. DOI: 10.1021/acs.jpca.7b09988.

(326) Villano, S. M.; Huynh, L. K.; Carstensen, H.-H.; Dean, A. M. High-Pressure Rate Rules for Alkyl + O2 Reactions. 1. The Dissociation, Concerted Elimination, and Isomerization Channels of the Alkyl Peroxy Radical. *J. Phys. Chem. A* **2011**, *115*, 13425–13442. DOI: 10.1021/jp2079204.

(327) Lee, J.; Bozzelli, J. W. Thermochemical and Kinetic Analysis of the Allyl Radical with O2 Reaction System. *Proc. Combust. Inst.* **2005**, *30*, 1015–1022. DOI: 10.1016/j.proci.2004.08.092.

(328) Srinivasan, N. K.; Su, M.-C.; Michael, J. V. High-Temperature Rate Constants for CH_3OH + Kr → Products, OH + CH_3OH → Products, OH + $(CH_3)_2CO$ → CH_2COCH_3 + H_2O, and OH + CH_3 → CH_2 + H_2O. *J. Phys. Chem. A* **2007**, *111*, 3951–3958. DOI: 10.1021/jp0673516.

(329) Elwardany, A.; Nasir, E. F.; Es-sebbar, E.; Farooq, A. Unimolecular Decomposition of Formic and Acetic Acids: A Shock Tube/Laser Absorption Study. *Proc. Combust. Inst.* **2015**, *35*, 429–436. DOI: 10.1016/j.proci.2014.06.141.

(330) Mousavipour, S. H.; Homayoon, Z. Multichannel RRKM-TST and CVT Rate Constant Calculations for Reactions of CH2OH or CH3O with HO2. *J. Phys. Chem. A* **2011**, *115*, 3291–3300. DOI: 10.1021/jp112081r.

(331) Skouteris, D.; Balucani, N.; Ceccarelli, C.; Vazart, F.; Puzzarini, C.; Barone, V.; Codella, C.; Lefloch, B. The Genealogical Tree of Ethanol: Gas-Phase Formation of Glycolaldehyde, Acetic Acid, and Formic Acid. *Astrophys. J.* **2018**, *854*, 135. DOI: 10.3847/1538-4357/aaa41e.

(332) Vichietti, R. M.; Spada, R. F. K.; Silva, A. B. F. da; Machado, F. B. C.; Haiduke, R. L. A. Accurate Calculations of Rate Constants for the Forward and Reverse H2O +

CO ↔ HCOOH Reactions. *ChemistrySelect* **2017**, *2*, 7267–7272. DOI: 10.1002/slct.201701137.

(333) Yetter, R. A.; Rabitz, H.; Dryer, F. L.; Maki, R. G.; Klemm, R. B. Evaluation of the Rate Constant for the Reaction OH+H2CO: Application of Modeling and Sensitivity Analysis Techniques for Determination of the Product Branching Ratio. *J. Chem. Phys.* **1989**, *91*, 4088–4097. DOI: 10.1063/1.456838.

(334) Chang, J. G.; Chen, H. T.; Xu, S.; Lin, M. C. Computational Study on the Kinetics and Mechanisms for the Unimolecular Decomposition of Formic and Oxalic Acids. *J. Phys. Chem. A* **2007**, *111*, 6789–6797. DOI: 10.1021/jp069036p.

(335) Galano, A.; Alvarez-Idaboy, J. R.; Ruiz-Santoyo, M. E.; Vivier-Bunge, A. Rate Coefficient and Mechanism of the Gas Phase OH Hydrogen Abstraction Reaction from Formic Acid: A Quantum Mechanical Approach. *J. Phys. Chem. A* **2002**, *106*, 9520–9528. DOI: 10.1021/jp020297i.

(336) Glarborg, P.; Marshall, P. The Rate Constant for the CO + H2O2 Reaction. *Chem. Phys. Lett.* **2009**, *475*, 40–43. DOI: 10.1016/j.cplett.2009.05.028.

(337) Senosiain, J. P.; Klippenstein, S. J.; Miller, J. A. The Reaction of Acetylene with Hydroxyl Radicals. *J. Phys. Chem. A* **2005**, *109*, 6045–6055. DOI: 10.1021/jp050737g.

(338) Petty, J. T.; Harrison, J. A.; Moore, C. B. Reactions of Trans-Hydroxycarbonyl Radical Studied by Infrared Spectroscopy. *J. Phys. Chem.* **1993**, *97*, 11194–11198. DOI: 10.1021/j100145a013.

(339) Golden, D. M.; Smith, G. P.; McEwen, A. B.; Yu, C.-L.; Eiteneer, B.; Frenklach, M.; Vaghjiani, G. L.; Ravishankara, A. R.; Tully, F. P. OH(OD) + CO: Measurements and an Optimized RRKM Fit. *J. Phys. Chem. A* **1998**, *102*, 8598–8606. DOI:

10.1021/jp982110m.

(340) Yu, H.-G.; Muckerman, J. T.; Francisco, J. S. Quantum Force Molecular Dynamics Study of the Reaction of O Atoms with HOCO. *J. Chem. Phys.* **2007**, *127*, 094302. DOI: 10.1063/1.2770463.

(341) Yu, H.-G.; Muckerman, J. T.; Francisco, J. S. Direct Ab Initio Dynamics Study of the OH + HOCO Reaction. *J. Phys. Chem. A* **2005**, *109*, 5230–5236. DOI: 10.1021/jp051458w.

(342) Larson, C. W.; Stewart, P. H.; Golden, D. M. Pressure and Temperature Dependence of Reactions Proceeding via a Bound Complex. An Approach for Combustion and Atmospheric Chemistry Modelers. Application to HO + CO → [HOCO] → H + CO2. *Int. J. Chem. Kinet.* **1988**, *20*, 27–40. DOI: 10.1002/kin.550200105.

(343) Xu, S.; Zhu, R. S.; Lin, M. C. Ab Initio Study of the OH + CH2O Reaction: The Effect of the OH··OCH2 Complex on the H-Abstraction Kinetics. *Int. J. Chem. Kinet.* **2006**, *38*, 322–326. DOI: 10.1002/kin.20166.

(344) Veyret, B.; Roussel, P.; Lesclaux, R. Mechanism of the Chain Process Forming H2 in the Photooxidation of Formaldehyde. *Int. J. Chem. Kinet.* **1984**, *16*, 1599–1608. DOI: 10.1002/kin.550161213.

(345) Veyret, B.; Rayez, J. C.; Lesclaux, R. Mechanism of the Photooxidation of Formaldehyde Studied by Flash Photolysis of Formaldehyde-Oxygen-Nitric Oxide Mixtures. *J. Phys. Chem.* **1982**, *86*, 3424–3430. DOI: 10.1021/j100214a032.

(346) Canosa-mas, C. E.; Frey, H. M.; Walsh, R. Studies of Methylene Chemistry by Pulsed Laser-Induced Decomposition of Ketene. Part 1.—Ketene in the Presence of Noble Gases. *J. Chem. Soc., Faraday Trans. 2* **1984**, *80*, 561–578. DOI:

10.1039/F29848000561.

(347) Faravelli, T.; Goldaniga, A.; Zappella, L.; Ranzi, E.; Dagaut, P.; Cathonnet, M. An Experimental and Kinetic Modeling Study of Propyne and Allene Oxidation. *Proc. Combust. Inst.* **2000**, *28*, 2601–2608. DOI: 10.1016/S0082-0784(00)80678-5.

(348) Vandooren, J.; Van Tiggelen, P. J. Reaction Mechanisms of Combustion in Low Pressure Acetylene-Oxygen Flames. *Symp. Combust.* **1977**, *16*, 1133–1144. DOI: 10.1016/S0082-0784(77)80402-5.

(349) Semenikhin, A. S.; Shubina, E. G.; Savchenkova, A. S.; Chechet, I. V.; Matveev, S. G.; Konnov, A. A.; Mebel, A. M. Mechanism and Rate Constants of the CH3 + CH2CO Reaction: A Theoretical Study. *Int. J. Chem. Kinet.* **2018**, *50*, 273–284. DOI: 10.1002/kin.21156.

(350) Banyard, S. A.; Canosa-Mas, C. E.; Ellis, M. D.; Frey, H. M.; Walsh, R. Keten Photochemistry. Some Observations on the Reactions and Reactivity of Triplet Methylene. *J. Chem. Soc. Chem. Commun.* **1980**, No. 23, 1156–1157. DOI: 10.1039/c39800001156.

(351) Xiong, S. Z.; Yao, Q.; Li, Z. R.; Li, X. Y. Reaction of Ketenyl Radical with Hydroxyl Radical over C2H2O2 Potential Energy Surface: A Theoretical Study. *Combust. Flame* **2014**, *161*, 885–897. DOI: 10.1016/j.combustflame.2013.10.013.

(352) Hassinen, E.; Kalliorinne, K.; Koskikallio, J. Kinetics of Reactions between Methyl and Acetyl Radicals in Gas Phase Produced by Flash Photolysis of Acetic Anhydride. *Int. J. Chem. Kinet.* **1990**, *22*, 741–745. DOI: 10.1002/kin.550220709.

(353) Yasunaga, K.; Kubo, S.; Hoshikawa, H.; Kamesawa, T.; Hidaka, Y. Shock-Tube and Modeling Study of Acetaldehyde Pyrolysis and Oxidation. *Int. J. Chem. Kinet.* **2007**, *40*, 73–102. DOI: 10.1002/kin.20294.

(354) Wang, H.; Bozzelli, J. W. Thermochemistry and Kinetic Analysis of the Unimolecular Oxiranyl Radical Dissociation Reaction: A Theoretical Study. *ChemPhysChem* **2016**, *17*, 1983–1992. DOI: 10.1002/cphc.201600152.

(355) Xu, Z. F.; Xu, K.; Lin, M. C. Thermal Decomposition of Ethanol. 4. Ab Initio Chemical Kinetics for Reactions of H Atoms with CH3CH2O and CH3CHOH Radicals. *J. Phys. Chem. A* **2011**, *115*, 3509–3522. DOI: 10.1021/jp110580r.

(356) Fagerström, K.; Lund, A.; Mahmoud, G.; Jodkowski, J. T.; Ratajczak, E. Kinetics of the Gas-Phase Reaction between Ethyl and Hydroxyl Radicals. *Chem. Phys. Lett.* **1993**, *208*, 321–327. DOI: 10.1016/0009-2614(93)89083-T.

(357) Heicklen, J. The Decomposition of Alkyl Nitrites and the Reactions of Alkoxyl Radicals. In *Advances in Photochemistry*; 1988; Vol. 14, pp 177–272. DOI: 10.1002/9780470133446.ch4.

(358) Aders, W.-K.; Wagner, H. G. Untersuchungen Zur Reaktion von Wasserstoffatomen Mit Äthanol Und Tert. Butanol. *Berichte der Bunsengesellschaft für Phys. Chemie* **1973**, *77*, 712–718. DOI: 10.1002/bbpc.19730770911.

(359) Olm, C.; Varga, T.; Valkó, É.; Hartl, S.; Hasse, C.; Turányi, T. Development of an Ethanol Combustion Mechanism Based on a Hierarchical Optimization Approach. *Int. J. Chem. Kinet.* **2016**, *48*, 423–441. DOI: 10.1002/kin.20998.

(360) Li, J.; Kazakov, A.; Dryer, F. L. Experimental and Numerical Studies of Ethanol Decomposition Reactions. *J. Phys. Chem. A* **2004**, *108*, 7671–7680. DOI: 10.1021/jp0480302.

(361) Kato, A.; Cvetanović, R. J. Reaction of Oxygen Atoms with Ethanol. *Can. J. Chem.* **1967**, *45*, 1845–1861. DOI: 10.1139/v67-297.

(362) Noell, A. C.; Alconcel, L. S.; Robichaud, D. J.; Okumura, M.; Sander, S. P. Near-Infrared Kinetic Spectroscopy of the HO2 and C2H5O2 Self-Reactions and Cross Reactions. *J. Phys. Chem. A* **2010**, *114*, 6983–6995. DOI: 10.1021/jp912129j.

(363) Bozzelli, J. W.; Dean, A. M. Chemical Activation Analysis of the Reaction of Ethyl Radical with Oxygen. *J. Phys. Chem.* **1990**, *94*, 3313–3317. DOI: 10.1021/j100371a021.

(364) Denisov, E. T. Mechanisms of the Reactions of Radicals with Ozone. *Russ. J. Phys. Chem. B* **2008**, *2*, 58–66. DOI: 10.1134/S1990793108010090.

(365) Zhang, P.; Wang, W.; Zhang, T.; Chen, L.; Du, Y.; Li, C.; Lü, J. Theoretical Study on the Mechanism and Kinetics for the Self-Reaction of C2H5O2 Radicals. *J. Phys. Chem. A* **2012**, *116*, 4610–4620. DOI: 10.1021/jp301308u.

(366) Sheng, C. Y.; Bozzelli, J. W.; Dean, A. M.; Chang, A. Y. Detailed Kinetics and Thermochemistry of C2H5 + O2: Reaction Kinetics of the Chemically-Activated and Stabilized CH3CH2OO. Adduct. *J. Phys. Chem. A* **2002**, *106*, 7276–7293. DOI: 10.1021/jp014540+.

(367) Harding, L. B.; Klippenstein, S. J.; Georgievskii, Y. Reactions of Oxygen Atoms with Hydrocarbon Radicals: A Priori Kinetic Predictions for the CH3+O, C2H5+O, and C2H3+O Reactions. *Proc. Combust. Inst.* **2005**, *30*, 985–993. DOI: 10.1016/j.proci.2004.08.184.

(368) Atkinson, R.; Finlayson, B. J.; Pitts, J. N. Photoionization Mass Spectrometer Studies of Gas Phase Ozone-Olefin Reactions. *J. Am. Chem. Soc.* **1973**, *95*, 7592–7599. DOI: 10.1021/ja00804a008.

(369) Atkinson, R.; Baulch, D. L.; Cox, R. A.; Crowley, J. N.; Hampson, R. F.; Hynes, R. G.; Jenkin, M. E.; Rossi, M. J.; Troe, J. Evaluated Kinetic and Photochemical Data for

Atmospheric Chemistry: Volume II – Gas Phase Reactions of Organic Species. *Atmos. Chem. Phys.* **2006**, *6*, 3625–4055. DOI: 10.5194/acp-6-3625-2006.

(370) Edelbüttel-Einhaus, J.; Hoyermann, K.; Rohde, G.; Seeba, J. The Detection of the Hydroxyethyl Radical by Rempi/Mass-Spectrometry and the Application to the Study of the Reactions CH3CHOH+O and CH3CHOH+H. *Symp. Combust.* **1992**, *24*, 661–668. DOI: 10.1016/S0082-0784(06)80081-0.

(371) Xu, Z. F.; Xu, K.; Lin, M. C. Ab Initio Kinetics for Decomposition/Isomerization Reactions of C2H5O Radicals. *ChemPhysChem* **2009**, *10*, 972–982. DOI: 10.1002/cphc.200800719.

(372) Zhang, Y.; Zhang, S.; Li, Q. S. Ab Initio Calculations and Mechanism of Two Proton Migration Reactions of Ethoxy Radical. *Chem. Phys.* **2005**, *308*, 109–116. DOI: 10.1016/j.chemphys.2004.08.004.

(373) da Silva, G.; Bozzelli, J. W. Role of the α-Hydroxyethylperoxy Radical in the Reactions of Acetaldehyde and Vinyl Alcohol with HO2. *Chem. Phys. Lett.* **2009**, *483*, 25–29. DOI: 10.1016/j.cplett.2009.10.045.

(374) Atkinson, R.; Baulch, D. L.; Cox, R. A.; Hampson, R. F.; Kerr, J. A.; Rossi, M. J.; Troe, J. Evaluated Kinetic and Photochemical Data for Atmospheric Chemistry, Organic Species: Supplement VII. *J. Phys. Chem. Ref. Data* **1999**, *28*, 191–393. DOI: 10.1063/1.556048.

(375) Galano, A.; Alvarez-Idaboy, J. R.; Bravo-Pérez, G.; Ruiz-Santoyo, M. E. Gas Phase Reactions of C1 –C4 Alcohols with the OH Radical: A Quantum Mechanical Approach. *Phys. Chem. Chem. Phys.* **2002**, *4*, 4648–4662. DOI: 10.1039/B205630E.

(376) Rosado-Reyes, C.; Tsang, W. Bond Cleavage During Isobutanol Thermal

Decomposition and the Breaking of C–C Bonds in Alcohols at High Temperatures. *J. Phys. Chem. A* **2013**, *117*, 10170–10177. DOI: 10.1021/jp404877t.

(377) Pokidova, T. S.; Denisov, E. T.; Shestakov, A. F. Kinetic Parameters and Geometry of the Transition State in the Unimolecular Degradation of Alcohols. *Pet. Chem.* **2009**, *49*, 343–353. DOI: 10.1134/S0965544109050016.

(378) Goldsmith, C. F.; Green, W. H.; Klippenstein, S. J. Role of O2 + QOOH in Low-Temperature Ignition of Propane. 1. Temperature and Pressure Dependent Rate Coefficients. *J. Phys. Chem. A* **2012**, *116*, 3325–3346. DOI: 10.1021/jp210722w.

(379) Villano, S. M.; Carstensen, H.-H.; Dean, A. M. Rate Rules, Branching Ratios, and Pressure Dependence of the HO2 + Olefin Addition Channels. *J. Phys. Chem. A* **2013**, *117*, 6458–6473. DOI: 10.1021/jp405262r.

(380) Huang, H.; Merthe, D. J.; Zádor, J.; Jusinski, L. E.; Taatjes, C. A. New Experiments and Validated Master-Equation Modeling for OH Production in Propyl+O2 Reactions. *Proc. Combust. Inst.* **2011**, *33*, 293–299. DOI: 10.1016/j.proci.2010.06.039.

(381) Kerr, J. A.; Lloyd, A. C. Kinetics and Pressure Dependence of the Decomposition of the Propionyl Radical. *Trans. Faraday Soc.* **1967**, *63*, 2480–2488. DOI: 10.1039/tf9676302480.

(382) Wagner, A. F.; Slagle, I. R.; Sarzynski, D.; Gutman, D. Experimental and Theoretical Studies of the Ethyl + Oxygen Reaction Kinetics. *J. Phys. Chem.* **1990**, *94*, 1853–1868. DOI: 10.1021/j100368a026.

(383) Baker, R. R.; Baldwin, R. R.; Walker, R. W. The Use of the H2+O2 Reaction in Determining the Velocity Constants of Elementary Reaction in Hydrocarbon Oxidation. *Symp. Combust.* **1971**, *13*, 291–299. DOI: 10.1016/S0082-

0784(71)80032-2.

(384) Singleton, D. L.; Irwin, R. S.; Cvetanović, R. J. Arrhenius Parameters for the Reactions of O(3 P) Atoms with Several Aldehydes and the Trend in Aldehydic C—H Bond Dissociation Energies. *Can. J. Chem.* **1977**, *55*, 3321–3327. DOI: 10.1139/v77-463.

(385) Dixon, D. J.; Skirrow, G.; Tipper, C. F. H. Low Temperature Gas-Phase Oxidation of Aldehydes. Part 1.—The Reaction below 120°C. *J. Chem. Soc. Faraday Trans. 1 Phys. Chem. Condens. Phases* **1974**, *70*, 1078–1089. DOI: 10.1039/f19747001078.

(386) Zügner, G. L.; Szilágyi, I.; Zádor, J.; Szabó, E.; Dóbé, S.; Song, X.; Wang, B. OH Yields for C2H5CO+O2 at Low Pressure: Experiment and Theory. *Chem. Phys. Lett.* **2010**, *495*, 179–181. DOI: 10.1016/j.cplett.2010.06.089.

(387) Baldwin, R. R.; Lewis, K. A.; Walker, R. W. Carbon Dioxide Formation in Oxidation of Propionaldehyde. *Combust. Flame* **1979**, *34*, 275–283. DOI: 10.1016/0010-2180(79)90102-0.

(388) Peter, A.; Acs, G.; Horvath, I.; Huhn, P. Decomposition of Propionaldehyde Initiated by the Thermal Decomposition of Azoethane. *Acta Chim. Hung.* **1981**, *108*.

(389) Ganguli, B.; Biondi, M. A.; Johnsen, R.; Dulaney, J. L. Electron-Temperature Dependence of the Recombination of HCO^+ Ions with Electrons. *Phys. Rev. A* **1988**, *37*, 2543–2547. DOI: 10.1103/PhysRevA.37.2543.

(390) Geppert, W. D.; Thomas, R.; Ehlerding, A.; Semaniak, J.; Österdahl, F.; Ugglas, M. A.; Djurić, N.; Paál, A.; Larsson, M. Extraordinary Branching Ratios in Astrophysically Important Dissociative Recombination Reactions. *Faraday Discuss.* **2004**, *127*, 425–437. DOI: 10.1039/b314005a.

(391) Russell D. Johnson III. *NIST Computational Chemistry Comparison and Benchmark Database NIST Standard Reference Database Number 101 Release 22*. **2022**. DOI: 10.18434/T47C7Z.

(392) Capitelli, M.; Ferreira, C. M.; Gordiets, B. F.; Osipov, A. I. *Plasma Kinetics in Atmospheric Gases*; Springer Series on Atomic, Optical, and Plasma Physics; Springer Berlin Heidelberg: Berlin, Heidelberg, 2000; Vol. 31. DOI: 10.1007/978-3-662-04158-1.

(393) Wagner, H. G.; Zabel, F. Neuere Untersuchungen Zum Thermischen Zerfall von CO2. Teil II. *Berichte der Bunsengesellschaft für Phys. Chemie* **1974**, *78*, 705–712. DOI: 10.1002/bbpc.19740780717.

(394) Rabinowitz, M. J.; Sutherland, J. W.; Patterson, P. M.; Klemm, R. B. Direct Rate Constant Measurements for H + CH_4 → CH_3 + H_2, 897-1729 K, Using the Flash Photolysis-Shock Tube Technique. *J. Phys. Chem.* **1991**, *95*, 674–681. DOI: 10.1021/j100155a033.

(395) Lu, K.-W.; Matsui, H.; Huang, C.-L.; Raghunath, P.; Wang, N.-S.; Lin, M. C. Shock Tube Study on the Thermal Decomposition of CH_3OH. *J. Phys. Chem. A* **2010**, *114*, 5493–5502. DOI: 10.1021/jp100535r.

(396) Tabayashi, K.; Bauer, S. H. The Early Stages of Pyrolysis and Oxidation of Methane. *Combust. Flame* **1979**, *34*, 63–83. DOI: 10.1016/0010-2180(79)90079-8.

(397) Böhland, T.; Dõbẽ, S.; Temps, F.; Wagner, H. G. Kinetics of the Reactions between $CH_2(\tilde{X}^3B_1)$-Radicals and Saturated Hydrocarbons in the Temperature Range 296 K ≤ T ≤ 707 K. *Berichte der Bunsengesellschaft für Phys. Chemie* **1985**, *89*, 1110–1116. DOI: 10.1002/bbpc.19850891018.

(398) Han, P.; Su, K.; Liu, Y.; Wang, Y.; Wang, X.; Zeng, Q.; Cheng, L.; Zhang, L. Reaction

Rate of Propene Pyrolysis. *J. Comput. Chem.* **2011**, *32*, 2745–2755. DOI: 10.1002/jcc.21854.

(399) Ge, Y.; Gordon, M. S.; Battaglia, F.; Fox, R. O. Theoretical Study of the Pyrolysis of Methyltrichlorosilane in the Gas Phase. 3. Reaction Rate Constant Calculations. *J. Phys. Chem. A* **2010**, *114*, 2384–2392. DOI: 10.1021/jp911673h.

(400) Lissianski, V.; Yang, H.; Qin, Z.; Mueller, M. R.; Shin, K. S.; Gardiner, W. C. High-Temperature Measurements of the Rate Coefficient of the H + CO_2 → CO + OH Reaction. *Chem. Phys. Lett.* **1995**, *240*, 57–62. DOI: 10.1016/0009-2614(95)00496-Q.

(401) Srinivasan, N. K.; Su, M.-C.; Sutherland, J. W.; Michael, J. V. Reflected Shock Tube Studies of High-Temperature Rate Constants for OH + CH_4 → CH_3 + H_2O and CH_3 + NO_2 → CH_3O + NO. *J. Phys. Chem. A* **2005**, *109*, 1857–1863. DOI: 10.1021/jp040679j.

(402) Cohen, N.; Westberg, K. R. Chemical Kinetic Data Sheets for High-Temperature Reactions. Part II. *J. Phys. Chem. Ref. Data* **1991**, *20*, 1211–1311. DOI: 10.1063/1.555901.

(403) Cohen, N.; Westberg, K. R. Chemical Kinetic Data Sheets for High-Temperature Chemical Reactions. *J. Phys. Chem. Ref. Data* **1983**, *12*, 531–590. DOI: 10.1063/1.555692.

(404) Brudnik, K.; Gola, A. A.; Jodkowski, J. T. Theoretical Kinetic Study of the Formation Reactions of Methanol and Methyl Hypohalites in the Gas Phase. *J. Mol. Model.* **2009**, *15*, 1061–1066. DOI: 10.1007/s00894-009-0461-x.

(405) Jodkowski, J. T.; Rayez, M.-T.; Rayez, J.-C.; Bérces, T.; Dóbé, S. Theoretical Study of the Kinetics of the Hydrogen Abstraction from Methanol. 3. Reaction of

Methanol with Hydrogen Atom, Methyl, and Hydroxyl Radicals. *J. Phys. Chem. A* **1999**, *103*, 3750–3765. DOI: 10.1021/jp984367q.

(406) Lendvay, G.; Bérces, T.; Márta, F. An Ab Initio Study of the Three-Channel Reaction between Methanol and Hydrogen Atoms: BAC-MP4 and Gaussian-2 Calculations. *J. Phys. Chem. A* **1997**, *101*, 1588–1594. DOI: 10.1021/jp963188a.

(407) Ohmori, K.; Miyoshi, A.; Matsui, H.; Washida, N. Studies on the Reaction of Acetaldehyde and Acetyl Radicals with Atomic Hydrogen. *J. Phys. Chem.* **1990**, *94*, 3253–3255. DOI: 10.1021/j100371a006.

(408) Aders, W. K.; Wagner, H. G. Untersuchungen Zur Reaktion von Wasserstoffatomen Mit Acetaldehyd. *Berichte der Bunsen-Gesellschaft* **1973**, *77*, 332–335. DOI: 10.1002/bbpc.19730770509.

(409) Dodd, R. E. Rate Constants in the High Temperature Photolysis of Acetaldehyde. *Trans. Faraday Soc.* **1951**, *47*, 56–62. DOI: 10.1039/tf9514700056.

(410) Höhlein, G.; Freeman, G. R. Radiation-Sensitized Pyrolysis of Diethyl Ether. Free-Radical Reaction Rate Parameters. *J. Am. Chem. Soc.* **1970**, *92*, 6118–6125. DOI: 10.1021/ja00724a004.

(411) Zhang, X.; Ye, L.; Li, Y.; Zhang, Y.; Cao, C.; Yang, J.; Zhou, Z.; Huang, Z.; Qi, F. Acetaldehyde Oxidation at Low and Intermediate Temperatures: An Experimental and Kinetic Modeling Investigation. *Combust. Flame* **2018**, *191*, 431–441. DOI: 10.1016/j.combustflame.2018.01.027.

(412) Held, T. J.; Dryer, F. L. A Comprehensive Mechanism for Methanol Oxidation. *Int. J. Chem. Kinet.* **1998**, *30*, 805–830. DOI: 10.1002/(SICI)1097-4601(1998)30:11<805::AID-KIN4>3.0.CO;2-Z.

(413) Dombrowsky, C.; Hoffmann, A.; Klatt, M.; Gg. Wagner, H. An Investigation of the

Methanol Decomposition Behind Incident Shock Waves. *Berichte der Bunsengesellschaft für Phys. Chemie* **1991**, *95*, 1685–1687. DOI: 10.1002/bbpc.19910951217.

(414) Ing, W.-C.; Sheng, C. Y.; Bozzelli, J. W. Development of a Detailed High-Pressure Reaction Model for Methane/Methanol Mixtures under Pyrolytic and Oxidative Conditions and Comparison with Experimental Data. *Fuel Process. Technol.* **2003**, *83*, 111–145. DOI: 10.1016/S0378-3820(03)00062-6.

(415) Marinov, N. M. A Detailed Chemical Kinetic Model for High Temperature Ethanol Oxidation. *Int. J. Chem. Kinet.* **1999**, *31*, 183–220. DOI: 10.1002/(SICI)1097-4601(1999)31:3<183::AID-KIN3>3.0.CO;2-X.

(416) *Obtained from LXCAT (Biagi database)*. www.lxcat.net.

(417) *Obtained from LXCAT (Itikawa database)*. www.lxcat.net.

(418) Verheyen, C.; Silva, T.; Guerra, V.; Bogaerts, A. The Effect of H_2O on the Vibrational Populations of CO_2 in a CO_2 /H_2O Microwave Plasma: A Kinetic Modelling Investigation. *Plasma Sources Sci. Technol.* **2020**, *29*, 095009. DOI: 10.1088/1361-6595/aba1c8.

(419) Itikawa, Y.; Mason, N. Cross Sections for Electron Collisions with Water Molecules. *J. Phys. Chem. Ref. Data* **2005**, *34*, 1–22. DOI: 10.1063/1.1799251.

(420) *Obtained from LXCAT (TRINITI database)*. www.lxcat.net (accessed 2023-01-04).

(421) De Meyer, R.; Gorbanev, Y.; Ciocarlan, R.-G.; Cool, P.; Bals, S.; Bogaerts, A. Importance of Plasma Discharge Characteristics in Plasma Catalysis: Dry Reforming of Methane vs. Ammonia Synthesis. *Chem. Eng. J.* **2024**, *488*, 150838. DOI: 10.1016/j.cej.2024.150838.

(422) Kossyi, I. A.; Kostinsky, A. Y.; Matveyev, A. A.; Silakov, V. P. Kinetic Scheme of the Non-Equilibrium Discharge in Nitrogen-Oxygen Mixtures. *Plasma Sources Sci. Technol.* **1992**, *1*, 207–220. DOI: 10.1088/0963-0252/1/3/011.

(423) Park, C. A Review of Reaction Rates in High Temperature Air. In *24th Thermophysics Conference*; American Institute of Aeronautics and Astronautics: Reston, Virigina, 1989. DOI: 10.2514/6.1989-1740.

(424) Belostotsky, S. G.; Economou, D. J.; Lopaev, D. V.; Rakhimova, T. V. Negative Ion Destruction by $O(^3P)$ Atoms and $O_2(a\ ^1\Delta_g)$ Molecules in an Oxygen Plasma. *Plasma Sources Sci. Technol.* **2005**, *14*, 532–542. DOI: 10.1088/0963-0252/14/3/016.

(425) Atkinson, R.; Baulch, D. L.; Cox, R. A.; Crowley, J. N.; Hampson, R. F.; Hynes, R. G.; Jenkin, M. E.; Rossi, M. J.; Troe, J. Evaluated Kinetic and Photochemical Data for Atmospheric Chemistry: Volume I - Gas Phase Reactions of Ox, HOx, NOx and SOx Species. *Atmos. Chem. Phys.* **2004**, *4*, 1461–1738. DOI: 10.5194/acp-4-1461-2004.

(426) Lifshitz, C.; Wu, R. L. C.; Haartz, J. C.; Tiernan, T. O. Associative Detachment Reactions of Negative Ions with O_3. *J. Chem. Phys.* **1977**, *67*, 2381–2382. DOI: 10.1063/1.435078.

(427) Stafford, D. S.; Kushner, M. J. $O_2(^1\Delta)$ Production in He/O_2 Mixtures in Flowing Low Pressure Plasmas. *J. Appl. Phys.* **2004**, *96*, 2451–2465. DOI: 10.1063/1.1768615.

(428) Gudmundsson, J. T.; Thorsteinsson, E. G. Oxygen Discharges Diluted with Argon: Dissociation Processes. *Plasma Sources Sci. Technol.* **2007**, *16*, 399–412. DOI: 10.1088/0963-0252/16/2/025.

(429) Thomas G. Beuthe, T. G. B.; Jen-Shih Chang, J.-S. C. Chemical Kinetic Modelling of Non-Equilibrium Ar-CO_2 Thermal Plasmas. *Jpn. J. Appl. Phys.* **1997**, *36*, 4997–5002. DOI: 10.1143/JJAP.36.4997.

(430) Park, C.; Howe, J. T.; Jaffe, R. L.; Candler, G. V. Review of Chemical-Kinetic Problems of Future NASA Missions, II: Mars Entries. *J. Thermophys. Heat Transf.* **1994**, *8*, 9–23. DOI: 10.2514/3.496.

(431) Dean, A. J.; Davidson, D. F.; Hanson, R. K. A Shock Tube Study of Reactions of C Atoms with H_2 and O_2 Using Excimer Photolysis of C_3O_2 and C Atom Atomic Resonance Absorption Spectroscopy. *J. Phys. Chem.* **1991**, *95*, 183–191. DOI: 10.1021/j100154a037.

(432) Petuchowski, S. J.; Dwek, E.; Allen, J. E., J.; Nuth, J. A., I. CO Formation in the Metal-Rich Ejecta of SN 1987A. *Astrophys. J.* **1989**, *342*, 406. DOI: 10.1086/167601.

(433) Prasad, S. S.; Huntress, W. T., J. A Model for Gas Phase Chemistry in Interstellar Clouds. I - The Basic Model, Library of Chemical Reactions, and Chemistry among C, N, and O Compounds. *Astrophys. J. Suppl. Ser.* **1980**, *43*, 1–35. DOI: 10.1086/190665.

(434) Albritton, D. L. Ion-Neutral Reaction-Rate Constants Measured in Flow Reactors through 1977. *At. Data Nucl. Data Tables* **1978**, *22*, 1–89. DOI: 10.1016/0092-640X(78)90027-X.

(435) Arin, L. M.; Warneck, P. Reaction of Ozone with Carbon Monoxide. *J. Phys. Chem.* **1972**, *76*, 1514–1516. DOI: 10.1021/j100655a002.

(436) McFarland, M.; Albritton, D. L.; Fehsenfeld, F. C.; Ferguson, E. E.; Schmeltekopf, A. L. Flow-Drift Technique for Ion Mobility and Ion-Molecule Reaction Rate Constant Measurements. III. Negative Ion Reactions of O^- with CO, NO, H_2, and D_2. *J. Chem. Phys.* **1973**, *59*, 6629–6635. DOI: 10.1063/1.1680043.

(437) Fehsenfeld, F. C.; Ferguson, E. E. Thermal Energy Reaction Rate Constants for H+

and CO+ with O and NO. *J. Chem. Phys.* **1972**, *56*, 3066–3070. DOI: 10.1063/1.1677642.

(438) Adams, N. G.; Smith, D.; Grief, D. Reactions of H_nCO^+ Ions with Molecules at 300 K. *Int. J. Mass Spectrom. Ion Phys.* **1978**, *26*, 405–415. DOI: 10.1016/0020-7381(78)80059-X.

(439) Husain, D.; Young, A. N. Kinetic Investigation of Ground State Carbon Atoms, $C(2^3P_J)$. *J. Chem. Soc. Faraday Trans. 2* **1975**, *71*, 525. DOI: 10.1039/f29757100525.

(440) Fahey, D. W.; Fehsenfeld, F. C.; Ferguson, E. E. Rate Constant for the Reaction $C^+ + CO_2$ at Collision Energies 0.04 to 2.5eV. *Geophys. Res. Lett.* **1981**, *8*, 1115–1117. DOI: 10.1029/GL008i010p01115.

(441) Burmeister, M.; Roth, P. ARAS Measurements on the Thermal Decomposition of CO_2 behind Shock Waves. *AIAA J.* **1990**, *28*, 402–405. DOI: 10.2514/3.10406.

(442) Cenian, A.; Chernukho, A.; Borodin, V.; Śliwiński, G. Modeling of Plasma-Chemical Reactions in Gas Mixture of CO_2 Lasers I. Gas Decomposition in Pure CO_2 Glow Discharge. *Contrib. to Plasma Phys.* **1994**, *34*, 25–37. DOI: 10.1002/ctpp.2150340105.

(443) Abreu, V. J.; Yee, J. H.; Solomon, S. C.; Dalgarno, A. The Quenching Rate of $O(^1D)$ by $O(^3P)$. *Planet. Space Sci.* **1986**, *34*, 1143–1145. DOI: 10.1016/0032-0633(86)90026-7.

(444) Tully, J. C. Reactions of $O(^1D)$ with Atmospheric Molecules. *J. Chem. Phys.* **1975**, *62*, 1893–1898. DOI: 10.1063/1.430675.

(445) Dunlea, E. J.; Ravishankara, A. R. Kinetic Studies of the Reactions of $O(^1D)$ with Several Atmospheric Molecules. *Phys. Chem. Chem. Phys.* **2004**, *6*, 2152–2161.

DOI: 10.1039/b400247d.

(446) Beverly, R. E. Ion Aging Effects on the Dissociative-Attachment Instability in CO_2 Lasers. *Opt. Quantum Electron.* **1982**, *14*, 501–513. DOI: 10.1007/BF00610306.

(447) Shields, H.; Smith, A. L. S.; Norris, B. Negative Ion Effects in TEA CO_2 Lasers. *J. Phys. D: Appl. Phys.* **1976**, *9*, 1587–1603. DOI: 10.1088/0022-3727/9/11/007.

List of Publications

As first author

- **Loenders, B.**; Engelmann, Y.; Bogaerts, A. Plasma-Catalytic Partial Oxidation of Methane on Pt(111): A Microkinetic Study on the Role of Different Plasma Species. J. Phys. Chem. C 2021, 125, 2966–2983. DOI: 10.1021/acs.jpcc.0c09849

- Biswas, A. N.;‡ Winter, L. R.;‡ **Loenders, B.**;‡ Xie, Z.; Bogaerts, A.; Chen, J. G. Oxygenate Production from Plasma-Activated Reaction of CO_2 and Ethane. ACS Energy Lett. 2022, 7, 236–241. DOI: 10.1021/acsenergylett.1c02355

- **Loenders, B.**; Michiels, R.; Bogaerts, A. Is a Catalyst Always Beneficial in Plasma Catalysis? Insights from the Many Physical and Chemical Interactions. J. Energy Chem. 2023, 85, 501–533. DOI: 10.1016/j.jechem.2023.06.016

- **Loenders, B.**; Michiels, R.; Bogaerts, A. How Plasma Reaction Conditions Affect the Optimal Catalyst: A Microkinetic Study of Plasma-Catalytic CO_2 Splitting. Plasma Chem. Plasma Process. 2025, 45, 1849–1899. DOI: 10.1007/s11090-025-10599-4

‡) These authors contributed equally.

As co-author

- Biondo, O.; Hughes, A.; van de Steeg, A.; Maerivoet, S.; **Loenders, B.**; van Rooij, G.; Bogaerts, A. Power Concentration Determined by Thermodynamic Properties in Complex Gas Mixtures: The Case of Plasma-Based Dry Reforming of Methane. Plasma Sources Sci. Technol. 2023, 32, 045001. DOI: 10.1088/1361-6595/acc6ec

- Li, S.; Sun, J.; Gorbanev, Y.; van't Veer, K.; **Loenders, B.**; Yi, Y.; Kenis, T.; Chen, Q.; Bogaerts, A. Plasma-Assisted Dry Reforming of CH_4 : How Small Amounts of O_2 Addition Can Drastically Enhance the Oxygenate Production–Experiments and Insights from Plasma Chemical Kinetics Modeling. ACS Sustain. Chem. Eng. 2023, 11, 15373–15384. DOI: 10.1021/acssuschemeng.3c04352

- Slaets, J.; **Loenders, B.**; Bogaerts, A. Plasma-Based Dry Reforming of CH_4: Plasma Effects vs. Thermal Conversion. Fuel 2024, 360, 130650. DOI: 10.1016/j.fuel.2023.130650

- Ceulemans, S.; Morais, E.; **Loenders, B.**; Bogaerts, A. Microkinetic Modelling of Post-Plasma Catalysis to Improve the Conversion of Dry Reforming of Methane in a Gliding Arc Plasmatron. J. Catal. 2026, 453, 116474. DOI: 10.1016/j.jcat.2025.116474

Presentations

Conference contributions

- Oral presentation: "Modelling of plasma-catalytic dry reforming of CH_4: How do radicals affect the behaviour of different transition metal catalysts?" at the 5th International Symposium on Plasmas for Catalysis and Energy Materials (ISPCEM) in Liverpool, United Kingdom (July, 2022).
    - **Recipient of the Best Oral Presentation Award**

- Oral presentation: "Effect of radicals on trends between transition metal catalysts in plasma catalysis: A microkinetic modeling study" at the International Symposium Plasma Catalysis for CO_2 Recycling in Krakau, Poland (September, 2022).

Project meetings

- PlasMaCatDesign Partner meeting on 29/04/2020
- PlasMaCatDesign Partner meeting on 01/10/2020
- PlasMaCatDesign Advisory Board meeting on 26/11/2020
- Research presentation: “Surface kinetics modeling of plasma-catalytic CH_4 partial oxidation” at ERC SCOPE meeting on 18/02/2021
- PlasMaCatDesign Partner meeting on 18/10/2021
- PlasMaCatDesign Advisory Board meeting on 08/11/2021
- PlasMaCatDesign Partner meeting on 31/03/2022
- PlasMaCatDesign Advisory Board meeting on 21/11/2022
- PlasMaCatDesign Partner meeting on 12/04/2023

Other Achievements

Teaching

- “Microkinetic modeling” as part of the Plasma modeling master’s course (2020)
- “Microkinetic modeling” as part of the Plasma modeling master’s course (2022)